

nature

PREDICTING THE PAST

Artificial intelligence restores, locates and dates ancient Greek texts

Early intervention
Can treatment before symptoms show keep Alzheimer's at bay?

National parks
Biodiversity lessons from Argentina'srewilding project

Complex manoeuvre
Electron-catalysed self-assembly of molecules

Vol. 593 No. 7890

Nature.2022.03.12

[Sat, 12 Mar 2022]

- [This Week](#)
- [News in Focus](#)
- [Books & Arts](#)
- [Opinion](#)
- [Work](#)
- [Research](#)
- [Amendments & Corrections](#)

This Week

- **[Russia's brutal attack on Ukraine is wrong and must stop](#)**

[04 March 2022]

Editorial • Nature stands in solidarity with the Ukrainian research community — and continues to support the global exchange of scholarly knowledge.

- **[Landmark treaty on plastic pollution must put scientific evidence front and centre](#)** [08 March 2022]

Editorial • United Nations resolution on greening plastics is a positive step. As negotiations begin, they must be evidence-based.

- **[Taiwan's pandemic vice-president — from lab bench to public office and back](#)** [08 March 2022]

World View • Successful policy and preparedness require more diverse evidence than researchers often encounter.

- **[Wispy clouds are born of dust in the wind](#)** [08 March 2022]

Research Highlight • Dust from deserts and plains drives the formation of cirrus clouds, particularly in the Northern Hemisphere.

- **[Soft gels assemble into hard plastic — and it's recyclable](#)**

[02 March 2022]

Research Highlight • Sturdy 3D-printed objects can be broken down into materials that can be used to print new objects.

- **[Even six-legged diners can't resist sweet-and-salty snacks](#)**

[02 March 2022]

Research Highlight • Bees and butterflies prefer sodium-spiked nectar to plain, according to experiments conducted in a flowery meadow.

- **[Huge comet is biggest of its kind](#)** [01 March 2022]

Research Highlight • Gargantuan object is roughly 140 kilometres across — making it by far the largest comet from the farthest reaches of the Solar System.

- **[How itchy vicuñas remake a vast wilderness](#)** [04 March 2022]

Research Highlight • An outbreak of mange among a population of the llama-like beasts kicked off a cascade of ecological effects in the high Andes.

- **Massive trial shows COVID rapid tests excel at detecting silent cases** [04 March 2022]

Research Highlight • In a trial in 73 workplaces, the tests detected hundreds of people with asymptomatic COVID-19 and generated very few false positives.

- **Short on sleep? Taking a trip could actually help** [01 March 2022]

Research Highlight • Travel is a sleep-balancing activity: the tired catch up, and the well-rested become less so.

- EDITORIAL
- 04 March 2022

Russia's brutal attack on Ukraine is wrong and must stop

Nature stands in solidarity with the Ukrainian research community — and continues to support the global exchange of scholarly knowledge.



Attacks on civilian infrastructure, such as the V. N. Karazin Kharkiv National University, will need to be assessed by the International Criminal Court as part of an investigation into war crimes. Credit: Sergey Bobok/AFP/Getty

In little over a week, many thousands of people have been killed as a result of Russia's brutal invasion of Ukraine, a sovereign nation. The United Nations has condemned what is happening as a violation of the UN Charter. The International Criminal Court is investigating potential war crimes and crimes against humanity, because innocent people and civilian infrastructure — including universities and cultural centres — are being targeted.

Along with [the world's scientific community](#), *Nature* condemns this horrific invasion in the strongest terms — and calls on Russia to immediately end its attack. We support and stand in solidarity with Ukraine's people, including its research community.

As this editorial was published, one million people, mostly children and women, had been forced to abandon their homes and flee to neighbouring countries. These numbers will multiply in the coming days and weeks. Ukrainian researchers are among those enduring unconscionable violence and suffering. Many have [bravely taken up arms to defend their country](#). Others are remaining in cities that are being bombed, to care for their families. “We are not thinking of research,” Illya Khadzhynov, vice-rector for scientific work at Vasyl’ Stus Donetsk National University, told *Nature*.

The global research community has mobilized rapidly to offer practical support. #ScienceForUkraine, [Ukrainian scientists working abroad](#), the [Global Young Academy](#) (GYA) and [Cara](#) (the Council for At-Risk Academics, in the United Kingdom) are among those collating offers of help from the world’s universities to place Ukrainian scientists in universities outside the country.

Members of Russia’s scientific community [are also condemning the invasion](#), potentially putting their own safety at risk. At the same time, numerous national and international scientific organizations have written open letters and statements urging an immediate ceasefire and support for Ukraine.

Russia’s government is rightly facing severe financial, economic and trade sanctions, and these are extending to research and higher education. Denmark and Germany have told universities to suspend cooperation with

institutions in Russia, and the European Union is halting payments to Russian partners taking part in EU-funded projects.

Some scientists are calling for a comprehensive and worldwide boycott of all Russian research, and for scientific journals to refuse to consider papers by researchers from Russia. Given the horror of what is happening in Ukraine, such calls are understandable. But *Nature*, in common with many other journals, will continue to consider manuscripts from researchers anywhere in the world. That is because we think at this time that such a boycott would do more harm than good. It would divide the global research community and restrict the exchange of scholarly knowledge — both of which have the potential to damage the health and well-being of humanity and the planet. The world must keep generating the knowledge needed to deal with this and other crises. The ability to communicate research and scholarship freely across national borders has been foundational to science and international relations — and has endured during some of the world's worst historical conflicts.

The GYA is also rightly calling for the research community to uphold scientific collaborations with Russian scholars amid the invasion and is urging researchers to “not let war divide us”. And, in its statement about the invasion, the InterAcademy Partnership, a network of the world's science academies, emphasizes the need for science to “leave no one behind”.

The whole scientific community — including *Nature* — must and will stand united in opposition to Russia's aggression.

Nature **603**, 201 (2022)

doi: <https://doi.org/10.1038/d41586-022-00647-w>

This article was downloaded by **calibre** from <https://www.nature.com/articles/d41586-022-00647-w>

- EDITORIAL
- 08 March 2022

Landmark treaty on plastic pollution must put scientific evidence front and centre

United Nations resolution on greening plastics is a positive step. As negotiations begin, they must be evidence-based.



Leila Benali (left), Morocco's minister for energy and sustainability, and UN Environment Programme chief Inger Andersen celebrate the decision to begin talks on a plastics treaty. Credit: Tony Karumba/AFP/Getty

On 2 March, world leaders and environment ministers agreed to start negotiations on the world's first legally binding international treaty to eliminate one of humanity's most devastating sources of pollution: plastics. This hugely positive step has the power to attack the problem as never

before. But to achieve this goal, science needs to be front and centre in the negotiations.

Plastic pollution is a massive problem. Some 400 million tonnes of the material is produced each year, a figure that could double by 2040. Of all the plastic that has ever been produced, only about 9% has been recycled and 12% incinerated. Almost all other waste plastic has ended up in the ocean or in huge landfill sites. More than 90% of plastics are made from fossil fuels. If left unchecked, plastics production and disposal will be responsible for 15% of permitted carbon emissions by 2050 if the world is to limit global warming to 1.5 °C above pre-industrial temperatures.

Talks on the treaty are expected to take between two and three years and will be organized by the United Nations Environment Programme, based in Nairobi. A significant feature of the treaty is that it will be legally binding, like the 2015 Paris climate agreement and the Montreal Protocol, a 1987 treaty that led to the production and use of ozone-depleting substances being phased out.

A team of negotiators from different regions is being established. By the end of May, they will start work on the treaty's text. According to last week's UN decision, these negotiators will consider "the possibility of a mechanism to provide policy relevant scientific and socio-economic information and assessment related to plastic pollution". But they need to do more than just consider a mechanism. The UN must urgently set up a scientists' group that can give the negotiators expert advice and respond to their questions. These science advisers would need to reflect the necessary expertise in the natural and social sciences, as well as in engineering, and represent different regions of the world.

Nations want the plastics treaty to be more ambitious than most existing environmental agreements. Unlike the Montreal Protocol, which replaced around 100 ozone-depleting substances with ozone-friendly alternatives, countries have agreed that a plastics treaty must lock sustainability into the 'full life-cycle' of polluting materials. This means plastics manufacturing must become a zero-carbon process, as must plastics recycling and waste disposal. These are not straightforward ambitions, which is why research — and access to research — is so important as negotiations get under way.

Most plastics are designed in a ‘linear’ one-way process: small, carbon-based molecules are knitted together with chemical bonds to make long and cross-linked polymer molecules. These bonds are hard to break, which makes plastics extremely long-lasting. They [do not degrade easily and are difficult to recycle](#).

Marine litter often grabs the headlines, but plastic pollution is everywhere. Landfill sites containing mountains of plastic blight our planet, and minuscule particles of plastic are found in even the most pristine environments. Such is the scale and persistence of plastics that they are now entering the fossil record. And a new human-made ecosystem — the plastisphere — has emerged that hosts microorganisms and algae¹.

As negotiators get to work, they will need scientists to help them address several key questions. Which types of plastic can be recycled^{2,3}? Which plastics can be designed to biodegrade, and under what conditions? And which plastics offer the best chances for reuse⁴? Moreover, [social-sciences research will be essential](#) to understanding the implications of — and inter-relationships between — the solutions that countries and industries will have to choose from. For example, new technologies and processes will have impacts on jobs. These impacts need to be studied so that risks to people’s livelihoods can be mitigated.

Mapping out the implications of various approaches to greening the plastics industry will also require cooperation between governments, industry and campaign organizations — building on the cooperation that has brought the world to the start of negotiations.

Plastics have made the modern world. They are a staple of daily life, from construction to clothing, technology to transport. But plastics use is also increasing at a rapid rate, and this is no longer tenable — around half of all plastics ever produced have been made since 2004.

It is clear from the UN’s ongoing efforts to tackle climate change that it is not enough for a treaty to be legally binding. Signatories must also be held accountable, with regular reporting and checks on progress. Equally important is the need for science advice to be embedded in the talks from the earliest possible stage.

Last week's decision is the best start the planet could have had to tackling our plastics addiction. But as the hard work begins, decision-makers must be able to quickly and easily access the very best available evidence that research can provide.

Nature **603**, 202 (2022)

doi: <https://doi.org/10.1038/d41586-022-00648-9>

References

1. Amaral-Zettler, L. A., Zettler, E. R. & Mincer, T. J. *Nature Rev. Microbiol.* **18**, 139–151 (2020).
2. Hopewell, J., Dvorak, R. & Edward, K. *Phil. Trans. R. Soc. B* **364**, 2115–2126 (2009).
3. Coates, G. W. & Getzler, Y. D. Y. L. *Nature Rev. Mater.* **5**, 501–516 (2020).
4. Grigore, M. E. *Recycling* **2**, 24 (2017).

This article was downloaded by **calibre** from <https://www.nature.com/articles/d41586-022-00648-9>

| [Section menu](#) | [Main menu](#) |

- WORLD VIEW
- 08 March 2022

Taiwan's pandemic vice-president — from lab bench to public office and back



Successful policy and preparedness require more diverse evidence than researchers often encounter.

- [Chen Chien-jen](#) 0

My CV is a strange one for an epidemiologist. Twenty years ago, I was at the National Taiwan University, training field researchers and studying liver disease, a major cause of death. When the severe acute respiratory syndrome (SARS) epidemic broke out in 2003, I became the minister of health and led reforms that allowed Taiwan to successfully contain epidemics of H5N1 avian influenza in 2005–08, H1N1 flu in 2009–10 and COVID-19. After a brief stint back in academia, I became the minister of

the National Science Council, promoting science and technology for the development of a knowledge-based economy. I was tapped to run for vice-president in 2015 and was elected to that position the following year.

Taiwan has a lower COVID-19 case rate than the 38 members of the Organisation for Economic Co-operation and Development, and has a lower mortality rate than all members but New Zealand. It also had positive economic growth in the first phase of containment, before vaccines were available. As of May 2020, I am back in academia, trying to fill knowledge gaps to make public-health interventions, such as cancer prevention and early detection, more effective.

Two years on from the World Health Organization's official declaration of the pandemic, I've been thinking about lessons I've learnt toggling between science and public service. I think all researchers — from bench scientists to physicists to computational social scientists — might find this exercise useful. Government advisers, too.

The first lesson: scientific training teaches us to seek out all the variables that might affect a system. My work as a minister taught me to expand that list of variables far beyond what is typical. Budgets, laws, staffing levels and more enter the picture. So do values and priorities.

Consider: as health minister, I set up how and when to pay for antiviral therapy for people with chronic viral hepatitis. As a researcher, disease severity and treatment efficacy were top of mind. As a minister, I had to take more into account: accessibility, equity (especially reaching marginalized groups), feasibility and financial resources. People in rural and mountainous regions could not afford to travel to medical centres, so we set up outreach units. I argued that fixed, separate budgets for distinct categories of disease hindered smart decisions: antiviral therapy is expensive, but liver transplants and cancer treatments are more so. I also adapted governing structures to decision-making needs. To build in sustained focus for other tricky, crucial issues, for example, I created units to focus on international cooperation and long-term care.

The second lesson: science is never enough to bring about a thriving society. That takes trust, robust institutions and social cohesion. Solidarity

is essential to inspire the public to comply with epidemic-prevention guidelines. Without solidarity, there cannot be effective border control, quarantine, contact tracing and isolation. The government must do its part to encourage compliance, such as paying for low-income people to get to vaccination centres and sending them free face masks and hand sanitizer. We targeted economic support where it was needed most, such as restaurants, vendors, grocery stores and taxi drivers.

The third lesson: infectious and toxic agents have impacts that last for decades, so long-range investments in scientific infrastructure pay off. But action must be quick. When SARS happened so long ago, neither the public-health nor the hospital system in Taiwan was prepared. Ineffective quarantine and shut-down procedures led to infections and deaths. The ministry trained staff at major medical centres, then dispatched them to hundreds of regional hospitals, which launched training at local hospitals — establishing an island-wide protocol in just two weeks. Steps to track down sources of infection with a standard set of questions were important, as was a computerized system to find out who had travelled to hotspots. This existing infrastructure has served Taiwan well through subsequent epidemics.

Each time I return to academia, my government experience leads me to pay more attention to the earlier parts of the disease process: more prevention, swifter detection and less time to treatment. In particular, that means rapid, practical diagnostics and vaccines. And that requires consideration of the socio-economic and political components of public-health programmes. For treatments to be effective, patients must receive them, which depends on where they are offered, what patients have to pay and what makes them inconvenient and uncomfortable.

In the 1990s, as a young professor at the National Taiwan University in Taipei, I got my first inkling of these lessons. My team discovered multiple health hazards caused by arsenic in drinking water. The more arsenic ingested, the higher the rate of internal cancers and cardiovascular diseases. I worked with environmental-health scientists, civil engineers, geologists, economists and lawyers to convert our data into regulatory standards, eventually lowering the maximum permitted contamination levels of

arsenic from 50 parts per billion to 10. Initially, I expected it would all be straightforward — arsenic levels should go as low as possible. Then, I realized more-expensive water bills have health impacts as well.

That experience opened my eyes to the limitations of science and technology alone in promoting human well-being, and to the need for interdisciplinary integration and co-creation. I feel fortunate to have had so many opportunities to apply these lessons in the service of my fellow citizens.

Nature **603**, 203 (2022)

doi: <https://doi.org/10.1038/d41586-022-00649-8>

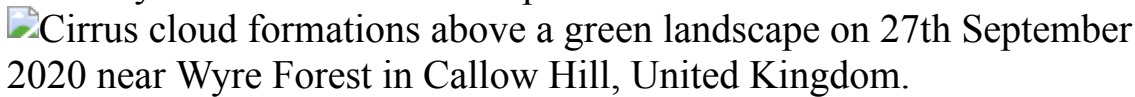
This article was downloaded by **calibre** from <https://www.nature.com/articles/d41586-022-00649-8>

| [Section menu](#) | [Main menu](#) |

- RESEARCH HIGHLIGHT
- 08 March 2022

Wispy clouds are born of dust in the wind

Dust from deserts and plains drives the formation of cirrus clouds, particularly in the Northern Hemisphere.



Many of the high-altitude clouds called cirrus clouds are spawned by dust from Earth's surface. Credit: Mike Kemp/In Pictures via Getty

Dust from windswept deserts and plains plays an outsized part in the formation of thin, wispy clouds around the globe¹.

Access options

Subscribe to Nature+

Get immediate online access to the entire Nature family of 50+ journals

\$29.99

monthly

[Subscribe](#)

Subscribe to Journal

Get full journal access for 1 year

\$199.00

only \$3.90 per issue

Subscribe

All prices are NET prices.

VAT will be added later in the checkout.

Tax calculation will be finalised during checkout.

Buy article

Get time limited or full article access on ReadCube.

\$32.00

Buy

All prices are NET prices.

Additional access options:

- [Log in](#)
- [Learn about institutional subscriptions](#)

Nature **603**, 204 (2022)

doi: <https://doi.org/10.1038/d41586-022-00587-5>

References

1. Froyd, K. D. *et al.* *Nature Geosci.* <https://doi.org/10.1038/s41561-022-00901-w> (2022).

This article was downloaded by **calibre** from <https://www.nature.com/articles/d41586-022-00587-5>

- RESEARCH HIGHLIGHT
- 02 March 2022

Soft gels assemble into hard plastic — and it's recyclable

Sturdy 3D-printed objects can be broken down into materials that can be used to print new objects.

 Microgels are printed into a blue Moai figure, left; then the microgels are regenerated and 3D printed again into a red boat.

A 3D-printed sculpture (left) depicts a statue from Rapa Nui, also known as Easter Island. The object can be degraded into its constituent microgel particles, which can be printed into a model boat (right). Credit: Alvaro Charlet *et al.*/*Small*

Researchers 3D printed a model Easter Island head using a novel ink, then degraded the figure into numerous tiny particles, created a new ink from the particles and used this to 3D print a toy boat¹.

Access options

Subscribe to Nature+

Get immediate online access to the entire Nature family of 50+ journals

\$29.99

monthly

[Subscribe](#)

Subscribe to Journal

Get full journal access for 1 year

\$199.00

only \$3.90 per issue

[Subscribe](#)

All prices are NET prices.

VAT will be added later in the checkout.

Tax calculation will be finalised during checkout.

Buy article

Get time limited or full article access on ReadCube.

\$32.00

[Buy](#)

All prices are NET prices.

Additional access options:

- [Log in](#)
- [Learn about institutional subscriptions](#)

Nature **603**, 204 (2022)

doi: <https://doi.org/10.1038/d41586-022-00590-w>

References

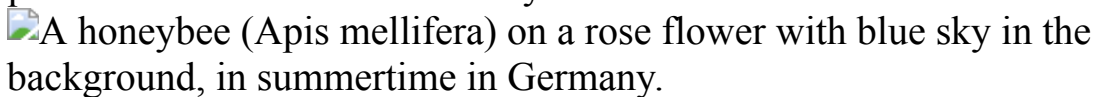
1. Charlet, A., Hirsch, M., Schreiber, S. & Amstad, E. *Small* <https://doi.org/10.1002/smll.202107128> (2022).

| [Section menu](#) | [Main menu](#) |

- RESEARCH HIGHLIGHT
- 02 March 2022

Even six-legged diners can't resist sweet-and-salty snacks

Bees and butterflies prefer sodium-spiked nectar to plain, according to experiments conducted in a flowery meadow.



Western honeybees have a taste for nectar that's salty as well as sweet.
Credit: Solvin Zankl/Nature Picture Library

Bees get a buzz out of salty nectar, researchers have found after doctoring flowers with sodium-laced sugar water¹.

Access options

Subscribe to Nature+

Get immediate online access to the entire Nature family of 50+ journals

\$29.99

monthly

[Subscribe](#)

Subscribe to Journal

Get full journal access for 1 year

\$199.00

only \$3.90 per issue

[Subscribe](#)

All prices are NET prices.

VAT will be added later in the checkout.

Tax calculation will be finalised during checkout.

Buy article

Get time limited or full article access on ReadCube.

\$32.00

[Buy](#)

All prices are NET prices.

Additional access options:

- [Log in](#)
- [Learn about institutional subscriptions](#)

Nature **603**, 204 (2022)

doi: <https://doi.org/10.1038/d41586-022-00591-9>

References

1. Finkelstein, C. J. *et al.* *Biol. Lett.* <https://doi.org/10.1098/rsbl.2022.0016> (2022).

This article was downloaded by **calibre** from <https://www.nature.com/articles/d41586-022-00591-9>

- RESEARCH HIGHLIGHT
- 01 March 2022

Huge comet is biggest of its kind

Gargantuan object is roughly 140 kilometres across — making it by far the largest comet from the farthest reaches of the Solar System.

An illustration of the distant Comet Bernardinelli-Bernstein as it might look in the outer Solar System.

Comet Bernardinelli–Bernstein (pictured, artist's illustration) is nearly twice as large as Comet Hale–Bopp, which is nicknamed 'the great comet'. Credit: NOIRLab/NSF/AURA/J. da Silva (Spaceengine)

Observations of the ‘megacomet’ Bernardinelli–Bernstein show that it is around 137 kilometres in diameter, confirming its status as the largest known classical comet¹.

Access options

Subscribe to Nature+

Get immediate online access to the entire Nature family of 50+ journals

\$29.99

monthly

[Subscribe](#)

Subscribe to Journal

Get full journal access for 1 year

\$199.00

only \$3.90 per issue

[Subscribe](#)

All prices are NET prices.

VAT will be added later in the checkout.

Tax calculation will be finalised during checkout.

Buy article

Get time limited or full article access on ReadCube.

\$32.00

[Buy](#)

All prices are NET prices.

Additional access options:

- [Log in](#)
- [Learn about institutional subscriptions](#)

Nature **603**, 204 (2022)

doi: <https://doi.org/10.1038/d41586-022-00588-4>

References

1. Lellouch, E., Moreno, R., Bockelée-Morvan, D., Biver, N. & Santos-Sanz, P. *Astron. Astrophys.* **659**, L1 (2022).

This article was downloaded by **calibre** from <https://www.nature.com/articles/d41586-022-00588-4>

- RESEARCH HIGHLIGHT
- 04 March 2022

How itchy vicuñas remade a vast wilderness

An outbreak of mange among a population of the llama-like beasts kicked off a cascade of ecological effects in the high Andes.

 Vicuna (*Vicugna vicugna*) male in defensive posture, in Laguna de los Pozuelos Natural Monument, Andes, northwestern Argentina.

A male vicuña strikes a defensive pose. The density of vicuña in a national park in Argentina dropped by 90% after mange broke out among the animals. Credit: Sebastian Kennerknecht/Nature Picture Library

When mange began to kill llama-like animals called vicuñas in the high Andes, their loss reverberated through the food web to affect grasslands and, eventually, condors¹.

Access options

Subscribe to Nature+

Get immediate online access to the entire Nature family of 50+ journals

\$29.99

monthly

[Subscribe](#)

Subscribe to Journal

Get full journal access for 1 year

\$199.00

only \$3.90 per issue

[Subscribe](#)

All prices are NET prices.

VAT will be added later in the checkout.

Tax calculation will be finalised during checkout.

Buy article

Get time limited or full article access on ReadCube.

\$32.00

[Buy](#)

All prices are NET prices.

Additional access options:

- [Log in](#)
- [Learn about institutional subscriptions](#)

Nature **603**, 205 (2022)

doi: <https://doi.org/10.1038/d41586-022-00592-8>

References

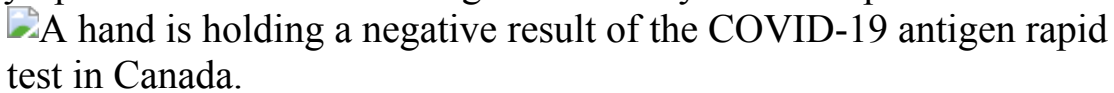
1. Monk, J. D. *et al.* *Ecol. Lett.* <https://doi.org/10.1111/ele.13983> (2022).

| [Section menu](#) | [Main menu](#) |

- RESEARCH HIGHLIGHT
- 04 March 2022

Massive trial shows COVID rapid tests excel at detecting silent cases

In a trial in 73 workplaces, the tests detected hundreds of people with asymptomatic COVID-19 and generated very few false positives.



Rapid COVID-19 testing in Canadian workplaces yielded only 75 confirmed false-positive results out of nearly 322,000 administered tests.
Credit: Artur Widak/NurPhoto via Getty

A large-scale testing campaign in Canadian workplaces shows that the regular use of rapid antigen tests is highly effective at ferreting out asymptomatic SARS-CoV-2 infections¹.

Rapid antigen tests identify proteins on the virus's surface and are faster and cheaper than more-sensitive polymerase chain reaction (PCR) tests, which can pinpoint tiny amounts of the virus by detecting its RNA. To determine the usefulness of rapid antigen tests, Laura Rosella at the University of Toronto in Canada and her colleagues studied a programme that implemented twice-a-week COVID-19 screening at Canadian companies that ranged from fewer than 100 employees to more than 10,000.

From January 2021 to June 2021, nearly 322,000 rapid tests were conducted at 73 workplaces. Testing yielded 604 positives; 473 of those were confirmed by PCR to be true positives. Only about one in 4,300 rapid-test results was confirmed by PCR as a false positive, which the authors note was not enough to disrupt workplace operations.

Of the 116 workplace-testing organizers who responded to a survey, 99% said they were either satisfied or very satisfied with the programme.

Nature **603**, 205 (2022)

doi: <https://doi.org/10.1038/d41586-022-00589-3>

References

1. Rosella, L. C. *et al.* *Sci. Adv.* **8**, eabm3608 (2022)

This article was downloaded by **calibre** from <https://www.nature.com/articles/d41586-022-00589-3>

| [Section menu](#) | [Main menu](#) |

- RESEARCH HIGHLIGHT
- 01 March 2022

Short on sleep? Taking a trip could actually help

Travel is a sleep-balancing activity: the tired catch up, and the well-rested become less so.

 Airplane passengers sleep in a designated 'Quiet Area' at Heathrow International Airport in London, England.

People who are relatively sleep-deprived at home increase the amount of time they sleep when they travel. Credit: Robert Alexander/Getty

Data from thousands of wearable monitors suggest that travelling can help people to catch up on sleep, contrary to popular belief¹.

Access options

Subscribe to Nature+

Get immediate online access to the entire Nature family of 50+ journals

\$29.99

monthly

[Subscribe](#)

Subscribe to Journal

Get full journal access for 1 year

\$199.00

only \$3.90 per issue

Subscribe

All prices are NET prices.

VAT will be added later in the checkout.

Tax calculation will be finalised during checkout.

Buy article

Get time limited or full article access on ReadCube.

\$32.00

Buy

All prices are NET prices.

Additional access options:

- [Log in](#)
- [Learn about institutional subscriptions](#)

Nature **603**, 205 (2022)

doi: <https://doi.org/10.1038/d41586-022-00586-6>

References

1. Jonasdottir, S. S., Bagrow, J. & Lehmann, S. *Nature Hum. Behav.* <https://doi.org/10.1038/s41562-022-01291-0> (2022).

This article was downloaded by **calibre** from <https://www.nature.com/articles/d41586-022-00586-6>

News in Focus

- **[Sci-Hub downloads, Mars rover delay and academic strikes in Nigeria](#)** [09 March 2022]
News Round-Up • The latest science news, in brief.
- **[Global research community condemns Russian invasion of Ukraine](#)** [01 March 2022]
News • Rebuke against Russian science grows as the deadly conflict enters its sixth day.
- **[‘I thought I had forgotten this horror’: Ukrainian scientists stand in defiance](#)** [02 March 2022]
News • Researchers tell Nature about their experiences of the Russian invasion.
- **[The next variant: three key questions about what’s after Omicron](#)** [28 February 2022]
News Explainer • The emergence of a new variant is just a matter of time, scientists say.
- **[How to protect the first ‘CRISPR babies’ prompts ethical debate](#)** [25 February 2022]
News • Fears of excessive interference cloud proposal for protecting children whose genomes were edited, as He Jiankui’s release from jail looks imminent.
- **[The controversial China Initiative is ending — researchers are relieved](#)** [24 February 2022]
News • The US Department of Justice has announced major changes to the espionage-detection programme. But scientists hope for further acknowledgement of the damage done.
- **[Could drugs prevent Alzheimer’s? These trials aim to find out](#)** [09 March 2022]
News Feature • Researchers are giving drugs to healthy people in hope of clearing away toxic proteins in the brain and warding off neurodegeneration.

- NEWS ROUND-UP
- 09 March 2022

Sci-Hub downloads, Mars rover delay and academic strikes in Nigeria

The latest science news, in brief.



The rover is equipped with a drill to allow it to search for signs of life beneath the surface of Mars. Credit: Aaron Chown/PA/Alamy

Ukraine invasion jeopardizes Mars rover launch

The future of a €1.3-billion (US\$1.4-billion) programme to explore Mars has been thrown into doubt by [Russia's invasion of Ukraine](#), after the European Space Agency (ESA) said that the launch of its rover this year is now “very unlikely”.

The plan to send a rover mission to Mars is the second part of the joint ExoMars mission between ESA and the Russian space agency Roscosmos. The rover was scheduled to take off on a Russian rocket from Baikonur, Kazakhstan, in September.

Following a meeting of its member states, ESA said on 28 February that the economic sanctions imposed by Western nations on Russia and the wider context of the war [have made a 2022 launch unlikely](#). ESA said it deplored “the human casualties and tragic consequences of the war in Ukraine”, and that its decisions take into account not only its workforce, but European values. ESA’s director-general, Josef Aschbacher, will now analyse possible options for a way forward. The next launch opportunity will be in November 2024.

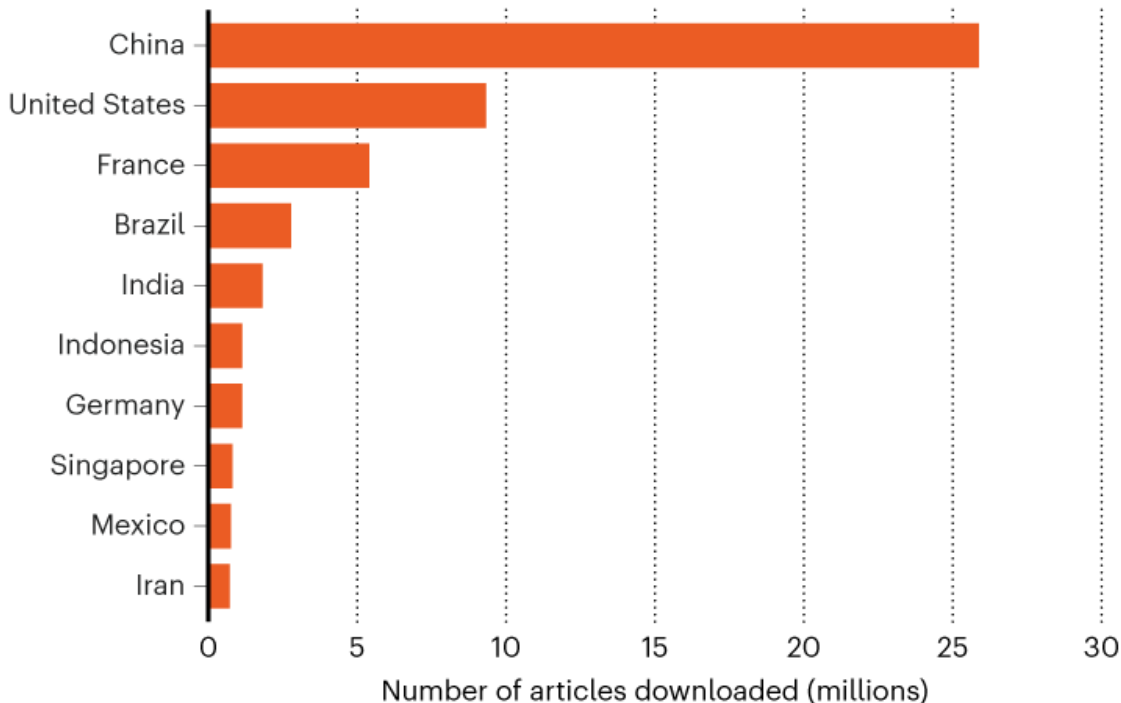
This will be the third time the mission has been postponed from its original planned launch in 2018. Each delay comes with mounting costs.

Sci-Hub downloads show where site is most used

[Download figures for Sci-Hub](#), the popular but controversial website that hosts pirated copies of scientific papers, reveal where people are using the site most. The statistics show that users accessing Sci-Hub from China are by far the most active — and that, with more than 25 million downloads, use in China outstrips the rest of the top 10 countries combined (see ‘Global resource’). The statistics are updated daily and show the number of downloads from each country over the past month — but they are not normalized for the size of the research population.

GLOBAL RESOURCE

In the last month, researchers downloaded millions of articles from Sci-Hub. These statistics might not reflect the true location of users — many access the resource through VPNs or mirror sites.



©nature

Data correct as of 24th February 2022.

Source: Sci-Hub

Researchers in countries whose universities lack the resources to pay for bulk subscriptions seem to be making heavy use of the service. Many nations with fewer scientific resources appear in the top 20, including Brazil (2.8 million downloads), Mexico (750,000) and Colombia (375,000).

The data come with several important caveats. The figures include only downloads from original Sci-Hub websites, not any replica or ‘mirror’ sites, which can have high traffic in places where the original domain is banned. And virtual private networks (VPNs) can skew the results by making it appear that users are in a different country.



There have been more than a dozen strikes at Nigeria's public universities over the past two decades. Credit: Pius Utomi Ekpei/AFP via Getty

Nigeria's strikes are disrupting research

Teaching and research are at a standstill across Nigeria's public universities as [thousands of academics strike over pay and lack of funding for research infrastructure.](#)

The Academic Staff Union of Universities, the Nigerian body representing lecturers and professors, says its members are on strike to force the government to implement a 2009 agreement to fund higher salaries, provide compensation for unpaid work (such as reviewing grants or acting as external examiners) and invest in Nigeria's public universities.

A spokesperson says the government is committed to implementing the agreement. The two sides are in talks to try to resolve the dispute. If they cannot, the union says it will continue the strike indefinitely.

“The government should fulfil whatever agreements they have reached with the university lecturers,” says virologist Oyewale Tomori, who chairs the government’s COVID-19 advisory committee.

The median monthly salary for lecturers ranges from US\$330 for an entry-level assistant lecturer to \$1,200 for a more experienced professor.

Nature **603**, 207 (2022)

doi: <https://doi.org/10.1038/d41586-022-00650-1>

This article was downloaded by **calibre** from <https://www.nature.com/articles/d41586-022-00650-1>

| [Section menu](#) | [Main menu](#) |

- NEWS
- 01 March 2022
- Update [07 March 2022](#)

Global research community condemns Russian invasion of Ukraine

Rebuke against Russian science grows as the deadly conflict enters its sixth day.

- [Nisha Gaind](#) &
- [Holly Else](#)



Ukrainian soldiers walk in the centre of Kyiv, which is being bombarded by Russian forces. Credit: Sergei Supinsky/AFP/Getty

Russia's unprovoked invasion of Ukraine has unleashed an outpouring of condemnation from scientists and research organizations worldwide. Some organizations in Western nations have moved quickly to sever links with Russia — cutting off funding and resources and ending collaborations with Russian scientists. And from Mauritius to Latvia, national science academies and groups of researchers have issued statements sharply criticizing the conflict and supporting their Ukrainian colleagues.

In Ukraine, scientists are pressuring nations to freeze Russia out of their science programmes, and calling on Russian institutes and scientific leaders to condemn the invasion.

"There should be a complete boycott of the Russian academic community. No cooperation," says Maksym Strikha, a physicist at the Taras Shevchenko National University of Kyiv, who is in the centre of the Ukrainian capital

and said the frontline was 30 kilometres away. That includes barring Russian-authored articles from Western journals and banning researchers with Russian affiliations from international research teams, he says. “The Russian academic community should also pay its own price for supporting [Russian President Vladimir] Putin.”

The chorus of condemnation includes the voices of thousands of scientists in Russia, who say that they are appalled by their government’s actions. In a letter organized by researchers in Russia and signed by more than 5,000 people, scientists strongly condemn the hostilities and say that the Russian leadership has launched an unjustifiable war for the sake of its “geopolitical ambitions”. The letter includes around 85 scientists who are members of the Russian Academy of Sciences, a government body that oversees much of the nation’s research. One academician, biologist Eugene Koonin at the US National Center for Biotechnology Information in Bethesda, Maryland, has resigned his foreign membership citing the inaction of the academy’s leadership. (The Russian Academy of Sciences did not respond to *Nature*’s request for comment.)



People in St Petersburg, Russia, protest against their government's military invasion of Ukraine. Credit: Valya Egorshin/NurPhoto/Getty

Collaborations cancelled

Among the strongest actions taken so far is the decision by a group of Germany's largest research funders, including the German Research Foundation, to freeze all scientific cooperation with Russia. In a 25 February statement, the group — the Alliance of Science Organisations in Germany — says that the country's research funds will no longer benefit Russia, that no joint scientific events will take place and that no new collaborations will begin. “The Alliance is aware of the consequences of these measures and at the same time deeply regrets them for science,” it said.

“My former student lives in Germany and we still collaborate. She was informed by her superiors that any contact with Russian scientists would be strongly discouraged,” says Mikhail Gelfand, a co-organizer of the Russian

scientists' letter and a biology lecturer at the Skoltech Center of Life Sciences in Moscow. "From what I see, it's happening in many places."

The mood among colleagues in Russia is "terrible", he says. "Nobody thought it would come as far as direct invasion," he says. "Nobody thought that Russia would attack Kyiv." Gelfand says that he hopes there is a way that general sanctions don't harm individual scientists, many of whom publicly oppose the war.

In the United States, the Massachusetts Institute of Technology in Cambridge has ended its relationship with the Skolkovo Foundation, a Moscow-based non-profit organization focusing on innovation. In 2011, the partners launched the Skolkovo Institute of Science and Technology, or Skoltech, in Moscow. "We take it with deep regret because of our great respect for the Russian people and our profound appreciation for the contributions of the many extraordinary Russian colleagues we have worked with," says a 25 February statement from MIT.

And on 27 February, UK science minister George Freeman tweeted that he had launched a rapid review of research-innovation funding from the UK government to Russian beneficiaries.

Total boycott

Ukrainian scientists, meanwhile, are rallying to convince international organizations to take stronger action against Russia. More than 130 people have signed an open letter to the European Commission and member states of the European Union calling for an urgent suspension of all funding to, and international collaboration with, Russian institutions. "The European Union cannot provide funding to the institutions subordinated to Putin's regime anymore" if it wishes to act in accordance with its "declared values", the letter says.

The statement, initiated by Ukraine's Council of Young Scientists, says that Russia must not be involved in EU programmes such as the flagship research programme Horizon Europe; the exchange scheme Erasmus+e; international collaborations such as the particle-physics research laboratory

CERN near Geneva, Switzerland; and the international nuclear-fusion project ITER, in southern France. On 5 March, the European Commission said that it was suspending scientific cooperation with Russia. In a statement, it said it would stop payments to Russian research partners and review all projects that involve Russian research organizations under its flagship Horizon Europe programme and its predecessor Horizon 2020. “The European Union stands with Ukraine and its people,” a commission spokesperson said.

Another high-profile cancellation is the four-yearly conference of the International Mathematical Union, which awards the prestigious Fields Medal and was scheduled to be held in St Petersburg in July. After mounting pressure from national mathematical societies and more than 100 of its invited speakers, the union said on 26 February that it would hold the International Congress of Mathematicians online in light of the conflict.

Further action

Some Ukrainian scientists say that although they appreciate the support of their Russian counterparts, the actions announced do not go far enough. In particular, Russian academic institutions have failed to condemn the aggression, says an open letter from the Academy of Sciences of the Higher School of Ukraine. Restrictions on Russian scientists must be all-encompassing, they say: “We urge that researchers with an affiliation of such institutions not be admitted to international grant teams, not be invited to international conferences, and not be published in leading international scientific journals.”

The editorial board of at least one journal, the *Journal of Molecular Structure*, has decided to no longer consider manuscripts authored by scientists working at institutions in Russia.

Alexander Kabanov, a Russian-US chemist at the University of North Carolina at Chapel Hill who co-organized a letter from the Russian researchers living overseas, says that support for Ukrainian researchers is the next crucial step. “Right now, many Ukrainians are fighting for their country and some are refugees,” he says. The Western academic community should

develop programmes of support for Ukrainians who need education and scientific training. “I believe the laboratories should be open for them.”

Nature **603**, 209-210 (2022)

doi: <https://doi.org/10.1038/d41586-022-00601-w>

Updates & Corrections

- **Update 07 March 2022:** This story has been updated with details of the European Commission’s response to Russia’s invasion of Ukraine.

This article was downloaded by **calibre** from <https://www.nature.com/articles/d41586-022-00601-w>

| [Section menu](#) | [Main menu](#) |

- NEWS
- 02 March 2022

‘I thought I had forgotten this horror’: Ukrainian scientists stand in defiance

Researchers tell *Nature* about their experiences of the Russian invasion.

- [Nisha Gaind](#),
- [Holly Else](#) &
- [Antoaneta Roussi](#)



People clear debris from a damaged military base in Okhtyrka in the Sumy region of Ukraine. Credit: Irina Rybakova/Handout/Reuters

“I survived this already eight years ago,” says economist Illya Khadzhynov. “I am from Donetsk.”

As the world awoke to news on 24 February that [Russia had invaded Ukraine](#), including its capital Kyiv, Ukraine’s people were being forced to make impossible decisions about whether to stay and shelter, attempt to flee or fight for their country.

As the conflict approaches the one-week mark, Ukrainian researchers have described to *Nature* how they have responded. Some scientists say that their colleagues and students have taken up arms to defend their country. Others have remained in cities, looking after their families and watching the devastation wrought by Russian shelling on apartment and university buildings. “We are not thinking about research,” says Khadzhynov.

Air-raid alerts

Khadzhynov is vice-rector for scientific work at Vasyl’ Stus Donetsk National University. In 2014, the 85-year-old university relocated to Vinnytsia in central Ukraine, displaced by the conflict in the Donbas region, parts of which are claimed by separatists. “It moved to Vinnytsia with no resources, no buildings. It had a rebirth,” says Khadzhynov.

For Khadzhynov, the events of the past week remind him of that time, when he was forced to leave his hometown of 35 years. “It’s the second time in my life this is happening. I thought I had forgotten all this horror. Unfortunately, it is repeated.”

When the attack came on 24 February, Khadzhynov was on the train to Kyiv. He received a text from his brother telling him the invasion had started, got off at the next stop and went back to Vinnytsia. Lectures at the university immediately moved online. Alongside his colleagues, Khadzhynov’s priority was his students’ well-being.

“We are thinking first of our students and personnel — what should we do and what should we say to them,” he says. “The main point for us is to give students psychological help and assistance for mental health.” Khadzhynov had not seen Russian forces in Vinnytsia when he spoke to *Nature* on 2 March, and had been going to his university to work every day. But he said air-raid alerts were ongoing. “The air alarms help us. In Donetsk, there were no air alarms, they simply started shelling.”

Many students at Khadzhynov’s university have entered the territorial defence forces, which are handing out weapons to any adult willing to defend the country; about 18,000 arms have been given out. Ukraine has announced conscription of all men aged 18–60, but students and those teaching in universities or in scientific positions are exempt, says Khadzhynov.

Picture from Kyiv

“It is probably coming to the next Russian bombardment,” says Maksym Strikha, a physicist at the Taras Shevchenko National University of Kyiv, from his apartment in central Kyiv on 1 March. “We hear shelling every day.”

The front line is about 30 kilometres away, he says, and small groups of Russian soldiers are continually trying to penetrate the city, but have so far been stopped by Ukrainian soldiers. Many younger students at his institute have also taken up arms. “They are either on the battlefield or supporting the army,” he says. (Colleagues his age and older — Strikha is 60 — are too old to fight, he says.)

“I can make no plans,” says Strikha. “Yesterday, I sent my colleagues a draft of my manual in Ukraine of solid-state physics. If the situation will not be good for me, maybe someone can edit this manual and publish it.”



The Kharkiv National University building in Ukraine's second city has been badly damaged by Russian bombardments. Credit: Oleksandr Lapshyn/Reuters

Due east of Kyiv, 30 kilometres from the northeastern Russian border, is Sumy National Agrarian University. Yuriy Danko, an economist and vice-rector for scientific work at the institute, says that shelling has damaged dormitory and university buildings. "All windows were broken, all doors were broken, all floors were destroyed."

"There are victims," says Danko. "Including many among the civilian population."

Danko says that some students left but most remained. The city has formed a territorial defence unit that accepts all types of people. "Students and scientists took up arms today."

On 1 March, Danko was at the university helping students who hadn't had time to leave and were still in dormitories — about 400. These include 170 students from other countries, including China, India and Nigeria. "It is

currently impossible to evacuate them and they are in bomb shelters. We are in bomb shelters during bombings and at night.”

Coordinating help

From Riga, Sanita Reinsone, a digital-humanities researcher at the University of Latvia, is coordinating efforts to help Ukrainian scientists. On 26 February, she made a dedicated Twitter account for the hashtag [#ScienceforUkraine](#), which has garnered more than 4,000 followers.

At first, institutes, universities and research organizations worldwide were offering moral support. But within days, many were providing detailed information about scholarships, fellowships and even offering to pay salaries for Ukrainian researchers. “I didn’t expect the calls of support to be so wide,” said Reinsone. “So far, I’ve compiled 50 organizations, but there could be more than 100 worldwide.” Offers have come in from Chile to Japan.

Reinsone took on the task of organizing the opportunities after feeling that she couldn’t sit and watch as a neighbouring country struggled under Russian aggression. “It was personal for me,” she says. An information-technology specialist from her department helped to create a [website that shows a map](#) of universities around the world and support they’re offering. “Ukrainian scholars don’t have the time to search these offers individually, so we want to aggregate all the details in one place,” she says.

A continent away in Lexington, Massachusetts, the situation in Ukraine reminds physicist George Gamota of his childhood. He fled Ukraine with his family in 1944, aged 5, and arrived in the United States in 1949. After a career working at Bell Labs, the Pentagon and as a institute director at the University of Michigan, he spent many years helping Ukraine to develop its scientific system after it gained independence, including as part of a nine-person international committee appointed by the Ukrainian government.

“Six months ago, I was excited to see young people working in labs and heading departments, which was very unusual,” says Gamota. “What will happen now is anybody’s guess,” he says. In one scenario, Russia could

impose regime change and install a Kremlin-friendly government. “That would be a tragedy, because more young people would flee, and the chances of Ukraine really developing would be stymied.”

For Khadzhynov, the suggestion of regime change prompts a swift answer: “In this case, I will move abroad.”

Nature **603**, 210-211 (2022)

doi: <https://doi.org/10.1038/d41586-022-00621-6>

This article was downloaded by **calibre** from <https://www.nature.com/articles/d41586-022-00621-6>

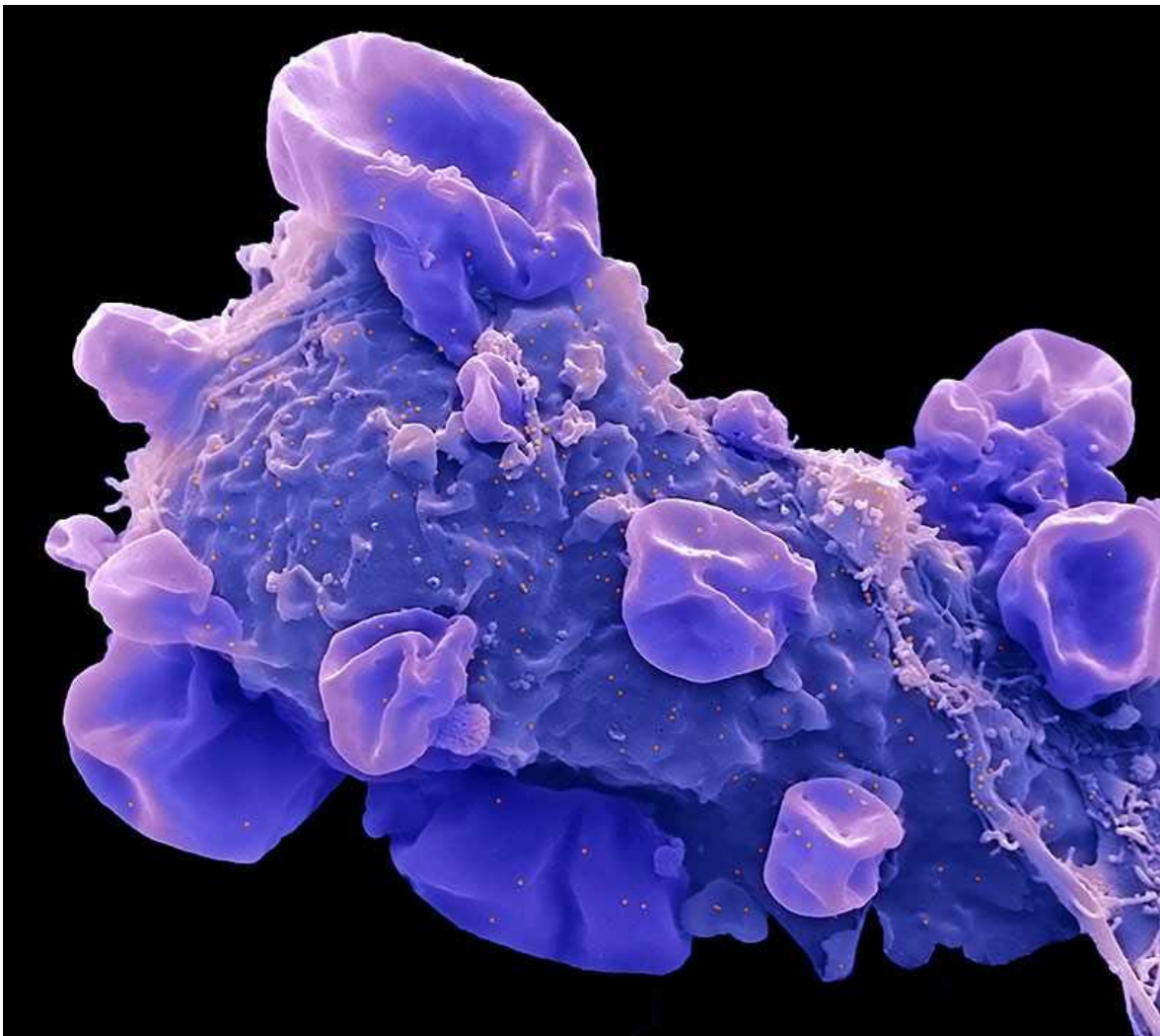
| [Section menu](#) | [Main menu](#) |

- NEWS EXPLAINER
- 28 February 2022

The next variant: three key questions about what's after Omicron

The emergence of a new variant is just a matter of time, scientists say.

- [Heidi Ledford](#)



Particles (orange; artificially coloured) of the SARS-CoV-2 Omicron variant bud from a cell.Credit: Steve Gschmeissner/SPL

Now what?

After the [Omicron variant](#) brought a fresh wave of SARS-CoV-2 infections and anxiety at the start of 2022, some nations are starting to record a decline in case numbers. But after two years of oscillating between pandemic surges and retreats, even people in these countries cannot help but wonder [when the next blow will come](#) — and what form it will take.

“I think it is inevitable that we will see new variants with varying degrees of immune evasion,” says Andrew Rambaut, who studies viral evolution at the

University of Edinburgh, UK. “They could emerge from wherever there is widespread transmission.”

As they wait for the next variant to enter the scene, scientists are studying the currently dominant Omicron variant to better predict the future; this research is described in a separate [Feature](#). Here are three key questions scientists would like that research to answer.

When will the next variant of concern emerge?

There is no way to know for sure when a variant will become dominant, or whether it will rise to the status of a ‘variant of concern’ — meaning that there are signs that it has picked up worrying new properties, such as [spreading more rapidly](#), causing more-severe disease or evading immune responses.

The public is most familiar with the first dominant sub-variants of Omicron and Delta. But researchers have been tracking a host of related sub-variants that are jockeying for dominance. In the United Kingdom, for example, one Delta variant called AY.4 was in the process of being rapidly displaced by another, called AY.4.2, in late 2021. “And then Omicron came along and just blew up,” says bioinformatician Andrew Page at the Quadram Institute in Norwich, UK.

The history of these viral dynamics suggests that a new variant will sweep through every few months, says Page. “They seem to happen quite regularly,” he says. “It’s probably just going to tick along.”

But whether that variant will rise to the level of a variant of concern remains an open question. At present, the original BA.1 Omicron lineage is being replaced by another, called BA.2. This lineage, although [probably more transmissible](#) than BA.1, does not seem to be a major change from the original one that swept through many countries earlier this year.

Such dynamics are probably common in viral pathogens. But the world has not followed a viral infection so closely before, says Page, and as a result, scientists had been missing out on the fine print. That close scrutiny, however, is already diminishing: COVID-19 testing rates in the United

Kingdom have declined, he notes, in part because Omicron tends to produce relatively mild disease. With a mild disease, people are less likely to seek testing, and governments become less proactive in encouraging tests.

Eventually, this will weaken [SARS-CoV-2 genomic surveillance efforts](#). When Omicron was discovered, the alarm was sounded very quickly, Page says, but in the future, it could take weeks longer to realize a new variant of concern is afoot. “There’s no way that we can keep up the pace we’ve had so far,” he says. “But if it’s not causing severe disease, do you need to have such intense surveillance?”

Will the next variant cause severe disease?

Omicron is less likely to cause severe disease than previous variants of concern — a feature that has helped to temper the impact of the variant’s rampant spread.

Although that has fed speculation that the virus could be evolving towards a strain that induces a milder disease, SARS-CoV-2’s evolutionary path remains unclear, says Rambaut. Thus far, new variants of concern have not evolved from the dominant preceding one. Instead, [they have emerged from separate lineages](#). There is no guarantee that the next dominant variant will sprout from the ‘mild’ Omicron branch of the SARS-CoV-2 family tree. “It is possible that a later variant may be back to a Delta or Alpha lineage, with sufficient immune evasion to sweep Omicron away,” says Rambaut.

Researchers also still don’t know the extent to which Omicron’s relative mildness is due to the prevalence of immunity against SARS-CoV-2, rather than intrinsic properties of the virus itself. As more of the world’s population becomes vaccinated, infected or both, immunity is likely to grow and so, too, will resilience against severe COVID-19.

But there were some differences in how Omicron behaved compared with previous variants, notes immunologist Wendy Burgers at the University of Cape Town in South Africa. Several animal studies, for example, have found that [Omicron is less likely to affect the lungs](#), than previous variants¹. “Will

the next mutated variant have different properties?” she says. “I don’t think there’s any guarantee that those intrinsic differences might not be worse.”

“We know a lot about the humans, but it’s the virus that’s unpredictable,” she says. “And I’m a little scared of that.”

Will vaccines protect against emerging variants?

The 54 mutations in Omicron’s genome — and particularly the 34 clustered in a key viral protein called spike — severely weakens the ability of COVID-19 vaccines to prevent SARS-CoV-2 infection. But protection against severe disease seems to have remained high, and probably contributed to the perceived mild disease caused by Omicron.

That bodes well for the resilience of vaccine-mediated immunity against future variants of concern, says Burgers. Although Omicron’s spike mutations seem to weaken antibody defences, scientists have detected only slight declines in the ability of immune cells called T cells to recognize the virus. These cells are thought to be particularly important in limiting the scope of a viral infection, killing off infected cells and limiting the virus’s spread. “I really breathed a sigh of relief after Omicron,” Burgers says. “I’m optimistic that the T-cell response will be quite resilient even if a new variant emerges.”

But Burgers notes that as antibodies become less relevant for SARS-CoV-2 immunity, T cells become more important, and a viral variant that can evade T-cell surveillance will have a key survival advantage. “The T-cell response is doing much more of the heavy lifting,” she says. “So one thing we might start seeing is T-cell escape.”

In other viruses, such as influenza, the ability to escape T-cell immunity develops gradually over the course of years. But it’s hard to predict how quickly it will proceed in the middle of a raging pandemic, Burgers says.

It is also becoming more difficult for immunologists to anticipate how population immunity will shape the course of the pandemic, as the drivers of that immunity grow increasingly complex. People might have received one

of a number of vaccines, or a combination of vaccines, or experienced an [infection from one or more variants, with or without vaccination.](#)

In general, this [accumulation of exposures](#) to SARS-CoV-2 variants should boost immunity, says infectious-disease specialist Santiago Ávila Ríos at Mexico's National Institute of Respiratory Diseases in Mexico City. In a preprint, Ríos and his team reported that multiple exposures to SARS-CoV-2, either through [vaccination or infection](#), amplified antibody responses, as well as responses by immune cells called B cells². "Thus, as more persons become exposed to the virus through different mechanisms, the emergence of new variants of concern may impose a lower disease burden," he says.

But some types of exposure might be better than others for preparing the body to fight off new variants. One study³, which has not yet been peer reviewed, found that people who had been vaccinated and then were infected with Omicron experienced "whopping increases in antibodies", says virologist Penny Moore at the University of the Witwatersrand in Johannesburg, South Africa. Those antibodies could attach to and disarm multiple SARS-CoV-2 variants besides Omicron, a property called cross-reactivity.

But antibodies produced by people who have been infected with Omicron but not previously exposed to SARS-CoV-2 — either by vaccination or infection — were not as robust in blocking other variants. "We can't assume that those people would be particularly well protected against incoming variants of concern," Moore says.

Ultimately, the data continue to point to the importance of vaccination, says Burgers. "We know that vaccines shore up our immunity and that immunity will be cross-reactive, when it comes to T cells, with another variant," she says. "There's a lot that we don't know, but there's a lot that's in our control."

Nature **603**, 212-213 (2022)

doi: <https://doi.org/10.1038/d41586-022-00510-y>

References

1. Diamond, M. *et al.* Preprint at Research Square
<https://doi.org/10.21203/rs.3.rs-1211792/v1> (2021).
2. Bednarski, E. *et al.* Preprint at medRxiv
<https://www.medrxiv.org/content/10.1101/2022.02.07.22270626v1> (2022).
3. Richardson, S.I. *et al.* Preprint at medRxiv
<https://www.medrxiv.org/content/10.1101/2022.02.10.22270789v1> (2022).

This article was downloaded by **calibre** from <https://www.nature.com/articles/d41586-022-00510-y>.

| [Section menu](#) | [Main menu](#) |

- NEWS
- 25 February 2022

How to protect the first ‘CRISPR babies’ prompts ethical debate

Fears of excessive interference cloud proposal for protecting children whose genomes were edited, as He Jiankui’s release from jail looks imminent.

- [Smriti Mallapaty](#)



He Jiankui should bear some responsibilities for the children whose genomes he edited, say scientists. Credit: Mark Schiefelbein/AP/Shutterstock

Two prominent bioethicists in China are calling on the government to set up a research centre dedicated to ensuring the well-being of the first children born with edited genomes. Scientists have welcomed the discussion, but many are concerned that the pair's approach would lead to unnecessary surveillance of the children.

The proposal comes ahead of the possibly imminent release from prison of He Jiankui, the researcher who in 2018 [shocked the world](#) by announcing that he had created babies with altered genomes. He's actions were widely condemned by scientists around the world, who called for a [global moratorium](#) on editing embryos destined for implantation. Several ethics committees have since concluded that the technology should not be used to make changes that can be passed on.

Researchers say that the latest proposal, in a document by Qiu Renzong at the Chinese Academy of Social Science in Beijing and Lei Ruipeng at the Huazhong University of Science and Technology in Wuhan, is the first to discuss how to manage the children's unique situation. "It's an important document," and a welcome move by researchers in China, says Gaetan Burgio, a geneticist at the Australian National University in Canberra.

The document — which Qiu and Lei have shared with various scientists, several Chinese ministries and to *Nature*, but which has not yet been published — states that the children need special protections because they're a "vulnerable group". Gene editing could have created errors in the children's genomes, which could be passed to their children. They recommend regular sequencing of the children's genomes to check for "abnormalities", including conducting genetic tests of their embryos in the future.

Qiu and Ruipeng also recommend that He contribute to the children's medical expenses, and take primary financial, moral and legal responsibility for their health and well-being, along with the Southern University of Science and Technology in Shenzhen, with which He was affiliated, and the government.

But Joy Zhang, a sociologist at the University of Kent in Canterbury, UK, says it is difficult for scientists to know what recommendations to make

because there is almost no information about the children's current condition, and the circumstances of their conception. "China has kept everything so tight," she says.

Global shock

In 2018, the world learned that He had implanted embryos in which he had used CRISPR–Cas9 to edit a gene known as *CCR5*, which encodes an HIV co-receptor, with the goal of making them resistant to the virus. The implantation led to the birth of twins in 2018, and a third child was later born to separate parents. The parents had agreed to the treatment because the fathers were HIV-positive and the mothers were HIV-negative, and the couples were barred from access to alternative assisted-reproduction technologies in China.

In December 2019, He was sentenced to [three years in prison](#). Sources close to him say that he should be released soon. Qiu says he might be assigned a research position.

Eben Kirksey, a medical anthropologist at Alfred Deakin Institute in Melbourne, Australia, who has written a book on human genome-editing¹, agrees that He should shoulder some responsibility for the children. He promised that they would receive health insurance for the first 18 years of their lives, but because the twins were born prematurely, they were initially denied coverage, which He initially stepped in to pay, according to Kirksey's investigations. He and the university should make good on promises of medical assistance, Kirksey says.

The children, who are now toddlers, are the only known children with edited genomes. It is possible that others have been born since, but Qiu says that this is unlikely to have happened in China, where researchers would have been deterred by He's harsh punishment. "No scientist will dare to further cross the line," he says.

But other researchers have stated their interest in implanting genome-edited embryos, including Denis Rebrikov, a molecular biologist and geneticist at the Kulakov National Medical Research Center for Obstetrics, Gynecology

and Perinatology in Moscow. He has developed a technique to use CRISPR to edit mutations in a gene linked to deafness, called *GJB2*, but he has yet to implant a genome-edited embryo owing to a lack of interest among deaf couples in Russia. “I am sure that sooner or later we will find a couple who want to give birth to a hearing child,” says Rebrikov. When he does, he plans to edit the embryos and store them before requesting permission from Russian regulatory bodies to implant them.

The three children in China “will not be the last” babies with edited genomes, says Ayo Wahlberg, an anthropologist specializing in reproductive technologies at the University of Copenhagen.

Excessive surveillance

Qiu and Lei drafted their recommendations with the three girls in mind, although Qiu says they could apply to future children. But researchers have expressed several concerns.

Kirksey agrees that the girls are vulnerable because they could encounter psychological and social risks. Their experiences should be researchers’ and societies’ main concern. But he disagrees with the level of testing that Qiu and Lei propose, which he sees as excessive, because there is no clear evidence that genome-editing has harmed the children. “Special protections could also translate into more intense surveillance.”

Qiu agrees that the children could be unaffected. “This is our wish. But who could be sure of it?” He says that their proposal, including regular genome monitoring, addresses that uncertainty.

Burgio says that regular sequencing will be needed for the rest of the girls’ lives to assess the extent of the edits and their potential health implications. More advanced techniques have emerged since 2018, and these should be used to take a closer look at the site where the genomes were edited, for signs of any unwanted changes, he says. “We don’t know which type of genetic mutations will be carried out into adulthood and passed on to the next generation,” says Burgio.

But Zhang worries that without clearly defined roles and responsibilities, the document opens up future abuses of power. The main risk to the children is likely to be the sociopolitical stigma that they could face, so “putting them in the hands of a few elites will only add to that, not help”, she says.

Kirksey says that lessons should be taken from the story of Louise Brown, who in 1978 became the first person to be born through *in vitro* fertilization — a procedure that was highly controversial at the time. “She was subjected to all kinds of medical tests through the course of her life,” says Kirksey, who says Brown has described her struggles with leading a normal life. “The story in the long run about these children will be about a struggle to be normal if they do become public figures like Louise Brown.”

Nature **603**, 213-214 (2022)

doi: <https://doi.org/10.1038/d41586-022-00512-w>

References

1. Kirksey, E. *The Mutant Project: Inside the Global Race to Genetically Modify Humans* (Bristol University Press, 2021).

This article was downloaded by **calibre** from <https://www.nature.com/articles/d41586-022-00512-w>

- NEWS
- 24 February 2022

The controversial China Initiative is ending — researchers are relieved

The US Department of Justice has announced major changes to the espionage-detection programme. But scientists hope for further acknowledgement of the damage done.

- [Natasha Gilbert](#) &
- [Max Kozlov](#)



Matthew Olsen, the US assistant attorney-general for national security, spent three months reviewing the China Initiative, which was launched in 2018, under the administration of former president Donald Trump. Credit: Alamy

The US Department of Justice (DoJ) announced on 23 February that it will effectively terminate the controversial China Initiative, a programme that sought to protect US laboratories and businesses from espionage. Instead of focusing on China, the programme will be broadened to cover other countries of concern, and will be renamed.

Scientists who spoke to *Nature* are relieved to see the initiative end — the programme frequently targeted academic researchers for failing to disclose funds from China or partnerships with institutions in that country. But they fear that the damage to collaborations with researchers in China will be long-lasting, and hope the US government will make amends for the harm that the initiative caused.

“These changes are long overdue and certainly welcome,” says Jenny Lee, a social scientist at the University of Arizona in Tucson who studies research collaborations and geopolitics. In particular, she was glad to see that, during the DoJ’s announcement, “it seemed there was an acknowledgement that the China Initiative failed in some respects”.

In a speech announcing that the agency would be shuttering the programme, Matthew Olsen, the US assistant attorney-general for national security, said that “safeguarding the integrity and transparency of research institutions is a matter of national security. But so is ensuring that we continue to attract the best and the brightest researchers and scholars to our country from all around the world.”

Olsen maintained that China is a threat to US research security. The DoJ, however, will pursue a broader plan called the Strategy for Countering Nation-State Threats to tackle the increasingly “aggressive” and “nefarious” activity of what he called hostile nations in addition to China, including Russia, Iran and North Korea.

“These nations seek to undermine our core democratic, economic and scientific institutions,” he said. “And they employ a growing range of tactics to advance their interests and to harm the United States.”

Initiative drift

Scientists and civil-liberties groups had been calling for the China Initiative to end for more than a year. Critics of the initiative said it was biased against researchers of Chinese descent, and pointed to the damaged lives and careers of those who have been arrested. For instance, nanotechnology researcher Anming Hu at the University of Tennessee, Knoxville, [was acquitted in September last year after a mistrial](#). He had been under house arrest for over a year while awaiting trial, and was fired from his job (the university rehired him this month).

Although the US government has caught genuine Chinese spies stealing US trade secrets and scientific and technological developments, many think that the China Initiative veered off course by focusing on academics who had

improperly filled in applications for funding from US agencies. One of the initiative's architects, Andrew Lelling, a former US attorney for the district of Massachusetts, acknowledged this shift [in a statement he posted online last year](#): "This was sound policy, but the Initiative has drifted and, in some significant ways, lost its focus."

The reforms to the China Initiative were driven in part by concerns from the academic and scientific community, Olsen said. A number of university and advocacy groups submitted letters to US attorney-general Merrick Garland asking for a review of the programme last year. Olsen was asked to evaluate the initiative, a process that took three months. He acknowledged that the cases brought against researchers under the China Initiative gave a perception of bias against those of Chinese descent, and undermined international collaboration. However, he said he hadn't seen any evidence to suggest that the DoJ had taken any decisions owing to racial prejudice.

The volunteer group APA Justice, which has been advocating on behalf of researchers of Asian descent, disagrees with Olsen's assessment but welcomes "the end of the ill-conceived initiative and DOJ's openness to listen and respond to community concerns". In December, an analysis [by the news outlet MIT Technology Review](#) found that nearly 90% of all China Initiative defendants were of Chinese origin — a fact that Lee says is indisputable evidence of racial profiling.

[An October report co-authored by Lee](#) surveyed nearly 2,000 scientists in the United States. About half of respondents of Chinese descent reported experiencing "considerable" fear, anxiety or a mixture of both that they are being surveilled by the US government. Only 12% of non-Chinese scientists reported the same concern. The survey also found that many US scientists of Chinese heritage had become less inclined to communicate with scholars in China. "All of those impacts combined means that there's damage that's already been done," Lee says.

Seeking accountability

Olsen said that the DoJ will continue to pursue all current China Initiative cases, a move that Gang Chen, a mechanical engineer at the Massachusetts

Institute of Technology in Cambridge, called “disappointing” in an e-mail to *Nature*. Chen was arrested under the China Initiative in January 2021 for allegedly failing to disclose on grant applications that he had ties to China and had received funding from Chinese institutions. He maintained his innocence until prosecutors acknowledged in January this year that he had not been obligated to disclose those affiliations, and dropped the charges.



Mechanical engineer Gang Chen at the Massachusetts Institute of Technology in Cambridge was arrested under the China Initiative. Prosecutors later dropped the charges. Credit: Tony Luong/New York Times/Redux/eyevine

The DoJ’s National Security Division (NSD), which was set up after the 11 September 2001 terrorist attacks in the United States to coordinate the government’s national security work, will now take an “active supervisory role” in assessing evidence and guiding decisions on whether to pursue criminal prosecution for cases involving academic integrity and research security, Olsen noted in his speech. Rather than pursue criminal cases

against academic researchers, the agency might decide that the offences should be remedied through civil suits or fines, he added. Wyn Hornbuckle, a DoJ spokesperson, declined to elaborate on what these changes might look like in practice, or whether the NSD had previously had an “active supervisory role” over cases associated with the China Initiative.

Hu says that the reforms are “encouraging” and could be a positive start to healing the hurt caused by his and others’ wrongful prosecution. However, he is waiting to see what action the government actually takes, and whether the FBI and other law-enforcement agencies are held to account for their behaviour. Some researchers have been trying to get the US government to make amends for wrongful prosecutions. For instance, Xiaoxing Xi, a physicist at Temple University in Philadelphia, Pennsylvania, [has been attempting to sue for compensation](#) after his wrongful arrest for allegedly sharing restricted technological know-how with China. His case pre-dates the China Initiative, but shares features with those brought under the programme. Prosecutors dropped his charges ahead of trial.

Chen told *Nature* that he applauds the changes but also thinks that the US Congress should hold the DoJ and FBI to account for the “harassment” of academic researchers. “The chilling effect will have a long-lasting damaging effect to US higher education and America’s ability to attract and retain world talents unless the government acknowledges its own wrongdoings,” he says.

Nature **603**, 214-215 (2022)

doi: <https://doi.org/10.1038/d41586-022-00555-z>

This article was downloaded by **calibre** from <https://www.nature.com/articles/d41586-022-00555-z>

- NEWS FEATURE
- 09 March 2022

Could drugs prevent Alzheimer's? These trials aim to find out

Researchers are giving drugs to healthy people in hope of clearing away toxic proteins in the brain and warding off neurodegeneration.

- [Alison Abbott](#) ⁰



Trial coordinator Eric McDade assesses participant Marty Reiswig for cognitive ability.Credit: Matt Miller/Washington University School of Medicine

Every two weeks, a nurse visits 43-year-old Marty Reiswig in Denver, Colorado, and injects him with an experimental drug called gantenerumab. Every month, Reiswig drives into town for a brain scan to make sure the drug has not caused any bleeds. And every year he flies to St Louis, Missouri, for four days of brain scans, spinal taps, blood analyses and exhaustive tests of his memory and reasoning capacity.

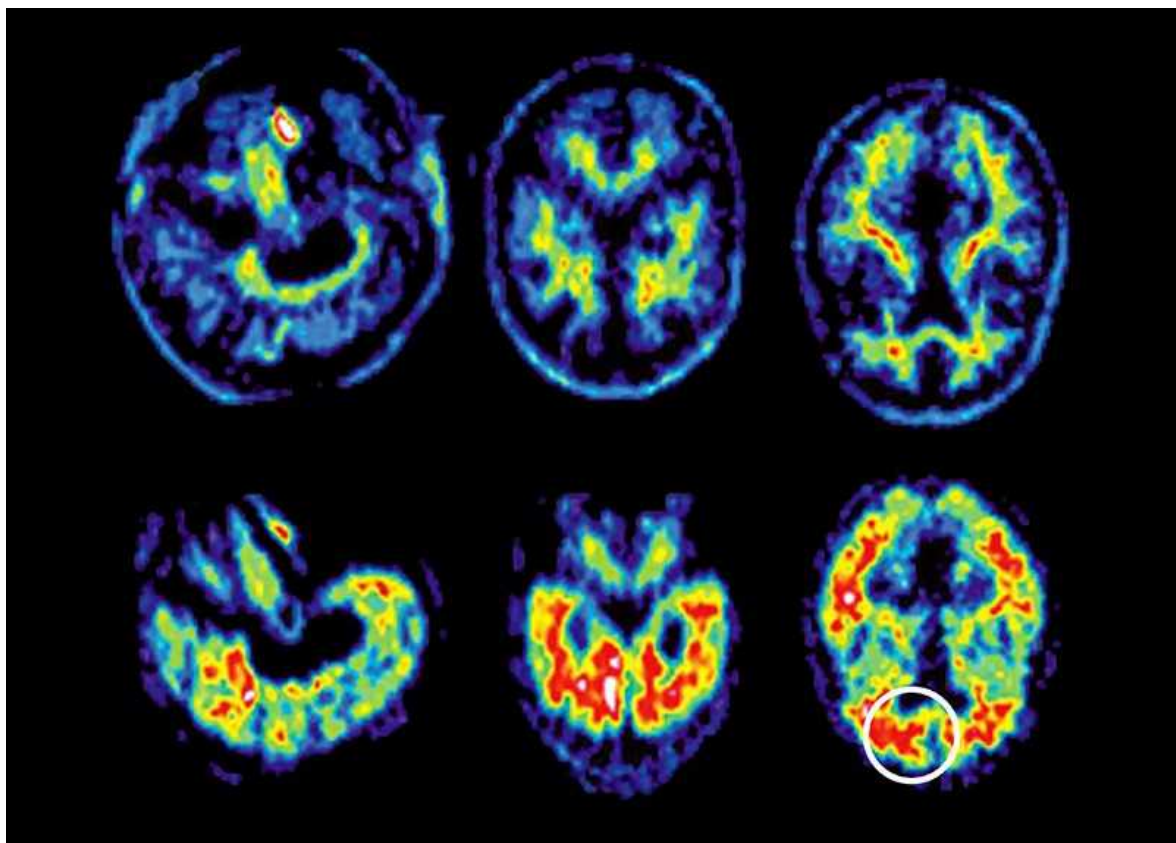
Reiswig is fit and healthy and runs two local businesses. He goes through all of this because he has a rare genetic mutation that almost guarantees he will develop early-onset Alzheimer's disease. He hopes that the international clinical trial he has been part of for nine years might prevent, or at least delay, the onset of symptoms that will otherwise arise in just a few years' time.

"I always do my best to give the researchers as much as I can — even if it turns out not to help me, it might help my children," he says.

The trial is one of several trying to understand whether treating the root cause of Alzheimer's before symptoms start might be the best way to handle a disease that exacts such a large toll. The drugs under scrutiny are all antibodies that have been developed to target and clear amyloid- β proteins in the brain, which clog together into toxic masses called plaques (see 'Antibodies against amyloid'). These drugs are of the same type as aducanumab, made by Biogen in Cambridge, Massachusetts, which was provisionally approved last year by the US Food and Drug Administration (FDA) for the treatment of mild Alzheimer's, in large part owing to its ability to remove amyloid- β .

And because such toxic proteins are a feature of several types of dementia, these antibody studies might also offer hints for how to treat the 55 million people around the world who have these conditions, says neurologist Paul Aisen at the University of Southern California in San Diego, who is a leader of the US Alzheimer's Clinical Trials Consortium. Most dementias hit after 65 years of age; all have proved to be stubbornly incurable. Of more than 100 trials around the world, most are aiming to treat symptoms of the disease rather than its root cause.

But Aisen foresees a future — maybe just a decade or so down the line — in which much of the burden of Alzheimer's disease might actually be prevented. "We're heading towards screening people from middle age on with blood tests, and treating those who show amyloid abnormalities with drugs that reduce the generation of amyloid plaques," he says. "I am optimistic."



PET (positron emission tomography) scans of the brain of a person with Alzheimer's show the build-up of amyloid plaques (circled) not present in healthy brains. Credit: Science Source/SPL

A lot needs to go right for this hopeful view to become reality. Large clinical trials will have to show that these therapies work, and amyloid-clearing drugs will have to be proven to be safe and affordable. After decades of setbacks and failed clinical trials, some dementia researchers prefer to express caution. "The field is taking tremendous risks by engaging in studies that can cost billions of dollars," says neurologist David Knopman at the Mayo Clinic in Rochester, Minnesota.

It will take a while for answers to emerge. Some trials of Alzheimer's disease prevention are just getting started, and some ongoing ones could stretch into the next decade.

Getting in early

It was 1986 when Carol Jennings in Nottingham, UK, wrote a letter to geneticist John Hardy asking whether she could be of use in his research. Just like Reiswig, Jennings had many relatives who succumbed to early-onset dementia. Hardy's team, now at University College London, was interested in the genetics of Alzheimer's and invited the Jennings family to donate blood to its project.

A few years later, the team identified a mutation shared by the affected family members¹. It was in a gene that codes for a large protein that sits in the membranes of neurons, the amyloid precursor protein (APP).

APP in the brain is chopped into amyloid- β and other short chains of amyloid protein by a suite of enzymes. In healthy brains, these amyloid peptides might serve useful functions, but over time they can accumulate — perhaps because the brain's molecular system for clearing them loses efficiency — and clump together into plaques. In someone with a mutation in the gene that codes for APP, the amyloid- β proteins are stickier or more profuse, and the disease manifests earlier than in people who do not have the mutation.

This is the basis of the amyloid hypothesis of Alzheimer's disease, first formulated by Hardy and his colleagues after their discovery of a disease-causing *APP* mutation. According to that theory, preventing the triggering event of amyloid- β accumulation might slow the disease process — or even stop it happening in the first place.

Pharmaceutical and biotechnology companies set about targeting the amyloid system, developing drugs to block the enzymes that cleave APP, or creating antibodies to the amyloid- β peptides. But their drugs continuously bombed in clinical trials. Five phase III clinical trials of a drug that blocks an amyloid-chopping enzyme, β -secretase, were discontinued because of

side effects that made cognition temporarily worse. Blockers of another enzyme, γ -secretase, went the same way. Time and time again, trials of antibodies designed to latch onto and bind to amyloid- β [failed to improve people's clinical symptoms](#). At least one major pharmaceutical company, Pfizer, left the Alzheimer's field, in 2018.

The serial failures divided the research community into camps. One camp argued that if targeting amyloid hadn't worked, then the amyloid hypothesis must be wrong. Knopman accepts that APP processing is part of the disease initiation process, but says that the role of amyloid- β has not been proved. "It's plausible, for example, that other APP cleavage products are more important to the disease process," he says.

The other camp argued that the trials had been poorly designed, in particular because they recruited people who had already begun to show early signs of Alzheimer's disease.

"The fact is that, to optimize the potential impact of removing amyloid, you need to do so as early as possible," says Aisen. Amyloid- β accumulation begins its slow and silent campaign of destruction in the brain many years before its damage is extensive enough to cause symptoms, he says. "The total duration of Alzheimer's disease is over 25 years, and the trials were only engaging in the final decade when there is constant worsening of neurodegeneration."

Animal studies back up this insight. In mice that were genetically altered to overexpress *APP*, treating young animals with aducanumab before amyloid- β deposits were detectable resulted in significant reductions in deposits and fewer signs of disease in the brain six months later².

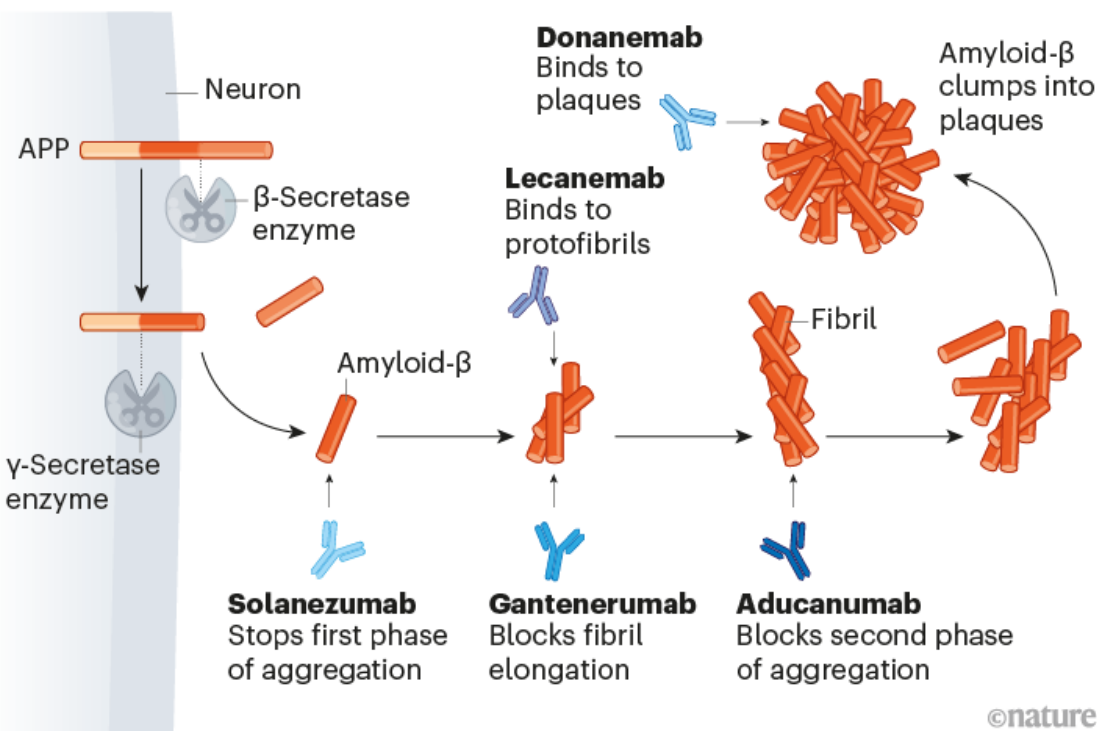
When the FDA made the controversial decision to [approve Biogen's aducanumab in June last year](#), it was recognizing this long-term picture: that the drug's ability to remove amyloid- β made it likely that it could reduce Alzheimer's symptoms down the line. Biogen's large, placebo-controlled trials of aducanumab in people with mild Alzheimer's had not unambiguously improved their clinical symptoms, but the drug did a good job of clearing amyloid plaques from their brains. The agency declared that

aducanumab was the first treatment to affect the biological cause of the disease.

The decision enraged many researchers who claimed that the FDA had lowered its standards. (Knopman resigned from the FDA's advisory committee over this issue.) But in the following months, more data emerged from other trials of different drugs, showing trends towards a modest slowing of cognitive decline as amyloid- β was cleared, as well as reductions in other biomarkers of Alzheimer's progression, such as the build-up of a protein called tau. Later that year, the agency put [three further antibodies onto a fast-track review process](#): Genentech–Roche's gantenerumab, Biogen–Eisai's lecanemab and Eli Lilly's donanemab. Similarly to aducanumab, all three have been shown in early trials to clear plaques.

ANTIBODIES AGAINST AMYLOID

Several clinical trials are testing whether drugs called monoclonal antibodies can stem the symptoms of Alzheimer's by preventing the toxic clumping of amyloid- β proteins. This process starts when enzymes cleave the amyloid precursor protein (APP). Amyloid- β proteins elongate into fibrils and then nucleate into plaques. All of the drugs bind to amyloid- β , but their primary targets in the process are different.



Credit: Nik Spencer/*Nature*

“These drugs are big, big game changers,” says neuroscientist Bart de Strooper, director of the UK Dementia Research Institute at University College London. “They will allow the amyloid hypothesis to be tested definitively.”

Many researchers agree that the best test of the hypothesis — and the best way to stop the disease in its tracks — is to give people these drugs early, without waiting for Alzheimer’s symptoms to set in first.

Timing is everything

According to Hardy, designers of even the earliest trials might have realized that they were recruiting too late in the disease. “Through the retrospectoscope, it was clear — the data were already there,” he says. In the 1980s, pathologist George Glenner at the University of California, San Diego, and his colleagues discovered that individuals with Down’s syndrome developed dementia relatively young³. They suggested that this was because people with Down’s syndrome have an extra chromosome 21 (where the *APP* gene sits). Their post-mortem studies⁴ showed that plaques developed many years before cognitive symptoms did.

The field is not ignoring the importance of finding treatments for symptomatic Alzheimer’s, says Aisen. But clinical researchers are now turning more attention to drug trials for the treatment of presymptomatic Alzheimer’s disease. It is not easy to find participants for such trials, however. People need to be symptomless but highly likely to begin developing symptoms on a measurable timescale. There are two approaches to identifying these individuals: find people like Reiswig with a rare genetic predisposition, or people in the general population with a high risk of developing Alzheimer’s because of the presence of amyloid- β in their brains.

To identify the rare genetic cases, the US National Institute on Aging (NIA) in Bethesda, Maryland, funded the launch of the Dominantly Inherited Alzheimer Network (DIAN) in 2008. It now includes more than 600 people

from 20 countries, representing around 300 families who have mutations in one of the three genes associated with early-onset Alzheimer's. Each family member has a 50% chance of inheriting a mutation.

The network quickly gathered more funding and research partners, and began enrolling families, including Reiswig's, into an observational programme. The researchers conducted positron emission tomography (PET) scans of the brain to check for amyloid- β and other biomarkers of Alzheimer's at regular intervals, and compared family members who carried the gene with those who didn't. They also noted when symptoms tended to begin in each family. The network's 2018 report confirmed that the first signs of amyloid abnormalities occur up to 25 years before symptoms start⁵.

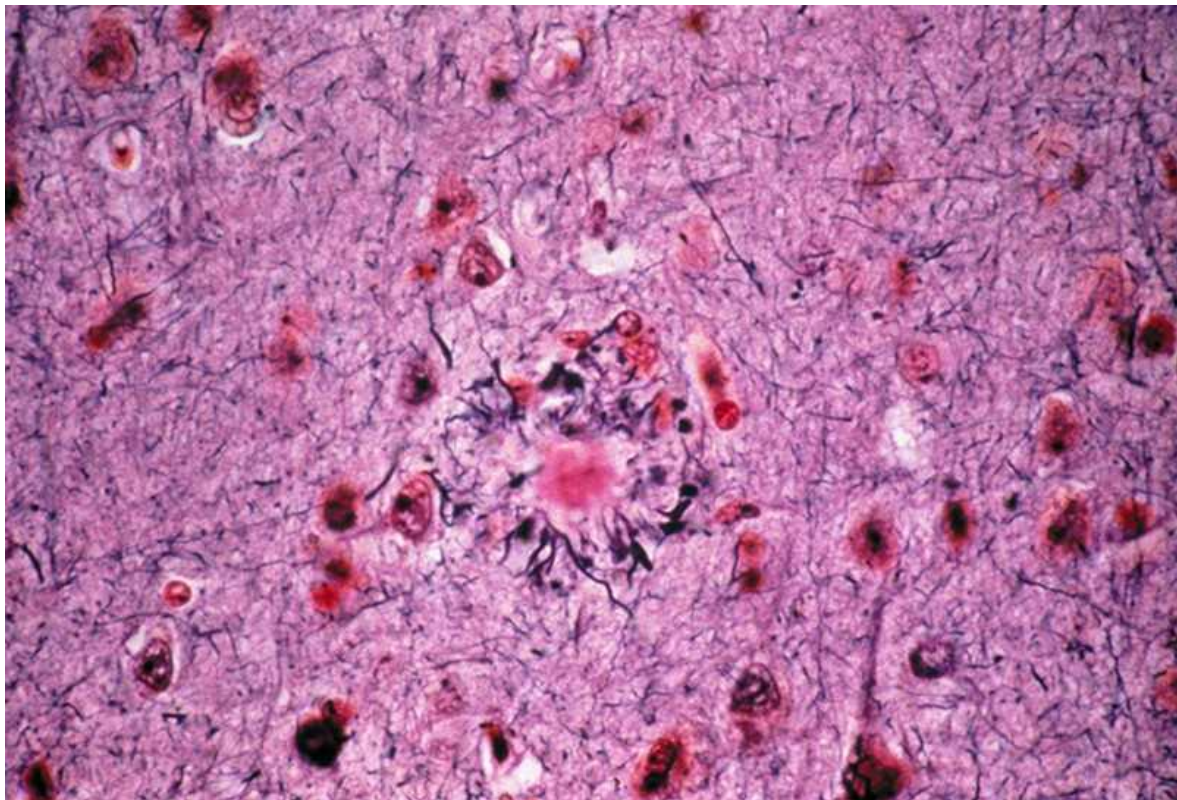
The DIAN consortium began a seven-year trial of amyloid-binding antibodies in 2012. It aimed to delay the progress of disease in people who have no cognitive symptoms but who have started to develop the primary markers of Alzheimer's — amyloid plaques — in their brains. The trial recruited 194 participants at various stages of their condition, and divided them into groups to receive either one of two antibodies, gantenerumab or solanezumab, or a placebo.

But the results of the trial, announced in 2020, were disappointing. The trial failed to prove that the drugs could slow cognitive decline — although there was little decline in treated presymptomatic participants, there was also little decline in the placebo group⁶. "That meant that we were simply unable to say whether the drugs would eventually help an asymptomatic population or not," says Randall Bateman at Washington University School of Medicine in St. Louis, who leads the DIAN Trials Unit that conducted the study.

Still, one of the antibodies, gantenerumab, had a notable impact on the biological markers of the disease. It not only reduced amyloid plaques, but also reduced levels of tau protein and of another marker of neurodegeneration, a neuronal protein that shows up in the blood.

These results encouraged Bateman and the DIAN consortium to continue studying gantenerumab for a further three years, dropping the solanezumab and placebo arms but allowing participants in those groups to convert to gantenerumab, and letting them know what drug they were taking.

That presented Reiswig with a dilemma. When he was originally tested for the gene mutation, he had chosen not to be informed of the result. But the extension of the study was only available to mutation carriers, so a request to participate would automatically reveal his genetic status. “I decided it was time for me to know, but I planned things carefully,” he says. He retreated to a holiday rental in Colorado with his wife to receive the phone call from his genetic counsellor. “I didn’t want to find out in my own house — that was at least something I wanted to have control over.” Reiswig wept when he learnt that he carried the mutation, and decided that his only chance was to continue with the trial.



An amyloid plaque (centre) in the brain tissue of a person who had Alzheimer’s disease.Credit: Martin M. Rotker/SPL

Last year, the consortium decided to try treating people with no cognitive symptoms and no plaques in their brains. “It’s really going to be the ultimate trial of Alzheimer’s prevention,” says Bateman. In the next few months, the team plans to begin recruiting 160 mutation carriers, some as young as 18, who are not expected to develop symptoms for another 11–25 years. The

placebo-controlled trial will run for four years, monitoring people's amyloid status at regular intervals. Then it will move into an 'open label study' for a further few years: the placebo arm will be dropped and all the participants will receive the trial drug. At that point, it will also measure other biomarkers of disease progression.

It would be impractical to run the trial for the decades it might take for participants to develop symptoms, says Eric McDade, the trial's principal investigator at Washington University in St. Louis. Instead, the team will monitor changes in biomarkers, such as amyloid- β and tau, that are now known to predict symptom onset during the long silent period of the disease. "The more of these other biomarkers that we can alter, the higher the probability that we can offset or at least significantly delay onset." The researchers will continue to monitor as many participants as possible after the trial's second phase, he says.

Outside the DIAN consortium, other trials for early-onset Alzheimer's are under way, testing drugs in people who already have some amyloid build-up. Genentech–Roche is studying individuals from a large family in Colombia, half of whom carry a pathological mutation in a gene that encodes part of one of the amyloid-chopping secretase enzymes. Its trial of the drug crenezumab will finish this year. Studies are also gearing up to test Alzheimer's drugs in people with Down's syndrome.

Stopping symptoms

The second approach to preventive trials is to identify those in the general population who are at high risk of developing late-onset Alzheimer's. The international Alzheimer's Disease Neuroimaging Initiative, a public–private partnership headquartered at the University of California, San Francisco, tracks Alzheimer's biomarkers in many hundreds of people through normal ageing and all stages of the disease. Its data show that around one-third of cognitively normal people aged over 65 have amyloid plaques in their brains, and that more than 85% of them will go on to develop symptoms of Alzheimer's within 10 years⁷.

On this basis, three large, placebo-controlled clinical trials are under way, each recruiting more than 1,000 people who are cognitively fit but have brain plaques, as seen by PET scanning. Each trial is testing a different antibody. All three will run for four years, by which time cognitive decline is usually measurable after plaques begin to accumulate.

Aisen's institute is coordinating the A4 trial — Anti-Amyloid treatment in Asymptomatic Alzheimer's — which is testing the Lilly drug solanezumab. Results are expected next year. Aisen also co-leads the AHEAD 3-45 trial, which began in 2020 and is testing lecanemab. That same year, Lilly started a trial called-Alz 2 with donanemab. And this year, Roche is launching its own phase III trial with gantenerumab, which will run for sixyears.

The costs of such trials “is typically hundreds of millions of dollars”, says Aisen. Just recruiting the 1,169 participants in the A4 trial required around 4,500 PET scans, each costing an average of US\$7,000. “But costs to society of this disease in terms of suffering, mortality and economic impact justify enormous investments in effective treatment,” he says.

In recent years, there has been substantial progress in developing simpler, [blood-based biomarkers of Alzheimer's disease](#). Two of these prevention trials are using such biomarkers to help select people for PET screening, chipping away at the cost of PET scans and the inconvenience for participants. One biomarker measures the ratio of two slightly different forms of amyloid- β , and another measures a tau-related molecule.

So far, the preventive trials all use antibodies against amyloid- β . These drugs have two disadvantages. They can have side effects: small brain bleeds or swellings, which are mostly harmless, but which can be serious. And they are expensive. Biogen initially fixed its price of a year's treatment with aducanumab at \$56,000, although it halved it in December 2021.

But the field is thinking about revisiting simpler, small-molecule drugs, which would be much cheaper to produce than antibody-based therapies. Some companies are starting to consider revisiting the secretase enzymes, says Aisen, perhaps tweaking the structure of the enzyme-blocking molecules that failed in early trials, or finding better ways to administer them.

Complex causes

Researchers in the field are aware that addressing dementia also requires an effort beyond amyloid- β . “Alzheimer’s disease is more complex,” says neurobiologist Roger Nitsch, one of the original developers of aducanumab at the University of Zurich, Switzerland. “Amyloid is a very slow-burning neurotoxin which initiates the disease, but brain cells — including those connecting to blood vessels and cells of the immune system — fight back.” There will be more ways to target established disease, he says. Also, only around two-thirds of all dementias are of the Alzheimer’s type, and post-mortem studies show that half of these have mixed pathology —the brains contain other toxic proteins in addition to amyloid and tau, or signs of blood-vessel damage.⁸

Prevention trials are important and promising, says NIA director Richard Hodes, “but we are not giving up on people who already have disease”. Because there will probably be multiple contributors to dementia — even in the same individual — a range of treatments will be needed, he says. The NIA is funding 72 clinical trials for dementia, trialling drugs aimed at various targets. Some, for example, aim to lower blood pressure to reduce the risk of small blood vessels breaking in the brain; others target tau. Only 20 target amyloid. The NIA is also supporting at least 120 trials to study the impact of non-pharmacological interventions, such as cognitive training, exercise and diet.

Researchers estimate that, in 2021, a total of at least 126 different agents — including those in NIA studies — were being investigated in clinical trials around the world.⁹

As a volunteer, Reiswig has had to accept the special burden that his particular trial brings — not just the time commitment, but also the constant reminders of the fate that awaits him if the trial drug doesn’t work. It helps, he says, that the DIAN consortium brings participants from all over the world together once a year to share their experiences. “We’ve created a wonderful community and we know we contribute strongly to science.”

doi: <https://doi.org/10.1038/d41586-022-00651-0>

References

1. Goate, A. *et al.* *Nature* **349**, 704–706 (1991).
2. Uhlmann, R. E. *et al.* *Nature Neurosci.* **23**, 1580–1588 (2020).
3. Glenner, G. G. & Wong, C. W. *Biochem. Biophys. Res. Commun.* **122**, 1131–1135 (1984).
4. Ikeda, S., Yanagisawa, N., Allsop, D. & Glenner, G. G. *Lab. Invest.* **61**, 133–137 (1989).
5. Gordon, B. A. *et al.* *Lancet Neurol.* **17**, 241–250 (2018).
6. Salloway, S. *et al.* *Nature Med.* **27**, 1187–1196 (2021).
7. Donohue, M. C. *et al.* *JAMA* **317**, 2305–2316 (2017).
8. Kapasi, A., DeCarli, C. & Schneider, J. A. *Acta Neuropathol.* **134**, 171–186 (2017).
9. Cummings, J., Lee, G., Zhong, K., Fonseca, J. & Taghva, K. *Alzheimers Dement.* **7**, e12179 (2021).

This article was downloaded by **calibre** from <https://www.nature.com/articles/d41586-022-00651-0>

Books & Arts

- **[A tour of the evolution of minds](#)** [07 March 2022]
Book Review • An informative guide takes in archaea, birds, primates and more — overconfidently.
- **[Microbes are the future, and the joy of games: Books in brief](#)** [18 February 2022]
Book Review • Andrew Robinson reviews five of the week's best science picks.

- BOOK REVIEW
- 07 March 2022

A tour of the evolution of minds

An informative guide takes in archaea, birds, primates and more — overconfidently.

- [Philip Ball](#) 0



A male bowerbird creates an intricate arrangement of found objects to attract a mate. Credit: Martin Willis/Nature Picture Library

Journey of the Mind: How Thinking Emerged from Chaos *Ogi Ogas and Sai Gaddam* W. W. Norton & Company (2022)

Look through a microscope at a macrophage cell pursuing, engulfing and consuming a bacterium, and it is hard not to impose a narrative: one is trying to catch the other, which is in turn trying to escape. In *Journey of the Mind*, neuroscientists Ogi Ogas and Sai Gaddam imply that this interpretation is not fanciful. They argue that minds of a sort have existed since the first archaea colonized the planet, billions of years ago.

Ogas and Gaddam's tour of the evolution of minds starts with the first cells on Earth and continues from flatworms to insects, reptiles and mammals. Along the way, biological brains amass sophisticated functions and capabilities, from navigation to memory, pattern recognition and sociality. The story doesn't end with humans: the authors argue that civilizations represent a kind of collective super-mind, augmented with wholly artificial AI minds. The narrative is enjoyable and illuminating, but it is flawed by a failure to separate fact from speculation.

The book offers an admirable survey of how minds might comprise modules that control simple operations, which are combined to solve complex problems of survival. For instance, a bacterium can move towards food sources thanks to motor systems that switch between directional swimming and random tumbling, depending on how it senses nutrient concentrations changing in its environment. In this way, a spatial problem acquires a temporal solution — how does the situation now compare with a moment ago? — and the microbe acquires a memory of sorts.

A rat finding food in a maze breaks down a visual scene into component features of edges, foreground and so on. And there's more: the rat mind holds a complex internal representation of the world against which to compare sensory input; it is constantly checking this inner map. The authors lean here towards the 'free-energy minimization' model proposed by neuroscientist Karl Friston and others, in which organisms strive to shrink the mismatch between expectation and experience.

Ogas and Gaddam take a very broad view of mind as "a physical system that converts sensations into action". At face value, this grants a mind to thermostats and robots as much as to living entities. "A mind responds. A mind transforms. A mind acts," they write. But the same is true of many machines. What, then, distinguishes a mind? If it's sentience or awareness,

the authors give a confusing picture. They say the “self-awareness” of an amoeba is “piddling” — and later seem to deny this quality to all organisms except vertebrates.

Many assertions go beyond the facts. The discussion of consciousness rests on the belief that the problem has been solved by cognitive scientist Stephen Grossberg (whom the authors thank for “guidance and support”). Since the late 1960s, Grossberg has developed the idea that consciousness arises from ‘resonance’ between specific modules of the brain. Ogas and Gaddam are vague about what resonance means here, beyond saying that the modules amplify and prolong each other’s outputs, and they give the reader little indication of what empirical evidence exists to support the idea. Grossberg’s theory is provocative and stimulating, but, couched in the abstract mathematical framework of dynamical systems theory, it remains contingent on his supposition that “all conscious states are resonant states”. I’m not convinced it amounts to the revolution that the authors assert.

There are many other proposals for what consciousness is and how it arises. Better-known is global workspace theory, championed in the past three decades by Bernard Baars, Stanislas Dehaene and others. They present consciousness as a phenomenon of information exchange in the brain, positing that awareness simply ‘ignites’ once certain criteria in the interaction of brain circuits are satisfied. Their corollary is that this would apply to any information-processing circuits with the correct architecture. Others, including neuroscientist Anil Seth, suspect that consciousness might be supported by only certain kinds of entities — as far as we know right now, ones that are alive. Ogas and Gaddam jump the gun, in my view, when they suggest that Grossberg has all the answers.

There are other instances in which they present contentious ideas with certainty. For all of the minds they discuss, much remains open. They write that birds didn’t develop language “because they don’t have hands”, but in fact it’s still debated whether gestures helped lead to the origin of language. They state that insects have no consciousness, when there is good reason to suppose that bees, at least, have many of the mental attributes associated with consciousness, such as foresight and the ability to imagine. Even bacteria are not the simple automata portrayed here; other researchers describe bacterial behaviours in the language of cognition.

The structure of a progression from the seemingly simple minds of bacteria and amoebas to the complex ones of primates makes narrative sense, but recalls the outdated image of evolution with humans at the apex. Our minds do excel in certain respects, most obviously in developing language and complex culture — but in dexterity, vision, navigation and more, other species eclipse us. There is more than a hint that evolution is striving to a particular end in Ogas and Gaddam's suggestion that, once early single-celled organisms acquired the ability to sense and move, "the royal road to consciousness beckoned".

The authors deploy some unedifying metaphors to tell their tale. One is the story of the nineteenth-century US anti-slavery campaigner Frederick Douglass, offered (I think) in an attempt to illustrate the social construction of the self. And they trivialize a pivotal social moment when they compare the mind's attentive focus to the media presentation of the murder of George Floyd in Minneapolis in 2020.

There is plenty to like in *Journey of the Mind*. It is so often informative and entertaining that it feels mean to cavil. But the book exemplifies a persistent problem in popular science, in which pet theories are presented with too much confidence and too little context. Readers deserve the full picture — less definitive and satisfying, perhaps, but ultimately more honest and illuminating.

Nature **603**, 221-222 (2022)

doi: <https://doi.org/10.1038/d41586-022-00652-z>

This article was downloaded by **calibre** from <https://www.nature.com/articles/d41586-022-00652-z>

- BOOK REVIEW
- 18 February 2022

Microbes are the future, and the joy of games: Books in brief

Andrew Robinson reviews five of the week's best science picks.

- [Andrew Robinson](#) 0

THE GENESIS MACHINE

OUR QUEST TO REWRITE LIFE IN THE
AGE OF SYNTHETIC BIOLOGY



AMY WEBB +
ANDREW HESSEL

The Genesis Machine

Amy Webb & Andrew Hessel *PublicAffairs* (2022)

Two moving stories bracket this fascinating survey of the present and future of biotechnology. Futurist Amy Webb and synthetic biologist Andrew Hessel describe their attempts to bypass personal fertility struggles by using cutting-edge technologies. Very soon, they argue, such difficulties could be obsolete, thanks to a “genesis machine” of people, labs, computer systems, government agencies and businesses that are “creating new interpretations, as well as new forms, of life” — along with unprecedented ethical, legal and political dilemmas.

Seven Games



A HUMAN HISTORY

Oliver Roeder

Seven Games

Oliver Roeder Norton (2022)

In a cautionary Aesop fable, a grasshopper asks an ant to play games on a summer day, rather than seeking food for winter. Ant refuses. Come winter, ant eats well; grasshopper goes hungry. But to journalist Oliver Roeder, the ludic grasshopper is the “diligent hero”. Roeder’s appealing biography of seven games — draughts (checkers), backgammon, chess, Go, poker, Scrabble and bridge — explores why play is both fascinating and necessary. Judging by the pandemic boom in online games, especially chess and Scrabble, many agree.

"A witty and compelling account of the many unexpected ways space rocks have impacted life on Earth. Brennecka's enthusiasm for his subject is utterly contagious."

—LEWIS DARTNELL, professor and author of *Origins: How the Earth Shaped Human History*

IMPACT

How Rocks

from Space

Led to Life,

Culture,

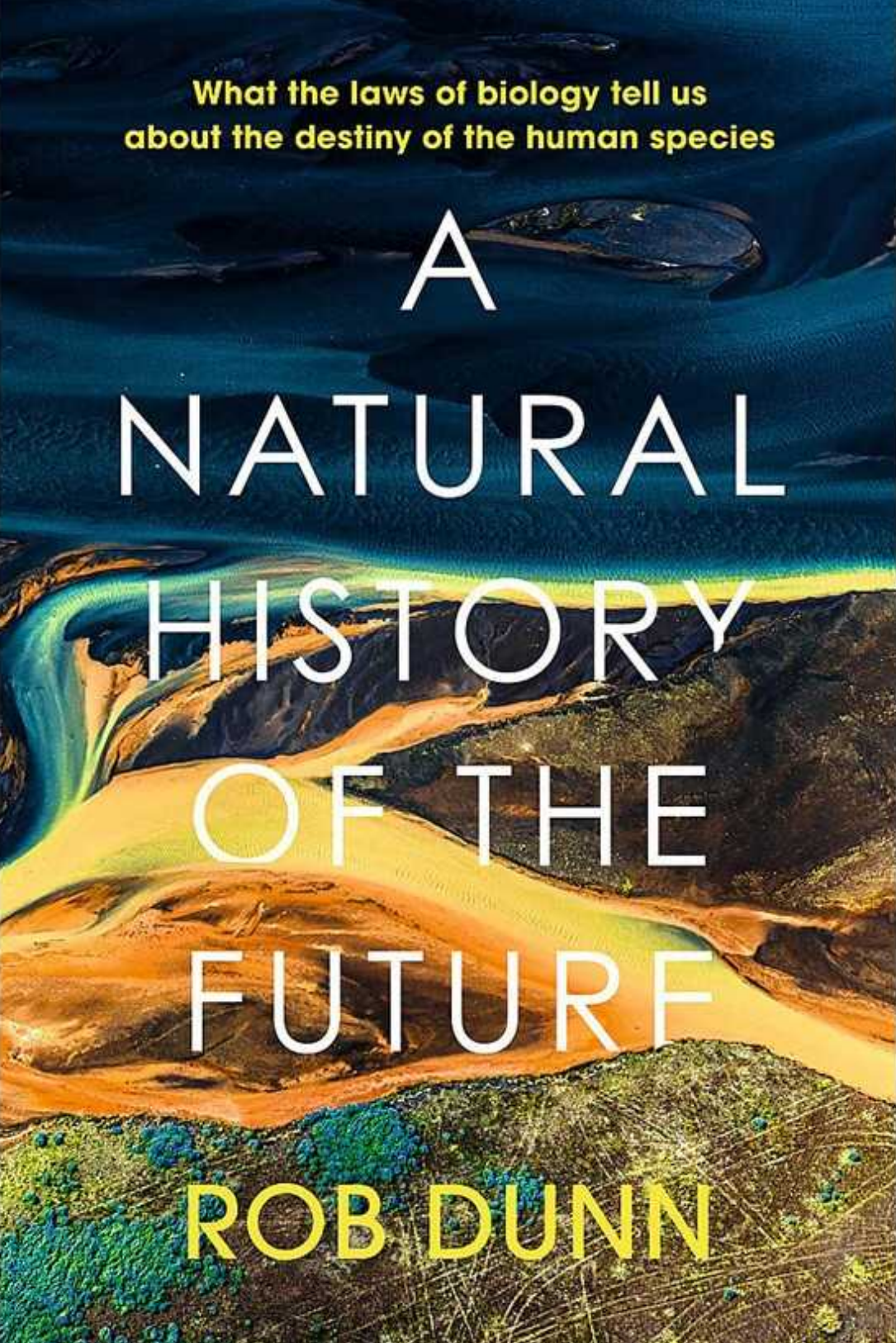
and Donkey Kong

**GREG
BRENNECKA**

Impact

Greg Brennecka *William Morrow* (2022)

Some meteorites contain diamonds older than the Sun, along with, astonishingly, predominantly left-handed amino acids and large amounts of water — the ingredients of life on Earth. Did meteors feature in the inception of the Solar System and of life? “To study meteorites truly is about studying origins,” concludes Greg Brennecka, one of only about 100 full-time, professional meteoricists around the world. His far-ranging and entertaining study deserves to win converts, although its ‘pop’ comparisons can be off-putting.



What the laws of biology tell us
about the destiny of the human species

A NATURAL HISTORY OF THE FUTURE

ROB DUNN

A Natural History of the Future

Rob Dunn *Basic* (2021)

“Most depictions of the future do not even include non-human life, except on distant farms (tended by robots) or in indoor gardens,” notes ecologist Rob Dunn. This is misleading, argues his articulate study of the relationship between humans and other life. Non-human life will survive us, suggests an experiment by microbiologist Michael Baym: bacteria exposed to increasingly concentrated antibiotics evolved resistance in just 10–12 days. Microorganisms will probably dominate the post-human world, as in the beginning of life on Earth.

BEN RAWLENCE

The Treeline



THE LAST FOREST
and the
FUTURE OF LIFE ON EARTH

The Treeline

Ben Rawlence *Jonathan Cape* (2022)

The concept of a fixed treeline, beyond which trees will not grow, has become redundant because of climate change. In the boreal forest encircling the globe, “the trees are on the move” towards the North Pole, notes writer and environmental activist Ben Rawlence. Having seen this migration for himself, he writes with accuracy, beauty and urgency about six key treeline species: Scots pine in Scotland, birch in Scandinavia, larch in Siberia, spruce in Alaska, poplar in Canada and mountain ash in Greenland.

Nature **603**, 222 (2022)

doi: <https://doi.org/10.1038/d41586-022-00485-w>

This article was downloaded by **calibre** from <https://www.nature.com/articles/d41586-022-00485-w>

| [Section menu](#) | [Main menu](#) |

Opinion

- **[Luc Montagnier \(1932–2022\)](#)** [04 March 2022]
Obituary • Virologist who won a Nobel prize for discovering HIV.
- **[Rewilding Argentina: lessons for the 2030 biodiversity targets](#)** [07 March 2022]
Comment • A foundation that turns private land into national parks is reintroducing native species to restore ecosystems and build ecotourism.
- **[President of National Academy of Sciences of Ukraine calls for solidarity](#)** [08 March 2022]
Correspondence •
- **[Pandemic preparedness — Europe launches research consortium](#)** [08 March 2022]
Correspondence •
- **[Proactive investment for virus research](#)** [08 March 2022]
Correspondence •
- **[Use of ‘nano’ prefix is no small matter](#)** [01 March 2022]
Correspondence •

- OBITUARY
- 04 March 2022

Luc Montagnier (1932–2022)

Virologist who won a Nobel prize for discovering HIV.

- [Heidi Ledford](#)



Credit: Jean Guichard/Gamma-Rapho/Getty

Luc Montagnier rose to scientific prominence and won a Nobel prize for co-discovering HIV. His work made it possible to develop diagnostic tests and treatments that have saved countless lives. He spent his later years dismantling that hard-won reputation by espousing fringe theories and opposing vaccination. His baseless claims about COVID-19 — that vaccines

would drive the emergence of dangerous variants, or that the virus was engineered — were weaponized by misinformation campaigns. He died on 8 February at the age of 89.

Montagnier was born on 18 August 1932 in Chabris, France. The Second World War marked his childhood with hunger and uncertainty, but his interest in science blossomed early. He embarked on the activity that has spawned countless researchers: tinkering with explosive compounds in a home laboratory. Later, he rigged a time-lapse camera to a microscope and studied chloroplasts' response to light. He was inspired to become a virologist after learning of the 1957 discovery that RNA from the tobacco mosaic virus could transmit infection.

Montagnier worked in several laboratories before landing at the Pasteur Institute in Paris in 1972, building up his virology expertise along the way. He specialized in retroviruses — RNA viruses that can insert a DNA copy of their genetic material into the genome of their host. This, along with advances in culturing immune cells and his use of reagents that block antiviral proteins called interferons to awaken dormant retroviruses in cells, came in handy in 1983. A colleague sent him lymph node tissue taken from a French fashion designer thought to be in the early stages of AIDS.

At the time, when people were diagnosed with AIDS, they were often already living with a variety of infections, cancers and other disorders that complicated the search for the source of the disease. Researchers speculated wildly: some blamed fungi or chemical exposure. Others saw that a class of immune cells called CD4⁺ T cells were depleted in people with AIDS, and wondered whether the body's immune system was targeting them.

Montagnier was reminded of a known retrovirus that could infect CD4⁺ T cells, and that was transmitted through blood and sexual activity.

In Montagnier's virology unit at the Pasteur Institute, Françoise Barré-Sinoussi isolated a new retrovirus from the lymph node biopsy; the team called it lymphadenopathy associated virus (LAV; [F. Barre-Sinoussi et al. Science 220, 868–871; 1983](#)). When, in September 1983, Montagnier presented the results at a small, late-night session of a scientific meeting at Cold Spring Harbor Laboratory in New York, his audience was sceptical.

“This situation is not infrequent in science, since new discoveries often raise controversy,” he wrote in his Nobel prize biography.

Soon after that presentation, a team led by virologist Robert Gallo, then at the US National Cancer Institute in Bethesda, Maryland, helped to solidify the link between AIDS and the virus that Montagnier’s team had found (formally named HIV in 1986). Gallo had previously discovered other retroviruses that infect human cells, called human T-lymphotropic virus (HTLV)-I and HTLV-II. In 1984, his team isolated a retrovirus from samples taken from people with AIDS, and he called it HTLV-III. But it turned out to be identical to LAV, samples of which Montagnier had supplied to his lab.

The two teams then waged an epic patent war over who should have the intellectual-property rights to a diagnostic test based on the virus. Finally, in 1987, peace was brokered by US president Ronald Reagan and French prime minister Jacques Chirac, who agreed to divide the royalties from the test between the two countries, and to establish an international AIDS research and education fund.

Given this history, many were surprised when, in 2008, Gallo did not receive a share of the Nobel prize. Instead, Montagnier shared the prize for physiology or medicine with Barré-Sinoussi; virologist Harald zur Hausen was also honoured, for his unconnected discovery that human papillomaviruses are linked to cervical cancer.

After the discovery of HIV, Montagnier’s work took a dismaying turn. He published a series of controversial articles claiming that highly diluted DNA from some pathogens emits electromagnetic waves. He invoked the debunked notion of ‘water memory’, arguing that the water is altered by the DNA in a way that retains some properties of the molecules even when they have been heavily diluted. (The concept of water memory had been championed by French immunologist Jacques Benveniste in a 1988 *Nature* paper that was later found to be irreproducible ([J. Maddox et al. *Nature* 334, 287–290; 1988](#))). At the age of 78, Montagnier left France to lead a research institute at Shanghai Jiao Tong University in China, to study the matter.

Over time, Montagnier seemed not only to be comfortable with controversy, but to court it. He embraced homoeopathy and pseudoscientific ideas about

autism. “He reached a stage where no researchers were able to provide comments or explanations for his late evolution,” says Bernard Meunier, former president of the French Academy of Sciences. Others were more direct: “Luc Montagnier has lost it,” wrote *Science* columnist and chemist Derek Lowe in 2012.

During the COVID-19 pandemic, Montagnier’s Nobel prize lent weight to his damaging views that the COVID-19 vaccine could be harmful. By the end of his life, the image of his face was circulating on social media in anti-vaccination memes. Hard to credit that it had once been on commemorative postage stamps in honour of his contributions to public health.

Nature **603**, 223 (2022)

doi: <https://doi.org/10.1038/d41586-022-00653-y>

This article was downloaded by **calibre** from <https://www.nature.com/articles/d41586-022-00653-y>.

| [Section menu](#) | [Main menu](#) |

- COMMENT
- 07 March 2022

Rewilding Argentina: lessons for the 2030 biodiversity targets

A foundation that turns private land into national parks is reintroducing native species to restore ecosystems and build ecotourism.

- [Emiliano Donadio](#)⁰,
- [Sebastian Di Martino](#)¹ &
- [Sofia Heinonen](#)²



Ecologist Marianela Masat checks on a giant anteater and her pup after the animals were reintroduced to the Iberá wetlands in Argentina. Credit: Rafael Abuin

When Mariuá, a 1.5-year-old female jaguar, set foot in our breeding centre in Argentina in December 2018, we did not know that she would make history. Two years later, she walked out with two cubs: the first jaguars to roam the 1.4 million hectares of the Iberá wetlands of northeastern Argentina for at least 70 years. Mariuá and her cubs have started to reverse a process that some had thought irreversible.

Within decades, one million species out of a total of some eight million could go extinct globally¹. Hunting, habitat loss and ecosystem degradation are propelling this unprecedented biodiversity crisis. Current extinction rates are 100 to 1,000 times higher than in the past several million years.

Argentina is no exception. Over the past 150 years, 5 bird and 4 mammal species have gone extinct. Today, about 17% of the country's 3,000 vertebrate species are imperilled², and 13 out of the 18 extant species of large mammal, from anteaters to tapirs, are experiencing catastrophic declines, in terms of both number and geographical range (see <http://cma.sarem.org.ar>).

In 1998, we started a rewilding programme in Argentina to try to reverse this appalling loss. Our non-profit foundation, Fundación Rewilding Argentina, was spun out from the US non-profit organization Tompkins Conservation. We create protected areas where we can reintroduce native species, re-establish their interactions, restore ecosystem functionality and build valuable ecotourism based on wildlife viewing.

Both rewilding and ecotourism can be controversial. We think that our work is an instructive example of how active restoration of crucial species, when done responsibly, can benefit both ecosystems and local people. It should be in the toolkit for meeting the 2030 biodiversity targets that will be discussed at the Convention on Biological Diversity's Conference of the Parties in Kunming, China, next month.

Three steps

The popularity of rewilding projects is growing. These include: wolves brought back to Yellowstone National Park in Wyoming, beavers to England, bison and musk ox to northern Russia, leopards to Mozambique and Tasmanian devils to mainland Australia. The International Union for Conservation of Nature reports that, since 2008, at least 418 reintroduction projects have been started³. Most of these projects occur in protected areas and involve one or a few species. Our work in Argentina is broader.

As a first step, we acquire private lands with philanthropic funds, reintroduce many species and form government-protected areas that are donated to federal and provincial governments. So far, we have purchased and donated about 400,000 hectares, with an estimated market value of US\$91 million. This has created and enlarged six national parks, one national reserve and two provincial parks. Another 100,000 hectares are

being donated. Together, these lands comprise a little over 10% of the total terrestrial area currently managed by the National Parks Administration of Argentina.

The second step is to restore ecosystems, mainly by reintroducing species at an unprecedented scale. We spend more than \$3 million each year on rewilding activities in three regions: the Iberá wetlands in the northeast, the dry Chaco forests in the north and the Patagonian steppe and coast in the south. Most often, we work with species deemed to have large impacts at the ecosystem level, such as large predators and herbivores.



Jaguars now roam Argentina's Iberá wetlands for the first time in more than 70 years.Credit: Matías Rebak

Thus far, we have successfully reintroduced pampas deer, giant anteaters and collared peccaries (a pig-like, hoofed animal). We have also started founding populations of jaguars, coypus (large aquatic rodents), Wolffsohn's viscachas (rodents that resemble a large chinchilla), red-and-green macaws and bare-faced curassows (birds related to chickens and pheasants). We are currently working on the reintroduction of 14 species.

As they become abundant, reintroduced species re-weave the fabric of ecological relationships. For example, jaguars (*Panthera onca*) and macaws (*Ara chloropterus*) are reviving a crucial interaction: predation. Jaguars have begun to prey on eight species, including native rodents and feral hogs, which could limit those populations and thus benefit vegetation growth. The macaws are consuming 49 plant species, which could enhance seed dispersal, although this remains to be tested.

Third, we invest heavily in infrastructure, capacity building and publicity to create an economy based on ecotourism. The species we work with are often highly charismatic, which benefits local communities, creating an economic incentive to conserve native wildlife and habitats. We organize workshops and courses so that locals can train as nature guides, cooks, craftspeople and more. In Iberá, where our work is most advanced, tourist visits increased by 87% between 2015 and 2021, according to official data from the Iberá wetland management agency. There were more than 50,000 visitors last year, despite the COVID-19 pandemic.

All of these steps are important: simply setting aside protected areas is not enough. Globally, most modern ecosystems are ecologically damaged⁴, even in long-standing protected areas⁵. In Argentina, for example, functional populations of jaguars are missing from 19 of 22 national parks where historical distribution data suggest this key apex predator should occur.

Jaguars and capybaras

Our flagship project is the rewilding of the Iberá wetland. There, we are working on the restoration of nine species, including jaguars, which were eradicated from this area more than 70 years ago. We have now established a founding population of eight individuals: one adult male and three adult females, two of which (including Mariuá) were each released with two cubs aged four months. Our goal is to release a total of 20 individuals by 2027.

Of all the species we work with, giant otters (*Pteronura brasiliensis*) and macaws have been the most difficult. Both species are extinct in the wild in Argentina. Bureaucratic hurdles have made sourcing wild individuals from neighbouring countries impossible.

We obtained two pairs of giant otters from European zoos, and are holding them in pens in the core of Iberá. After several attempts, one pair bred successfully and the female gave birth to three cubs, producing the first litter born in the country for more than 30 years. We plan to release this family to the wild next year.



This female giant river otter, together with a male and their three cubs, will be released to the wild in Argentina next year to create a founding population. Credit: Matías Rebak

We source macaws, which have been extinct in the wild in Argentina for 100 years, from zoos, wildlife shelters and breeding centres. Because of their captive origin, we must give them the opportunity to practise flying in an aviary. We provide them with native foods, so that they learn what to eat, and we use a remote-controlled stuffed fox to teach them to avoid predators. This training isn't always successful. Out of the 87 macaws that we have worked with, 48 were healthy and skilled enough to release. Two founding populations now thrive in the wild; one of them began reproducing in 2020.

Efforts elsewhere have demonstrated the powerful effects of restoring species. In the northeast Pacific Ocean, reintroduced sea otters (*Enhydra lutris*) have voraciously eaten sea urchins, which in turn has allowed the return of lush kelp forests⁶. In Yellowstone Park, some researchers argue that reintroduced wolves have discouraged herbivores from foraging along stream edges, which might have increased tree growth and stabilized stream banks⁷. In Mozambique's Gorongosa Park, the return of wildebeest and other large herbivores has curtailed *Mimosa pigra*, an undesirable invasive shrub⁸.

Our rewilding work in Argentina could also have profound impacts. Close monitoring of the female jaguars and their cubs in the Iberá wetland has shown that they are largely feeding on the most abundant native prey: capybaras (*Hydrochoerus hydrochaeris*). Reducing the number of capybaras is expected to allow more vegetation to thrive, providing habitat for arthropods and small vertebrates, and possibly increasing carbon sequestration⁹. It could also help to reduce the transmission of sarcoptic mange, a density-dependent disease plaguing the capybara population. Jaguars also prey on foxes, which might benefit threatened bird species. We are working with several academic institutions to test how the return of the jaguar is reshaping the ecosystem.

Challenges and caveats

As our rewilding work gained momentum, critics ramped up from different fronts. At first, some were fearful of our policy of acquiring private lands with funds provided largely by foreign philanthropists. Those concerns faded when we began donating the land to federal and provincial governments.

Then, ranchers argued that we were taking agricultural land out of production and reintroducing or boosting populations of animals that would conflict with their livestock. For example, in Patagonia, we established several protected areas where pumas (*Puma concolor*) and guanacos (*Lama guanicoe*, a relative of the llama) thrive. For almost a century, ranchers have trapped, shot and poisoned these animals, blaming them for killing sheep and competing for forage, respectively. We are conducting research to

quantify the impact of pumas and guanacos on livestock, and offering alternative job opportunities based on wildlife viewing.



Red-and-green macaws went extinct in Argentina in the late 1800s. Rewilding efforts that began in 2016 have now established two founding populations in the Iberá wetlands. Credit: Matías Rebak

Federal and state managers, and often academics, argue that some founding populations of reintroduced species are too small and genetically related to create a viable, long-term population. This is true in some cases. But careful releases of unrelated animals can sidestep this issue. Worries about the spread of diseases when translocating individuals is also often invoked as a reason to halt rewilding activities. We implement thorough health checks and rigorous quarantines to decrease the risk of introducing unwanted diseases in the regions where we work.

Concerns are sometimes raised about whether reintroduced species will recreate historical conditions, or instead create something new. Rewilding, however, seeks to regenerate and maintain ecological processes and biodiversity, rather than reaching some specific, historical equilibrium¹⁰. We

think it is preferable to assume the uncertainties in trying to restore ecosystems, rather than accepting their degraded state.

Another worry is the possible impacts that tourism can have on climate, biodiversity and society — for instance, on water use, aviation emissions, road building and so on. Our strategy is to limit visitor numbers and avoid crowding by constructing multiple access gates on existing dirt roads.

There are many policies that hinder rather than help rewilding. In Argentina, the laws that regulate transportation of wildlife species are built on the assumption that such activities always represent a threat to conservation. Wild animals can typically be imported to the country only through an airport in Buenos Aires. Because of this, an animal that could be driven in a truck from Brazil in a few hours must instead fly more than 1,500 kilometres and then be driven all the way back to its release area. Receiving wild animals at another international port, or moving them around within the country, requires special permits that often take months to obtain. Regulations could be altered to ease rewilding efforts while still policing the illegal wildlife trade.

Next steps

Nature-based tourism has been growing globally at rates of more than 4% per year, particularly in low- and middle-income countries¹¹. Charismatic fauna, including large predators, are becoming increasingly important. In the Brazilian Pantanal, the world's largest wetland, wildlife viewing — mostly of jaguars — generated an annual revenue of \$6.8 million in 2015. This is three times the revenue obtained from traditional cattle ranching in that region¹².

With about 97% of the planet's land surface ravaged by humans⁴, nature is facing its last stand. Urgent measures are needed not only to halt but also to reverse ecosystem and biodiversity loss. The active reintroduction of key species is one powerful way to heal some degraded ecosystems.

This daunting task should not fall solely to non-profit organizations that have limited funds and staff, like us. The United Nations launched its

Decade on Ecosystem Restoration in June 2021, calling for massive restoration efforts worldwide to heal nature and the climate. To achieve meaningful results at a global scale, rewilding needs the support of many stakeholders and effective international cooperation. Crucially, it requires the active involvement of governments to facilitate, fund and lead restoration efforts.

Nature **603**, 225–227 (2022)

doi: <https://doi.org/10.1038/d41586-022-00631-4>

References

1. IPBES. *Summary for Policymakers of the Global Assessment Report on Biodiversity and Ecosystem Services of the Intergovernmental Science-Policy Platform on Biodiversity and Ecosystem Services* (eds Diaz, S. *et al.*) (IPBES, 2019).
2. Bauni, V. *et al.* *Zookeys* **1085**, 101–127 (2022).
3. Soorae, P. S. (ed.) *Global Conservation Translocation Perspectives: 2021. Case Studies from Around the Globe* (IUCN SSC Conservation Translocation Specialist Group, Environment Agency — Abu Dhabi & Calgary Zoo, 2021).
4. Plumptre, A. J. *et al.* *Front. For. Glob. Chang.* <https://doi.org/10.3389/ffgc.2021.626635> (2021).
5. Jones, K. R. *et al.* *Science* **360**, 788–791 (2018).
6. Estes, J. A. & Duggins, D. O. *Ecol. Monogr.* **65**, 75–100 (1995).
7. Allen, B. L. *et al.* *Food Webs* **12**, 64–75 (2017).
8. Guyton, J. A. *et al.* *Nature Ecol. Evol.* **4**, 712–724 (2020).
9. Schmitz, O. J. *et al.* *Science* **362**, eaar3213 (2018).

10. Svenning, J. C., Munk, M. & Schweiger, A. in *Rewilding* (eds Pettorelli, N., Durant, S. M. & Du Toit, J. T.) 73–98 (Cambridge Univ. Press, 2019).
 11. Balmford, A. *et al.* *PLoS Biol.* **7**, e1000144 (2009).
 12. Tortato, F. R., Izzo, T. J., Hoogesteijn, R. & Peres, C. A. *Glob. Ecol. Conserv.* **11**, 106–114 (2017).
-

This article was downloaded by **calibre** from <https://www.nature.com/articles/d41586-022-00631-4>

| [Section menu](#) | [Main menu](#) |

- CORRESPONDENCE
- 08 March 2022

President of National Academy of Sciences of Ukraine calls for solidarity

- [Anatoly Zagorodny](#) ⁰

As president of the National Academy of Sciences of Ukraine, I call on researchers around the world to bear witness to the tragedy occurring in my country.

Ukraine has a highly developed scientific and industrial complex and significant research potential. It has industries based around nuclear energy, mechanical engineering, aviation and space industries.

The National Academy of Sciences of Ukraine comprises more than 150 research institutions — known for their strengths in physics, material sciences and computing, among others. Many of these institutions are under military attack.

Along with killing Ukrainians, the barbarous Russian invasion aims to destroy infrastructure — both industrial and scientific. One unit seriously at risk is the Kharkov Institute of Physics and Technology's flagship nuclear facility, which is used for nuclear-physics and materials-science research and to create medical isotopes.

All of the academy's institutions are currently still managing to work online. However, the continual explosions and howl of air-raid sirens are making it increasingly difficult for many scientists to carry on with their research.

Ukraine now needs widespread support and massive practical help to end the bloodshed swiftly, to offer safety for our citizens and to rebuild.

Nature **603**, 228 (2022)

doi: <https://doi.org/10.1038/d41586-022-00668-5>

This article was downloaded by **calibre** from <https://www.nature.com/articles/d41586-022-00668-5>

| [Section menu](#) | [Main menu](#) |

- CORRESPONDENCE
- 08 March 2022

Pandemic preparedness — Europe launches research consortium

- [Audrey Richard ORCID: http://orcid.org/0000-0002-0207-0139](#)¹,
- [Diana Stepanyan](#)¹ &
- [Jonathan Ewbank ORCID: http://orcid.org/0000-0002-1257-6862](#)²

To improve Europe's responsiveness to pandemic-prone pathogens, as well as resilience against major infectious-disease threats, the European Union has launched a consortium called Integrated Services for Infectious Disease Outbreak Research (ISIDORe; see go.nature.com/3hdjmet).

Access options

Subscribe to Nature+

Get immediate online access to the entire Nature family of 50+ journals

\$29.99

monthly

[Subscribe](#)

Subscribe to Journal

Get full journal access for 1 year

\$199.00

only \$3.90 per issue

Subscribe

All prices are NET prices.

VAT will be added later in the checkout.

Tax calculation will be finalised during checkout.

Buy article

Get time limited or full article access on ReadCube.

\$32.00

Buy

All prices are NET prices.

Additional access options:

- [Log in](#)
- [Learn about institutional subscriptions](#)

Nature **603**, 228 (2022)

doi: <https://doi.org/10.1038/d41586-022-00669-4>

This article was downloaded by **calibre** from <https://www.nature.com/articles/d41586-022-00669-4>

- CORRESPONDENCE
- 08 March 2022

Proactive investment for virus research

- [Michael Head](#) ORCID: <http://orcid.org/0000-0003-1189-0531> ①

Soumya Swaminathan and her colleagues call for a reboot of biomedical research and development (R&D) for the global good ([Nature 602, 207–210; 2022](#)). I agree that a more proactive approach to R&D decision-making is needed to help improve preparedness, particularly in relation to infectious diseases (see, for example, go.nature.com/3hx7rgh).

Access options

Subscribe to Nature+

Get immediate online access to the entire Nature family of 50+ journals

\$29.99

monthly

[Subscribe](#)

Subscribe to Journal

Get full journal access for 1 year

\$199.00

only \$3.90 per issue

Subscribe

All prices are NET prices.

VAT will be added later in the checkout.

Tax calculation will be finalised during checkout.

Buy article

Get time limited or full article access on ReadCube.

\$32.00

Buy

All prices are NET prices.

Additional access options:

- [Log in](#)
- [Learn about institutional subscriptions](#)

Nature **603**, 228 (2022)

doi: <https://doi.org/10.1038/d41586-022-00670-x>

This article was downloaded by **calibre** from <https://www.nature.com/articles/d41586-022-00670-x>

- CORRESPONDENCE
- 01 March 2022

Use of ‘nano’ prefix is no small matter

- [Seyed M. Moghimi](#) ORCID: <http://orcid.org/0000-0003-0836-926X>
0

The overuse and misuse of the prefix ‘nano’ — to denote size on the nanometre scale — is creating a misleading terminology that threatens to undermine nanoscience. I urge scientists to instead use standard nomenclature and classification systems for precision and clarity in their communications.

Access options

Subscribe to Nature+

Get immediate online access to the entire Nature family of 50+ journals

\$29.99

monthly

[Subscribe](#)

Subscribe to Journal

Get full journal access for 1 year

\$199.00

only \$3.90 per issue

Subscribe

All prices are NET prices.

VAT will be added later in the checkout.

Tax calculation will be finalised during checkout.

Buy article

Get time limited or full article access on ReadCube.

\$32.00

Buy

All prices are NET prices.

Additional access options:

- [Log in](#)
- [Learn about institutional subscriptions](#)

doi: <https://doi.org/10.1038/d41586-022-00537-1>

This article was downloaded by **calibre** from <https://www.nature.com/articles/d41586-022-00537-1>

Work

- **[Marching in the streets for climate-crisis action](#)** [22 February 2022]
Career Q&A • Conservationist Charlie Gardner explains why he joined Scientists for Extinction Rebellion and its civil-disobedience protests.
- **[An engineer advances fire-management laws in Colombia](#)** [23 February 2022]
Career Q&A • María Constanza Meza Elizalde wants to change fire laws and attitudes.
- **[Neuroscience saved my life and gave me a vocation](#)** [23 February 2022]
Career Q&A • Christin Godale campaigns for bigger research budgets and better care for people with epilepsy.
- **[Staring into the human genome to diagnose COVID](#)** [07 March 2022]
Where I Work • Bioinformatician Lucía Spangenberg is helping to make genetic sequencing available to anyone who needs it.

- CAREER Q&A
- 22 February 2022
- Correction [22 February 2022](#)

Marching in the streets for climate-crisis action

Conservationist Charlie Gardner explains why he joined Scientists for Extinction Rebellion and its civil-disobedience protests.

- [Christine Ro](#) ⁰



Charlie Gardner speaks at an Extinction Rebellion protest. Credit: Louise Jasper Photography

Conservationist, consultant and activist Charlie Gardner is an associate senior lecturer in conservation biology at the Durrell Institute of Conservation and Ecology at the University of Kent in Canterbury, UK. He regularly participates in protests with Scientists for Extinction Rebellion, an offshoot of [a broader movement](#) that uses nonviolent civil disobedience to push for action on the climate and biodiversity crises. He has also advised on legislation such as the [UK Climate and Ecological Emergency Bill](#), which seeks to curb UK greenhouse-gas emissions and biodiversity loss, and is currently making its way through Parliament.

What drove you to activism?

Teaching. Five or six years ago, I was standing in front of a lecture theatre, full of young people who are going to suffer the consequences of climate change much more than I am. I couldn't stand that I wasn't doing everything I could. When Extinction Rebellion (XR) was launched in the United Kingdom in October 2018, it felt like the answer. As conservationists, we silently wish that members of the general public cared more about the destruction of nature. Now they are taking to the streets and I have this moral obligation to be there in support.

How have you been working with Scientists for XR?

In October 2019, a group of scientists came together to create [Scientists for XR](#), which has carried out many actions. These include pasting scientific papers to the walls of the London headquarters of News Corp in 2021 in protest against inadequate climate-change coverage in the company's newspapers.

The group has different functions. One is to provide scientific support for the wider XR movement, so that it remains founded on solid scientific ground. And a second is to advocate. Scientists vocally supporting XR sends a powerful message. Society trusts scientists.

A third function is direct action. Scientists for XR groups have been involved in a number of XR events, such as marches and roadblocks. For example, at the 2021 opening of a London Science Museum exhibition sponsored by oil and gas company Shell, some scientists locked themselves to parts of the exhibition in protest against the sponsorship, while our scientist group set up a table outside to demonstrate principles of atmospheric cooling to engage with the public. Events such as this serve to highlight the issue of science museums accepting sponsorship from fossil-fuel companies.

How can scientists dip their toes into this type of work?

What the public sees of these direct actions is the tip of the iceberg. For every person out on the streets, there are 20 more behind the scenes involved in other tasks: organizing, producing press releases, baking cakes for marchers. Whatever you enjoy doing and have skills in, there is a role for you.

Taking part does not have to involve engaging in civil disobedience yourself, or putting yourself in a risky position. One of the most important jobs at a protest is for people to stand at the edges, engaging the public in conversations. That's a role that scientists can perform fantastically.

How have your advocacy and activism benefited you?

There's this crazy notion that scientists shouldn't speak out because it will damage their reputations. But activism has had the opposite effect on my career. My research is based on conservation in Madagascar; it's fairly niche. I previously had no global reputation. Since becoming a vocal scientist-activist, my reputation and my visibility as a scientist have soared.

Also, activism is great for my mental health. Knowing I'm doing what I can is important to me. There are simply the best people in these movements, and there's a sense of community.

Does being a vocal activist diminish your scientific credibility?

Popular perception holds that scientists must be neutral purveyors of information and not speak up about what that information means. Somehow, if we do so, it could damage our credibility.

But when scientists take personal risks and make personal sacrifices, that communicates the urgency of the situation in an important way. If scientists are saying that it's time for action, but not acting themselves, that undermines their own arguments.

How do you balance your academic responsibilities with advocacy?

For five years, I worked half-time at the University of Kent. I did this deliberately, to allow me the freedom to engage in other activities, including conservation consultancy, activism and writing popular non-fiction. I left that post last year, partly to focus on activism and writing, and partly out of frustration with the precarity of academic life.

There are things that enable me to be less single-minded in the pursuit of my career: I come from a position of relative privilege; I'm not interested in accumulating money; and I don't have children. So I think academia has been a good fit for me, but only because it doesn't fill my life.

Nature **603**, 349-351 (2022)

doi: <https://doi.org/10.1038/d41586-022-00518-4>

This interview has been edited for length and clarity.

Updates & Corrections

- **Correction 22 February 2022:** An earlier version of this story misstated Charlie Gardner's current job title; he is an associate senior

lecturer. The text has been updated.

This article was downloaded by **calibre** from <https://www.nature.com/articles/d41586-022-00518-4>

| [Section menu](#) | [Main menu](#) |

- CAREER Q&A
- 23 February 2022

An engineer advances fire-management laws in Colombia

María Constanza Meza Elizalde wants to change fire laws and attitudes.

- [Christine Ro](#) ⁰



Wildfires are becoming more frequent in the Orinoquía region of Colombia. Credit: María Meza

María Constanza Meza Elizalde is a forest engineer and PhD student at the National University of Colombia in Bogotá, where she researches fire

ecology and conducts fieldwork in hard-to-reach areas with recurring fire problems. With her adviser and other students in her research group, she's been drafting and lobbying for [legislation that aims to reduce fire risk overall](#), while recognizing diverse business and cultural practices related to fire.

Why is there a need for a science-backed fire-management bill?

I study the Orinoquía region, near the border with Venezuela. It's an area of extensive savannahs, where the number of wildfires is increasing, mainly because of activities such as hunting, along with agricultural burning that gets out of control. Landscape-management decisions, very frequent burning or total fire suppression in the savannah are also factors. And climate change is affecting the wildfire dynamics.

As a result, we are seeing changing patterns, with more frequent and intense wildfires in forest areas where they were not common before, and covering larger areas. This leads to forest degradation and to political decisions in which only the negative side of fire is seen.

Communities living in fire-dependent ecosystems know how to reduce risks, but environmental authorities don't recognize these practices. Right now, there are no laws or conservation strategies in Colombia that recognize the ecological role of fire.

How did you get involved in drafting fire legislation?

Because there were no public forums to talk about fires and develop strategies for reducing the risks, we began a dialogue with local communities about the problems and benefits of fires, while also involving non-governmental organizations, public entities, fire departments and national parks.

The great challenge is to articulate scientific, local and institutional knowledge to guarantee a fire-management plan that will result in safe and resilient landscapes. People think that only legislators can make laws. This is not true — citizens can propose them. We had the support of Congressman Mauricio Toro, who is a member of Colombia's Green Alliance party, and his technical legislative staff. We designed a bill that recognizes both scientific and ancestral, traditional knowledge, while respecting ecological heritage and regulations for integrated fire management. The bill would also promote research to develop strategies for reducing the risk of wildfires, and encouraging ecological restoration, environmental rehabilitation and recovery of natural ecosystems affected by forest fires.



Forest engineer María Constanza Meza Elizalde has helped to draft legislation to reduce wildfires. Credit: Arturo Cortés

How do you balance this advocacy work with your PhD commitments?

It is difficult. Fortunately, my network of academic and family support allows me to raise my voice. Dolors Armenteras, my PhD supervisor, listened to my suggestion and taught me and the rest of the group to organize ourselves and work collaboratively.

When it comes to research, all the students in the group have our own theses, but we are a team, whose research and joint work contribute to our influence in decision-making. Alone, we couldn't have had much impact.

Have you encountered people who don't take you or your science seriously?

At the regional and local levels, the reaction has been mostly positive. And although not all national-level institutions take us seriously, we've found that legislators, regardless of their political position, take our science-based recommendations seriously. For me, as a PhD student, it has been very gratifying to have support from members of all political parties.

As a woman, I have other challenges to being heard. Being a woman in discussion spaces where the majority of participants are men, it takes more time to build your confidence. For example, I am an early-career researcher but I am also an engineer and I have a master's degree. Yet, in some workspaces, people keep calling me a 'girl'.

What's your advice for early-career scientists who want to influence policy?

First, I want to express my admiration for scientists who work in remote areas affected by armed conflict. I know how difficult and even dangerous it is for environmental defenders to discuss controversial ideas to influence policies.

The greatest lesson I've learnt about the legislative process is how to communicate science more effectively and contribute to politicians' capacity for understanding complex scientific problems.

As scientists, we do not always consider other stakeholders' access to information, but it's important that research results reach interested parties outside academia in a timely manner.

A communication strategy that considers economic disparities or technological barriers is essential. For example, written pamphlets are useless in communities with high illiteracy. So our group has been incorporating different communication strategies, including an art exhibition and a radio soap opera, to make the messages more effective.

This feels important, because in Colombia, we have many problems of climate change and armed conflict. We're facing huge challenges but they are not insurmountable. If scientists work together, we can influence the attitudes and actions of communities and governments. The only way forward is collaborative work.

Nature **603**, 350-351 (2022)

doi: <https://doi.org/10.1038/d41586-022-00529-1>

This interview has been edited for length and clarity.

This article was downloaded by **calibre** from <https://www.nature.com/articles/d41586-022-00529-1>

- CAREER Q&A
- 23 February 2022

Neuroscience saved my life and gave me a vocation

Christin Godale campaigns for bigger research budgets and better care for people with epilepsy.

- [Christine Ro](#) ⁰



Christin Godale in the Danzer lab at Cincinnati Children's Hospital Medical Centre, Ohio, where she is doing her graduate studies. Credit: Christin

Godale

Christin Godale has lived with epilepsy since being diagnosed around the age of two. She credits neuroscience with saving her life and giving her a vocation; in 2016, she started a PhD in neuroscience at the University of Cincinnati in Ohio. Godale advocates for neuroscience funding, as both a patient and a scientist.

Describe your advocacy for neuroscience funding

I work with the US Society for Neuroscience (SfN) as an early-career policy ambassador. In this role, I have opportunities to meet policymakers, maintain relationships with the offices of elected officials and contribute to collaborative advocacy through phone calls, social media and letter-writing with the SfN.

We're advocating for increases in federal funding of \$49.4 billion for the US National Institutes of Health; \$612 million for the BRAIN Initiative, a research-technology project focusing on brain disorders; and \$904 million for neuroscience-related research at the US Department of Veterans Affairs.

We're also advocating for extra funding for federal research agencies to allow scientists to complete work halted by the COVID-19 pandemic, and to extend employment or training for people whose projects have been disrupted. The legislation to authorize this was introduced into the US House of Representatives in November 2021. This was a result, we think, of many scientist-advocates holding '[Hill Days](#)', events at which scientists discuss research with policymakers.

What support would you like to see for people with epilepsy?

I work on various local and national initiatives, including the Safe Step Act. This proposed federal legislation would allow exemptions from 'step therapy', whereby health insurers require patients to try, and fail on, multiple alternative medications before they can receive the drug initially prescribed

by their doctors. The process is meant to lower costs for the insurers, because some drugs are cheaper to prescribe; however, they might not be the correct ones for a specific case of epilepsy.

The act would exempt people with epilepsy from step-therapy protocols if they are stable on their anti-seizure medication or have already had a bad reaction to a treatment. Individuals with epilepsy who are forced by step therapy to go on multiple medications are at higher risk of developing breakthrough seizures¹, which can prove fatal.

Another bill, proposed in Ohio, would require publicly funded schools to create a ‘seizure action plan’ for each student with a seizure disorder. These plans include first aid and medication to help staff care for a student who has a seizure at school. Astonishingly, these plans are not commonly used or required in schools across the United States. I am campaigning for seizure action plans to be implemented at the University of Cincinnati.

How does your lived experience of epilepsy shape your science advocacy?

Navigating graduate studies while living with epilepsy was challenging at first, but my adviser, Steve Danzer, and my lab-mates have provided me with the support that I needed to be successful. A lot of that support is made possible because they understand epilepsy not only at a mechanistic level, but also at a personal level. My colleagues always make themselves available to help with experiments on days when I have an unexpected seizure; they also ask for resources to educate themselves on the patient perspective of epilepsy, and volunteer at events for [Epilepsy Alliance Ohio](#) in Cincinnati, part of the nationwide support network Epilepsy Alliance America.

Like many people with epilepsy, I rely on anti-seizure medications, which allow me to pursue my dreams and ambitions. Advocating for basic science is very personal for the epilepsy community and myself. Researchers should consider the voices of patient advocates when performing basic research, writing a grant application or giving a scientific presentation.

How has the pandemic affected your advocacy work?

Early in the COVID-19 crisis, my university shut down non-essential scientific research. When my lab was not in service, I had more time to focus on advocacy efforts, specifically with the SfN. I participated in the SfN's NeuroAdvocate Challenge, which encouraged US neuroscientists to attend meetings of the Congressional Neuroscience Caucus, a bipartisan group that raises awareness of neurological conditions and mental illnesses, and to support researchers affected by the pandemic.

The crisis also brought to light shortcomings in the academic system – explicitly, a lack of training in science communication, which is needed to battle misinformation and pseudoscience. Many universities are now trying to improve in this area.

How do you balance your advocacy and research with your personal life?

When I started my graduate programme, I would work an insane number of hours a day. However, my work and mental health suffered from the resulting burnout. I learnt that I needed to have my own time, to spend with my family and cats and to dabble in some of my hobbies, such as cooking and listening to true-crime podcasts. I wish I'd discovered a healthy work-life balance earlier on, but I'm happy that I finally found it.

Nature **603**, 352 (2022)

doi: <https://doi.org/10.1038/d41586-022-00548-y>

This interview has been edited for length and clarity.

References

1. Finamore, J. M. *et al. Epilepsia* **57**, 1294–1300 (2016).

This article was downloaded by **calibre** from <https://www.nature.com/articles/d41586-022-00548-y>.

| [Section menu](#) | [Main menu](#) |

- WHERE I WORK
- 07 March 2022

Staring into the human genome to diagnose COVID

Bioinformatician Lucía Spangenberg is helping to make genetic sequencing available to anyone who needs it.

- [Patricia Maia Noronha](#) ⁰

Lucía Spangenberg uses the Mk1c Sequencer to determine the DNA sequence of an organism or portions of the human genome.

Lucía Spangenberg is a bioinformatician affiliated with the Pasteur Institute of Montevideo in Uruguay and co-founder of the company GenLives. She is also a teacher at the Catholic University of Uruguay. Credit: Pablo Albarenga for *Nature*

In this picture I'm using a MinION Mk1C, a portable, cheap and easy-to-use DNA-sequencing machine, to detect SARS-CoV-2 in a nasal swab. This is part of the work the Pasteur Institute of Montevideo is doing to combat coronavirus in Uruguay. Our team has been analysing DNA samples from all over the country to detect clusters of the virus and its variants.

Doing genetic sequencing this easily is still exciting to me. About 20 years ago, this work was very time-consuming, and the price tag of sequencing the whole human genome was around US\$3 billion. Today, it can be done in a week for around \$1,000. That means the technology is increasingly available, and can help more people worldwide.

In 2002, when I finished secondary school, I was torn between studying biology and informatics. So, I googled ‘informatics and biology’ and the

term ‘bioinformatics’ came up. It was not something I’d ever heard of, but it combined the two subjects I loved most.

This field has such huge potential to help people with rare diseases, who might otherwise spend years without a correct diagnosis. This science can help to steer patients to better treatments.

That is why I and two colleagues formed a start-up, called GenLives. In Uruguay, genetic sequencing is still used mainly for research purposes. The goal of GenLives is to make it available to anyone who needs it. Since we started in 2015, we’ve helped hundreds of patients.

There are still illnesses that remain a mystery — about 50% of our cases remain unsolved, which is pretty standard in this sort of work. That is why, in this field, sharing your data is so important. One patient’s data could help with another person’s diagnosis. International DNA databases are growing fast, and I hope that, soon, all the remaining cases will be solved.

Nature **603**, 354 (2022)

doi: <https://doi.org/10.1038/d41586-022-00654-x>

This article was downloaded by **calibre** from <https://www.nature.com/articles/d41586-022-00654-x>

| [Section menu](#) | [Main menu](#) |

Research

- **[Self-assembly of molecules triggered by electricity](#)** [09 March 2022]
News & Views • The options for controlling molecular self-assembly processes have been limited. A fresh approach uses electrons to facilitate self-assembly, and thereby provides precise external control over the process.
- **[Epstein–Barr virus sparks brain autoimmunity in multiple sclerosis](#)** [15 February 2022]
News & Views • Understanding factors that lead to the development of multiple sclerosis might aid efforts to develop new therapies. Clinical data now implicate a viral culprit and immune-system dysfunction as underlying factors in this condition.
- **[Light arrays measure up on a chip the size of a fingertip](#)** [09 March 2022]
News & Views • An optical device enables high-speed, high-resolution distance measurements to be made over a large field of view. Clever switching gives the integrated design a tiny footprint and keeps its power consumption low.
- **[Letters and cards telling people about local police reduce crime](#)** [02 March 2022]
News & Views • A combination of Internet-based and field experiments suggests that being given personal information about a stranger leads people to believe that they themselves are known to that person — and to change their behaviour accordingly.
- **[AI minds the gap and fills in missing Greek inscriptions](#)** [09 March 2022]
News & Views • The use of artificial intelligence (AI) is transforming many areas of research. A new AI tool helps to fill in missing text and estimate the timeframe and geographical origin of ancient inscriptions.
- **[AGN as potential factories for eccentric black hole mergers](#)** [09 March 2022]
Article • The accretion disk environments surrounding active galactic nuclei are potential locations where there is an excess of eccentric mergers of large black holes, which have different spin-orbit tilts compared with circular mergers.
- **[Ultra-narrow optical linewidths in rare-earth molecular crystals](#)** [09 March 2022]
Article • A study reports europium molecular crystals with optically addressable spin states that exhibit ultra-narrow linewidths, demonstrating the use of rare-earth molecular crystals as a

platform for photonic quantum technologies.

- **Structure of the moiré exciton captured by imaging its electron and hole** [09 March 2022]
Article • Imaging the electron and hole that bind to form interlayer excitons in a 2D moiré material enables direct measurement of its diameter and indicates the localization of its centre of mass.
- **A large-scale microelectromechanical-systems-based silicon photonics LiDAR** [09 March 2022]
Article • A large focal plane switch array is constructed to steer the laser beam of a LiDAR system, leading to 3D imaging with 16,384 pixels, improving the resolution and coverage of solid-state LiDARs.
- **Vertical MoS₂ transistors with sub-1-nm gate lengths** [09 March 2022]
Article • Ultra-scaled transistors based on two-dimensional MoS₂ with physical gate lengths of 0.34 nm are reported, which show relatively good electrical characteristics and can be switched off.
- **Electron-catalysed molecular recognition** [09 March 2022]
Article • A simple and versatile strategy is established to facilitate molecular recognition by extending electron catalysis for use in supramolecular non-covalent chemistry.
- **Au–Pd separation enhances bimetallic catalysis of alcohol oxidation** [17 January 2022]
Article • ‘Cooperative redox enhancement (CORE) effects, which arise through the coupling of oxidative dehydrogenation and oxygen reduction reactions, can lead to increased rates of reaction over spatially separated bimetallic heterogeneous catalysts.
- **Weak cubic CaSiO₃ perovskite in the Earth’s mantle** [09 March 2022]
Article • At temperatures and pressures typical of the Earth’s lower mantle, cubic CaSiO₃ perovskite is found to have lower strength and viscosity compared to bridgmanite and ferropericlase, providing clues to its role in subduction regions.
- **Restoring and attributing ancient texts using deep neural networks** [09 March 2022]
Article • Ithaca—a deep neural network for textual restoration, geographical attribution and dating of ancient Greek inscriptions—collaboratively aids historians’ study of damaged texts.
- **Innovative ochre processing and tool use in China 40,000 years ago** [02 March 2022]
Article • A cultural assembly of traits at a 40,000-year-old archaeological site at Xiamabei, China supports a model of repeated early human expansions, cultural exchange and innovation in east Asia.

- **Ancient DNA and deep population structure in sub-Saharan African foragers** [23 February 2022]

Article • DNA analysis of 6 individuals from eastern and south-central Africa spanning the past approximately 18,000 years, and of 28 previously published ancient individuals, provides genetic evidence supporting hypotheses of increasing regionalization at the end of the Pleistocene.
- **Knowledge about others reduces one's own sense of anonymity** [02 March 2022]

Article • When people learn more about a stranger, they think a stranger knows more about them, and when tested in a field experiment, this shifted residents' perceptions of police officers' knowledge of illegal activity.
- **Differential mechanisms underlie trace and delay conditioning in Drosophila** [16 February 2022]

Article • Trace and delay conditioning experiments in Drosophila reveal the different neurons and signalling mechanisms that underlie this behaviour and highlight similarities with observations of learning experiences in mammals.
- **Molecular hallmarks of heterochronic parabiosis at single-cell resolution** [02 March 2022]

Article • A transcriptomics study demonstrates cell-type-specific responses to differentially aged blood and shows young blood to have restorative and rejuvenating effects that may be invoked through enhanced mitochondrial function.
- **The bacterial toxin colibactin triggers prophage induction** [23 February 2022]

Article • The bacterial genotoxin colibactin triggers prophage-mediated lysis of neighbouring bacteria, a finding that provides insight into the dynamics of microbial communities and relationships between bacterial metabolite production and phage behaviour.
- **Clonally expanded B cells in multiple sclerosis bind EBV EBNA1 and GlialCAM** [24 January 2022]

Article • The identification of high-affinity molecular mimicry between the Epstein–Barr virus (EBV) transcription factor EBNA1 and the CNS protein GlialCAM provides a mechanistic link between multiple sclerosis and EBV.
- **A trispecific antibody targeting HER2 and T cells inhibits breast cancer growth via CD4 cells** [23 February 2022]

Article • A trispecific antibody targeting HER2 and T cells stimulates CD4 T cell-dependent inhibition of breast cancer cell proliferation in vitro and tumor regression in a humanized mouse model.

- **Silent mutations reveal therapeutic vulnerability in RAS Q61 cancers** [02 March 2022]

Article • A translationally silent KRASG60G mutation, preventing the formation of a cryptic splice donor site and enabling expression of KRAS(Q61K), reveals a vulnerability in RASQ61 cancers that are therapeutically exploitable in a mutant-selective manner.

- **Structural basis for mismatch surveillance by CRISPR-Cas9** [02 March 2022]

Article • Cryo-electron microscopy structures of Cas9 during mismatch cleavage provide insight into the mechanisms that control off-target effects of Cas9, which will aid in the future design of high-fidelity Cas9 variants with reduced off-target cleavage.

- **Aquaculture will continue to depend more on land than sea**

[09 March 2022]

Matters Arising •

- NEWS AND VIEWS
- 09 March 2022

Self-assembly of molecules triggered by electricity

The options for controlling molecular self-assembly processes have been limited. A fresh approach uses electrons to facilitate self-assembly, and thereby provides precise external control over the process.

- [Robert Francke](#) 9

Molecular recognition is the formation of specific interactions between two or more molecules through non-covalent bonding, and has a crucial role in biological systems. Chemists have long been working to achieve molecular recognition between synthetic molecules under non-biological conditions: when molecules with specific properties are brought together, they self-assemble spontaneously until an equilibrium ratio between the number of free and assembled molecules is reached. However, so far, only a few options have been available for steering the time course of the process.

[Writing in Nature](#), Jiao *et al.*¹ present a method that uses electrochemical reduction of the components to trigger molecular assembly. This ground-breaking approach enables assembly to be switched on and off at will, allows the assembly rate to be tuned, and can generate stable solutions containing almost any possible ratio of assemblies and free molecules.

Access options

Subscribe to Nature+

Get immediate online access to the entire Nature family of 50+ journals

\$29.99

monthly

[Subscribe](#)

Subscribe to Journal

Get full journal access for 1 year

\$199.00

only \$3.90 per issue

[Subscribe](#)

All prices are NET prices.

VAT will be added later in the checkout.

Tax calculation will be finalised during checkout.

Buy article

Get time limited or full article access on ReadCube.

\$32.00

[Buy](#)

All prices are NET prices.

Additional access options:

- [Log in](#)
- [Learn about institutional subscriptions](#)

Nature **603**, 229-230 (2022)

doi: <https://doi.org/10.1038/d41586-022-00640-3>

References

1. Jiao, Y. *et al.* *Nature* **603**, 265–270 (2022).
2. Philp, D. & Stoddart, J. F. *Angew. Chem. Int. Edn* **35**, 1154–1196 (1996).
3. Persch, E., Dumele, O. & Diederich, F. *Angew. Chem. Int. Edn* **54**, 3290–3327 (2015).
4. Studer, A. & Curran, D. P. *Nature Chem.* **6**, 765–773 (2014).
5. Francke, R. & Little, R. D. *ChemElectroChem* **6**, 4373–4382 (2019).
6. Aida, T., Meijer, E. W. & Stupp, S. I. *Science* **335**, 813–817 (2012).

This article was downloaded by **calibre** from <https://www.nature.com/articles/d41586-022-00640-3>

| [Section menu](#) | [Main menu](#) |

- NEWS AND VIEWS
- 15 February 2022

Epstein–Barr virus sparks brain autoimmunity in multiple sclerosis

Understanding factors that lead to the development of multiple sclerosis might aid efforts to develop new therapies. Clinical data now implicate a viral culprit and immune-system dysfunction as underlying factors in this condition.

- [Hartmut Wekerle](#) 0

Most people who study multiple sclerosis (MS) propose that the factors underlying initiation of the disease enter the central nervous system (CNS) from outside the brain. The debate about the nature of these factors has split researchers into two main camps. Most see autoimmunity as the driving factor for the illness, but a minority invoke viral culprits. [Writing in Nature](#), Lanz *et al.*¹ report evidence that might settle this debate through a compromise solution.

Access options

Subscribe to Nature+

Get immediate online access to the entire Nature family of 50+ journals

\$29.99

monthly

[Subscribe](#)

[Subscribe to Journal](#)

Get full journal access for 1 year

\$199.00

only \$3.90 per issue

[Subscribe](#)

All prices are NET prices.

VAT will be added later in the checkout.

Tax calculation will be finalised during checkout.

[Buy article](#)

Get time limited or full article access on ReadCube.

\$32.00

[Buy](#)

All prices are NET prices.

Additional access options:

- [Log in](#)
- [Learn about institutional subscriptions](#)

Nature **603**, 230-232 (2022)

doi: <https://doi.org/10.1038/d41586-022-00382-2>

References

1. Lanz, T. V. *et al.* *Nature* **603**, 321–327 (2022).

2. Hohlfeld, R., Dornmair, K., Meinl, E. & Wekerle, H. *Lancet Neurol.* **15**, 198–209 (2016).
3. Bjornevik, K. *et al.* *Science* **375**, 296–301 (2022).
4. Brändle, S. *et al.* *Proc. Natl Acad. Sci. USA* **113**, 7864–7869 (2016).
5. Elsner, R. A. & Shlomchik, M. J. *Immunity* **53**, 1136–1150 (2020).
6. Obermeier, B. *et al.* *Nature Med.* **14**, 688–693 (2008).
7. Serafini, B. *et al.* *J. Exp. Med.* **204**, 2899–2912 (2007).
8. Lünemann, J. D. *et al.* *J. Exp. Med.* **205**, 1763–1773 (2008).
9. Bosch, A. & Estevez, R. *Front. Cell. Neurosci.* **14**, 627887 (2021).
10. Roemer, S. F. *et al.* *Brain* **130**, 1194–1205 (2007).
11. Olsson, T., Barcellos, L. F. & Alfredsson, L. *Nature Rev. Neurol.* **13**, 25–36 (2017).
12. Hauser, S. L. *Ann. Neurol.* **90**, 539–541 (2021).
13. Keegan, M. *et al.* *Lancet* **366**, 579–582 (2005).

This article was downloaded by **calibre** from <https://www.nature.com/articles/d41586-022-00382-2>

- NEWS AND VIEWS
- 09 March 2022

Light arrays measure up on a chip the size of a fingertip

An optical device enables high-speed, high-resolution distance measurements to be made over a large field of view. Clever switching gives the integrated design a tiny footprint and keeps its power consumption low.

- [H. Y. Fu](#) ^⑨ &
- [Qian Li](#) ¹

Our eyes use 3D information to sense our surroundings, but few imaging systems are capable of emulating this feat. Light detection and ranging (lidar) systems are an exception: they use 3D imaging to measure targets over long distances with high precision, and for this reason, they have been widely applied in technologies ranging from autonomous driving to complex cartography¹. The next challenges for lidar methods are miniaturization and integration into a single chip. But these advances can come at the cost of a limited field of view and low resolution. [Writing in Nature](#), Zhang *et al.*² report an integrated lidar system that offers an exceptional field of view and high resolution in a compact, low-power device.

Access options

Subscribe to Nature+

Get immediate online access to the entire Nature family of 50+ journals

\$29.99

monthly

[Subscribe](#)

Subscribe to Journal

Get full journal access for 1 year

\$199.00

only \$3.90 per issue

[Subscribe](#)

All prices are NET prices.

VAT will be added later in the checkout.

Tax calculation will be finalised during checkout.

Buy article

Get time limited or full article access on ReadCube.

\$32.00

[Buy](#)

All prices are NET prices.

Additional access options:

- [Log in](#)
- [Learn about institutional subscriptions](#)

Nature **603**, 232-233 (2022)

doi: <https://doi.org/10.1038/d41586-022-00642-1>

References

1. Schwarz, B. *Nature Photon.* **4**, 429–430 (2010).
2. Zhang, X., Kwon, K., Henriksson, J., Luo, J. & Wu, M. C. *Nature* **603**, 253–258 (2022).
3. Jiang, Y., Karpf, S. & Jalali, B. *Nature Photon.* **14**, 14–18 (2020).
4. Li, Z., Zang, Z., Han, Y., Wu, L. & Fu, H. Y. *Opt. Express* **29**, 16547–16562 (2021).
5. Poulton, C. V. *et al.* *Opt. Lett.* **42**, 4091–4094 (2017).
6. Sun, J., Timurdogan, E., Yaacobi, A., Hosseini, E. S. & Watts, M. R. *Nature* **493**, 195–199 (2013).
7. Rogers, C. *et al.* *Nature* **590**, 256–261 (2021).

This article was downloaded by **calibre** from <https://www.nature.com/articles/d41586-022-00642-1>

| [Section menu](#) | [Main menu](#) |

- NEWS AND VIEWS
- 02 March 2022

Letters and cards telling people about local police reduce crime

A combination of Internet-based and field experiments suggests that being given personal information about a stranger leads people to believe that they themselves are known to that person — and to change their behaviour accordingly.

- [Elicia John](#) ⁰ &
- [Shawn D. Bushway](#) ¹

Community policing is often held up as an instrumental part of reforms to make policing less harmful, particularly in low-income communities that have high rates of violence. But building collaborative relationships between communities and police is hard. [Writing in Nature](#), Shah and LaForest¹ describe a large field experiment revealing that giving residents cards and letters with basic information about local police officers can prevent crime. Combining these results with those from Internet-based experiments, the authors attribute the observed reduction in crime to perceived ‘information symmetry’.

Access options

Subscribe to Nature+

Get immediate online access to the entire Nature family of 50+ journals

\$29.99

monthly

Subscribe

Subscribe to Journal

Get full journal access for 1 year

\$199.00

only \$3.90 per issue

Subscribe

All prices are NET prices.

VAT will be added later in the checkout.

Tax calculation will be finalised during checkout.

Buy article

Get time limited or full article access on ReadCube.

\$32.00

Buy

All prices are NET prices.

Additional access options:

- [Log in](#)
- [Learn about institutional subscriptions](#)

Nature **603**, 233-235 (2022)

doi: <https://doi.org/10.1038/d41586-022-00152-0>

References

1. Shah, A. K. & LaForest, M. *Nature* **603**, 297–301 (2022).

2. Levay, K. E., Freese, J. & Druckman, J. N. *Sage Open* <https://doi.org/10.1177/2158244016636433> (2016).
3. Mullinix, K. J., Leeper, T. J., Druckman, J. N. & Freese, J. *J. Exp. Polit. Sci.* **2**, 109–138 (2015).
4. National Academies of Sciences, Engineering, and Medicine. *Proactive Policing: Effects on Crime and Communities* (National Academies Press, 2018).
5. Liberman, N., Trope, Y. & Stephan, E. *Social Psychology: Handbook of Basic Principles* 2nd edn (eds Kruglanski, A. W. & Higgins, E. T.) 353–381 (Guilford, 2007).
6. Mussweiler, T. *Psychol. Rev.* **110**, 472–489 (2003).
7. Hershfield, H. E., John, E. M. & Reiff, J. S. *Policy Insights Behav. Brain Sci.* **5**, 209–215 (2018).
8. van Gelder, J. L., Luciano, E. C., Weulen Kranenbarg, M. & Hershfield, H. E. *Criminology* **53**, 158–179 (2015).
9. Silver, E. & Miller, L. L. *Criminology* **42**, 551–584 (2004).

This article was downloaded by **calibre** from <https://www.nature.com/articles/d41586-022-00152-0>

- NEWS AND VIEWS
- 09 March 2022

AI minds the gap and fills in missing Greek inscriptions

The use of artificial intelligence (AI) is transforming many areas of research. A new AI tool helps to fill in missing text and estimate the timeframe and geographical origin of ancient inscriptions.

- [Charlotte Roueché](#) 

The possibility that artificial intelligence (AI) will automate tasks and thus destroy certain jobs is advancing steadily into more and more areas of life; the waves are now lapping even on the quiet shores of ancient-world studies. In [a paper in *Nature*](#), Assael *et al.*¹ present an AI tool called Ithaca, which has been developed to bring deep learning to the world of classical studies and the interpretation of transcribed ancient Greek texts, which were originally inscribed on stone. But this advance should not be interpreted as a threat to centuries of tradition — rather as a complement to them.

Access options

Subscribe to Nature+

Get immediate online access to the entire Nature family of 50+ journals

\$29.99

monthly

[Subscribe](#)

Subscribe to Journal

Get full journal access for 1 year

\$199.00

only \$3.90 per issue

[Subscribe](#)

All prices are NET prices.

VAT will be added later in the checkout.

Tax calculation will be finalised during checkout.

Buy article

Get time limited or full article access on ReadCube.

\$32.00

[Buy](#)

All prices are NET prices.

Additional access options:

- [Log in](#)
- [Learn about institutional subscriptions](#)

Nature **603**, 235-236 (2022)

doi: <https://doi.org/10.1038/d41586-022-00641-2>

References

1. Assael, Y. *et al.* *Nature* **603**, 280–283 (2022).
-

This article was downloaded by **calibre** from <https://www.nature.com/articles/d41586-022-00641-2>

| [Section menu](#) | [Main menu](#) |

- Article
- [Published: 09 March 2022](#)

AGN as potential factories for eccentric black hole mergers

- [J. Samsing](#) [ORCID: orcid.org/0000-0003-0607-8741](#)¹,
- [I. Bartos](#) [ORCID: orcid.org/0000-0001-5607-3637](#)²,
- [D. J. D’Orazio](#)¹,
- [Z. Haiman](#) [ORCID: orcid.org/0000-0003-3633-5403](#)³,
- [B. Kocsis](#) [ORCID: orcid.org/0000-0002-4865-7517](#)^{4,5},
- [N. W. C. Leigh](#)^{6,7},
- [B. Liu](#)¹,
- [M. E. Pessah](#) [ORCID: orcid.org/0000-0001-8716-3563](#)¹ &
- [H. Tagawa](#)⁸

[Nature](#) volume **603**, pages 237–240 (2022)

- 961 Accesses
- 195 Altmetric
- [Metrics details](#)

Subjects

- [Compact astrophysical objects](#)
- [General relativity and gravity](#)
- [High-energy astrophysics](#)

Abstract

There is some weak evidence that the black hole merger named GW190521 had a non-zero eccentricity^{1,2}. In addition, the masses of the component black holes exceeded the limit predicted by stellar evolution³. The large masses can be explained by successive mergers^{4,5}, which may be efficient in gas disks surrounding active galactic nuclei, but it is difficult to maintain an eccentric orbit all the way to the merger, as basic physics would argue for circularization⁶. Here we show that active galactic nuclei disk environments can lead to an excess of eccentric mergers, if the interactions between single and binary black holes are frequent⁵ and occur with mutual inclinations of less than a few degrees. We further illustrate that this eccentric population has a different distribution of the inclination between the spin vectors of the black holes and their orbital angular momentum at merger⁷, referred to as the spin–orbit tilt, compared with the remaining circular mergers.

This is a preview of subscription content

Access options

Subscribe to Nature+

Get immediate online access to the entire Nature family of 50+ journals

\$29.99

monthly

[Subscribe](#)

Subscribe to Journal

Get full journal access for 1 year

\$199.00

only \$3.90 per issue

Subscribe

All prices are NET prices.
VAT will be added later in the checkout.
Tax calculation will be finalised during checkout.

Buy article

Get time limited or full article access on ReadCube.

\$32.00

Buy

All prices are NET prices.

Additional access options:

- [Log in](#)
- [Learn about institutional subscriptions](#)

Fig. 1: Illustration of an eccentric LIGO-Virgo source forming in an AGN disk.

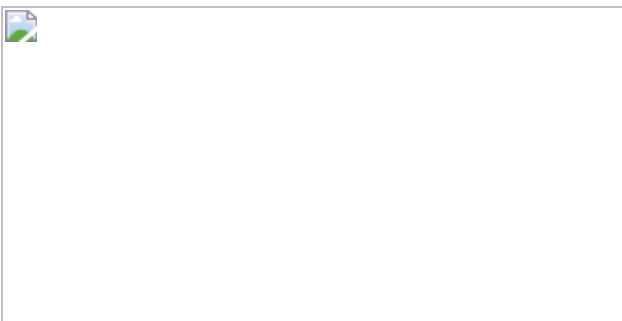


Fig. 2: Merger probability.

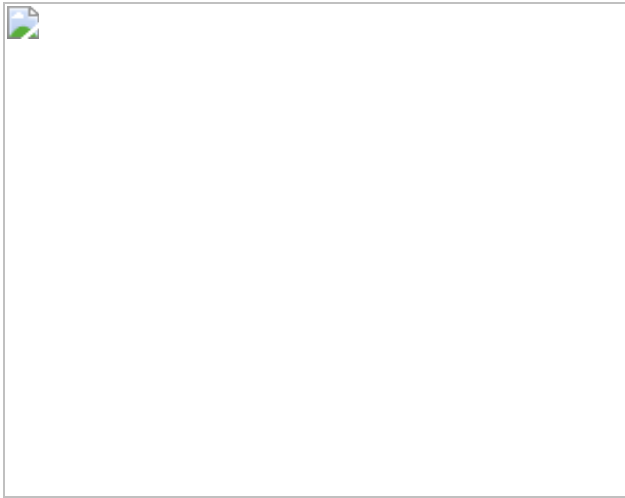


Fig. 3: Dependence on orbital inclination.

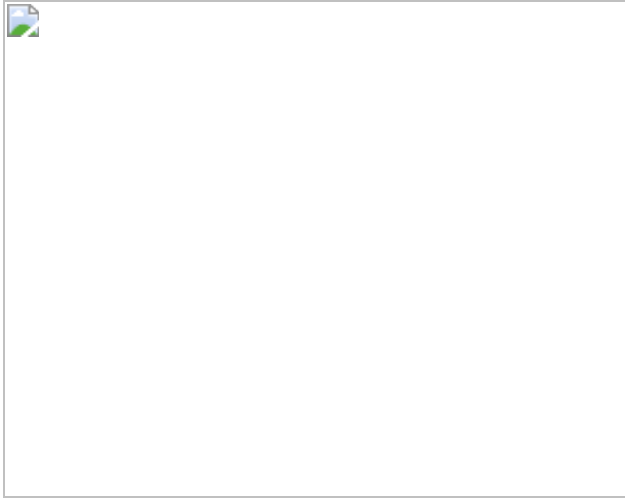


Fig. 4: Distribution of orbital plane orientations.

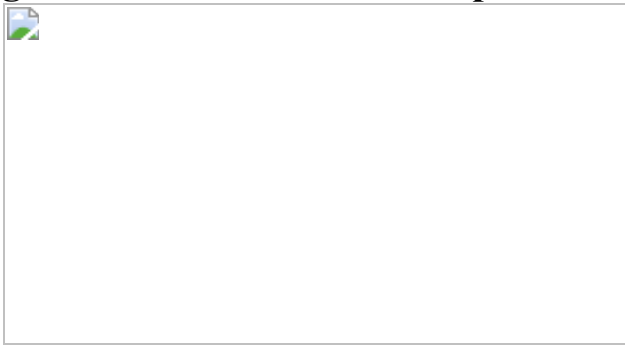
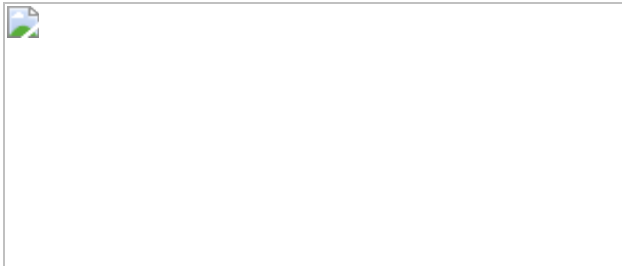


Fig. 5: Eccentricity and gravitational-wave frequency distributions.



Data availability

The data that support the findings of this study are available from the corresponding author on reasonable request.

Code availability

Requests for codes should be addressed to the corresponding author.

References

1. Gayathri, V. et al. Eccentricity estimate for black hole mergers with numerical relativity simulations. *Nat. Astron.* <https://doi.org/10.1038/s41550-021-01568-w> (2022).
2. Romero-Shaw, I., Lasky, P. D., Thrane, E. & Calderón Bustillo, J. GW190521: orbital eccentricity and signatures of dynamical formation in a binary black hole merger signal. *Astrophys. J. Lett.* **903**, L5 (2020).
3. Abbott, R. et al. Properties and astrophysical implications of the $150M_{\odot}$ binary black hole merger GW190521. *Astrophys. J. Lett.* **900**, L13 (2020).
4. Yang, Y. et al. Hierarchical black hole mergers in active galactic nuclei. *Phys. Rev. Lett.* **123**, 181101 (2019).
5. Tagawa, H., Haiman, Z. & Kocsis, B. Formation and evolution of compact-object binaries in AGN disks. *Astrophys. J.* **898**, 25 (2020).

6. Peters, P. Gravitational radiation and the motion of two point masses. *Phys. Rev.* **136**, B1224–B1232 (1964).
7. Abbott, R. et al. GW190521: a binary black hole merger with a total mass of $150 M_{\odot}$. *Phys. Rev. Lett.* **125**, 101102 (2020).
8. Bartos, I., Kocsis, B., Haiman, Z. & Márka, S. Rapid and bright stellar-mass binary black hole mergers in active galactic nuclei. *Astrophys. J.* **835**, 165 (2017).
9. Levin, Y. Formation of massive stars and black holes in self-gravitating AGN discs, and gravitational waves in LISA band. Preprint at <https://arxiv.org/abs/astro-ph/0307084> (2003).
10. Stone, N. C., Metzger, B. D. & Haiman, Z. Assisted inspirals of stellar mass black holes embedded in AGN discs: solving the ‘final au problem’. *Mon. Not. R. Astron. Soc.* **464**, 946–954 (2017).
11. Cantiello, M., Jermyn, A. S. & Lin, D. N. C. Stellar evolution in AGN disks. *Astrophys. J.* **910**, 94 (2021).
12. McKernan, B., Ford, K. E. S., Lyra, W. & Perets, H. B. Intermediate mass black holes in AGN discs—I. Production and growth. *Mon. Not. R. Astron. Soc.* **425**, 460–469 (2012).
13. McKernan, B. et al. Constraining stellar-mass black hole mergers in AGN disks detectable with LIGO. *Astrophys. J.* **866**, 66 (2018).
14. Leigh, N. W. C. et al. On the rate of black hole binary mergers in galactic nuclei due to dynamical hardening. *Mon. Not. R. Astron. Soc.* **474**, 5672–5683 (2018).
15. Secunda, A. et al. Orbital migration of interacting stellar mass black holes in disks around supermassive black holes. *Astrophys. J.* **878**, 85 (2019).
16. Tagawa, H., Haiman, Z., Bartos, I. & Kocsis, B. Spin evolution of stellar-mass black hole binaries in active galactic nuclei. *Astrophys. J.*

17. Kocsis, B., Gáspár, M. E. & Márka, S. Detection rate estimates of gravity waves emitted during parabolic encounters of stellar black holes in globular clusters. *Astrophys. J.* **648**, 411–429 (2006).
18. Rodriguez, C. L. et al. Post-Newtonian dynamics in dense star clusters: formation, masses, and merger rates of highly-eccentric black hole binaries. *Phys. Rev. D* **98**, 123005 (2018).
19. Samsing, J. Eccentric black hole mergers forming in globular clusters. *Phys. Rev. D* **97**, 103014 (2018).
20. Graham, M. J. et al. Candidate electromagnetic counterpart to the binary black hole merger gravitational-wave event S190521g. *Phys. Rev. Lett.* **124**, 251102 (2020).
21. Blanchet, L. Gravitational radiation from post-Newtonian sources and inspiralling compact binaries. *Living Rev. Relativ.* **17**, 2 (2014).
22. Samsing, J. & D’Orazio, D. J. Black hole mergers from globular clusters observable by LISA I: eccentric sources originating from relativistic N -body dynamics. *Mon. Not. R. Astron. Soc.* **481**, 5445–5450 (2018).
23. Monaghan, J. J. A statistical theory of the disruption of three-body systems — II. High angular momentum. *Mon. Not. R. Astron. Soc.* **177**, 583–594 (1976).
24. Valtonen, M. & Karttunen, H. *The Three-Body Problem* (Cambridge Univ. Press, 2006).
25. Stone, N. C. & Leigh, N. W. C. A statistical solution to the chaotic, non-hierarchical three-body problem. *Nature* **576**, 406–410 (2019).
26. Thompson, T. A., Quataert, E. & Murray, N. Radiation pressure-supported starburst disks and active galactic nucleus fueling. *Astrophys. J.* **630**, 167–185 (2005).

27. Rodriguez, C. L., Zevin, M., Pankow, C., Kalogera, V. & Rasio, F. A. Illuminating black hole binary formation channels with spins in advanced LIGO. *Astrophys. J.* **832**, L2 (2016).
28. Ostriker, E. C. Dynamical friction in a gaseous medium. *Astrophys. J.* **513**, 252–258 (1999).
29. Kim, H. & Kim, W.-T. Dynamical friction of a circular-orbit perturber in a gaseous medium. *Astrophys. J.* **665**, 432–444 (2007).
30. Samsing, J., MacLeod, M. & Ramirez-Ruiz, E. The formation of eccentric compact binary inspirals and the role of gravitational wave emission in binary-single stellar encounters. *Astrophys. J.* **784**, 71 (2014).
31. Samsing, J., MacLeod, M. & Ramirez-Ruiz, E. Formation of tidal captures and gravitational wave inspirals in binary-single interactions. *Astrophys. J.* **846**, 36 (2017).
32. Samsing, J., MacLeod, M. & Ramirez-Ruiz, E. Dissipative evolution of unequal-mass binary–single interactions and its relevance to gravitational-wave detections. *Astrophys. J.* **853**, 140 (2018).
33. Heggie, D. C. Binary evolution in stellar dynamics. *Mon. Not. R. Astron. Soc.* **173**, 729–787 (1975).
34. Samsing, J., Askar, A. & Giersz, M. MOCCA-SURVEY database. I. Eccentric black hole mergers during binary–single interactions in globular clusters. *Astrophys. J.* **855**, 124 (2018).
35. Gondán, L. & Kocsis, B. Measurement accuracy of inspiraling eccentric neutron star and black hole binaries using gravitational waves. *Astrophys. J.* **871**, 178 (2019).
36. Zevin, M., Samsing, J., Rodriguez, C., Haster, C.-J. & Ramirez-Ruiz, E. Eccentric black hole mergers in dense star clusters: the role of binary–binary encounters. *Astrophys. J.* **871**, 91 (2019).

37. Li, Y.-P., Dempsey, A. M., Li, S., Li, H. & Li, J. Orbital evolution of binary black holes in active galactic nucleus disks: a disk channel for binary black hole mergers? *Astrophys. J.* **911**, 124 (2021).
38. Samsing, J., Hamers, A. S. & Tyles, J. G. Effect of distant encounters on black hole binaries in globular clusters: systematic increase of in-cluster mergers in the LISA band. *Phys. Rev. D* **100**, 043010 (2019).

Acknowledgements

We are grateful to N. Bose, K. Holley-Bockelmann, A. Pai, M. Zevin and M. Safarzadeh for their useful suggestions. J.S. is supported by the European Union’s Horizon 2020 research and innovation programme under the Marie Skłodowska-Curie grant agreement no. 844629. D.J.D. received funding from the European Union’s Horizon 2020 research and innovation programme under the Marie Skłodowska-Curie grant agreement no. 101029157 and through Villum Fonden grant no. 29466. I.B. acknowledges the support of the Alfred P. Sloan Foundation and NSF grants PHY-1911796 and PHY-2110060. H.T. is financially supported by the Grants-in-Aid for Basic Research by the Ministry of Education, Science and Culture of Japan (17H01102, 17H06360) and the Japan Society for the Promotion of Science (JSPS) KAKENHI grant number JP21J00794. N.W.C.L. acknowledges the support of a Fondecyt Iniciación grant 11180005, the financial support from Millenium Nucleus NCN19-058 (TITANs) and the BASAL Centro de Excelencia en Astrofísica y Tecnologías Afines (CATA) grant CATA AFB170002 along with ANID BASAL projects ACE210002 and FB210003. Z.H. acknowledges support from NASA grant NNX15AB19G and NSF grants AST-1715661 and AST-2006176. B.L. gratefully acknowledges support from the European Union’s Horizon 2020 research and innovation program under the Marie Skłodowska-Curie grant agreement no. 847523 ‘INTERACTIONS’. This project has received funding from the European Research Council (ERC) under the European Union’s Horizon 2020 research and innovation programme ERC-2014-STG under grant agreement no. 638435 (GalNUC) to B.K. M.E.P. gratefully acknowledges support from the Independent Research Fund Denmark (DFF) via grant no. DFF 8021-00400B.

Author information

Affiliations

1. Niels Bohr International Academy, Niels Bohr Institute, Copenhagen, Denmark

J. Samsing, D. J. D’Orazio, B. Liu & M. E. Pessah

2. Department of Physics, University of Florida, Gainesville, FL, USA

I. Bartos

3. Department of Astronomy, Columbia University, New York, NY, USA

Z. Haiman

4. Rudolf Peierls Centre for Theoretical Physics, Clarendon Laboratory, Oxford, UK

B. Kocsis

5. St Hugh’s College, Oxford, UK

B. Kocsis

6. Departamento de Astronomía, Facultad Ciencias Físicas y Matemáticas, Universidad de Concepción, Concepción, Chile

N. W. C. Leigh

7. Department of Astrophysics, American Museum of Natural History, New York, NY, USA

N. W. C. Leigh

8. Astronomical Institute, Tohoku University, Sendai, Miyagi, Japan

H. Tagawa

Contributions

J.S. led the work, carried out the simulations and calculations, and wrote the initial manuscript together with I.B. and D.J.D. The remaining authors, Z.H., B.K., N.W.C.L., B.L., M.E.P. and H.T., all contributed equally to the intellectual development of the ideas and the preparation of the final manuscript.

Corresponding author

Correspondence to [J. Samsing](#).

Ethics declarations

Competing interests

The authors declare no competing interests.

Peer review

Peer review information

Nature thanks the anonymous reviewers for their contribution to the peer review of this work.

Additional information

Publisher's note Springer Nature remains neutral with regard to jurisdictional claims in published maps and institutional affiliations.

Rights and permissions

[Reprints and Permissions](#)

About this article

Cite this article

Samsing, J., Bartos, I., D’Orazio, D.J. *et al.* AGN as potential factories for eccentric black hole mergers. *Nature* **603**, 237–240 (2022).
<https://doi.org/10.1038/s41586-021-04333-1>

- Received: 08 October 2020
- Accepted: 10 December 2021
- Published: 09 March 2022
- Issue Date: 10 March 2022
- DOI: <https://doi.org/10.1038/s41586-021-04333-1>

Share this article

Anyone you share the following link with will be able to read this content:

[Get shareable link](#)

Sorry, a shareable link is not currently available for this article.

[Copy to clipboard](#)

Provided by the Springer Nature SharedIt content-sharing initiative

This article was downloaded by **calibre** from <https://www.nature.com/articles/s41586-021-04333-1>

- Article
- [Published: 09 March 2022](#)

Ultra-narrow optical linewidths in rare-earth molecular crystals

- [Diana Serrano](#) ORCID: [orcid.org/0000-0002-9478-3776](#)^{1 na1},
- [Senthil Kumar Kuppusamy](#) ORCID: [orcid.org/0000-0002-1501-7759](#)^{2,3 na1},
- [Benoît Heinrich](#)⁴,
- [Olaf Fuhr](#)^{3,5},
- [David Hunger](#) ORCID: [orcid.org/0000-0001-6156-6145](#)^{2,6},
- [Mario Ruben](#) ORCID: [orcid.org/0000-0002-7718-7016](#)^{2,3,7} &
- [Philippe Goldner](#) ORCID: [orcid.org/0000-0001-8517-0911](#)¹

[Nature](#) volume **603**, pages 241–246 (2022)

- 1481 Accesses
- 94 Altmetric
- [Metrics details](#)

Subjects

- [Quantum information](#)
- [Quantum optics](#)

Abstract

Rare-earth ions (REIs) are promising solid-state systems for building light–matter interfaces at the quantum level^{1,2}. This relies on their potential to

show narrow optical and spin homogeneous linewidths, or, equivalently, long-lived quantum states. This enables the use of REIs for photonic quantum technologies such as memories for light, optical–microwave transduction and computing^{3,4,5}. However, so far, few crystalline materials have shown an environment quiet enough to fully exploit REI properties. This hinders further progress, in particular towards REI-containing integrated nanophotonics devices^{6,7}. Molecular systems can provide such capability but generally lack spin states. If, however, molecular systems do have spin states, they show broad optical lines that severely limit optical-to-spin coherent interfacing^{8,9,10}. Here we report on europium molecular crystals that exhibit linewidths in the tens of kilohertz range, orders of magnitude narrower than those of other molecular systems. We harness this property to demonstrate efficient optical spin initialization, coherent storage of light using an atomic frequency comb, and optical control of ion–ion interactions towards implementation of quantum gates. These results illustrate the utility of rare-earth molecular crystals as a new platform for photonic quantum technologies that combines highly coherent emitters with the unmatched versatility in composition, structure and integration capability of molecular materials.

This is a preview of subscription content

Access options

Subscribe to Nature+

Get immediate online access to the entire Nature family of 50+ journals

\$29.99

monthly

[Subscribe](#)

Subscribe to Journal

Get full journal access for 1 year

\$199.00

only \$3.90 per issue

[Subscribe](#)

All prices are NET prices.

VAT will be added later in the checkout.

Tax calculation will be finalised during checkout.

Buy article

Get time limited or full article access on ReadCube.

\$32.00

[Buy](#)

All prices are NET prices.

Additional access options:

- [Log in](#)
- [Learn about institutional subscriptions](#)

Fig. 1: Material and low-temperature optical spectroscopy.

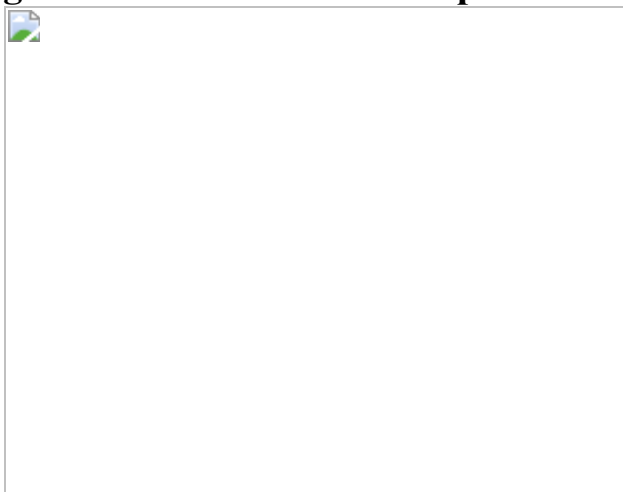


Fig. 2: Ultra-narrow optical homogeneous linewidths.

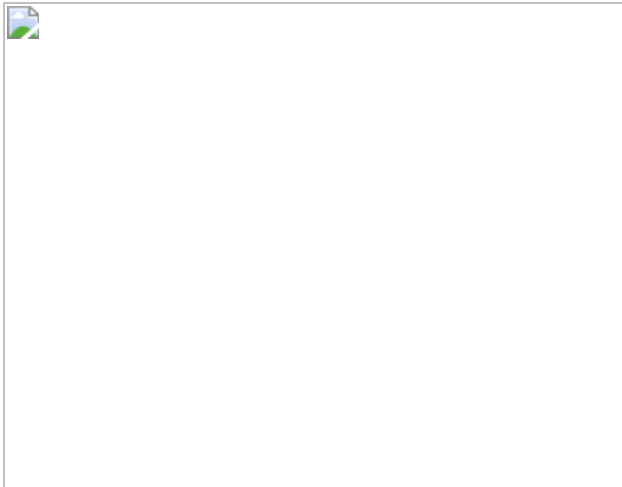


Fig. 3: Optically addressable nuclear spins.

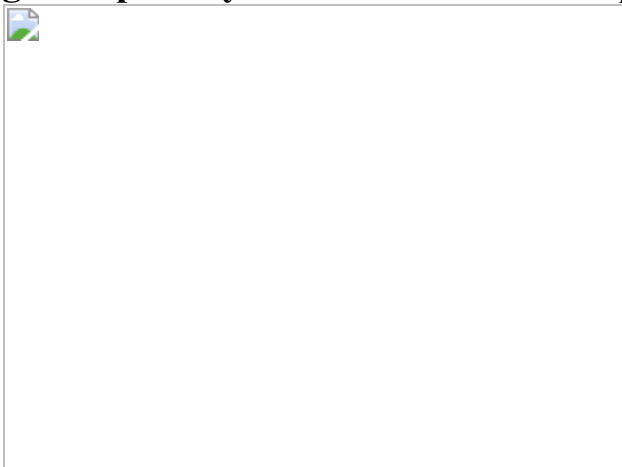


Fig. 4: Coherent light storage and optically controlled ion–ion interactions.



Data availability

Datasets generated and/or analysed during the current study are available in the Zenodo repository (<https://doi.org/10.5281/zenodo.5652030>). [Source data](#) are provided with this paper.

References

1. Awschalom, D. D., Hanson, R., Wrachtrup, J. & Zhou, B. B. Quantum technologies with optically interfaced solid-state spins. *Nat. Photon.* **12**, 516–527 (2018).
2. Goldner, P., Ferrier, A. & Guillot-Noël, O. in *Handbook on the Physics and Chemistry of Rare Earths* Vol. 46 (eds Bünzli, J.-C. G. & Pecharsky, V. K.) 1–78 (Elsevier, 2015).
3. Bussières, F. et al. Quantum teleportation from a telecom-wavelength photon to a solid-state quantum memory. *Nat. Photon.* **8**, 775–778 (2014).
4. Bartholomew, J. G. et al. On-chip coherent microwave-to-optical transduction mediated by ytterbium in YVO₄. *Nat. Commun.* **11**, 3266 (2020).
5. Kinoshita, A. et al. Roadmap for rare-earth quantum computing. Preprint at <https://arxiv.org/abs/2103.15743> (2021).
6. Kindem, J. M. et al. Control and single-shot readout of an ion embedded in a nanophotonic cavity. *Nature* **580**, 201–204 (2020).
7. Chen, S., Raha, M., Phenicie, C. M., Ourari, S. & Thompson, J. D. Parallel single-shot measurement and coherent control of solid-state spins below the diffraction limit. *Science* **370**, 592–595 (2020).
8. Bayliss, S. L. et al. Optically addressable molecular spins for quantum information processing. *Science* **370**, 1309–1312 (2020).
9. Kumar, K. S. et al. Optical spin-state polarization in a binuclear europium complex towards molecule-based coherent light-spin

interfaces. *Nat. Commun.* **12**, 2152 (2021).

10. Toninelli, C. et al. Single organic molecules for photonic quantum technologies. *Nat. Mater.* **20**, 1615–1628 (2021).
11. Zhong, M. et al. Optically addressable nuclear spins in a solid with a six-hour coherence time. *Nature* **517**, 177–180 (2015).
12. de Riedmatten, H., Afzelius, M., Staudt, M. U., Simon, C. & Gisin, N. A solid-state light–matter interface at the single-photon level. *Nature* **456**, 773–777 (2008).
13. Seri, A. et al. Quantum storage of frequency-multiplexed heralded single photons. *Phys. Rev. Lett.* **123**, 080502 (2019).
14. Zhong, T. & Goldner, P. Emerging rare-earth doped material platforms for quantum nanophotonics. *Nanophotonics* **8**, 2003–2015 (2019).
15. Casabone, B. et al. Dynamic control of Purcell enhanced emission of erbium ions in nanoparticles. *Nat. Commun.* **12**, 3570 (2021).
16. Zhong, T. et al. Optically addressing single rare-earth ions in a nanophotonic cavity. *Phys. Rev. Lett.* **121**, 183603 (2018).
17. Zhong, T. et al. Nanophotonic rare-earth quantum memory with optically controlled retrieval. *Science* **357**, 1392–1395 (2017).
18. Bhaskar, M. K. et al. Experimental demonstration of memory-enhanced quantum communication. *Nature* **580**, 60–64 (2020).
19. Zirkelbach, J. et al. Partial cloaking of a gold particle by a single molecule. *Phys. Rev. Lett.* **125**, 103603 (2020).
20. Melby, L. R., Rose, N. J., Abramson, E. & Caris, J. C. Synthesis and fluorescence of some trivalent lanthanide complexes. *J. Am. Chem. Soc.* **86**, 5117–5125 (1964).
21. Binnemans, K. Interpretation of europium (III) spectra. *Coord. Chem. Rev.* **295**, 1–45 (2015).

22. Könz, F. et al. Temperature and concentration dependence of optical dephasing, spectral-hole lifetime, and anisotropic absorption in Eu³⁺:Y₂SiO₅. *Phys. Rev. B* **68**, 085109 (2003).
23. Thiel, C. W., Böttger, T. & Cone, R. L. Rare-earth-doped materials for applications in quantum information storage and signal processing. *J. Lumin.* **131**, 353–361 (2011).
24. Abella, I. D., Kurnit, N. A. & Hartmann, S. R. Photon echoes. *Phys. Rev.* **141**, 391 (1966).
25. Perrot, A. et al. Narrow optical homogeneous linewidths in rare earth doped nanocrystals. *Phys. Rev. Lett.* **111**, 203601 (2013).
26. Riesen, H. Hole-burning spectroscopy of coordination compounds. *Coord. Chem. Rev.* **250**, 1737–1754 (2006).
27. Shelby, R. & Macfarlane, R. M. Frequency-dependent optical dephasing in the stoichiometric material EuP₅O₁₄. *Phys. Rev. Lett.* **45**, 1098–1101 (1980).
28. Flinn, G. P. et al. Sample-dependent optical dephasing in bulk crystalline samples of Y₂O₃:Eu³⁺. *Phys. Rev. B* **49**, 5821 (1994).
29. Kozankiewicz, B. & Orrit, M. Single-molecule photophysics, from cryogenic to ambient conditions. *Chem. Soc. Rev.* **43**, 1029–1043 (2014).
30. Serrano, D., Karlsson, J., Fossati, A., Ferrier, A. & Goldner, P. All-optical control of long-lived nuclear spins in rare-earth doped nanoparticles. *Nat. Commun.* **9**, 2127 (2018).
31. Afzelius, M. & Simon, C. Impedance-matched cavity quantum memory. *Phys. Rev. A* **82**, 022310 (2010).
32. Macfarlane, R. M. Optical Stark spectroscopy of solids. *J. Lumin.* **125**, 156–174 (2007).

33. Altner, S. B., Mitsunaga, M., Zumofen, G. & Wild, U. P. Dephasing-rephasing balancing in photon echoes by excitation induced frequency shifts. *Phys. Rev. Lett.* **76**, 1747–1750 (1996).
34. Wernsdorfer, W. & Ruben, M. Synthetic Hilbert space engineering of molecular qudits: isotopologue chemistry. *Adv. Mater.* **31**, 1806687 (2019).
35. Godfrin, C. et al. Operating quantum states in single magnetic molecules: implementation of Grover's quantum algorithm. *Phys. Rev. Lett.* **119**, 187702 (2017).

Acknowledgements

We thank M. Afzelius for useful discussions, and N. Harada and P. Vermaut for assistance during scanning electron microscopy measurements. This project has received funding from the European Union's Horizon 2020 research and innovation programme under grant agreement number 820391 (SQUARE) and EUCOR Marie Skłodowska-Curie COFUND project number 847471 (QUSTEC), the French Agence Nationale de la Recherche under grant ANR-20-CE09-0022 (UltraNanOSpec), the Frontiers Research in Chemistry Foundation CIRFC number 93 "Optically controlled qudits" and KIT Future Fields Project "Optically addressable qubits".

Author information

Author notes

1. These authors contributed equally: Diana Serrano, Senthil Kumar Kuppusamy

Affiliations

1. Chimie ParisTech, PSL University, CNRS, Institut de Recherche de Chimie Paris, Paris, France

Diana Serrano & Philippe Goldner

2. Institute for Quantum Materials and Technologies (IQMT), Karlsruhe Institute of Technology (KIT), Karlsruhe, Germany

Senthil Kumar Kuppusamy, David Hunger & Mario Ruben

3. Institute of Nanotechnology, Karlsruhe Institute of Technology (KIT), Karlsruhe, Germany

Senthil Kumar Kuppusamy, Olaf Fuhr & Mario Ruben

4. Institut de Physique et Chimie des Matériaux de Strasbourg (IPCMS), CNRS-Université de Strasbourg, Strasbourg, France

Benoît Heinrich

5. Karlsruhe Nano Micro Facility (KNMF), Karlsruhe Institute of Technology (KIT), Karlsruhe, Germany

Olaf Fuhr

6. Physikalisches Institut, Karlsruhe Institute of Technology (KIT), Karlsruhe, Germany

David Hunger

7. Centre Européen de Sciences Quantiques (CESQ), Institut de Science et d'Ingénierie Supramoléculaire (ISIS), Université de Strasbourg, Strasbourg, France

Mario Ruben

Contributions

P.G., M.R. and D.H. conceived and supervised the project. D.S. and S.K.K. were involved in the conceptual development of the project. S.K.K. and M.R. were responsible for the synthesis and characterization of the isotopologue complexes. B.H. performed powder X-ray diffraction studies

and indexed the patterns. O.F. solved the X-ray structure of the complex. D.S. and P.G. performed the optical experiments and analysed the results. D.S. and P.G. wrote the manuscript with input from all authors.

Corresponding authors

Correspondence to [Diana Serrano](#), [Senthil Kumar Kuppusamy](#), [Mario Ruben](#) or [Philippe Goldner](#).

Ethics declarations

Competing interests

The authors declare no competing interests.

Peer review

Peer review information

Nature thanks David Mills and the other, anonymous, reviewer(s) for their contribution to the peer review of this work. Peer reviewer reports are available.

Additional information

Publisher's note Springer Nature remains neutral with regard to jurisdictional claims in published maps and institutional affiliations.

Extended data figures and tables

[Extended Data Fig. 1 Eu³⁺ complex preparation and X-ray crystal structure.](#)

Upper: Schematic representation of the preparation of the europium complex discussed in this study. Lower: X-ray crystal structure of the complex. As shown, the piperidin-1-ium cation is involved in hydrogen bonding interactions with two oxygen atoms of benzoylacetonate ligands.

Extended Data Fig. 2 Photostability of the Eu³⁺ complex.

⁵D₀ photoluminescence (PL) intensity under continuous wave excitation measured at 8 K for the ¹⁵¹Eu³⁺ isotopically enriched complex. The constant PL signal confirms absence of photobleaching. See SI section 3 for more details.

[Source data](#)

Extended Data Fig. 3 2-pulse photon echo decay from the 5% Eu³⁺-95% Y³⁺ diluted complex.

The experimental decay (black circles) was fitted with a double exponential model (red curve) with $T_{2,fast} = 18 \mu\text{s}$ and $T_{2,slow} = 68 \mu\text{s}$ decay time constants.

[Source data](#)

Extended Data Fig. 4 Spectral tailoring prior to AFC storage.

a. Spectral pit of 9 MHz dug in the absorption profile at 30 MHz to create a high absorption region at 0 MHz. **b.** Atomic frequency comb (AFC) with teeth of 0.9 MHz separated by 1.75 MHz (finesse $F=1.9$). The FFT of the storage pulse is presented over the AFC (blue line) showing good spectral overlap. The input pulse intensity was estimated by sending it through the spectral pit in **a**, taking advantage of the pit's almost full transparency. A correction was made to account for residual absorption.

[Source data](#)

Supplementary information

Supplementary Information

This file contains the table of contents; supplementary text, figures, tables and references.

Peer Review File

Source data

Source Data Fig. 1

Source Data Fig. 2

Source Data Fig. 3

Source Data Fig. 4

Source Data Extended Data Fig. 2

Source Data Extended Data Fig. 3

Source Data Extended Data Fig. 4

Rights and permissions

Reprints and Permissions

About this article

Cite this article

Serrano, D., Kuppusamy, S.K., Heinrich, B. *et al.* Ultra-narrow optical linewidths in rare-earth molecular crystals. *Nature* **603**, 241–246 (2022). <https://doi.org/10.1038/s41586-021-04316-2>

- Received: 21 May 2021
- Accepted: 07 December 2021
- Published: 09 March 2022
- Issue Date: 10 March 2022
- DOI: <https://doi.org/10.1038/s41586-021-04316-2>

Share this article

Anyone you share the following link with will be able to read this content:

[Get shareable link](#)

Sorry, a shareable link is not currently available for this article.

[Copy to clipboard](#)

Provided by the Springer Nature SharedIt content-sharing initiative

This article was downloaded by **calibre** from <https://www.nature.com/articles/s41586-021-04316-2>

- Article
- [Published: 09 March 2022](#)

Structure of the moiré exciton captured by imaging its electron and hole

- [Ouri Karni](#)^{1,2 na1},
- [Elyse Barré](#)^{2,3 na1},
- [Vivek Pareek](#) [ORCID: orcid.org/0000-0002-9262-427X](#)^{4 na1},
- [Johnathan D. Georgaras](#)^{5 na1},
- [Michael K. L. Man](#) [ORCID: orcid.org/0000-0001-6043-3631](#)^{4 na1},
- [Chakradhar Sahoo](#)^{4 na1 naAff11},
- [David R. Bacon](#)⁴,
- [Xing Zhu](#)⁴,
- [Henrique B. Ribeiro](#)²,
- [Aidan L. O'Beirne](#)^{2,6},
- [Jenny Hu](#)¹,
- [Abdullah Al-Mahboob](#)⁴,
- [Mohamed M. M. Abdelrasoul](#)⁴,
- [Nicholas S. Chan](#)⁴,
- [Arka Karmakar](#)⁴,
- [Andrew J. Winchester](#)⁴,
- [Bumho Kim](#) [ORCID: orcid.org/0000-0002-5671-5641](#)⁷,
- [Kenji Watanabe](#) [ORCID: orcid.org/0000-0003-3701-8119](#)⁸,
- [Takashi Taniguchi](#) [ORCID: orcid.org/0000-0002-1467-3105](#)⁹,
- [Katayun Barmak](#) [ORCID: orcid.org/0000-0003-0070-158X](#)¹⁰,
- [Julien Madéo](#) [ORCID: orcid.org/0000-0002-1711-5010](#)⁴,
- [Felipe H. da Jornada](#) [ORCID: orcid.org/0000-0001-6712-7151](#)⁵,
- [Tony F. Heinz](#)^{1,2} &

- [Keshav M. Dani](#) [ORCID: orcid.org/0000-0003-3917-6305⁴](#)

[*Nature*](#) volume **603**, pages 247–252 (2022)

- 2024 Accesses
- 84 Altmetric
- [Metrics details](#)

Subjects

- [Optical materials and structures](#)
- [Two-dimensional materials](#)

Abstract

Interlayer excitons (ILXs) — electron–hole pairs bound across two atomically thin layered semiconductors — have emerged as attractive platforms to study exciton condensation^{1,2,3,4}, single-photon emission and other quantum information applications^{5,6,7}. Yet, despite extensive optical spectroscopic investigations^{8,9,10,11,12}, critical information about their size, valley configuration and the influence of the moiré potential remains unknown. Here, in a WSe₂/MoS₂ heterostructure, we captured images of the time-resolved and momentum-resolved distribution of both of the particles that bind to form the ILX: the electron and the hole. We thereby obtain a direct measurement of both the ILX diameter of around 5.2 nm, comparable with the moiré-unit-cell length of 6.1 nm, and the localization of its centre of mass. Surprisingly, this large ILX is found pinned to a region of only 1.8 nm diameter within the moiré cell, smaller than the size of the exciton itself. This high degree of localization of the ILX is backed by Bethe–Salpeter equation calculations and demonstrates that the ILX can be localized within small moiré unit cells. Unlike large moiré cells, these are uniform over large regions, allowing the formation of extended arrays of localized excitations for quantum technology.

This is a preview of subscription content

Access options

Subscribe to Nature+

Get immediate online access to the entire Nature family of 50+ journals

\$29.99

monthly

[Subscribe](#)

Subscribe to Journal

Get full journal access for 1 year

\$199.00

only \$3.90 per issue

[Subscribe](#)

All prices are NET prices.

VAT will be added later in the checkout.

Tax calculation will be finalised during checkout.

Buy article

Get time limited or full article access on ReadCube.

\$32.00

[Buy](#)

All prices are NET prices.

Additional access options:

- [Log in](#)
- [Learn about institutional subscriptions](#)

Fig. 1: Sample structure and experimental configuration.

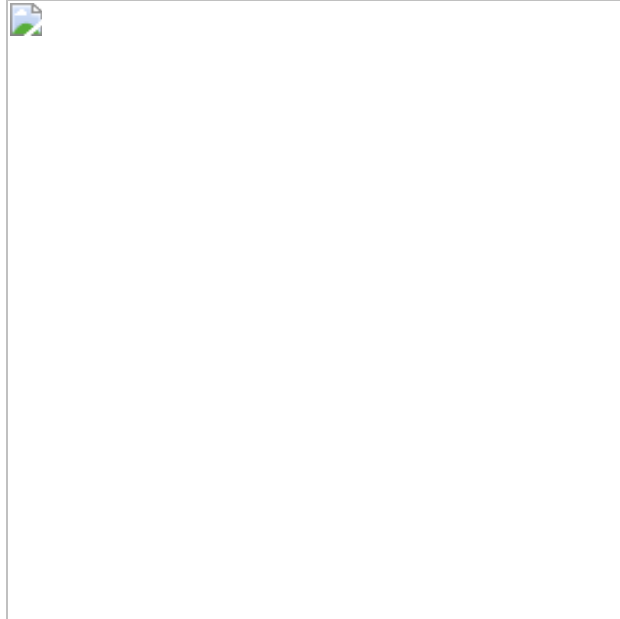


Fig. 2: Static and photoexcited TR- μ -ARPES measurements.

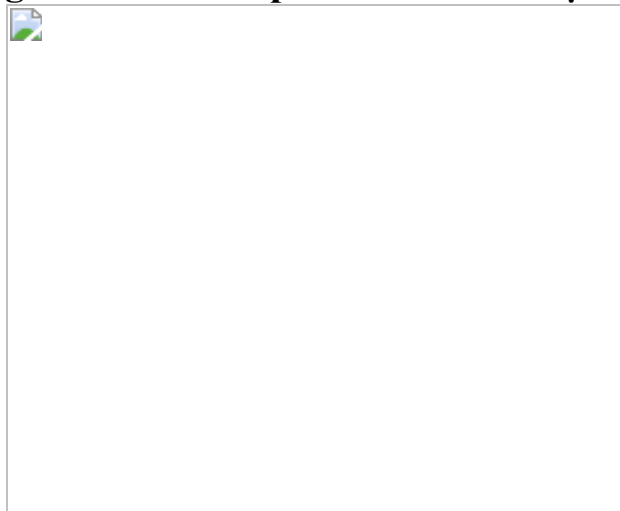


Fig. 3: Time-resolved and momentum-resolved distributions of the ILX electrons and holes.

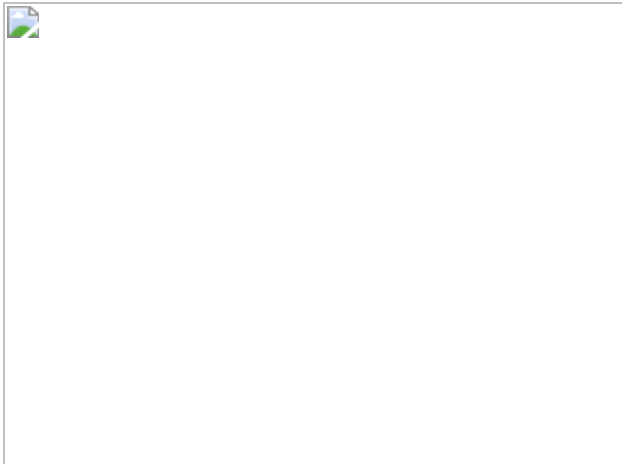
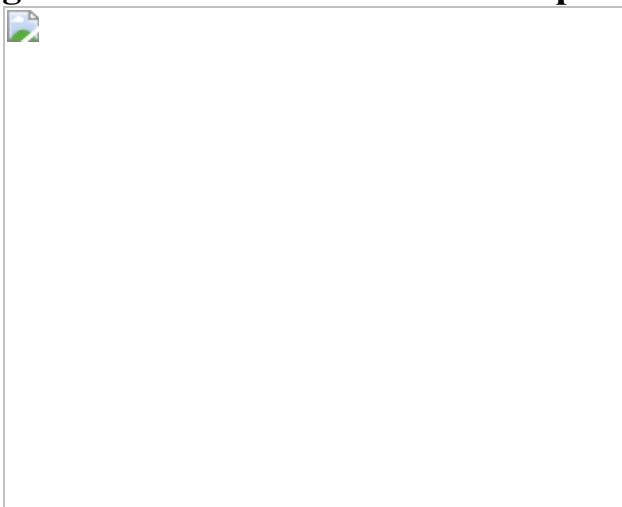


Fig. 4: ILX wavefunctions in real space.



Data and materials availability

All data are available in the main text or the [Supplementary Material](#).

References

1. Wang, Z. et al. Evidence of high-temperature exciton condensation in two-dimensional atomic double layers. *Nature* **574**, 76–80 (2019).
2. Wang, J. et al. Optical generation of high carrier densities in 2D semiconductor heterobilayers. *Sci. Adv.* **5**, eaax0145 (2019).

3. Li, W., Lu, X., Dubey, S., Devenica, L. & Srivastava, A. Dipolar interactions between localized interlayer excitons in van der Waals heterostructures. *Nat. Mater.* **19**, 624–629 (2020).
4. Kremser, M. et al. Discrete interactions between a few interlayer excitons trapped at a MoSe₂–WSe₂ heterointerface. *Npj 2D Mater. Appl.* **4**, 8 (2020).
5. Yu, H., Liu, G.-B., Tang, J., Xu, X. & Yao, W. Moiré excitons: from programmable quantum emitter arrays to spin–orbit-coupled artificial lattices. *Sci. Adv.* **3**, e1701696 (2017).
6. Liu, X. & Hersam, M. C. 2D materials for quantum information science. *Nat. Rev. Mater.* **4**, 669–684 (2019).
7. Kennes, D. M. et al. Moiré heterostructures as a condensed-matter quantum simulator. *Nat. Phys.* **17**, 155–163 (2021).
8. Rivera, P. et al. Interlayer valley excitons in heterobilayers of transition metal dichalcogenides. *Nat. Nanotechnol.* **13**, 1004 (2018).
9. Tran, K. et al. Evidence for moiré excitons in van der Waals heterostructures. *Nature* **567**, 71–75 (2019).
10. Seyler, K. L. et al. Signatures of moiré-trapped valley excitons in MoSe₂/WSe₂ heterobilayers. *Nature* **567**, 66–70 (2019).
11. Karni, O. et al. Infrared interlayer exciton emission in MoS₂/WSe₂ heterostructures. *Phys. Rev. Lett.* **123**, 247402 (2019).
12. Zhang, L. et al. Highly valley-polarized singlet and triplet interlayer excitons in van der Waals heterostructure. *Phys. Rev. B* **100**, 041402 (2019).
13. Fogler, M. M., Butov, L. V. & Novoselov, K. S. High-temperature superfluidity with indirect excitons in van der Waals heterostructures. *Nat. Commun.* **5**, 4555 (2014).

14. Wu, F., Lovorn, T. & MacDonald, A. H. Theory of optical absorption by interlayer excitons in transition metal dichalcogenide heterobilayers. *Phys. Rev. B* **97**, 035306 (2018).
15. Jin, C. et al. Identification of spin, valley and moiré quasi-angular momentum of interlayer excitons. *Nat. Phys.* **15**, 1140–1144 (2019).
16. Jin, C. et al. Observation of moiré excitons in WSe₂/WS₂ heterostructure superlattices. *Nature* **567**, 76–80 (2019).
17. Gillen, R. & Maultzsch, J. Interlayer excitons in MoSe₂/WSe₂ heterostructures from first principles. *Phys. Rev. B* **97**, 165306 (2018).
18. Shabani, S. et al. Deep moiré potentials in twisted transition metal dichalcogenide bilayers. *Nat. Phys.* **17**, 720–725 (2021).
19. Man, M. K. L. et al. Experimental measurement of the intrinsic excitonic wave function. *Sci. Adv.* **7**, eabg0192 (2021).
20. Dong, S. et al. Direct measurement of key exciton properties: energy, dynamics, and spatial distribution of the wave function. *Nat. Sci.* **1**, e10010 (2021).
21. Wallauer, R. et al. Momentum-resolved observation of exciton formation dynamics in monolayer WS₂. *Nano Lett.* **21**, 5867–5873 (2021).
22. Li, H. et al. Imaging moiré flat bands in three-dimensional reconstructed WSe₂/WS₂ superlattices. *Nat. Mater.* **20**, 945–950 (2021).
23. Madéo, J. et al. Directly visualizing the momentum-forbidden dark excitons and their dynamics in atomically thin semiconductors. *Science* **370**, 1199–1204 (2020).
24. Schönhense, G., Medjanik, K. & Elmers, H.-J. Space-, time- and spin-resolved photoemission. *J. Electron. Spectrosc. Relat. Phenom.* **200**, 94–118 (2015).

25. Medjanik, K. et al. Direct 3D mapping of the Fermi surface and Fermi velocity. *Nat. Mater.* **16**, 615–621 (2017).
26. Kunstmann, J. et al. Momentum-space indirect interlayer excitons in transition-metal dichalcogenide van der Waals heterostructures. *Nat. Phys.* **14**, 801–805 (2018).
27. Moser, S. An experimentalist’s guide to the matrix element in angle resolved photoemission. *J. Electron. Spectrosc. Relat. Phenom.* **214**, 29–52 (2017).
28. Beaulieu, S. et al. Revealing hidden orbital pseudospin texture with time-reversal dichroism in photoelectron angular distributions. *Phys. Rev. Lett.* **125**, 216404 (2020).
29. Rustagi, A. & Kemper, A. F. Photoemission signature of excitons. *Phys. Rev. B* **97**, 235310 (2018).
30. Ohnishi, H., Tomita, N. & Nasu, K. Direct determination of exciton wavefunction amplitudes by the momentum-resolved photo-electron emission experiment. *Int. J. Mod. Phys. B* **32**, 1850094 (2017).
31. Wang, Y. H., Steinberg, H., Jarillo-Herrero, P. & Gedik, N. Observation of Floquet–Bloch states on the surface of a topological insulator. *Science* **342**, 453–457 (2013).
32. Mahmood, F. et al. Selective scattering between Floquet–Bloch and Volkov states in a topological insulator. *Nat. Phys.* **12**, 306–310 (2016).
33. Cui, X. et al. Transient excitons at metal surfaces. *Nat. Phys.* **10**, 505–509 (2014).
34. Liu, E. et al. Signatures of moiré trions in WSe₂/MoSe₂ heterobilayers. *Nature* **594**, 46–50 (2021).
35. Hybertsen, M. S. & Louie, S. G. Electron correlation in semiconductors and insulators: band gaps and quasiparticle energies.

Phys. Rev. B **34**, 5390–5413 (1986).

36. Rohlfing, M. & Louie, S. G. Electron–hole excitations and optical spectra from first principles. *Phys. Rev. B* **62**, 4927–4944 (2000).
37. Meckbach, L., Stroucken, T. & Koch, S. W. Giant excitation induced bandgap renormalization in TMDC monolayers. *Appl. Phys. Lett.* **112**, 061104 (2018).
38. Sun, D. et al. Observation of rapid exciton–exciton annihilation in monolayer molybdenum disulfide. *Nano Lett.* **14**, 5625–5629 (2014).
39. Wu, F., Lovorn, T., Tutuc, E. & MacDonald, A. H. Hubbard model physics in transition metal dichalcogenide moiré bands. *Phys. Rev. Lett.* **121**, 026402 (2018).
40. Brown, D. Decentering distortion of lenses. *Photogramm. Eng.* **32**, 444–462 (1966).
41. Xian, R. P., Rettig, L. & Ernstorfer, R. Symmetry-guided nonrigid registration: the case for distortion correction in multidimensional photoemission spectroscopy. *Ultramicroscopy* **202**, 133–139 (2019).
42. Ye, Z. et al. Efficient generation of neutral and charged biexcitons in encapsulated WSe₂ monolayers. *Nat. Commun.* **9**, 3718 (2018).
43. Giannozzi, P. et al. QUANTUM ESPRESSO: a modular and open-source software project for quantum simulations of materials. *J. Phys. Condens. Matter* **21**, 395502 (2009).
44. Schlipf, M. & Gygi, F. Optimization algorithm for the generation of ONCV pseudopotentials. *Comput. Phys. Commun.* **196**, 36–44 (2015).
45. Ismail-Beigi, S. Truncation of periodic image interactions for confined systems. *Phys. Rev. B* **73**, 233103 (2006).
46. Dion, M., Rydberg, H., Schröder, E., Langreth, D. C. & Lundqvist, B. I. Van der Waals density functional for general geometries. *Phys. Rev.*

Lett. **92**, 246401 (2004).

47. Cooper, V. R. Van der Waals density functional: an appropriate exchange functional. *Phys. Rev. B* **81**, 161104 (2010).
48. Deslippe, J. et al. BerkeleyGW: a massively parallel computer package for the calculation of the quasiparticle and optical properties of materials and nanostructures. *Comput. Phys. Commun.* **183**, 1269–1289 (2012).
49. da Jornada, F. H., Qiu, D. Y. & Louie, S. G. Nonuniform sampling schemes of the Brillouin zone for many-electron perturbation-theory calculations in reduced dimensionality. *Phys. Rev. B* **95**, 035109 (2017).
50. Alexeev, E. M. et al. Resonantly hybridized excitons in moiré superlattices in van der Waals heterostructures. *Nature* **567**, 81–86 (2019).
51. Zhang, C. et al. Interlayer couplings, Moiré patterns, and 2D electronic superlattices in MoS₂/WSe₂ hetero-bilayers. *Sci. Adv.* **3**, e1601459 (2017).

Acknowledgements

We acknowledge support for optical spectroscopy measurements, data analysis, sample characterization, and sample fabrication from the AMOS program, Chemical Sciences, Geosciences, and Biosciences Division, Basic Energy Sciences, U.S. Department of Energy. Sample preparation was also supported by the Gordon and Betty Moore Foundation’s EPiQS Initiative through grant number GBMF9462 and made use of the facilities in the Stanford Nano Shared Facilities (SNSF), supported by the National Science Foundation under award ECCS-1542152. We thank the OIST engineering support section and Y. Yamauchi from the OIST Facilities Operations and Use section for their support. The TR-μ-ARPES instrumentation, data acquisition and preliminary analysis were supported by the Femtosecond Spectroscopy Unit, Kick-start fund KICKS. XUV generation technology

was supported by OIST Innovative Technology – Proof of Concept Program at the Okinawa Institute of Science and Technology Graduate University. The computational work was supported by the Center for Computational Study of Excited-State Phenomena in Energy Materials, which is funded by the U.S. Department of Energy (DOE), Office of Science, Basic Energy Sciences, Materials Sciences and Engineering Division, under contract no. DE-AC02-05CH11231, as part of the Computational Materials Sciences Program. We acknowledge the use of computational resources at the National Energy Research Scientific Computing Center, a DOE Office of Science User Facility supported by the Office of Science of the US DOE under the above contract. Funding: AMOS program, Chemical Sciences, Geosciences, and Biosciences Division, Basic Energy Sciences, U.S. Department of Energy (T.F.H., O.K., E.B., H.B.R.). Gordon and Betty Moore Foundation’s EPiQS Initiative through grant number GBMF9462 (J.H., A.L.O.). Koret Foundation (O.K.). Natural Science and Engineering Research Council (NSERC) of Canada, fellowship PGSD3-502559-2017 (E.B.). NTT Research Fellowship (J.H.). Femtosecond Spectroscopy Unit – Okinawa Institute of Science and Technology Graduate University (V.P., M.K.L.M., C.S., D.R.B., X.Z., A.A.-M., M.M.M.A., N.S.C., A.K., A.J.W., J.M., K.M.D.). Okinawa Institute of Science and Technology Graduate University Innovative Technology Research – Proof of Concept Program (K.M.D.). JSPS KAKENHI grant no. JP17K04995 (M.K.L.M.). Kick-start fund KICKS – Okinawa Institute of Science and Technology Graduate University (K.M.D., N.S.C.). JSPS KAKENHI grant no. 21H01020 (J.M.). FAPESP for post-doctoral fellowships, grant nos. 2018/04926-9 and 2017/20100-00 (H.B.R.). National Science Foundation Materials Research Science and Engineering Centers DMR-1420634 and DMR-2011738 (K.B., B.K.). Elemental Strategy Initiative, conducted by the MEXT, Japan, grant no. JPMXP0112101001 (K.W., T.T.). JSPS KAKENHI grant nos. 19H05790 and JP20H00354 (K.W., T.T.). Department of Energy Office of Science, Basic Energy Sciences, Materials Sciences and Engineering Division, under contract no. DE-AC02-05CH11231 (F.H.dJ., J.D.G.).

Author information

Author notes

1. Chakradhar Sahoo

Present address: Tata Institute of Fundamental Research, Hyderabad,
Gopanpally, Serlingampalli, Telangana, India

2. These authors contributed equally: Ouri Karni, Elyse Barré, Vivek Pareek, Johnathan D. Georgaras, Michael K. L. Man, Chakradhar Sahoo

Affiliations

1. Department of Applied Physics, Stanford University, Stanford, CA, USA

Ouri Karni, Jenny Hu & Tony F. Heinz

2. SLAC National Accelerator Laboratory, Menlo Park, CA, USA

Ouri Karni, Elyse Barré, Henrique B. Ribeiro, Aidan L.
O'Beirne & Tony F. Heinz

3. Department of Electrical Engineering, Stanford University, Stanford, CA, USA

Elyse Barré

4. Femtosecond Spectroscopy Unit, Okinawa Institute of Science and Technology Graduate University, Onna-son, Okinawa, Japan

Vivek Pareek, Michael K. L. Man, Chakradhar Sahoo, David R.
Bacon, Xing Zhu, Abdullah Al-Mahboob, Mohamed M. M.
Abdelrasoul, Nicholas S. Chan, Arka Karmakar, Andrew J.
Winchester, Julien Madéo & Keshav M. Dani

5. Department of Materials Science and Engineering, Stanford University, Stanford, CA, USA

Johnathan D. Georgaras & Felipe H. da Jornada

6. Department of Physics, Stanford University, Stanford, CA, USA

Aidan L. O’Beirne

7. Department of Mechanical Engineering, Columbia University, New York, NY, USA

Bumho Kim

8. Research Center for Functional Materials, National Institute for Materials Science, Tsukuba, Japan

Kenji Watanabe

9. International Center for Materials Nanoarchitectonics, National Institute for Materials Science, Tsukuba, Japan

Takashi Taniguchi

10. Department of Applied Physics and Applied Mathematics, Columbia University, New York, NY, USA

Katayun Barmak

Contributions

O.K., E.B. and K.M.D. conceived the project. K.W., T.T., B.K. and K.B. supplied raw materials for sample fabrication. E.B. and O.K., supported by A.L.O., H.B.R. and J.H. fabricated the samples. V.P., M.K.L.M. and C.S. collected the data, with assistance from D.R.B., X.Z., A.A.-M., M.M.M.A., A.K., A.J.W. and J.M. V.P., M.K.L.M., C.S., N.S.C. and X.Z. performed preliminary analysis. E.B. and O.K. analysed the data. F.H.dJ. and J.D.G. performed theoretical calculations. J.D.G. was supervised by F.H.dJ. A.L.O., E.B., H.B.R., J.H. and O.K. were supervised by T.F.H. K.M.D. supervised the project. All authors contributed to discussions and manuscript preparations.

Corresponding author

Correspondence to [Keshav M. Dani](#).

Ethics declarations

Competing interests

J.M., M.K.L.M. and K.M.D. are inventors on a patent application related to this work filed by the Okinawa Institute of Science and Technology School Corporation (US 2020/0333559 A1 published on October 22, 2020). The authors declare no other competing interests.

Peer review

Peer review information

Nature thanks the anonymous reviewers for their contribution to the peer review of this work.

Additional information

Publisher's note Springer Nature remains neutral with regard to jurisdictional claims in published maps and institutional affiliations.

Extended data figures and tables

[Extended Data Fig. 1 Reflection contrast spectra of the sample.](#)

Top, reflection of the 1L WSe₂ region, showing its lowest excitonic resonance at 1.7 eV, marked with a grey dashed line. Middle, the same, for 1L MoS₂, with its lowest resonance at 1.95 eV. Bottom, the same, for the heterobilayer region. It shows several resonances, marked I, II and III, instead of a single line in the vicinity of the WSe₂ resonance. This signature has been categorized as evidence for the emergence of the moiré pattern¹⁶. All measurements were done at 80 K.

Extended Data Fig. 2 Distortion correction procedures in the momentum microscope.

a, Schematic of the imaging optics in the momentum microscope. To correct for the distortions in the imaging optics, a physical grid was inserted at the back focal plane of the objective lens. **b**, A cut in the k_x - k_y plane in the presence of the grid as imaged by the detector before correction. Overlaid on top is a yellow box representing a perfect square. It can be seen that the pattern of the grid is not perfectly square. A weak pincushion distortion is also visible. **c**, The same, after correction, showing the grid lines conforming to the yellow square. **d**, A 2D projection of the grid at different electron kinetic energies E_{kin} , before corrections. The variation of the distortion and magnification with different E_{kin} is obvious. **e**, The same, after energy-dependent grid distortion corrections.

Extended Data Fig. 3 Static ARPES data with VB assignment near the K points.

A rescaled version of Fig. 2a, highlighting the MoS₂ VBs around the K valleys.

Extended Data Fig. 4 Extracting the exciton-bound electron dispersion.

a, k_x ARPES cut of the photoexcited electron signal around the K point. The dashed yellow line is the VB dispersion. **b**, Selected spectra (EDC) along the dashed orange, green and red lines marked in a, together with the Gaussian fits, demonstrating the negative dispersion of the signal.

Extended Data Fig. 5 TR- μ -ARPES data with above bandgap photoexcitation.

a, A momentum slice along the Γ -K axis of the BZ at $t = 0$ ps. The photoexcited electrons are scattered over a wide momentum and the shaded energy range above the dashed orange line, with a clear CB dispersion

around the K point (yellow dashed indicator). **b**, Normalized EDC at the K point. The green plot is the equilibrium data. The black plot refers to the data at $t = 0$ ps. **c**, The same as **a**, at $t = 50$ ps. The photoexcited electrons are concentrated at 1 eV energy (magenta dashed line) with an anomalous dispersion curvature. **d**, The same as **b**, for $t = 50$ ps. The red plot refers to the data at 50-ps delay. This highlights the spectral differences between the unbound (at $t = 0$ ps) and exciton-bound (at later times) electrons showing up at different energies. The dashed magenta lines at energies below 0 eV indicate the band-edge energies for each VB. In comparison with the equilibrium VB EDC, at $t = 50$ ps, a reduction in counts is clearly registered for VB 1, associated with WSe₂, whereas none is registered for the other VBs, deducing that no holes are accumulating in MoS₂. **e**, Average momentum deviation from the VBM, $(k_x, k_y) = (0, 0)$ Å⁻¹, of the ILX-bound hole distributions, determined at various time delays using the Gaussian fit. The distribution are clustered on average around $(k_x, k_y) = (0.002, 0.0088) \pm (0.0056, 0.0042)$ Å⁻¹, effectively (within a single-pixel error) at the VBM. **f**, The same for the ILX-bound electrons. Their distributions are broadly clustered around $(k_x, k_y) = (-0.0139, 0.0381) \pm (0.0019, 0.0035)$ Å⁻¹, deviating from the hole momentum. This is attributed to the expected momentum mismatch between the ILX-bound electrons and holes of a moiré exciton.

Extended Data Fig. 6 Extracting the photoexcited hole distribution.

a, APRES energy–momentum cut along the K–Γ direction around a specific K point for unexcited conditions. **b**, Fitting the VB with three Gaussians in energy near the centre of the plot in **a**. **c**, The same as **a**, after the photoexcitation. **d**, The same as **b**, after the photoexcitation. **e**, Heat map of the photoemitted counts associated with the top VB of the unperturbed sample. **f**, The same, after the excitation. Red squares mark the region around $[k_{x0}, k_{y0}]$ used to normalize the counts from each measurement. **g**, The hole occupation distribution map resulting from the comparison between panels **e** and **f**.

Extended Data Fig. 7 Temperature dependence of ILX density and momentum distribution widths at 50-ps delay.

a, ILX density, acquired for two excitation powers, at 100 K and 300 K. The reduction of ILX density with temperature is in line with the expected shortening of their lifetime at elevated temperatures. **b**, Fitted Gaussian widths of the ILX-bound hole and electron distributions at 100 K and 300 K. The width of the ILX-bound hole distribution hardly changes, whereas the electron distribution shows some broadening within our experimental accuracy. This is consistent with the analysis in the [Supplementary Material](#) that predicts little temperature dependence for the widths of $I_e(\mathbf{k})$ and $I_h(\mathbf{k})$. Both excitation powers show very similar distribution widths, ruling out low signal-to-noise ratio issues or many-body effects. The latter is also consistent with the ILX densities being lower than their broadening onset described in Fig. [3e](#).

Supplementary information

Supplementary Information

This file contains supplementary text, Supplementary Figs. 1–3, supplementary equations and supplementary references

Rights and permissions

Reprints and Permissions

About this article

Cite this article

Karni, O., Barré, E., Pareek, V. *et al.* Structure of the moiré exciton captured by imaging its electron and hole. *Nature* **603**, 247–252 (2022). <https://doi.org/10.1038/s41586-021-04360-y>

- Received: 29 July 2021
- Accepted: 14 December 2021
- Published: 09 March 2022
- Issue Date: 10 March 2022
- DOI: <https://doi.org/10.1038/s41586-021-04360-y>

Share this article

Anyone you share the following link with will be able to read this content:

[Get shareable link](#)

Sorry, a shareable link is not currently available for this article.

[Copy to clipboard](#)

Provided by the Springer Nature SharedIt content-sharing initiative

This article was downloaded by **calibre** from <https://www.nature.com/articles/s41586-021-04360-y>.

| [Section menu](#) | [Main menu](#) |

- Article
- Open Access
- [Published: 09 March 2022](#)

A large-scale microelectromechanical-systems-based silicon photonics LiDAR

- [Xiaosheng Zhang](#) [ORCID: orcid.org/0000-0003-4435-1796¹](#),
- [Kyungmok Kwon¹](#),
- [Johannes Henriksson](#) [ORCID: orcid.org/0000-0003-3130-9775¹](#),
- [Jianheng Luo¹](#) &
- [Ming C. Wu¹](#)

Nature volume 603, pages 253–258 (2022)

- 9115 Accesses
- 85 Altmetric
- [Metrics details](#)

Subjects

- [Imaging and sensing](#)
- [Optical sensors](#)
- [Silicon photonics](#)

Abstract

Three-dimensional (3D) imaging sensors allow machines to perceive, map and interact with the surrounding world¹. The size of light detection and ranging (LiDAR) devices is often limited by mechanical scanners. Focal plane array-based 3D sensors are promising candidates for solid-state LiDARs because they allow electronic scanning without mechanical moving parts. However, their resolutions have been limited to 512 pixels or smaller². In this paper, we report on a 16,384-pixel LiDAR with a wide field of view (FoV, $70^\circ \times 70^\circ$), a fine addressing resolution ($0.6^\circ \times 0.6^\circ$), a narrow beam divergence ($0.050^\circ \times 0.049^\circ$) and a random-access beam addressing with sub-MHz

operation speed. The 128×128 -element focal plane switch array (FPSA) of grating antennas and microelectromechanical systems (MEMS)-actuated optical switches are monolithically integrated on a $10 \times 11\text{-mm}^2$ silicon photonic chip, where a 128×96 subarray is wire bonded and tested in experiments. 3D imaging with a distance resolution of 1.7 cm is achieved with frequency-modulated continuous-wave (FMCW) ranging in monostatic configuration. The FPSA can be mass-produced in complementary metal–oxide–semiconductor (CMOS) foundries, which will allow ubiquitous 3D sensors for use in autonomous cars, drones, robots and smartphones.

[Download PDF](#)

Main

Autonomous systems powered by artificial intelligence will have a transformative impact on our society. 3D sensors that directly measure the coordinates, shapes and velocities of objects have seen an increasing number of applications in autonomous vehicles, drones and robots^{3,4}. LiDAR systems can work in darkness and offer high resolution and high accuracy thanks to the short wavelength of light⁵. Small-form-factor LiDARs with single-photon avalanche diode arrays^{6,7,8} have started to be featured in smartphones and other consumer electronics; however, their ranges are limited, owing to flood illumination. Scanning LiDARs with collimated laser beams have much longer reach but often require bulky scanners that are difficult to integrate.

Recently, there has been intensive research on integrated optical beam scanners capable of high-speed operation over a large FoV with high resolution and low power consumption, which are the key requirements for solid-state LiDARs. Two common architectures are the optical phased array (OPA) and the FPSA. OPAs have been demonstrated on photonic integrated circuit platforms^{9,10,11,12,13,14,15,16,17,18,19} and MEMS platforms^{20,21,22}. They are capable of random-access beam scanning but require precise amplitude and phase control of all the optical antennas in the array, which makes scaling challenging. So far, most OPAs with large pixel number and large FoV are only 1D arrays. Scanning in the orthogonal direction is achieved by wavelength tuning using a widely tunable laser. For example, Chung et al. demonstrated a 1,024-element 1D OPA with 45° FoV in 2018 (ref. ¹³) and Poulton et al. demonstrated an 8,192-element 1D OPA with 100° FoV in 2020 (ref. ¹⁹). 2D OPAs with large pixel number have been reported on MEMS platforms^{21,22} but their FoV is usually small, owing to the large array pitch to accommodate the MEMS actuators. The performances of some state-of-the-art OPAs are summarized in Extended Data Table 1.

By contrast, the FPSA uses a camera-like optical system that maps each angle within the FoV to a pixel at the back focal plane of an imaging lens. Instead of integrating a ranging unit at each pixel, the optical switch network in the FPSA allows all pixels to share one (or more) LiDAR ranging unit(s). Each pixel consists of only an optical antenna and a switch, making it possible to integrate a large array on a single chip. Small-scale FPSAs with tens of pixels have been demonstrated using thermally tuned Mach-Zehnder interferometer (MZI) switches^{[23,24,25,26,27,28,29](#)}. However, their integration density is limited by the large footprint of the MZIs and the high power consumption of thermo-optic phase shifters. MEMS-based silicon photonic switches offer many advantages, including small footprint, low loss (nearly zero loss in the OFF state), low power consumption and fast switching time. These advantages have been demonstrated in large-scale optical switches for optical communication networks^{[30,31](#)}. Proof-of-concept scanners with a small number of pixels (≤ 400) were recently reported^{[32,33](#)}. The performances of the reported FPSAs are summarized in Extended Data Table 2 and Extended Data Fig. 1.

In this paper, we experimentally demonstrate a 16,384-pixel FMCW imaging LiDAR with a monolithically integrated 128×128 -element silicon photonic MEMS FPSA (a 128×96 subarray is wire bonded and tested in experiments). With a 5-mm-focal-length compound lens, the system can randomly direct the laser beam to 16,384 distinct directions in a $70^\circ \times 70^\circ$ FoV with a 0.05° divergence angle and a microsecond switching time. To the best of our knowledge, this is the largest integrated 2D FPSA ever reported. 3D imaging is realized by combining the FPSA with FMCW ranging. The FPSA presented here is highly scalable. Megapixel 3D imaging LiDAR is possible by leveraging the Moore's law-like scaling that has propelled the explosive growth of CMOS imaging sensors over the past few decades.

FPSA scanner architecture and design

The schematic of the FPSA is shown in Fig. 1a. The working principle of the beam scanner is shown in Fig. 1b using a 1D FPSA as an example. An array of optical antennas is placed on the back focal plane of a convex lens with a focal length of f and each antenna is connected to the input light source by means of an optical switch. When one of the optical switches is turned on, the input light is routed to the corresponding antenna. The emitted light from the antenna is then converted to a collimated beam by the lens. The angle between the output beam and the lens optical axis is $\theta = \tan^{-1}(-x/f)$, in which x is the coordinate of the emitting antenna relative to the optical axis. By turning on antennas at different locations, the output beam can be steered to the corresponding angles. The FoV is $2\tan^{-1}(L/2f)$, in which L is the overall size of the array. The divergence angle of the output beam can be estimated by l/f , in

which l is the size of an individual grating antenna. The angular resolution can be estimated by p/f , in which p is the array pitch.

Fig. 1: Architecture and working principle of the FPSA.

 figure 1



a, Perspective-view schematic of the 2D FPSA with the lens and output beam. Light is coupled onto the FPSA chip by means of one of the input ports and then routed to the selected grating antenna by turning on the corresponding row-selection and column-selection switches. The lens converts the emitted light to a collimated beam. **b**, Schematic of a 1D FPSA beam scanner demonstrating the working principle. **c**, Top-view schematic of the 2D FPSA design. **d**, Schematics of the MEMS optical switches and grating antennas in the ON and OFF states. In the ON state, the tip of the polysilicon coupler waveguide (green) is pulled down close to the bus waveguides (yellow) to couple light to the grating antenna.

The architecture of the 2D FPSA is shown in Fig. 1c using a 4×4 array as an example. Each optical antenna (grating) is connected to a row waveguide by means of a MEMS optical switch (hereafter called a column-selection switch) and each row waveguide is connected to one of the two input waveguides by means of a MEMS optical switch (hereafter called a row-selection switch). To reduce the total number of control signals from N^2 to $2N$ in an $N \times N$ FPSA, we used a row–column addressing scheme: all switches in the same column are electrically connected, whereas the row-selection switch is individually addressed. By turning on one row-selection switch and one

column-selection switch, light from one of the two input ports is routed to the selected grating antenna and emitted to the prescribed angle in free space.

We used a MEMS optical switch design similar to those reported in refs. [30,31](#), in which the tip of a polysilicon coupler is physically moved by an electrostatic MEMS actuator to control the light path, as shown in Fig. [1d](#). The row-selection switch has two actuators coupling light between the input and row waveguides, whereas the column-selection switch has only one actuator, as the grating is directly connected to the polysilicon waveguide.

We designed a 128×128 -element FPSA with a $55\text{-}\mu\text{m}$ pitch in both directions, thus the overall array size is $7 \times 7 \text{ mm}^2$. The overall chip including the routing waveguides, input/output couplers and bonding pads is $10 \times 11 \text{ mm}^2$ in size. The device is fabricated on a silicon-on-insulator (SOI) wafer with a 220-nm-thick device layer. Figure [2a–c](#) shows the optical microscope images of the entire chip, unit cells comprising grating antennas and column-selection switches, and the row-selection switches, respectively. The scanning electron micrographs of the array are shown in Fig. [2d](#), with the close-up views of the unit cell and the grating antenna in Fig. [2e,f](#), respectively. Confocal microscopic images of the device are shown in Extended Data Fig. [2](#). The waveguides are defined on the device layer of the SOI wafer by a partial etch. The grating antennas are patterned on the polysilicon layer with a focusing-curved shape of around $10 \times 5 \text{ }\mu\text{m}^2$ in size. The orientation and grating period of each antenna are individually tailored so that the output beam points towards the centre of the lens to increase the light-collection efficiency and reduce the aberration effects of the lens. The emission efficiencies of all the gratings are kept higher than 65%. The details of the grating antenna design are described in [Methods](#) and Extended Data Fig. [3](#). The device lens (Thorlabs MVL5M23, $f = 5 \text{ mm}$, F/2.8) maps each grating antenna to a distinctive far-field angle, resulting in a $70^\circ \times 70^\circ$ FoV, 0.6° resolution and 0.05° divergence angle.

Fig. 2: Microscopic images of the fabricated FPSA device.

 **figure 2**

a–c, Microscopic images showing the FPSA chip (**a**), the grating antennas with column-selection switches (**b**) and the row-selection switch (**c**). **d–f**, Scanning electron micrographs of the FPSA chip (**d**), the column-selection switches (**e**) and the grating antennas (**f**). Scale bars: **a**, 2 mm; **b** and **c**, 40 μ m; **d**, 100 μ m; **e**, 20 μ m; **f**, 4 μ m.

Device characterization

The fabricated FPSA device is wire bonded to a ceramic pin grid array (PGA) and controlled by a field-programmable gate array (FPGA) and a driver circuit board (details are described in [Methods](#)). Owing to the limited PGA pin count, only three-quarters of the row-addressing signals and all column-addressing signals are bonded, skipping every fourth row of the FPSA.

To demonstrate optical beam steering, the electrically addressed 128×96 grating antennas are turned on one at a time. The captured images of the output beam projection onto a paper screen are overlapped and shown in Fig. [3a](#). This clearly demonstrates that the fabricated FPSA is able to steer the output beam across the 70°

$\times 70^\circ$ FoV as designed, albeit with a small number of dark spots caused by minor defects on the device. To demonstrate the random-access beam-steering capability, we program the FPSA to sequentially turn on 475 selected grating antennas to display a ‘Cal’ logo, as shown in Fig. 3b. Figure 3c shows an enlarged far-field pattern with the output beam raster scanned at 100 kHz and captured by a single frame of the infrared camera running at 33 frames per second. We also characterized the beam quality by measuring the far-field beam profile with an infrared camera at 0.71 m distance away from the lens. Figure 3d shows that the measured full width at half maximum beam divergence is $0.050^\circ \times 0.049^\circ$, which matches well with the diffraction limit of the lens aperture. Measured beam profiles of more pixels are shown in Extended Data Fig. 4 and output-power-variation measurement results are shown in Extended Data Fig. 5. Details of the optical characterization setups are described in [Methods](#) and Extended Data Fig. 6.

Fig. 3: Characterization of the FPSA beam scanner.



a, Beam-steering pattern projected on a paper screen showing a $70^\circ \times 70^\circ$ FoV. **b**, A scanned ‘Cal’ logo pattern with 475 distinct output beam directions projected on a paper screen. **c**, Zoomed-in beam-steering pattern captured at the focal plane of a Fourier lens. **d**, Beam profile measured at 0.71 m away from the FPSA beam scanner. **e**, **f**, Dynamic responses of the row-selection switch (average of 22 measurements of optical power measured at the drop port) (**e**) and the column-selection switch (average of 32 measurements of optical power measured at the through port) (**f**) in the FPSA. The red curves show the applied voltage waveform and the blue curves show the measured optical power.

The temporal responses of the row-selection and column-selection switches are characterized by measuring the optical power at the switch output ports while applying a square-wave voltage signal, as shown in Fig. 3e,f, respectively. The on and off response times of the row-selection switch are 1.1 μ s and 0.6 μ s, respectively. The response times of the column-selection switch are slightly longer (2.7 μ s and 2.0 μ s for on and off switching, respectively), owing to the more compact design of the MEMS actuator. The results indicate that the device can be operated at a sub-MHz frequency for beam steering, which is suitable for scanning LiDARs.

3D imaging

An imaging LiDAR is constructed by combining the FPSA with a frequency-modulated laser and a coherent receiver. A schematic of the system is shown in Fig. 4a, with further details described in [Methods](#) and Extended Data Fig. 7. The components of the FMCW ranging system are off-chip in this demonstration; however, they could also be integrated on-chip, as demonstrated by Bhargava et al.³⁴. Linear frequency chirps with an excursion of 8.6 GHz and a ramp time of 80 μ s are generated by directly modulating a 1,550 nm-wavelength distributed feedback (DFB) laser with a pre-distorted waveform obtained from an iterative learning method³⁵. The returned light from the target is mixed with a reference light at the photodetector. A Fourier transform then extracts the beat frequency that is proportional to the target distance. We use a monostatic configuration in which the same grating antenna on the FPSA is used to transmit the FMCW light and receive the returned signal from the target.

Fig. 4: 3D imaging results.

 **figure 4**

a, Schematic of the FMCW LiDAR with the FPSA beam scanner. **b**, Representative FMCW LiDAR spectrum with a target at 0.84 m. **c**, **d**, Point clouds and camera images of the targets composed of three letters in the same plane (**c**) and in different planes (**d**) at about 0.8 m. **e**, **f**, Representative FMCW LiDAR spectra with targets at 5.5 m (**e**)

and 10.8 m (**f**). **g, h**, Point clouds and camera images of targets at about 5.2 m (**g**) and 10 m (**h**). The point clouds are colour-coded by the z -coordinate values.

To demonstrate 3D imaging, we used a 25-mm-focal-length F/1.4 lens (Navitar SWIR-25) with the FPSA, achieving a $16^\circ \times 16^\circ$ FoV and a 0.13° addressing resolution. Reflective targets made of materials similar to those used for traffic signs are placed at distances of roughly 0.8 m, 5 m and 10 m from the imaging lens. The output beam is scanned sequentially in the FoV. The LiDAR ranging resolution is 1.7 cm and the output power at the device lens is about 1 mW for the 0.8-m measurements and 2 mW for the 5-m and 10-m measurements. Example beat signal spectra of the FMCW LiDAR measurements are shown in Fig. [4b, e, f](#) and the measured point clouds are shown in Figs. [4c, d, g, h](#). Good 3D image fidelity is achieved with lateral resolution matched to that of the FPSA and distance resolution agreeing well with the frequency excursion.

Scalability of imaging LiDAR

To further increase the resolution, we can increase the chip size and/or shrink the footprint of the pixel. The footprint of the current pixel ($55 \times 55 \mu\text{m}^2$) can be reduced by optimizing the design of the MEMS actuators and the switch couplers. It is feasible to shrink the pixel to $10 \times 10 \mu\text{m}^2$ for megapixel LiDAR with a $1 \times 1\text{-cm}^2$ FPSA, which will improve the angular resolution to 0.11° with an $f=5$ mm lens or 0.02° with an $f=25$ mm lens. For such high-resolution FPSA, it is important to minimize the switch loss, as there are a large number of switches (1,000) along each row. A salient feature of our FPSA is that the MEMS-actuated switches have nearly zero loss in the OFF state (the only loss is waveguide propagation loss), unlike the MZI-based thermo-optic switches. This makes it possible to keep the optical insertion loss low for high-density FPSAs. The FPSA is fabricated using standard semiconductor processes and can be mass-produced at commercial CMOS foundries.

One unique advantage of the FPSA LiDAR is its flexibility. The FoV and angular resolution can be easily adjusted by selecting imaging lenses with different focal lengths, taking advantage of the large library of well-optimized camera lenses designed for a wide range of focal lengths and image sensor sizes. For example, compact mobile phone camera lenses are suitable for small FPSA chips aiming at a small footprint and large FoV, whereas lenses designed for professional cameras are suitable for large FPSA chips aiming at low divergence and high angular resolution. Full 180° or even larger FoV can also be achieved with fisheye lenses.

Conclusions and discussions

We have presented the performance of a large-scale (16,384-pixel) imaging LiDAR using a 128×128 silicon photonic FPSA, in which a 128×96 subarray is wire bonded and tested in experiments. The grating antenna in each pixel is digitally controlled by an integrated MEMS optical switch within an area of $55 \times 55 \mu\text{m}^2$. Random-access beam steering with a FoV of $70^\circ \times 70^\circ$, an addressing resolution of 0.6° in both directions, a beam divergence of 0.05° and a sub-MHz operation speed is achieved with a 5-mm-focal-length imaging lens. 3D imaging with 1.7-cm range resolution has also been demonstrated. The angular resolution of the current system can be further increased by optimizing the optical design and fabrication technology. In addition to 3D sensing applications, the FPSA can also be used in other applications that require optical beam steering, such as free-space optical communication³⁶ and trapped-ion quantum computation³⁷.

Methods

Comparison of FPSAs and OPAs

Extended Data Table 1 compares the performance of state-of-the-art OPAs reported in the literature. Extended Data Table 2 and Extended Data Fig. 1 compare the performance of the FPSAs reported here with other 1D and 2D FPSAs reported in the literature. Note that, although some of the 1D FPSAs and OPAs use wavelength tuning to steer the beam in the orthogonal direction, here we only summarize their beam-steering performances in the FPSA or OPA direction.

Device fabrication and characterization

The FPSA device fabrication process starts with a standard silicon photonics process on SOI, followed by the deposition and patterning of an extra polysilicon layer for MEMS actuators, polysilicon coupler waveguides and grating antennas, similar to that described in ref. ³⁰. Extended Data Figure 2 shows confocal microscopic images of the fabricated FPSA device.

The far-field beam profiles of 13 pixels in addition to the one shown in Fig. 3d are measured with an infrared camera at a distance of 0.71 m away from the lens (the same condition as for Fig. 3d) and the beam profiles and cross sections are shown in Extended Data Fig. 4. The results show that the beam divergence angles are consistent throughout the array, with an average divergence of $0.048^\circ \times 0.047^\circ$ and a standard deviation of $0.0026^\circ \times 0.0029^\circ$.

The free-space output power from 256 pixels (128 pixels in row 22 and 128 pixels in row 62) of the FPSA beam scanner after the device lens is measured by an optical

power meter and histograms of the normalized optical power are shown in Extended Data Fig. 5. The data show that 105 of 128 pixels (82%) in row 22 and 86 of 128 pixels (67%) in row 62 have an output-power variation within 5 dB. The output-power variation is partly caused by the variation of optical losses; that is, light emitted from grating antennas at different locations experience different waveguide propagation losses, grating emission losses and lens collection losses, which will be further discussed in the ‘Optical efficiency’ section. Fabrication imperfections also contribute to the output-power variation. Reducing optical losses and improving the fabrication process will help improve the power uniformity. The pixels with no measured output power (corresponding to dark spots in Fig. 3a) are attributable to damaged MEMS actuators or electrical connections caused by fabrication and handling imperfections, and we expect that the yield can be largely improved with professional nanofabrication foundries.

Grating antenna design and simulation

The grating antennas are patterned on the 350-nm-thick polysilicon layer with a 250-nm partial etch. Each grating antenna has seven grooves with a constant width of 290 nm. We customize the grating periods according to the grating locations in the array so that the output light is directed towards the centre of the lens aperture. This will increase the lens collection efficiency and reduce aberrations. Finite-difference time-domain (FDTD) simulation results of the grating emission angle and efficiency as a function of the grating period are shown in Extended Data Fig. 3. The simulations show that the grating emission efficiency will notably decrease when the output is close to 0° (vertical direction). On the other hand, the grating pattern width will approach the minimum feature size of our lithography (ASML DUV Stepper Model 5500/300) when the output angle is smaller than –20°. Considering these trade-offs, we set the output directions of the grating antennas to be from –10° to –20° from the vertical direction, corresponding to grating periods in the range 550–580 nm. This is by no means a fundamental limit for grating antenna design, and a higher emission efficiency can be achieved with an optimized design of grating geometry^{38,39}.

Optical efficiency

The on-chip optical losses of the FPSA reported here mainly come from three sources: (1) waveguide propagation loss (3.8 dB cm^{-1}); note that grating antennas at different locations are connected to different waveguide lengths and, thus, have different waveguide propagation losses; (2) row-selection-switch loss (2 dB) and column-selection-switch loss (2.5 dB); (3) grating antenna emission loss (about 1.9 dB, depending on the grating antenna locations, as shown in Extended Data Fig. 3). For example, a grating antenna with a 1-cm waveguide has an on-chip loss of 10.2 dB. By optimizing the parameters in the fabrication process for the same device layout, we

can reduce the waveguide propagation loss to 1 dB cm⁻¹ and the switch losses to less than 1 dB for both row-selection and column-selection switches, therefore the on-chip loss of a grating antenna with a 1-cm waveguide can be reduced to 4.9 dB. The on-chip optical efficiency can be further improved by optimizing the design of grating antennas and MEMS switch actuators.

In addition to the on-chip losses, the demonstrated LiDAR setup also has two off-chip losses: (1) fibre-to-chip coupling loss (5 dB for each coupling) and (2) loss owing to limited device lens transmittance and collection efficiency of grating antenna emitted light (total about 3 dB). The fibre-to-chip coupling loss can be eliminated if the LiDAR ranging system components are integrated on-chip³⁴. The device lens loss can be reduced by applying anti-reflection coating for the operating wavelength, as well as improving the optical design to better match the lens aperture with the grating antenna emitting pattern.

Packaging and control

The FPSA chip is attached and wire bonded to a 256-pin ceramic PGA. Owing to the in-plane fibre array for optical I/O coupling, some electrical pads on the PGA are blocked by the fibre array, therefore the total number of available pads is smaller than the required control signals (256 + ground). Instead of missing a contiguous block of the array, every fourth row of the array is skipped for wire bonding, whereas all columns are wire bonded, so a 128 × 96 subarray is tested in experiments. A driver circuit board with two HV583 (128-channel low-voltage serial to high-voltage parallel converter) chips generates the electrical control signals for the FPSA and the output is controlled by an FPGA. The driver circuit board can update the FPSA electrical control signal at a rate of up to 1.25 MHz for random-access beam steering. Light is coupled between the external fibre-based optical setup and the FPSA chip using an off-chip fibre array and on-chip grating couplers.

Optical characterization methods and setup

The beam-steering patterns in the 70° × 70° FoV shown in Fig. 3a,b are captured by projecting the output beam from the 5-mm-focal-length lens on a sheet of paper as a diffuser screen and imaging the screen pattern using an infrared camera (Xenics Bobcat 320) with a 3.5-mm-focal-length wide-angle lens. The optical setup is shown in Extended Data Fig. 6a.

The zoomed-in far-field beam-steering pattern shown in Fig. 3c is measured by collecting the output beam from the device lens using a 30-mm-focal-length lens as the Fourier lens and capturing the intensity distribution on the focal plane of the Fourier lens using the infrared camera sensor, which is effectively the far-field

intensity distribution of the beam scanner. The optical setup is shown in Extended Data Fig. 6b.

The beam profiles shown in Fig. 3d and Extended Data Fig. 4 are captured by the bare infrared camera sensor at a distance of 0.71 m away from the device lens, and the optical setup is shown in Extended Data Fig. 6c.

FMCW LiDAR 3D imaging setup

The optical and electrical setup for the 3D imaging demonstration is shown in Extended Data Fig. 7. The DFB laser (Optilab DFB-1550) is linearly frequency modulated by a pre-distorted current waveform obtained by the iterative learning pre-distortion process³⁵. An erbium-doped fibre amplifier boosts the optical power to compensate for the loss along the optical path. The amplified light passes through a fibre circulator and then splits into two paths by a 50/50 splitter for the two input waveguides (for 5-m and 10-m LiDAR measurements, light is coupled into one of the input waveguides). Light is coupled to the FPSA chip by means of an angled polished fibre array and on-chip grating couplers, and then directed to the target from one of the grating antennas through the imaging lens. The returned light from the target is received by the same grating antenna on the FPSA and coupled back to the fibre array. The fibre array facet and the surface of the grating coupler on the FPSA chip together have about –34 dB of reflection, which is used as the reference path (local oscillator) of the FMCW LiDAR. The reference and probe light passes through the circulator to the photodetector (Thorlabs PDB480C-AC), generating a beat signal sampled by an analogue-to-digital converter (National Instruments PXIe-5114). The data are transferred to a laptop computer and the beat frequency that is proportional to the target distance is extracted by performing a fast Fourier transform. For each beam direction, the distance measurements are repeated ten times and the results are averaged to increase the measurement precision. The FPSA chip is also controlled by the laptop computer by means of the FPGA and the driver circuit board.

Data availability

The data used to produce the plots in this paper and the extended data plots are available in Dryad with the identifier <https://doi.org/10.6078/D1HB0C>.

Code availability

The code used to analyse the data and produce the plots are available in Dryad with the identifier <https://doi.org/10.6078/D1HB0C>.

References

1. Schwarz, B. Mapping the world in 3D. *Nat. Photon.* **4**, 429–430 (2010).
2. Rogers, C. et al. A universal 3D imaging sensor on a silicon photonics platform. *Nature* **590**, 256–261 (2021).
3. Shi, J., Guo, J., Kagami, M., Suni, P. & Zieman, O. Photonic technologies for autonomous cars: feature introduction. *Opt. Express* **27**, 7627–7628 (2019).
4. Javidi, B. et al. Roadmap on 3D integral imaging: sensing, processing, and display. *Opt. Express* **28**, 32266–32293 (2020).
5. Behroozpour, B., Sandborn, P. A. M., Wu, M. C. & Boser, B. E. Lidar system architectures and circuits. *IEEE Commun. Mag.* **55**, 135–142 (2017).
6. Shin, D. et al. Photon-efficient imaging with a single-photon camera. *Nat. Commun.* **7**, 12046 (2016).
7. Morimoto, K. et al. Megapixel time-gated SPAD image sensor for 2D and 3D imaging applications. *Optica* **7**, 346–354 (2020).
8. Kuzmenko, K. et al. 3D LIDAR imaging using Ge-on-Si single-photon avalanche diode detectors. *Opt. Express* **28**, 1330–1344 (2020).
9. Doylend, J. K. et al. Two-dimensional free-space beam steering with an optical phased array on silicon-on-insulator. *Opt. Express* **19**, 21595–21604 (2011).
10. Sun, J., Timurdogan, E., Yaacobi, A., Hosseini, E. S. & Watts, M. R. Large-scale nanophotonic phased array. *Nature* **493**, 195–199 (2013).
11. Aflatouni, F., Abiri, B., Rekhi, A. & Hajimiri, A. Nanophotonic projection system. *Opt. Express* **23**, 21012–21022 (2015).
12. Hutchison, D. N. et al. High-resolution aliasing-free optical beam steering. *Optica* **3**, 887–890 (2016).
13. Chung, S., Abediasl, H. & Hashemi, H. A monolithically integrated large-scale optical phased array in silicon-on-insulator CMOS. *IEEE J. Solid-State Circuits* **53**, 275–296 (2018).
14. Fatemi, R., Khachaturian, A. & Hajimiri, A. A nonuniform sparse 2-D large-FOV optical phased array with a low-power PWM drive. *IEEE J. Solid-State Circuits*

54, 1200–1215 (2019).

15. Zhang, Y. et al. Sub-wavelength-pitch silicon-photonic optical phased array for large field-of-regard coherent optical beam steering. *Opt. Express* **27**, 1929–1940 (2019).
16. Kim, T. et al. A single-chip optical phased array in a wafer-scale silicon photonics/CMOS 3D-integration platform. *IEEE J. Solid-State Circuits* **54**, 3061–3074 (2019).
17. Ashtiani, F. & Aflatouni, F. N × N optical phased array with 2N phase shifters. *Opt. Express* **27**, 27183–27190 (2019).
18. Miller, S. A. et al. Large-scale optical phased array using a low-power multi-pass silicon photonic platform. *Optica* **7**, 3–6 (2020).
19. Poulton, C. V. et al. 8192-element optical phased array with 100° steering range and flip-chip CMOS. In *2020 Conference on Lasers and Electro-Optics (CLEO)* paper JTh4A.3 (Optical Society of America, 2020).
20. Yoo, B. et al. A 32 × 32 optical phased array using polysilicon sub-wavelength high-contrast-grating mirrors. *Opt. Express* **22**, 19029–19039 (2014).
21. Wang, Y. et al. 2D broadband beamsteering with large-scale MEMS optical phased array. *Optica* **6**, 557–562 (2019).
22. Bartlett, T. A., McDonald, W. C. & Hall, J. N. Adapting Texas Instruments DLP technology to demonstrate a phase spatial light modulator. In *Emerging Digital Micromirror Device Based Systems and Applications XI* paper 109320S (International Society for Optics and Photonics, 2019).
23. Abe, H. et al. Two-dimensional beam-steering device using a doubly periodic Si photonic-crystal waveguide. *Opt. Express* **26**, 9389–9397 (2018).
24. López, J. J. et al. Planar-lens enabled beam steering for chip-scale LIDAR. In *2018 Conference on Lasers and Electro-Optics (CLEO)* paper SM3I.1 (Optical Society of America, 2018).
25. Inoue, D., Ichikawa, T., Kawasaki, A. & Yamashita, T. Demonstration of a new optical scanner using silicon photonics integrated circuit. *Opt. Express* **27**, 2499–2508 (2019).
26. Ito, H. et al. Wide beam steering by slow-light waveguide gratings and a prism lens. *Optica* **7**, 47–52 (2020).

27. Chang, Y. et al. Metalens-enabled low-power solid-state 2D beam steering. In *2019 Conference on Lasers and Electro-Optics (CLEO)* paper SF3N.5 (Optical Society of America, 2019).
28. Li, C., Cao, X., Wu, K., Li, X. & Chen, J. Lens-based integrated 2D beam-steering device with defocusing approach and broadband pulse operation for Lidar application. *Opt. Express* **27**, 32970–32983 (2019).
29. Cao, X., Qiu, G., Wu, K., Li, C. & Chen, J. Lidar system based on lens assisted integrated beam steering. *Opt. Lett.* **45**, 5816–5819 (2020).
30. Seok, T. J., Quack, N., Han, S., Muller, R. S. & Wu, M. C. Large-scale broadband digital silicon photonic switches with vertical adiabatic couplers. *Optica* **3**, 64–70 (2016).
31. Seok, T. J., Kwon, K., Henriksson, J., Luo, J. & Wu, M. C. Wafer-scale silicon photonic switches beyond die size limit. *Optica* **6**, 490–494 (2019).
32. Cook, E. H. et al. Polysilicon grating switches for LiDAR. *J. Microelectromech. Syst.* **29**, 1008–1013 (2020).
33. Zhang, X., Kwon, K., Henriksson, J., Luo, J. & Wu, M. C. A 20x20 focal plane switch array for optical beam steering. In *2020 Conference on Lasers and Electro-Optics (CLEO)* paper SM1O.3 (Optical Society of America, 2020).
34. Bhargava, P. et al. Fully integrated coherent LiDAR in 3D-integrated silicon photonics/65nm CMOS. In *2019 Symposium on VLSI Circuits* C262–C263 (IEEE, 2019).
35. Zhang, X., Pouls, J. & Wu, M. C. Laser frequency sweep linearization by iterative learning pre-distortion for FMCW LiDAR. *Opt. Express* **27**, 9965–9974 (2019).
36. Kaymak, Y. et al. A survey on acquisition, tracking, and pointing mechanisms for mobile free-space optical communications. *IEEE Commun. Surv. Tutor.* **20**, 1104–1123 (2018).
37. Kim, J. et al. Enabling trapped ion quantum computing with MEMS technology. In *2017 International Conference on Optical MEMS and Nanophotonics (OMN)* (IEEE, 2017).
38. Michaels, A. & Yablonovitch, E. Inverse design of near unity efficiency perfectly vertical grating couplers. *Opt. Express* **26**, 4766–4779 (2018).

39. Khajavi, S. et al. Compact and highly-efficient broadband surface grating antenna on a silicon platform. *Opt. Express* **29**, 7003–7014 (2021).

Acknowledgements

This research project is funded by Bakar Fellows Program at UC Berkeley. The devices are fabricated in the Marvell Nanofabrication Laboratory at UC Berkeley. We thank V. Stojanovic and P. Bhargava for helpful discussions, and J. Tremblay and K. Yu for the driver circuit board design.

Author information

Author notes

1. These authors contributed equally: Xiaosheng Zhang, Kyungmok Kwon

Affiliations

1. Department of Electrical Engineering and Computer Sciences, University of California, Berkeley, Berkeley, CA, USA

Xiaosheng Zhang, Kyungmok Kwon, Johannes Henriksson, Jianheng Luo & Ming C. Wu

Contributions

X.Z. contributed to the layout design of the FPSA, tested the optical characterizations of the devices and performed the LiDAR measurements. K.K. contributed to the layout design of the FPSA, fabricated the devices and tested the mechanical performance of the devices. J.H. contributed to the MEMS optical switch design and optical simulations. J.L. contributed to the MEMS optical switch design and mechanical simulations. M.C.W. conceived the FPSA architecture and supervised the project.

Corresponding author

Correspondence to [Ming C. Wu](#).

Ethics declarations

Competing interests

All authors, with the exception of J.H. and J.L., are shareholders of nEYE Systems Inc., a start-up company that makes 3D sensors.

Peer review

Peer review information

Nature thanks Hongyan Fu and the other, anonymous, reviewers for their contribution to the peer review of this work.

Additional information

Publisher's note Springer Nature remains neutral with regard to jurisdictional claims in published maps and institutional affiliations.

Extended data figures and tables

[Extended Data Fig. 1 Comparison of integrated FPSAs in the literature and this work.](#)

1D and 2D arrays are indicated by dots and squares, respectively, and this work is indicated by a star.

[Extended Data Fig. 2 Confocal microscopic images of the fabricated FPSA device.](#)

a, Confocal microscopic image showing the grating antennas with column-selection switches. **b**, Confocal microscopic image showing the row-selection switch.

[Extended Data Fig. 3 FDTD simulation results of the grating antenna.](#)

The emission angle and efficiency as a function of the grating period are simulated for a focusing-curved grating antenna of $10 \mu\text{m} \times 5 \mu\text{m}$ in size. The green-shaded region shows the grating periods selected for the FPSA grating antenna design.

[Extended Data Fig. 4 Measured beam profiles of 13 pixels across the FPSA.](#)

The beam profiles are measured at 0.71 m away from the FPSA beam scanner.

Extended Data Fig. 5 Histograms of measured free-space output power of the FPSA beam scanner.

The output power is measured from 128 pixels in row 22 (**a**) and 128 pixels in row 62 (**b**). The bars at -27 dB represent pixels with no output power measured.

Extended Data Fig. 6 Schematics of the optical characterization setups.

- a**, Schematic of the setup for capturing the beam-steering pattern in the $70^\circ \times 70^\circ$ FoV.
- b**, Schematic of the setup for capturing the zoomed-in beam-steering pattern.
- c**, Schematic of the setup for measuring the beam profiles.

Extended Data Fig. 7 Optical and electrical control setup of the FMCW LiDAR with the FPSA beam scanner for 3D imaging.

The LiDAR is operated in a monostatic configuration, in which the same grating antenna on the FPSA is used to transmit the FMCW light and receive the returned signal from the target.

Extended Data Table 1 Comparison of OPAs in the literature

Extended Data Table 2 Comparison of integrated FPSAs in the literature and this work

Rights and permissions

Open Access This article is licensed under a Creative Commons Attribution 4.0 International License, which permits use, sharing, adaptation, distribution and reproduction in any medium or format, as long as you give appropriate credit to the original author(s) and the source, provide a link to the Creative Commons license, and indicate if changes were made. The images or other third party material in this article are included in the article's Creative Commons license, unless indicated otherwise in a credit line to the material. If material is not included in the article's Creative Commons license and your intended use is not permitted by statutory regulation or exceeds the permitted use, you will need to obtain permission directly from the copyright holder. To view a copy of this license, visit <http://creativecommons.org/licenses/by/4.0/>.

[Reprints and Permissions](#)

About this article

Cite this article

Zhang, X., Kwon, K., Henriksson, J. *et al.* A large-scale microelectromechanical-systems-based silicon photonics LiDAR. *Nature* **603**, 253–258 (2022).
<https://doi.org/10.1038/s41586-022-04415-8>

- Received: 03 September 2021
- Accepted: 12 January 2022
- Published: 09 March 2022
- Issue Date: 10 March 2022
- DOI: <https://doi.org/10.1038/s41586-022-04415-8>

Share this article

Anyone you share the following link with will be able to read this content:

[Get shareable link](#)

Sorry, a shareable link is not currently available for this article.

[Copy to clipboard](#)

Provided by the Springer Nature SharedIt content-sharing initiative

[Light arrays measure up on a chip the size of a fingertip](#)

- H. Y. Fu
- Qian Li

News & Views 09 Mar 2022

This article was downloaded by **calibre** from <https://www.nature.com/articles/s41586-022-04415-8>

- Article
- [Published: 09 March 2022](#)

Vertical MoS₂ transistors with sub-1-nm gate lengths

- [Fan Wu](#) ORCID: orcid.org/0000-0003-3427-2955^{1,2 na1},
- [He Tian](#) ^{1,2 na1},
- [Yang Shen](#)^{1,2 na1},
- [Zhan Hou](#)^{1,2},
- [Jie Ren](#)^{1,2},
- [Guangyang Gou](#)^{1,2},
- [Yabin Sun](#)³,
- [Yi Yang](#)^{1,2} &
- [Tian-Ling Ren](#) ORCID: orcid.org/0000-0002-7330-0544^{1,2}

[Nature](#) volume 603, pages 259–264 (2022)

- 3759 Accesses
- 42 Altmetric
- [Metrics details](#)

Subjects

- [Electronic devices](#)

Abstract

Ultra-scaled transistors are of interest in the development of next-generation electronic devices^{1,2,3}. Although atomically thin molybdenum disulfide (MoS_2) transistors have been reported⁴, the fabrication of devices with gate lengths below 1 nm has been challenging⁵. Here we demonstrate side-wall MoS_2 transistors with an atomically thin channel and a physical gate length of sub-1 nm using the edge of a graphene layer as the gate electrode. The approach uses large-area graphene and MoS_2 films grown by chemical vapour deposition for the fabrication of side-wall transistors on a 2-inch wafer. These devices have On/Off ratios up to 1.02×10^5 and subthreshold swing values down to 117 mV dec^{-1} . Simulation results indicate that the MoS_2 side-wall effective channel length approaches 0.34 nm in the On state and 4.54 nm in the Off state. This work can promote Moore's law of the scaling down of transistors for next-generation electronics.

This is a preview of subscription content

Access options

Subscribe to Nature+

Get immediate online access to the entire Nature family of 50+ journals

\$29.99

monthly

[Subscribe](#)

Subscribe to Journal

Get full journal access for 1 year

\$199.00

only \$3.90 per issue

[Subscribe](#)

All prices are NET prices.
VAT will be added later in the checkout.
Tax calculation will be finalised during checkout.

Buy article

Get time limited or full article access on ReadCube.

\$32.00

[Buy](#)

All prices are NET prices.

Additional access options:

- [Log in](#)
- [Learn about institutional subscriptions](#)

Fig. 1: Comparison of the 0.34 nm L_g side-wall transistor with other typical structure transistors.

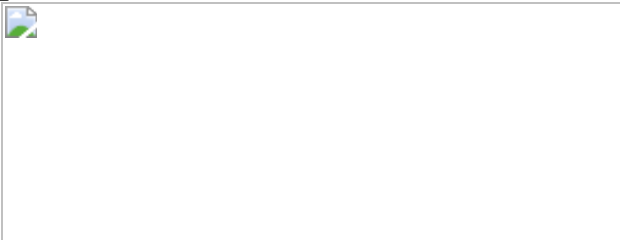


Fig. 2: The 0.34 nm gate-length side-wall monolayer MoS₂ transistor device structure and characterization.

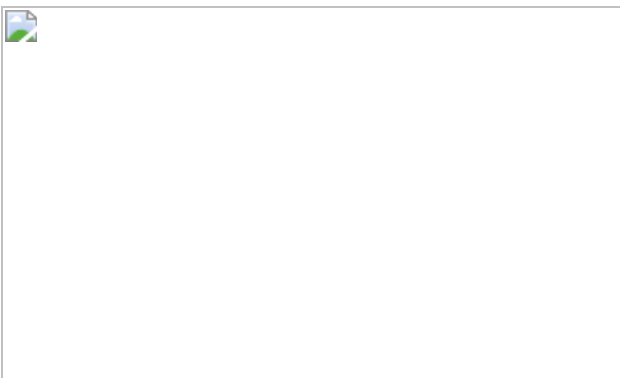


Fig. 3: Electrical characterization of 0.34 nm gate-length side-wall transistors.

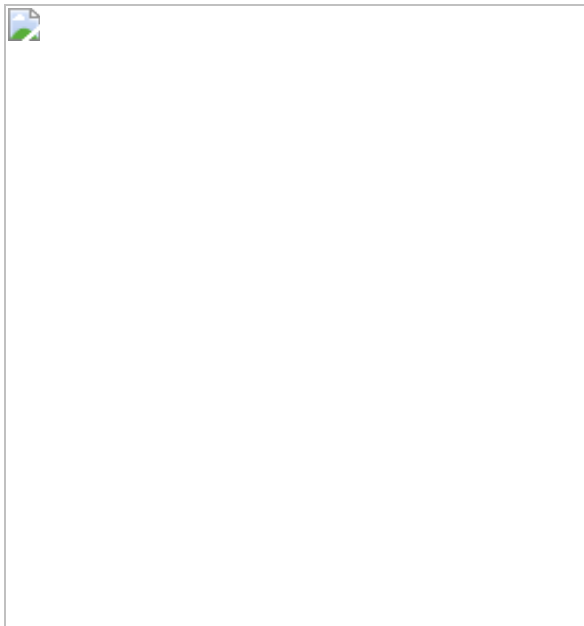
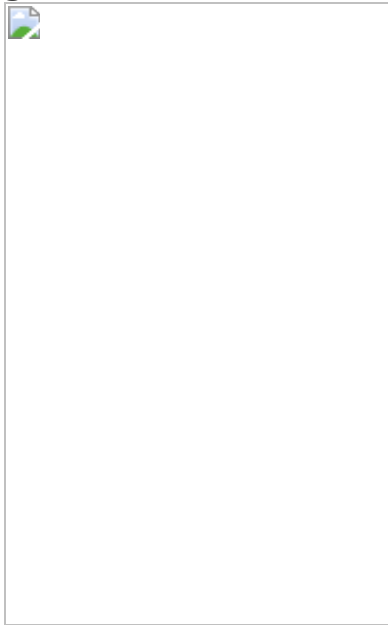


Fig. 4: TCAD simulation results and benchmark.



Data availability

The data that support the findings of this study are available from the corresponding author upon reasonable request.

References

1. Liu, Y. et al. Promises and prospects of two-dimensional transistors. *Nature* **591**, 43–53 (2021).
2. Chhowalla, M., Jena, D. & Zhang, H. Two-dimensional semiconductors for transistors. *Nat. Rev. Mater.* **1**, 16052 (2016).
3. Akinwande, D. et al. Graphene and two-dimensional materials for silicon technology. *Nature* **573**, 507–518 (2019).
4. Radisavljevic, B., Radenovic, A., Brivio, J., Giacometti, V. & Kis, A. Single-layer MoS₂ transistors. *Nat. Nanotechnol.* **6**, 147–150 (2011).
5. Desai, S. B. et al. MoS₂ transistors with 1-nanometer gate lengths. *Science* **354**, 99–102 (2016).
6. Moore, G. E. Cramming more components onto integrated circuits. *Proc. IEEE* **86**, 82–85 (1998).
7. Chau, R., Doyle, B., Datta, S., Kavalieros, J. & Zhang, K. Integrated nanoelectronics for the future. *Nat. Mater.* **6**, 810–812 (2007).
8. Lundstrom, M. Moore’s law forever? *Science* **299**, 210–211 (2003).
9. Migita, S., Morita, Y., Matsukawa, T., Masahara, M. & Ota, H. Experimental demonstration of ultrashort-channel (3 nm) junctionless FETs utilizing atomically sharp V-grooves on SOI. *IEEE Trans. Nanotechnol.* **13**, 208–215 (2014).
10. Novoselov, K. S. et al. Electric field effect in atomically thin carbon films. *Science* **306**, 666–669 (2004).
11. Deng, N. et al. Black phosphorus junctions and their electrical and optoelectronic applications. *J. Semicond.* **42**, 081001 (2021).
12. Kim, K. S. et al. Large-scale pattern growth of graphene films for stretchable transparent electrodes. *Nature* **457**, 706–710 (2009).

13. Lee, S., Sohn, J., Jiang, Z., Chen, H.-Y. & Wong, H.-S. P. Metal oxide-resistive memory using graphene-edge electrodes. *Nat. Commun.* **6**, 8407 (2015).
14. Sohn, J., Lee, S., Jiang, Z., Chen, H. & Wong, H. P. Atomically thin graphene plane electrode for 3D RRAM. In *2014 IEEE International Electron Devices Meeting (IEDM)* 5.3.1–5.3.4 (IEEE, 2014).
15. Wu, F. et al. A 10 nm short channel MoS₂ transistor without the resolution requirement of photolithography. *Adv. Electron. Mater.* **7**, 2100543 (2021).
16. Yoon, Y., Ganapathi, K. & Salahuddin, S. How good can monolayer MoS₂ transistors be? *Nano Lett.* **11**, 3768–3773 (2011).
17. Dunlap, W. C. & Watters, R. L. Direct measurement of the dielectric constants of silicon and germanium. *Phys. Rev.* **92**, 1396–1397 (1953).
18. Xie, L. et al. Graphene-contacted ultrashort channel monolayer MoS₂ transistors. *Adv. Mater.* **29**, 1702522 (2017).
19. Liu, C. et al. Two-dimensional materials for next-generation computing technologies. *Nat. Nanotechnol.* **15**, 545–557 (2020).
20. Yu, Z. et al. Realization of room-temperature phonon-limited carrier transport in monolayer MoS₂ by dielectric and carrier screening. *Adv. Mater.* **28**, 547–552 (2016).
21. Tseng, A. A., Kuan, C., Chen, C. D. & Ma, K. J. Electron beam lithography in nanoscale fabrication: recent development. *IEEE Trans. Electron. Packag. Manuf.* **26**, 141–149 (2003).
22. Sinha, S., Cline, B., Yeric, G., Chandra, V. & Cao, Y. Design benchmarking to 7 nm with FinFET predictive technology models. In *Proc. 2012 ACM/IEEE International Symposium on Low Power Electrons and Design* 15–20 (Association for Computing Machinery, 2012).

23. Suzuki, K., Tanaka, T., Tosaka, Y., Horie, H. & Arimoto, Y. Scaling theory for double-gate SOI MOSFET's. *IEEE Trans. Electron Devices* **40**, 2326–2329 (1993).
24. Xuejue, H. et al. Sub 50-nm FinFET: PMOS. In *International Electron Devices Meeting (IEDM) Technical Digest Paper* 67–70 (IEEE, 1999).
25. Yang-Kyu, C. et al. Sub-20nm CMOS FinFET technologies. In *International Electron Devices Meeting (IEDM) Technical Digest Paper* 19.11.11–19.11.14 (IEEE, 2001).
26. Bin, Y. et al. FinFET scaling to 10 nm gate length. In *International Electron Devices Meeting (IEDM) Technical Digest Paper* 10.2.1–10.2.4 (IEEE, 2002).
27. Fu-Liang, Y. et al. 5nm-gate nanowire FinFET. In *Proc. Symposium on VLSI Technology, Digest of Technical Papers* 196–197 (IEEE, 2004).
28. Lee, H. et al. Sub-5nm all-around gate FinFET for ultimate scaling. In *Proc. Symposium on VLSI Technology, Digest of Technical Papers* 58–59 (IEEE, 2006).
29. Yeo, K. H. et al. Gate-all-around (GAA) twin silicon nanowire MOSFET (TSNWFET) with 15 nm length gate and 4 nm radius nanowires. In *International Electron Devices Meeting (IEDM)* 1–4 (IEEE, 2006).
30. Loubet, N. et al. Stacked nanosheet gate-all-around transistor to enable scaling beyond FinFET. In *Symposium on VLSI Technology* T230–T231 (IEEE, 2017).
31. Franklin, A. D. et al. Sub-10 nm carbon nanotube transistor. *Nano Lett.* **12**, 758–762 (2012).
32. Cao, Q., Tersoff, J., Farmer, D. B., Zhu, Y. & Han, S.-J. Carbon nanotube transistors scaled to a 40-nanometer footprint. *Science* **356**, 1369–1372 (2017).

33. Qiu, C. et al. Scaling carbon nanotube complementary transistors to 5-nm gate lengths. *Science* **355**, 271–276 (2017).
34. English, C. D., Smithe, K. K. H., Xu, R. L. & Pop, E. Approaching ballistic transport in monolayer MoS₂ transistors with self-aligned 10 nm top gates. In *International Electron Devices Meeting (IEDM)* 5.6.1–5.6.4 (IEEE, 2016).
35. Jiang, J. et al. Ultrashort vertical-channel van der Waals semiconductor transistors. *Adv. Sci.* **7**, 1902964 (2020).
36. Zou, X., Liu, L., Xu, J., Wang, H. & Tang, W.-M. Few-layered MoS₂ field-effect transistors with a vertical channel of sub-10 nm. *ACS Appl. Mater. Inter.* **12**, 32943–32950 (2020).
37. *International Roadmap for Devices and Systems (IRDS™) 2021 Edition* (IEEE, 2021); <https://irds.ieee.org/editions/2021>
38. Bohr, M. A 30 year retrospective on Dennard’s MOSFET scaling paper. *IEEE Solid-State Circuits Soc. Newslett.* **12**, 11–13 (2007).

Acknowledgements

We thank W.-Z. Bao from Fudan University for valuable discussions. This work was supported by the National Natural Science Foundation of China (grant nos. 62022047, 61874065, U20A20168 and 51861145202), the National Key R&D Program (grant no. 2021YFC3002200 and 2020YFA0709800), The Beijing Natural Science Foundation (grant no. M22020), the Fok Ying-Tong Education Foundation (grant no. 171051), the Beijing National Research Center for Information Science and Technology Youth Innovation Fund (grant no. BNR2021RC01007), State Key Laboratory of New Ceramic and Fine Processing of Tsinghua University (grant no. KF202109) and the Research Fund from Beijing Innovation Center for Future Chip, Center for Flexible Electronics Technology of Tsinghua University and the Independent Research Program of Tsinghua University (grant no. 20193080047).

Author information

Author notes

1. These authors contributed equally: Fan Wu, He Tian, Yang Shen

Affiliations

1. School of Integrated Circuits, Tsinghua University, Beijing, China

Fan Wu, He Tian, Yang Shen, Zhan Hou, Jie Ren, Guangyang Gou, Yi Yang & Tian-Ling Ren

2. The Beijing National Research Center for Information Science and Technology (BNRist), Tsinghua University, Beijing, China

Fan Wu, He Tian, Yang Shen, Zhan Hou, Jie Ren, Guangyang Gou, Yi Yang & Tian-Ling Ren

3. Department of Electrical Engineering, East China Normal University, Shanghai, China

Yabin Sun

Contributions

H.T. and T.-L.R. proposed the idea and the project. H.T. and F.W. designed the experiment. Y. Shen and Y. Sun performed the simulation. F.W., Z.H., G.G. and J.R. performed the device fabrication and characterization. Y.Y. provided suggestions to the manuscript. T.-L.R. and H.T. supervised the project. All the authors discussed the results and commented on the manuscript.

Corresponding authors

Correspondence to [He Tian](#) or [Tian-Ling Ren](#).

Ethics declarations

Competing interests

The authors declare no competing interests.

Peer review

Peer review information

Nature thanks Dennis Lin and the other, anonymous, reviewers(s) for their contribution to the peer review of this work.

Additional information

Extended data

is available for this paper at <https://doi.org/10.1038/s41586-021-04323-3>.

Publisher's note Springer Nature remains neutral with regard to jurisdictional claims in published maps and institutional affiliations.

Extended data figures and tables

[Extended Data Fig. 1 As-fabricated, Al-contacted graphene transistors.](#)

(a, b) The I_{DS} - V_{GS} transfer curves and I_{DS} - V_{DS} output curves. The electrical conductivity is $\sim 10^6$ S/m at $V_{GS} = 0$ V. (c) The optical image. After Al deposition and lift-off process, the samples were stored at 10^{-5} bar vacuum to avoid oxidization. (d) The device structure diagram. The channel width and channel length are 8 μm and 22 μm , respectively.

Extended Data Fig. 2 The quality verification of self-oxidized AlO_x.

(a) The $I-V$ curves another 10 devices. The 2.4 V voltage drop between graphene and Al is a safe value for the measurements. (b) A typical optical image of the measured structure. (c) The diagram of the measured structure. After Al deposited on graphene, the samples are stored in clean atmosphere condition for more than 3 days. Then, Al is surrounded by dense AlO_x layer, and Pt is deposited after EBL process.

Extended Data Fig. 3 The EDS mapping of 0.34 nm gate-length side-wall transistor.

(a) The TEM image of this EDS mapping region in BF mode. (b–i) The EDS mapping of carbon (C), oxygen (O), aluminum (Al), silicon (Si), sulfur (S), titanium (Ti), molybdenum (Mo) and hafnium (Hf). The mapping of Mo and S verifies the presence of the 2D MoS₂ channel. The C element seen on the top of MoS₂ can be attributed to the organic residue like PMMA or contaminants from fabrication.

Extended Data Fig. 4 Back-gated planar MoS₂ transistors.

(a) The measured structure. The channel width and channel length are 4 μm and 5 μm , respectively. (b–p) The $I_{\text{DS}}-V_{\text{BG}}$ transfer curves under different V_{DS} bias of the 15 typical back-gated planar MoS₂ transistors. The MoS₂ channel is highly n-doped when $V_{\text{BG}} = 50$ V.

Extended Data Fig. 5 The tunability of the Al screening layer of the 0.34 nm gate-length side-wall transistor.

(a) The measured structure and signal input. (b) The $I_{\text{DS}}-V_{\text{BS}}$ characteristics under different V_{Al} bias, when graphene gate is fixed at 0 V.

Extended Data Fig. 6 The detailed tunability of the Al screening layer.

(a) The basic 0.34 nm graphene side-wall edge gated MoS₂ transistor and signal input, the Al screening layer is connected to ground. (b) The I_{DS} - V_{Gr} characteristics at $V_{BS} = 0$ V and $V_{Al} = 0$ V. The V_{DS} varies from 10 mV to 3.0 V. (c) The 0.34 nm graphene side-wall edge gated MoS₂ transistor and signal input, the Al screening layer is fixed at different bias. (d) The I_{DS} - V_{Gr} characteristics at $V_{DS} = 0$ V and $V_{Al} = 0$ V. The V_{Al} varies from -2.0 V to 2.0 V with 0.5 V step. (e) The Al side-wall gated MoS₂ transistor and signal input, the graphene layer is connected to ground. (f) The I_{DS} - V_{Al} characteristics at $V_{BS} = 0$ V and $V_{Gr} = 0$ V. The V_{DS} varies from 10 mV to 3.0 V.

Extended Data Fig. 7 The reproducibility of the 0.34 nm gate-length side-wall transistors.

Additional 49 devices are measured at $V_{BS} = 50$ V, $V_{Al} = 0$ V and $V_{DS} = 1$ V. From additional device 1 to device 28, the measured 0.34 nm gate-length side-wall transistors are with $L_{ch} = 1 \mu\text{m}$; from additional device 29 to device 49, the measured 0.34 nm gate-length side-wall transistors are with $L_{ch} = 0.5 \mu\text{m}$.

Extended Data Fig. 8 TCAD simulation for extracting the effective gate length in the Off state.

(a) The simulated transfer curve under $V_{BS} = 50$ V, $V_{Al} = 0$ V and $V_{DS} = 50$ mV. (b) The carrier density along vertical MoS₂ channel. By definition of $I_{off} = 10^{-12}\text{A}$ and $n_{threshold} = 2 \times 10^{12} \text{ cm}^{-3}$ (correspond to $1.3 \times 10^5 \text{ cm}^{-2}$), the L_{eff} is 4.54 nm.

Extended Data Fig. 9 The TCAD simulation results of the 0.34 nm gate-length side-wall transistors to boost On-state

performance.

The transfer curves by scaling down L_{ch} from 500 nm to 4.54 nm shown in **(a)** log-scale and **(b)** linear-scale. The transfer curves under extreme $L_{ch} = 4.54$ nm with different fixed Al bias shown in **(c)** log-scale and **(d)** linear-scale. The transfer curves under extreme $L_{ch} = 4.54$ nm by scaling down gate dielectric thickness from 14 nm to 5 nm shown in **(e)** log-scale and **(f)** linear-scale. Under 14 nm HfO₂ as gate dielectric, $V_{BS} = 50$ V, $V_{Al} = 0$ V and $V_{DS} = 50$ mV condition, the On-state current can be further improved ~ 2 orders of magnitude.

Extended Data Table 1 The detailed parameters for MoS₂ channel with different layer numbers.

Extended Data Table 2 The detailed parameters for HfO₂ and natural AlO_x. Here, T_{ch} is the channel thickness, E_g is the band gap, ϵ is the relative dielectric constant, χ is the electron affinity, m_e is the electron effective mass, μ_e is the electron mobility, the initial doping of MoS₂ is $10^{16}\text{--}10^{17}$ cm⁻³, and graphene is modeled as metal with work function set as 4.6 eV.

Rights and permissions

Reprints and Permissions

About this article

Cite this article

Wu, F., Tian, H., Shen, Y. *et al.* Vertical MoS₂ transistors with sub-1-nm gate lengths. *Nature* **603**, 259–264 (2022). <https://doi.org/10.1038/s41586-021-04323-3>

- Received: 01 December 2020

- Accepted: 09 December 2021
- Published: 09 March 2022
- Issue Date: 10 March 2022
- DOI: <https://doi.org/10.1038/s41586-021-04323-3>

Share this article

Anyone you share the following link with will be able to read this content:

[Get shareable link](#)

Sorry, a shareable link is not currently available for this article.

[Copy to clipboard](#)

Provided by the Springer Nature SharedIt content-sharing initiative

This article was downloaded by **calibre** from <https://www.nature.com/articles/s41586-021-04323-3>

| [Section menu](#) | [Main menu](#) |

- Article
- [Published: 09 March 2022](#)

Electron-catalysed molecular recognition

- [Yang Jiao^{1 na1}](#),
- [Yunyan Qiu ORCID: orcid.org/0000-0001-9279-4714^{1 na1}](#),
- [Long Zhang ORCID: orcid.org/0000-0002-4631-158X¹](#),
- [Wei-Guang Liu²](#),
- [Haochuan Mao^{1,3}](#),
- [Hongliang Chen^{1,4,5}](#),
- [Yuanning Feng ORCID: orcid.org/0000-0002-8832-0767¹](#),
- [Kang Cai^{1,6}](#),
- [Dengke Shen^{1,7}](#),
- [Bo Song ORCID: orcid.org/0000-0002-4337-848X¹](#),
- [Xiao-Yang Chen ORCID: orcid.org/0000-0003-3449-4136¹](#),
- [Xuesong Li¹](#),
- [Xingang Zhao¹](#),
- [Ryan M. Young^{1,3}](#),
- [Charlotte L. Stern ORCID: orcid.org/0000-0002-9491-289X¹](#),
- [Michael R. Wasielewski ORCID: orcid.org/0000-0003-2920-5440^{1,3}](#),
- [R. Dean Astumian ORCID: orcid.org/0000-0001-7472-187X⁸](#),
- [William A. Goddard III²](#) &
- [J. Fraser Stoddart ORCID: orcid.org/0000-0003-3161-3697^{1,4,5,9}](#)

Nature volume **603**, pages 265–270 (2022)

- 4313 Accesses
- 99 Altmetric

- [Metrics details](#)

Subjects

- [Catalytic mechanisms](#)
- [Self-assembly](#)

Abstract

Molecular recognition^{1,2,3,4} and supramolecular assembly^{5,6,7,8} cover a broad spectrum^{9,10,11} of non-covalently orchestrated phenomena between molecules. Catalysis¹² of such processes, however, unlike that for the formation of covalent bonds, is limited to approaches^{13,14,15,16} that rely on sophisticated catalyst design. Here we establish a simple and versatile strategy to facilitate molecular recognition by extending electron catalysis¹⁷, which is widely applied^{18,19,20,21} in synthetic covalent chemistry, into the realm of supramolecular non-covalent chemistry. As a proof of principle, we show that the formation of a trisradical complex²² between a macrocyclic host and a dumbbell-shaped guest—a molecular recognition process that is kinetically forbidden under ambient conditions—can be accelerated substantially on the addition of catalytic amounts of a chemical electron source. It is, therefore, electrochemically possible to control²³ the molecular recognition temporally and produce a nearly arbitrary molar ratio between the substrates and complexes ranging between zero and the equilibrium value. Such kinetically stable supramolecular systems²⁴ are difficult to obtain precisely by other means. The use of the electron as a catalyst in molecular recognition will inspire chemists and biologists to explore strategies that can be used to fine-tune non-covalent events, control assembly at different length scales^{25,26,27} and ultimately create new forms of complex matter^{28,29,30}.

This is a preview of subscription content

Access options

Subscribe to Nature+

Get immediate online access to the entire Nature family of 50+ journals

\$29.99

monthly

[Subscribe](#)

Subscribe to Journal

Get full journal access for 1 year

\$199.00

only \$3.90 per issue

[Subscribe](#)

All prices are NET prices.

VAT will be added later in the checkout.

Tax calculation will be finalised during checkout.

Buy article

Get time limited or full article access on ReadCube.

\$32.00

[Buy](#)

All prices are NET prices.

Additional access options:

- [Log in](#)
- [Learn about institutional subscriptions](#)

Fig. 1: Design of an electron-catalysed molecular recognition process.



Fig. 2: Molecular recognition accelerated by catalytic amounts of cobaltocene (CoCp_2).

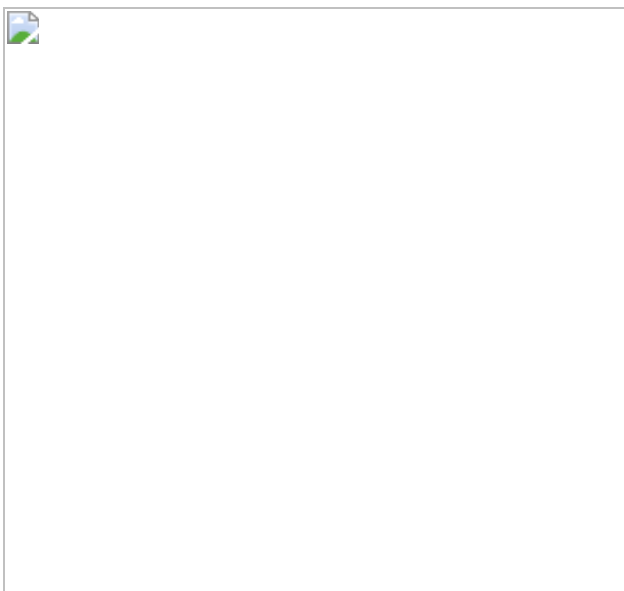


Fig. 3: Detection and verification of the key intermediate in the electron-catalysed molecular recognition process.

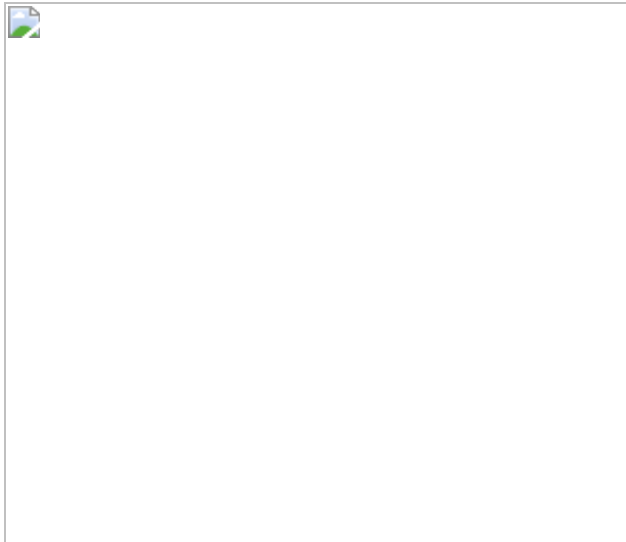
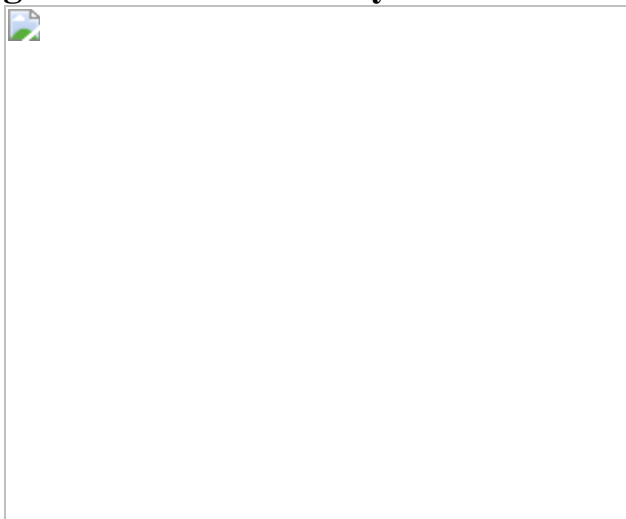


Fig. 4: Electrochemically controlled molecular recognition.



Data availability

The data that support the findings of this study are available within the paper and its [Supplementary Information](#) files.

References

1. Lehn, J.-M. Supramolecular chemistry—Scope and perspectives. Molecules, supermolecules, and molecular devices (Nobel lecture). *Angew. Chem. Int. Ed. Engl.* **27**, 89–112 (1988).

2. Cram, D. J. The design of molecular hosts, guests, and their complexes (Nobel lecture). *Angew. Chem. Int. Ed. Engl.* **27**, 1009–1020 (1988).
3. Philp, D. & Stoddart, J. F. Self-assembly in natural and unnatural systems. *Angew. Chem. Int. Ed. Engl.* **35**, 1154–1196 (1996).
4. Persch, E., Dumele, O. & Diederich, F. Molecular recognition in chemical and biological systems. *Angew. Chem. Int. Ed.* **54**, 3290–3327 (2015).
5. Aida, T., Meijer, E. W. & Stupp, S. I. Functional supramolecular polymers. *Science* **335**, 813–817 (2012).
6. Das, K., Gabrielli, L. & Prins, L. J. Chemically fueled self-assembly in biology and chemistry. *Angew. Chem. Int. Ed.* **60**, 20120–20143 (2021).
7. Weißenfels, M., Gemen, J. & Klajn, R. Dissipative self-assembly: fueling with chemicals versus light. *Chem* **7**, 23–37 (2021).
8. Yin, Z. et al. Dissipative supramolecular polymerization powered by light. *CCS Chem.* **1**, 335–342 (2019).
9. Wiester, M. J., Ulmann, P. A. & Mirkin, C. A. Enzyme mimics based upon supramolecular coordination chemistry. *Angew. Chem. Int. Ed.* **50**, 114–137 (2010).
10. Webber, M. J., Appel, E. A., Meijer, E. W. & Langer, R. Supramolecular biomaterials. *Nat. Mater.* **15**, 13–26 (2015).
11. Amabilino, D. B., Smith, D. K. & Steed, J. W. Supramolecular materials. *Chem. Soc. Rev.* **46**, 2404–2420 (2017).
12. Wang, Y. et al. What molecular assembly can learn from catalytic chemistry. *Chem. Soc. Rev.* **43**, 399–411 (2014).
13. Turberfield, A. J. et al. DNA fuel for free-running nanomachines. *Phys. Rev. Lett.* **90**, 118102 (2003).

14. Zhang, D. Y., Turberfield, A. J., Yurke, B. & Winfree, E. Engineering entropy-driven reactions and networks catalyzed by DNA. *Science* **318**, 1121–1125 (2007).
15. Song, T. & Liang, H. Synchronized assembly of gold nanoparticles driven by a dynamic DNA-fueled molecular machine. *J. Am. Chem. Soc.* **134**, 10803–10806 (2012).
16. Li, H. et al. Proton-assisted self-assemblies of linear di-pyridyl polyaromatic molecules at solid/liquid interface. *J. Phys. Chem. C* **116**, 21753–21761 (2012).
17. Studer, A. & Curran, D. P. The electron is a catalyst. *Nat. Chem.* **6**, 765–773 (2014).
18. Francke, R. & Little, R. D. Electrons and holes as catalysts in organic electrosynthesis. *ChemElectroChem* **6**, 4373–4382 (2019).
19. Yan, M., Kawamata, Y. & Baran, P. S. Synthetic organic electrochemical methods since 2000: on the verge of a renaissance. *Chem. Rev.* **117**, 13230–13319 (2017).
20. Prier, C. K., Rankic, D. A. & MacMillan, D. W. C. Visible light photoredox catalysis with transition metal complexes: applications in organic synthesis. *Chem. Rev.* **113**, 5322–5363 (2013).
21. Romero, N. A. & Nicewicz, D. A. Organic photoredox catalysis. *Chem. Rev.* **116**, 10075–10166 (2016).
22. Trabolsi, A. et al. Radically enhanced molecular recognition. *Nat. Chem.* **2**, 42–49 (2010).
23. Aubert, S., Bezagu, M., Spivey, A. C. & Arseniyadis, S. Spatial and temporal control of chemical processes. *Nat. Rev. Chem.* **3**, 706–722 (2019).
24. Mattia, E. & Otto, S. Supramolecular systems chemistry. *Nat. Nanotechnol.* **10**, 111–119 (2015).

25. Whitesides, G. M. Self-assembly at all scales. *Science* **295**, 2418–2421 (2002).
26. Harada, A., Kobayashi, R., Takashima, Y., Hashidzume, A. & Yamaguchi, H. Macroscopic self-assembly through molecular recognition. *Nat. Chem.* **3**, 34–37 (2010).
27. Santos, P. J., Gabrys, P. A., Zornberg, L. Z., Lee, M. S. & Macfarlane, R. J. Macroscopic materials assembled from nanoparticle superlattices. *Nature* **591**, 586–591 (2021).
28. Lehn, J. M. Toward self-organization and complex matter. *Science* **295**, 2400–2403 (2002).
29. Vantomme, G. & Meijer, E. W. The construction of supramolecular systems. *Science* **363**, 1396–1397 (2019).
30. Pezzato, C., Cheng, C., Stoddart, J. F. & Astumian, R. D. Mastering the non-equilibrium assembly and operation of molecular machines. *Chem. Soc. Rev.* **46**, 5491–5507 (2017).
31. Luca, O. R., Gustafson, J. L., Maddox, S. M., Fenwick, A. Q. & Smith, D. C. Catalysis by electrons and holes: formal potential scales and preparative organic electrochemistry. *Org. Chem. Front.* **2**, 823–848 (2015).
32. Whitesides, G. M. et al. Noncovalent synthesis: using physical-organic chemistry to make aggregates. *Acc. Chem. Res.* **28**, 37–44 (1995).
33. Reinhoudt, D. N. Synthesis beyond the molecule. *Science* **295**, 2403–2407 (2002).
34. Frasconi, M. et al. Redox control of the binding modes of an organic receptor. *J. Am. Chem. Soc.* **137**, 11057–11068 (2015).
35. Wang, Y. et al. Symbiotic control in mechanical bond formation. *Angew. Chem. Int. Ed.* **55**, 12387–12392 (2016).
36. Cai, K. et al. Molecular Russian dolls. *Nat. Commun.* **9**, 5275 (2018).

Acknowledgements

We thank Northwestern University (NU) for its continued support of this research and acknowledge the Integrated Molecular Structure Education and Research Center (IMSERC) at NU for providing access to equipment for relevant experiments. The computational investigations at California Institute of Technology were supported by National Science Foundation grant no. CBET-2005250 (W.-G.L. and W.A.G.). This work was also supported by the Department of Energy, Office of Science, Office of Basic Energy Sciences under Award DE-FG02-99ER14999 (M.R.W.) and the Natural Science Foundation of Anhui Province grant no. 2108085MB31 (D.S.).

Author information

Author notes

1. These authors contributed equally: Yang Jiao, Yunyan Qiu

Affiliations

1. Department of Chemistry, Northwestern University, Evanston, IL, USA

Yang Jiao, Yunyan Qiu, Long Zhang, Haochuan Mao, Hongliang Chen, Yuanning Feng, Kang Cai, Dengke Shen, Bo Song, Xiao-Yang Chen, Xuesong Li, Xingang Zhao, Ryan M. Young, Charlotte L. Stern, Michael R. Wasielewski & J. Fraser Stoddart

2. Materials and Process Simulation Center, California Institute of Technology, Pasadena, CA, USA

Wei-Guang Liu & William A. Goddard III

3. Institute for Sustainability and Energy at Northwestern, Northwestern University, Evanston, IL, USA

Haochuan Mao, Ryan M. Young & Michael R. Wasielewski

4. Stoddart Institute of Molecular Science, Department of Chemistry,
Zhejiang University, Hangzhou, China

Hongliang Chen & J. Fraser Stoddart

5. ZJU-Hangzhou Global Scientific and Technological Innovation Center,
Hangzhou, China

Hongliang Chen & J. Fraser Stoddart

6. Department of Chemistry, Nankai University, Tianjin, China

Kang Cai

7. Institutes of Physical Science and Information Technology, Anhui
University, Hefei, China

Dengke Shen

8. Department of Physics and Astronomy, University of Maine, Orono,
ME, USA

R. Dean Astumian

9. School of Chemistry, University of New South Wales, Sydney, New
South Wales, Australia

J. Fraser Stoddart

Contributions

Y.J., Y.Q. and J.F.S. conceived the idea for this project. L.Z. proposed a key mechanistic conjecture. W.-G.L. and W.A.G. performed quantum mechanical calculations. Y.J. and Y.Q. synthesized and characterized the materials with the help of H.C., Y.F., K.C., D.S., B.S., X.-Y.C., X.L. and X.Z. H.M., R.M.Y. and M.R.W. performed the electron paramagnetic resonance characterizations and detailed analyses. C.L.S. performed the

single-crystal X-ray diffraction. R.D.A. contributed to the theoretical analyses on the mechanism of electron catalysis. Y.J., Y.Q. and J.F.S. wrote the first and second drafts of the paper. J.F.S. and W.A.G. directed the project. All the authors participated in evaluating the results and commented on the manuscript.

Corresponding authors

Correspondence to [William A. Goddard III](#) or [J. Fraser Stoddart](#).

Ethics declarations

Competing interests

Y.J., Y.Q. and J.F.S. have filed a patent application lodged with Northwestern University (INVO reference no. NU 2021-248) based on this work.

Peer review

Peer review information

Nature thanks Robert Francke and the other, anonymous, reviewer(s) for their contribution to the peer review of this work. Peer reviewer reports are available.

Additional information

Publisher's note Springer Nature remains neutral with regard to jurisdictional claims in published maps and institutional affiliations.

Extended data figures and tables

Extended Data Fig. 1 The electron as an efficient catalyst for both covalent reactions and molecular recognition.

a, Electron-catalysed covalent reactions are well established in synthetic covalent chemistry, particularly for radical-mediated photoredox catalysis and organic electrosynthesis. Consider a reaction $\mathbf{A} + \mathbf{B} \rightarrow \mathbf{A}-\mathbf{B}$, where a high energy barrier causes the reaction to be very slow. Injection of an electron reduces one of the substrates (**A**) to a highly reactive radical species ($\mathbf{A}^{\bullet-}$), which can rapidly form a covalent bond with the other substrate (**B**). The resulting intermediate ($\mathbf{A}^{\bullet-}-\mathbf{B}$) releases the electron to afford the final product ($\mathbf{A}-\mathbf{B}$). Whereas the overall process is redox neutral, i.e., the redox state remains the same during the transformation from the substrates to product, the catalytic pathway, which involves the temporary addition of an electron, leads to a substantially lower energy barrier, thereby expediting the formation of the covalent bond. In this process, the electron has acted as an effective catalyst. **b**, The research reported in this article aims to extend the paradigm of electron catalysis to promoting and controlling molecular recognition. The trajectory for this noncovalent process is similar to that for electron-catalysed covalent reactions, except that the product is a supramolecular complex wherein molecular components are assembled courtesy of noncovalent bonding interaction(s), rather than a molecule whose atoms are connected by covalent bond(s).

Supplementary information

Supplementary Information

Supplementary Figs. 1–45, Schemes 1–9, Tables 1–8, supplementary text and notes, extensive experimental data, quantum mechanical calculation results and detailed discussions.

Supplementary Data

The crystallographic data for the [2]catenane in its bisradical dicationic state, which is available free of charge from the Cambridge

Crystallographic Data Centre. The CCDC number is 2125118.

Peer Review File

Rights and permissions

Reprints and Permissions

About this article

Cite this article

Jiao, Y., Qiu, Y., Zhang, L. *et al.* Electron-catalysed molecular recognition. *Nature* **603**, 265–270 (2022). <https://doi.org/10.1038/s41586-021-04377-3>

- Received: 06 September 2021
- Accepted: 22 December 2021
- Published: 09 March 2022
- Issue Date: 10 March 2022
- DOI: <https://doi.org/10.1038/s41586-021-04377-3>

Share this article

Anyone you share the following link with will be able to read this content:

[Get shareable link](#)

Sorry, a shareable link is not currently available for this article.

[Copy to clipboard](#)

Provided by the Springer Nature SharedIt content-sharing initiative

Self-assembly of molecules triggered by electricity

- Robert Francke

News & Views 09 Mar 2022

This article was downloaded by **calibre** from <https://www.nature.com/articles/s41586-021-04377-3>

| [Section menu](#) | [Main menu](#) |

- Article
- [Published: 17 January 2022](#)

Au–Pd separation enhances bimetallic catalysis of alcohol oxidation

- [Xiaoyang Huang](#) ORCID: [orcid.org/0000-0002-7221-2075^{1,na1}](https://orcid.org/0000-0002-7221-2075),
- [Ouardia Akdim](#) ORCID: [orcid.org/0000-0003-3915-7681^{1,na1}](https://orcid.org/0000-0003-3915-7681),
- [Mark Douthwaite](#) ORCID: [orcid.org/0000-0002-9162-3363¹](https://orcid.org/0000-0002-9162-3363),
- [Kai Wang](#) ORCID: [orcid.org/0000-0002-1918-4781¹](https://orcid.org/0000-0002-1918-4781),
- [Liang Zhao](#) ORCID: [orcid.org/0000-0002-4956-9447¹](https://orcid.org/0000-0002-4956-9447),
- [Richard J. Lewis](#) ORCID: [orcid.org/0000-0001-9990-7064¹](https://orcid.org/0000-0001-9990-7064),
- [Samuel Pattisson](#) ORCID: [orcid.org/0000-0002-6520-2194¹](https://orcid.org/0000-0002-6520-2194),
- [Isaac T. Daniel](#) ORCID: [orcid.org/0000-0002-3103-6415¹](https://orcid.org/0000-0002-3103-6415),
- [Peter J. Miedziak](#)^{1,2},
- [Greg Shaw](#) ORCID: [orcid.org/0000-0002-3119-0631¹](https://orcid.org/0000-0002-3119-0631),
- [David J. Morgan](#) ORCID: [orcid.org/0000-0002-6571-5731¹](https://orcid.org/0000-0002-6571-5731),
- [Sultan M. Althahban](#)^{3,4},
- [Thomas E. Davies](#) ORCID: [orcid.org/0000-0002-8930-5067¹](https://orcid.org/0000-0002-8930-5067),
- [Qian He](#)^{1,5},
- [Fei Wang](#)¹,
- [Jile Fu](#)¹,
- [Donald Bethell](#) ORCID: [orcid.org/0000-0002-7320-7585¹](https://orcid.org/0000-0002-7320-7585),
- [Steven McIntosh](#) ORCID: [orcid.org/0000-0003-4664-2028⁶](https://orcid.org/0000-0003-4664-2028),
- [Christopher J. Kiely](#)^{3,6} &
- [Graham J. Hutchings](#) ORCID: [orcid.org/0000-0001-8885-1560¹](https://orcid.org/0000-0001-8885-1560)

Nature volume 603, pages 271–275 (2022)

- 7697 Accesses
- 24 Altmetric
- [Metrics details](#)

Subjects

- [Heterogeneous catalysis](#)
- [Other nanotechnology](#)

Abstract

In oxidation reactions catalysed by supported metal nanoparticles with oxygen as the terminal oxidant, the rate of the oxygen reduction can be a limiting factor. This is exemplified by the oxidative dehydrogenation of alcohols, an important class of reactions with modern commercial applications^{1,2,3}. Supported gold nanoparticles are highly active for the dehydrogenation of the alcohol to an aldehyde⁴ but are less effective for oxygen reduction^{5,6}. By contrast, supported palladium nanoparticles offer high efficacy for oxygen reduction^{5,6}. This imbalance can be overcome by alloying gold with palladium, which gives enhanced activity to both reactions^{7,8,9}; however, the electrochemical potential of the alloy is a compromise between that of the two metals, meaning that although the oxygen reduction can be improved in the alloy, the dehydrogenation activity is often limited. Here we show that by separating the gold and palladium components in bimetallic carbon-supported catalysts, we can almost double the reaction rate compared with that achieved with the corresponding alloy catalyst. We demonstrate this using physical mixtures of carbon-supported monometallic gold and palladium catalysts and a bimetallic catalyst comprising separated gold and palladium regions. Furthermore, we demonstrate electrochemically that this enhancement is attributable to the coupling of separate redox processes occurring at isolated gold and palladium sites. The discovery of this catalytic effect—a cooperative redox enhancement—offers an approach to the design of multicomponent heterogeneous catalysts.

This is a preview of subscription content

Access options

Subscribe to Nature+

Get immediate online access to the entire Nature family of 50+ journals

\$29.99

monthly

[Subscribe](#)

Subscribe to Journal

Get full journal access for 1 year

\$199.00

only \$3.90 per issue

[Subscribe](#)

All prices are NET prices.

VAT will be added later in the checkout.

Tax calculation will be finalised during checkout.

Buy article

Get time limited or full article access on ReadCube.

\$32.00

[Buy](#)

All prices are NET prices.

Additional access options:

- [Log in](#)
- [Learn about institutional subscriptions](#)

Fig. 1: Catalytic performance for aqueous HMF oxidation.



Fig. 2: Proposed reaction scheme for the aqueous phase oxidation of alcohols and formyls over a physical mixture of Au/C and Pd/C.

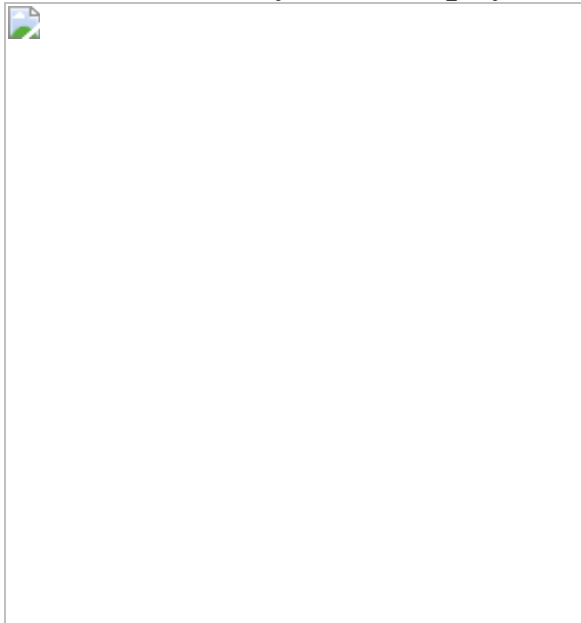


Fig. 3: Electrocatalytic performance.

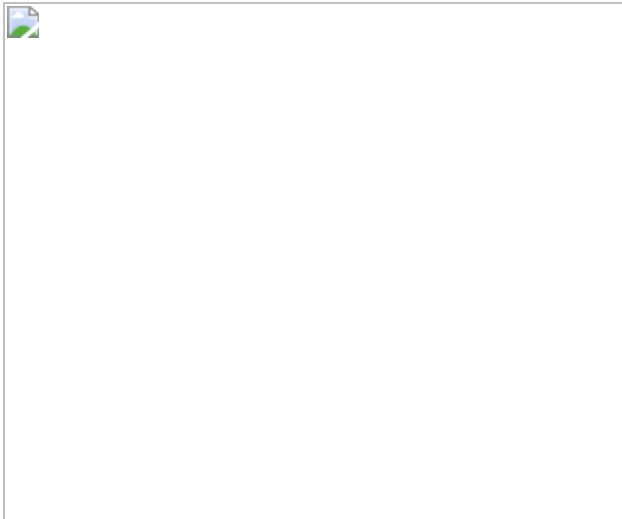
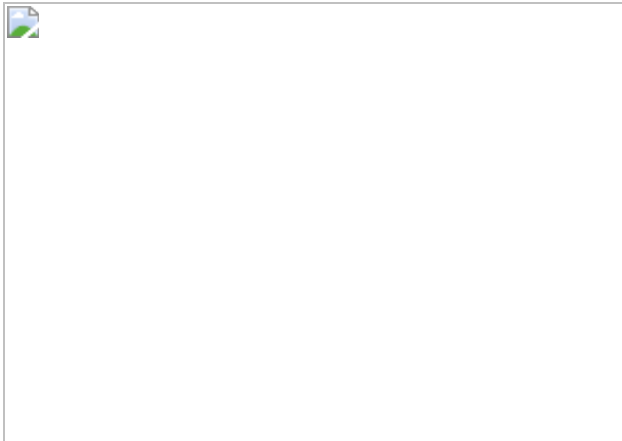


Fig. 4: Representative STEM-HAADF images and the corresponding particle size distribution.



Data availability

All data that led us to understand the results presented here are available with the Article or from the corresponding author upon reasonable request. [Source data](#) are provided with this paper.

References

1. Mallat, T. & Baiker, A. Oxidation of alcohols with molecular oxygen on solid catalysts. *Chem. Rev.* **104**, 3037–3058 (2004).

2. Ciriminna, R., Pandarus, V., Béland, F., Xu, Y. J. & Pagliaro, M. Heterogeneously catalyzed alcohol oxidation for the fine chemical industry. *Org. Process Res. Dev.* **19**, 1554–1558 (2015).
3. Sheldon, R. A., Arends, I. W. C. E., Brink, G. J., Ten, & Dijksman, A. Green, catalytic oxidations of alcohols. *Acc. Chem. Res.* **35**, 774–781 (2002).
4. Abad, A., Concepción, P., Corma, A. & García, H. A collaborative effect between gold and a support induces the selective oxidation of alcohols. *Angew. Chem. Int. Ed.* **44**, 4066–4069 (2005).
5. Kulkarni, A., Siahrostami, S., Patel, A. & Nørskov, J. K. Understanding catalytic activity trends in the oxygen reduction reaction. *Chem. Rev.* **118**, 2302–2312 (2018).
6. Nørskov, J. K. et al. Origin of the overpotential for oxygen reduction at a fuel-cell cathode. *J. Phys. Chem. B* **108**, 17886–17892 (2004).
7. Zhu, X. et al. Optimising surface d charge of AuPd nanoalloy catalysts for enhanced catalytic activity. *Nat. Commun.* **10**, 1428 (2019).
8. Enache, D. I. et al. Solvent-free oxidation of primary alcohols to aldehydes using Au–Pd/TiO₂ catalyst. *Science* **311**, 362–365 (2006).
9. Trindell, J. A., Duan, Z., Henkelman, G. & Crooks, R. M. Au_xPd_(300-x) alloy nanoparticles for the oxygen reduction reaction in alkaline media. *ChemElectroChem* **7**, 3824–3831 (2020).
10. Hutchings, G. J. & Kiely, C. J. Strategies for the synthesis of supported gold palladium nanoparticles with controlled morphology and composition. *Acc. Chem. Res.* **46**, 1759–1772 (2013).
11. Wang, A., Liu, X. Y., Mou, C. Y. & Zhang, T. Understanding the synergistic effects of gold bimetallic catalysts. *J. Catal.* **308**, 258–271 (2013).

12. Wang, D., Villa, A., Porta, F., Prati, L. & Su, D. Bimetallic gold/palladium catalysts: correlation between nanostructure and synergistic effects. *J. Phys. Chem. C* **112**, 8617–8622 (2008).
13. Gao, F. & Goodman, D. W. Pd–Au bimetallic catalysts: understanding alloy effects from planar models and (supported) nanoparticles. *Chem. Soc. Rev.* **41**, 8009–8020 (2012).
14. Han, S. & Mullins, C. B. Catalytic reactions on Pd–Au bimetallic model catalysts. *Acc. Chem. Res.* **54**, 379–387 (2020).
15. Davis, S. E., Ide, M. S. & Davis, R. J. Selective oxidation of alcohols and aldehydes over supported metal nanoparticles. *Green Chem.* **15**, 17–45 (2013).
16. Parmeggiani, C., Matassini, C. & Cardona, F. A step forward towards sustainable aerobic alcohol oxidation: new and revised catalysts based on transition metals on solid supports. *Green Chem.* **19**, 2030–2050 (2017).
17. Pelaez, M. et al. A review on the visible light active titanium dioxide photocatalysts for environmental applications. *Appl. Catal. B* **125**, 331–349 (2012).
18. Golberg, D. et al. Boron nitride nanotubes and nanosheets. *ACS Nano* **4**, 2979–2993 (2010).
19. Suo, Y., Zhuang, L. & Lu, J. First-principles considerations in the design of Pd-alloy catalysts for oxygen reduction. *Angew. Chem. Int. Ed.* **46**, 2862–2864 (2007).
20. Zope, B. N., Hibbitts, D. D., Neurock, M. & Davis, R. J. Reactivity of the gold/water interface during selective oxidation catalysis. *Science* **330**, 74–78 (2010).
21. Han, Y. F. et al. Au promotional effects on the synthesis of H₂O₂ directly from H₂ and O₂ on supported Pd–Au alloy catalysts. *J. Phys. Chem. C* **111**, 8410–8413 (2007).

22. Chadderdon, D. J. et al. Electrocatalytic oxidation of 5-hydroxymethylfurfural to 2,5-furandicarboxylic acid on supported Au and Pd bimetallic nanoparticles. *Green Chem.* **16**, 3778–3786 (2014).
23. Zhu, Y. et al. Boosting oxygen reduction reaction activity of palladium by stabilizing its unusual oxidation states in perovskite. *Chem. Mater.* **27**, 3048–3054 (2015).
24. Ringeisen, B. R. et al. High power density from a miniature microbial fuel cell using *Shewanella oneidensis* DSP10. *Environ. Sci. Technol.* **40**, 2629–2634 (2006).
25. Mackay, A. L. A dense non-crystallographic packing of equal spheres. *Acta Cryst.* **15**, 916–918 (1962).
26. Siyo, B. et al. Influence of support on the aerobic oxidation of HMF into FDCA over preformed Pd nanoparticle based materials. *Appl. Catal. A* **478**, 107–116 (2014).
27. Villa, A., Schiavoni, M., Campisi, S., Veith, G. M. & Prati, L. Pd-modified Au on carbon as an effective and durable catalyst for the direct oxidation of HMF to 2,5-furandicarboxylic acid. *ChemSusChem* **6**, 609–612 (2013).
28. Han, X. et al. Base-free aerobic oxidation of 5-hydroxymethylfurfural to 2,5-furandicarboxylic acid over a Pt/C–O–Mg catalyst. *Green Chem.* **18**, 1597–1604 (2016).
29. Zhou, C. et al. Functionalized carbon nanotubes for biomass conversion: the base-free aerobic oxidation of 5-hydroxymethylfurfural to 2,5-furandicarboxylic acid over platinum supported on a carbon nanotube catalyst. *ChemCatChem* **7**, 2853–2863 (2015).
30. Artz, J. & Palkovits, R. Base-free aqueous-phase oxidation of 5-hydroxymethylfurfural over ruthenium catalysts supported on covalent triazine frameworks. *ChemSusChem* **8**, 3832–3838 (2015).

31. Mishra, D. K. et al. MnCo₂O₄ spinel supported ruthenium catalyst for air-oxidation of HMF to FDCA under aqueous phase and base-free conditions. *Green Chem.* **19**, 1619–1623 (2017).
32. Schade, O. et al. The influence of the gold particle size on the catalytic oxidation of 5-(hydroxymethyl)furfural. *Catalysts* **10**, 342 (2020).
33. Megías-Sayago, C. et al. Effect of gold particles size over Au/C catalyst selectivity in HMF oxidation reaction. *ChemCatChem* **12**, 1177–1183 (2020).
34. Ferraz, C. P. et al. 5-Hydroxymethylfurfural and furfural base-free oxidation over AuPd embedded bimetallic nanoparticles. *Catalysts* **10**, 75 (2020).
35. Yang, J. et al. Effect of the oxygen coordination environment of CaMn oxides on the catalytic performance of Pd supported catalysts for aerobic oxidation of 5-hydroxymethyl-2-furfural. *Catal. Sci. Technol.* **9**, 6659–6668 (2019).
36. Liu, Y. et al. Active oxygen species promoted catalytic oxidation of 5-hydroxymethyl-2-furfural on facet-specific Pt nanocrystals. *ACS Catal.* **9**, 8306–8315 (2019).
37. Megias-Sayago, C. et al. Understanding the role of the acid sites in 5-hydroxymethylfurfural oxidation to 2,5-furandicarboxylic acid reaction over gold catalysts: surface investigation on Ce_xZr_{1-x}O₂ compounds. *ACS Catal.* **8**, 11154–11164 (2018).
38. Yu, K. et al. The role of Bi-doping in promoting electron transfer and catalytic performance of Pt/3DOM-Ce_{1-x}BixO_{2-δ}. *J. Catal.* **365**, 292–302 (2018).
39. Schade, O. R., Kalz, K. F., Neukum, D., Kleist, W. & Grunwaldt, J. D. Supported gold- and silver-based catalysts for the selective aerobic oxidation of 5-(hydroxymethyl)furfural to 2,5-furandicarboxylic acid and 5-hydroxymethyl-2-furancarboxylic acid. *Green Chem.* **20**, 3530–3541 (2018).

40. Masoud, N., Donoeva, B. & de Jongh, P. E. Stability of gold nanocatalysts supported on mesoporous silica for the oxidation of 5-hydroxymethyl furfural to furan-2,5-dicarboxylic acid. *Appl. Catal. A* **561**, 150–157 (2018).
41. Wan, X. et al. Base-free aerobic oxidation of 5-hydroxymethyl-furfural to 2,5-furandicarboxylic acid in water catalyzed by functionalized carbon nanotube-supported Au–Pd alloy nanoparticles. *ACS Catal.* **4**, 2175–2185 (2014).
42. Bonincontro, D. et al. AuPd-nNiO as an effective catalyst for the base-free oxidation of HMF under mild reaction conditions. *Green Chem.* **21**, 4090–4099 (2019).
43. Gui, Z. et al. Efficient aerobic oxidation of 5-hydroxymethylfurfural in aqueous media with Au–Pd supported on zinc hydroxycarbonate. *ChemCatChem* **8**, 3636–3643 (2016).
44. Kerdi, F. et al. Evaluation of surface properties and pore structure of carbon on the activity of supported Ru catalysts in the aqueous-phase aerobic oxidation of HMF to FDCA. *Appl. Catal. A* **506**, 206–219 (2015).
45. Ait Rass, H., Essayem, N. & Besson, M. Selective aerobic oxidation of 5-HMF into 2,5-furandicarboxylic acid with Pt catalysts supported on TiO₂- and ZrO₂-based supports. *ChemSusChem* **8**, 1206–1217 (2015).
46. Chen, H. et al. Atomic layer deposition of Pt nanoparticles on low surface area zirconium oxide for the efficient base-free oxidation of 5-hydroxymethylfurfural to 2,5-furandicarboxylic acid. *Appl. Catal. A* **555**, 98–107 (2018).

Acknowledgements

We thank L. Kang and R. Wang from University College London and Cardiff University for access and assistance with the electron microscopy; and the Diamond Light Source for access to beamline E01 (proposal

number EM18909). C.J.K. acknowledges funding from the National Science Foundation Major Research Instrumentation programme (GR# MRI/DMR-1040229). S.M.A. thanks the Saudi Arabian government for his PhD scholarship. X.H. and Q.H. thank Cardiff University School of Chemistry for financial support. Q.H. also acknowledges the support by National Research Foundation (NRF) Singapore, under its NRF Fellowship (NRF-NRFF11-2019-0002). K.W. and L.Z. thank the Chinese Scholarship Council (CSC) for financial support. XPS data collection was performed at the EPSRC National Facility for XPS ('HarwellXPS'), operated by Cardiff University and UCL, under contract number PR16195. We thank Cardiff University and the Max Planck Centre for Fundamental Heterogeneous Catalysis (FUNCAT) for financial support.

Author information

Author notes

1. These authors contributed equally: Xiaoyang Huang, Ouardia Akdim

Affiliations

1. Max Planck-Cardiff Centre on the Fundamentals of Heterogeneous Catalysis FUNCAT, Cardiff Catalysis Institute, School of Chemistry, Cardiff University, Cardiff, UK

Xiaoyang Huang, Ouardia Akdim, Mark Douthwaite, Kai Wang, Liang Zhao, Richard J. Lewis, Samuel Pattisson, Isaac T. Daniel, Peter J. Miedziak, Greg Shaw, David J. Morgan, Thomas E. Davies, Qian He, Fei Wang, Jile Fu, Donald Bethell & Graham J. Hutchings

2. School of Applied Sciences, University of South Wales, Pontypridd, UK

Peter J. Miedziak

3. Department of Materials Science and Engineering, Lehigh University, Bethlehem, PA, USA

Sultan M. Althahban & Christopher J. Kiely

4. Department of Mechanical Engineering, Jazan University, Jazan, Saudi Arabia

Sultan M. Althahban

5. Department of Materials Science and Engineering, Faculty of Engineering, National University of Singapore, Singapore, Singapore

Qian He

6. Department of Chemical and Biomolecular Engineering, Lehigh University, Bethlehem, PA, USA

Steven McIntosh & Christopher J. Kiely

Contributions

X.H., O.A., M.D., R.J.L., S.P., P.J.M. and G.J.H. contributed to the design of the study. X.H., O.A., L.Z., I.T.D., R.J.L., K.W., J.F. and F.W. conducted experiments and data analysis. O.A. and X.H. conceived the mechanism. X.H., O.A., M.D., R.J.L., S.P., P.J.M., G.S., D.B., S.M., C.J.K. and G.J.H. provided technical support, conceptual advice and result interpretation. X.H., O.A., S.P., G.S., D.J.M., S.M.A., T.E.D., Q.H. and C.J.K. conducted catalyst characterization and corresponding data processing. M.D., O.A., D.B. and G.J.H. wrote the manuscript. X.H. wrote the Extended Data figures and tables. X.H., O.A., M.D., R.J.L., S.P., G.S., D.B., S.M., C.J.K. and G.J.H commented on and amended both documents. All authors discussed and contributed to the work.

Corresponding author

Correspondence to [Graham J. Hutchings](#).

Ethics declarations

Competing interests

The authors declare no competing interests.

Peer review

Peer review information

Nature thanks Bin Wang and the other, anonymous, reviewer(s) for their contribution to the peer review of this work.

Additional information

Publisher's note Springer Nature remains neutral with regard to jurisdictional claims in published maps and institutional affiliations.

Extended data figures and tables

Extended Data Fig. 1 Diagrammatic representation of the solid-immobilisation method used for catalyst preparation.

a, Monometallic Au/C and Pd/C. **b**, Au=Pd/C. **c**, Au@Pd/C catalysts. **d**, alloyed Au–Pd/C. **e**, Schematic representation of our reactor set-up for the thermocatalytic experiments.

Extended Data Fig. 2 Time-on-line data of aqueous HMF oxidation over series of Au/Pd catalysts and their TOF.

a, Au/C. **b**, Pd/C. **c**, Au–Pd/C alloy. **d**, Physical mixture of Au/C + Pd/C. **e**, Au@Pd/C. **f**, Au/C followed by the addition of Pd/C after 30 min. **g**, Au/C followed by the addition of C after 30 min. Reaction conditions: HMF (0.1 M); NaHCO₃ (0.4 M); H₂O (16 ml); Au/C: 72.1 mg; Pd/C: 71 mg; Au–Pd/C alloy: 143.1 mg; Au@Pd/C: 143.1 mg; C: 71 mg; 80 °C; ρO_2 = 3 bar. Key: FDCA yield (■), FFCA yield (♦), HMFCA yield (▲), HMF

conversion (●), mass balance (*). Associated error bars correspond to mean ± s.d. ($n = 5$). **h**, The influence on ODH activity when various quantities of Pd/C (▲) and C (●) are added to Au/C (72.1 mg); ODH activity exhibited by various quantities of Pd/C, in the absence of Au/C, is also displayed (◀). **i**, The influence of oxygen pressure (0.6–3.0 bar) on ODH activity over a physical mixture of Au/C + Pd/C (▲) and Au/C (◆) is displayed. The reaction conditions used for **h** and **i** are given in Methods. **j**, Summary of each catalyst in terms of HMF conversion, initial rate and TOF at a 5-min reaction time. The total active sites available in each catalyst was estimated using the Mackay model, based on the presented particle size distributions²⁵. Further information relating to how the TOFs were calculated, can be found in Methods.

[Source data](#)

[Extended Data Fig. 3 Catalytic performance over Au/C, Pd/C, Au–Pd/C alloy, Au/C + Pd/C physical mixture and Au@Pd/C catalysts in series of alcohol oxidation reactions.](#)

a, Glycerol oxidation. **b**, Ethanol oxidation. **c**, 5-Formyl-2-furancarboxylic acid (FFCA) oxidation. **d**, 5-Hydroxymethylfuroicacid (HMFCa) oxidation. Reaction conditions were all listed in Methods. **e**, Conversion values for the HMF oxidation reaction after 5 and 15 min time-on-line for the various catalysts studied in this work. Reaction conditions: HMF (0.1 M); NaHCO₃ (0.4 M); H₂O (16 ml); Au/(C/TiO₂/BN): 72.1 mg, Pd/(C/TiO₂/BN): 71 mg, Au@Pd/C, Au–Pd/(C/TiO₂/BN) and Au/(C/TiO₂/BN) + Pd/(C/TiO₂/BN): 143.1 mg; 80 °C; $p\text{O}_2 = 3$ bar; reaction time: 5 and 15 min. * presents the test on bare supports in HMF oxidation, HMF (0.1 M); NaHCO₃ (0.4 M); H₂O (16 ml); C/TiO₂/BN: 60 mg; 80 °C; $p\text{O}_2 = 3$ bar; reaction time: 30 min.

[Source data](#)

[Extended Data Fig. 4 Electron microscopy analysis of Au/C + Pd/C \(physical mixture\) catalyst after one cycle of use in the](#)

oxidation of HMF.

a, b, Representative complementary BF- and HAADF-STEM micrographs showing metal nanoparticle size and spatial distribution. **c**, Atomic resolution HAADF-STEM micrograph of a C grain supporting Au particles. **d**, A C grain supporting Pd particles confirming that the Au and Pd remain separated under our reaction conditions. **e, f**, Representative XEDS spectra of individual Au particles and Pd particles in the catalyst, respectively. No evidence of Au or Pd migration or intermixing after the catalytic reaction was observed.

[Source data](#)

Extended Data Fig. 5 XPS data.

a, b, Au 4f and **c, d**, Pd 3d /Au 4d regions for Au/C and Pd/C monometallic catalysts before and after a typical HMF oxidation reaction as a physical mixture. Among which, **a**, fresh Au/C; **b**, used Au/C; **c**, fresh Pd/C; and **d**, used Pd/C. TPR data for the physically mixed Au/C + Pd/C catalyst and the Au@Pd/C catalyst **e**, before and **f**, after HMF oxidation.

[Source data](#)

Extended Data Fig. 6 Electrochemical and thermal catalytic oxidation of aqueous HMF over Au/Pd catalysts.

a, Correlation between the thermo- and electro-catalytic HMF oxidation over the series of catalysts. For thermocatalytic experiments, the initial rates were from a 5-min reaction. The current densities were from the maxima observed in the corresponding CV experiments (Fig. 3a). Associated error bars correspond to mean \pm s.d. ($n = 3$). **b**, Aqueous HMF oxidation over the mono- and bi-metallic Au–Pd catalysts. Reaction conditions: HMF (0.1 M); NaOH (0.4 M); H₂O (16 ml); 25 °C; $p\text{O}_2$ = 3 bar; 30 min; catalyst amounts for Au@Pd/C and Au–Pd/C: 143.1 mg, Au/C: 72.1 mg, Pd/C: 71 mg, carbon balance: ca 92%. **c**, Catalytic performance in short circuit with current density (normalized by an electrode surface area of 0.07 cm²) generated as a

function of time in the single cell. Reaction conditions: 0.1 M NaOH and 0.02 M HMF in 50 ml H₂O; Au (working electrode) and Pd or C (counter electrode); 25 °C; O₂ flow: 50 ml min⁻¹. **d**, H-type dual cell consists of Au as the anode in an N₂ flow, Pd as cathode in an O₂ flow. The two cells connect via an anion exchange membrane. Reaction conditions: each cell contains 0.1 M NaOH and 0.02 M HMF in 35 ml H₂O; 25 °C; gas flow O₂/N₂: 50 ml min⁻¹. **e**, Reaction conditions: i: 0.1 M NaOH and 0.02 M HMF in 50 ml H₂O, 25 °C, N₂ flow: 50 ml min⁻¹; ii: same as i, except for the O₂ flow: 50 ml min⁻¹; iii: each cell contains 0.1 M NaOH and 0.02 M HMF in 35 ml H₂O, 25 °C, O₂/N₂ flow: 50 ml min⁻¹; iv: same as iii, except for the disconnection of Au and Pd electrodes; v- same as iii, except the mass of Pd/C is doubled.

[Source data](#)

Extended Data Fig. 7 Representative STEM-HAADF images and X-ED spectra of nanoparticles in the Au=Pd/C catalysts and its corresponding activities.

a, Lower magnification STEM-HAADF image of the Au = Pd/C catalyst. **b**, **c**, X-ED spectra obtained from individual nanoparticles, showing a Au-only and a Pd-only nanoparticle. **d**, STEM-HAADF image and the corresponding X-ED spectrum (inlet) of a Janus-like particle occasionally found in this Au=Pd/C catalyst. **e**, Activity comparison to the physical mixture **f**. Reaction conditions: HMF (0.1 M); NaHCO₃ (0.4 M); H₂O (16 ml); Au/C: 72.1 mg; Pd/C: 71 mg; Au=Pd/C: 143.1 mg; 80 °C; pO₂ = 3 bar; reaction time: 30 min. Associated error bars correspond to mean ± s.d. (*n* = 3).

[Source data](#)

Extended Data Fig. 8 Electron microscopy analysis of Au@Pd/C catalyst after one use in the oxidation of HMF.

a, b, Representative complementary pair of BF- and HAADF-STEM micrographs showing metal nanoparticle size and spatial distribution. **c–e**, Atomic resolution HAADF-STEM micrographs of particles. The yellow arrows in e highlight certain atomic columns that appear lower in contrast, indicating some alloying of Pd with the Au matrix. **f**, A representative XEDS spectrum obtained from a typical nanoparticle, showing the presence of both Au and Pd.

[Source data](#)

Extended Data Fig. 9 Reusability data for the prepared Au/Pd catalysts in HMF oxidation reaction.

a, c, The Au@Pd/C catalyst. **b, d**, the physical mixture Au/C + Pd/C catalyst. Reaction conditions: HMF (0.1 M); NaHCO₃ (0.4 M); H₂O (16 ml); Au/C: 72.1 mg; Pd/C: 71 mg; Au@Pd/C: 143.1 mg; 80 °C; pO₂ = 3 bar; reaction time: 60 min. Key: FDCA yield (■), FFCA yield (◆), HMFCA yield (▲), HMF conversion (●), mass balance (*).

[Source data](#)

**Extended Data Table 1 The performance of supported metal catalysts in the aqueous phase aerobic oxidation of 5-hydroxymethyl furfural to furan dicarboxylic acid
(FDCA)** [15](#),[26](#),[27](#),[28](#),[29](#),[30](#),[31](#),[32](#),[33](#),[34](#),[35](#),[36](#),[37](#),[38](#),[39](#),[40](#),[41](#),[42](#),[43](#),[44](#),[45](#),[46](#)

Source data

[**Source Data Fig. 1**](#)

[**Source Data Fig. 3**](#)

[**Source Data Fig. 4**](#)

[**Source Data Extended Data Fig. 2**](#)

[**Source Data Extended Data Fig. 3**](#)

[**Source Data Extended Data Fig. 4**](#)

[**Source Data Extended Data Fig. 5**](#)

[**Source Data Extended Data Fig. 6**](#)

[**Source Data Extended Data Fig. 7**](#)

[**Source Data Extended Data Fig. 8**](#)

[**Source Data Extended Data Fig. 9**](#)

Rights and permissions

[Reprints and Permissions](#)

About this article

Cite this article

Huang, X., Akdim, O., Douthwaite, M. *et al.* Au–Pd separation enhances bimetallic catalysis of alcohol oxidation. *Nature* **603**, 271–275 (2022).
<https://doi.org/10.1038/s41586-022-04397-7>

- Received: 12 January 2021
- Accepted: 04 January 2022
- Published: 17 January 2022
- Issue Date: 10 March 2022
- DOI: <https://doi.org/10.1038/s41586-022-04397-7>

Share this article

Anyone you share the following link with will be able to read this content:

[Get shareable link](#)

Sorry, a shareable link is not currently available for this article.

[Copy to clipboard](#)

Provided by the Springer Nature SharedIt content-sharing initiative

This article was downloaded by **calibre** from <https://www.nature.com/articles/s41586-022-04397-7>

| [Section menu](#) | [Main menu](#) |

- Article
- [Published: 09 March 2022](#)

Weak cubic CaSiO₃ perovskite in the Earth's mantle

- [J. Immoor](#)¹,
- [L. Miyagi](#)²,
- [H.-P. Liermann](#) [ORCID: orcid.org/0000-0001-5039-1183](#)³,
- [S. Speziale](#)⁴,
- [K. Schulze](#)⁵,
- [J. Buchen](#) [ORCID: orcid.org/0000-0001-5671-5214](#)⁶ nAff⁷,
- [A. Kurnosov](#)¹ &
- [H. Marquardt](#) [ORCID: orcid.org/0000-0003-1784-6515](#)⁷

[Nature](#) volume 603, pages 276–279 (2022)

- 774 Accesses
- 83 Altmetric
- [Metrics details](#)

Subjects

- [Geodynamics](#)
- [Geophysics](#)
- [Mineralogy](#)

Abstract

Cubic CaSiO₃ perovskite is a major phase in subducted oceanic crust, where it forms at a depth of about 550 kilometres from majoritic garnet^{1,2,28}. However, its rheological properties at temperatures and pressures typical of the lower mantle are poorly known. Here we measured the plastic strength of cubic CaSiO₃ perovskite at pressure and temperature conditions typical for a subducting slab up to a depth of about 1,200 kilometres. In contrast to tetragonal CaSiO₃, previously investigated at room temperature^{3,4}, we find that cubic CaSiO₃ perovskite is a comparably weak phase at the temperatures of the lower mantle. We find that its strength and viscosity are substantially lower than that of bridgmanite and ferropericlase, possibly making cubic CaSiO₃ perovskite the weakest lower-mantle phase. Our findings suggest that cubic CaSiO₃ perovskite governs the dynamics of subducting slabs. Weak CaSiO₃ perovskite further provides a mechanism to separate subducted oceanic crust from the underlying mantle. Depending on the depth of the separation, basaltic crust could accumulate at the boundary between the upper and lower mantle, where cubic CaSiO₃ perovskite may contribute to the seismically observed regions of low shear-wave velocities in the uppermost lower mantle^{5,6}, or sink to the core–mantle boundary and explain the seismic anomalies associated with large low-shear-velocity provinces beneath Africa and the Pacific^{7,8,9}.

This is a preview of subscription content

Access options

Subscribe to Nature+

Get immediate online access to the entire Nature family of 50+ journals

\$29.99

monthly

[Subscribe](#)

Subscribe to Journal

Get full journal access for 1 year

\$199.00

only \$3.90 per issue

[Subscribe](#)

All prices are NET prices.

VAT will be added later in the checkout.

Tax calculation will be finalised during checkout.

Buy article

Get time limited or full article access on ReadCube.

\$32.00

[Buy](#)

All prices are NET prices.

Additional access options:

- [Log in](#)
- [Learn about institutional subscriptions](#)

Fig. 1: Deviatoric stress measured in cubic CaSiO₃ perovskite at lower-mantle pressures and T = 1,150 ± 50 K.

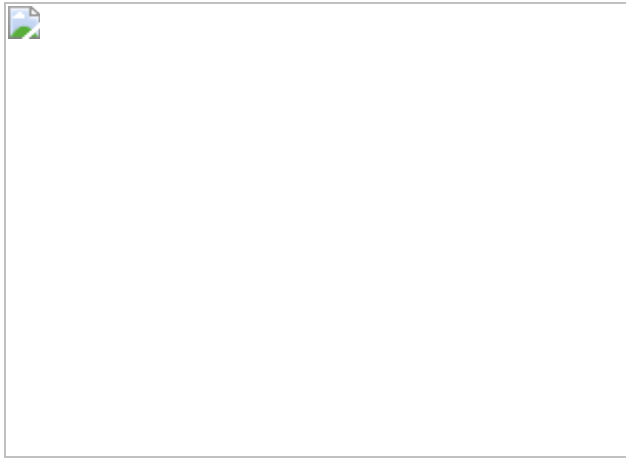


Fig. 2: Strength of major lower-mantle phases at high pressures.

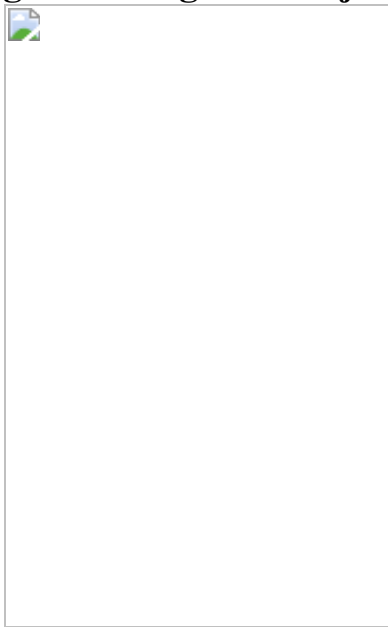
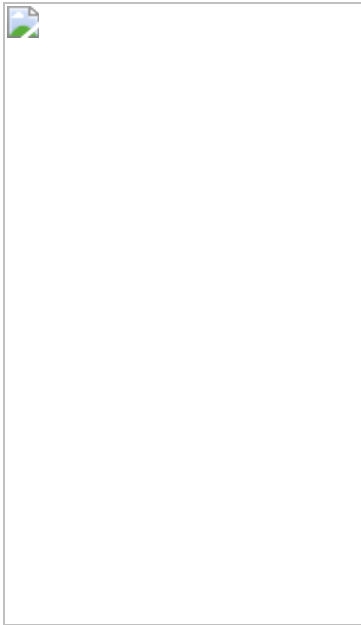


Fig. 3: Depth-dependent viscosity contrast between major lower-mantle phases at approximately 1,150 K.



Data availability

Raw data were generated at the Deutsches Elektronen-Synchrotron (DESY) and are available at <https://doi.org/10.6084/m9.figshare.17287361>. All derived data supporting the findings of this study are available within the article and the Extended Data. Source data for Figs. 2, 3 and Extended Data Fig. 2 are provided with the paper.

References

1. Irifune, T. & Tsuchiya, T. Mineralogy of the Earth – phase transitions and mineralogy of the lower mantle. In Treatise on Geophysics. Volume 2: Mineral Physics 1st edn (ed. Schubert, G.) 33–62 (Elsevier, 2007).
2. Hirose, K., Sinmyo, R. & Hernlund, J. Perovskite in Earth’s deep interior. *Science* **358**, 734–738 (2017).
3. Miyagi, L. et al. Diamond anvil cell deformation of CaSiO₃ perovskite up to 49 GPa. *Phys. Earth Planet. Inter.* **174**, 159–164 (2009).

4. Shieh, S. R., Duffy, T. S. & Shen, G. Elasticity and strength of calcium silicate perovskite at lower mantle pressures. *Phys. Earth Planet. Inter.* **143–144**, 93–105 (2004).
5. Ballmer, M. D., Schmerr, N. C., Nakagawa, T. & Ritsema, J. Compositional mantle layering revealed by slab stagnation at ~1000-km depth. *Sci. Adv.* **1**, e1500815 (2015).
6. Gréaux, S. et al. Sound velocity of CaSiO_3 perovskite suggests the presence of basaltic crust in the Earth's lower mantle. *Nature* **565**, 218–221 (2019).
7. Thomson, A. R. et al. Calcium silicate perovskite's acoustic velocities can explain LLSVPs in Earth's lower mantle. *Nature* **572**, 643–647 (2019).
8. Jones, T. D., Maguire, R. R., van Keken, P. E., Ritsema, J. & Koelemeijer, P. Subducted oceanic crust as the origin of seismically slow lower-mantle structures. *Prog. Earth Planet. Sci.* **7**, 17 (2020).
9. Garnero, E. J., McNamara, A. K. & Shim, S.-H. Continent-sized anomalous zones with low seismic velocity at the base of Earth's mantle. *Nat. Geosci.* **9**, 481–489 (2016).
10. Tschauner, O. et al. Discovery of davemaoite, CaSiO_3 -perovskite, as a mineral from the lower mantle. *Science* **374**, 891–894 (2021).
11. Nestola, F. et al. CaSiO_3 perovskite in diamond indicates the recycling of oceanic crust into the lower mantle. *Nature* **555**, 237–241 (2018).
12. Komabayashi, T., Hirose, K., Sata, N., Ohishi, Y. & Dubrovinsky, L. S. Phase transition in CaSiO_3 perovskite. *Earth Planet. Sci. Lett.* **260**, 564–569 (2007).
13. Sun, N. et al. Confirming a pyrolytic lower mantle using self-consistent pressure scales and new constraints on CaSiO_3 perovskite. *J. Geophys. Res. Solid Earth* **121**, 4876–4894 (2016).

14. Ferré, D., Cordier, P. & Carrez, P. Dislocation modeling in calcium silicate perovskite based on the Peierls–Nabarro model. *Am. Mineral.* **94**, 135–142 (2009).
15. Ferré, D., Carrez, P. & Cordier, P. Peierls dislocation modelling in perovskite (CaTiO_3): comparison with tausonite (SrTiO_3) and MgSiO_3 perovskite. *Phys. Chem. Miner.* **36**, 233–239 (2009).
16. Immoor, J. et al. An improved setup for radial diffraction experiments at high pressures and high temperatures in a resistive graphite-heated diamond anvil cell. *Rev. Sci. Instrum.* **91**, 045121 (2020).
17. Merkel, S. et al. Deformation of polycrystalline MgO at pressures of the lower mantle. *J. Geophys. Res.* **107**, 2271 (2002).
18. Immoor, J. et al. Evidence for $\{100\} \langle 011 \rangle$ slip in ferropericlase in Earth’s lower mantle from high-pressure/high-temperature experiments. *Earth Planet. Sci. Lett.* **489**, 251–257 (2018).
19. Couper, S., Speziale, S., Marquardt, H., Liermann, H. P. & Miyagi, L. Does heterogeneous strain act as a control on seismic anisotropy in Earth’s lower mantle? *Front. Earth Sci.* **8**, 540449 (2020).
20. Girard, J., Amulele, G., Farla, R., Mohiuddin, A. & Karato, S.-i Shear deformation of bridgmanite and magnesiowüstite aggregates at lower mantle conditions. *Science* **351**, 144–147 (2016).
21. Merkel, S. et al. Deformation of $(\text{Mg}_{0.9}\text{Fe}_{0.1})\text{SiO}_3$ pPerovskite aggregates up to 32 GPa. *Earth Planet. Sci. Lett.* **209**, 351–360 (2003).
22. Marquardt, H. & Miyagi, L. Slab stagnation in the shallow lower mantle linked to an increase in mantle viscosity. *Nat. Geosci.* **8**, 311–314 (2015).
23. Yamazaki, D. & Karato, S.-i Some mineral physics constraints on the rheology and geothermal structure of Earth’s lower mantle. *Am. Mineral.* **86**, 385–391 (2001).

24. Thielmann, M., Golabek, G. J. & Marquardt, H. Ferropericlase control of lower mantle rheology: impact of phase morphology. *Geochim. Geophys. Geosys.* **21**, e2019GC008688 (2020).
25. Goryaeva, A. M., Carrez, P. & Cordier, P. Low viscosity and high attenuation in MgSiO₃ post-perovskite inferred from atomic-scale calculations. *Sci. Rep.* **6**, 34771 (2016).
26. Muir, J. M. R. & Brodholt, J. P. Water distribution in the lower mantle: implications for hydrolytic weakening. *Earth Planet. Sci. Lett.* **484**, 363–369 (2018).
27. Kavner, A., Sinogeikin, S. V., Jeanloz, R. & Bass, J. D. Equation of state and strength of natural majorite. *J. Geophys. Res. Solid Earth* **105**, 5963–5971 (2000).
28. Saikia, A., Frost, D. J. & Rubie, D. C. Splitting of the 520-kilometer seismic discontinuity and chemical heterogeneity in the mantle. *Science* **319**, 1515–1518 (2008).
29. Takeda, Y.-T. Flow in rocks modelled as multiphase continua: application to polymineralic rocks. *J. Struc. Geol.* **20**, 1569–1578 (1998).
30. Hunt, S. A. et al. An experimental investigation of the relative strength of the silica polymorphs quartz, coesite, and stishovite. *Geochim. Geophys. Geosys.* **20**, 1975–1989 (2019).
31. van Keken, P. E., Karato, S. & Yuen, D. A. Rheological control of oceanic crust separation in the transition zone. *Geophys. Res. Lett.* **23**, 1821–1824 (1996).
32. Hirose, K., Fei, Y., Ma, Y. & Mao, H.-K. The fate of subducted basaltic crust in the Earth's lower mantle. *Nature* **397**, 53–56 (1999).
33. Hirose, K., Takafuji, N., Sata, N. & Ohishi, Y. Phase transition and density of subducted MORB crust in the lower mantle. *Earth Planet. Sci. Lett.* **237**, 239–251 (2005).

34. Hofmann, A. W. Mantle geochemistry: the message from oceanic volcanism. *Nature* **385**, 219–229 (1997).
35. Kurashina, T., Hirose, K., Ono, S., Sata, N. & Ohishi, Y. Phase transition in Al-bearing CaSiO₃ perovskite: implications for seismic discontinuities in the lower mantle. *Phys. Earth Planet. Inter.* **145**, 67–74 (2004).
36. Fukao, Y. & Obayashi, M. Subducted slabs stagnant above, penetrating through, and trapped below the 660 km discontinuity. *J. Geophys. Res.* **118**, 5920–5938 (2013).
37. Liermann, H.-P. et al. Experimental method for in situ determination of material textures at simultaneous high pressure and high temperature by means of radial diffraction in the diamond anvil cell. *Rev. Sci. Instrum.* **80**, 104501 (2009).
38. Liermann, H.-P. et al. The Extreme Conditions Beamline P02.2 and the Extreme Conditions Science Infrastructure at PETRA III. *J. Synchr. Rad.* **22**, 908–924 (2015).
39. Fei, Y. et al. Toward an internally consistent pressure scale. *Proc. Natl Acad. Sci.* **104**, 9182–9186 (2007).
40. Hammersley, A. P., Svensson, S. O., Hanfland, M., Fitch, A. N. & Hausermann, D. Two-dimensional detector software: from real detector to idealised image or two-theta scan. *High Press. Res.* **14**, 235–248 (1996).
41. Lutterotti, L., Matthies, S., Wenk, H.-R., Schultz, A. S. & Richardson, J. W. Jr Combined texture and structure analysis of deformed limestone from time-of-flight neutron diffraction spectra. *J. Appl. Phys.* **81**, 594–600 (1997).
42. Singh, A. K., Balasingh, C., Mao, H.-K., Hemley, R. J. & Shu, J. Analysis of lattice strains measured under nonhydrostatic pressure. *J. Appl. Phys.* **83**, 7567–7575 (1998).

43. Matthies, S. & Vinel, G. W. On the reproduction of the orientation distribution function of texturized samples from reduced pole figures using the conception of a conditional ghost correction. *Phys. Status Solidi B* **112**, K111–K114 (1982).
44. Wenk, H.-R., Matthies, S., Donovan, J. & Chateigner, D. BEARTEX: a Windows-based program system for quantitative texture analysis. *J. Appl. Crystallogr.* **31**, 262–269 (1998).
45. Lebensohn, R. A. & Tomé, C. N. A self-consistent anisotropic approach for the simulation of plastic deformation and texture development of polycrystals: application to zirconium alloys. *Acta Metall. Mater.* **41**, 2611–2624 (1993).

Acknowledgements

We acknowledge technical assistance by A. Ehnes and I. Schwark. We thank A. R. Thomson for providing a table with the high-temperature shear modulus of CaSiO₃ perovskite. This research was supported through the German Science Foundation (grants MA4534/3-1 and MA4534/4-1) as well the European Union’s Horizon 2020 research and innovation programme (ERC grant 864877). H.M. acknowledges support from the Bavarian Academy of Sciences. L..M acknowledges support from the NSF (EAR-1654687) and US Department of Energy National Nuclear Security Administration through the Chicago-DOE Alliance Center (DE-NA0003975).

Author information

Author notes

1. J. Buchen

Present address: Department of Earth Sciences, University of Oxford, Oxford, UK

Affiliations

1. Bayerisches Geoinstitut (BGI), University of Bayreuth, Bayreuth, Germany
J. Immoor & A. Kurnosov
2. University of Utah, Salt Lake City, UT, USA
L. Miyagi
3. Deutsches Elektronen-Synchrotron (DESY), Hamburg, Germany
H.-P. Liermann
4. German Research Center for Geosciences (GFZ), Potsdam, Germany
S. Speziale
5. Independent researcher, Bayreuth, Germany
K. Schulze
6. Seismological Laboratory, California Institute of Technology, Pasadena, CA, USA
J. Buchen
7. Department of Earth Sciences, University of Oxford, Oxford, UK
H. Marquardt

Contributions

H.M., H.-P.L., L.M. and S.S. designed the research. J.I. prepared the experiments. All authors contributed to the synchrotron experiments. J.I. and L.M. analysed the data. H.M. performed the modelling. H.M. wrote the

initial draft of the manuscript. All authors contributed to the final writing of the manuscript.

Corresponding author

Correspondence to [H. Marquardt](#).

Ethics declarations

Competing interests

The authors declare no competing interest.

Peer review

Peer review information

Nature thanks Patrick Cordier and the other, anonymous, reviewer(s) for their contribution to the peer review of this work.

Additional information

Publisher's note Springer Nature remains neutral with regard to jurisdictional claims in published maps and institutional affiliations.

Extended data figures and tables

[Extended Data Fig. 1 Unrolled diffraction image](#)

Data were collected at 52.5 GPa and $1,150 \pm 50$ K (bottom) along with the best-fit model (top). The curvature is a measure of lattice strains and was used to calculate the strength of CaSiO₃ perovskite.

Extended Data Fig. 2 Experimentally derived lattice strains of cubic CaSiO₃ at a temperature of 1,150 ± 50 K.

The error of the derived lattice strains is similar to the symbol sizes, as shown in the lower right corner.

Extended Data Fig. 3 Texture development observed in experiments.

Texture strength is indicated by the colours. 100 texture increases with pressure throughout the experiment, increasing from about 1.5 mrd to 1.75 mrd, indicating plastic flow.

[Source data](#)

Extended Data Fig. 4 VPSC modelling of texture development.

The measured experimental texture after sample synthesis was used as starting texture. 20% of plastic strain leads to a texture strength comparable to that measured at 52.2 GPa (see Extended Data Fig. 3).

Extended Data Table 1 Viscosity contrast between CaSiO₃ perovskite and bridgmanite (left) or ferropericlase (right)

Source data

[Source Data Fig. 2](#)

[Source Data Fig. 3](#)

[Source Data Extended Data Fig. 3](#)

Rights and permissions

[Reprints and Permissions](#)

About this article

Cite this article

Immoor, J., Miyagi, L., Liermann, HP. *et al.* Weak cubic CaSiO₃ perovskite in the Earth's mantle. *Nature* **603**, 276–279 (2022).
<https://doi.org/10.1038/s41586-021-04378-2>

- Received: 04 February 2021
- Accepted: 22 December 2021
- Published: 09 March 2022
- Issue Date: 10 March 2022
- DOI: <https://doi.org/10.1038/s41586-021-04378-2>

Share this article

Anyone you share the following link with will be able to read this content:

[Get shareable link](#)

Sorry, a shareable link is not currently available for this article.

[Copy to clipboard](#)

Provided by the Springer Nature SharedIt content-sharing initiative

This article was downloaded by **calibre** from <https://www.nature.com/articles/s41586-021-04378-2>

- Article
- Open Access
- [Published: 09 March 2022](#)

Restoring and attributing ancient texts using deep neural networks

- [Yannis Assael](#) [ORCID: orcid.org/0000-0001-7408-3847¹](#), [na1](#),
- [Thea Sommerschield](#) [ORCID: orcid.org/0000-0002-6965-8105^{2,3}](#), [na1](#),
- [Brendan Shillingford¹](#),
- [Mahyar Bordbar¹](#),
- [John Pavlopoulos](#) [ORCID: orcid.org/0000-0001-9188-7425⁴](#),
- [Marita Chatzipanagiotou⁴](#),
- [Ion Androutsopoulos⁴](#),
- [Jonathan Prag⁵](#) &
- [Nando de Freitas¹](#)

Nature volume **603**, pages 280–283 (2022)

- 5415 Accesses
- 1 Citations
- 606 Altmetric
- [Metrics details](#)

Subjects

- [Archaeology](#)
- [Computer science](#)
- [History](#)

Abstract

Ancient history relies on disciplines such as epigraphy—the study of inscribed texts known as inscriptions—for evidence of the thought, language, society and history of

past civilizations¹. However, over the centuries, many inscriptions have been damaged to the point of illegibility, transported far from their original location and their date of writing is steeped in uncertainty. Here we present Ithaca, a deep neural network for the textual restoration, geographical attribution and chronological attribution of ancient Greek inscriptions. Ithaca is designed to assist and expand the historian’s workflow. The architecture of Ithaca focuses on collaboration, decision support and interpretability. While Ithaca alone achieves 62% accuracy when restoring damaged texts, the use of Ithaca by historians improved their accuracy from 25% to 72%, confirming the synergistic effect of this research tool. Ithaca can attribute inscriptions to their original location with an accuracy of 71% and can date them to less than 30 years of their ground-truth ranges, redating key texts of Classical Athens and contributing to topical debates in ancient history. This research shows how models such as Ithaca can unlock the cooperative potential between artificial intelligence and historians, transformationally impacting the way that we study and write about one of the most important periods in human history.

[Download PDF](#)

Main

Epigraphy is the study of texts—inscriptions—written directly on durable materials (stone, pottery, metal) by individuals, groups and institutions of the ancient world^{2,3}. Thousands of inscriptions have survived to our time, but many have been damaged over the centuries and their texts are now fragmentary. Inscriptions may also be moved or trafficked far from their original location⁴, and radiocarbon dating is unusable owing to the inorganic nature of most inscribed supports. Specialist epigraphers must then reconstruct the missing text, a process known as text restoration (Fig. 1), and establish the original place and date of writing, tasks known as geographical attribution and chronological attribution, respectively⁵. These three tasks are crucial steps towards placing an inscription both in history and within the world of the people who wrote and read it^{6,7}. However, these tasks are non-trivial, and traditional methods in epigraphy involve highly complex, time-consuming and specialized workflows.

Fig. 1: Restoration of a damaged inscription.



This inscription (*Inscriptiones Graecae*, volume 1, edition 3, document 4, face B (*IG I³ 4B*)) records a decree concerning the Acropolis of Athens and dates to 485/4 bc. Marsyas, Epigraphic Museum, WikiMedia CC BY 2.5.

When restoring damaged inscriptions, epigraphers rely on accessing vast repositories of information to find textual and contextual parallels⁸. These repositories primarily consist of a researcher's mnemonic repertoire of parallels and, more recently, of digital corpora for performing 'string matching' searches. However, differences in the search query can exclude or obfuscate relevant results, and it is almost impossible to estimate the true probability distribution of possible restorations. Attributing an inscription is equally problematic—if it was moved, or if useful internal dating elements are missing, historians must find alternative criteria to attribute the place and date of writing (such as letterforms, dialects)⁹. Inevitably, a high level of generalization is often involved (chronological attribution intervals can be very long).

Deep learning for epigraphy

Here we overcome the constraints of current epigraphic methods by using state-of-the-art machine learning research. Inspired by biological neural networks, deep neural networks can discover and harness intricate statistical patterns in vast quantities of data¹⁰. Recent increases in computational power have enabled these models to tackle challenges of growing sophistication in many fields^{11,12,13,14}, including the study of ancient languages^{15,16,17,18}.

We present Ithaca, a deep neural network architecture trained to simultaneously perform the tasks of textual restoration, geographical attribution and chronological attribution. Ithaca, which was named after the Greek island that eluded the hero Odysseus' homecoming, was trained on inscriptions written in the ancient Greek language and across the ancient Mediterranean world between the seventh century bc and the fifth century ad. This choice was due to two main reasons. First, the variability

of contents and context of the Greek epigraphic record, which makes it an excellent challenge for language processing; and second, the availability of digitized corpora for ancient Greek, an essential resource for training machine learning models.

Working with Greek inscriptions

To train Ithaca, we developed a pipeline to retrieve the unprocessed Packard Humanities Institute (PHI)^{19,20} dataset, which consists of the transcribed texts of 178,551 inscriptions. This process required rendering the text machine-actionable, normalizing epigraphic notations, reducing noise and efficiently handling all irregularities. Each PHI inscription is assigned a unique numerical ID, and is labelled with metadata relating to the place and time of writing. PHI lists a total of 84 ancient regions; whereas the chronological information is noted in a wide variety of formats, varying from historical eras to precise year intervals, written in several languages, lacking in standardized notation and often using fuzzy wording²¹. After crafting an extended ruleset to process and filter the data (Methods), the resulting dataset I.PHI is to our knowledge the largest multitask dataset of machine-actionable epigraphical text, containing 78,608 inscriptions.

Ithaca is a model for epigraphic tasks

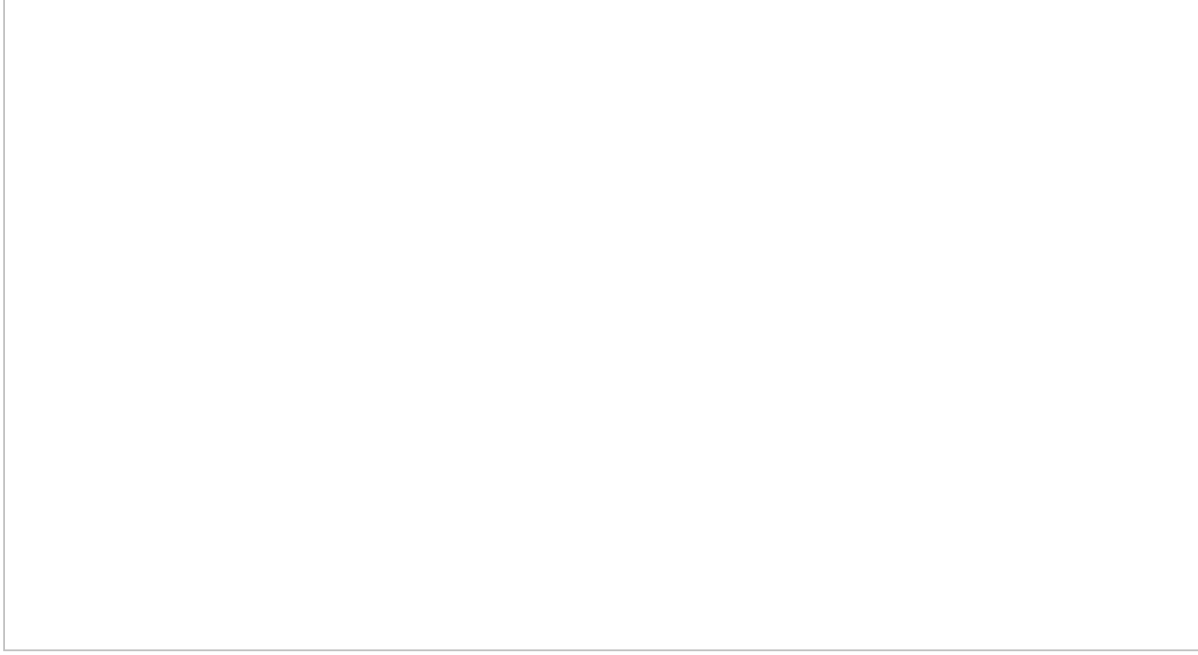
The architecture of Ithaca was carefully tailored to each of the three epigraphic tasks, meaningfully handling long-term context information and producing interpretable outputs to enhance the potential for human–machine cooperation. To begin, contextual information is captured more comprehensively by representing the inputs as words; however, parts of words could have been lost over the centuries. To address this challenge, we process the input text as character and word representations jointly, representing damaged, missing or unknown words with a special symbol ‘[unk]’.

Next, to enable large-scale processing, Ithaca’s torso is based on a neural network architecture called the transformer²², which uses an attention mechanism to weigh the influence of different parts of the input (such as characters, words) on the model’s decision-making process. The attention mechanism is informed of the position of each part of the input text by concatenating the input character and word representations with their sequential positional information. Ithaca’s torso consists of stacked transformer blocks: each block outputs a sequence of processed representations of which the length is equal to the number of input characters, and the output of each block becomes the input of the next. The final output of the torso is passed to three different task heads that handle restoration, geographical attribution and chronological attribution, respectively. Each head consists of a shallow feedforward neural network, specifically trained for each task. In the example shown in Fig. 2, the restoration head predicts the three missing characters; the geographical attribution head classifies the

inscription among 84 regions; and the chronological attribution head dates it to between 800 bc and ad 800.

Fig. 2: Ithaca’s architecture processing the phrase ‘δῆμο το αθηναίων’ (‘the people of Athens’).

 figure 2



The first three characters of the phrase were hidden and their restoration is proposed. In tandem, Ithaca also predicts the inscription’s region and date.

Interpreting the outputs

Our intention was to maximize the collaborative potential between historians and deep learning. Ithaca’s architecture was therefore designed to provide intelligible outputs, while featuring multiple visualization methods to augment the interpretability of the model’s predictive hypotheses. For the task of restoration, instead of providing historians with a single restoration hypothesis, Ithaca offers a set of the top 20 decoded predictions ranked by probability (Fig. 3a). This first visualization facilitates the pairing of Ithaca’s suggestions with historians’ contextual knowledge, therefore assisting human decision-making. This is complemented by saliency maps, a method used to identify which unique input features contributed the most to the model’s predictions, for both the restoration and attribution tasks (Fig. 3d and Extended Data Fig. 5a).

Fig. 3: Ithaca’s outputs.

 figure 3

a, Restoration predictions for six missing characters (dashes) in an Athenian inscription (*IG II² 116*). The top restoration, in green, is correct (συμμαχία, ‘alliance’). Note how the following hypotheses (ἐκκλησία, ‘assembly’; and προξενία, ‘treaty between state and foreigner’), highlighted in red, typically occur in Athenian political decrees²³, revealing Ithaca’s receptivity to context. **b**, Geographical attribution of an inscription from Amorgos (*IG XII 7, 2*). Ithaca’s top prediction is correct, and the closest predictions are neighbouring regions. **c**, Date distribution for an inscription from Delos (*IG XI 4, 579*). The ground-truth date interval 300–250 bc is shown in grey; Ithaca’s predicted distribution is shown in yellow and has a mean at 273 bc (green). Ithaca’s predictions show a higher confidence for the interval’s higher date margin, therefore potentially narrowing the broad ground-truth dating bracket. **d**, Chronological attribution saliency map for an Athenian inscription (*IG I³ 371*). The colour intensity illustrates the importance of each input. Ithaca focuses on the personal name (Νικίας, ‘Nikias’) and the Greek commanders’ rank (στρατεγοίς, ‘generals’). Nikias had a key role in the great Athenian expedition to Sicily^{24,25,26}, the historical event to which this very inscription pertains. Ithaca dates the inscription to 413 bc, matching the exact range proposed by historians (414–413 bc).

For the geographical attribution task, Ithaca classifies the input text among 84 regions, and the ranked list of possible region predictions is visually implemented with both a map and a bar chart (Fig. 3b). Finally, to expand interpretability for the chronological attribution task, instead of outputting a single date value, we predict a categorical distribution over dates (Fig. 3c). By so doing, Ithaca can handle ground-truth labels more effectively, as the labels correspond to date intervals. More precisely, Ithaca discretizes all dates between 800 bc and ad 800 into 10-year bins, resulting in 160 decades. For example, the date range 300–250 bc is represented as 5 decades of equal

20% probability, whereas an inscription dated to 305 bc would be assigned to the single-decade-bin 300–310 bc with 100% probability.

Experimental evaluation

To compare performance in the three epigraphic tasks, we use four methods. First, we evaluate the difficulty of the restoration task by assigning two evaluators with epigraphical expertise ('ancient historian') a set of damaged inscriptions to restore, using the training set to search for textual parallels. Second, we provide the human experts with a ranked list of Ithaca's top 20 restoration hypotheses to inform their predictions ('ancient historian and Ithaca'), therefore assessing the true impact of our work as a cooperative research aid. Third, as a computational baseline we reimplement our previous work Pythia¹⁵—a sequence-to-sequence recurrent neural network for the task of ancient-text restoration. Finally, for the attribution tasks, we introduce an ablation of the epigrapher's workflow, the 'onomastics' baseline: annotators were tasked with attributing a set of texts, exclusively using the known distribution of Greek personal names across time and space to infer geographical and chronological indicia²⁷.

We introduce the following metrics to measure each method's performance. For restoration, to obviate the lack of ground truths in damaged inscriptions, we artificially hide 1 to 10 characters of undamaged input text and treat the original sequences as the target. The first metric used is the character error rate (CER), which counts the normalized differences between the top predicted restoration sequence and the target sequence. Furthermore, we use top- k accuracy to measure whether the correct restoration or region label for geographical attribution is among the top k predictions, therefore quantifying Ithaca's potential as an assistive tool. For chronological attribution, we use a distance metric (Methods) to measure the distance in years from the predictive distribution's mean and the ground-truth interval, the latter being defined by a minimum and a maximum date.

As shown in Table 1, for the task of restoration, Ithaca consistently outperforms the competing methods, scoring a 26.3% CER and 61.8% top 1 accuracy. Specifically, our model achieves a 2.2× lower (that is, better) CER compared with human experts, whereas Ithaca's top 20 predictions achieve a 1.5× improved performance compared with Pythia, with an accuracy of 78.3%. Notably, when pairing historians with Ithaca (ancient historian and Ithaca), human experts achieve an 18.3% CER and 71.7% top 1 accuracy, therefore demonstrating a considerable 3.2× and 2.8× improvement compared with their original CER and top 1 scores. Regarding the attribution to regions, Ithaca has 70.8% top 1 and 82.1% top 3 predictive accuracy. Finally, for chronological attribution, whereas the onomastics human baseline predictions are within an average of 144.4 and median of 94.5 years from the ground-truth date

intervals, Ithaca’s predictions, based on the totality of texts, have an average distance of 29.3 years from the target dating brackets, with a median distance of only 3 years.

Table 1 Experimental results

Contributing to historical debates

Our experimental evaluation effectively demonstrates Ithaca’s impact on the study of inscriptions, and their consequent value as historical evidence. First, Ithaca can discover epigraphic patterns on an unprecedented scale and in unparalleled detail, harnessing substantial quantities of epigraphic data (I.PHI) to achieve the high performance observed in all three epigraphic tasks. Moreover, whereas Ithaca may have outperformed historians in the first baseline, the combination of a historian’s own (contextual) knowledge alongside Ithaca’s assistive input resulted in an even greater improvement over the model’s performance. This collaborative potential is augmented by Ithaca’s design decisions, and by the different visualization aids increasing the interpretability of outputs, therefore enabling historians to evaluate multiple hypotheses. As a consequence, Ithaca could help historians narrow the wide or vague date brackets they are sometimes forced to resort to, by helping increase precision and establish relative datings for historical events, and even contributing to current methodological debates in ancient history.

Indeed, to demonstrate Ithaca’s creative potential, we applied our model to a contemporary dispute concerning the dating of a group of inscriptions whose interpretation is central to the political history of classical Athens. Historians disagree on whether these decrees should pre- or post-date 446/5 bc depending on the (dis)belief in using specific letterforms as dating criteria (the three-bar sigma dating convention)²⁸. In recent years, the validity of this dating convention was called into question²⁹—the dates of many decrees have been pushed to the 420s bc, therefore profoundly influencing our understanding of Athenian imperialism³⁰.

This group of disputed Athenian decrees exists in our dataset: their dating labels follow the conventional ‘higher’ dates (pre-446/5 bc). We excluded these texts from the dataset and trained Ithaca on all of the remaining inscriptions. Notably, Ithaca’s predictions for these held-out texts independently align with the most recent dating breakthroughs, therefore overturning the conventional historical reading based on the sigma dating criterion. More specifically, whereas the I.PHI labels are on average 27 years off the ‘lower’ dating proposed by modern re-evaluations, Ithaca’s predictions are on average only 5 years off the newly proposed ground truths.

This example eloquently illustrates how models such as Ithaca can contribute to key methodological debates on the chronological reorganization of Athenian imperialism,

one of the most important moments in Greek history. In no instance do Ithaca’s predictions for this group of inscriptions exceed 433 bc: Ithaca’s average predicted date for all of these decrees is 421 bc. Historians may now use Ithaca’s interpretability-augmenting aids (such as saliency maps) to examine these predictions further and bring more clarity to Athenian history.

Conclusions

Ithaca is to our knowledge the first epigraphic restoration and attribution model of its kind. By substantially improving the accuracy and speed of the epigrapher’s pipeline, it may assist the restoration and attribution of newly discovered or uncertain inscriptions, transforming their value as historical sources and helping historians to achieve a more holistic understanding of the distribution and nature of epigraphic habits across the ancient world. To achieve this goal, our interdisciplinary team created an open-source and publicly available interface (<https://ithaca.deeplmind.com>), enabling historians to use Ithaca for their personal research, while facilitating its development for further applications.

In fact, the methods introduced in this research apply to all disciplines dealing with ancient text (papyrology, numismatics, codicology), to any language (ancient or modern), also integrating additional metadata (inscription images, stylometrics). Furthermore, Ithaca’s quintessentially interactive nature as a cooperative research aid lends itself as an effective set-up for future machine learning research by adding humans into the training loop.

In conclusion, the transformational impact of this work lies in delivering state-of-the-art research aids that extend the scope of ancient history and the humanities.

Methods

Previous work

In recent years, several works have proposed traditional machine learning approaches to the study of ancient texts. This body of work has focused on optical character recognition and visual analysis^{31,32,33,34}, writer identification^{35,36,37} and text analysis^{38,39,40,41,42,43,44}, stylometrics⁴⁵ and document dating⁴⁶. It is only very recently that scholarship has begun to use deep learning and neural networks for optical character recognition^{47,48,49,50,51,52,53,54,55}, text analysis⁵⁶, machine translation of ancient texts^{57,58,59}, authorship attribution^{60,61} and deciphering ancient languages^{62,63}, and been applied to study the form and style of epigraphic monuments⁶⁴.

The closest work to Ithaca is our 2019 research on ancient text restoration: Pythia¹⁵. Pythia was to our knowledge the first ancient text restoration model to use deep neural networks, and was followed by blank language models¹⁸, Babylonian⁶⁵ and Korean text translation and restoration¹⁷, Latin BERT for language modelling, part-of-speech tagging, word sense disambiguation and word similarity¹⁶, and the classification of Cuneiform tablets by period⁶⁶.

Ithaca is to our knowledge the first model to tackle the three central tasks in the epigrapher’s workflow holistically. Not only does it advance the previous state-of-the-art set by Pythia, but it also uses deep learning for geographical and chronological attribution for the very first time and on an unprecedented scale. Ithaca offers interpretable outputs, showcasing the rising importance of cooperation between human experts and machine learning⁶⁷—as exemplified by our experimental evaluation.

Most importantly, this work shows how matching human experts with deep learning architectures to tackle tasks collaboratively can surpass the individual (unaided) performance of both humans and model on the same tasks. Indeed, recent medical research^{68,69} further confirms the importance of hybrid architectures in addressing real-world problems. The present work makes human expert interaction possible by visualizing the output probability distributions for all tasks using multiple charts and maps, and augmenting their interpretability by means of saliency maps. It is our hope that this work may set a new standard for the field of digital epigraphy, by using advanced deep learning architectures to support the work of ancient historians.

Generating the I.PHI corpus

When restoring damaged inscriptions, epigraphers conjecture the total number of missing characters based on grammatical and syntactical considerations, and on the reconstructed physical form of the text⁵. Conjectured missing characters that cannot be restored are conventionally marked with periods or hyphens, one hyphen equating to one missing character. Moreover, PHI presents interpretive transcriptions of the texts (including capitalization, punctuation, word division, lower-case letter conversion).

Thus, moving from the PHI dataset, we substantially expand the ruleset for filtering human annotations previously conceived for Pythia, rendering the text machine-actionable. We removed 9,441 duplicate texts and filtered out all inscriptions under 50 characters in length, whereas, in Pythia’s dataset, we had excluded all texts with fewer than 100 characters. To increase the amount of available text, we retained the supplements proposed by epigraphers (conventionally added between square brackets), and we matched the number of unrestored characters with an equal number of ‘–’ symbols, as is commonly done by epigraphers (Extended Data Fig. 1).

Each PHI inscription is assigned to a region of the ancient Mediterranean world (Extended Data Fig. 2), and includes an additional metadata string referring to the date proposed by epigraphers for the text (Extended Data Fig. 1). The chronological information is noted in a variety of formats (historical eras, precise year intervals); in several languages (including Latin); ranging before (bce) and after (ce) the Common Era; lacking in standardized notation ('early', 'first half', '1st half', 'beginning', 'beg.') and often using fuzzy wording ('late 7th/6th ac.', 'ca. 100 a.?', 'bef. 64 ad'). After crafting an extended ruleset, we succeeded in generating well-defined date intervals for 60% of all PHI inscriptions, as the chronological metadata of the remaining 40% is either missing or unprocessable. The resulting I.PHI dataset contains $1.93\times$ more inscriptions than the previous Pythia's dataset. The texts of which the numerical PHI identifier (PHI ID) ended in 3 or 4 were held out and used as test and validation sets, respectively (Extended Data Table 1).

Ithaca architecture

Inputs

For each inscription, the input of the model consists of (1) a sequence of character embeddings (real-valued vectors, each representing the character of the alphabet that occurs at the corresponding position of the inscription); (2) an equally long sequence of word embeddings (real-valued vectors, each representing the vocabulary word at the corresponding character position of the inscription; Fig. 2); and (3) positional embeddings (also real-valued vectors, each representing a position of the input sequence). The first two kinds of embeddings are randomly initialized and learned when training Ithaca (via backpropagation). The positional embeddings are also trainable and they are initialized with a separate sinusoidal function per dimension²² to maintain a symmetrical distance between neighbouring steps and smoothly decay over the maximum length of 768 characters. Our vocabulary includes every word appearing more than 10 times in I.PHI (35,884 words), while damaged or 'unknown' (under-represented) words are rendered with an '[unk]' symbol. The joint use of character and word embeddings enables the architecture of Ithaca to be both character- and context-aware^{70,71,72}. Finally, the input sequence is padded with a start-of-sentence character '<'.

Torso

The three input sequences are combined by concatenating the different embeddings per-character position and the resulting sequence is fed through the torso of the model. The architecture of Ithaca's torso consists of eight stacked transformer decoder blocks, inspired by the large-scale transformer model BigBird⁷³. Every block uses four sparse

attention heads (using global, local and random attention mechanisms), which reduce the context-length dependency from quadratic to linear, therefore enabling the model to handle lengthier sequences⁷³ compared with classical transformers. Furthermore, the attention mechanism is ‘multi-head’ (Fig. 2) in the sense that it can learn to consider different types of information extracted from the input. For example, different attention heads may be sensitive to particular character sequences, or more perceptive to certain words and phrases with distinctive morphosyntactic or semantic features. Finally, to overcome problems that hinder the stacking of such complicated blocks, each transformer block uses residual connections and layer normalization (shown as ‘add and normalize’ in Fig. 2).

Task heads

Ithaca’s torso outputs a sequence whose length is equal to the number of input characters, and each item in this sequence is a 2,048-dimensional embedding vector. Each task head consists of a two-layer feedforward network followed by a softmax function. There are three different task heads, handling region attribution, chronological attribution and restoration respectively. To predict the regions and dates, Ithaca uses the first output embedding ($t = 1$) and passes it on to the two corresponding heads. This arrangement is similar to that of DocBERT⁷⁴ and works better than other pooling methods (such as mean- and max-pooling over the output embeddings) in our experimental evaluation. Finally, for the restoration task, Ithaca uses the remaining output embeddings ($t > 1$) as there is a direct correspondence with the input text characters: for each missing character position, the corresponding output embedding of the torso is fed to the head of the restoration task, which predicts the missing character.

Data preparation and augmentation

I.PHI may be the first multitask dataset of machine-actionable epigraphical text, but its size is still several orders of magnitude smaller than modern typical language datasets. To avert the risk of overfitting, which is common in large-scale deep neural network architectures, we apply several data augmentation methods, described below, to artificially increase the size of I.PHI’s training set. Our preliminary experimental evaluation found that these methods are crucial in achieving the reported performance. These augmentation methods are applied anew whenever a training inscription is re-encountered in each training epoch.

Text clipping

For each inscription, we select an arbitrary section of its text and ignore the remaining text. We implement this by first sampling a segment length between 50 and 768 characters, and then sampling the starting index of the segment. This method helps Ithaca to generalize and improve the handling of partial inputs.

Text masking

Forcing the model to rely on contextual information often leads to improvements in prediction. To achieve this in our model, during training, we randomly hide up to half of the input text by replacing sequences of characters sampled from a geometric distribution ($P = 0.1$) with ‘–’. This span masking is intended to replicate the distribution over the length of missing characters estimated from the dataset, and uses the hidden ground-truth characters as target labels for the restoration task.

Word deletion

During training, we also delete words from each input text (without replacing them with any special characters in this case) with a 20% probability. Here, the goal is again to increase variability in the training data to improve the model’s ability to generalize over all possible ways in which inscriptions are damaged⁷⁵.

Sentence swap

By randomly swapping sentences in the input text with a 25% probability, we generate multiple input–label pairs for the auxiliary task of next-sentence prediction (NSP)⁷⁵ (see below).

Data circularity

Ithaca’s source dataset (PHI) is a synthesis of generations of scholarly research. Epigraphers typically restore texts and attribute them chronologically through a process of induction. Textual restorations are proposed on the basis of parallels, mediated by wider historical and linguistic knowledge; chronological attributions are proposed partly from archaeological and contextual information, partly from textual form and content, and partly from textual and material parallels. The texts on which Ithaca trains include previous scholarly restorations; and the dates recorded are the product of accumulated scholarly knowledge and induction from archaeological, historical and textual study. This might be thought to imply circularity, but that would be true only if Ithaca were operating in a world of objective data and aiming to offer a single objectively true solution. Rather, Ithaca is an assistive tool aiming to improve

on and facilitate a scholarly process of induction, model uncertainty and propose possible solutions for the scholar to consider.

Considering textual restoration, Ithaca avoids the risk of ‘history from square brackets’^{76,77,78} (assuming any proposed restoration to be ground truth, meaning the accepted consensus, rather than merely one of several hypotheses), because none of Ithaca’s proposed restorations are assumed to be objectively certain—instead, they are presented as plausible suggestions. Furthermore, the inclusion of existing scholarly conjectures within the training set itself does not constitute a form of ‘history from square brackets’, as such conjectures are themselves plausible restorations achieved by a process of induction and considered acceptable by one or more experts, and as such are precisely the sort of result that Ithaca itself aims to generate. The value of Ithaca is indeed its ability to learn from the largest possible dataset of attested and possible texts, making the underlying process of inductive reasoning as powerful as possible, and so generating possible restorations for scholars to evaluate.

As for chronological attribution, the dataset on which Ithaca trains is founded in the past study of multiple elements (such as archaeological provenance, material form, textual content and form). Ithaca in turn learns through close attention to the text alone. The attributions proposed by Ithaca therefore have their basis in the inductive study of a vast textual dataset and its correlation to chronological data that are more broadly derived. Ithaca is therefore able to bring some refinement to those attempts to date the texts through the application of machine learning specifically to the textual patterns in that data. Thus, Ithaca is, in this case, a part of that scholarly process, and no more or less circular in its reasoning than any other scholar.

Training on epigraphic tasks

For the task of restoration, we use the text-masking augmentation method to mask parts of the input and produce ground truths. We subsequently use a cross-entropy loss to train Ithaca to predict the missing characters. The cross-entropy loss is also used for geographical attribution, using the region metadata as target labels. We further apply label smoothing with a coefficient of 10% to avoid overfitting and to provide historians with a smoother distribution of predicted hypotheses. For the task of chronological attribution, Ithaca discretizes all dates between 800 bc and ad 800 with a bin size of 10 years. This range covers the majority of the PHI dataset entries and encompasses the conventional date range for Greek epigraphy. The processed ground-truth date intervals are discretized into bins of equal probability, forming the target probability distribution. The limitations of discretizing and amalgamating date ranges of different levels of precision based on past scholarship have been noted^{79,80}—the scale of data on which Ithaca trains, together with the increased attention to textual patterns (compared with the previous paragraph), at least partially meet that challenge.

We then use the Kullback–Leibler divergence to minimize the difference between target and predicted probability distribution (Fig. 3c).

Finally, to allow for better modelling of context, we introduce a next sentence prediction loss, an auxiliary function common to language modelling tasks⁸¹. During training, we randomly shuffle some of the sentences of the input text, and at the end of each (non-final) sentence (marked by a full stop, '.') we predict whether the next sentence is in the correct order (valid) or a product of the shuffling augmentation. By deploying the torso’s output embeddings for the full stops, we introduce an additional feedforward network that uses binary cross-entropy to predict the validity of the next sentence whenever a ‘.’ character appears.

Using this setup, Ithaca was trained for a week on 128 Tensor Processing Units (TPU) v4 pods on the Google Cloud Platform. The effective batch size was 8,192 texts and a LAMB optimizer⁸² was used to optimize Ithaca’s parameters with a learning rate of 3×10^{-4} . Using Bayesian optimization hyperparameter search, the loss functions of each task were combined using the following function:

$$\$\$L=3\times \text{Loss}_{\text{Restoration}} + 2\times \text{Loss}_{\text{Region}} + 1.25\times \text{Loss}_{\text{Date}} + 0.01\times \text{Loss}_{\text{NSP}}.\$\$$$

We do not use a separate masked (token) language modelling loss, which is commonly used when pretraining language models, as it is very similar to the restoration loss, although the latter masks characters instead of tokens.

To obtain Ithaca’s textual restoration predictions, we select a sequence of missing characters to predict and use Beam Search with a beam width of 100. Instead of using a standard sequential Beam Search, we take advantage of Ithaca’s non-autoregressive nature^{83,84,85}, and use a non-sequential one instead. Each beam starts with the prediction scoring the highest confidence⁸⁶, then proceeds iteratively to restore at each time-step the characters of which the certainty is the highest. We found that this version of Beam Search performed substantially better in our evaluation metrics. For region attribution, the outputs are presented as a plot of the top 10 predictions; for chronological attributions, we visualize the model’s predictive distribution over possible date bins. Finally, to reduce the variance of random segment selections, we repeat the process ten times and report results averaged over the iterations.

Ancient historian baseline

The evaluators for ancient text restoration were two graduate students of ancient history, with 7 years of historical and linguistic training and specializing in Greek history and epigraphic documents. Thus, they can be assumed to be more capable than

the ‘average’ ancient historian, but not yet equivalent to (the very small number) of established specialists in the field. The scholars were allowed to use the training set to search for textual ‘parallels’, and made an average of 50 restorations in 2 h.

Although Ithaca can indeed propose restoration hypotheses faster, and model its prediction uncertainty, it cannot make choices on the basis of historical and material context. Thus, the experimental setup cannot be considered to be direct comparison between human historians and machine learning, nor are the evaluators assumed to be a proxy for all historians. Instead, the experiment was intended to measure the difficulty of the task and the potential for cooperative artificial intelligence.

Onomastics baseline

Greek nomenclature is commonly used by epigraphers as one of several elements to inform their attribution predictions⁸⁷. Inspired by this method in the wider epigraphic workflow, we designed an ‘onomastic’ baseline, of which the predictions are based exclusively on the metadata associated with Greek personal names. Five annotators searched for name(s) appearing in a set of inscriptions in the Lexicon of Greek Personal Names (LGPN), a database recording the geographical and chronological distribution of ancient names²⁷, and based their attribution hypotheses on the LGPN’s distribution data. Evaluators were also provided with the inscription’s date or place of writing for the geographical or chronological attribution tasks, respectively.

Restoration metrics

To evaluate different restoration methods, for every inscription, we predict a sequence of 1–10 contiguous missing characters. These lengths account for 83% of the distribution of missing character lengths in I.PHI, and enable comparisons with both previous work and the human baselines. Note that, thanks to the text-masking augmentation adopted during training, Ithaca could potentially restore up to half of the input text.

Although the number of characters to be predicted reflects the difficulty of the task, the restored sequences in the test sets held out for human evaluation might not necessarily maintain the same distribution of lengths (as they were a subset of the test set). Thus, instead of reporting only the average scores over the entire test set (as done in previous work), we chose to account for these length discrepancies and compute the average scores for each restored sequence length. First, we computed a separate CER for all samples of each length (between 1–10 characters),

$$\text{CER} = \frac{1}{\sum_{i=1}^N \text{len}_i} \sum_{i=1}^N \text{CER}_i$$

$$\{I\}_{i=1}^N \frac{\text{EditDistance}(\text{pred}_i, \text{target}_i)}{N},$$

where I is the indicator function, len_i denotes the length of the i -th sample, N is the number of samples, pred_i is the predicted sequence of missing characters of the i -th sample and target_i the corresponding target sequence. We next calculate the average for all lengths:

$$\text{CER} = \frac{1}{L} \sum_{i=1}^L \frac{\text{EditDistance}(\text{pred}_i, \text{target}_i)}{\text{len}_i}$$

where $L = 10$ is the maximum length.

As human annotators annotated only a subset of the test set owing to time constraints, macro-averaging assigns equal importance to all sample lengths to represent the difficulty of the task independently of dataset statistics, and therefore enabling a fair comparison of the methods. Similarly, for accuracy, we first computed a separate accuracy per length, and then the average:

$$\begin{aligned} \text{accuracy} &= \frac{1}{N} \sum_{i=1}^N \frac{\text{EditDistance}(\text{pred}_i, \text{target}_i)}{\text{len}_i} \\ &= \frac{1}{N} \sum_{i=1}^N \frac{\text{EditDistance}(\text{pred}_i, \text{target}_i)}{\text{len}_i} \end{aligned}$$

Chronological attribution metric

As our model outputs a predictive distribution in the chronological attribution task, we introduce an interpretable metric to measure the distance in years between a prediction and the ground-truth interval (Fig. 3c). More specifically, we use a distance metric between the mean of the predictive distribution and the target ground-truth interval; the latter is defined by a minimum (gt_{\min}) and a maximum (gt_{\max}) date in years:

$$\begin{aligned} \text{Years} &= \begin{cases} 0, & \text{if } \text{pred} \geq \text{gt}_{\max} \\ \text{avg} - \text{gt}_{\min}, & \text{if } \text{pred} < \text{gt}_{\min} \\ \text{gt}_{\max} - \text{pred}, & \text{if } \text{pred} > \text{gt}_{\max} \\ \text{gt}_{\min} - \text{pred}, & \text{if } \text{pred} < \text{gt}_{\min} \end{cases} \end{aligned}$$

Model selection

The final model was obtained by storing the best-performing model on the validation set by using a combined metric that sums the accuracy for textual restoration and geographical attribution, and the distance in years divided by 100 for chronological attribution to make the magnitude comparable. The extensive computational resources required to train our model made the Pareto frontier computation infeasible.

Chronological attribution results

Ithaca’s predictions are 5× closer to ground truths than those recorded in the onomastics baseline (144.4 years). More specifically, Ithaca’s average date prediction is within 28.7 years of the ground-truth date interval, and the median is only 3 years. The results are shown in detail in Extended Data Fig. 3.

Restoring full texts with Ithaca

To overcome memory constraints and length limitations for long inscriptions (>768 characters), Ithaca can be applied iteratively to restore all missing text in a damaged inscription. We experimented with this option on inscription *IG II² 116*, which is missing 378 characters, and compared Ithaca’s predictions with those of our previous work Pythia on the same text, using the authoritative edition published by Rhodes and Osborne as ground truths⁸⁸. The models’ correct restorations are highlighted in green (Extended Data Fig. 4), and the erroneous ones in red. In a real-world scenario, both Ithaca and Pythia would provide a ranked set of 20 restoration hypotheses. The comparison in performance between Pythia and Ithaca is stark (74 versus 45 mistakes): moreover, in all cases in which the restoration is in red, the ground-truth sequence existed within the beam of Ithaca’s top 20 hypotheses.

Geographical attribution of Delphic inscriptions

Epigraphers determine the original location where an inscription was written by examining the personal names, local or regional dialectal varieties, and idiosyncratic lexicon or style of an inscription. Moving from this methodological premise, and to discover underlying patterns in Ithaca’s geographical predictions, we compute statistics to track the words that appear most frequently in texts whose region Ithaca predicts correctly. Thus, for each word of the test set, we compute an average accuracy and a frequency of appearance. This visualization is intended to evaluate whether the occurrence of particular words could be correlated to the model’s geographical attributions.

The most frequent words that appear in texts with high prediction accuracy clustered primarily in inscriptions from the region of Delphi, and pertained to the epigraphic genre of ‘manumission inscriptions’ (Extended Data Table 2 for an example). Ancient Greek society depended heavily on unfree labour, but slaves could be freed through a process known as ‘manumission’, which was publicly documented and certified by inscriptions^{89,90}. Over 1,000 such texts dating between around 201 bc and ad 100 have been found in Delphi^{91,92}. The words appearing in Ithaca’s accuracy statistics are identified as typical of these manumission texts, which are in turn distinctive of this region (for example, ἐπίστευσε, ἀποδμενος, καταδουλισμωι, βεβαιωτήρ, ωνάν): these words could therefore be underpinning the correct attribution predictions (a detailed example is offered in Extended Data Table 2). Further study can now be dedicated to investigating stylized manumissions as distinctive of Delphi.

To further assess the impact of Ithaca’s output visualization techniques in a real-world scenario, we also analysed the saliency maps for geographical attribution of the manumission inscriptions. Indeed, the saliency maps for the Delphic inscription *BCH* 66/67 (1942/3) 82,9, for example, highlight words typically found in manumission texts and which also appear in Ithaca’s word statistics: these words (ἐπίστευσε, ἐλευθερος, ποιέουσα, ἀποτρέχουσα) have the most important role in the geographical attribution of the inscription, while also betraying the text’s genre as a typical slave manumission inscription (Extended Data Fig. 5b).

Redating disputed Athenian decrees

In the absence of helpful internal evidence of a text’s date (for example, the mention of known historical figures⁹³), epigraphers typically derive an approximate date on the basis of a text’s content, letterforms and grammatical criteria. For example, one of the most notorious methodological debates in epigraphy concerns the ‘three-bar sigma’ dating convention, which holds that no Athenian public document containing the three-bar sigma letter (ϟ) could be dated after the year 446/5 bc, when the letter was supplanted by the four-bar sigma (Σ). On the basis of this chronological benchmark, a group of inscriptions whose interpretation is central to the political history of Classical Athens, and which feature the earlier letter ϟ, were dated to pre-446/5 bc by many authoritative corpora^{28, 94}. This set of decrees exists in the PHI dataset (Extended Data Table 3), and their dating labels follow the conventional ‘higher’ dating of the three-bar sigma criterion.

However, this orthodox dating system soon proved to be problematic: the high dates proposed for these decrees did not agree with contemporary literary accounts reporting on Athenian imperialist policies. Few historians contested the validity of the sigma criterion^{29,95}, but in 1990 photo-enhancement and laser scanning confirmed the down-dating of an inscription featuring the three-bar sigma (the Egesta decree, *IG* I³ 11)

from 458 to 418 bc⁹⁶. Over the following decade, the sigma's traditional cut-off date was revisited, and the dates of other decrees were also pushed back^{28,97}.

Ithaca's predictions for this set of disputed inscriptions independently align with the most recent dating breakthroughs (Extended Data Fig. 6). For example, the (in)famous Chalcis decree (*IG I³ 40*; Extended Data Fig. 7), which records an oath of allegiance sworn by the city of Chalcis to Athens⁹⁸ and traditionally dated to 446/5 bc²⁸, is attributed by Ithaca to 420 bc, therefore concurring with the lower dating hypothesis of 424/3 bc proposed by more recent scholarship⁹⁹. Perhaps the most compelling example of Ithaca's prediction independently aligning with a lower dating hypothesis is the decree of Kleinias (*IG I³ 34*)¹⁰⁰, regulating the collection of tribute across the Athenian empire. The sigma dating system would assign the inscription to 448/7 bc²⁸, but scholars have recently challenged this orthodoxy and proposed the earlier date of 425/4 bc¹⁰¹. Ithaca's prediction agrees precisely with the latter, dating the famous decree to 424 bc.

Ithaca has re-dated a number of these key inscriptions with striking accuracy (Extended Data Table 3). Although it may seem slight, this 40/30-year chronological reorganization has considerable implications for our grasp of Athenian imperial behaviour, leading historians to a more profound understanding of one of the most momentous periods of ancient history^{28,97}. The fact that Ithaca was trained on the largest available dataset of Greek epigraphic texts makes it possible to challenge or overcome individual biases or, indeed, errors in the existing academic tradition, notwithstanding the fact that the dataset in question is originally based on the accumulated academic tradition.

Reporting summary

Further information on research design is available in the [Nature Research Reporting Summary](#) linked to this paper.

Data availability

Ithaca was trained on The Packard Humanities Institute's Searchable Greek Inscriptions public dataset, PHI, which is available online (<https://inscriptions.packhum.org/>). The complete processing workflow for transforming the dataset to a machine-actionable format suitable for training Ithaca (I.PHI) is available at GitHub (<https://github.com/sommerschield/iphil>) under Apache License 2.0. The LGPN (<https://www.lgpn.ox.ac.uk/>) was used by annotators for the onomastics baseline to track the geographical and chronological distribution of ancient names. The PeriodO gazetteer (<https://client.perio.do/>) was used as a reference for

mapping the PHI historical time periods to the chronological range metadata of I.PHI. The Pleiades gazetteer (<https://pleiades.stoa.org/>) was used as a reference for mapping the PHI region names to the geographical coordinates used in the geographical attribution map visualizations.

Code availability

Ithaca's training and inference source code is available at GitHub (<https://github.com/deepmind/ithaca>) under Apache License 2.0, along with the trained weights, licensed under Creative Commons Attribution-ShareAlike 4.0 International. A public interface for historians using Ithaca for their research (that is, restoration and attribution of Greek inscriptions, use of all visualization tools discussed in the present paper) is available online (<https://ithaca.deepmind.com>). Neural networks were developed with JAX v.0.2.9 (<https://github.com/google/jax>), Flax v.0.3.0 (<https://github.com/google/flax>), and Haiku v.0.0.4 (<https://github.com/deepmind/dm-haiku>). The XLA compiler is bundled with JAX and does not have a separate version number. Dataset processing and analysis used Python v.3.7 (<https://www.python.org>), NumPy v.1.19.2 (<https://github.com/numpy/numpy>), SciPy v.1.5.2 (<https://www.scipy.org>), pandas v.1.1.3 (<https://github.com/pandas-dev/pandas>), BeautifulSoup4 v.4.9.0 (<https://www.crummy.com/software/BeautifulSoup>) and Google Colab (<https://research.google.com/colaboratory>), which is an online service and does not have a version number. Visualizations were generated using matplotlib v.3.4.2 (<https://matplotlib.org>), seaborn v.0.11.1 (<https://seaborn.pydata.org>) and GeoPandas v.0.9.0 (<https://geopandas.org>).

References

1. Davies, J. & Wilkes, J. Epigraphy and the Historical Sciences (British Academy, 2012).
2. Osborne, R. In *The Oxford History of Historical Writing: Volume 1: Beginnings to AD 600* (eds Feldherr, A. & Hardy, G.) 97–121 (Oxford Univ. Press, 2011).
3. Bodel, J. P. Epigraphic Evidence: Ancient History from Inscriptions (Routledge, 2001).
4. Tsirogiannis, C. The itinerary of a stolen stele. *UNESCO Cour.* **4**, 18–20 (2020).
5. Bruun, C. & Edmondson, J. C. in *The Oxford Handbook of Roman Epigraphy* (eds Bruun, C. & Edmondson, J. C.) 13–20 (Oxford University Press, 2015).

6. Macmullen, R. The epigraphic habit in the Roman empire. *Am. J. Philol.* **103**, 233–246 (1982).
7. Nawotka, K. Epigraphic Culture in the Eastern Mediterranean in Antiquity (Routledge, 2021).
8. Osborne, R. & Rhodes, P. J. Greek Historical Inscriptions 478–404 BC xvii–xviii (Oxford Univ. Press, 2017).
9. Cooley, A. The Cambridge Handbook to Latin Epigraphy 398–434 (Cambridge Univ. Press, 2012).
10. Goodfellow, I., Bengio, Y. & Courville, A. Deep Learning (MIT Press, 2016).
11. Brown, T. B. et al. Language models are few-shot learners. In *Proc. Advances in Neural Information Processes (NeurIPS)* Vol. 33 (eds Larochelle, H., Ranzato, M., Hadsell, R., Balcan, M. F. & Lin, H.) 1877–1901 (Curran Associates, 2020).
12. LeCun, Y., Bengio, Y. & Hinton, G. Deep learning. *Nature* **521**, 436–444 (2015).
13. Senior, A. W. et al. Improved protein structure prediction using potentials from deep learning. *Nature* **577**, 706–710 (2020).
14. Silver, D. et al. Mastering the game of go without human knowledge. *Nature* **550**, 354–359 (2017).
15. Assael, Y., Sommerschield, T. & Prag, J. Restoring ancient text using deep learning: a case study on Greek epigraphy. In *Proc. 2019 Conference on Empirical Methods in Natural Language Processing and the 9th International Joint Conference on Natural Language Processing (EMNLP-IJCNLP)* 6368–6375 (Association for Computational Linguistics, 2019).
16. Bamman, D. & Burns, P. J. Latin BERT: a contextual language model for classical philology. Preprint at <https://arXiv.org/abs/2009.10053> (2020).
17. Kang, K. et al. Restoring and mining the records of the Joseon dynasty via neural language modeling and machine translation. In *Proc. 2021 Conference of the North American Chapter of the Association for Computational Linguistics: Human Language Technologies (NAACL)* 4031–4042 (Association for Computational Linguistics, 2021).
18. Shen, T., Quach, V., Barzilay, R. & Jaakkola, T. Blank language models. In *Proc. 2020 Conference on Empirical Methods in Natural Language Processing*

(EMNLP) (eds Webber, B., Cohn, T., He, Y. & Liu, Y.) 5186–5198 (Association for Computational Linguistics, 2020).

19. Packard Humanities Institute. The Packard Humanities Institute's Searchable Greek Inscriptions (2005); <https://inscriptions.packhum.org/>
20. Gawlinski, L. Review: Packard Humanities Institute's Searchable Greek Inscriptions (2017); <https://classicalstudies.org/scs-blog/laura-gawlinski/review-packard-humanities-institutes-searchable-greek-inscriptions>
21. Iversen, P. A. The Packard Humanities Institute (PHI) Greek epigraphy project and the revolution in Greek epigraphy. *Abgadiyat* 2, 51–55 (2007).
22. Vaswani, A. et al. Attention is all you need. In *Proc. Advances in Neural Information Processing Systems (NeurIPS)* Vol. 30 (eds Guyon, E. et al.) 5998–6008 (Curran Associates, 2017).
23. Hedrick, C. W. Jr Democracy and the Athenian epigraphical habit. *Hesperia* 68, 387–438 (1999).
24. Wesley, E. T. A new restoration of *I.G. I² 297*. *Class. Q.* 14, 230–231 (1964).
25. Thucydides. 6.31.
26. Kagan, D. The Peace of Nicias and the Sicilian Expedition (Cornell University Press, 1991).
27. Parker, R. Data in Online Database “Lexicon of Greek Personal Names (LGPN)” (Univ. Oxford, 2019).
28. Rhodes, P. After the three-bar sigma controversy: the history of Athenian imperialism reassessed. *Class. Q.* 58, 500–506 (2008).
29. Mattingly, H. B. The Athenian Empire Restored: Epigraphic and Historical Studies 1–4 (Univ. Michigan Press, 1996).
30. Ma, J., Papazarkadas, N. & Parker, R. Interpreting the Athenian Empire (Duckworth, 2009).
31. Garz, A., Eichenberger, N., Liwicki, M. & Ingold, R. HisDoc 2.0: toward computer-assisted paleography. *Manuscr. Cult.* 7, 19–28 (2015).
32. Shaus, A. Computer Vision and Machine Learning Methods for Analyzing First Temple Period Inscriptions. PhD thesis, Tel Aviv Univ. (2017).

33. Soumya, A. & Kumar, G. H. Classification of ancient epigraphs into different periods using random forests. In *Proc. 2014 Fifth International Conference on Signal and Image Processing* 171–178 (IEEE Computer Society, 2014).
34. Terras, M. & Robertson, P. Image to Interpretation: An Intelligent System to Aid Historians in Reading the Vindolanda Texts (Oxford Univ. Press, 2006).
35. Faigenbaum-Golovin, S. et al. Algorithmic handwriting analysis of Judah's military correspondence sheds light on composition of biblical texts. *Proc Natl Acad. Sci. USA* **113**, 4664–4669 (2016).
36. Panagopoulos, M., Papaodysseus, C., Rousopoulos, P., Dafi, D. & Tracy, S. Automatic writer identification of ancient Greek inscriptions. *Trans. Pattern Anal. Mach. Intel.* **31**, 1404–1414 (2009).
37. Tracy, S. V. & Papaodysseus, C. The study of hands on Greek inscriptions: the need for a digital approach. *A. J. Archaeol.* **113**, 99–102 (2009).
38. Koppel, M., Michaely, M. & Tal, A. Reconstructing ancient literary texts from noisy manuscripts. In *Proc. Fifth Workshop on Computational Linguistics for Literature (NAACL-HLT)* (eds Feldman, A., Kazantseva, A. & Szpakowicz, S.) 40–46 (Association for Computational Linguistics, 2016).
39. Lee, J. & Haug, D. Porting an ancient Greek and Latin treebank. In *Proc. Seventh International Conference on Language Resources and Evaluation (LREC)* (eds Calzolari, N. et al.) (European Language Resources Association, 2010).
40. Rao, R. P. et al. A Markov model of the Indus script. *Proc. Natl Acad. Sci. USA* **106**, 13685–13690 (2009).
41. Rao, R. P. et al. Entropic evidence for linguistic structure in the Indus script. *Science* **324**, 1165–1165 (2009).
42. Rao, R. P. et al. Entropy, the Indus script, and language: a reply to R. Sproat. *Comput. Linguist.* **36**, 795–805 (2010).
43. Vatri, A. & McGillivray, B. The Diorisis ancient Greek corpus: linguistics and literature. *Res. Data J. Hum. Soc. Sci.* **3**, 55–65 (2018).
44. Yadav, N. et al. Statistical analysis of the Indus script using n -grams. *PLoS ONE* **5**, e9506 (2010).
45. Gianitsos, E., Bolt, T., Chaudhuri, P. & Dexter, J. Stylometric classification of ancient Greek literary texts by genre. In *Proc. 3rd Joint SIGHUM Workshop on*

Computational Linguistics for Cultural Heritage, Social Sciences, Humanities and Literature 52–60 (Association for Computational Linguistics, 2019).

46. Baledent, A., Hiebel, N. & Lejeune, G. Dating ancient texts: an approach for noisy French documents. In *Proc. LT4HALA 2020 1st Workshop on Language Technologies for Historical and Ancient Languages* 17–21 (European Language Resources Association, 2020).
47. Amato, G., Falchi, F. & Vadicamo, L. Visual recognition of ancient inscriptions using convolutional neural network and Fisher vector. *J. Comput. Cult. Herit.* **9**, 1–24 (2016).
48. Avadesh, M. & Goyal, N. Optical character recognition for Sanskrit using convolution neural networks. In *2018 13th IAPR International Workshop on Document Analysis Systems (DAS)* 447–452 (IEEE Computer Society, 2018).
49. Can, G., Odobezi, J. M. & Gatica-Perez, D. Evaluating shape representations for Maya glyph classification. *J. Comput. Cult. Herit.* **9**, 1–26 (2016).
50. Chen, L., Lyu, B., Tomiyama, H. & Meng, L. A method of Japanese ancient text recognition by deep learning. *Proced. Comp. Sci.* **174**, 276–279 (2020).
51. Dencker, T., Klinkisch, P., Maul, S. M. & Ommer, B. Deep learning of cuneiform sign detection with weak supervision using transliteration alignment. *PLoS ONE* **15**, e0243039 (2020).
52. Hussien, R. S., Elkhidir, A. A. & Elnourani, M. G. Optical character recognition of Arabic handwritten characters using neural network. In *Proc. International Conference on Computing, Control, Networking, Electronics and Embedded Systems Engineering (ICCNEEE)* 456–461 (IEEE, 2015).
53. Narang, S. R., Kumar, M. & Jindal, M. K. DeepNetDevanagari: a deep learning model for Devanagari ancient character recognition. *Multimed. Tools Appl.* **80**, 20671–20686 (2021).
54. Palaniappan, S. & Adhikari, R. Deep learning the indus script. Preprint at <https://arxiv.org/abs/1702.00523> (2017).
55. Suganya, T. S. & Murugavalli, S. Feature selection for an automated ancient Tamil script classification system using machine learning techniques. In *Proc. International Conference on Algorithms, Methodology, Models and Applications in Emerging Technologies (ICAMMAET)* 1–6 (IEEE, 2017).

56. Burns, P. J., Brofos, J., Li, K., Chaudhuri, P. & Dexter, J. P. Profiling of intertextuality in Latin literature using word embeddings. In *Proc. 2021 Conference of the North American Chapter of the Association for Computational Linguistics (NAACL): Human Language Technologies* 4900–4907 (Association for Computational Linguistics, 2021).
57. Pagé-Perron, E., Sukhareva, M., Khait, I. & Chiarcos, C. Machine translation and automated analysis of the Sumerian language. In *Proc. Joint SIGHUM Workshop on Computational Linguistics for Cultural Heritage, Social Sciences, Humanities and Literature* 10–16 (Association for Computational Linguistics, 2017).
58. Park, C., Lee, C., Yang, Y. & Lim, H. Ancient Korean neural machine translation. *IEEE Access* **8**, 116617–116625 (2020).
59. Punia, R. N., Schenk, N., Chiarcos, C. & Pagé-Perron, É. Towards the first machine translation system for Sumerian transliterations. In *Proc. 28th International Conference on Computational Linguistics (COLING)* 3454–3460 (International Committee on Computational Linguistics, 2020).
60. Cilia, N. D. et al. An experimental comparison between deep learning and classical machine learning approaches for writer identification in Medieval documents. *J. Imaging* **6**, 89–104 (2020).
61. Reisi, E. & Mahboob Farimani, H. Authorship attribution in historical and literary texts by a deep learning classifier. *J. Appl. Intel. Syst. Inform. Sci.* **1**, 118–127 (2020).
62. Luo, J., Cao, Y. & Barzilay, R. Neural decipherment via minimum-cost flow: from Ugaritic to Linear B. In *Proc. 57th Annual Meeting of the Association for Computational Linguistics* 3146–3155 (Association for Computational Linguistics, 2019).
63. Luo, J., Hartmann, F., Santus, E., Barzilay, R. & Cao, Y. Deciphering undersegmented ancient scripts using phonetic prior. *Trans. Assoc. Comput. Linguis.* **9**, 69–81 (2021).
64. Tupman, C., Kangin, D. & Christmas, J. Reconsidering the Roman workshop: using computer vision to analyse the making of ancient inscriptions. *Umanist. Digit.* **10**, 461–473 (2021).
65. Fetaya, E., Lifshitz, Y., Aaron, E. & Gordin, S. Restoration of fragmentary Babylonian texts using recurrent neural networks. *Proc. Natl Acad. Sci. USA* **117**, 22743–22751 (2020).

66. Bogacz, B. & Mara, H. Period classification of 3D cuneiform tablets with geometric neural networks. In *Proc. 2020 17th International Conference on Frontiers in Handwriting Recognition (ICFHR)* 246–251 (IEEE, 2020).
67. Dafoe, A. et al. Cooperative AI: machines must learn to find common ground. *Nature* **593**, 33–36 (2021).
68. Farzaneh, N., Williamson, C. A., Gryak, J. & Najarian, K. A hierarchical expert-guided machine learning framework for clinical decision support systems: an application to traumatic brain injury prognostication. *NPJ Digit. Med.* **4**, 78 (2021).
69. Wu, N. et al. Deep neural networks improve radiologists' performance in breast cancer screening. *IEEE Trans. Med. Imaging* **39**, 1184–1194 (2019).
70. Kim, Y., Jernite, Y., Sontag, D. & Rush, A. M. Character-aware neural language models. In *Proc. Thirtieth AAAI Conference on Artificial Intelligence* 2741–2749 (AAAI Press, 2016).
71. Ling, W., Trancoso, I., Dyer, C. & Black, A. W. Character-based neural machine translation. Preprint at <https://arxiv.org/abs/1511.04586> (2015).
72. Miyamoto, Y. & Cho, K. J. Gated word-character recurrent language model. In *Proc. 2016 Conference on Empirical Methods in Natural Language Processing (EMNLP)* 1992–1997 (Association for Computational Linguistics, 2016).
73. Zaheer, M. et al. Advances in neural information processing systems. In *Proc. Advances in Neural Information Processes (NeurIPS)* Vol. 33 17283–17297 (Curran Associates, 2020).
74. Adhikari, A., Ram, A., Tang, R. & Lin, J. DocBERT: BERT for document classification. Preprint at <https://arxiv.org/abs/1904.08398> (2019).
75. Wei, J. & Eda, K. Z. EDA: easy data augmentation techniques for boosting performance on text classification tasks. In *Proc. 2019 Conference on Empirical Methods in Natural Language Processing and the 9th International Joint Conference on Natural Language Processing (EMNLP-IJCNLP)* 6382–6388 (Association for Computational Linguistics, 2019).
76. Badian, E. History from “square brackets”. *Z. Papyrologie Epigraphik* **79**, 59–70 (1989).
77. Bodel, J. P. Epigraphic Evidence: Ancient History from Inscriptions 52–55 (Routledge, 2001).

78. Cooley, A. *The Cambridge Handbook to Latin Epigraphy* 355–357 (Cambridge Univ. Press, 2012).
79. Beltrán Lloris, F. in *The Oxford Handbook of Roman Epigraphy* (eds Bruun, C. & Edmondson, J. C.) 141–143 (Oxford Univ. Press, 2015).
80. Cherry, D. Re-figuring the Roman epigraphic habit. *Anc. Hist. Bull.* **9**, 143–156 (1995).
81. Devlin, J., Chang, M. W., Lee, K. & Toutanova, K. BERT: pre-training of deep bidirectional transformers for language understanding. In *Proc. 2019 Conference of the North American Chapter of the Association for Computational Linguistics: Human Language Technologies (NAACL-HLT)* Vol. 1 4171–4186 (Association for Computational Linguistics, 2019).
82. You, Y. et al. Large batch optimization for deep Learning: training BERT in 76 minutes. In *Proc. International Conference on Learning Representations (ICLR)* (ICLR, 2020).
83. Ghazvininejad, M., Levy, O., Liu, Y. & Zettlemoyer, L. N. Mask-predict: parallel decoding of conditional masked language models. In *Proc. 2019 Conference on Empirical Methods in Natural Language Processing and the 9th International Joint Conference on Natural Language Processing (EMNLP-IJCNLP)* 6112–6121 (Association for Computational Linguistics, 2019).
84. Mansimov, E., Wang, A., Welleck, S. & Cho, K. A generalized framework of sequence generation with application to undirected sequence models. Preprint at <https://arxiv.org/abs/1905.12790> (2019).
85. Wang, A. & Cho, K. BERT has a mouth, and it must speak: BERT as a Markov random field language model. In *Proc. Workshop on Methods for Optimizing and Evaluating Neural Language Generation* 30–36 (Association for Computational Linguistics, 2019).
86. Schick, T. & Schütze, H. It's not just size that matters: small language models are also few-shot learners. In *Proc. 2021 Conference of the North American Chapter of the Association for Computational Linguistics: Human Language Technologies (NAACL-HLT)* 2339–2352 (Association for Computational Linguistics, 2021).
87. Hornblower, S. & Matthews, E. *Greek Personal Names: Their Value as Evidence* (British Academy, 2000).
88. Rhodes, P. J. & Osborne, R. *Greek Historical Inscriptions 404-323 BC* (Oxford University Press, 2003).

89. Lewis, D. M. In *The Oxford Handbook of Ancient Greek Law* (eds Harris, E. M. & Canevaro, M.) 1–32 (Oxford Univ. Press, 2015).
90. Zelnick-Abramovitz, R. *The Concept of Manumission and the Status of Manumitted Slaves in the Ancient Greek World* (Brill, 2005).
91. Kamen, D. Sale for the purpose of freedom: slave manumission in ancient Greece. *Class. J.* **109**, 281–307 (2014).
92. Mulliez, D. Les actes d'affranchissement delphiques. *Cah. Cent. Gustave Glotz* **3**, 31–44 (1992).
93. Develin, R. Athenian Officials 684–321 BC (Cambridge Univ. Press, 1989).
94. Meiggs, R. & Lewis, D. M. A Selection of Greek Historical Inscriptions to the End of the Fifth Century B.C (Oxford Univ. Press, 1969).
95. Mattingly, H. B. The growth of Athenian imperialism. *Historia* **12**, 257–273 (1963).
96. Chambers, M. H., Galluci, R. & Spanos, P. Athens' alliance with Egesta in the year of Antiphon. *Z. PapYROLOGIE Epigraphik* **83**, 38–57 (1990).
97. Papazarkadas, N. in *Interpreting the Athenian Empire* (eds Ma, J., Papazarkadas, N. & Parker, R.) 67–88 (Duckworth, 2009).
98. Lambert, S. D. Two inscribed documents of the Athenian empire: the Chalkis decree and the Tribute Reassessment decree. *Attic Inscr. Online Papers* **8**, 11–31 (2017).
99. Mattingly, H. B. The Athenian decree for Chalcis (IG 13.40). *Class. Q.* **52**, 377–379 (2002).
100. Lambert, S. Decrees of the council and assembly. *Attic Inscr. UK Collect.* **4**, 56–60 (2020).
101. Matthaiou, A. P. The Athenian Empire on Stone Revisited: David Lewis Lecture in Ancient History (Ellenike Epigrafike Etaireia, 2009).

Acknowledgements

We acknowledge Ç. Gulçehre, P. Kohli, M. Zaheer and J. Ainslie for their scientific insights; K. Kavukcuoglu and D. Hassabis for reviewing the manuscript; J. Grayston,

B. Maynard, R. Cardenas and the staff at Psyche Interactive for developing the backend of the public interface; E. Karakozoglou, A. Berger, A. Vora and D. Chou for their strategic counselling; V. Margaritis and K.-I. Naltsa for their artistic advice; and M. Tsitonas for his legal counsel. We thank R. Bagnall, L. Calvelli, A. Cooley, R. Parker and C. Roueché for their comments and insights; the contributors of PHI, LGPN, PeriodO and Pleiades for the online resources; the staff at the Acropolis museum for the permission to use the photographic reproduction of the Chalcis decree (*IG I³ 40*); and the student annotators and baseline evaluators of the Athens University of Economics and Business (MSc in Digital Methods for the Humanities) and the University of Oxford (Faculty of Classics). T.S. acknowledges that this project has received funding from the European Union's Horizon 2020 research and innovation programme under the Marie Skłodowska-Curie grant agreement no. 101026185. T.S. also thanks Harvard University's Center for Hellenic Studies for its support.

Author information

Author notes

1. These authors contributed equally: Yannis Assael, Thea Sommerschield

Affiliations

1. DeepMind, London, UK

Yannis Assael, Brendan Shillingford, Mahyar Bordbar & Nando de Freitas

2. Department of Humanities, Ca' Foscari University of Venice, Venice, Italy

Thea Sommerschield

3. Center for Hellenic Studies, Harvard University, Washington, DC, USA

Thea Sommerschield

4. Department of Informatics, Athens University of Economics and Business, Athens, Greece

John Pavlopoulos, Marita Chatzipanagiotou & Ion Androutsopoulos

5. Faculty of Classics, University of Oxford, Oxford, UK

Jonathan Prag

Contributions

Y.A. and T.S. are co-first authors and the order of the names is alphabetical. B.S was a major contributor to the project. M.B. contributed to the execution. J. Pavlopoulos, M.C. and I.A. contributed to the dataset analysis, the evaluations and advised the project. J. Prag and N.d.F. supervised the project.

Corresponding authors

Correspondence to [Yannis Assael](#) or [Thea Sommerschield](#).

Ethics declarations

Competing interests

The authors declare no competing interests.

Peer review

Peer review information

Nature thanks John Bodel, Kyunghyun Cho and the other, anonymous, reviewer(s) for their contribution to the peer review of this work.

Additional information

Publisher's note Springer Nature remains neutral with regard to jurisdictional claims in published maps and institutional affiliations.

Extended data figures and tables

[Extended Data Fig. 1 Raw and processed PHI inscription, text and metadata.](#)

A fragmentary early-fifth century sacrificial calendar from the Acropolis of Athens (*IG I³ 234*), face A, lines 10-23. In (a) transcription of the inscription text as it currently appears in PHI; (b) the same text's processed rendition in I.PHI; (c) the unprocessed metadata of this inscription as it currently appears in the PHI dataset; (d) the processed metadata rendition in I.PHI.

Extended Data Fig. 2 Geographical distribution of Greek inscriptions in I.PHI.

Each red circle represents a region across the ancient Mediterranean world (84 in total), the circle size is directly proportional to the number of inscriptions found in that region (total inscriptions in I.PHI n = 78,608).

Extended Data Fig. 3 Comparison between Ithaca and the onomastics baseline's chronological predictions.

The box plot shows the median and the mean distance between the predicted date and the ground-truth time interval, measured in years using the chronological distance metric (see Methods). In this plot, the bounds of the boxes are defined by the first and the third quartiles, and the whiskers by the minimum and maximum values. Ithaca's mean distance is 2.2x lower than that of the onomastics baseline. Ithaca's average prediction loss was 29.3 years from the ground-truth interval, while the median prediction loss was only 3 years. The onomastics baseline consists of n = 142 attributions provided by the human annotators.

Extended Data Fig. 4 Restoration performance comparison.

(a) The original inscription (*IG II² 116*) has 378 missing characters. (b) The restorations of the missing characters proposed in the authoritative edition by Rhodes - Osborne 2003 for this text⁸⁸, and which we use as ground truths in our evaluation. (c) Pythia's restoration shows 74 mismatches with the Rhodes-Osborne edition, while (d) Ithaca's shows only 45. Correct restorations are highlighted in green, incorrect ones in red.

Extended Data Fig. 5 Restoration and geographical attribution saliency maps.

(a) The decree (*IG II² 116*) from the Acropolis of Athens recording an alliance between the Athenians and the Thessalian federation (360/1 bc). At each step of the restoration of the missing word “alliance” (συμμοχία), Ithaca is clearly attending to the contextually important words “Athenians” (‘Αθηναίων) and “Thessalians” (Θετταλῶν). (b) The manumission inscription (*BCH* 66/67 (1942/3) 82,9) is correctly attributed to the Delphi region (left), and the generated saliency map (right) highlights words correlated to high accuracy predictions from the word statistics table.

Extended Data Fig. 6 PHI vs. Ithaca's dating distance in years for disputed Athenian decrees.

The box plot shows the median and the mean of the distribution, the bounds of the boxes are defined by the first and the third quartiles and the whiskers by the minimum and maximum values of $n = 21$ inscriptions. Ithaca's chronological predictions (average distance of 5 years from the modern "lower" ground truth) compared to PHI meta-data for time intervals (older estimates, average distance of 27 years from the modern ground truth). Lower distance in years is better. Exploiting the features of our full dataset, Ithaca's predictions are better and closer to modern re-evaluations compared to the original PHI ground-truth dates. The latter reflect the dates assigned by the published editions which PHI is reporting, and which almost all reflect the old three-bar sigma dating. We refer the reader to Extended Data Table 3 for detailed results.

Extended Data Fig. 7 Chalcis decree (*IG I³ 40*).

The inscription records an oath of allegiance sworn by the city of Chalcis to Athens. It has been traditionally dated to 446/5 bc based on the 3-bar sigma criterion²⁸, but was more recently redated to 424/3 bc⁹⁹. Photograph by kind concession of the Acropolis Museum. Acrop. 6509 © Acropolis Museum (photo: Socratis Mavrommatis).

Extended Data Table 1 Dataset statistics for the size of the I.PHI corpus

Extended Data Table 2 Word statistics for geographical attribution

Extended Data Table 3 Downdating Athenian decrees with Ithaca

Supplementary information

Reporting Summary

Rights and permissions

Open Access This article is licensed under a Creative Commons Attribution 4.0 International License, which permits use, sharing, adaptation, distribution and reproduction in any medium or format, as long as you give appropriate credit to the original author(s) and the source, provide a link to the Creative Commons license, and indicate if changes were made. The images or other third party material in this article are included in the article's Creative Commons license, unless indicated otherwise in a credit line to the material. If material is not included in the article's Creative Commons license and your intended use is not permitted by statutory regulation or exceeds the permitted use, you will need to obtain permission directly from the copyright holder. To view a copy of this license, visit <http://creativecommons.org/licenses/by/4.0/>.

Reprints and Permissions

About this article

Cite this article

Assael, Y., Sommerschield, T., Shillingford, B. *et al.* Restoring and attributing ancient texts using deep neural networks. *Nature* **603**, 280–283 (2022).
<https://doi.org/10.1038/s41586-022-04448-z>

- Received: 16 August 2021
- Accepted: 19 January 2022
- Published: 09 March 2022
- Issue Date: 10 March 2022
- DOI: <https://doi.org/10.1038/s41586-022-04448-z>

Share this article

Anyone you share the following link with will be able to read this content:

[Get shareable link](#)

Sorry, a shareable link is not currently available for this article.

[Copy to clipboard](#)

Provided by the Springer Nature SharedIt content-sharing initiative

Further reading

- [**AI minds the gap and fills in missing Greek inscriptions**](#)
 - Charlotte Roueché

Nature (2022)

[**The AI historian: A new tool to decipher ancient texts**](#)

- Shamina Bundell

Nature Video 09 Mar 2022

The AI that deciphers ancient Greek graffiti

- Nick Petrić Howe
- Benjamin Thompson

Nature Podcast 09 Mar 2022

AI minds the gap and fills in missing Greek inscriptions

- Charlotte Roueché

News & Views 09 Mar 2022

This article was downloaded by **calibre** from <https://www.nature.com/articles/s41586-022-04448-z>

| [Section menu](#) | [Main menu](#) |

- Article
- [Published: 02 March 2022](#)

Innovative ochre processing and tool use in China 40,000 years ago

- [Fa-Gang Wang^{1 na1}](#),
- [Shi-Xia Yang](#) [ORCID: orcid.org/0000-0002-7039-8128^{2,3,4,5 na1}](#),
- [Jun-Yi Ge](#) [ORCID: orcid.org/0000-0002-4569-2915^{2,3}](#),
- [Andreu Ollé](#) [ORCID: orcid.org/0000-0002-8643-5536^{6,7}](#),
- [Ke-Liang Zhao](#) [ORCID: orcid.org/0000-0002-5802-9098^{2,3}](#),
- [Jian-Ping Yue](#) [ORCID: orcid.org/0000-0002-8544-9522⁸](#),
- [Daniela Eugenia Rosso](#) [ORCID: orcid.org/0000-0003-0499-0497^{9,10}](#),
- [Katerina Douka](#) [ORCID: orcid.org/0000-0002-0558-0011^{4,11}](#),
- [Ying Guan](#) [ORCID: orcid.org/0000-0002-1021-9917^{2,3}](#),
- [Wen-Yan Li¹](#),
- [Hai-Yong Yang¹²](#),
- [Lian-Qiang Liu¹](#),
- [Fei Xie¹](#),
- [Zheng-Tang Guo¹³](#),
- [Ri-Xiang Zhu](#) [ORCID: orcid.org/0000-0002-4985-925X¹⁴](#),
- [Cheng-Long Deng](#) [ORCID: orcid.org/0000-0003-1848-3170^{14,15}](#),
- [Francesco d'Errico](#) [^{16,17}](#) &
- [Michael Petraglia](#) [ORCID: orcid.org/0000-0003-2522-5727^{4,18,19,20}](#)

[Nature](#) volume 603, pages 284–289 (2022)

- 3564 Accesses
- 518 Altmetric
- [Metrics details](#)

Subjects

- [Archaeology](#)

Abstract

Homo sapiens was present in northern Asia by around 40,000 years ago, having replaced archaic populations across Eurasia after episodes of earlier population expansions and interbreeding^{1,2,3,4}. Cultural adaptations of the last Neanderthals, the Denisovans and the incoming populations of *H. sapiens* into Asia remain unknown^{1,5,6,7}. Here we describe Xiamabei, a well-preserved, approximately 40,000-year-old archaeological site in northern China, which includes the earliest known ochre-processing feature in east Asia, a distinctive miniaturized lithic assemblage with bladelet-like tools bearing traces of hafting, and a bone tool. The cultural assembly of traits at Xiamabei is unique for Eastern Asia and does not correspond with those found at other archaeological site assemblages inhabited by archaic populations or those generally associated with the expansion of *H. sapiens*, such as the Initial Upper Palaeolithic^{8,9,10}. The record of northern Asia supports a process of technological innovations and cultural diversification emerging in a period of hominin hybridization and admixture^{2,3,6,11}.

This is a preview of subscription content

Access options

Subscribe to Nature+

Get immediate online access to the entire Nature family of 50+ journals

\$29.99

monthly

[Subscribe](#)

[Subscribe to Journal](#)

Get full journal access for 1 year

\$199.00

only \$3.90 per issue

[Subscribe](#)

All prices are NET prices.

VAT will be added later in the checkout.

Tax calculation will be finalised during checkout.

[Buy article](#)

Get time limited or full article access on ReadCube.

\$32.00

[Buy](#)

All prices are NET prices.

Additional access options:

- [Log in](#)
- [Learn about institutional subscriptions](#)

Fig. 1: Location of Xiamabei in the Nihewan Basin, China, and archaeological site excavations.

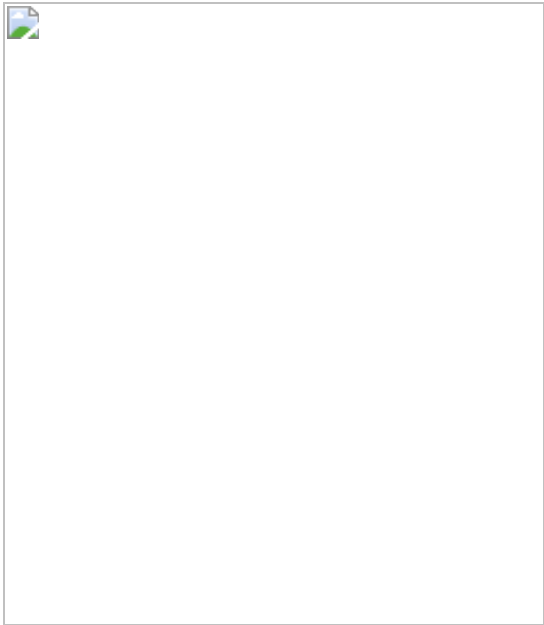


Fig. 2: Stratigraphy, sedimentary sequence and the position of luminescence and radiocarbon samples at Xiamabei.

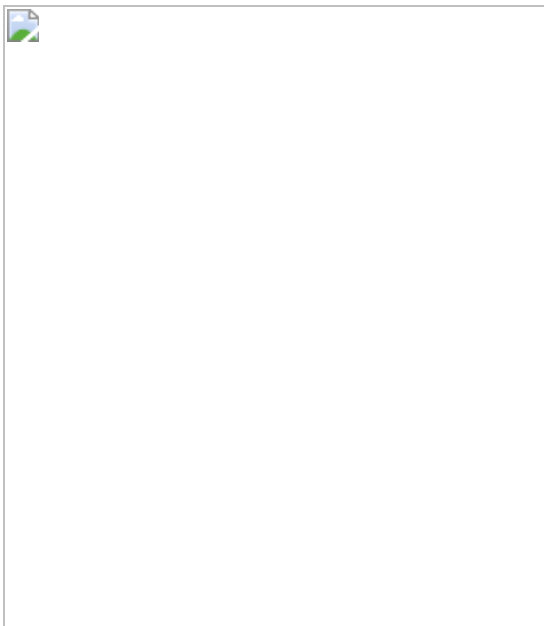


Fig. 3: Artefacts laying on the red-stained sediment patch.

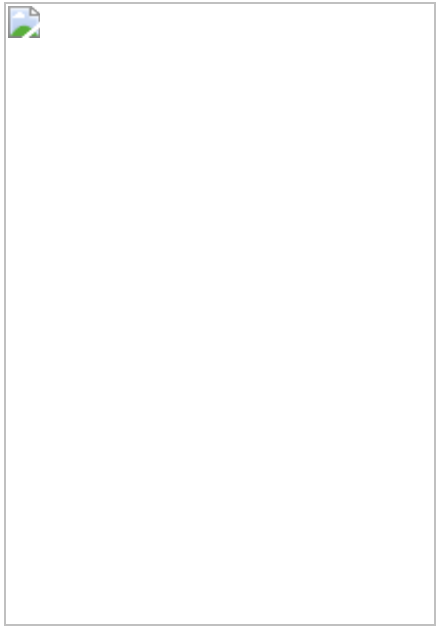
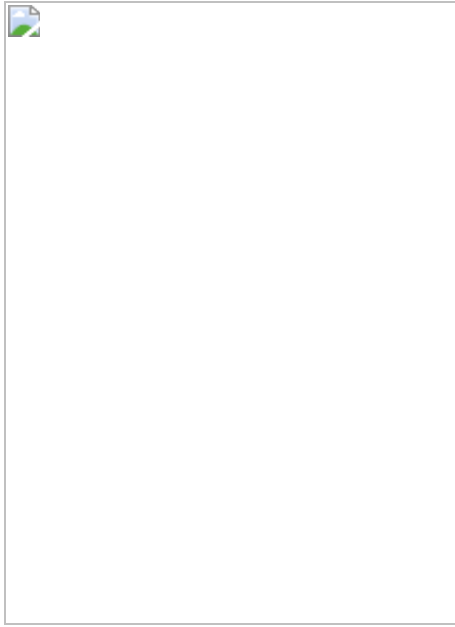


Fig. 4: Examples of use wear on lithics and residues on hafted pieces.



Data availability

AMS ^{14}C and OSL age data used in Fig. 2 are presented in Supplementary Tables C1, C3, respectively. The data from X-ray diffraction spectra, Raman spectra, high-temperature magnetic susceptibility measurements, and magnetic component analysis of coercivity distributions used in Extended Data Fig. 6 can be downloaded at

<https://doi.org/10.5061/dryad.9s4mw6mj0>. Other data generated during this study are included in the Article, Extended Data and Supplementary Information, and/or are available from the corresponding author/s on reasonable request.

Code availability

CQL code for the Bayesian age model is provided in Supplementary Table C4

References

1. Bae, C. J., Douka, K. & Petraglia, M. On the origin of modern humans: Asian perspectives. *Science* **358**, 1269–1269 (2017).
2. Fu, Q. et al. DNA analysis of an early modern human from Tianyuan Cave, China. *Proc. Natl Acad. Sci. USA* **110**, 2223–2227 (2013).
3. Massilani, D. et al. Denisovan ancestry and population history of early East Asians. *Science* **370**, 579–583 (2020).
4. Li, F., Bae, C. J., Ramsey, B., Chen, F. & Gao, X. Re-dating Zhoukoudian Upper Cave, northern China and its regional significance. *J. Hum. Evol.* **121**, 170–177 (2018).
5. Timmermann, A. & Friedrich, T. Late Pleistocene climate drivers of early human migration. *Nature* **538**, 92–95 (2016).
6. Kuhlwilm, M. I. et al. Ancient gene flow from early modern humans into Eastern Neanderthals. *Nature* **530**, 429–433 (2016).
7. Bae, C. J. et al. Late Pleistocene human evolution in Eastern Asia behavioral perspectives. *Curr. Anthropol.* **58**, 514–526 (2017).
8. Hajdinjak, M. et al. Initial Upper Palaeolithic humans in Europe had recent Neanderthal ancestry. *Nature* **592**, 253–257 (2021).

9. Bar-Yosef, O. & Wang, Y. Palaeolithic Archaeology in China. *Annu. Rev. Anthropol.* **41**, 319–335 (2012).
10. Li, F., Petraglia, M., Roberts, P. & Gao, X. The northern dispersal of early modern humans in eastern Eurasia. *Chin. Sci. Bull.* **65**, 1699–1701 (2020).
11. Dennell, R., Martinón-Torres, M., de Castro, J. M. B. & Gao, X. A demographic history of late Pleistocene China. *Quat. Int.* **559**, 4–13 (2020).
12. deMenocal, P. B. & Stringer, C. Climate and the peopling of the world. *Nature* **538**, 49–50 (2016).
13. Harvati, K. et al. Apidima Cave fossils provide earliest evidence of *Homo sapiens* in Eurasia. *Nature* **571**, 500–504 (2019).
14. Dennell, R. *From Arabia to the Pacific: How Our Species Colonised Asia* (Routledge, 2020).
15. Hovers, E., Ilani, S., Bar-Yosef, O. & Vandermeersch, B. An early case of color symbolism: ochre use by modern humans in Qafzeh Cave. *Curr. Anthropol.* **44**, 491–522 (2003).
16. Watts, I. Red ochre, body painting, and language: interpreting the Blombos ochre. *Cradle Lang.* **2**, 93–129 (2009).
17. Zipkin, A. M. *Material Symbolism and Ochre Exploitation in Middle Stone Age East-Central Africa*. Doctoral dissertation. The George Washington Univ. (2015).
18. Villa, P. et al. Border Cave and the beginning of the Later Stone Age in South Africa. *Proc. Natl Acad. Sci. USA* **109**, 13208–13213 (2012).
19. Pargeter, J. & Shea, J. Going big versus going small: lithic miniaturization in hominin lithic technology. *Evol. Anthropol.* **28**, 72–85 (2019).

20. Zwyns, N. et al. The northern route for human dispersal in central and Northeast Asia: new evidence from the site of Tolbor-16, Mongolia. *Sci. Rep.* **9**, 11759 (2019).
21. Peng, F., Lin, S. C., Patania, I. & Levchenko, V. A chronological model for the Late Paleolithic at Shuidonggou Locality 2, North China. *PLoS ONE* **15**, e023268 (2020).
22. Li, F. et al. The easternmost Middle Paleolithic (Mousterian) from Jinsitai Cave, North China. *J. Hum. Evol.* **114**, 76–84 (2018).
23. Li, F. et al. Chronology and techno-typology of the Upper Palaeolithic sequence in the Shuidonggou area, northern China. *J. World Prehistory* **32**, 111–141 (2019).
24. Yue, J. et al. Human adaptations during MIS 2: evidence from microblade industries of Northeast China. *Palaeogeogr. Palaeoclimatol. Palaeoecol.* **567**, 110286 (2021).
25. Li, Z., Doyon, L., Li, H., Wang, Q. & d'Errico, F. Engraved bones from the archaic hominin site of Lingjing, Henan Province. *Antiquity* **93**, 886–900 (2019).
26. Wei, Y., d'Errico, F., Vanhaeren, M., Peng, F. & Gao, X. A technological and morphological study of Late Paleolithic ostrich eggshell beads from Shuidonggou, North China. *J. Archaeol. Sci.* **85**, 83–104 (2017).
27. Qu, T., Bar-Yosef, O., Wang, Y. & Wu, X. The Chinese Upper Paleolithic: geography, chronology, and techno-typology. *J. Archaeol. Res.* **21**, 1–73 (2013).
28. Martí, A. P., Wei, Y., Gao, X., Chen, F. & d'Errico, F. The earliest evidence of coloured ornaments in China: the ochred ostrich eggshell beads from Shuidonggou Locality 2. *J. Anthropol. Archaeol.* **48**, 102–113 (2017).

29. Guan, Y. et al. Microblade remains from the Xishahe site, North China and their implications for the origin of microblade technology in Northeast Asia. *Quat. Int.* **535**, 38–47 (2020).
30. Pargeter, J. & Faith, T. J. Lithic miniaturization as adaptive strategy: a case study from Boomplaas Cave, South Africa. *Archaeol. Anthropol. Sci.* **12**, 225 (2020).
31. Guo, Y. J. et al. Luminescence ages for three ‘Middle Paleolithic’ sites in the Nihewan Basin, northern China, and their archaeological and palaeoenvironmental implications. *Quat. Res.* **85**, 456–470 (2016).
32. Yang, S., Deng, C., Zhu, R. & Petraglia, M. The Paleolithic in the Nihewan Basin, China: evolutionary history of an Early to Late Pleistocene record in Eastern Asia. *Evol. Anthropol.* **29**, 125–142 (2020).
33. Scerri, E. et al. Did our species evolve in subdivided populations across Africa, and why does it matter? *Trends Ecol. Evol.* **33**, 582–594 (2018).
34. Ramsey, B. C., Higham, T. & Leach, P. Towards high-precision AMS: progress and limitations. *Radiocarbon* **46**, 17–24 (2004).
35. Brock, F., Higham, T., Ditchfield, P. & Ramsey, C. B. Current pretreatment methods for AMS radiocarbon dating at the Oxford Radiocarbon Accelerator Unit (ORAU). *Radiocarbon* **52**, 103–112 (2010).
36. Reimer, P. et al. The IntCal20 Northern Hemisphere radiocarbon age calibration curve (0–55 cal kBP). *Radiocarbon* **62**, 725–757 (2020).
37. Bronk, C. B. Bayesian analysis of radiocarbon dates. *Radiocarbon* **51**, 337–360 (2009).
38. Huntley, D. J., Godfrey-Smith, D. I. & Thewalt, M. L. W. Optical dating of sediments. *Nature* **313**, 105–107 (1985).

39. Duller, G. Distinguishing quartz and feldspar in single grain luminescence measurements. *Radiat. Meas.* **37**, 161–165 (2003).
40. Rhodes, E. J. Optically stimulated luminescence dating of sediments over the past 200,000 years. *Annu. Rev. Earth Planet. Sci.* **39**, 461–488 (2011).
41. Zhang, X. L. et al. The earliest human occupation of the high-altitude Tibetan Plateau 40 thousand to 30 thousand years ago. *Science* **362**, 1049–1051 (2018).
42. Ge, J. Y. et al. Evidence from the Dayao Palaeolithic site, Inner Mongolia for human migration into arid northwest China during mid-Pleistocene interglacials. *Quat. Res.* **103**, 113–129(2021)
43. Duller, G. Luminescence dating of Quaternary sediments: recent advances. *J. Quat. Sci.* **19**, 183–192 (2004).
44. Aitken, M. J. *Introduction to Optical Dating: The Dating of Quaternary Sediments by the Use of Photon-Stimulated Luminescence* (Clarendon, 1998).
45. Ramsey, B. C. Deposition models for chronological records. *Quat. Sci. Rev.* **27**, 42–60 (2008).
46. Ramsey, B. C. Bayesian analysis of radiocarbon dates. *Radiocarbon* **51**, 337–360 (2009).
47. Ramsey, B. C. Dealing with outliers and offsets in radiocarbon dating. *Radiocarbon* **51**, 1023–1045 (2009).
48. Ramsey, B. C. *Bayesian Approaches to the Building of Archaeological Chronologies* (CRC, 2015).
49. Ramsey, B. C. Methods for summarizing radiocarbon datasets. *Radiocarbon* **59**, 1809–1833 (2017).
50. Adams, J. et al. in *Non-Flint Raw Material Use in Prehistory: Old Prejudices and New Directions* (eds Sternke, F. et al.) 43–66

(Archaeopress, 2009).

51. de Beaune, S. *Pour une Archéologie du Geste: Broyer, Moudre, Piler, des Premiers Chasseurs aux Premiers Agriculteurs* (CNRS Editions, 2000).
52. Rosso, D. E., Martí, I. A. P. & d'Errico, F. Middle Stone Age ochre processing and behavioural complexity in the Horn of Africa: evidence from Porc-Epic Cave, Dire Dawa, Ethiopia. *PLoS ONE* **11**, e0164793 (2016).
53. Hodgskiss, T. Identifying grinding, scoring and rubbing use-wear on experimental ochre pieces. *J. Archaeol. Sci.* **37**, 3344–3358 (2010).
54. Rifkin, R. F. Processing ochre in the Middle Stone Age: testing the inference of prehistoric behaviours from actualistically derived experimental data. *J. Anthropol. Archaeol.* **31**, 174–195 (2012).
55. Rosso, D. E., d'Errico, F. & Queffelec, A. Patterns of change and continuity in ochre use during the late Middle Stone Age of the Horn of Africa: the Porc-Epic Cave record. *PLoS ONE* **12**, e0177298 (2017).
56. Lafuente, B., Downs, R. T., Yang, H. & Stone N. In *Highlights in Mineralogical Crystallography* (eds Armbruster, T. & Danisi, R. M.) 1–30 (W. De Gruyter, 2015) pp. 1–30.
57. Bassel, L. et al. Fluorescence-based knife-edge beam diameter measurement to characterize X-ray beam profiles in reflection geometry. *Spectroc. Acta B* **118**, 98–101 (2016).
58. Dayet, L. et al. Manganese and iron oxide use at Combe-Grenal (Dordogne, France): a proxy for cultural change in Neanderthal communities. *J. Archaeol. Sci. Rep.* **25**, 239–256 (2019).
59. Queffelec, A., d'Errico, F. & Vanhaeren, M. In *Munibe Monographs* 493–503 (Anthropology and Archaeology Series, 2017).

60. Lucas-Tooth, H. J. & Price, B. J. A mathematical method for the investigation of inter-element effects in X-ray fluorescence. *Metallurgia* **64**, 149–152 (1961).
61. Anthony, J. W., Bideaux, R. A., Bladh, K. W. & Nichols, M. C. *Handbook of Mineralogy* (Mineral Data Publishing, 1990).
62. Hanesch, M. Raman spectroscopy of iron oxides and (oxy)hydroxides at low laser power and possible applications in environmental magnetic studies. *Geophys. J. Int.* **17**, 941–948 (2009).
63. Li, J. H. et al. Micro-XRF study of the troodontid dinosaur *Jianianhualong Tengi* reveals new biological and taphonomical signals. *At. Spectrosc.* **42**, 1–11 (2021).
64. Deng, C., Zhu, R., Jackson, M. J., Verosub, K. L. & Singer, M. J. Variability of the temperature-dependent susceptibility of the Holocene eolian deposits in the Chinese loess plateau: a pedogenesis indicator. *Phys. Chem. Earth A* **26**, 873–878 (2001).
65. Dunlop, D. J. & Özdemir Ö. *Rock Magnetism: Fundamentals and Frontiers* (Cambridge Univ. Press, 1997).
66. Kruiver, P. P., Dekkers, M. J. & Heslop, D. Quantification of magnetic coercivity components by the analysis of acquisition curves of isothermal remanent magnetization. *Earth Planet. Sci. Lett.* **189**, 269–276 (2001).
67. Jiang, Z. et al. Ferro and antiferromagnetism of ultrafine-grained hematite. *Geochem. Geophys. Geosyst.* **15**, 2699–2712 (2014).
68. Özdemir, Ö. & Dunlop, D. J. Hysteresis and coercivity of hematite. *J. Geophys. Res. Solid Earth* **119**, 2582–2594 (2014).
69. Roberts, A. P., Cui, Y. & Verosub, K. L. Wasp-waisted hysteresis loops: mineral magnetic characteristics and discrimination of components in mixed magnetic systems. *J. Geophys. Res.* **100**, 17909–17924 (1995).

70. Yuan, J. et al. Rapid drift of the Tethyan Himalaya terrane before two-stage India–Asia collision. *Natl Sci. Rev.* **8**, nwaal73 (2021).
71. Roberts, A. P. et al. Hematite (α -Fe₂O₃) quantification in sedimentary magnetism: limitations of existing proxies and ways forward. *Geosci. Lett.* **7**, 8 (2020).
72. Semenov, S. A. *Prehistoric Technology. An Experimental Study of the Oldest Tools and Artefacts from Traces of Manufacture and Wear* (Cory, Adams and Mackay, 1964).
73. Hayden, B. (ed.) *Lithic Use-Wear Analysis* (Academic, 1979).
74. Keeley, L. H. *Experimental Determination of Stone Tools Uses: A Microwear Analysis* (Univ. of Chicago Press, 1980).
75. Vaughan, P. C. *Use-Wear Analysis of Flaked Stone Tools* (Univ. of Arizona Press, 1985).
76. Knutsson, K. *Patterns of Tools Use. Scanning Electron Microscopy of Experimental Quartz Tools* (Societas Archaeologica Upsalensis, 1988).
77. González, J. E. & Ibáñez, J. J. *Metodología de Análisis Funcional de Instrumentos Tallados en Sílex* (Univ. de Deusto, 1994).
78. Levi Sala, I. *A Study of Microscopic Polish on Flint Implements* (Tempus Reparatum, 1996). BAR IS629.
79. Marreiros, J. M., Gibaja Bao, J. F. & Ferreira Bicho, N. *Use-Wear and Residue Analysis in Archaeology* (Springer, 2015).
80. Stemp, W. J., Watson, A. S. & Evans, A. A. Surface analysis of stone and bone tools. *Surf. Topogr. Metrol. Prop.* **4**, 13001 (2016).
81. Ollé, A. & Vergès, J. M. SEM functional analysis and the mechanism of microwear formation. In *Proc. International Congress Verona* (eds Longon, L. & Skakun, N.) 39–49 (Archaeopress, 2008).

82. Ollé, A. & Vergès, J. M. The use of sequential experiments and SEM in documenting stone tool microwear. *J. Archaeol. Sci.* **48**, 60–72 (2014).
83. Fernández-Marchena, J. L. & Ollé, A. Microscopic analysis of technical and functional traces as a method for the use-wear analysis of rock crystal tools. *Quat. Int.* **424**, 171–190 (2016).
84. Pedergnana, A. & Ollé, A. Monitoring and interpreting the use-wear formation processes on quartzite flakes through sequential experiments. *Quat. Int.* **427**, 35–65 (2017).
85. Borel, A., Ollé, A., Vergès, J. M. & Sala, R. Scanning electron and optical light microscopy: two complementary approaches for the understanding and interpretation of usewear and residues on stone tools. *J. Archaeol. Sci.* **48**, 46–59 (2014).
86. Ollé, A. et al. Microwear features on vein quartz, rock crystal and quartzite: a study combining optical light and scanning electron microscopy. *Quat. Int.* **424**, 154–170 (2016).
87. Pedergnana, A., Ollé, A. & Evans, A. A. A new combined approach using confocal and scanning electron microscopy to image surface modifications on quartzite. *J. Archaeol. Sci. Rep.* **30**, 102237 (2020).
88. Martín-Viveros, J. I. & Ollé, A. Use-wear and residue mapping on experimental chert tools. A multi-scalar approach combining digital 3D, optical, and scanning electron microscopy. *J. Archaeol. Sci. Rep.* **30**, 102236 (2020).
89. Monnier, F., Ladwig, J. & Porter, L. S. T. Swept under the rug: the problem of unacknowledged ambiguity in lithic residue identification. *J. Archaeol. Sci.* **39**, 3284–3300 (2012).
90. Pedergnana, A., Asryan, L., Fernández-Marchena, J. L. & Ollé, A. Modern contaminants affecting microscopic residue analysis on stone tools: a word of caution. *Micron* **86**, 1–21 (2016).

91. Pedergnana, A. & Ollé, A. Building an experimental comparative reference collection for lithic micro-residue analysis based on a multi-analytical approach. *J. Archaeol. Method Theory* **25**, 117–154 (2018).
92. Xhaufclair, H. et al. Use-related or contamination? Residue and use-wear mapping on stone tools used for experimental processing of plants from Southeast Asia. *Quat. Int.* **427**, 80–93 (2017).
93. Martín-Viveros, J. I. & Ollé, A. Using 3D digital microscopy and SEM–EDX for in-situ residue analysis: a multi-analytical contextual approach on experimental stone tools. *Quat. Int.* **569–570**, 228–262 (2020).
94. Hayes, E., Cnuds, D. & Rots, V. Integrating SEM–EDS in a sequential residue analysis protocol: benefits and challenges. *J. Archaeol. Sci. Rep.* **23**, 116–126 (2019).
95. Ollé, A. *Variabilitat i Patrons Funcionals en els Sistemes Tècnics de Mode 2. Anàlisi de les Deformacions d'ús en els Conjunts Lítics del Ripar Esterno de Grotta Paglicci (Rignano Garganico, Foggia), Áridos (Arganda, Madrid) i Galería-TN (Sierra de Atapuerca, Burgos)*. Thesis, Universitat Rovira i Virgili (2003).
96. Fernández-Marchena, J. L. et al. Rainbow in the dark. The identification of diagnostic projectile impact features on rock crystal. *J. Archaeol. Sci. Rep.* **31**, 102315 (2020).
97. Martín-Viveros, J. I. et al. Use-wear analysis of a specific mobile toolkit from the Middle Palaeolithic site of Abric Romaní (Barcelona, Spain): a case study from level M. *Archaeol. Anthropol. Sci.* **12**, 16 (2020).
98. Downs, R. T. The RRUFF Project: an integrated study of the chemistry, crystallography, Raman and infrared spectroscopy of minerals. In *Program and Abstracts of the 19th General Meeting of the International Mineralogical Association in Kobe, Japan*. 3–13 (2006).

99. Robertson, D. J. & France, D. E. Discrimination of remanence-carrying minerals in mixtures, using isothermal remanent magnetisation acquisition curves. *Phys. Earth Planet. Inter.* **82**, 223–234 (1994).
100. Swanson-Hywel, N. L., Fairchild, L. M. & Slotznick, S. P. Primary and secondary red bed magnetization constrained by fluvial intraclasts. *J. Geophys. Res. Solid Earth* **124**, 4276–4289 (2019).

Acknowledgements

We thank Y. Lefrais (IRAMAT-CRP2A, UMR 5060 CNRS) and F. Orange for assistance with SEM–EDS analyses; A. Queffelec (PACEA UMR 5199) and L. Geis (PACEA UMR 5199) for assistance with the EDXRF analyses and the 3D imaging; C. X. Zhang, B. Hu, M. L. Zhou, J. H. Li, Y. Liu, S. H. Yang, X. G. Li, Y. Chen, J. Yuan, Z. S. Shen, S. Zhang and Z. X. Jiang for assistance with the sediment analysis; B. Xu and Y. Li for discussions on dating results; and R. P. Tang and F. X. Huan for assistance with figure preparation. Financial support for this research was provided by the National Natural Science Foundation of China (41888101, 42177424, 41977380, 42072212 and 41690112), the Strategic Priority Research Program of Chinese Academy of Sciences (XDB26000000), the Key Research Program of the Institute of Geology and Geophysics, Chinese Academy of Sciences (IGGCAS-201905), the State Key Laboratory of Loess and Quaternary Geology, Institute of Earth Environment (SKLLQGZR2002), the Youth Innovation Promotion Association of Chinese Academy of Sciences (2020074), the Humboldt Foundation, and the Max Planck Society. A.O. was supported by the Spanish MICIU/Feder (PGC2018-093925-B-C32), the Catalan AGAUR (SGR2017-1040) and the Univ. Rovira i Virgili (2019-PFR-URV-91) in the context of a MICIN ‘María de Maeztu’ excellence accreditation (CEX2019-000945). D.E.R. was funded by the Fyssen Foundation, France, and the Juan de la Cierva-Formación Research Fellowship (FJC2018-035605-I; Ministerio de Ciencia e Innovación, Spain). F.d. was funded by the Research Council of Norway through its Centre of Excellence funding scheme (SFF Centre for Early Sapiens Behaviour–Sapien CE project number 262618), the ERC Synergy grant QUANTA (grant no. 951388), the Talents programme (Grant No.

191022-001) and the GPR Human Past of the University of Bordeaux Initiative of Excellence. K.D. received funding from the ERC under the European Union's Horizon 2020 research and innovation programme, grant agreement 715069-FINDER-ERC-2016-STG.

Author information

Author notes

1. These authors contributed equally: Fa-Gang Wang, Shi-Xia Yang

Affiliations

1. Hebei Provincial Institute of Cultural Relics and Archeology, Shijiazhuang, China

Fa-Gang Wang, Wen-Yan Li, Lian-Qiang Liu & Fei Xie

2. Key Laboratory of Vertebrate Evolution and Human Origins, Institute of Vertebrate Palaeontology and Palaeoanthropology, Chinese Academy of Sciences, Beijing, China

Shi-Xia Yang, Jun-Yi Ge, Ke-Liang Zhao & Ying Guan

3. Center for Excellence in Life and Palaeoenvironment, Chinese Academy of Sciences, Beijing, China

Shi-Xia Yang, Jun-Yi Ge, Ke-Liang Zhao & Ying Guan

4. Department of Archaeology, Max Planck Institute for the Science of Human History, Jena, Germany

Shi-Xia Yang, Katerina Douka & Michael Petraglia

5. State Key Laboratory of Loess and Quaternary Geology, Institute of Earth Environment, Chinese Academy of Sciences, Xi'an, China

Shi-Xia Yang

6. Institut Català de Palaeoecologia Humana i Evolució Social (IPHES-CERCA), Tarragona, Spain

Andreu Ollé

7. Universitat Rovira i Virgili, Departament d'Història i Història de l'Art, Tarragona, Spain

Andreu Ollé

8. Department of History, Anhui University, Hefei, China

Jian-Ping Yue

9. Université Côte d'Azur, CNRS, CEPAM, Nice, France

Daniela Eugenia Rosso

10. Departament de Prehistòria, Arqueologia i Història Antiga, Grupo de Investigación Prehistoria del Mediterráneo Occidental (PREMEDOC), Universitat de València, Valencia, Spain

Daniela Eugenia Rosso

11. Department of Evolutionary Anthropology, University of Vienna, Vienna, Austria

Katerina Douka

12. Museum of Yuzhou, Yuxian, China

Hai-Yong Yang

13. Key Laboratory of Cenozoic Geology and Environment, Institute of Geology and Geophysics, Chinese Academy of Sciences, Beijing, China

Zheng-Tang Guo

14. State Key Laboratory of Lithospheric Evolution, Institute of Geology and Geophysics, Chinese Academy of Sciences, Beijing, China

Ri-Xiang Zhu & Cheng-Long Deng

15. College of Earth and Planetary Sciences, University of Chinese Academy of Sciences, Beijing, China

Cheng-Long Deng

16. PACEA UMR 5199, Université de Bordeaux, CNRS, Pessac, France

Francesco d'Errico

17. SFF Centre for Early Sapiens Behaviour (SapienCE), University of Bergen, Bergen, Norway

Francesco d'Errico

18. Human Origins Program, National Museum of Natural History, Smithsonian Institution, Washington, DC, USA

Michael Petraglia

19. School of Social Science, The University of Queensland, Brisbane, Queensland, Australia

Michael Petraglia

20. Australian Research Centre for Human Evolution (ARCHE), Griffith University, Brisbane, Australia

Michael Petraglia

Contributions

F.-G.W., S.-X.Y., C.-L.D., R.-X.Z., Z.-T.G., F.d. and M.P. obtained funding and initiated the project; F.-G.W., S.-X.Y., J.-Y.G., L.-Q.L., F.X., H.-Y.Y., Y.G. and W.-Y.L. conducted field excavation and site sampling; J.-

Y.G., K.-L.Z., K.D. and C.-L.D. conducted stratigraphic and palaeoenvironmental studies; J.-Y.G. performed the OSL dating; K.D. performed the ^{14}C dating; S.-X.Y., J.-P.Y., M.P. and A.O. analysed the stone artefacts; F.d., D.E.R., Y.G., S.-X.Y. and C.-L.D. analysed the ochre-processing artefacts and the sediment; and S.-X.Y., C.-L.D., F.d. and M.P. wrote the main text and supplementary materials with specialist contributions from the other authors.

Corresponding authors

Correspondence to [Shi-Xia Yang](#), [Cheng-Long Deng](#), [Francesco d'Errico](#) or [Michael Petraglia](#).

Ethics declarations

Competing interests

The authors declare no competing interests.

Peer review

Peer review information

Nature thanks Andrew Murray, Pamela Willoughby and the other, anonymous, reviewers for their contribution to the peer review of this work. Peer reviewer reports are available.

Additional information

Publisher's note Springer Nature remains neutral with regard to jurisdictional claims in published maps and institutional affiliations.

Extended data figures and tables

Extended Data Fig. 1 Bone tool from Layer 6.

a, Periosteal view of the shaft fragment. **b**, Close-up view of the distal area showing microflake scars, smoothing and striations. **c**, Scraping regularizing the edge close to the opposite end. The object is an elongated fragment of a long bone from a medium-sized mammal. The bone is in an excellent state of preservation, apart from a large notch and post-depositional chipping located on both sides and rare flaking of the periosteal surface, at places removing primary bone lamellae. The edge of the rounded end displays micro flake scars strongly worn by usewear. The adjacent surface is covered with groups of microscopic striations subparallel or oblique to the main axis of the object that fade in frequency away from the edge. The left edge of the opposite end, which is pointed in shape, has been regularized by scraping with a lithic tool so as to make the edges of the bone less sharp. The adjacent periosteal surface also bears longitudinal striations, due to scraping, as well as groups of short striations perpendicular to the major axis of the object. The marks present on the rounded end are consistent with the object being used as a scraper on a soft material, strewn with abrasive particles. The modifications on the opposite end were intended to facilitate hafting of the object or its gripping during work.

Extended Data Fig. 2 Ochre piece OP1.

a, Ochre piece OP1, numbers indicate the analyzed areas (zone 1: grey polished area; zone 2: purple granular area; zone 3: coarse-grained area; zone 4: blistered area). **b**, drawing of ochre piece OP1, grey areas represent flake scars. **c–f**, SEM images of ochre piece OP1 (zones 1 to 4 respectively): grey polished area (**c**); purple granular area (**d**); coarse-grained area (**e**); blistered area (**f**). **g**, μ -Raman spectra obtained from the analysis of zone 1 (grey polished area, spectrum 1) and zone 3 (coarse-grained area, spectrum 2) showing the presence of hematite (H) and quartz (Q). The hematite reference spectrum is indicated in red: RRUFF ID R110013⁹⁸. OP1 (28 x 20 mm in size; 12,4 g in mass) is a fragment of a larger nodule showing a portion of the original curved outer surface and several flake scars. The outer surface features a cracked and pitted texture alternating compact (grey polished area, zone 1 in **a**) and granular zones

(purple granular and coarse-grained areas, zones 2 and 3 respectively in **a**). The flake scars feature a homogeneously blistered structure partially hidden on one surface by a yellow and on another by a dark red coating (blistered area, zone 4 in **a**). The blisters are smoother on some surfaces. Differential alteration indicates different episodes of fragmentation, probably due to knapping.

Extended Data Fig. 3 Ochre piece OP2.

a, Ochre piece OP2, number indicates the area analyzed using SEM-EDS. **b, c**, SEM images of ochre piece OP2. **d**, μ -Raman spectrum obtained from the analysis of OP2 showing the presence of hematite (H), quartz (Q), and an undetermined manganese oxide (Und). The hematite reference spectrum is indicated in red: RRUFF ID R110013⁹⁸. OP2 (11 x 8 mm in size; 0.6 g in mass) preserves at its base (at the bottom) a dark brown flat area representing the outer surface of an originally larger ochre lump of which OP2 is a small fragment. OP2 likely results from pounding that larger piece. More heterogeneous and porous than OP1, it bears no other evidence of deliberate modification.

Extended Data Fig. 4 Quartzite cobble (QC) and limestone slab (LS).

a, Views of the QC with indication of the area enlarged in **b**. **b**, Flat pitted area of the QC. **c**, Views of the LS with indication of the area enlarged in **(d)** and the area on which fragment OMF was retrieved (1). **d**, Smoothed area with diffused ochre stain. **e**, Residue OMF with indication of the area analysed using SEM-EDS (1). **f, g**, SEM images of sample OMF. **h**, μ -Raman spectrum obtained from sample OMF showing the presence of hematite (H) and an undetermined manganese oxide (Und). The hematite reference spectrum is indicated in red: RRUFF ID R110013⁹⁸. The quartzite cobble (10 x 9 cm in size) bears pits consistent with grinding and pounding actions on a flat facet (**a, b**) and on a protuberant zone of the edge. No ochre residues were identified on the surface of the cobble, or on the sediment covering the piece before cleaning. The limestone slab (24 x 16 cm in size) bears smoothed areas on one flat face and one edge as well as a

diffuse red stain on the latter (**c**, **d**). Sample OMF (**e–g**) was identified on the edge of the limestone slab that features a red stain (**c**, zone 1). However, since the smoothed surfaces of the artefact were found in direct contact with the red stain on the sediment (Fig. [3b](#)), it is not clear whether the red residues come from the stained sediment or whether they result from a processing of ochre directly on the surface of the tool.

Extended Data Fig. 5 Anthropogenic modifications observed on ochre piece OP1.

a, squares indicate areas presented in **c–g** with same letters. **b**, grey areas represent surfaces that bear striations produced by grinding. Arrows indicate the direction of the grinding motions. **c–e**, **g**, striations observed on OP1. **f**, 3D reconstruction of an area showing striations. The outer surface of the nodule bears five adjacent areas, each covered by parallel striations produced by abrading the nodule on a grindstone with a to-and-from motion (**a**, **b**). OP1 contains inclusions of almost pure iron in a more granular matrix. Abrasion has differentially smoothed areas of different hardness with the harder remaining more prominent. The orientation of the striations slightly differs on each facet indicating changes in the direction of the movement and possibly different sessions of use. The latter hypothesis is supported by substantial differences in the size of the striations between modified areas suggesting abrasion on grindstones of different granulometry (**c–g**).

Extended Data Fig. 6 Sediment analyses.

Samples X1 and X2 come from the red stained area on which the ochre fragments OP1 and OP2, stone slab LS and quartzite cobble QC were found; and samples X3 and X6 were retrieved Layer 6 but at about 2 m far from the stained area (Supplementary Fig. [G1](#)). **a**, XRD spectra clearly showing that hematite is abundant in samples X1 and X2, and that it is not detected in samples X3 and X6. **b**, Raman spectra. Data of the reference hematite (CIT-2058) with RRUFF ID X050102 come from the RRUFF Project website (<https://rruff.info/hematite/display=default/X050102>), see also Anthony et al.^{[61](#)}. **c**, High-temperature magnetic susceptibility measurements. Blue arrows represent the feature of partially-oxidized

magnetite; and red arrows, of hematite. **d**, Magnetic component analysis of coercivity distributions calculated with the IRM-CLG program⁶⁶. Green, purple, blue and red lines indicate the low-coercivity component (IRM_L), middle-coercivity component (IRM_M), high-coercivity component (IRM_H), and the sum of these components (sum), respectively. $B_{1/2}$ is the field at which half of the saturation IRM (SIRM) is reached; and the dispersion parameter (DP) represents one standard deviation⁹⁹. $B_{L1/2}$, $B_{M1/2}$ and $B_{H1/2}$ represent $B_{1/2}$ of the low-, middle- and high-coercivity component, respectively. DP_L , DP_M and DP_H represent DP of the low-, middle- and high-coercivity component, respectively. The high-coercivity component (IRM_H) with median acquisition field ($B_{H1/2}$) of up to 575 mT is interpreted as single domain (SD) hematite, because the SD threshold grain size of hematite is considerably larger than 15 µm, and even up to 100 µm⁶⁸. This kind of hematite grains with high coercivities up to several hundreds of mT is usually of detrital origin^{70,100}. **e**, Fe element distribution via Micro-XRF imaging. The yellow arrows point to large (up to 150–200 µm) Fe-rich agglomerates, which probably contain a high proportion of hematite, whose presence is detected by XRD analyses (**a**), Raman spectroscopy (**b**) and mineral magnetic measurements (**c**, **d**).

Extended Data Fig. 7 Bladelet-like chert piece with a bone fragment attached (no. 129).

(1) mosaic of the ventral face showing the location of the bone (3D DM). (2–4) detail of the bone film adhering to a layer of calcium carbonate (3D DM, SEM-LFD and SEM BSD respectively). (5) detail of the bone imprint (SEM-LFD). (6) calcium carbonate layer sandwiched between the bone and the tool surface (SEM-BSD). (7) EDX spectrum from the bone film taken in the center of images 3 and 4. (8–10) plant fiber imprints, present on both edges at the proximal end, associated with some ochre particles (3D DM, SEM-LFD and SEM-BSD respectively).

Extended Data Fig. 8 Bladelet-like chert piece, dorsal face, use-wear after removing residues (no. 129).

(1) mosaic of the distal left portion (3D DM). (3, 4) edge micro-scarring covered by an invasive, grid-influenced plant polish produced by a whittling action (SEM-LFD). (5, 6) portion of the dorsal ridge with a well-developed polish, ploughed by transversal striations (SEM-LFD and OM 50x-lens).

Extended Data Fig. 9 Bladelet-like chert piece, ventral face, use-wear after removing residues (no. 129).

(1) central part of the active edge with micro-scarring and well-developed polish (SEM-LFD). (2) detail from image 1 (OM 10x-lens). (3–5) details of image 2 (ON 20x-lens, SEM-LFD and OM 50x-lens respectively); (6) mosaic of the distal portion (SEM-LFD). (7) detail of the area interpreted as the limit of the hafted area, with some binding scars and no polish. (8, 9) intensively polished areas covered with fine transverse striations (SEM LFD and SEM-BSD).

Extended Data Fig. 10 Map, site location, stratigraphy and archaeological site distributions.

a, distribution of MIS 3 sites in northern China (see Supplementary Table A1 for site names. The source of the map <https://resources.arcgis.com/>). **b**, field view of Xiamabei. **c**, view of the excavated section. **d**, archaeological site distributions. Key features include a red stained patch with artefacts and a hearth and surrounding ashy area. Sediment samples for composition analysis within the excavation area are shown. Notable is the distribution of lithic artefacts and fauna, including the location of a bone tool. Stone tools submitted to use-wear analysis provide evidence for the following activities: hafting to handles; processing of vegetal material; involvement in butchery activities and hide working; perforation of hard material; use as wedges.

Supplementary information

Supplementary Information

This file contains supplementary text, Figures, Tables and references.

Reporting Summary

Peer Review File

Rights and permissions

Reprints and Permissions

About this article

Cite this article

Wang, FG., Yang, SX., Ge, JY. *et al.* Innovative ochre processing and tool use in China 40,000 years ago. *Nature* **603**, 284–289 (2022).
<https://doi.org/10.1038/s41586-022-04445-2>

- Received: 13 June 2021
- Accepted: 19 January 2022
- Published: 02 March 2022
- Issue Date: 10 March 2022
- DOI: <https://doi.org/10.1038/s41586-022-04445-2>

Share this article

Anyone you share the following link with will be able to read this content:

[Get shareable link](#)

Sorry, a shareable link is not currently available for this article.

[Copy to clipboard](#)

Provided by the Springer Nature SharedIt content-sharing initiative

This article was downloaded by **calibre** from <https://www.nature.com/articles/s41586-022-04445-2>

| [Section menu](#) | [Main menu](#) |

- Article
- Open Access
- [Published: 23 February 2022](#)

Ancient DNA and deep population structure in sub-Saharan African foragers

- [Mark Lipson](#)^{1,2 na1},
- [Elizabeth A. Sawchuk](#) [ORCID: orcid.org/0000-0003-4398-2174](#)^{3,4 na1},
- [Jessica C. Thompson](#) [ORCID: orcid.org/0000-0003-1627-4949](#)^{5,6},
- [Jonas Oppenheimer](#)⁷,
- [Christian A. Tryon](#) [ORCID: orcid.org/0000-0002-2354-3273](#)^{8,9,10},
- [Kathryn L. Ranhorn](#) [ORCID: orcid.org/0000-0002-9048-5966](#)⁶,
- [Kathryn M. de Luna](#) [ORCID: orcid.org/0000-0002-3496-2115](#)¹¹,
- [Kendra A. Sirak](#) [ORCID: orcid.org/0000-0003-2347-3479](#)^{1,2},
- [Iñigo Olalde](#) [ORCID: orcid.org/0000-0002-2660-6807](#)^{1,12},
- [Stanley H. Ambrose](#) [ORCID: orcid.org/0000-0002-8785-0512](#)¹³,
- [John W. Arthur](#) [ORCID: orcid.org/0000-0002-4968-5843](#)¹⁴,
- [Kathryn J. W. Arthur](#)¹⁴,
- [George Ayodo](#)¹⁵,
- [Alex Bertacchi](#) [ORCID: orcid.org/0000-0002-2269-2437](#)⁵,
- [Jessica I. Cerezo-Román](#) [ORCID: orcid.org/0000-0002-7752-8079](#)¹⁶,
- [Brendan J. Culleton](#)¹⁷,
- [Matthew C. Curtis](#) [ORCID: orcid.org/0000-0003-4692-3241](#)¹⁸,
- [Jacob Davis](#)¹⁹,
- [Agness O. Gidna](#)²⁰,
- [Annalys Hanson](#)²¹,
- [Potiphar Kaliba](#)²²,
- [Maggie Katongo](#) [ORCID: orcid.org/0000-0002-5286-1350](#)^{23,24},
- [Amandus Kwekason](#)²⁰,
- [Myra F. Laird](#) [ORCID: orcid.org/0000-0002-8636-0407](#)²⁵,
- [Jason Lewis](#) [ORCID: orcid.org/0000-0001-8325-1128](#)⁴,
- [Audax Z. P. Mabulla](#)²⁶,

- [Fredrick Mapemba²²](#),
- [Alan Morris²⁷](#),
- [George Mudenda²⁴](#),
- [Raphael Mwafulirwa²⁸](#),
- [Daudi Mwangomba²⁹](#),
- [Emmanuel Ndiema³⁰](#),
- [Christine Ogola³⁰](#),
- [Flora Schilt ORCID: orcid.org/0000-0002-2144-3017³¹](#),
- [Pamela R. Willoughby³](#),
- [David K. Wright ORCID: orcid.org/0000-0003-1704-0423^{32,33}](#),
- [Andrew Zipkin ORCID: orcid.org/0000-0002-3813-8051³⁴](#),
- [Ron Pinhasi ORCID: orcid.org/0000-0003-1629-8131^{35,36}](#),
- [Douglas J. Kennett ORCID: orcid.org/0000-0001-6144-7365³⁷](#),
- [Fredrick Kyalo Manthi³⁰](#),
- [Nadin Rohland¹](#),
- [Nick Patterson²](#),
- [David Reich ORCID: orcid.org/0000-0002-7037-5292^{1,2,38,39}](#) &
- [Mary E. Prendergast ORCID: orcid.org/0000-0003-0275-6795^{1,23}](#)

Nature volume 603, pages 290–296 (2022)

- 65k Accesses
- 924 Altmetric
- [Metrics details](#)

Subjects

- [Archaeology](#)
- [Biological anthropology](#)
- [Population genetics](#)

Abstract

Multiple lines of genetic and archaeological evidence suggest that there were major demographic changes in the terminal Late Pleistocene epoch and early Holocene epoch of sub-Saharan Africa^{1,2,3,4}. Inferences about this period are challenging to make because demographic shifts in the past 5,000 years have obscured the structures of more ancient populations^{3,5}. Here we present genome-wide ancient DNA data for

six individuals from eastern and south-central Africa spanning the past approximately 18,000 years (doubling the time depth of sub-Saharan African ancient DNA), increase the data quality for 15 previously published ancient individuals and analyse these alongside data from 13 other published ancient individuals. The ancestry of the individuals in our study area can be modelled as a geographically structured mixture of three highly divergent source populations, probably reflecting Pleistocene interactions around 80–20 thousand years ago, including deeply diverged eastern and southern African lineages, plus a previously unappreciated ubiquitous distribution of ancestry that occurs in highest proportion today in central African rainforest hunter-gatherers. Once established, this structure remained highly stable, with limited long-range gene flow. These results provide a new line of genetic evidence in support of hypotheses that have emerged from archaeological analyses but remain contested, suggesting increasing regionalization at the end of the Pleistocene epoch.

[Download PDF](#)

Main

Models for the expression of human behavioural complexity during the Late Pleistocene (around 125–12 thousand years ago (ka)) often invoke demographic change^{1,2}. By around 50 ka, technological innovations and symbolic behaviours (such as ornaments, bone tools, pigments and microliths) that were present earlier in the Middle Stone Age (MSA) become more consistently expressed across sub-Saharan Africa^{4,6,7}. Archaeologists refer to this as the transition to the Later Stone Age (LSA)^{1,7,8,9}. By around 20 ka, these material culture components were nearly ubiquitous, but regionally diverse. One explanation is that people began living in larger and/or more connected groups, with variations in population size and connectivity driving differences in material culture across space and time. Given the morphological variation among Late Pleistocene skeletons, interactions may have involved deeply structured populations^{2,10}, consistent with some population history models based on genetics³.

The advent of genome-wide ancient DNA (aDNA) technology holds promise for better understanding major changes in material culture and hypothesized demographic shifts among ancient African foragers (Supplementary Notes 1, 2). Compared to elsewhere, especially Europe, there has been little genomic investigation of ancient African peoples. Previously available aDNA sequences from sub-Saharan African foraging contexts^{11,12,13,14}, despite being relatively recent (younger than about 9 ka), provide evidence of ancient genetic structure that has since been disrupted by demographic transformations (such as the spread of food production, as well as colonialism, imperialism, enslavement and modern sociopolitical reorganization). The

structure of ancient populations cannot be robustly reconstructed based solely on genetic data from present-day people.

Here we present new genome-wide aDNA data and radiocarbon dates from three Late Pleistocene and three early to middle Holocene individuals associated with LSA technologies at five sites in eastern and south-central Africa: Kisese II and Mlambalasi Rockshelters in Tanzania, Fingira and Hora 1 Rockshelters in Malawi, and Kalemba Rockshelter in Zambia (Fig. 1a and Extended Data Table 1). Direct and indirect dates range from around 18 ka to 5 ka, doubling the time depth of aDNA reported from sub-Saharan Africa. We analyse these data together with the published sequences of 28 other ancient African individuals recovered from contexts spanning the past 8,000 years and largely associated with foraging at 17 sites in eastern, central and southern Africa. We also provide higher-coverage data for 15 of these individuals. Analysis of the ancient data together with sequences from present-day groups, aided by new statistical methods, enables a reconstruction of changes in regional- and continental-scale population structures among people who lived before the sweeping demographic changes of the past approximately 5,000 years. It also enables comparisons of Pleistocene forager population dynamics between the tropics and more temperate regions.

Fig. 1: Locations of the individuals analysed and PCA analysis.

 figure 1



a, Locations of individuals analysed in this study. The shapes and colours of the symbols correspond to the PCA in **b**. 1, Shum Laka; 2, Mota Cave; 3, Kakapel RS (Rockshelter); 4, Nyarindi RS; 5, Jauyoyo RS; 6, White Rock Point; 7, Panga ya Saidi; 8, Makangale Cave; 9, Kuumbi Cave; 10, Gishimangeda Cave; 11, Kisese II

RS; 12, Mlambalasi RS; 13, Fingira; 14, Hora 1; 15, Chencherere II; 16, Kalemba RS; 17, Ballito Bay; 18, Faraoskop RS; 19, St Helena. **b**, PCA results. Axes were computed using present-day groups from eastern (Dinka pastoralists), southern (Jul'hoansi foragers) and central Africa (Mbuti foragers). Small circles represent present-day individuals; other symbols represent ancient individuals (larger points corresponding to earlier individuals and black outlines to newly reported individuals). The lowest-coverage individual (from Mlambalasi), shown with an asterisk, has the most uncertain position. The base map in **a** is from Natural Earth (<https://www.naturalearthdata.com>). E., east.

The dataset

Of 31 samples (Supplementary Table 1), five petrous bones and one distal phalanx yielded aDNA sequences, which, after preparation of up to six libraries from each sample and enrichment for a panel of around 1.2 million single-nucleotide polymorphisms (SNPs), ranged in coverage from 0.001–3.2× (median, 0.06×) of targeted genome-wide SNP positions (Extended Data Table 1 and Supplementary Table 2). Additional archaeological and bioarchaeological information for these individuals is summarized in Supplementary Note 3. Direct ^{14}C dates were attempted for the five petrous bones, but only two preserved sufficient collagen: Kalemba (I10726; 5,280–4,880 calibrated years before present (cal. bp), PSUAMS-4764) and Kisese II (I18821; 7,240–6,985 cal. bp, PSUAMS-4718) (Supplementary Table 3 and Supplementary Note 4). Moreover, a new date was generated on enamel carbonate for a published individual from Hora 1 (I2966; previously estimated around 8,100 bp, now directly dated to 9,090–8,770 cal. bp, PSUAMS-5145). Individuals from Mlambalasi (I13976; about 20–17 ka) and Hora 1 (I19528, I19529; 17–14 ka) are well constrained to the Late Pleistocene based on multiple indirect dates (Supplementary Table 4 and Supplementary Note 3). One individual from Fingira (I11019) is represented by a distal phalanx that was recovered in isolation near the surface during excavation. This sample was too small to be both dated and assessed for aDNA; its age is constrained to around 6,200–2,300 cal. bp by association with direct dates on other human remains from the site. The 15 previously published individuals^{11,13,15,16} (Supplementary Note 3) for which we increase sequence coverage include approximately 26× shotgun coverage for the individual from Mota Cave in Ethiopia¹⁵ (I5950), enabling reliable calling of diploid genotypes (Extended Data Table 1, [Methods](#) and Supplementary Table 2). The authenticity of the new aDNA data was assessed through a combination of several criteria; detectable contamination was observed for only two samples ([Methods](#), Extended Data Fig. 1a, Supplementary Table 2 and Supplementary Note 5). In Supplementary Table 5 and Supplementary Note 5, we report genotypes at SNPs associated with lactase persistence, sickle cell trait and the Duffy antigen, with derived

alleles observed only at the DARC (Duffy) locus (four published individuals from Cameroon).

Uniparental markers

All four newly reported males are similar to most published ancient foragers from this region of Africa in carrying the widely distributed Y chromosome haplogroup B2 (Extended Data Table 1). Among the 23 individuals in our dataset with known mtDNA haplogroups, up to 14—almost all from Kenya and Tanzania—have haplogroups that are today associated with eastern Africa (Extended Data Table 1 and Supplementary Table 6). Eight individuals—all from Malawi and Zambia—have haplogroups that are associated with some ancient and present-day southern African people, specifically groups for whom foraging is the main mode of subsistence^{17,18,19,20}. Two individuals from Malawi (I19529 from Hora 1, dating to about 16 ka and carrying L5b, and I4426 from Fingira, dating to about 2.3 ka and carrying L0f/L0f3) have eastern-Africa-associated haplogroups, whereas a different individual from Malawi (I2967 from Hora 1, dating to about 8.2 ka with L0a2/L0a2b) and possibly one from Kenya (I8930 from White Rock Point with L2a4) belong to lineages that are characteristic of present-day central African foragers (such as Mbuti and Aka). These results show that eastern and south-central Africa was home to, and an area of interaction among, diverse ancient foraging groups, and also that several of these haplogroup lineages were formerly more widespread than they are today.

Three-way cline of genome-wide ancestry

For the bulk of our analyses, we used the genome-wide genotype data to gain insights into the ancestry of the ancient forager individuals and their connections to other groups. We performed a supervised principal component analysis (PCA) ([Methods](#)) in which we used three present-day groups—Ju'hoansi (San) from southern Africa, Mbuti from central Africa and Dinka from northeastern Africa—to define a two-dimensional plane of variation, and projected all other individuals (ancient and present day) onto this plane (Fig. 1b). Consistent with previous studies^{5,11,13,14}, we observed an ancient latitudinal gradient of ancestry, represented at its northern extreme by an individual from around 4.5 ka from Mota Cave, Ethiopia, and its southern extreme by individuals from around 2 ka from South Africa. The newly reported individuals generally cluster with their geographical neighbours but extend documentation of the cline both geographically (southwest to Kalemba, at the corresponding extreme on PCA) and temporally (to a maximum of approximately 18–16 ka, with no apparent temporal subclusters). Furthermore, we found complexity in the cline in the form of deviations from a straight line: (1) the main direction of variation does not align with ancient southern African foragers; and (2) several individuals appear to shift in the

direction of present-day and ancient central African foragers. Both observations may indicate that some of the ancient eastern and south-central African individuals sampled here trace part of their ancestry to groups that are related to foragers currently living in central Africa. Furthermore, (1) could indicate that the southern-African-related ancestry among the ancient individuals is only distantly related to present-day Ju'hoansi and ancient southern African foragers.

We used allele-sharing tests (*f*-statistics) ([Methods](#)) to further investigate which individuals differed in their degree of relatedness to ancient South African foragers (AncSA) (Extended Data Table [1](#)), the Mota individual or present-day Mbuti. Consistent with the PCA, most pairs of individuals from the same region (including from different time points) were nearly symmetric in their ancestry ($|Z| < 3$) (Supplementary Table [2](#)). The exceptions were (1) excess affinity between Mbuti and KPL001 (Kakapel; max $Z = 5.1$); (2) excess affinity between AncSA and I0589 (Kuumbi Cave; max $Z = 4.1$); and (3) modest differences within Malawi and Zambia (max $Z = 3.8$). By contrast, well-powered cross-region statistics were highly significantly non-zero, for example, $f_4(I8808 \text{ (Jawuoyo)}, I8821 \text{ (Kisese II)}; \text{Mota, AncSA}) > 0$, $Z = 7.8$. We also used the qpWave program in ADMIXTOOLS to combine multiple *f*-statistic-based signals into a test for the number of distinct components of ancestry (relative to a specified outgroup set) present among the (sampled) ancient forager individuals ([Methods](#)). We found that at least three sources are necessary ($P = 6.4 \times 10^{-14}$ for rejecting a two-source model) but, interestingly (with our available statistical power), that three sources are also sufficient ($P = 0.73$; four versus three sources $P = 0.15$), even with Mota, San (here, both Ju'hoansi and †Khomani) and Mbuti among the outgroups. When we added the Mota individual to the test set, we found increased evidence for a fourth source, despite the less stringent outgroups ($P = 0.07$; four versus three sources $P = 0.019$) ([Methods](#)). This result could reflect a highly divergent ancestry component contributing to the Mota individual inferred in previous work¹⁶; additional lineages may also have been present among as-yet unsampled ancient individuals from these regions.

We attempted to estimate the dates of admixture (potentially involving any distinct sources of ancestry) for the ancient foragers using DATES²¹. With the caveat that our power is limited by data availability, we obtained only two robust estimates (Supplementary Table [8](#)), both for previously published individuals, and both (given the additional results below) are probably connected to admixture from food producers: for I4421 (Chencherere II, no direct age, past approximately 5,000 years), a date of 10 ± 2 generations before the individual lived; and for I1048 (Makangale Cave, direct age, past approximately 1,500 years), 79 ± 24 generations before the individual lived.

Inter- and intraregional relationships

Next, we modelled the ancestry of the ancient foragers in an admixture graph framework to test additional hypotheses concerning their relationships, aided by a new methodology to increase available information from low-coverage data (Figs. 2 and 3, [Methods](#), Supplementary Notes 6 and 7 and Extended Data Figs. 2–5). In model 1, along with other populations, we included three geographically and genetically diverse ancient eastern and south-central African individuals with high sequencing coverage: I4426 (Fingira, about 2.5 ka), I8821 (Kisese II) and I8808 (Jawuoyo). On the basis of the results in the previous section, we hypothesized that they could be fit with mixtures of three ancestry components: one related to the Mota individual (representing an ancient group of foragers from the northern part of eastern Africa), one related to central African foragers (represented by present-day Mbuti) and one related to southern African foragers (represented by four ancient individuals from South Africa). Indeed, we obtained a good fit to the data in model 1 (max residual $Z = 2.0$), even when specifying identical sources for all three individuals, and the relative ancestry proportions were as expected: Mota-related ancestry decreased from north to south, and Jawuoyo (I8808) had the highest ratio of central-African-related ancestry to southern-African-related ancestry. Omitting any of the three components for any of the individuals results in a poor fit ($Z \geq 4.0$) (Supplementary Note 6). As in ref. 16, we also estimated around 30% of a separate and deeply diverged ‘ghost’ ancestry component in the Mota individual (replicated here using new higher-coverage diploid whole-genome data).

Fig. 2: Schematic of admixture graph results.

 **figure 2**

Branch lengths are not to scale. The arrows denote admixture events, with the three primary components of ancestry shown as dashed arrows, and other inferred gene flow as small solid arrows (with colours corresponding to related groups). Subclusters of ancient eastern and south-central African foragers reflect the inferred instances of excess relatedness among individuals, with internal branch lengths shown in genetic-drift units. Mixture proportions are shown in Fig. 3 and Supplementary Table 9 and the full results are shown in Extended Data Fig. 4. Individual laboratory numbers are shown at the bottom (Extended Data Table 1). N., north; W., west.

Fig. 3: Distribution of main ancestry components.

 **figure 3**

Kriged distribution of the proportions of each of the three main ancestry components (summing to 1) found in ancient eastern and south-central African foragers analysed in this study (details are provided in Supplementary Table 9). The approximate present-day Mbuti home region is from ref. 41. Individuals from the same site were included using locations that differed by 0.000001 decimal degrees latitude to ensure representation in the interpolation. Scale bars, 250 km. Topographical data are from the Shuttle Radar Topography Mission (SRTM)⁴². SA, southern African.

When we added more individuals to create models 2 and 3 (max residuals $Z = 3.0$ and $Z = 3.7$), we found that the overall inferred structure and parameters were similar to those of model 1 (Supplementary Tables 9 and 10; see below for specific individuals and regions). The Mota-related and southern-African-related ancestry sources are inferred to split deeply along their respective lineages, meaning that, in some sense, they represent ‘ghost’ populations (without closely related sampled representatives). The central-African-related component is inferred to be closer to Mbuti (including an ancestral admixture event; Supplementary Note 6) than to Aka, and therefore to not split as deeply relative to the initial divergence of the central African forager lineage. Almost all of the additional significant allele-sharing signals that we observed beyond those in model 1 can be attributed to one of the three following causes (Supplementary Table 11): (1) excess relatedness at short-distance scales (see below); (2) admixture from pastoralists and/or farmers more recent than our period of focus (four individuals); or (3) contamination (two individuals). In these cases, we adjusted our final model by (1) allowing shared history (that is, genetic drift) between the relevant individuals; (2) adding the inferred admixture events; or (3) incorporating extra admixture to represent the contamination source (Supplementary Note 6).

For sites in western Kenya, we found that all three individuals in model 3 have excess relatedness beyond the baseline expectation (Fig. 2). The individuals from Jawuoyo

(I8808) and Nyarindi (NYA002/NYA003) are the closest, and they can be modelled with Mota-related, central-African-related and southern-African-related ancestry in respective proportions of about 62%, 19% and 19%, while the individual from Kakapel (KPL001) is inferred to have around 12% additional central-African-related ancestry (s.e. of approximately 2–4% with some assumptions) (Fig. 3 and Supplementary Note 6). For north-central Tanzanian sites, again all four individuals have signals of mutual excess allele sharing, with the three individuals from Gishimangeda (I13763, I13982 and I13983) being the closest. One of the three (I13763) shows excess relatedness to non-African individuals, which we interpret as evidence of a small proportion of contamination (Supplementary Notes 5 and 6); otherwise, all four can be fit as a clade with 54%, 12% and 34% Mota-related, central-African-related and southern-African-related ancestry, respectively. Similarly, the three island and coastal individuals (Makangale Cave I1048, Kuumbi Cave I10589, Panga ya Saidi I0595) display excess relatedness, with those from Kuumbi Cave and Panga ya Saidi closest to one another, and with 49% Mota-related, 12% central-African-related and 39% southern-African-related ancestry. These individuals also have ancestry admixed from populations that are associated with food production: Agaw-related for all three, plus western-African-related for Panga ya Saidi (I0595) (Supplementary Note 6).

In contrast to Kenya and Tanzania, we did not observe widespread signals of excess relatedness in Malawi and Zambia. After adjusting for ancestry proportions, most individuals within this geographical cluster are no more related to one another than they are to individuals from Kenya and Tanzania. The only notable exceptions that we found among those in model 3 (Supplementary Note 6) were as follows: (1) among individuals from Fingira (I4426, I4427 and I4468), in particular, two dating to about 6.1 ka; and (2) between the individuals from 9–8 ka from Hora 1 (I2966 and I2967). However, other individuals separated by as little as 100–150 km (Fingira-Hora 1 and Chencherere II-Kalembo) can be fit well with independent mixtures of the same ancestry sources used across the entire study region, including some individuals around 700–1,500 km away. At the same time, the inferred ancestry proportions for the individuals from Malawi and Zambia are quite similar (about 20–30% Mota-related, 5–10% central-African-related and 60–70% southern-African-related), with significant (but small) differences observed for I4426 from Fingira (approximately 11% additional central-African-related ancestry), I4421 from Chencherere (approximately 4% ancestry related to pastoralists), I10726 from Kalembo (approximately 5% less Mota-related ancestry than in Malawi) and I2966 from Hora 1 (a small amount of contamination). We also built an alternative version of our model in which we specified the Malawi individuals as forming a clade descended from a shared three-way admixture event (plus small proportions of additional admixture for the aforementioned individuals) that had only a slightly worse fit—confirming the very similar ancestry proportions among the individuals—but that featured zero shared drift

at the base of the clade and almost none on the internal branches (Supplementary Note 6 and Extended Data Fig. 6).

We examined the relationship between geographical distance and genetic relatedness using a new approach based on the residuals of a model assuming that there is no excess shared genetic drift—that is, we observed the similarity of genotypes within pairs of individuals relative to that predicted solely by differential proportions of the three ancestry sources ([Methods](#)). Using pairs of individuals from either Kenya and Tanzania, or Malawi and Zambia, together with inter-region pairs to plot the residuals as a function of distance, we found greater relatedness at short distances, but with different length scales for the decay of the fitted curves (about 60 km and about 3 km, respectively) (Extended Data Fig. 7a). Similar patterns are also observed if we omit pairs of individuals that were buried at the same site (Extended Data Fig. 7b). Thus, with the caveats that our sampling is not uniform and that not all of the individuals lived contemporaneously, we found on average that (1) individuals from the same or nearby sites are more closely related than predicted solely on the basis of the broad regional genetic structure, but (2) this relatedness extends only over short distances, particularly within Malawi and Zambia.

For a comparative perspective from contemporaneous ancient foragers in temperate environments, where there are more extensive available data, we performed similar analyses for individuals from Mesolithic Europe ($n = 36$, about 12–7 ka) ([Methods](#), Supplementary Table 12 and Extended Data Fig. 7c,d). Both western and eastern/northern Europe also show a pattern of greater relatedness at shorter distances; western Europe is similar to Malawi and Zambia in that almost all of the signal comes from same-site pairs, but eastern/northern Europe has a substantially longer geographical decay scale.

Finally, we compared the ancient individuals to the present-day Sandawe and Hadza groups in Tanzania, who historically or recently practiced foraging lifeways. Previous studies have shown that the Hadza and Sandawe have distinctive ancestry from their neighbours, with unusually high proportions of ancestry related to ancient African foragers^{11,13,14,22}. We built an extended version of model 2 including both groups (Extended Data Fig. 8 and Supplementary Note 6). In contrast to the general pattern for ancient individuals, we could not fit Hadza and Sandawe into a simple regional clade, even after accounting for recent admixture that is probably related to incoming pastoralists and farmers (contributing a total of about 41% and about 62% ancestry for these Hadza and Sandawe individuals, respectively). In particular, both were inferred to share a lineage closest to ancient foragers from north-central Tanzania, but the Hadza had excess allele sharing with the Mota individual, while the Sandawe had excess allele sharing with southern African foragers.

Effective population sizes

We inferred recent (up to about 500 years before the individual's birth) ancestral effective population sizes (N_e) for the higher-coverage ancient individuals by scanning for long runs of homozygosity (ROH), which are expected to be present in the genomes of individuals either from populations with small sizes or whose parents have familial relatedness (the latter resulting in especially long ROH) (Methods and Extended Data Fig. 9). The calculation of N_e depends on several factors in addition to census population size; in particular, N_e is a function of both population density and the distance scale of those social interactions that lead to reproduction. All of the ancient individuals are inferred to have at least one long ROH (> 4 centimorgans (cM)), consistent with broad worldwide trends towards smaller population sizes in more ancient societies²³. However, the N_e estimates vary by an order of magnitude, from individuals with minimal ROH, suggesting relatively larger population sizes (I5950 (Mota): $N_e = 5,470$, 95% confidence interval (CI) = 1,237 to unbounded; I8821 (Kisese II): $N_e = 2,640$, 95% CI = 881–16,424) to those with an ROH of longer than 100 cM, indicative of much smaller population sizes (for example, I8808 (Jawuoyo): $N_e = 377$, 95% CI = 229–678). Overall, the range is similar to many African forager groups today (N_e , around 500–1,500)²⁴ and towards the low end when compared with present-day population sizes worldwide²³.

Discussion

In contrast to previous studies, our results show that a two-way clinal model extending latitudinally from eastern to southern Africa is insufficient to explain observed patterns of genetic variation in ancient sub-Saharan African foragers. Here we demonstrate that central-African-related ancestry (closest to present-day Mbuti among sampled populations), along with Mota-related and southern African-related ancestry, was ubiquitous (in varying proportions) from southwestern Kenya to southeastern Zambia (Fig. 3), with all three components present by at least about 7 ka in Tanzania and about 16 ka in Malawi. Furthermore, when considering ancient African foragers from a wide range of time periods, ecological contexts and archaeological associations, geographical proximity remains the strongest predictor of genetic similarity^{5,11}. Such a pattern may indicate that long-range migrations were rare in the terminal Pleistocene and Holocene, when these individuals lived. This hypothesis is supported by the signals in our admixture graphs of excess genetic relatedness at subregional scales but not at longer-distance scales. Although it is not possible at present to estimate when and how quickly this three-way cline emerged, it must have post-dated both the emergence of the Mota-related lineage around 80–60 ka^{12,16} and, with respect to the

central-African-related ancestry, the split between Aka and Mbuti less than around 50 ka^{25,26}.

Although the observed cline of ancestry remained stable for thousands of years, we propose that it initially arose closer to this split time than to the terminal Pleistocene, and under qualitatively different patterns of mobility and admixture than after it was established. Dispersals, interactions and extensive admixture across eastern and south-central Africa before around 16 ka are evidenced by substantial proportions of ancestry related to the Mota (Ethiopia) individual as far south as Zambia, and ancestry related to southern African foragers as far north as Kenya, in combination with a high degree of homogeneity of ancestry in each subregion after that time. If patterns of mobility and social interactions had remained consistent throughout the Late Pleistocene and Holocene, we would expect to find broad evidence of longer-range ancestry connections within eastern and south-central Africa and beyond, but we observed only two significant plausible instances among our sampled individuals (involving extra central-African-related ancestry in one individual each from Kenya and Malawi).

However, within the three-way population structure, we observed distinct regional trajectories. Individuals from Kenya and Tanzania form three clusters (western Kenya, north-central Tanzania and coastal/island), with individuals in the same cluster showing excess allele sharing even beyond what would be expected from having similar ancestry proportions. This suggests that there is elevated gene flow within each subregion, on a distance scale estimated as approximately 0–100 km. By contrast, the only signals of elevated relatedness detected for individuals from Malawi and Zambia involve those buried at the same site, and can span 1,000–3,600 years (for example, at Fingira). This pattern is best explained by low average human dispersal/interaction distances during much of the Late Pleistocene and Holocene, with the establishment of the broad-scale ancestry cline followed by, on average, more local interactions that differed by region. We observed a similar pattern in ancient foragers from western Europe, whereas those from northern and eastern Europe show longer distance scales of relatedness. This provides genetic evidence that the average distances between where people lived and where their ancestors lived (and therefore the average distances of human movement, especially with respect to reproductive partners) differed among foragers in different regions.

Our genetic findings offer new insights on demographic processes of the Late Pleistocene to Holocene that were previously studied using bioarchaeological, archaeological and linguistic evidence. Beginning approximately 300 ka, archaeological evidence attests to the long-distance movement of materials such as obsidian, presumably facilitated by social networks²⁷. Exchange intensified through the Late Pleistocene to become a hallmark of the LSA, culminating in elaborate transport networks and shared material culture traditions by the Early

Holocene^{1,4,28,29}. However, the extent to which people were moving with objects remains an open question. Our genetic results support a scenario in which human mobility and longer-range gene flow occurred with the development and elaboration of long-distance networks approximately 80–20 ka, contributing to the formation of a population structure that persisted over tens of thousands of years during a period when people were living locally.

Genetic evidence also adds weight to arguments for changing Late Pleistocene interaction spheres, with limited gene flow accompanying changes in behaviour and possibly linguistic boundaries. However, at this juncture, we are unable to assess hypothesized population density shifts, based on heightened evidence for symbolic expression at LSA sites and the appearance and disappearance of specific artefact types^{8,9,30,31,32}. Our genetic estimates of recent effective population size are consistent with those of at least some present-day African foragers²⁴, but they are not good comparators due to demographic pressures recently placed on such groups³³. Furthermore, small subpopulations with limited gene flow could result in low ancestral effective population sizes even if the region's total population is high. Preservation of genetic diversity through the existence of many subpopulations over long time scales could also be a contributor to the high levels of genetic diversity observed in most present-day sub-Saharan African groups.

The LSA archaeological record testifies to the appearance of well-defined, temporally and spatially bounded material culture traditions^{34,35}, a phenomenon that is sometimes referred to as regionalization. Faunal data indicate subsistence intensification after around 20 ka^{36,37}, and linguistic data also suggest shifts toward local interactions, reflected in the fact that, today, communities that are presently or historically associated with foraging in central, eastern and southern Africa speak languages of different families (in central Africa, adopted from recent arrivals). At the same time, past regional connectivity and borrowing was such that linguists previously characterized 'click' languages as a single family, and the proposed grouping of Khoë–Kwadi–Sandawe strengthens evidence for longer-distance ties between eastern and southern Africa^{38,39}. Our genetic results confirm that trends toward regionalization extended to human population structure, suggesting that decreasing gene flow accompanied changes in behaviour and possibly language.

Conclusions

Demographic transformations in the past approximately 5,000 years have fundamentally altered regional population structures and largely erased what was, by the Late Pleistocene, a well-established three-way cline of eastern-, southern- and central-African-related ancestry that extended across eastern and south-central Africa.

Groups who historically forage have frequently been pushed to marginal environments and have experienced transformative demographic changes, making it difficult to learn about deep history from present-day DNA. Today, Africa houses the greatest human genetic diversity, but undersampling of both living and ancient individuals obscures the origins of this diversity⁴⁰. We show that aDNA from tropical Africa can survive from the Pleistocene and reveal patterns that could not be inferred from populations that lived even a few millennia later, underscoring the breadth of African genetic diversity and the importance of eastern and south-central Africa as long-term reservoirs of human interaction and innovation.

Methods

Skeletal samples

The skeletal remains that were sampled in this study are curated at the National Museum of Kenya (Kisese II), the National Museum of Tanzania (Mlambalasi), the Malawi Department of Museums and Monuments (Hora 1 and Fingira) and the Livingstone Museum (Kalembo), and sampling permissions and protocols are described in Supplementary Note 3. Individuals were chosen based on their associated LSA archaeological contexts, and skeletal samples were selected to maximize the likelihood of yielding authentic aDNA and to minimize damage. The Fingira phalanx was an isolated find from a mixed excavation context, and too small to provide both aDNA and a direct date. A list of both successful and failing samples is provided in Supplementary Table 1. Direct radiocarbon dating was attempted on five of the six successful individuals at the Pennsylvania State University Radiocarbon Laboratory using established methods and quality control measures for collagen purification^{43,44} before accelerator mass spectrometry analysis (Supplementary Note 4). A list of direct date and stable isotopic results for the two successfully dated individuals, and indirect dates where available for the other individuals, is provided in Supplementary Tables 3 and 4. All dates were calibrated using OxCal (v.4.4)⁴⁵, with a uniform prior ($U(0,100)$) to model a mixture of two curves: IntCal20 (ref. 46) and SHCal20 (ref. 47).

aDNA laboratory work

We successfully generated genome-wide aDNA data from a total of six human skeletal elements: five petrous bones and one phalanx. We processed an additional six petrous bones, eight teeth and 11 other bones in the same manner but did not obtain usable DNA (Supplementary Table 1). In clean room facilities at Harvard Medical School, we cleaned the outer surfaces of the samples and then sandblasted (petrous bones)⁴⁸ or drilled (other bones and teeth) to obtain powder (additional information for the 15 previously published samples reported here with increased coverage can be found in

refs. [11](#),[13](#),[15](#),[16](#)). We extracted DNA [49](#),[50](#),[51](#) and prepared barcoded sequencing libraries (between one and six libraries for the six newly reported individuals, and between one and eight additional libraries for the previously reported individuals: from Mota Cave in Ethiopia [15](#) (I5950); White Rock Point in Kenya [13](#) (I8930); Gishmangeda Cave in Tanzania [13](#) (I13763, I13982 and I13983); Chencherere II (I4421 and I4422), Fingira (I4426, I4427 and I4468) and Hora 1 (I2967) in Malawi [11](#); and Shum Laka in Cameroon [16](#) (I10871, I10872, I10873 and I10874), treating in almost all cases with uracil-DNA-glycosylase (UDG) to reduce aDNA damage artefacts [52](#),[53](#),[54](#). We used two rounds of targeted in-solution hybridization to enrich the libraries for molecules from the mitochondrial genome and overlapping a set of around 1.2 million nuclear SNPs [55](#),[56](#),[57](#),[58](#) and sequenced in pools on the Illumina NextSeq 500 and HiSeqX10 machines with 76 bp or 101 bp paired-end reads. Further details on each library are provided in Supplementary Table [2](#). For the Mota individual (I5950), we also generated whole-genome shotgun sequencing data, using the same (pre-enrichment) library, with seven lanes with 101 bp paired-end reads (on Illumina HiSeq X Ten machines) yielding approximately 26× coverage (1,176,635 sites covered from the capture SNP set).

Bioinformatics procedures

From the raw sequencing data, we used barcode information to assign reads to the proper libraries (allowing at most one mismatch per read pair). We merged overlapping reads (at least 15 bases), trimmed barcode and adapter sequences from the ends, and mapped to the mtDNA reference genome RSRS [59](#) and the human reference genome hg19 using BWA (v.0.6.1) [60](#). After alignment, we removed duplicate reads and reads with mapping quality less than 10 (30 for shotgun data) or with length less than 30 bases. To prepare data for analysis, we disregarded terminal bases of the reads (2 for UDG-treated libraries and 5 for untreated, to eliminate most damage-induced errors), merged the .bam files for all libraries from each individual, and called pseudohaploid genotypes (one allele chosen at random from the reads aligning at each SNP). The high coverage for the Mota whole-genome shotgun data enabled us to call diploid genotypes; we used the procedure from ref. [26](#), including storing the genotypes in a fasta-style format that is easily accessible through the cascertain and cTools software. Code for bioinformatics tools and data workflows is provided at GitHub (<https://github.com/DReichLab/ADNA-Tools> and <https://github.com/DReichLab/adna-workflow>).

Uniparental markers and authentication

We determined the genetic sex of each individual according to the ratio of DNA fragments mapping to the X and Y chromosomes [61](#). We called mtDNA haplogroups

using HaploGrep2 (ref. [62](#)), comparing informative positions to PhyloTree Build 17 (ref. [63](#)) (Supplementary Table [6](#)). For four individuals (I2967, I4422, I4426 and I19528) with evidence of haplogroups that split partially but not fully along more specific lineages, we use the notation [HaploGrep2 call]/[sub-clade direction] (for example, L0f/L0f3 for a split on the lineage leading to L0f3 but not within L0f3). For males, we called Y-chromosome haplogroups by comparing their derived mutations with the Y-chromosome phylogeny provided by YFull (<https://yfull.com>).

We evaluated the authenticity of the data first by measuring the rate of characteristic aDNA damage-induced errors at the ends of sequenced molecules. We next searched directly for possible contamination by examining (1) the X/Y ratio mentioned above (in case of contamination by sequences from the opposite sex), (2) the consistency of mtDNA-mapped sequences with the haplogroup call for each individual^{[64](#)} and (3) the heterozygosity rate at variable sites on the X chromosome (for males only)^{[65](#)}. Two individuals (I2966 from Hora 1 and I13763 from Gishmageda Cave) had non-negligible evidence of contamination from these metrics and also displayed excess allele sharing with non-Africans in the admixture graph analysis; we were able to fit them in the final model after allowing ‘artificial’ admixture from a European-related source (6% and 9%, respectively). We also restricted ourselves to damaged reads in making the mtDNA haplogroup call for I2966. Further details are provided in Supplementary Table [2](#) and Supplementary Note [5](#).

Familial relatives

We searched for close family relatives by computing, for each pair of individuals, the proportion of matching alleles (from all targeted SNPs) when sampling one read at random per site from each. We then compared these proportions to the rates when sampling two alleles from the same individual—mismatches are expected to be twice as common for unrelated individuals as for within-individual comparisons, with family relatives intermediate. We found one possible instance between the two individuals from White Rock Point (approximately second-degree relatives, but uncertain due to low coverage) (Extended Data Fig. [1b](#))

Dataset for genome-wide analyses

We merged our newly generated data with published data from ancient and present-day individuals^{[11,12,13,14,16,25,26,66,67](#)}. We performed our genome-wide analyses using the set of autosomal SNPs from our target enrichment (about 1.1 million).

PCA

We performed a supervised PCA using the smartpca software⁶⁸, using three populations (Jul'hoansi, Mbuti and Dinka; four individuals each, from ref. ²⁶, were chosen to create a broad separation in the PCA between highly divergent ancestral lineages from southern, central and eastern Africa) to define a two-dimensional plane of variation, and projected all other present-day and ancient individuals (using the lsqproject and shrinkmode options). This procedure captures the genetic structure of the projected individuals in relation to the groups used to create the axes, reducing the effects of population-specific genetic drift in determining the positions of the individuals shown in the plot, as well as bias due to missing data for the ancient individuals.

f-statistics

We computed *f*-statistics in ADMIXTOOLS⁶⁹, with standard errors estimated by block jackknife. To facilitate the use of low-coverage data, we used a new program, qpstats (included as part of the ADMIXTOOLS package), together with the option ‘allsnps: YES,’ for both stand-alone f_4 -statistics and statistics for use in qpWave and qpGraph (see below). In brief, qpstats solves a system of equations based on *f*-statistic identities to enable the estimation of a consistent set of statistics while maximizing the available coverage and reducing noise in the presence of missing data; full details are provided in Supplementary Note ⁷. We computed statistics of the form $f_4(\text{Ind1}, \text{Ind2}; \text{Ref1}, \text{Ref2})$, where Ind1 and Ind2 are ancient individuals from Kenya, Tanzania or Malawi/Zambia, and Ref1 and Ref2 are either ancient southern African foragers (AncSA, listed in Extended Data Table ¹), the Mota individual or present-day Mbuti. These groups were chosen in light of our PCA results and the previous evidence for ancestry related to some or all of them among ancient eastern and south-central African foragers^{5,11,14}.

qpWave analysis

The qpWave software⁷⁰ estimates how many distinct sources of ancestry (from 1 to the size of the test set) are necessary to explain the allele-sharing relationships between the specified test populations and the outgroups (where ‘distinct’ means different phylogenetic split points relative to the outgroups). Each test returns results for different ranks of the allele-sharing matrix, where rank k implies $k + 1$ ancestry sources. For absolute fit quality, we give the ‘tail’ P value, where a higher value indicates a better fit. We also give ‘taildiff’ P values as relative measures comparing consecutive rank levels, where a higher value indicates less improvement in the fit when adding another ancestry source. As our base test set, we used the 12 ancient eastern and south-central African forager individuals (3 from Kenya, 3 from Tanzania, 5 from Malawi and 1 from Zambia) from our admixture graph Model 3 who did not

have evidence of either admixture from food producers or contamination. We also compared results when adding the Mota individual to the test set. As outgroups, we used Altai Neanderthal, Mota and the following eight present-day groups: Ju'hoansi, †Khomani, Mbuti, Aka, Yoruba, French, Agaw and Aari, with the last two (as well as Mota) omitted when we moved Mota to the test set.

Dates of admixture

We inferred dates of admixture using the DATES software²¹. We used a minimum genetic distance of 0.6 cM, a maximum of 1 M and a bin size of 0.1 cM. As reference populations, we used ancient southern African foragers together with one of Mota, Dinka, Luhya, Yoruba or European-American individuals (the latter three from 1000 Genomes: LWK, YRI and CEU). The results assume an average generation interval of 28 years, and standard errors were estimated by block jackknife.

Admixture graph fitting

We built admixture graphs using the qpGraph software in ADMIXTOOLS⁶⁹. We chose to analyse each eastern and south-central forager individual separately rather than form subgroups (for example, by site or time period) to study both broad- and fine-scale structure (through relationships between individuals with both low and high degrees of ancestral similarity). Although such an approach was facilitated by our relatively manageable sample sizes, it also relied on the ability to compute *f*-statistics with our qpfstats methodology (further details are provided in Supplementary Note 7 and the ‘*f*-statistics’ section above) to make use of all available SNPs for individuals with low-coverage data. For all of the models, we used the options ‘outpop: NULL’, ‘lambdascale: 1’ and ‘diag: 0.0001.’ We also specified larger values of the ‘initmix’ parameter to explore the space of graph parameters more thoroughly: 100,000, 150,000 and 200,000 for models 1–3 (and additional models built from them), respectively.

We began with a version of the admixture graph from ref. 16, to which we added three high-coverage ancient forager individuals (from Jawuoyo, Kisese II and Fingira) to create model 1. We then extended our model to more individuals. We used a procedure in which we (1) added each other ancient individual one by one to model 1 and evaluated the fit; (2) built an intermediate-size model 2 including a total of 11 geographically diverse eastern and south-central African foragers; (3) added the remaining individuals one by one to model 2; and (4) built our final Model 3 with all 18 individuals above a coverage threshold of 0.05× (Supplementary Note 6). In steps (1) and (3), as a starting point, we assumed a simple form of admixture (as in model 1) whereby all eastern and south-central African individuals derived their ancestry from exactly the same three sources (in varying proportions). If we found that an individual

did not fit well when added in this manner, we noted the specific violation(s) to determine whether the likely cause(s) were excess relatedness to certain other individuals, distinct source(s) for the three-way admixture, admixture from other populations, or contamination or other artefacts. For the two individuals (one from Hora 1 and one from Gishimangeda) with evidence of appreciable contamination, we included dummy admixture events contributing non-African-related ancestry. Full details on our fitting procedures are provided in Supplementary Note 6.

Excess relatedness analysis

To study excess relatedness between individuals after correcting for different proportions of Mota-related, central-African-related and southern-African-related ancestry, we built an admixture graph similar to our main model 3, but in which each forager individual is descended from an independent mixture of the three ancestry components, without accounting for excess shared genetic drift. We also included four additional individuals with lower coverage (three from Kenya and one from Chenchere II in Malawi), but excluded the two early individuals from Hora 1 due to their much greater time depth compared with other individuals in the model. Finally, for individuals modelled with admixture beyond the primary three sources (that is, pastoralist-related ancestry for four individuals, western-African-related ancestry for the Panga ya Saidi individual and the excess central-African-related ancestry for the Kakapel individual, plus dummy admixture for contamination), we locked the relevant branch lengths and mixture proportions at their values from model 3 to prevent compensation for the inaccuracies in the model by these parameters. We next used the residuals (fitted minus observed values) of each outgroup f_3 -statistic $f_3(\text{Neanderthal}; X, Y)$ to quantify the excess relatedness between individuals X and Y that is unaccounted for by the model. In other words, we fit each individual as we did during the add-one phase of the main admixture graph inference procedure (except here all simultaneously) but now, instead of using the model violations to inform the building of a well-fitting model, we used them directly as the output of the analysis.

We plotted the excess relatedness residuals for each pair of individuals as a function of great-circle distance between sites, as computed using the haversine formula (also adding a dummy value of 0.001 km to each distance). We fit curves to the data with the functional form $1/mx$, additionally allowing for translation (full equation: $y = 1/(mx + a) + b$, where y is excess relatedness, x is distance, and m , a and b are fitted constants) through inverse-variance-weighted least squares. We also omitted the point corresponding to the pair of individuals from White Rock Point (Kenya) because of their evidence for close familial relatedness (see above). Finally, we computed a decay scale for the curves given by the formula $(e - 1) \times a/m$ (where e is Euler's number). We note that a residual (that is, y axis) value of zero has no special meaning in the plots.

For Mesolithic Europe, we performed two analogous analyses, one for the western part of the continent and one for eastern and northern. In the first analysis, we selected individuals with predominantly western hunter-gatherer (WHG)-related ancestry, while in the second analysis, we selected individuals who could be modelled as admixed with WHG as well as eastern hunter-gatherer (EHG)-related ancestry (Supplementary Table 12). In both cases, we built simple admixture graph models to estimate the residuals. For western Europe, we used the Upper Palaeolithic Ust'-Ishim individual from Russia⁷¹ as an outgroup and fit all of the test individuals as descending from a single ancestral lineage. For eastern and northern Europe, we used Ust'-Ishim as an outgroup, Mal'ta 1 from Siberia⁷² for a representative of ancient northern Eurasian ancestry, Villabruna from Italy⁷³ for WHG, Karelia from Russia^{56,58,73} for EHG (admixed with ancestry related to Mal'ta and to Villabruna) and finally the test individuals each with independent mixtures of WHG and EHG-related ancestry in varying proportions.

Effective population size inference

We called ROH starting with counts of reads for each allele at the set of target SNPs (rather than our pseudohaploid genotype data), which we converted to normalized Phred-scaled likelihoods. We performed the calling using BCFtools/RoH⁷⁴, which is able to accommodate unphased, relatively low-coverage data (at least for calling long ROH) and does not rely on a reference haplotype panel. The method is also robust to modest rates of genotype error, such as that which could occur here as a result of aDNA damage or contamination, although we recommend some caution in interpreting the results for I2966 (Hora 1) and I0589 (Kuumbi Cave; for this analysis only, we used the version of the published data with UDG-minus libraries included, for a total of around 2× average coverage). We also note that the nature of any possible effect on the final inferences is uncertain; errors could deflate the population size estimates by breaking up ROH, but they could also break very long ROH into shorter but still long blocks, which have the strongest influence on the population size estimates. In the absence of population-level data from related groups, we specified a single default allele frequency ('--AF-dflt 0.4') and no genetic map (although we subsequently converted physical positions to genetic distances using ref. ⁷⁵, which we expect to be reasonably accurate at the length scales that we are interested in). For our analyses, we retained ROH blocks with length >4 cM. In three instances, we merged blocks with a gap of <0.5 cM and at most two apparent heterozygous sites between them.

From the ROH results, we applied the maximum likelihood approach from ref. ²³ to estimate recent ancestral effective population sizes (N_e). We used all ROH blocks of longer than 4 cM, except for three individuals (KPL001 from Kakapel in Kenya, I9028

from St Helena, South Africa, and I9133 from Faraoskop, South Africa) with high proportions of very long ROH (a sign of familial relatedness between parents—approximately at the first-cousin level in these cases—rather than of longer-term low population size), for whom we used only blocks from 4–8 cM.

We note that, even within a randomly mating population, the number and extent of ROH can vary substantially between individuals, which is reflected in the large standard errors of the N_e estimates for small sample sizes. We also note that recent admixture can influence ROH (and therefore N_e estimates) by making coalescence between an individual's two chromosomes less likely, but on the basis of the other results of our study, we do not expect a substantial effect for these individuals.

Reporting summary

Further information on research design is available in the [Nature Research Reporting Summary](#) linked to this paper.

Data availability

The aligned sequences are available through the European Nucleotide Archive under accession number [PRJEB49291](#). Genotype data used in the analysis are available online (<https://reich.hms.harvard.edu/datasets>). Any other relevant data are available from the corresponding authors on reasonable request.

Code availability

Code for the bioinformatics tools and data workflows is provided at GitHub (<https://github.com/DReichLab/ADNA-Tools> and <https://github.com/DReichLab/adna-workflow>).

References

1. Tryon, C. A. The Middle/Later Stone Age transition and cultural dynamics of late Pleistocene East Africa. *Evol. Anthropol. Issues News Rev.* **28**, 267–282 (2019).
2. Mirazón Lahr, M. The shaping of human diversity: filters, boundaries and transitions. *Philos. Trans. R. Soc. B* **371**, 20150241 (2016).
3. Hollfelder, N., Breton, G., Sjödin, P. & Jakobsson, M. The deep population history in Africa. *Hum. Mol. Genet.* **30**, R2–R10 (2021).

4. Miller, J. M. & Wang, Y. V. Ostrich eggshell beads reveal 50,000-year-old social network in Africa. *Nature* **601**, 234–239 (2021).
5. Vicente, M. & Schlebusch, C. M. African population history: an ancient DNA perspective. *Curr. Opin. Genet. Dev.* **62**, 8–15 (2020).
6. McBrearty, S. & Brooks, A. S. The revolution that wasn't: a new interpretation of the origin of modern human behavior. *J. Hum. Evol.* **39**, 453–563 (2000).
7. d'Errico, F. et al. Trajectories of cultural innovation from the Middle to Later Stone Age in Eastern Africa: personal ornaments, bone artifacts, and ochre from Panga ya Saidi, Kenya. *J. Hum. Evol.* **141**, 102737 (2020).
8. Shipton, C. et al. The Middle to Later Stone Age transition at Panga ya Saidi, in the tropical coastal forest of eastern Africa. *J. Hum. Evol.* **153**, 102954 (2021).
9. Ambrose, S. H. Chronology of the Later Stone Age and food production in East Africa. *J. Archaeol. Sci.* **25**, 377–392 (1998).
10. Scerri, E. M. L. et al. Did our species evolve in subdivided populations across Africa, and why does it matter? *Trends Ecol. Evol.* **33**, 582–594 (2018).
11. Skoglund, P. et al. Reconstructing prehistoric African population structure. *Cell* **171**, 59–71 (2017).
12. Schlebusch, C. M. et al. Southern African ancient genomes estimate modern human divergence to 350,000 to 260,000 years ago. *Science* **358**, 652–655 (2017).
13. Prendergast, M. E. et al. Ancient DNA reveals a multistep spread of the first herders into sub-Saharan Africa. *Science* **365**, eaaw6275 (2019).
14. Wang, K. et al. Ancient genomes reveal complex patterns of population movement, interaction, and replacement in sub-Saharan Africa. *Sci. Adv.* **6**, eaaz0183 (2020).
15. Gallego Llorente, M. et al. Ancient Ethiopian genome reveals extensive Eurasian admixture in Eastern Africa. *Science* **350**, 820–822 (2015).
16. Lipson, M. et al. Ancient West African foragers in the context of African population history. *Nature* **577**, 665–670 (2020).
17. Rito, T. et al. A dispersal of *Homo sapiens* from southern to eastern Africa immediately preceded the out-of-Africa migration. *Sci. Rep.* **9**, 4728 (2019).

18. Tishkoff, S. A. et al. History of click-speaking populations of Africa inferred from mtDNA and Y chromosome genetic variation. *Mol. Biol. Evol.* **24**, 2180–2195 (2007).
19. Soares, P. et al. The expansion of mtDNA haplogroup L3 within and out of Africa. *Mol. Biol. Evol.* **29**, 915–927 (2012).
20. Silva, M. et al. 60,000 years of interactions between Central and Eastern Africa documented by major African mitochondrial haplogroup L2. *Sci. Rep.* **5**, 12526 (2015).
21. Narasimhan, V. M. et al. The formation of human populations in South and Central Asia. *Science* **365**, eaat7487 (2019).
22. Tishkoff, S. A. et al. The genetic structure and history of Africans and African Americans. *Science* **324**, 1035–1044 (2009).
23. Ringbauer, H., Novembre, J. & Steinrücken, M. Parental relatedness through time revealed by runs of homozygosity in ancient DNA. *Nat. Commun.* **12**, 5425 (2021).
24. Hitchcock, R. K. Foragers and food production in Africa: a cross-cultural and analytical perspective. *World J. Agric. Soil Sci.* **1**, WJASS.MS.ID.000522 (2019).
25. Fan, S. et al. African evolutionary history inferred from whole genome sequence data of 44 indigenous African populations. *Genome Biol.* **20**, 82 (2019).
26. Mallick, S. et al. The Simons Genome Diversity Project: 300 genomes from 142 diverse populations. *Nature* **538**, 201–206 (2016).
27. Brooks, A. S. et al. Long-distance stone transport and pigment use in the earliest Middle Stone Age. *Science* **360**, 90–94 (2018).
28. Merrick, H., Brown, F. H. & Nash, W. P. in *Society, Culture and Technology in Africa* (ed. Childs, S. T.) 29–44 (MASCA, 1994).
29. Stewart, B. A. et al. Ostrich eggshell bead strontium isotopes reveal persistent macroscale social networking across late Quaternary southern Africa. *Proc. Natl Acad. Sci. USA* **117**, 6453–6462 (2020).
30. Archer, W. Carrying capacity, population density and the later Pleistocene expression of backed artefact manufacturing traditions in Africa. *Philos. Trans. R. Soc. B* **376**, 20190716 (2021).

31. Mackay, A., Stewart, B. A. & Chase, B. M. Coalescence and fragmentation in the late Pleistocene archaeology of southernmost Africa. *J. Hum. Evol.* **72**, 26–51 (2014).
32. Tryon, C. A. & Faith, J. T. A demographic perspective on the Middle to Later Stone Age transition from Nasera rockshelter, Tanzania. *Philos. Trans. R. Soc. B* **371**, 20150238 (2016).
33. Hitchcock, R. K., Sapignoli, M. & Babchuk, W. A. Settler colonialism, conflicts, and genocide: interactions between hunter-gatherers and settlers in Kenya, and Zimbabwe and northern Botswana. *Settl. Colon. Stud.* **5**, 40–65 (2015).
34. Tryon, C. A. & Ranhorn, K. L. in *Culture History and Convergent Evolution* (ed. Groucutt, H. S.) 143–156 (Springer, 2020).
35. Barham, L. & Mitchell, P. *The First Africans: African Archaeology from the Earliest Toolmakers to Most Recent Foragers* (Cambridge University Press, 2008).
36. Prendergast, M. E. *The History of Eastern African Foragers*,
<https://doi.org/10.1093/acrefore/9780190277734.013.405> (Oxford Research Encyclopedias, 2020).
37. Thompson, J. C. *Faunal Analysis in African archaeology*,
<https://doi.org/10.1093/acrefore/9780190854584.013.44> (Oxford Research Encyclopedias, 2020).
38. Güldemann, T. & Elderkin, E. D. In *Khoisan Language and Linguistics: The Riezlern Symposium 2003* vol. 17 (eds Brenzinger, M. & König, C.) 15–52 (Rüdiger Köppe, 2010).
39. Güldemann, T. In *Beyond ‘Khoisan’: Historical Relations in the Kalahari Basin* (eds Güldemann, T. & Fehn, A.-M.) 1–41 (John Benjamins, 2014).
40. Choudhury, A. et al. High-depth African genomes inform human migration and health. *Nature* **586**, 741–748 (2020).
41. Abruzzi, W. S. In *Beyond the Myths of Culture: Essays in Cultural Materialism* (ed. Ross, E. B.) 1–31 (Academic, 1980).
42. NASA Shuttle Radar Topography Mission Global 3 arc second,
<https://doi.org/10.5067/MEASUREs/SRTM/SRTMGL3.003> (NASA, 2013).

43. Kennett, D. J. Archaeogenomic evidence reveals prehistoric matrilineal dynasty. *Nat. Commun.* **8**, 14115 (2017).
44. Lohse, J. C., Culleton, B. J., Black, S. L. & Kennett, D. J. A precise chronology of Middle to Late Holocene bison exploitation in the far southern Great Plains. *J. Tex. Archeol. Hist.* **1**, 94–126 (2014).
45. Bronk Ramsey, C. Bayesian analysis of radiocarbon dates. *Radiocarbon* **51**, 337–360 (2009).
46. Reimer, P. J. et al. The IntCal20 Northern Hemisphere radiocarbon age calibration curve (0–55 cal kBP). *Radiocarbon* **62**, 725–757 (2020).
47. Hogg, A. G. et al. SHCal20 Southern Hemisphere calibration, 0–55,000 years cal BP. *Radiocarbon* **62**, 759–778 (2020).
48. Pinhasi, R., Fernandes, D. M., Sirak, K. & Cheronet, O. Isolating the human cochlea to generate bone powder for ancient DNA analysis. *Nat. Protoc.* **14**, 1194–1205 (2019).
49. Dabney, J. et al. Complete mitochondrial genome sequence of a Middle Pleistocene cave bear reconstructed from ultrashort DNA fragment. *Proc. Natl Acad. Sci. USA* **110**, 15758–15763 (2013).
50. Korlevic, P. et al. Reducing microbial and human contamination in DNA extractions from ancient bones and teeth. *Biotechniques* **59**, 87–93 (2015).
51. Rohland, N., Glocke, I., Aximu-Petri, A. & Meyer, M. Extraction of highly degraded DNA from ancient bones, teeth and sediments for high-throughput sequencing. *Nat. Protoc.* **13**, 2447–2461 (2018).
52. Rohland, N., Harney, E., Mallick, S., Nordenfelt, S. & Reich, D. Partial uracil-DNA-glycosylase treatment for screening of ancient DNA. *Philos. Trans. R. Soc. Lond. B* **370**, 20130624 (2015).
53. Briggs, A. W. et al. Removal of deaminated cytosines and detection of in vivo methylation in ancient DNA. *Nucleic Acids Res.* **38**, e87 (2010).
54. Gansauge, M.-T., Aximu-Petri, A., Nagel, S. & Meyer, M. Manual and automated preparation of single-stranded DNA libraries for the sequencing of DNA from ancient biological remains and other sources of highly degraded DNA. *Nat. Protoc.* **15**, 2279–2300 (2020).

55. Fu, Q. et al. DNA analysis of an early modern human from Tianyuan Cave, China. *Proc. Natl Acad. Sci. USA* **110**, 2223–2227 (2013).
56. Haak, W. et al. Massive migration from the steppe was a source for Indo-European languages in Europe. *Nature* **522**, 207–211 (2015).
57. Lazaridis, I. et al. Genomic insights into the origin of farming in the ancient Near East. *Nature* **536**, 419–424 (2016).
58. Mathieson, I. et al. Genome-wide patterns of selection in 230 ancient Eurasians. *Nature* **528**, 499–503 (2015).
59. Behar, D. M. et al. A “Copernican” reassessment of the human mitochondrial DNA tree from its root. *Am. J. Hum. Genet.* **90**, 675–684 (2012).
60. Li, H. & Durbin, R. Fast and accurate long-read alignment with Burrows–Wheeler transform. *Bioinformatics* **26**, 589–595 (2010).
61. Skoglund, P., Storå, J., Götherström, A. & Jakobsson, M. Accurate sex identification of ancient human remains using DNA shotgun sequencing. *J. Archaeol. Sci.* **40**, 4477–4482 (2013).
62. Weissensteiner, H. et al. HaploGrep 2: mitochondrial haplogroup classification in the era of high-throughput sequencing. *Nucleic Acids Res.* **44**, W58–W63 (2016).
63. van Oven, M. & Kayser, M. Updated comprehensive phylogenetic tree of global human mitochondrial DNA variation. *Hum. Mutat.* **30**, E386–E394 (2009).
64. Fu, Q. et al. A revised timescale for human evolution based on ancient mitochondrial genomes. *Curr. Biol.* **23**, 553–559 (2013).
65. Korneliussen, T. S., Albrechtsen, A. & Nielsen, R. ANGSD: analysis of next generation sequencing data. *BMC Bioinform.* **15**, 356–356 (2014).
66. 1000 Genomes Project Consortium. A global reference for human genetic variation. *Nature* **526**, 68–74 (2015).
67. Bergström, A. et al. Insights into human genetic variation and population history from 929 diverse genomes. *Science* **367**, eaay5012 (2020).
68. Patterson, N., Price, A. L. & Reich, D. Population structure and eigenanalysis. *PLoS Genet.* **2**, e190 (2006).

69. Patterson, N. et al. Ancient admixture in human history. *Genetics* **192**, 1065–1093 (2012).
70. Reich, D. et al. Reconstructing Native American population history. *Nature* **488**, 370–374 (2012).
71. Fu, Q. et al. Genome sequence of a 45,000-year-old modern human from western Siberia. *Nature* **514**, 445–449 (2014).
72. Raghavan, M. et al. Upper Palaeolithic Siberian genome reveals dual ancestry of Native Americans. *Nature* **505**, 87–91 (2014).
73. Fu, Q. et al. The genetic history of Ice Age Europe. *Nature* **534**, 200–205 (2016).
74. Narasimhan, V. et al. BCFtools/RoH: a hidden Markov model approach for detecting autozygosity from next-generation sequencing data. *Bioinform. Oxf. Engl.* **32**, 1749–1751 (2016).
75. Myers, S., Bottolo, L., Freeman, C., McVean, G. & Donnelly, P. A fine-scale map of recombination rates and hotspots across the human genome. *Science* **310**, 321–324 (2005).
76. Pfeiffer, S., Harrington, L. & Lombard, M. The people behind the samples: biographical features of past hunter-gatherers from KwaZulu-Natal who yielded aDNA. *Int. J. Paleopathol.* **24**, 158–164 (2019).

Acknowledgements

We thank the authorities in Kenya, Tanzania, Malawi and Zambia for permission to study these ancient individuals (Supplementary Note 3); J. Stock, A. Manica and D. Bradley for previous work on the individual from Mota Cave, Ethiopia; J. Sealy for helping with the proposal to redate the Hora 1 individual; and L. Eccles for help with radiocarbon dating. Radiocarbon work was supported by the NSF Archaeometry programme (grant no. BCS-1460369) to D.J.K. and B.J.C. Excavations leading to recovery of Kahora 1 and 2 were supported by the National Geographic Society (NGS-53412R-18 to J.C.T.), Yale University and the Hyde Family Foundations. E.A.S. acknowledges support from the Social Sciences and Humanities Research Council of Canada (fellowships 756-2017-0456, BPF 169449). M.E.P. was supported the Radcliffe Institute for Advanced Study during project development. D.R. is an Investigator of the Howard Hughes Medical Institute and was also funded by NIH grants R01-GM100233 and R01-HG012287; by John Templeton Foundation grant 61220; by a private donation from J.-F. Clin; and by the Allen Discovery Center programme, a Paul G. Allen Frontiers Group advised programme of the Paul G. Allen

Family Foundation. Open access publication was made possible by The John Templeton Foundation, Yale University Council on African Studies and Rice University School of Social Sciences.

Author information

Author notes

1. These authors contributed equally: Mark Lipson, Elizabeth A. Sawchuk

Affiliations

1. Department of Genetics, Harvard Medical School, Boston, MA, USA

Mark Lipson, Kendra A. Sirak, Iñigo Olalde, Nadin Rohland, David Reich & Mary E. Prendergast

2. Department of Human Evolutionary Biology, Harvard University, Cambridge, MA, USA

Mark Lipson, Kendra A. Sirak, Nick Patterson & David Reich

3. Department of Anthropology, University of Alberta, Edmonton, Alberta, Canada

Elizabeth A. Sawchuk & Pamela R. Willoughby

4. Department of Anthropology, Stony Brook University, Stony Brook, NY, USA

Elizabeth A. Sawchuk & Jason Lewis

5. Department of Anthropology and Peabody Museum of Natural History, Yale University, New Haven, CT, USA

Jessica C. Thompson & Alex Bertacchi

6. Institute of Human Origins, School of Human Evolution and Social Change, Arizona State University, Tempe, AZ, USA

Jessica C. Thompson & Kathryn L. Ranhorn

7. Department of Biomolecular Engineering, University of California, Santa Cruz, Santa Cruz, CA, USA

Jonas Oppenheimer

8. Department of Anthropology, University of Connecticut, Storrs, CT, USA

Christian A. Tryon

9. Department of Anthropology, Harvard University, Cambridge, MA, USA

Christian A. Tryon

10. Human Origins Program, National Museum of Natural History, Smithsonian Institution, Washington, DC, USA

Christian A. Tryon

11. Department of History, Georgetown University, Washington, DC, USA

Kathryn M. de Luna

12. BIOMICs Research Group, University of the Basque Country UPV/EHU, Vitoria-Gasteiz, Spain

Iñigo Olalde

13. Department of Anthropology, University of Illinois Urbana-Champaign, Urbana, IL, USA

Stanley H. Ambrose

14. Department of Anthropology, University of South Florida, St Petersburg, FL, USA

John W. Arthur & Kathryn J. W. Arthur

15. School of Health Sciences, Jaramogi Oginga Odinga University of Science and Technology, Bondo, Kenya

George Ayodo

16. Department of Anthropology, University of Oklahoma, Norman, OK, USA

Jessica I. Cerezo-Román

17. Institutes of Energy and the Environment, Pennsylvania State University, University Park, PA, USA

Brendan J. Culleton

18. Anthropology Program, California State University—Channel Islands, Camarillo, CA, USA

Matthew C. Curtis

19. Independent researcher, New Haven, CT, USA

Jacob Davis

20. National Museums of Tanzania, Dar es Salaam, Tanzania

Agness O. Gidna & Amandus Kwekason

21. Sol Solutions LLC, Scottsdale, AZ, USA

Annalys Hanson

22. Malawi Department of Museums and Monuments, Lilongwe, Malawi

Potiphar Kaliba & Fredrick Mapemba

23. Department of Anthropology, Rice University, Houston, TX, USA

Maggie Katongo & Mary E. Prendergast

24. Livingstone Museum, Livingstone, Zambia

Maggie Katongo & George Mudenda

25. Department of Integrative Anatomical Sciences, University of Southern California, Los Angeles, CA, USA

Myra F. Laird

26. Department of Archaeology and Heritage Studies, University of Dar es Salaam, Dar es Salaam, Tanzania

Audax Z. P. Mabulla

27. Department of Human Biology, University of Cape Town, Cape Town, South Africa

Alan Morris

28. Mzuzu University, Mzuzu, Malawi

Raphael Mwafulirwa

29. University of Malawi, Zomba, Malawi

Daudi Mwangomba

30. Department of Earth Sciences, National Museums of Kenya, Nairobi, Kenya

Emmanuel Ndiema, Christine Ogola & Fredrick Kyalo Manthi

31. Interdisciplinary Center for Archaeology and Evolution of Human Behaviour (ICArEHB), FCHS, Universidade do Algarve, Faro, Portugal

Flora Schilt

32. Department of Archaeology, Conservation and History, University of Oslo, Oslo, Norway

David K. Wright

33. State Key Laboratory of Loess and Quaternary Geology, Institute of Earth Environment, Chinese Academy of Sciences, Xian, China

David K. Wright

34. School of Human Evolution and Social Change, Arizona State University, Tempe, AZ, USA

Andrew Zipkin

35. Department of Evolutionary Anthropology, University of Vienna, Vienna, Austria

Ron Pinhasi

36. Human Evolution and Archaeological Sciences – HEAS, University of Vienna, Vienna, Austria

Ron Pinhasi

37. Department of Anthropology, University of California, Santa Barbara, CA, USA

Douglas J. Kennett

38. Broad Institute of Harvard and MIT, Cambridge, MA, USA

David Reich

39. Howard Hughes Medical Institute, Harvard Medical School, Boston, MA, USA

David Reich

Contributions

M.L., E.A.S., J.C.T., D.R. and M.E.P. conceptualized the study. E.A.S., J.C.T., C.A.T., K.L.R., K.M.d.L., S.H.A., J.W.A., K.J.W.A., G.A., A.B., J.I.C.-R., M.C.C., J.D., A.O.G., A.H., P.K., M.K., A.K., M.F.L., J.L., A.Z.P.M., F.M., A.M., G.M., R.M., D.M., E.N., C.O., F.S., P.R.W., D.K.W., A.Z., F.K.M. and M.E.P. provided samples, and assembled archaeological and anthropological materials and information. B.J.C. and D.J.K. performed radiocarbon analysis. N.R., R.P., J.O. and D.R. performed aDNA laboratory and data-processing work. M.L., K.A.S., I.O., N.P. and D.R. analysed genetic data. M.L., E.A.S., J.C.T., M.E.P. and D.R. wrote the manuscript with contributions from the other authors.

Corresponding authors

Correspondence to [Mark Lipson](#), [Elizabeth A. Sawchuk](#), [Jessica C. Thompson](#), [David Reich](#) or [Mary E. Prendergast](#).

Ethics declarations

Competing interests

The authors declare no competing interests.

Peer review

Peer review information

Nature thanks Diyendo Massilani, Manuel Will and the other, anonymous, reviewer(s) for their contribution to the peer review of this work. Peer reviewer reports are available.

Additional information

Publisher's note Springer Nature remains neutral with regard to jurisdictional claims in published maps and institutional affiliations.

A list of affiliations appears at the end of the paper

Extended data figures and tables

Extended Data Fig. 1 Sex chromosome ratios and kinship analysis.

A, Sex chromosome ratios. For each library, we show the proportion of reads aligning to chromosome Y of the total aligning to either X or Y; individuals determined to be genetically female to the left and males to the right. Bars show 95% binomial confidence intervals (normal approximation) around the mean. See also Supplementary Table 2 and Supplementary Note 5. **B**, Kinship analysis. Different-individual allelic mismatch rates (orange points) are mostly approximately twice as high as same-individual rates (blue points), as expected for unrelated individuals. The labelled pair (I8930 and I8931, both from White Rock Point), have a rate that is roughly seven-eighths that of the other pairs, which would correspond to a second-degree familial relationship (but with relatively high uncertainty given the low SNP coverage). Bars show two standard errors in each direction around the mean as determined by a Block Jackknife; note log scale for the x-axis.

Extended Data Fig. 2 Full admixture graph results for Model 1.

Branch lengths are shown in units of average squared allele frequency divergence (multiplied by 1000, rounded to the nearest integer). All predicted and observed f -statistics agree to within $Z = 2.0$. AncSA = ancient southern African foragers.

Extended Data Fig. 3 Full admixture graph results for Model 2.

Branch lengths are shown in units of average squared allele frequency divergence (multiplied by 1000, rounded to the nearest integer). All predicted and observed f -statistics agree to within $Z = 3.0$. AncSA = ancient southern African foragers.

Extended Data Fig. 4 Full admixture graph results for Model 3.

Branch lengths are shown in units of average squared allele frequency divergence (multiplied by 1000, rounded to the nearest integer). All predicted and observed f -statistics agree to within $Z = 3.7$. AncSA = ancient southern African foragers.

Extended Data Fig. 5 Admixture graph results for a version of Model 1 using only overlapping SNPs (without the *qpfstats* program).

Branch lengths are shown in units of average squared allele frequency divergence (multiplied by 1000, rounded to the nearest integer). All predicted and observed f -statistics agree to within $Z = 2.0$. AncSA = ancient southern African foragers.

Extended Data Fig. 6 Admixture graph results for a version of Model 2 with the Malawi individuals fit using a shared three-way admixture clade.

Branch lengths are shown in units of average squared allele frequency divergence (multiplied by 1000, rounded to the nearest integer). All predicted and observed f -statistics agree to within $Z = 2.9$. AncSA = ancient southern African foragers.

Extended Data Fig. 7 Excess relatedness as a function of geographical distance.

Each point represents the model residual for one pair of individuals. The lines show best-fitting curves of the functional form $y = 1/kx$ (allowing for horizontal and vertical translation). See [Methods](#) for details. **A, B:** Eastern and south-central Africa, with same-site pairs omitted from the analysis in **B** (grey: different sub-regions; blue: both Kenya, both Tanzania, or both coastal; yellow: both Malawi/Zambia). **C:** Western Europe. Note the different y-axis range. **D:** Northern and eastern Europe, where fit #1 includes all pairs, while fit #2 omits same-site pairs.

Extended Data Fig. 8 Admixture graph results for a version of Model 2 with Hadza and Sandawe added.

Branch lengths are shown in units of average squared allele frequency divergence (multiplied by 1000, rounded to the nearest integer). All predicted and observed f -statistics agree to within $Z = 3.2$. AncSA = ancient southern African foragers.

Extended Data Fig. 9 ROH and effective population sizes.

A: total lengths of ROH per individual in segments of > 4 cM, divided by colours into length bins. Asterisks denote individuals with evidence of familial relatedness between parents. **B:** estimated recent effective population sizes by individual or group (note log scale). Colours correspond to those in Fig. 1. Bars show 95% confidence intervals centred around the maximum likelihood estimate, reflecting uncertainty in our inferences due to the limited number in the number of ROH segments available for

analysis; see [Methods](#) for details. SL, Shum Laka; western SA, western South African sites Faraoskop and St Helena.

Extended Data Table 1 Ancient individuals analysed in this study

Supplementary information

[Supplementary Notes 1–7](#)

Additional information on sampling and permissions, archaeological context and data analysis.

[Reporting Summary](#)

[Supplementary Tables 1–12](#)

Additional information about samples, radiocarbon dating and genomic data.

[Peer Review File](#)

Rights and permissions

Open Access This article is licensed under a Creative Commons Attribution 4.0 International License, which permits use, sharing, adaptation, distribution and reproduction in any medium or format, as long as you give appropriate credit to the original author(s) and the source, provide a link to the Creative Commons license, and indicate if changes were made. The images or other third party material in this article are included in the article's Creative Commons license, unless indicated otherwise in a credit line to the material. If material is not included in the article's Creative Commons license and your intended use is not permitted by statutory regulation or exceeds the permitted use, you will need to obtain permission directly from the copyright holder. To view a copy of this license, visit <http://creativecommons.org/licenses/by/4.0/>.

[Reprints and Permissions](#)

About this article

Cite this article

Lipson, M., Sawchuk, E.A., Thompson, J.C. *et al.* Ancient DNA and deep population structure in sub-Saharan African foragers. *Nature* **603**, 290–296 (2022).
<https://doi.org/10.1038/s41586-022-04430-9>

- Received: 22 June 2021
- Accepted: 14 January 2022
- Published: 23 February 2022
- Issue Date: 10 March 2022
- DOI: <https://doi.org/10.1038/s41586-022-04430-9>

Share this article

Anyone you share the following link with will be able to read this content:

[Get shareable link](#)

Sorry, a shareable link is not currently available for this article.

[Copy to clipboard](#)

Provided by the Springer Nature SharedIt content-sharing initiative

[Ancient DNA illuminates how humans travelled and interacted in Stone Age Africa](#)

Research Briefing 23 Feb 2022

This article was downloaded by **calibre** from <https://www.nature.com/articles/s41586-022-04430-9>

| [Section menu](#) | [Main menu](#) |

- Article
- [Published: 02 March 2022](#)

Knowledge about others reduces one's own sense of anonymity

- [Anuj K. Shah ORCID: orcid.org/0000-0001-5073-9362¹](#) &
- [Michael LaForest ORCID: orcid.org/0000-0001-9666-0457²](#)

Nature volume **603**, pages 297–301 (2022)

- 2865 Accesses
- 1 Citations
- 173 Altmetric
- [Metrics details](#)

Subjects

- [Human behaviour](#)

Abstract

Social ties often seem symmetric, but they need not be^{1,2,3,4,5}. For example, a person might know a stranger better than the stranger knows them. We explored whether people overlook these asymmetries and what consequences that might have for people's perceptions and actions. Here we show that when people know more about others, they think others know more about them. Across nine laboratory experiments, when participants learned more about a stranger, they felt as if the stranger also knew them

better, and they acted as if the stranger was more attuned to their actions. As a result, participants were more honest around known strangers. We tested this further with a field experiment in New York City, in which we provided residents with mundane information about neighbourhood police officers. We found that the intervention shifted residents' perceptions of officers' knowledge of illegal activity, and it may even have reduced crime. It appears that our sense of anonymity depends not only on what people know about us but also on what we know about them.

This is a preview of subscription content

Access options

Subscribe to Nature+

Get immediate online access to the entire Nature family of 50+ journals

\$29.99

monthly

[Subscribe](#)

Subscribe to Journal

Get full journal access for 1 year

\$199.00

only \$3.90 per issue

[Subscribe](#)

All prices are NET prices.

VAT will be added later in the checkout.

Tax calculation will be finalised during checkout.

Buy article

Get time limited or full article access on ReadCube.

\$32.00

[Buy](#)

All prices are NET prices.

Additional access options:

- [Log in](#)
- [Learn about institutional subscriptions](#)

Fig. 1: Treatment-control differences in crime after policing intervention.

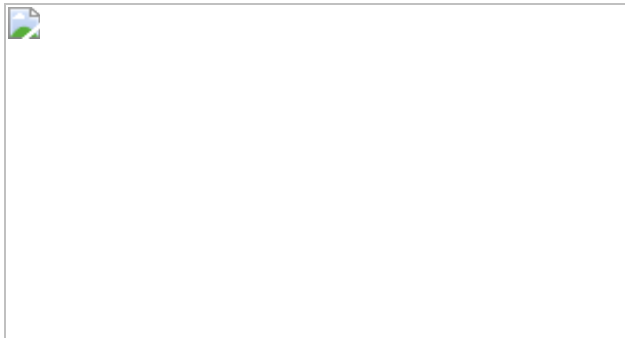
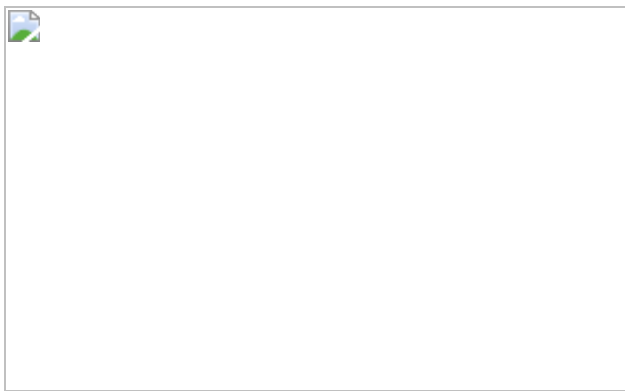


Fig. 2: Residents' perceptions of officer knowledge predict crime reductions.



Data availability

The Open Science Framework page for this project (<https://osf.io/mkgwr/>) includes all data from laboratory experiments and all data necessary to reproduce the results of the field experiment.

Code availability

The codes for running the laboratory experiments online and for analysing the data from the field experiment are available on the Open Science Framework (<https://osf.io/mkgwr/>).

References

1. Krackhardt, D. & Kilduff, M. Whether close or far: social distance effects on perceived balance in friendship networks. *J. Pers. Soc. Psychol.* **76**, 770–782 (1999).
2. Davis, J. A. In *Theories of Cognitive Consistency* (eds Abelson, R. P. et al.) 544–550 (Rand McNally, 1968).
3. Heider, F. *The Psychology of Interpersonal Relations* (Wiley, 1958).
4. DeSoto, C. B. Learning a social structure. *J. Abnorm. Soc. Psychol.* **60**, 417–421 (1960).
5. Freeman, L. C. Filling in the blanks: a theory of cognitive categories and the structure of social affiliation. *Soc. Psychol. Q.* **55**, 118–127 (1992).
6. Rand, D. G. et al. Social heuristics shape intuitive cooperation. *Nat. Commun.* **5**, 3677 (2014).
7. Holoiu, D. S., Bergsieker, H. B., Shelton, J. N. & Alegre, J. M. Do you really understand? Achieving accuracy in interracial relationships. *J. Pers. Soc. Psychol.* **108**, 76–92 (2015).
8. Epley, N., Keysar, B., Van Boven, L. & Gilovich, T. Perspective taking as egocentric anchoring and adjustment. *J. Pers. Soc. Psychol.* **87**,

327–339 (2004).

9. Nickerson, R. S. How we know—and sometimes misjudge—what others know: imputing one’s own knowledge to others. *Psychol. Bull.* **125**, 737–759 (1999).
10. Gilovich, T., Savitsky, K. & Medvec, V. H. The illusion of transparency: biased assessments of others’ ability to read one’s emotional states. *J. Pers. Soc. Psychol.* **75**, 332–346 (1998).
11. Gilovich, T. & Savitsky, K. The spotlight effect and the illusion of transparency: egocentric assessments of how we’re seen by others. *Curr. Dir. Psychol. Sci.* **8**, 165–168 (1999).
12. Milgram, S. The experience of living in cities. *Science* **167**, 1461–1468 (1970).
13. Diener, E., Fraser, S. C., Beaman, A. L. & Kelem, R. T. Effects of deindividuation variables on stealing among Halloween trick-or-treaters. *J. Pers. Soc. Psychol.* **33**, 178–183 (1976).
14. Zhong, C., Bohns, V. K. & Gino, F. Good lamps are the best police: darkness increases dishonesty and self-interested behavior. *Psychol. Sci.* **21**, 311–314 (2010).
15. Andreoni, J. & Petrie, R. Public goods experiments without confidentiality: a glimpse into fund-raising. *J. Public Econ.* **88**, 1605–1623 (2004).
16. Yoeli, E., Hoffman, M., Rand, D. & Nowak, M. Powering up with indirect reciprocity in a large-scale field experiment. *Proc. Natl Acad. Sci. USA* **110**, 10424–10429 (2013).
17. Ernest-Jones, M., Nettle, D. & Bateson, M. Effects of eye images on everyday cooperative behavior: a field experiment. *Evol. Hum. Behav.* **32**, 172–178 (2011).

18. Pronin, E., Kruger, J., Savitsky, K. & Ross, L. You don't know me, but I know you: the illusion of asymmetric insight. *J. Pers. Soc. Psychol.* **81**, 639–656 (2001).
19. Lakens, D. Equivalence tests: a practical primer for *t* tests, correlations, and meta-analyses. *Soc. Psychol. Pers. Sci.* **8**, 355–362 (2017).
20. Preacher, K. J., Rucker, D. D. & Hayes, A. F. Addressing moderated mediation hypotheses: theory, methods, and prescriptions. *Multivariate Behav. Res.* **42**, 185–227 (2007).
21. Parks, R. B., Mastrofski, S. D., DeJong, C. & Gray, M. K. How officers spend their time with the community. *Justice Q.* **16**, 483–518 (1999).
22. Ba, B. A., Knox, D., Mummolo, J. & Rivera, R. The role of officer race and gender in police-civilian interactions in Chicago. *Science* **371**, 696–702 (2021).
23. Fryer, R. G. An empirical analysis of racial differences in police use of force. *J. Pol. Econ.* **127**, 1210–1261 (2019).
24. Voigt, R. et al. Language from police body camera footage shows racial disparities in officer respect. *Proc. Natl Acad. Sci. USA* **114**, 6521–6526 (2017).
25. Braga, A. A., Papachristos, A. V. & Hureau, D. M. The effects of hot spots policing on crime: an updated systematic review and meta-analysis. *Justice Q.* **31**, 633–663 (2014).
26. National Academies of Sciences, Engineering, and Medicine. *Proactive Policing: Effects on Crime and Communities* (The National Academies Press, 2018).
27. National Research Council. *Fairness and Effectiveness in Policing: The Evidence* (The National Academies Press, 2004).

28. Sherman, L. W. & Eck, J. in *Evidence Based Crime Prevention* (eds Sherman, L. W. et al.) 295–329 (Routledge, 2002).
29. Peyton, K., Sierra-Arévalo, M. & Rand, D. G. A field experiment on community policing and police legitimacy. *Proc. Natl Acad. Sci. USA* **116**, 19894–19898 (2019).
30. Owens, E., Weisburd, D., Amendola, K. L. & Alpert, G. P. Can you build a better cop? Experimental evidence on supervision, training, and policing in the community. *Criminol. Public Policy* **17**, 41–87 (2018).
31. Sunshine, J. & Tyler, T. The role of procedural justice and legitimacy in shaping public support for policing. *Law Soc. Rev.* **37**, 513–548 (2003).
32. Chalfin, C., Hansen, B., Weisburst, E. K. & Williams, M. C. Police force size and civilian race. *Am. Econ. Rev. Insights* (in the press).
33. Belloni, A., Chernozhukov, V. & Hansen, C. High-dimensional methods and inference on structural and treatment effects. *J. Econ. Perspect.* **28**, 29–50 (2014).

Acknowledgements

This research was supported by the National Institute of Justice (award number 2013-R2-CX-0006). We are grateful to the New York City Police Department, particularly T. Coffey and D. Williamson in the Office of Management Analysis and Planning. Points of view or opinions contained within this document are those of the authors and do not necessarily represent the official position or policies of the New York City Police Department. We also thank the New York City Housing Authority for their assistance with the field experiment. Throughout this project, ideas42 was an essential research partner. We are also grateful to H. Furstenberg-Beckman for thoughtful guidance; A. Alhadeff and W. Tucker for valuable assistance; Crime Lab New York for critical support in the planning and evaluation of the policing intervention, particularly R. Ander, M. Barron, A. Chalfin, K. Falco, V. Gilbert, D. Hafetz, B. Jakubowski, Z. Jelveh, K.

Nguyen, L. Parker, J. Lerner, H. Golden, G. Stoddard and N. Weil; V. Nguyen for her support as a research assistant; and J. Ludwig, S. Mullainathan, A. Kumar, E. O'Brien and F. Goncalves for insightful feedback.

Author information

Affiliations

1. University of Chicago, Chicago, Illinois, USA

Anuj K. Shah

2. Pennsylvania State University, State College, Pennsylvania, USA

Michael LaForest

Contributions

A.K.S. developed the hypotheses. A.K.S. designed, conducted and analysed the laboratory experiments. A.K.S. and M.L. designed the field intervention. M.L. led the analysis of the field intervention. A.K.S. and M.L. contributed to the manuscript.

Corresponding author

Correspondence to [Anuj K. Shah](#).

Ethics declarations

Competing interests

The authors declare no competing interests.

Peer review

Peer review information

Nature thanks the anonymous reviewers for their contribution to the peer review of this work.

Additional information

Publisher's note Springer Nature remains neutral with regard to jurisdictional claims in published maps and institutional affiliations.

Extended data figures and tables

Extended Data Fig. 1 Outreach cards.

A sample outreach card (front and back) used in the field intervention. Identifying information has been redacted.

Extended Data Fig. 2 Outreach letters.

A sample letter used in the field intervention. Identifying information has been redacted.

Extended Data Fig. 3 Distribution of point estimates for treatment effect.

As a robustness check, we conducted analyses for various radii ranging up to three blocks around developments: 65 ft., 100 ft., 150 ft., 200 ft., 250 ft., 300 ft., 400 ft., 500 ft., and 750 ft. And, for each radius, we conducted analyses for cumulative time intervals ranging from one month after the intervention (i.e., February 2018) to the first nine months after the intervention (i.e., February through October 2018). Varying both of these dimensions produced 81 sets of results, based on our primary specification applied to each radius and time interval (see Supplementary Information [C.3](#)). This figure shows the distribution of point estimates for the crime reductions across these analyses, along with an Epanechnikov

kernel density function over the distribution. The red dot highlights where the 250-ft, 3-month result falls in the distribution, suggesting it is in line with the central estimates across all 81 analyses.

Extended Data Fig. 4 Heat map of P-values for treatment effect over time and distance.

As a robustness check, we conducted analyses for various radii ranging up to three blocks around developments: 65 ft., 100 ft., 150 ft., 200 ft., 250 ft., 300 ft., 400 ft., 500 ft., and 750 ft. And, for each radius, we conducted analyses for cumulative time intervals ranging from one month after the intervention (i.e., February 2018) to the first nine months after the intervention (i.e., February through October 2018). Varying both of these dimensions produced 81 sets of results. This figure shows a heat map of P -values across these 81 specifications, with the 250-ft, 3-month result outlined in blue. P -values are from two-tailed tests based on our primary specification applied to each radius and time interval (see Supplementary Information C.3).

Extended Data Table 1 NYCHA development characteristics

Extended Data Table 2 Primary survey outcome estimates

Extended Data Table 3 Exploratory survey outcome estimates

Extended Data Table 4 Crime outcome estimates

Extended Data Table 5 Crime outcome treatment-on-the-treated estimates

Supplementary information

Supplementary Information

This file contains the following sections: A. Lab experiment methods, materials, and results; B. Field experiment methods and materials; C. Field experiment results, tables, and figures; D. Software Used; E. Supplementary references.

Reporting Summary

Rights and permissions

[Reprints and Permissions](#)

About this article

Cite this article

Shah, A.K., LaForest, M. Knowledge about others reduces one's own sense of anonymity. *Nature* **603**, 297–301 (2022). <https://doi.org/10.1038/s41586-022-04452-3>

- Received: 07 September 2020
- Accepted: 21 January 2022
- Published: 02 March 2022
- Issue Date: 10 March 2022
- DOI: <https://doi.org/10.1038/s41586-022-04452-3>

Share this article

Anyone you share the following link with will be able to read this content:

[Get shareable link](#)

Sorry, a shareable link is not currently available for this article.

[Copy to clipboard](#)

Provided by the Springer Nature SharedIt content-sharing initiative

Further reading

- [Letters and cards telling people about local police reduce crime](#)

- Elicia John
- Shawn D. Bushway

Nature (2022)

[COVID stimulus spending failed to deliver on climate promises](#)

- Benjamin Thompson
- Nick Petrić Howe

Nature Podcast 02 Mar 2022

[Letters and cards telling people about local police reduce crime](#)

- Elicia John
- Shawn D. Bushway

News & Views 02 Mar 2022

This article was downloaded by **calibre** from <https://www.nature.com/articles/s41586-022-04452-3>

- Article
- [Published: 16 February 2022](#)

Differential mechanisms underlie trace and delay conditioning in *Drosophila*

- [Dhruv Grover](#) ORCID: orcid.org/0000-0001-5438-233X¹,
- [Jen-Yung Chen](#)¹,
- [Jiayun Xie](#)¹,
- [Jinfang Li](#) ORCID: orcid.org/0000-0001-5754-8008¹,
- [Jean-Pierre Changeux](#)^{1,2,3} &
- [Ralph J. Greenspan](#) ORCID: orcid.org/0000-0002-6787-2845^{1,4}

[Nature](#) volume 603, pages 302–308 (2022)

- 3514 Accesses
- 190 Altmetric
- [Metrics details](#)

Subjects

- [Attention](#)
- [Classical conditioning](#)
- [Cognitive control](#)
- [Neural circuits](#)
- [Working memory](#)

Abstract

Two forms of associative learning—delay conditioning and trace conditioning—have been widely investigated in humans and higher-order mammals¹. In delay conditioning, an unconditioned stimulus (for example, an electric shock) is introduced in the final moments of a conditioned stimulus (for example, a tone), with both ending at the same time. In trace conditioning, a ‘trace’ interval separates the conditioned stimulus and the unconditioned stimulus. Trace conditioning therefore relies on maintaining a neural representation of the conditioned stimulus after its termination (hence making distraction possible²), to learn the conditioned stimulus–unconditioned stimulus contingency³; this makes it more cognitively demanding than delay conditioning⁴. Here, by combining virtual-reality behaviour with neurogenetic manipulations and *in vivo* two-photon brain imaging, we show that visual trace conditioning and delay conditioning in *Drosophila* mobilize R2 and R4m ring neurons in the ellipsoid body. In trace conditioning, calcium transients during the trace interval show increased oscillations and slower declines over repeated training, and both of these effects are sensitive to distractions. Dopaminergic activity accompanies signal persistence in ring neurons, and this is decreased by distractions solely during trace conditioning. Finally, dopamine D1-like and D2-like receptor signalling in ring neurons have different roles in delay and trace conditioning; dopamine D1-like receptor 1 mediates both forms of conditioning, whereas the dopamine D2-like receptor is involved exclusively in sustaining ring neuron activity during the trace interval of trace conditioning. These observations are similar to those previously reported in mammals during arousal⁵, prefrontal activation⁶ and high-level cognitive learning^{7,8}.

This is a preview of subscription content

Access options

Subscribe to Nature+

Get immediate online access to the entire Nature family of 50+ journals

\$29.99

monthly

[Subscribe](#)

Subscribe to Journal

Get full journal access for 1 year

\$199.00

only \$3.90 per issue

[Subscribe](#)

All prices are NET prices.

VAT will be added later in the checkout.

Tax calculation will be finalised during checkout.

Buy article

Get time limited or full article access on ReadCube.

\$32.00

[Buy](#)

All prices are NET prices.

Additional access options:

- [Log in](#)
- [Learn about institutional subscriptions](#)

Fig. 1: *Drosophila* visual trace conditioning, but not delay conditioning, is distraction-sensitive, and both require ellipsoid body R2 and R4m ring neurons.

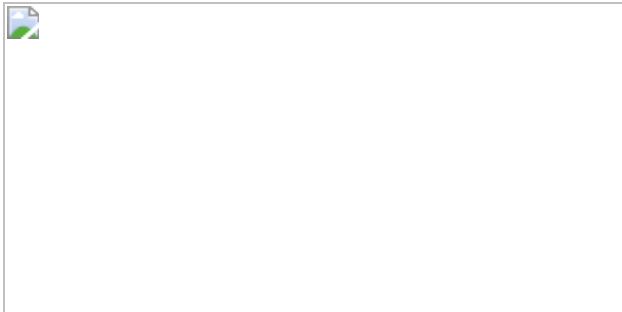


Fig. 2: Ellipsoid body ring neuron ratiometric calcium imaging during trace conditioning reveals an increasing, distraction-sensitive oscillatory component and persistence.

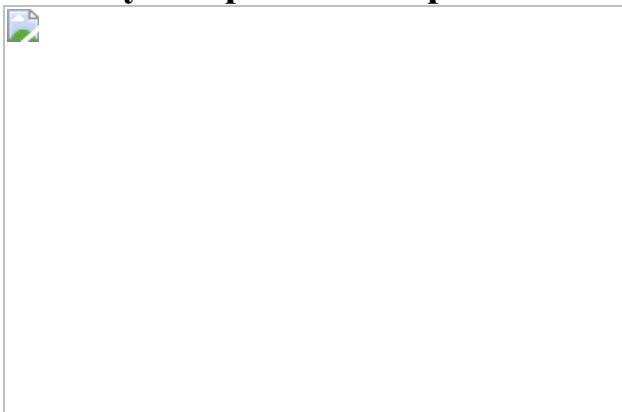
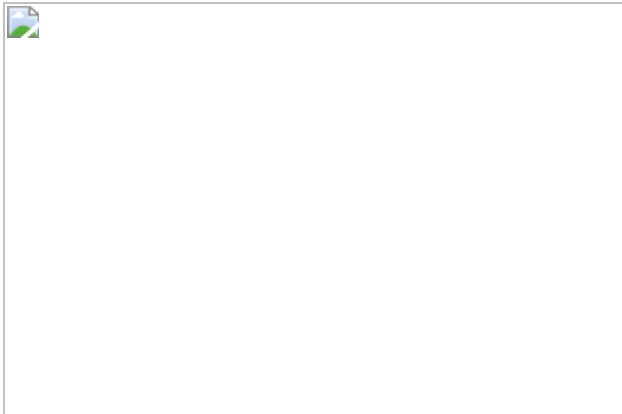


Fig. 3: Ellipsoid-body-projecting dopaminergic neurons are required for trace and delay conditioning, selectively active during the trace interval and negatively affected by distractions in trace conditioning.



Fig. 4: Dopamine receptor signalling in the ellipsoid body ring during delay and trace conditioning.



Data availability

Datasets generated as part of this study are available from the corresponding author on reasonable request. [Source data](#) are provided with this paper.

Code availability

The source code for the different assays developed is available for download from the public repository at
<https://github.com/dgrover/flyCAVE>.

References

1. Clark, R. E. & Squire, L. R. Classical conditioning and brain systems: the role of awareness. *Science* **280**, 77–81 (1998).
2. Han, C. J. et al. Trace but not delay fear conditioning requires attention and the anterior cingulate cortex. *Proc. Natl Acad. Sci. USA* **100**, 13087–13092 (2003).
3. Garner, A. R. et al. Generation of a synthetic memory trace. *Science* **335**, 1513–1516 (2012).
4. Raybuck, J. D. & Lattal, K. M. Bridging the interval: theory and neurobiology of trace conditioning. *Behav. Processes* **101**, 103–111

(2014).

5. Colgin, L. L. Mechanisms and functions of theta rhythms. *Annu. Rev. Neurosci.* **36**, 295–312 (2013).
6. Koechlin, E. Prefrontal executive function and adaptive behavior in complex environments. *Curr. Opin. Neurobiol.* **37**, 1–6 (2016).
7. Nichols, M. J. & Newsome, W. T. The neurobiology of cognition. *Nature* **402**, C35–C38 (1999).
8. Milner, B., Squire, L. R. & Kandel, E. R. Cognitive neuroscience and the study of memory. *Neuron* **20**, 445–468 (1998).
9. Knight, D. C., Cheng, D. T., Smith, C. N., Stein, E. A. & Helmstetter, F. J. Neural substrates mediating human delay and trace fear conditioning. *J. Neurosci.* **24**, 218–228 (2004).
10. Kronforst-Collins, M. A. & Disterhoft, J. F. Lesions of the caudal area of rabbit medial prefrontal cortex impair trace eyeblink conditioning. *Neurobiol. Learn. Mem.* **69**, 147–162 (1998).
11. Connor, D. A. & Gould, T. J. The role of working memory and declarative memory in trace conditioning. *Neurobiol. Learn. Mem.* **134**, 193–209 (2016).
12. LeDoux, J. E. & Lau, H. Seeing consciousness through the lens of memory. *Curr. Biol.* **30**, R1018–R1022 (2020).
13. Venken, K. J. T., Simpson, J. H. & Bellen, H. J. Genetic manipulation of genes and cells in the nervous system of the fruit fly. *Neuron* **72**, 202–230 (2011).
14. Haberkern, H. & Jayaraman, V. Studying small brains to understand the building blocks of cognition. *Curr. Opin. Neurobiol.* **37**, 59–65 (2016).
15. Tully, T. & Quinn, W. G. Classical conditioning and retention in normal and mutant *Drosophila melanogaster*. *J. Comp. Physiol. A* **157**,

263–277 (1985).

16. Owald, D. & Waddell, S. Olfactory learning skews mushroom body output pathways to steer behavioral choice in *Drosophila*. *Curr. Opin. Neurobiol.* **35**, 178–184 (2015).
17. Bustos, G. U., Cervantes-Sandoval, I. & Davis, R. L. Olfactory learning in *Drosophila*. *Physiology* **25**, 338–346 (2010).
18. Galili, D. S., Lüdke, A., Galizia, C. G., Szyszka, P. & Tanimoto, H. Olfactory trace conditioning in *Drosophila*. *J. Neurosci.* **31**, 7240–7248 (2011).
19. Shuai, Y., Hu, Y., Qin, H., Campbell, R. A. A. & Zhong, Y. Distinct molecular underpinnings of *Drosophila* olfactory trace conditioning. *Proc. Natl Acad. Sci. USA* **108**, 20201–20206 (2011).
20. Dill, M., Wolf, R. & Heisenberg, M. Visual pattern recognition in *Drosophila* involves retinotopic matching. *Nature* **365**, 751–753 (1993).
21. Kamikouchi, A. et al. The neural basis of *Drosophila* gravity-sensing and hearing. *Nature* **458**, 165–171 (2009).
22. Pacheco, D. A., Thibierge, S. Y., Pnevmatikakis, E. & Murthy, M. Auditory activity is diverse and widespread throughout the central brain of *Drosophila*. *Nat. Neurosci.* **24**, 93–104 (2021).
23. Neuser, K., Triphan, T., Mronz, M., Poeck, B. & Strauss, R. Analysis of a spatial orientation memory in *Drosophila*. *Nature* **453**, 1244–1247 (2008).
24. Ofstad, T. A., Zuker, C. S. & Reiser, M. B. Visual place learning in *Drosophila melanogaster*. *Nature* **474**, 204–209 (2011).
25. Liu, G. et al. Distinct memory traces for two visual features in the *Drosophila* brain. *Nature* **439**, 551–556 (2006).

26. Vogt, K. et al. Shared mushroom body circuits underlie visual and olfactory memories in *Drosophila*. *eLife* **3**, e02395 (2014).
27. Zhang, K., Guo, J. Z., Peng, Y., Xi, W. & Guo, A. Dopamine–mushroom body circuit regulates saliency-based decision-making in *Drosophila*. *Science* **316**, 1901–1904 (2007).
28. Aso, Y. et al. Mushroom body output neurons encode valence and guide memory-based action selection in *Drosophila*. *eLife* **3**, e04580 (2014).
29. Cognigni, P., Felsenberg, J. & Waddell, S. Do the right thing: neural network mechanisms of memory formation, expression and update in *Drosophila*. *Curr. Opin. Neurobiol.* **49**, 51–58 (2018).
30. Srinivasan, S., Greenspan, R. J., Stevens, C. F. & Grover, D. Deep(er) learning. *J. Neurosci.* **38**, 7365–7374 (2018).
31. Mao, Z. & Davis, R. L. Eight different types of dopaminergic neurons innervate the *Drosophila* mushroom body neuropil: anatomical and physiological heterogeneity. *Front. Neural Circuits* **3**, 5 (2009).
32. Liang, X. et al. Morning and evening circadian pacemakers independently drive premotor centers via a specific dopamine relay. *Neuron* **102**, 843–857 (2019).
33. Lebestky, T. et al. Two different forms of arousal in *Drosophila* are oppositely regulated by the dopamine D1 receptor ortholog DopR via distinct neural circuits. *Neuron* **64**, 522–536 (2009).
34. Aso, Y. et al. The neuronal architecture of the mushroom body provides a logic for associative learning. *eLife* **3**, e04577 (2014).
35. Knudsen, E. I. Fundamental components of attention. *Annu. Rev. Neurosci.* **30**, 57–78 (2007).
36. Carter, R. M. K., Hofstötter, C., Tsuchiya, N. & Koch, C. Working memory and fear conditioning. *Proc. Natl Acad. Sci. USA* **100**, 1399–

1404 (2003).

37. Kim, R. & Sejnowski, T. J. Strong inhibitory signaling underlies stable temporal dynamics and working memory in spiking neural networks. *Nat. Neurosci.* **24**, 129–139 (2021).
38. Renn, S. C. P. et al. Genetic analysis of the *Drosophila* ellipsoid body neuropil: organization and development of the central complex. *J. Neurobiol.* **41**, 189–207 (1999).
39. Hollerman, J. R. & Schultz, W. Dopamine neurons report an error in the temporal prediction of reward during learning. *Nat. Neurosci.* **1**, 304–309 (1998).
40. Sutton, R. S. & Barto, A. G. Toward a modern theory of adaptive networks: Expectation and prediction. *Psychol. Rev.* **88**, 135–170 (1981).
41. Schultz, W. Dopamine reward prediction error coding. *Dialogues Clin. Neurosci.* **18**, 23–32 (2016).
42. Tobler, P. N., Fiorillo, C. D. & Schultz, W. Adaptive coding of reward value by dopamine neurons. *Science* **307**, 1642–1645 (2005).
43. Lak, A. et al. Dopaminergic and prefrontal basis of learning from sensory confidence and reward value. *Neuron* **105**, 700–711 (2020).
44. Sabandal, J. M., Berry, J. A. & Davis, R. L. Dopamine-based mechanism for transient forgetting. *Nature* **591**, 426–430 (2021).
45. Seelig, J. D. & Jayaraman, V. Neural dynamics for landmark orientation and angular path integration. *Nature* **521**, 186–191 (2015).
46. Green, J., Vijayan, V., Mussells Pires, P., Adachi, A. & Maimon, G. A neural heading estimate is compared with an internal goal to guide oriented navigation. *Nat. Neurosci.* **22**, 1460–1468 (2019).
47. Shih, C. T. et al. Connectomics-based analysis of information flow in the drosophila brain. *Curr. Biol.* **25**, 1249–1258 (2015).

48. Franconville, R., Beron, C. & Jayaraman, V. Building a functional connectome of the drosophila central complex. *eLife* **7**, e37017 (2018).
49. Fisher, Y. E., Lu, J., D'Alessandro, I. & Wilson, R. I. Sensorimotor experience remaps visual input to a heading-direction network. *Nature* **576**, 121–125 (2019).
50. Mashour, G. A., Roelfsema, P., Changeux, J. P. & Dehaene, S. Conscious processing and the global neuronal workspace hypothesis. *Neuron* **105**, 776–798 (2020).
51. Xie, T. et al. A genetic toolkit for dissecting dopamine circuit function in *Drosophila*. *Cell Rep.* **23**, 652–665 (2018).
52. Baines, R. A., Uhler, J. P., Thompson, A., Sweeney, S. T. & Bate, M. Altered electrical properties in *Drosophila* neurons developing without synaptic transmission. *J. Neurosci.* **21**, 1523–1531 (2001).
53. McGuire, S. E., Mao, Z. & Davis, R. L. Spatiotemporal gene expression targeting with the TARGET and gene-switch systems in *Drosophila*. *Sci. STKE* **2004**, pl6 (2004).
54. Klapoetke, N. C. et al. Independent optical excitation of distinct neural populations. *Nat. Methods* **11**, 338–346 (2014).
55. Akerboom, J. et al. Optimization of a GCaMP calcium indicator for neural activity imaging. *J. Neurosci.* **32**, 13819–13840 (2012).
56. Weir, P. T. & Dickinson, M. H. Functional divisions for visual processing in the central brain of flying *Drosophila*. *Proc. Natl Acad. Sci. USA* **112**, E5523–E5532 (2015).
57. Savitzky, A. & Golay, M. J. E. Smoothing and differentiation of data by simplified least squares procedures. *Anal. Chem.* **36**, 1627–1639 (1964).
58. Wobbrock, J. O., Findlater, L., Gergle, D. & Higgins, J. J. The aligned rank transform for nonparametric factorial analyses using only

ANOVA procedures. In *Proc. SIGCHI Conference on Human Factors in Computing Systems* 143–146 (Association for Computing Machinery, 2011).

Acknowledgements

We thank F. Cardone and I. Freerkson for their assistance with designing and fabricating electronic and mechanical components; A. Calhoun, W. Joiner, M. Wu and V. Jayaraman for gifting fly stocks; T. Dawkins for advice and assistance with various experimental analyses; E. Huie for assistance with behavioural experiments; M. Nelson for assistance with in vivo imaging experiments; and T. Sejnowski for comments on the manuscript. This work was supported by the Air Force Office of Scientific Research grants FA9550-14-1-0211 and FA9550-19-1-0280 to D.G. and R.J.G.; awards from the Mathers Foundation 20154167 and National Science Foundation 1212778 to R.J.G.; and the European Union’s Horizon 2020 Framework Programme for Research and Innovation under specific grant agreement no. 945539 (Human Brain Project SGA3) and Kavli Institute for Brain and Mind International Faculty award to J.-P.C.

Author information

Affiliations

1. Kavli Institute for Brain and Mind, University of California, San Diego, La Jolla, CA, USA

Dhruv Grover, Jen-Yung Chen, Jiayun Xie, Jinfang Li, Jean-Pierre Changeux & Ralph J. Greenspan

2. CNRS UMR 3571, Institut Pasteur, Paris, France

Jean-Pierre Changeux

3. College de France, Paris, France

Jean-Pierre Changeux

4. Division of Biological Sciences, University of California, San Diego,
La Jolla, CA, USA

Ralph J. Greenspan

Contributions

D.G. designed the behaviour and imaging assay hardware and software. D.G. and J.-Y.C. performed behaviour, neural and receptor silencing and optogenetic activation experiments. J.X., J.L. and D.G. acquired *in vivo* imaging data. J.-Y.C. performed immunostaining experiments. D.G., J.-Y.C., J.X. and J.L. analysed the data. D.G., J.-P.C., J.-Y.C. and R.J.G. drafted the manuscript. All authors reviewed and approved the final manuscript.

Corresponding author

Correspondence to [Ralph J. Greenspan](#).

Ethics declarations

Competing interests

The authors declare no competing interests.

Peer review

Peer review information

Nature thanks Ronald Davis and the other, anonymous, reviewer(s) for their contribution to the peer review of this work.

Additional information

Publisher's note Springer Nature remains neutral with regard to jurisdictional claims in published maps and institutional affiliations.

Extended data figures and tables

Extended Data Fig. 1 *Drosophila* behaviour assay for visual trace and delay aversive conditioning.

a, Panoramic virtual-reality system components with real-time machine-vision based wingbeat amplitude tracking for tethered flying flies. 1) Projector, 2) 880 nm infrared diffused backlight, 3) Rear-projection coated acrylic sphere, 4) High-speed camera for wing tracking, 5) 850 nm long-pass optical filter, 6) photographic macro lens, 7) xyz-translation micro-manipulator, 8) Fly tether-rod, 9–10) Mirrors for re-directing projection patterns for panoramic visual stimulus presentation, 11) 808 nm infrared laser for delivery of heat punishment, 12) 850 nm long-pass dichroic filter (see [Methods](#), ‘Tethered-flight behaviour assay’, for optical configurations used in optogenetic experiments). **b**, Sample display frame consisting of three orthogonal views of a virtually created sphere that is projected onto the curved spherical projection screen from frontal and two lateral sides. The virtual sphere with warped T’s is programmatically calibrated to fit the dimensions and curvature of the physical display screen. Top, inverted-T displayed 45° from front-centre in CW direction with upright-T 180° away. Bottom, inverted-T displayed 45° from front-centre in CCW direction with upright-T 180° away. **c**, Internal body temperature of a tethered fly when exposed to infrared-laser-based heat punishment. Red bars indicate 0.5 s of infrared laser exposure, power-level of which was optimized to cause an immediate and robust rise in temperature from ambient room temperature of 25 °C to 35 °C. **d**, Delay learning PI ($n = 20$ flies per group) measured as a factor of CS duration and number of training trials. $PI > 0$ indicates successful learning as the fly spends more time fixating on CS⁻ than CS⁺. Peak learning (indicated with black arrow) occurred with CS duration of 10 s and 7 training trials. **e**, Change in flight orientation in the 5 s after air puff (0.5 s). See [Methods](#), ‘Tethered-flight behaviour assay’, for experimental details. Binned is the fraction of time each fly ($n = 40$ flies) spent orienting towards or away from the stimulus (orientation change greater than 20°), or

no change in flight orientation (less than or equal to 20°). **f**, Test of conditioning to distractor stimulus. Flies are subjected to full trace conditioning protocol (5-s TI) with distractors ($n = 40$ flies). Following training, same experimental protocol as **e** was followed to test distractor-only conditioning response. Binned is the fraction of time each fly spent orienting towards (attraction, positive conditioning) or away (aversion, negative conditioning) from the stimulus, or no change in flight orientation (neutral). Box plot centre (median), edges (IQR), whiskers (1.5x IQR). Groups were compared using a Kruskal–Wallis and post-hoc unpaired two-sided Mann–Whitney U -tests with Bonferroni corrected multiple comparisons. ** indicates p -value < 0.01, exact P values in Supplementary Table 1. Scatters represent individual fly PI scores.

Extended Data Fig. 2 Conditioning-related experimental controls.

a, Delay and trace conditioning experimental control protocols tested in **b**, **c**. **b**, PI (mean with s.e.m., $n = 20$ flies per group) for flies tested with US-only presentation (no CS), CS-only presentation (no US), reverse trace conditioning wherein US precedes CS⁺ presentation with a gap of 2 s. PI = 0 indicates no learning as the fly spends an equal amount of time fixating on CS⁻ and CS⁺ during the test trial. Groups were compared using Kruskal–Wallis and post-hoc unpaired two-sided Mann–Whitney U -tests with Bonferroni corrected multiple comparisons. No significant differences were observed between groups. **c**, PI (mean with s.e.m., $n = 40$ flies per group) for delay and trace conditioning (5–40-s TI) where CS⁺ precedes CS⁻ presentation (blue) and CS⁻ precedes CS⁺ (red). Group comparisons were performed using a two-factor ART-ANOVA test. No significant difference was observed between groups. Scatters represent individual fly PI scores.

Extended Data Fig. 3 Testing the effects of multi-modality distractors on conditioning.

a, Delay and trace conditioning protocols under different sets of (air puff and optogenetic) distractor conditions tested in **b–e**. **b**, PI (mean with s.e.m., $n = 40$ flies per group) for flies tested under delay and trace

conditioning (5–40-s TI) without (air puff) distractors (black), multiple distractors including during the TI (distractor set #1, blue), single distractor during the TI (distractor set #2, red), multiple distractors except during the TI (distractor set #3, grey). Groups were compared using a two-factor ART-ANOVA test. ** indicates p-value < 0.01, comparing no distractor conditions with corresponding distractor set #1 conditions (blue), and corresponding distractor set #2 conditions (red). Exact P values in Supplementary Table 1. **c**, PI (mean with s.e.m., n = 40 flies per group) for flies tested under delay and trace conditioning (5-s TI) testing the effect of amplified (air puff) distractions - distractor set #1 (white, control), distractor set #4 with double the normal air flow rate (regulated at a rate of 100 ml min⁻¹) (grey), distractor set #5 with double the normal air puff duration (1 s) (blue), and distractor set #6 with double the number of air puffs with an inter-pulse interval of 0.5 s, starting at times shown in **a**. Groups were compared using a Kruskal–Wallis and post-hoc unpaired two-sided Mann–Whitney U-tests with Bonferroni corrected multiple comparisons. **d**, PI (mean with s.e.m., n = 20 flies per group) delay and trace conditioning (5-s TI), with (distractor set #1, grey) and without distractors (white) by varying the number of training trials used for conditioning. Groups were compared using a two-factor ART-ANOVA test. **e**, Delay and trace learning (5-s TI) in flies where optogenetic activation (red-light pulse) of auditory sensory neurons (*JO_AB-Gal4>>UAS-CsChrimson*) was used as distractors in-lieu of the air puff, as shown in **a**. PI (mean with s.e.m., n = 20 flies per group) raised on standard food (white bars), and food supplemented with all-trans-retinal (grey). Gal4 control activation (*pBDPGal4>>UAS-CsChrimson*) with no brain expression included as a secondary control. Groups were compared using a Kruskal–Wallis and post-hoc unpaired two-sided Mann–Whitney U-tests with Bonferroni corrected multiple comparisons. ** indicates p-value < 0.01, exact P values in Supplementary Table 1. Scatters in all panels represent either individual fly probability or PI scores.

Extended Data Fig. 4 Effect of neural silencing of central complex and mushroom body structures on delay and trace conditioning.

a, Individual flies were tested under delay and trace conditioning (5 and 10-s TI). **b**, Top-left, illustration of implicated learning and memory structures

in the fly brain, ellipsoid body (yellow), fan-shaped body (purple) and mushroom body (red). PI for delay conditioning, and trace conditioning with **c**, 5-s TI, and **d**, 10-s TI. Shown are flies with neural activity silenced (*UAS-Kir2.1, Tub-Gal80ts*) in the ellipsoid body ring neurons – R1 (*c105-Gal4*), R3 and R4d (*c232-Gal4*) and R2 and R4m (*EB1-Gal4*), fan-shaped body columnar neurons – dorsal layers (*c205-Gal4*), dorsal and central layers (*R38E07-Gal4*), and dorsal and ventral layers (*104y-Gal4*), and neurons projecting to the mushroom body lobes – α and β lobes (*17d-Gal4*), α' and β' lobes (*c305a-Gal4*) and γ lobes (*MB009B-Gal4*), along with respective driver-less and effector-less controls. PI (mean with s.e.m., n = 20 flies per group) for flies with intact Gal80 repression of Kir2.1 (white), and warm-induction of Kir2.1 (grey). Scatters represent individual fly PI scores. Groups were compared (to both driver-less and effector-less controls) using a Kruskal–Wallis and post-hoc unpaired two-sided Mann–Whitney *U*-tests with Bonferroni corrected multiple comparisons. ** indicates p-value < 0.01, exact *P* values in Supplementary Table 1.

Extended Data Fig. 5 Ratiometric calcium imaging of ellipsoid body ring neurons during trace conditioning reveals an increased oscillatory component and slower decline with repeated training that is susceptible to distractions.

a, Ratiometric imaging of an *EB1-Gal4, UAS-GCaMP6f.myr-tdTomato* female during a single trace conditioning (5-s TI) experiment without (air puff) distractors (left), and with distractors (right). Shown, raw $dF_{\text{ratio}}/F_{\text{ratio}}$ activity traces (where $F_{\text{ratio}} = F_{\text{GCaMP6f}}/F_{\text{tdTomato}}$) for trials 1, 4, and 7. Red curve fits are single-term exponential model fits through the raw $dF_{\text{ratio}}/F_{\text{ratio}}$ activity traces starting at the end of CS presentation. **b**, Scree plots of cumulative variance explained by each of the top 50 principal components for all trace conditioning trials without distractors (blue), and with distractors (red). **c**, Cumulative variance explained by the top 12 components per trial for trace conditioning without distractors (blue), and with distractors (red). **d**, Exponential curve fit decay rates of EB1 neural activity post-CS for trials without distractors (blue), and with distractors (red). **e**, Normalized relative power of EB1 neural activity for trials 1, 4 and 7 (left to right) during CS. Shown are the detected frequencies at maximum

relative power for trials without distractors (blue), and with distractors (red), greater than peak mean baseline frequency. Black line represents mean baseline frequency spectrum (from $n = 51$ flies). **f**, Frequency (at maximum relative power) of EB1 neural activity during CS for trials without distractors (blue), and with distractors (red) (see [Methods](#), ‘Frequency and decay rate computation’). **g**, Normalized relative power of EB1 neural activity for trials 1, 4 and 7 (left to right) during the 5-s TI. Shown are the detected frequencies at maximum relative power for trials without distractors (blue), and with distractors (red), greater than peak mean baseline frequency. Black line represents mean baseline frequency spectrum (from $n = 51$ flies). **h**, Frequency (at maximum relative power) of EB1 neural activity across trials during the 5-s TI for trials without distractors (blue), and with distractors (red) (see [Methods](#), ‘Frequency and decay rate computation’). No distractor trials ($n = 16$ flies), distractor trials ($n = 16$ flies). Box plot centre (median), edges (IQR), whiskers (1.5x IQR). Scatters represent individual fly activity scores. Group comparisons were performed using a two-factor ART-ANOVA test. ** indicates p -value < 0.01 , exact P values in Supplementary Table 1.

[Extended Data Fig. 6 Ratiometric calcium imaging of ellipsoid body ring neurons during delay conditioning reveals an increased oscillatory component and steady decline with repeated training that is not susceptible to distractions.](#)

a, Ratiometric imaging of an *EB1-Gal4, UAS-GCaMP6f.myr-tdTomato* female during a single delay conditioning experiment without (air puff) distractors (left), and with distractors (right). Shown, raw $dF_{\text{ratio}}/F_{\text{ratio}}$ activity traces (where $F_{\text{ratio}} = F_{\text{GCaMP6f}}/F_{\text{tdTomato}}$) for trials 1, 4, and 7. Red curve fits are single-term exponential model fits through the raw $dF_{\text{ratio}}/F_{\text{ratio}}$ activity traces starting at the end of CS. **b**, Scree plots of cumulative variance explained by each of the top 50 principal components for all delay conditioning trials without distractors (blue), and with distractors (red). **c**, Cumulative variance explained by the top 12 components per trial for delay conditioning without distractors (blue), and with distractors (red). **d**, Exponential curve fit decay rates of EB1 neural activity post-CS for trials without distractors (blue), and with distractors

(red). **e**, Normalized relative power of EB1 neural activity for trials 1, 4 and 7 (left to right) during CS. Shown are the detected frequencies at maximum relative power for trials without distractors (blue), and with distractors (red), greater than peak mean baseline frequency. Black line represents mean baseline frequency spectrum (from $n = 51$ flies). **f**, Frequency (at maximum relative power) of EB1 neural activity across delay conditioning trials during CS for trials without distractors (blue), and with distractors (red) (see [Methods](#), ‘Frequency and decay rate computation’). No distractor trials ($n = 9$ flies), distractor trials ($n = 9$ flies). **g**, Frequency (from **f**) as a function of learning performance (see [Methods](#), ‘Correlating physiological and behavioural metrics’) for trace conditioning with (red, $R^2 0.72$) and without (blue, $R^2 0.77$) distractors. Curve fits are second degree polynomials through the median activity for each of the no distractor (blue) and distractor (red) trials. Box plot centre (median), edges (IQR), whiskers (1.5x IQR). Scatters represent individual fly activity scores. Group comparisons were performed using a two-factor ART-ANOVA test. No significant difference was observed between groups.

Extended Data Fig. 7 Ratiometric calcium imaging of ellipsoid body ring neuron activity in CS-only and US-only conditions.

a, Ratiometric imaging of *EB1-Gal4, UAS-GCaMP6f.myr-tdTomato* female during a single CS-only presentation (no US) experiment. Shown, raw dF_{ratio}/F_{ratio} activity traces (where $F_{ratio} = F_{GCaMP6f}/F_{tdTomato}$) for trials 1, 4, and 7. Red curve fits are single-term exponential model fits through the raw dF_{ratio}/F_{ratio} activity traces starting at the end of CS. **b**, Exponential curve fit decay rates of EB1 neural activity post-CS. **c**, Normalized relative power of EB1 neural activity for trials 1, 4 and 7 (left to right) during CS. Shown are the detected frequencies at maximum relative power greater than peak mean baseline frequency. Black line represents mean baseline frequency spectrum (from $n = 51$ flies). **d**, Frequency (at maximum relative power) of EB1 neural activity during CS (see [Methods](#), ‘Frequency and decay rate computation’). **e**, Normalized relative power of EB1 neural activity for trials 1, 4 and 7 (left to right) during the 5 s post-CS period. Shown are the detected frequencies at maximum relative power greater than peak mean baseline frequency. Black line represents mean baseline frequency spectrum

(from n = 51 flies). **f**, Frequency (at maximum relative power) of EB1 neural activity during the 5 s post-CS period (see [Methods](#), ‘Frequency and decay rate computation’). CS-only presentation trials, n = 17 flies. Box plot centre (median), edges (IQR), whiskers (1.5x IQR). Scatters represent individual fly activity scores. Friedman’s repeated measure ANOVA test was used for comparisons between trials. No significant difference was observed. **g**, Ratiometric imaging of an *EB1-Gal4, UAS-GCaMP6f.myr-tdTomato* female during a single US-only presentation (no CS) experiment. Shown, raw $dF_{\text{ratio}}/F_{\text{ratio}}$ activity traces (where $F_{\text{ratio}} = F_{\text{GCaMP6f}}/F_{\text{tdTomato}}$) for trials 1, 4, and 7. No notable calcium activity was detected. **h**, Normalized relative power of EB1 neural activity for trials 1, 4 and 7 (left to right) during the 10 s CS fictitious presentation (5–15 s). No frequencies of maximum relative power greater than peak mean baseline frequency were detected. Black line represents mean baseline frequency spectrum (from n = 51 flies). **i**, Normalized relative power of EB1 neural activity for trials 1, 4 and 7 (left to right) during the 5 s post-fictitious-CS presentation (15–20 s). No frequencies of maximum relative power greater than peak mean baseline frequency were detected. Black line represents mean baseline frequency spectrum (from n = 51 flies). US-only presentation trials, n = 8 flies.

[Extended Data Fig. 8 Ratiometric calcium imaging of ellipsoid-body-projecting dopaminergic neurons during delay conditioning.](#)

Confocal fluorescence images of **a**, *TH-Gal4>>UAS-myr-EGFP*, **b**, *MB504b-Gal4>>UAS-myr-EGFP*, **c**, *c346-Gal4>>UAS-myr-EGFP*, and **d**, *c346-Gal4, TH-FLP>>UAS-FRT-stop-FRT-mCD8-GFP* expression in female *Drosophila* brains staining the pattern of dopaminergic neurons in most of the brain (does not include the PAM cluster), PPL1 dopaminergic cluster projecting to the mushroom bodies, and PPM3 dopaminergic cluster projecting to the ellipsoid body, respectively. In **a**, left and right images correspond to different z-planes across the brain highlighting dopaminergic neuron subsets targeting the central complex and mushroom body structures. Scale bar is 50 μm . At least three brains were immunostained per genotype presented in **a–d**. **e**, Ratiometric imaging of a *c346-Gal4, UAS-*

GCaMP6m.myr-tdTomato female during a single delay conditioning experiment without (air puff) distractors (left), and with distractors (right). Shown, raw dF_{ratio}/F_{ratio} activity traces (where $F_{ratio} = F_{GCaMP6m}/F_{tdTomato}$) for each training trial. **f**, Peak dF_{ratio}/F_{ratio} activity of ellipsoid body DANs during CS (left), and post-US (right), across trials, without distractors (blue, n = 5 flies), and with distractors (red, n = 5 flies). Box plot centre (median), edges (IQR), whiskers (1.5x IQR). Scatters represent individual fly activity scores. Group comparisons were performed using a two-factor ART-ANOVA test. No significant difference was observed between groups.

Extended Data Fig. 9 Ratiometric calcium imaging of ellipsoid-body-projecting dopaminergic neurons in CS-only and US-only conditions.

a, Ratiometric imaging of a *c346-Gal4, UAS-GCaMP6m.myr-tdTomato* female during a single CS-only presentation (no US) experiment without (air puff) distractors (left), and with distractors (right). Shown, raw dF_{ratio}/F_{ratio} activity traces (where $F_{ratio} = F_{GCaMP6m}/F_{tdTomato}$) for each training trial. **b**, Peak dF_{ratio}/F_{ratio} activity of ellipsoid body DANs during CS (top), and post-CS (bottom), across trials, without distractors (blue, n = 5 flies), and with distractors (red, n = 5 flies). **c**, Ratiometric imaging of a *c346-Gal4, UAS-GCaMP6m.myr-tdTomato* female during a single US-only (no CS) experiment without (air puff) distractors (left), distractors with US in a simulated delay conditioning setting (middle), and distractors with US in a simulated trace conditioning (5-s TI) setting (right). Shown, raw dF_{ratio}/F_{ratio} activity traces (where $F_{ratio} = F_{GCaMP6m}/F_{tdTomato}$) for each training trial. **d**, Peak dF_{ratio}/F_{ratio} activity of ellipsoid body DANs prior to US (left), and post-US (right), across trials, without distractors (black, n = 5 flies), distractors with US in simulated delay conditioning setting (blue, n = 5 flies), and distractors with US in simulated trace conditioning (5-s TI) setting (red, n = 5 flies). Box plot centre (median), edges (IQR), whiskers (1.5x IQR). Scatters represent individual fly activity scores. Group comparisons were performed using a two-factor ART-ANOVA test. No significant difference was observed between groups.

Extended Data Fig. 10 Role of Dop1R2 and DopEcR dopamine receptor signalling in ellipsoid body ring neurons during delay and trace conditioning.

a, Frequency (with maximum power, see [Methods](#), ‘Frequency and decay rate computation’) of EB1 neural activity with either Dop1R2 or DopEcR dopamine receptor signalling impairment across trials for delay conditioning during CS for *EB1-Gal4, UAS-GCaMP6f.myr-tdTomato* flies (black), *EB1-Gal4, UAS-GCaMP6f.myr-tdTomato, UAS-Dop1R2^{RNAi}* flies (red), and *EB1-Gal4, UAS-GCaMP6f.myr-tdTomato, UAS-DopEcR^{RNAi}* flies (blue). n = 9 flies (black), n = 5 flies (red), n = 5 flies (blue). **b**, Frequency of EB1 neural activity with either Dop1R2 or DopEcR signalling impairment across trials for trace conditioning (5-s TI) (during CS, left; during TI, right) for *EB1-Gal4, UAS-GCaMP6f.myr-tdTomato* flies (black), *EB1-Gal4, UAS-GCaMP6f.myr-tdTomato, UAS-Dop1R2^{RNAi}* flies (red), and *EB1-Gal4, UAS-GCaMP6f.myr-tdTomato, UAS-DopEcR^{RNAi}* flies (blue) (see [Methods](#), ‘Frequency and decay rate computation’). n = 16 flies (black), n = 5 flies (red), n = 5 flies (blue). Box plot centre (median), edges (IQR), whiskers (1.5x IQR). Scatters represent individual fly metrics. Group comparisons were performed using a two-factor ART-ANOVA test. No significant difference was observed between groups.

Supplementary information

Reporting Summary

Supplementary Table 1

Statistical comparisons and exact P values for each experiment presented in the main and Extended Data figures.

Supplementary Video 1

EB ring neuron activity during trace conditioning. In vivo ratiometric calcium imaging in an *EB1-Gal4, UAS-GCaMP6f.myr-tdTomato* female

during trace conditioning (5 s trace interval). Left, tdTomato channel with a pseudocolour $F_{\text{ratio}} = F_{\text{GCaMP6f}}/F_{\text{tdTomato}}$ representation of the GCaMP6f signal. Frames with squares on top-right indicate CS (blue), and US (red). Right, $dF_{\text{ratio}}/F_{\text{ratio}}$ activity traces for the corresponding trial. Each row corresponds to a single training trial, wherein CS (blue) and US (red) are presented. Frame rate is 1.5x recording speed (9 Hz).

Supplementary Video 2

EB ring neuron activity during trace conditioning with distractions. In vivo ratiometric calcium imaging in an *EB1-Gal4, UAS-GCaMP6f.myr-tdTomato* female during trace conditioning (5 s trace interval) with (air puff) distractions. Left, tdTomato channel with a pseudocolour $F_{\text{ratio}} = F_{\text{GCaMP6f}}/F_{\text{tdTomato}}$ representation of the GCaMP6f signal. Frames with squares on top-right indicate CS (blue), US (red), and distractors (grey). Right, $dF_{\text{ratio}}/F_{\text{ratio}}$ activity traces for the corresponding trial. Each row corresponds to a single training trial, wherein CS (blue), US (red), and distractors (grey) are presented. Frame rate is 1.5x recording speed (9 Hz).

Supplementary Video 3

EB ring neuron activity during delay conditioning. In vivo ratiometric calcium imaging in an *EB1-Gal4, UAS-GCaMP6f.myr-tdTomato* female during delay conditioning. Left, tdTomato channel with a pseudocolour $F_{\text{ratio}} = F_{\text{GCaMP6f}}/F_{\text{tdTomato}}$ representation of the GCaMP6f signal. Frames with squares on top-right indicate CS (blue), and US (red). Right, $dF_{\text{ratio}}/F_{\text{ratio}}$ activity traces for the corresponding trial. Each row corresponds to a single training trial, wherein CS (blue) and US (red) are presented. Frame rate is 1.5x recording speed (9 Hz).

Supplementary Video 4

EB ring neuron activity during delay conditioning with distractions. In vivo ratiometric calcium imaging in an *EB1-Gal4, UAS-GCaMP6f.myr-tdTomato* female during delay conditioning with (air puff) distractions. Left,

tdTomato channel with a pseudocolour $F_{\text{ratio}} = F_{\text{GCaMP6f}}/F_{\text{tdTomato}}$ representation of the GCaMP6f signal. Frames with squares on top-right indicate CS (blue), US (red), and distractors (grey). Right, $dF_{\text{ratio}}/F_{\text{ratio}}$ activity traces for the corresponding trial. Each row corresponds to a single training trial, wherein CS (blue), US (red), and distractors (grey) are presented. Frame rate is 1.5x recording speed (9 Hz).

Supplementary Video 5

EB-projecting dopaminergic neuron activity during trace conditioning. In vivo ratiometric calcium imaging in a *c346-Gal4, UAS-GCaMP6m.myr-tdTomato* female during trace conditioning (5 s trace interval). Left, tdTomato channel with a pseudocolour $F_{\text{ratio}} = F_{\text{GCaMP6m}}/F_{\text{tdTomato}}$ representation of the GCaMP6m signal. Frames with squares on top-right indicate CS (blue), and US (red). Right, $dF_{\text{ratio}}/F_{\text{ratio}}$ activity traces for the corresponding trial. Each row corresponds to a single training trial, wherein CS (blue) and US (red) are presented. Frame rate is 1.5x recording speed (9 Hz).

Supplementary Video 6

EB-projecting dopaminergic neuron activity during trace conditioning with distractions. In vivo ratiometric calcium imaging in a *c346-Gal4, UAS-GCaMP6m.myr-tdTomato* female during trace conditioning (5 s trace interval) with (air puff) distractions. Left, tdTomato channel with a pseudocolour $F_{\text{ratio}} = F_{\text{GCaMP6m}}/F_{\text{tdTomato}}$ representation of the GCaMP6m signal. Frames with squares on top-right indicate CS (blue), US (red), and distractors (grey). Right, $dF_{\text{ratio}}/F_{\text{ratio}}$ activity traces for the corresponding trial. Each row corresponds to a single training trial, wherein CS (blue), US (red), and distractors (grey) are presented. Frame rate is 1.5x recording speed (9 Hz).

Supplementary Video 7

EB-projecting dopaminergic neuron activity during delay conditioning. In vivo ratiometric calcium imaging in a *c346-Gal4, UAS-GCaMP6m.myr-*

tdTomato female during delay conditioning. Left, tdTomato channel with a pseudocolour $F_{\text{ratio}} = F_{\text{GCaMP6m}}/F_{\text{tdTomato}}$ representation of the GCaMP6m signal. Frames with squares on top-right indicate CS (blue), and US (red). Right, $dF_{\text{ratio}}/F_{\text{ratio}}$ activity traces for the corresponding trial. Each row corresponds to a single training trial, wherein CS (blue) and US (red) are presented. Frame rate is 1.5x recording speed (9 Hz).

Supplementary Video 8

EB-projecting dopaminergic neuron activity during delay conditioning with distractions. In vivo ratiometric calcium imaging in a *c346-Gal4, UAS-GCaMP6m.myr-tdTomato* female during delay conditioning with (air puff) distractions. Left, tdTomato channel with a pseudocolour $F_{\text{ratio}} = F_{\text{GCaMP6m}}/F_{\text{tdTomato}}$ representation of the GCaMP6m signal. Frames with squares on top-right indicate CS (blue), US (red), and distractors (grey). Right, $dF_{\text{ratio}}/F_{\text{ratio}}$ activity traces for the corresponding trial. Each row corresponds to a single training trial, wherein CS (blue), US (red), and distractors (grey) are presented. Frame rate is 1.5x recording speed (9 Hz).

Source data

Source Data Fig. 1

Source Data Fig. 2

Source Data Fig. 3

Source Data Fig. 4

Rights and permissions

Reprints and Permissions

About this article

Cite this article

Grover, D., Chen, JY., Xie, J. *et al.* Differential mechanisms underlie trace and delay conditioning in *Drosophila*. *Nature* **603**, 302–308 (2022).
<https://doi.org/10.1038/s41586-022-04433-6>

- Received: 11 May 2020
- Accepted: 13 January 2022
- Published: 16 February 2022
- Issue Date: 10 March 2022
- DOI: <https://doi.org/10.1038/s41586-022-04433-6>

Share this article

Anyone you share the following link with will be able to read this content:

[Get shareable link](#)

Sorry, a shareable link is not currently available for this article.

[Copy to clipboard](#)

Provided by the Springer Nature SharedIt content-sharing initiative

This article was downloaded by **calibre** from <https://www.nature.com/articles/s41586-022-04433-6>

- Article
- [Published: 02 March 2022](#)

Molecular hallmarks of heterochronic parabiosis at single-cell resolution

- [Róbert Pálovics](#)¹ na1,
- [Andreas Keller](#) [ORCID: orcid.org/0000-0002-5361-0895](#)^{1,2} na1,
- [Nicholas Schaum](#)¹ na1,
- [Weilun Tan](#)³ na1,
- [Tobias Fehlmann](#) [ORCID: orcid.org/0000-0003-1967-2918](#)²,
- [Michael Borja](#)³,
- [Fabian Kern](#) [ORCID: orcid.org/0000-0002-8223-3750](#)²,
- [Liana Bonanno](#)¹,
- [Kruti Calcuttawala](#)¹,
- [James Webber](#)³,
- [Aaron McGeever](#)³,
- [The Tabula Muris Consortium](#),
- [Jian Luo](#) [ORCID: orcid.org/0000-0002-2064-8467](#)⁴,
- [Angela Oliveira Pisco](#) [ORCID: orcid.org/0000-0003-0142-2355](#)³,
- [Jim Karkanias](#) [ORCID: orcid.org/0000-0002-8057-6055](#)³,
- [Norma F. Neff](#) [ORCID: orcid.org/0000-0001-7141-5420](#)³,
- [Spyros Darmanis](#) ³,
- [Stephen R. Quake](#) [ORCID: orcid.org/0000-0002-1613-0809](#)^{3,5} &
- [Tony Wyss-Coray](#) [ORCID: orcid.org/0000-0001-5893-0831](#)^{1,6,7}

Nature volume **603**, pages 309–314 (2022)

- 8112 Accesses

- 108 Altmetric
- [Metrics details](#)

Subjects

- [Ageing](#)
- [Gene expression](#)
- [Transcriptomics](#)

Abstract

The ability to slow or reverse biological ageing would have major implications for mitigating disease risk and maintaining vitality¹. Although an increasing number of interventions show promise for rejuvenation², their effectiveness on disparate cell types across the body and the molecular pathways susceptible to rejuvenation remain largely unexplored. Here we performed single-cell RNA sequencing on 20 organs to reveal cell-type-specific responses to young and aged blood in heterochronic parabiosis. Adipose mesenchymal stromal cells, haematopoietic stem cells and hepatocytes are among those cell types that are especially responsive. On the pathway level, young blood invokes new gene sets in addition to reversing established ageing patterns, with the global rescue of genes encoding electron transport chain subunits pinpointing a prominent role of mitochondrial function in parabiosis-mediated rejuvenation. We observed an almost universal loss of gene expression with age that is largely mimicked by parabiosis: aged blood reduces global gene expression, and young blood restores it in select cell types. Together, these data lay the groundwork for a systemic understanding of the interplay between blood-borne factors and cellular integrity.

This is a preview of subscription content

Access options

Subscribe to Nature+

Get immediate online access to the entire Nature family of 50+ journals

\$29.99

monthly

[Subscribe](#)

Subscribe to Journal

Get full journal access for 1 year

\$199.00

only \$3.90 per issue

[Subscribe](#)

All prices are NET prices.

VAT will be added later in the checkout.

Tax calculation will be finalised during checkout.

Buy article

Get time limited or full article access on ReadCube.

\$32.00

[Buy](#)

All prices are NET prices.

Additional access options:

- [Log in](#)
- [Learn about institutional subscriptions](#)

Fig. 1: Cell-type-specific DGE.

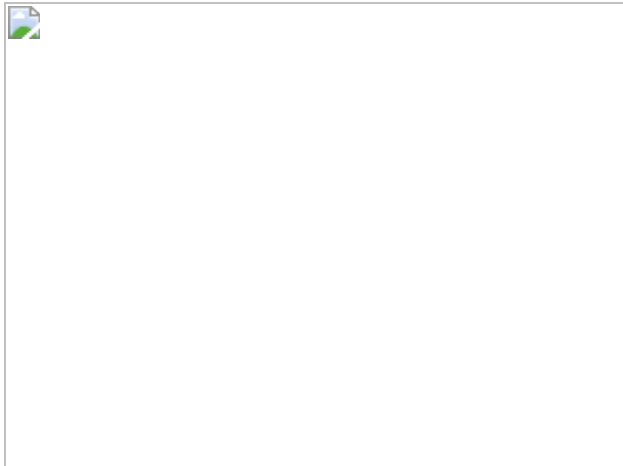


Fig. 2: Young blood reverses mitochondrial and global gene expression loss.

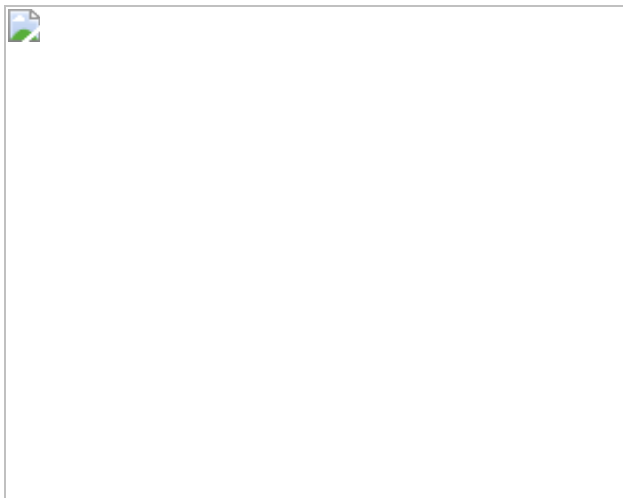


Fig. 3: Structured responses to parabiosis.

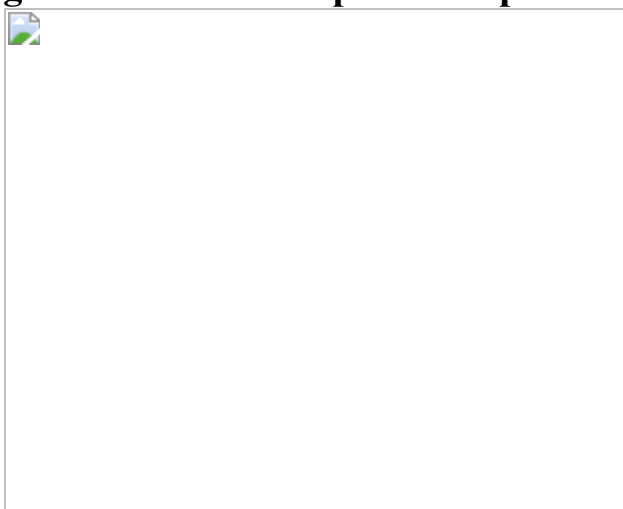
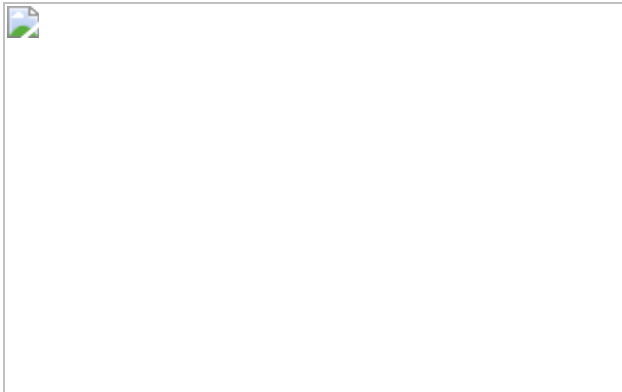


Fig. 4: Coordinated, organism-wide cellular responses to ageing and parabiosis.



Code availability

Code used for downstream analyses of the raw count matrices is available at GitHub: <https://github.com/rpalovics/parabiosis/releases/tag/0.1.0> (<https://doi.org/10.5281/zenodo.5762659>).

Data availability

The dataset can be explored interactively at <https://ccb-web.cs.uni-saarland.de/parabiosis/>. Gene counts and metadata are available on Figshare:

https://figshare.com/projects/Molecular_hallmarks_of_heterochronic_parabiosis_at_single_cell_resolution/127628. Raw sequencing data are available in the Gene Expression Omnibus under accession code [GSE132042](#) and via the following public AWS S3 bucket: <https://registry.opendata.aws/tabula-muris-senis/>. The versions of the noted databases used are available at the following URLs: STRING database, <https://version-11-0.string-db.org/>; MitoCarta 3.0, <https://www.broadinstitute.org/files/shared/metabolism/mitocarta/mouse.mitoCarta3.0.html>; GENCODE vM19, https://www.gencodegenes.org/mouse/release_M19.html.

References

1. López-Otín, C., Blasco, M. A., Partridge, L., Serrano, M. & Kroemer, G. The hallmarks of aging. *Cell* **153**, 1194–1217 (2013).

2. Mahmoudi, S., Xu, L. & Brunet, A. Turning back time with emerging rejuvenation strategies. *Nat. Cell Biol.* **21**, 32–43 (2019).
3. Schaum, N. et al. Single-cell transcriptomics of 20 mouse organs creates a *Tabula Muris*. *Nature* **562**, 367–372 (2018).
4. Schaum, N. et al. Ageing hallmarks exhibit organ-specific temporal signatures. *Nature* **583**, 596–602 (2020).
5. Almanzar, N. et al. A single-cell transcriptomic atlas characterizes ageing tissues in the mouse. *Nature* **583**, 590–595 (2020).
6. Castellano, J. M., Kirby, E. D. & Wyss-Coray, T. Blood-borne revitalization of the aged brain. *JAMA Neurol.* **72**, 1191–1194 (2015).
7. Villeda, S. A. et al. The ageing systemic milieu negatively regulates neurogenesis and cognitive function. *Nature* **477**, 90–96 (2011).
8. Katsimpardi, L. et al. Vascular and neurogenic rejuvenation of the aging mouse brain by young systemic factors. *Science* **344**, 630–634 (2014).
9. Smith, L. K. et al. β 2-microglobulin is a systemic pro-aging factor that impairs cognitive function and neurogenesis. *Nat. Med.* **21**, 932–937 (2015).
10. Khrimian, L. et al. Gpr158 mediates osteocalcin’s regulation of cognition. *J. Exp. Med.* **214**, 2859–2873 (2017).
11. Conboy, I. M. et al. Rejuvenation of aged progenitor cells by exposure to a young systemic environment. *Nature* **433**, 760–764 (2005).
12. Ma, S. et al. Caloric restriction reprograms the single-cell transcriptional landscape of *Rattus norvegicus* aging. *Cell* **180**, 984–1001 (2020).
13. Das, M. M. et al. Young bone marrow transplantation preserves learning and memory in old mice. *Commun. Biol.* **2**, 73 (2019).

14. Baht, G. S. et al. Exposure to a youthful circulation rejuvenates bone repair through modulation of β -catenin. *Nat. Commun.* **6**, 7131 (2015).
15. Kovina, M. V., Zuev, V. A., Kagarlitskiy, G. O. & Khodarovich, Y. M. Effect on lifespan of high yield non-myeloablating transplantation of bone marrow from young to old mice. *Front. Genet.* <https://doi.org/10.3389/fgene.2013.00144> (2013).
16. Wang, C.-H. et al. Bone marrow rejuvenation accelerates re-endothelialization and attenuates intimal hyperplasia after vascular injury in aging mice. *Circ. J.* **77**, 3045–3053 (2013).
17. Smith, L. K. et al. The aged hematopoietic system promotes hippocampal-dependent cognitive decline. *Aging Cell* **19**, e13192 (2020).
18. Lee, S. S. et al. A systematic RNAi screen identifies a critical role for mitochondria in *C. elegans* longevity. *Nat. Genet.* **33**, 40–48 (2003).
19. Zhang, M. J., Pisco, A. O., Darmanis, S. & Zou, J. Mouse Aging Cell Atlas analysis reveals global and cell type specific aging signatures revision 1. *Elife* **10**, e62293 (2021).
20. Kular, J. K., Basu, S. & Sharma, R. I. The extracellular matrix: structure, composition, age-related differences, tools for analysis and applications for tissue engineering. *J. Tissue Eng.* **5**, <https://doi.org/10.1177/2041731414557112> (2014).
21. Pinti, M. et al. Aging of the immune system: focus on inflammation and vaccination. *Eur. J. Immunol.* **46**, 2286–2301 (2016).
22. Villeda, S. A. et al. Young blood reverses age-related impairments in cognitive function and synaptic plasticity in mice. *Nat. Med.* **20**, 659–663 (2014).
23. Picelli, S. et al. Full-length RNA-seq from single cells using Smart-seq2. *Nat. Protoc.* **9**, 171–181 (2014).

24. Darmanis, S. et al. A survey of human brain transcriptome diversity at the single cell level. *Proc. Natl Acad. Sci. USA* **112**, 7285–7290 (2015).
25. Picelli, S. et al. Tn5 transposase and tagmentation procedures for massively scaled sequencing projects. *Genome Res.* **24**, 2033–2040 (2014).
26. Hennig, B. P. et al. Large-scale low-cost NGS library preparation using a robust Tn5 purification and tagmentation protocol. *G3 (Bethesda)* **8**, 79–89 (2018).
27. Luecken, M. D. & Theis, F. J. Current best practices in single-cell RNA-seq analysis: a tutorial. *Mol. Syst. Biol.* **15**, e8746 (2019).
28. Wolf, F. A., Angerer, P. & Theis, F. J. SCANPY: large-scale single-cell gene expression data analysis. *Genome Biol.* **19**, 15 (2018).
29. Polański, K. et al. BBKNN: fast batch alignment of single cell transcriptomes. *Bioinformatics* **36**, 964–965 (2020).
30. Traag, V. A., Waltman, L. & Van Eck, N. J. From Louvain to Leiden: guaranteeing well-connected communities. *Sci. Rep.* **9**, 5233 (2019).
31. McInnes, L., Healy, J. & Melville, J. UMAP: Uniform Manifold Approximation and Projection for Dimension Reduction. Preprint at <https://arxiv.org/abs/1802.03426> (2018) .
32. Korsunsky, I. et al. Fast, sensitive and accurate integration of single-cell data with Harmony. *Nat. Methods* **16**, 1289–1296 (2019).
33. Pedregosa, F. et al. Scikit-learn: machine Learning in Python. *J. Machine Learn. Res.* **12**, 2825–2830 (2011).
34. Mann, H. B. & Whitney, D. R. On a test of whether one of two random variables is stochastically larger than the other. *Ann. Math. Stat.* **18**, 50–60 (1947).

35. Benjamini, Y. & Hochberg, Y. Controlling the false discovery rate: a practical and powerful approach to multiple testing. *J. R. Stat. Soc. B* **57**, 289–300 (1995).
36. Enge, M. et al. Single-cell analysis of human pancreas reveals transcriptional signatures of aging and somatic mutation patterns. *Cell* **171**, 321–330 (2017).
37. Kimmel, J. C. et al. Murine single-cell RNA-seq reveals cell-identity- and tissue-specific trajectories of aging. *Genome Res.* **29**, 2088–2103 (2019).
38. Gerstner, N. et al. GeneTrail 3: advanced high-throughput enrichment analysis. *Nucleic Acids Res.* **48**, W515–W520 (2020).
39. Carbon, S. et al. The Gene Ontology Resource: 20 years and still GOing strong. *Nucleic Acids Res.* **47**, D330–D338 (2019).
40. Rath, S. et al. MitoCarta3.0: an updated mitochondrial proteome now with sub-organelle localization and pathway annotations. *Nucleic Acids Res.* **49**, D1541–D1547 (2021).
41. Gu, Z., Eils, R. & Schlesner, M. Complex heatmaps reveal patterns and correlations in multidimensional genomic data. *Bioinformatics* **32**, 2847–2849 (2016).
42. Wickham, H. *ggplot2*. *Wiley Interdiscip. Rev. Comput. Stat.* **3**, 180–185 (2011).
43. Hagberg, A., Swart, P. & Schult, D. Exploring Network Structure, Dynamics, and Function Using Networkx (Los Alamos National Laboratory, 2008); <https://www.osti.gov/servlets/purl/960616>.
44. Szklarczyk, D. et al. STRING v11: protein–protein association networks with increased coverage, supporting functional discovery in genome-wide experimental datasets. *Nucleic Acids Res.* **47**, D607–D613 (2019).

45. Ewels, P. A. et al. The nf-core framework for community-curated bioinformatics pipelines. *Nat. Biotechnol.* **38**, 276–278 (2020).
46. Dobin, A. et al. STAR: ultrafast universal RNA-seq aligner. *Bioinformatics* **29**, 15–21 (2013).
47. Li, B. & Dewey, C. N. RSEM: accurate transcript quantification from RNA-Seq data with or without a reference genome. *BMC Bioinform.* **12**, 323 (2011).
48. Soneson, C., Love, M. I. & Robinson, M. D. Differential analyses for RNA-seq: transcript-level estimates improve gene-level inferences [version 1; peer review: 2 approved]. *F1000Research* **4**, 1521 (2015).
49. Love, M. I., Huber, W. & Anders, S. Moderated estimation of fold change and dispersion for RNA-seq data with DESeq2. *Genome Biol.* **15**, 550 (2014).
50. Chen, E. Y. et al. Enrichr: interactive and collaborative HTML5 gene list enrichment analysis tool. *BMC Bioinform.* **14**, 128 (2013).

Acknowledgements

We thank the members of the laboratory of T.W.-C. and the Chan Zuckerberg Biohub for feedback and support. Financial support for library preparation, sequencing and AWS time was provided by the Chan Zuckerberg Biohub. Further financial support was provided by the Department of Veterans Affairs (BX004599 to T.W.-C.), the National Institute on Aging (R01-AG045034, AG064928, AG072255, and DP1-AG053015 to T.W.-C.), the NOMIS Foundation (T.W.-C.), The Glenn Foundation for Medical Research (T.W.-C.), Nan Fung Life Sciences (T.W.-C.), and the Wu Tsai Neurosciences Institute and Bertarelli Foundation (T.W.-C.). This work was supported by the National Institute of Aging and the National Institutes of Health under award number P30AG059307.

Author information

Author notes

1. These authors contributed equally: Róbert Pálovics, Andreas Keller, Nicholas Schaum, Weilun Tan

Affiliations

1. Department of Neurology and Neurological Sciences, Stanford University School of Medicine, Stanford, CA, USA

Róbert Pálovics, Andreas Keller, Nicholas Schaum, Liana Bonanno, Kruti Calcuttawala, Daniela Berdnik, Biter Bilen, Antoine de Morree, Qiang Gan, Oliver Hahn, Michael Seamus Haney, Albin Huang, Tal Iram, Nathalie Khoury, Davis P. Lee, Song E. Lee, Benoit Lehallier, Ling Liu, Maria F. Lugo-Fagundo, Thomas A. Rando, Daniel Staehli, Michael N. Wosczyna, Andrew C. Yang, Lakshmi P. Yerra, Macy E. Zardeneta, Hui Zhang & Tony Wyss-Coray

2. Clinical Bioinformatics, Saarland University, Saarbrücken, Germany

Andreas Keller, Tobias Fehlmann & Fabian Kern

3. Chan Zuckerberg Biohub, San Francisco, CA, USA

Weilun Tan, Michael Borja, James Webber, Aaron McGeever, Stephanie D. Conley, Aaron Demers, Tessa Divita, Hamid Ebadi, Rafael Gómez-Sjöberg, Foad Green, Geraldine Genetiano, Lincoln Harris, Shayan Hosseinzadeh, Kerwyn Casey Huang, Feather Ives, Robert C. Jones, Annie Lo, Andrew P. May, Ashley Maynard, Marina McKay, Lolita Penland, Robert Puccinelli, Rene V. Sit, Justin Sonnenburg, Michelle Tan, Cristina Tato, Lucas Waldburger, Kevin A. Yamauchi, Justin Youngyunipatkul, Brian Yu, Alexander Zee, Chunyu Zhao, James Zou, Angela Oliveira Pisco, Jim Karkanias, Norma F. Neff, Spyros Darmanis & Stephen R. Quake

4. Veterans Administration Palo Alto Healthcare System, Palo Alto, CA, USA

Haley du Bois, Olivia Leventhal, Thomas A. Rando & Jian Luo

5. Department of Bioengineering, Stanford University, Stanford, CA, USA

Michelle B. Chen, Kerwyn Casey Huang, Marco Mignardi, Soso Xue, Andrew C. Yang, Fabio Zanini & Stephen R. Quake

6. Paul F. Glenn Center for the Biology of Aging, Stanford University School of Medicine, Stanford, CA, USA

Thomas A. Rando, Macy E. Zardeneta & Tony Wyss-Coray

7. Wu Tsai Neurosciences Institute, Stanford University School of Medicine, Stanford, CA, USA

Philip A. Beachy & Tony Wyss-Coray

8. Department of Pediatrics, Pulmonary Medicine, Stanford University School of Medicine, Stanford, CA, USA

Nicole Almanzar, Christin S. Kuo, Dullei Min, Kenneth Weinberg & Sean M. Wu

9. Institute for Stem Cell Biology and Regenerative Medicine, Stanford University School of Medicine, Stanford, CA, USA

Jane Antony, Ankit S. Baghel, Isaac Bakerman, Ishita Bansal, Philip A. Beachy, Michael F. Clarke, Kubilay Demir, Matt Fish, Benson M. George, Gunsagar S. Gulati, Taichi Isobe, Kevin S. Kao, Aaron M. Kershner, Bernhard M. Kiss, William Kong, Wan-Jin Lu, Anoop Manjunath, Patricia K. Nguyen, Joseph Noh, Zhen Qi, Shaheen S. Sikandar, Rahul Sinha, Krzysztof Szade, Laughing Bear Torrez Dulgeroff, Linda J. van Weele, Irving L. Weissman & Jinyi Xiang

10. Stanford Cardiovascular Institute, Stanford University School of Medicine, Stanford, CA, USA

Isaac Bakerman, Patricia K. Nguyen & Sean M. Wu

11. Division of Cardiovascular Medicine, Department of Medicine, Stanford University School of Medicine, Stanford, CA, USA

Isaac Bakerman, Guang Li, Patricia K. Nguyen & Sean M. Wu

12. Department of Neurobiology, Stanford University School of Medicine, Stanford, CA, USA

Ben A. Barres, Qingyun Li & Lu Zhou

13. Department of Biochemistry, Stanford University School of Medicine, Stanford, CA, USA

Philip A. Beachy, Douglas Brownfield, F. Hernán Espinoza, Astrid Gillich, Mark A. Krasnow, Wan-Jin Lu, Ahmad N. Nabhan, Katharine M. Ng, Roel Nusse & Kyle J. Travaglini

14. Maternal & Child Health Research Institute, Stanford University School of Medicine, Stanford, CA, USA

Philip A. Beachy, Kubilay Demir, Matt Fish, Mark A. Krasnow, Roel Nusse & Sean M. Wu

15. Department of Developmental Biology, Stanford University School of Medicine, Stanford, CA, USA

Philip A. Beachy, Matt Fish, Xueying Gu, Yan Hang, Seung K. Kim, Jonathan Lam, Roel Nusse, Weng Chuan Peng, Eric J. Rulifson & Krissie Tellez

16. Flow Cytometry Core, Veterans Administration Palo Alto Healthcare System, Palo Alto, CA, USA

Corey Cain

17. Department of Surgery, Division of Plastic and Reconstructive Surgery, Stanford University, Stanford, CA, USA

Charles K. F. Chan

18. Department of Biomedicine, Aarhus University, Aarhus, Denmark

Antoine de Morree

19. Department of Physiology, University of California, San Francisco, CA, USA

Mu He

20. Department of Microbiology & Immunology, Stanford University School of Medicine, Stanford, CA, USA

Kerwyn Casey Huang, Bryan Merrill, Justin Sonnenburg & Carolina Tropini

21. Department of Medicine and Liver Center, University of California San Francisco, San Francisco, CA, USA

Guruswamy Karnam, Rasika Patkar, Joe M. Segal, Margaret Tsui & Bruce M. Wang

22. Department of Medicine and Stanford Diabetes Research Center, Stanford University, Stanford, CA, USA

Seung K. Kim

23. Department of Urology, Stanford University School of Medicine, Stanford, CA, USA

Bernhard M. Kiss

24. Sean N. Parker Center for Asthma and Allergy Research, Stanford University School of Medicine, Stanford, CA, USA

Maya E. Kumar

25. Department of Medicine, Division of Pulmonary and Critical Care,
Stanford University School of Medicine, Stanford, CA, USA

Maya E. Kumar

26. Department of Developmental Biology, University of Pittsburgh
School of Medicine, Pittsburgh, PA, USA

Guang Li

27. Mental Illness Research Education and Clinical Center, Veterans
Administration Palo Alto Healthcare System, Palo Alto, CA, USA

M. Windy McNerney

28. Department of Psychiatry, Stanford University School of Medicine,
Stanford, CA, USA

M. Windy McNerney

29. Vera Moulton Wall Center for Pulmonary and Vascular Disease,
Stanford University School of Medicine, Stanford, CA, USA

Ross J. Metzger & Fan Zhang

30. Department of Pediatrics, Division of Cardiology, Stanford University
School of Medicine, Stanford, CA, USA

Ross J. Metzger & Fan Zhang

31. Princess Máxima Center for Pediatric Oncology, Utrecht, The
Netherlands

Weng Chuan Peng

32. Department of Epidemiology and Biostatistics, University of
California, San Francisco, CA, USA

Katherine Pollard

33. Department of Pathology, Stanford University School of Medicine, Stanford, CA, USA

Rahul Sinha & Irving L. Weissman

34. Ludwig Center for Cancer Stem Cell Research and Medicine, Stanford University School of Medicine, Stanford, CA, USA

Rahul Sinha & Irving L. Weissman

35. Stanford Cancer Institute, Stanford University School of Medicine, Stanford, CA, USA

Rahul Sinha & Irving L. Weissman

36. Department of Medical Biotechnology, Faculty of Biochemistry, Biophysics and Biotechnology, Jagiellonian University, Krakow, Poland

Krzysztof Szade

37. School of Biomedical Engineering, University of British Columbia, Vancouver, British Columbia, Canada

Carolina Tropini

38. Department of Microbiology and Immunology, University of British Columbia, Vancouver, British Columbia, Canada

Carolina Tropini

39. Humans and the Microbiome Program, Canadian Institute for Advanced Research, Toronto, Ontario, Canada

Carolina Tropini

40. Department of Electrical Engineering, Stanford University, Palo Alto, CA, USA

Martin Jinye Zhang & James Zou

41. Department of Epidemiology, Harvard T.H. Chan School of Public Health, Boston, MA, USA

Martin Jinye Zhang

42. Department of Biomedical Data Science, Stanford University, Palo Alto, CA, USA

James Zou

Consortia

The Tabula Muris Consortium

- , Nicole Almanzar
- , Jane Antony
- , Ankit S. Baghel
- , Isaac Bakerman
- , Ishita Bansal
- , Ben A. Barres
- , Philip A. Beachy
- , Daniela Berdnik
- , Biter Bilen
- , Douglas Brownfield
- , Corey Cain
- , Charles K. F. Chan
- , Michelle B. Chen
- , Michael F. Clarke
- , Stephanie D. Conley
- , Spyros Darmanis
- , Aaron Demers
- , Kubilay Demir

- , Antoine de Morree
- , Tessa Divita
- , Haley du Bois
- , Hamid Ebadi
- , F. Hernán Espinoza
- , Matt Fish
- , Qiang Gan
- , Benson M. George
- , Astrid Gillich
- , Rafael Gòmez-Sjöberg
- , Foad Green
- , Geraldine Genetiano
- , Xueying Gu
- , Gunsagar S. Gulati
- , Oliver Hahn
- , Michael Seamus Haney
- , Yan Hang
- , Lincoln Harris
- , Mu He
- , Shayan Hosseinzadeh
- , Albin Huang
- , Kerwyn Casey Huang
- , Tal Iram
- , Taichi Isobe
- , Feather Ives
- , Robert C. Jones
- , Kevin S. Kao
- , Jim Karkanas
- , Guruswamy Karnam
- , Andreas Keller
- , Aaron M. Kershner
- , Nathalie Khoury
- , Seung K. Kim
- , Bernhard M. Kiss
- , William Kong
- , Mark A. Krasnow
- , Maya E. Kumar

- , Christin S. Kuo
- , Jonathan Lam
- , Davis P. Lee
- , Song E. Lee
- , Benoit Lehallier
- , Olivia Leventhal
- , Guang Li
- , Qingyun Li
- , Ling Liu
- , Annie Lo
- , Wan-Jin Lu
- , Maria F. Lugo-Fagundo
- , Anoop Manjunath
- , Andrew P. May
- , Ashley Maynard
- , Aaron McGeever
- , Marina McKay
- , M. Windy McNerney
- , Bryan Merrill
- , Ross J. Metzger
- , Marco Mignardi
- , Dullei Min
- , Ahmad N. Nabhan
- , Norma F. Neff
- , Katharine M. Ng
- , Patricia K. Nguyen
- , Joseph Noh
- , Roel Nusse
- , Róbert Pálovics
- , Rasika Patkar
- , Weng Chuan Peng
- , Lolita Penland
- , Angela Oliveira Pisco
- , Katherine Pollard
- , Robert Puccinelli
- , Zhen Qi
- , Stephen R. Quake

- , Thomas A. Rando
- , Eric J. Rulifson
- , Nicholas Schaum
- , Joe M. Segal
- , Shaheen S. Sikandar
- , Rahul Sinha
- , Rene V. Sit
- , Justin Sonnenburg
- , Daniel Staehli
- , Krzysztof Szade
- , Michelle Tan
- , Weilun Tan
- , Cristina Tato
- , Krissie Tellez
- , Laughing Bear Torrez Dulgeroff
- , Kyle J. Travaglini
- , Carolina Tropini
- , Margaret Tsui
- , Lucas Waldburger
- , Bruce M. Wang
- , Linda J. van Weele
- , Kenneth Weinberg
- , Irving L. Weissman
- , Michael N. Wosczyna
- , Sean M. Wu
- , Tony Wyss-Coray
- , Jinyi Xiang
- , Soso Xue
- , Kevin A. Yamauchi
- , Andrew C. Yang
- , Lakshmi P. Yerra
- , Justin Youngyunpipatkul
- , Brian Yu
- , Fabio Zanini
- , Macy E. Zardeneta
- , Alexander Zee
- , Chunyu Zhao

- , Fan Zhang
- , Hui Zhang
- , Martin Jinye Zhang
- , Lu Zhou
- & James Zou

Contributions

R.P., A.K., N.S. and W.T. contributed equally. N.S., S.R.Q. and T.W.-C. conceptualized the study. R.P., A.K., N.S., T.F. and T.W.-C. conceptualized the analysis. R.P., A.K., T.F. and F.K. conducted the analysis. N.S., L.B. and J.L. performed parabiosis surgeries. N.S. and K.C. collected and processed bulk organ samples for RNA-seq. The Tabula Muris Consortium processed organs and captured cells for scRNA-seq. W.T. and M.B. conducted cDNA and library preparation. R.P. created the web browser. W.T. and M.B. performed sequencing and library quality control. W.T., M.B., A.O.P., J.W. and A.M. processed raw sequencing data. R.P., A.K., N.S., S.R.Q. and T.W.-C. wrote and edited the manuscript. T.W.-C., S.R.Q., S.D., N.F.N., J.K. and A.O.P supervised the work.

Corresponding authors

Correspondence to [Andreas Keller](#), [Spyros Darmanis](#), [Stephen R. Quake](#) or [Tony Wyss-Coray](#).

Ethics declarations

Competing interests

The authors declare no competing interests.

Peer review

Peer review information

Nature thanks Johan Auwerx, Yousin Suh, Fan Zhang and the other, anonymous, reviewer(s) for their contribution to the peer review of this work.

Additional information

Publisher's note Springer Nature remains neutral with regard to jurisdictional claims in published maps and institutional affiliations.

Extended data figures and tables

[Extended Data Fig. 1 Outline of data analyses and tissue specific data overview.](#)

a, Outline of computational analyses. Single-cell count data are processed per tissue, see [Methods](#) ‘Quality control’-‘Cell type annotation’. Differential gene expression is then conducted per cell type and comparison (AGE, ACC, REJ) within each tissue, see [Methods](#) ‘Differential gene expression’. All of the next panels present data after quality control. **b**, Number of cells per tissue and replicate. Replicates are colored by their condition. **c**, Number of replicates per tissue. Replicates are colored by their condition. **d**, Total number of cells per tissue. **e**, Fraction of cells within each condition per tissue. **f-i**, For each experimental condition within each tissue: total read counts (**f**), the percent of reads mapped to ribosomal genes (**g**), mitochondrial genes (**h**), and ERCC spike-ins (**i**) plotted against the mean number of genes expressed. **j**, Average LISI scores of mouse replicates calculated over the batch corrected tissue specific UMAP embeddings plotted against the mean LISI scores of tissue specific UMAP embeddings calculated from neighborhood graphs without batch correction. **k**, Mean entropy batch mixing of mouse replicates calculated over the tissue specific batch-corrected neighborhood graph plotted against the mean entropy batch mixing calculated from neighborhood graphs without batch correction. **l**, Result of saturation analyses shown per condition (Y, A, IY, HY, IA, HA). Downsampling was carried out per condition within each tissue separately. Results indicate the number of detected genes as the function of the downsampled total counts.

Extended Data Fig. 2 Cell type specific data overview.

All panels present data after quality control. **a**, Number of cells per cell type and replicate. Replicates are colored by their condition. **b**, Number of replicates per cell type. Replicates are colored by their condition. **c**, Total number of cells per cell type. **d**, Fraction of cells within each condition per cell type. **e-h**, For each experimental condition within each cell type, total read counts (**e**), the percent of reads mapped to ribosomal genes (**f**), mitochondrial genes (**g**), and ERCC spike-ins (**h**) plotted against the mean number of genes expressed.

Extended Data Fig. 3 Validation of differential gene expression analysis.

a, Number of DEGs plotted against the total number of cells within the control and treatment groups. Each dot represents a DGE comparison of a cell type. **b-d**, Cumulative distributions of the calculated effect size (**b**), -log10(adj. p-value) (**c**) and log2 fold change values (**d**). Distributions are shown separately for ACC, REJ and AGE DGE. Vertical lines indicate the cutoffs applied throughout the study. **e**, Summary of ACC DGE results. Each cell type that has at least 50 cells in IY and HY is studied in the context of ACC and hence shown. From top to bottom: control and treatment sample sizes indicated separately for AGE and ACC, the number of genes differentially expressed in AGE and ACC, overlaps between AGE and ACC. Overlaps are normalized by the number of DEGs in the union of ACC and AGE DEGs. **f**, Summary of REJ DGE results. Each cell type that has at least 50 cells in IA and HA is studied in the context of REJ and hence shown. From top to bottom: control and treatment sample sizes indicated separately for AGE and REJ, the number of genes differentially expressed in AGE and REJ, overlaps between AGE and REJ. Overlaps are normalized by the number of DEGs in the union of REJ and AGE DEGs. **g**, Percent of DEGs that change in the same direction with AGE and ACC are plotted against the total number of DEGs within AGE and ACC for each comparison. Percentages are based on the union of DEGs as defined in (**e**) **h**, Percent of DEGs that change in the opposite direction with AGE and REJ are plotted against the total number of DEGs within AGE and REJ for each comparison. Percentages are based on the union of DEGs as defined in

(f). i, Fraction of DEGs changing in the same direction with AGE and ACC plotted against the fraction of DEGs changing in the opposite direction with AGE and ACC. Each dot represents a cell type of the study. Colored area indicates where more DEGs change in the same direction than in the opposite direction. **j**, Fraction of DEGs changing in the same direction with AGE and REJ plotted against the fraction of DEGs changing in the opposite direction with AGE and REJ. Each dot represents a cell type of the study. Colored area indicates where more DEGs change in the opposite direction than in the same direction.

Extended Data Fig. 4 Validation of differential gene expression analysis.

a, Violin plots showing the number of differentially expressed genes as the function of the number of replicates per comparison. The number of replicates are defined as the minimum number of replicates within the control and treatment groups. Results are shown separately for TMS (left) and parabiosis (right). **b**, Comparison of differential gene expression results with and without subsampling in case of each cell type specific comparison. Spearman correlation values indicate (dis)similarities between: p-values derived from the original and subsampled data (left), effect sizes calculated from the original and subsampled data (middle), and effect sizes calculated on the original data and p-values derived from the subsampled datasets. **c**, Number of DEGs identified at different p-value and effect size cutoffs per comparison in AGE (left), ACC (middle), and REJ (right).

Extended Data Fig. 5 Differential gene expression results.

a, Top list of the 50 most frequent DEGs identified for ACC and REJ. Results are shown separately for up and downregulation. Columns with darker bars indicate top lists where only changes consistent with AGE are shown. These include genes changing in the same direction with ACC and AGE, as well as genes changing in the opposite direction with REJ and AGE. **b**, DGE results for marrow HSCs for ACC (left) and for REJ (right). from top to bottom: volcano plots (top) show top DEGs. Comparisons of log2-fold changes (middle) show changes with parabiosis on the x-axis and with normal ageing on the y-axis. DEGs with adj. p-value < 0.05, eff. size >

0.6 are shown. Areas where ACC and AGE change in the same direction as well as where REJ and AGE change in the opposite direction are highlighted. Top pathways (GO Biological Process) with highest ‘Combined scores’ defined as in Enrichr⁵⁰ are shown at the bottom. **c**, Most enriched pathways (GO Biological Process) among the 100 most frequent DEGs shared across multiple cell types. Results shown for ACC and ACC-AGE same direction (top), and REJ and REJ-AGE opposite direction (bottom). Combined scores are defined as in Enrichr⁵⁰. **d**, Gene expression violin plots for liver hepatocytes, GAT MSCs and marrow HSCs of select genes encoding proteins of the electron transport chain. Significance values show the adj. p-values of the Wilcoxon–Mann–Whitney test (two-sided) based differential gene expression, see [Methods](#): ‘Differential gene expression’.

Extended Data Fig. 6 Analyses of genes associated with the 5 OXPHOS complexes.

a, Log2-fold changes with AGE, ACC and REJ of genes associated with the 5 OXPHOS complexes. Changes with adj. p-val.<0.05 and eff. size>0.6 are shown. Each column corresponds to one complex and the three separate colors distinguish between AGE, ACC and REJ. **b**, Spearman correlation of gene expression values with age in case of genes associated with the 5 OXPHOS complexes in the Tabula Muris Senis bulk dataset. Data has been analyzed as in². Correlation values with adj. p-value < 0.05 are shown. **c**, Log2-fold changes with ACC and REJ of genes associated with the 5 OXPHOS complexes in the bulk parabiosis dataset.

Extended Data Fig. 7 Analysis of transcriptional noise.

a–c, Mean number of genes expressed within each cell type, x and y axes indicate Y and A (**a**), IY and HY (**b**) and IA and HA (**c**), each dot represents a cell type. **d–f**, Cell-cell variability within each cell type in Y and A (**d**), IY and HY (**e**) and IA and HA (**f**), each dot represents a cell type. **g–i**, Overdispersion within each cell type in Y and A (**g**), IY and HY (**h**) and IA and HA (**i**), each dot represents a cell type.

Extended Data Fig. 8 Pathway analysis.

a, Top 10 most differently affected pathways over all ACC tissues and cell types (top, largest difference at the top) and top 10 most differently affected pathways over all AGE (bottom, largest difference at the bottom) tissues and cell types. **b**, Same as for **a**, comparing REJ and AGE pathways. **c**, Heatmap showing the top 30 most strongly affected pathways in AGE, ACC and REJ in hematopoietic stem cells (HSCs) of the marrow. Pathways related to mitochondria are highlighted in green on the left. Each entry of the heatmap shows the significance level and the number of genes associated with the pathway. **d**, Same as for **c**, showing the top 30 most strongly affected pathways for beta cells of the pancreas.

Extended Data Fig. 9 Ageing and rejuvenation similarity analysis.

a–c, AGE (**a**), ACC (**b**), and REJ (**c**) DGE based cosine similarity matrices of the cell types studied, see [Methods](#) section ‘Ageing and rejuvenation similarity analysis’. All matrices are clustered with complete link hierarchical clustering. **d**, Force-directed network visualization of the STRING links between DEGs common to MSCs from GAT, MAT, SCAT, bladder, limb muscle, and diaphragm. **e**, Force-directed network visualization of the STRING links between DEGs common to MSCs (GAT and MAT), hepatocytes, basal and epidermal cells (skin), and HSCs and macrophages (marrow). All links with >0.9 STRING confidence score (scale from 0-1) are queried and shown. **f, g** Most enriched pathways (GO Biological Process) among the nodes of the networks shown in (**d, e**), combined scores are defined as in Enrichr⁵⁰.

Supplementary information

Supplementary Fig. 1

Statistics related to quality control, batch correction and cell type annotation for the data used after quality control throughout the study. Results shown separately, for each tissue analysed.

Supplementary Fig. 2

AGE, ACC and REJ DGE results shown for each cell type separately. Blank plots indicate insufficient data (that is, fewer than 50 cells per control or treatment group of the specific comparison).

Supplementary Fig. 3

Heatmaps showing the top 30 most strongly affected pathways in AGE, ACC and REJ for each tissue and cell type. Pathways related to mitochondria are highlighted in green. Heatmaps show the significance level and the number of genes associated with the corresponding pathway.

Supplementary Information

This file contains the legends for Supplementary Tables 1–8.

Supplementary Tables

This file contains Supplementary Tables 1–8; see separate PDF for table legends.

Reporting Summary

Rights and permissions

Reprints and Permissions

About this article

Cite this article

Pálovics, R., Keller, A., Schaum, N. *et al.* Molecular hallmarks of heterochronic parabiosis at single-cell resolution. *Nature* **603**, 309–314 (2022). <https://doi.org/10.1038/s41586-022-04461-2>

- Received: 23 October 2020
- Accepted: 25 January 2022
- Published: 02 March 2022
- Issue Date: 10 March 2022
- DOI: <https://doi.org/10.1038/s41586-022-04461-2>

Share this article

Anyone you share the following link with will be able to read this content:

[Get shareable link](#)

Sorry, a shareable link is not currently available for this article.

[Copy to clipboard](#)

Provided by the Springer Nature SharedIt content-sharing initiative

[Single-cell survey of heterochronic parabiosis](#)

- Anna Kriebs

Research Highlight 02 Mar 2022

This article was downloaded by **calibre** from <https://www.nature.com/articles/s41586-022-04461-2>

- Article
- Open Access
- [Published: 23 February 2022](#)

The bacterial toxin colibactin triggers prophage induction

- [Justin E. Silpe](#) ORCID: [orcid.org/0000-0002-6264-8553^{1,na1}](https://orcid.org/0000-0002-6264-8553),
- [Joel W. H. Wong](#)^{1 na1},
- [Siân V. Owen](#) ORCID: [orcid.org/0000-0001-5330-3177²](https://orcid.org/0000-0001-5330-3177),
- [Michael Baym](#) ORCID: [orcid.org/0000-0003-1303-5598²](https://orcid.org/0000-0003-1303-5598) &
- [Emily P. Balskus](#) ORCID: [orcid.org/0000-0001-5985-5714^{1,3}](https://orcid.org/0000-0001-5985-5714)

Nature volume 603, pages 315–320 (2022)

- 13k Accesses
- 262 Altmetric
- [Metrics details](#)

Subjects

- [Natural products](#)
- [Phage biology](#)

Abstract

Colibactin is a chemically unstable small-molecule genotoxin that is produced by several different bacteria, including members of the human gut microbiome^{1,2}. Although the biological activity of colibactin has been extensively investigated in mammalian systems³, little is known about its effects on other microorganisms. Here we show that colibactin targets bacteria that contain prophages, and induces lytic development through the bacterial SOS response. DNA, added exogenously, protects bacteria from colibactin, as does expressing a colibactin resistance protein (ClbS) in non-colibactin-producing cells. The prophage-inducing effects that we observe apply broadly across different phage–bacteria systems and in complex communities. Finally,

we identify bacteria that have colibactin resistance genes but lack colibactin biosynthetic genes. Many of these bacteria are infected with predicted prophages, and we show that the expression of their ClbS homologues provides immunity from colibactin-triggered induction. Our study reveals a mechanism by which colibactin production could affect microbiomes and highlights a role for microbial natural products in influencing population-level events such as phage outbreaks.

[Download PDF](#)

Main

Microbial communities, including the human microbiome, are rich sources of bioactive natural products. However, the biological roles of natural products in these habitats are typically poorly understood. A bacterial natural product of particular relevance to human health is colibactin, a chemically reactive small-molecule genotoxin produced by gut bacteria that have a 54-kb hybrid nonribosomal peptide synthetase-polyketide synthase (NRPS-PKS) biosynthetic gene cluster known as the *pks* island (Fig. 1a). This gene cluster is predominantly found in human-associated strains of *Escherichia coli* that belong to phylogenetic group B2, but is also present in other human gut Enterobacteriaceae, as well as bacteria from the honey bee gut, a marine sponge and an olive tree knot^{4,5,6}. Mechanistic studies have revealed that colibactin induces inter-strand DNA cross-links in vitro, causes cell-cycle arrest in eukaryotic cell culture and affects tumour formation in mouse models of colorectal cancer. Colibactin–DNA adducts have been detected in mammalian cells and in mice⁷, and studies have identified colibactin-associated mutational signatures in cancer genomes, predominantly from colorectal cancer^{8,9}. Despite its important biological activity, colibactin has eluded traditional isolation and structural elucidation. Information regarding its chemical structure has largely been derived from bioinformatic analyses and biochemical characterization^{10,11,12,13}. These studies suggest that colibactin has a pseudodimeric structure, with a reactive cyclopropane warhead at each end that accounts for its characteristic DNA-alkylating ability^{7,14,15} (Fig. 1a).

Fig. 1: Colibactin production specifically affects prophage-carrying bacteria.

 **figure 1**

a, Biosynthetic organization and chemical structure of the genotoxic natural product colibactin. The proposed mode of action toward human cells as a DNA-damaging agent is shown. **b**, Growth and relative abundance of *pks⁻* and *pks⁺* *E. coli* in co-culture. Top, total culture density (optical density at 600 nm; OD_{600 nm}) of *pks⁻ lacZ⁻* *E. coli* co-cultured with *pks⁺ lacZ⁺* *E. coli*, at a starting ratio of 1:1. Bottom, the proportion of *lacZ⁺* versus *lacZ⁻* within the same co-culture (see Extended Data Fig. 1b for swapped markers). **c**, Plaque assay obtained from 24-h co-cultures between *pks⁺* or *pks⁻* *E. coli* with *E. coli* harbouring phage lambda. Supernatants were spotted onto wild-type (WT) *E. coli* (top) and the lambda-resistant $\Delta lamB$ mutant (bottom). **d**, Relative light units (RLU) produced from a bioluminescent reporter encompassing the DNA-damage-inducible region of phage lambda that regulates lysis–lysogeny (P_R-*lux*). Reporter output measured in *recA⁺* (black) and $\Delta recA$ (white) *E. coli* co-cultured with *pks⁺* or *pks⁻* *E. coli* in the absence or presence of MMC. RLU was calculated by dividing bioluminescence by OD_{600 nm}. Data are mean \pm s.d. with $n = 3$ biological replicates (**b**, **d**); or $n = 3$ biological replicates from which a single representative image is shown (**c**).

Source data

In contrast to its effects on eukaryotic organisms, the effect of colibactin on the surrounding microbial community remains largely unknown. Previous studies have indicated that colibactin production may cause broad shifts in the composition of the gut microbial community in mice and inhibit the growth of a subset of staphylococci^{16,17}. However, exposure to colibactin did not affect the growth of the

vast majority (97%) of bacterial species tested, and the mechanism that underlies these effects has remained elusive. We aimed to shed additional light on the activity of colibactin and its potential ecological roles in microbial communities by studying its effects on bacteria. To begin, we exposed a laboratory strain of non-colibactin-producing (*pks*⁻) *E. coli* (BW25113) to supernatants from overnight cultures of colibactin-producing *E. coli* (a heterologous expression strain called BAC-*pks*; hereafter *pks*⁺). Culture supernatants did not inhibit the growth of the laboratory *E. coli* strain (Extended Data Fig. 1a), in line with analogous reports in mammalian cells¹. To test whether growth inhibition requires the presence of live colibactin-producing cells, we co-cultured *pks*⁺ *E. coli* with *pks*⁻ *E. coli* carrying chromosomally distinguishable markers (*lacZ*) and monitored the growth of the two populations. When started at a 1:1 ratio, the proportion of *pks*⁺ *E. coli* did not change over the course of the experiment, and this outcome occurred irrespective of which strain carried the *lacZ* marker (Fig. 1b, Extended Data Fig. 1b). These results suggest that, under the conditions tested, colibactin production by one bacterium does not inhibit the growth of an isogenic, non-producing strain.

Colibactin induces prophages

Multiple lines of evidence suggest that bacteria should be susceptible to colibactin-mediated DNA damage. For example, the final gene in the *pks* gene cluster, *clbS*, encodes a self-resistance protein that is reported to hydrolyse and destroy the reactive cyclopropane warheads of colibactin^{18,19}, and another gene, *clbP*, encodes a periplasmic peptidase that converts an inactive late-stage biosynthetic intermediate (precolibactin) to the final genotoxic metabolite in the periplasm before export^{20,21}. Both bacterially encoded self-resistance mechanisms suggest that, like many toxic bacterial natural products, colibactin is potentially deleterious to non-producing bacteria. We next considered alternative consequences of colibactin-mediated DNA damage beyond inhibition of bacterial growth. One possible response of interest is phage induction. Specifically, it is known that DNA damage induced by ultraviolet irradiation or by chemical treatment (for example, mitomycin C (MMC)) activates lytic replication of prophages (a latent form of phage infection) in bacteria, killing the cell and potentially nucleating a phage epidemic within the larger microbial community²². We therefore wondered whether colibactin could affect bacterial populations by activating resident prophages.

To test whether colibactin production alters the behaviour of prophages in neighbouring, non-colibactin-producing lysogens, we infected wild-type *E. coli* BW25113 with phage lambda and co-cultured this lysogen with *pks*⁺ or *pks*⁻ *E. coli*. Twenty-four hours of co-culture with the *pks*⁺ strain increased phage titres by orders of magnitude above those obtained with the *pks*⁻ strain (Fig. 1c). Physical separation of

colibactin producers from the lysogen via a 0.4- μ m filter ablated this effect (Extended Data Fig. 1c), suggesting that cell–cell contact is required¹. Consistent with the resident prophage being the responsible agent, no plaques were observed for any condition on $\Delta lamB$ *E. coli*, which lacks the lambda phage receptor (Fig. 1c). Finally, we verified that levels of colibactin production were not markedly altered between co-culture and monoculture conditions and were unaffected by the presence of the prophage-containing strain (Extended Data Fig. 1d). These results suggest that colibactin production specifically affects prophage-carrying bacteria by inducing lytic development.

Regulation of lambda induction from the prophage state occurs via a repressor protein (cl) that is inactivated by the host-encoded SOS response, for which RecA is a master regulator²³. To test whether prophage induction by colibactin follows a similar sequence of events, we engineered a transcriptional reporter to track the lambda lysis–lysogeny decision by fusing the lambda immunity region to the luciferase operon (*lux*) on a plasmid (hereafter called P_R -*lux*). Light production by luciferase therefore reports the transcriptional de-repression of phage lambda lytic replication, which is induced by known DNA-damaging-agents, such as MMC (Extended Data Fig. 1e). To examine the effect of colibactin in this system, we co-cultured *E. coli* harbouring P_R -*lux* with *pks*⁺ or *pks*[−] *E. coli*. The *pks*⁺ strain induced P_R -*lux* in the reporter strain 40-fold compared to the *pks*[−] strain (Fig. 1d). Furthermore, the activating effect of both MMC and co-cultured *pks*⁺ cells was eliminated in $\Delta recA$ *E. coli* (Fig. 1d), showing that the transcriptional de-repression requires the canonical DNA-damage-inducible SOS response. Consistent with the active genotoxin being involved, deletion of the gene encoding the late-stage biosynthetic enzyme ClbP in the producing strain abolished the activation of P_R -*lux* activity in co-cultured reporter cells and markedly reduced phage titres when co-cultured with the lambda lysogen (Extended Data Fig. 2a–c). Similar results were obtained using a native *pks*⁺ adherent-invasive colibactin-producing *E. coli* (NC101, which is used in mouse models of colorectal cancer carcinogenesis²⁴) (Extended Data Fig. 2a–c, [Supplementary Discussion](#)). Finally, addition of extracellular DNA attenuated P_R -*lux* activity and phage activation in a concentration-dependent, sequence-motif-specific manner (Extended Data Fig. 2d–h, [Supplementary Discussion](#)). Together, these data suggest that the ability to produce and transmit the final genotoxic product is important for the effect of colibactin on bacteria.

***pks* induces human-associated prophages**

Given that bacteria frequently exist in polymicrobial communities, that prophages are pervasive in these communities and that the SOS response is highly conserved, we

wondered whether the genotoxic effect of colibactin could extend to prophages that reside in phylogenetically distinct, Gram-negative and Gram-positive bacteria. To investigate this, we co-cultured *pks⁺* or *pks⁻* *E. coli* with multiple isolates of prophage-carrying *Salmonella enterica* subsp. *enterica* serovar Typhimurium (*S. Typhimurium*) (one harbouring prophage P22 and another harbouring prophages BTP1 and Gifsy-1), multiple isolates of *Staphylococcus aureus* (one harbouring prophage phi11 and another harbouring phi80α), a Shiga toxin encoding isolate of *Citrobacter rodentium* (harbouring an *stx_{2dact}* prophage), and a commensal isolate of *Enterococcus faecium* obtained from human faeces (harbouring a temperate phage phi1). Each phage–bacteria system resulted in a *pks*-dependent increase in prophage induction, as measured by enumerating plaque-forming units, antibody-based toxin detection and quantitative PCR (qPCR), showing that colibactin functions as a broad inducer (Fig. [2a–d](#)). Notably, the increased Shiga toxin production from the *stx_{2dact}* prophage that was observed upon co-culture of *C. rodentium* with *pks⁺* *E. coli* reveals how the effects of colibactin on susceptible bacteria and prophage have functionally relevant consequences beyond microorganisms.

Fig. 2: Colibactin activates prophages in diverse bacteria and in complex communities.

 **figure 2**

a, b, Plaque assays obtained from co-cultures of *pks⁺* or *pks⁻* *E. coli* with a *S. Typhimurium* P22 lysogen (**a**, top), a *S. Typhimurium* BTP1 and Gifsy-1 polylysogen (**a**, bottom two panels) or two *S. aureus* lysogens (**b**). The indicator strains used for each plaque assay are specific to the different phages indicated. **c**, Relative quantities

of *E. faecium*-specific host and phage DNA as measured by qPCR after co-culture with *pks*[−] or *pks*⁺ *E. coli*. **d**, Enzyme-linked immunosorbent assay (ELISA) of Shiga toxin (*Stx*_{2dact}) in cultures of *C. rodentium* harbouring phage *stx*_{2dact} co-cultured with *pks*[−] or *pks*⁺ *E. coli* or induced with 1.5 µg ml^{−1} MMC. Negative and positive conditions (bars designated – and +) indicate Stx-negative and Stx-positive standards included with the ELISA kit ([Methods](#)). Top, image of representative assay results from microtitre wells. Bottom, absorbance measurements from above samples (absorbance at 450 nm; Abs_{450 nm}). **e**, Schematic of ex vivo community experiment. Faecal communities from C57BL/6J mice were cultivated anaerobically before the addition of *pks*[−] or *pks*⁺ *E. coli* along with each of the indicated phage-containing isolates indicated in **f–h**. Supernatants of the resulting samples were analysed for phage induction using plaque assays, qPCR and ELISA. **f**, Plaque forming units (PFU) of lysogens BTP1, Gifsy-1, phi80α and phi11 in ex vivo communities. ND, not detected. **g**, Relative quantities of *E. faecium*-specific host and phage DNA as measured by qPCR from ex vivo communities. **h**, Shiga toxin ELISA on *C. rodentium* harbouring phage *stx*_{2dact} in ex vivo communities. In **a**, **b**, data are shown as a single representative image from *n* = 3 biological replicates. In **d**, **f**, **h**, data are mean ± s.d. with *n* = 3 biological replicates. In **e**, schematic created with BioRender.com. In **c**, **g**, data are mean ± s.e.m. with *n* = 3 biological replicates, each with 2 and 3 technical replicates (**c** and **g**, respectively).

[Source data](#)

Having experimentally demonstrated prophage induction in these bacteria under in vitro co-culture conditions, we next sought to test the action of colibactin in a setting that more closely resembles the complex multispecies environment of the gut. To achieve this, we anaerobically co-cultured *pks*⁺ or *pks*[−] *E. coli* ex vivo with complex faecal microbiomes from C57BL/6J mice, to which we added the individual gut-associated bacteria from our above panel²⁵ (*S. Typhimurium*, *S. aureus*, *E. faecium* and *C. rodentium*) (Fig. [2e](#)). In all cases except for prophage BTP1 from the *S. Typhimurium* polylysogen, we observed an increase in phage or toxin production within the *pks*⁺ communities relative to the *pks*[−] communities (Fig. [2f–h](#)). The lack of *pks*-dependent induction for BTP1—which is possibly due to the high degree of spontaneous induction in anaerobic communities—is notable given the significant induction observed under the same conditions for Gifsy-1, which is co-harboured by the same host bacterium. Together, these results demonstrate that colibactin-producing bacteria induce prophages in human- and gut-relevant strains and in complex microbial communities.

***pks*[−] strains can be colibactin-resistant**

Our results predict that colibactin, like MMC, is a generally effective inducer of prophages. However, unlike MMC, in which self-protection to the producing organism is thought to require the combined action of multiple resistance proteins^{26,27}, protection from colibactin exposure in *pks*⁺ organisms involves one 170-amino-acid resistance protein, ClbS^{18,19} (Fig. 1a). Studies using genetic deletions of *clbS* found that colibactin producers deficient for ClbS are viable, but that their growth depends on RecA, indicating that DNA repair mechanisms are needed for growth¹⁸ (Extended Data Fig. 3a). Acquisition of *clbS* would therefore be a potential strategy for susceptible community members to protect themselves against the effects of colibactin. We thus wondered whether *clbS*-like genes exist in closely related, non-colibactin-producing bacteria, and whether the function of these genes may alter phage–host dynamics in response to colibactin. To gain insight into its context, we performed a bioinformatic search (tBLASTn) for genes that encode proteins with amino acid sequences identical to that of *E. coli* ClbS. In 97% of the examined hits (230 total; Supplementary Table 1), the *clbS* homologue was found in a *pks* gene cluster with the same genetic organization as that of known colibactin-producing strains. In the seven cases (3%) in which *clbS* was not associated with an intact *pks* gene cluster, the gene normally encoded upstream of *clbS*—*clbQ*—was present but truncated, and both genes were surrounded by predicted transposase-associated genes (Extended Data Fig. 3b, Supplementary Table 1), indicating that the region may be subject to horizontal transfer. This search, consistent with a recent report²⁸, reveals that the *clbS* gene found in *pks*⁺ *E. coli* also exists in isolates of the same species that lack a *pks* gene cluster.

To test whether expression of ClbS in non-colibactin-producing *E. coli* can provide protection from colibactin exposure, we introduced and expressed plasmid-encoded *clbS* (from *pks*⁺ *E. coli*, pTrc-*clbS*) in a *pks*[−] strain harbouring either the P_R-*lux* reporter or phage lambda (Extended Data Fig. 3c). When co-cultured with *pks*⁺ *E. coli*, the reporter strain harbouring the *clbS* expression vector prevented P_R-*lux* reporter activity, whereas the same reporter strain transformed with pTrc-Δ*clbS* did not (Extended Data Fig. 3d). ClbS did not inhibit P_R-*lux* reporter activity when MMC was used as the inducing agent, suggesting that protection is specific to colibactin (Extended Data Fig. 3e). Moreover, supernatants from ClbS-expressing cells did not provide protection against colibactin, indicating that ClbS-based resistance is intracellular and not shared between cells (Extended Data Fig. 3f). Consistent with the reporter activity, the lambda lysogen harbouring pTrc-*clbS* yielded 1,000-fold fewer phage particles than the same lysogen carrying pTrc-Δ*clbS* when co-cultured with *pks*⁺ *E. coli* (Extended Data Fig. 3g). The pTrc-*clbS* construct also repressed the induction of phage P22 when introduced into *S. Typhimurium*, indicating that this resistance mechanism is functional beyond *E. coli* (Extended Data Fig. 3g).

We next sought to examine whether *clbS*-like genes exist in more distantly related bacteria that lack the *pks* gene cluster; and, if so, whether they also have a protective function in this context. Hypothesizing that organisms that are found in close proximity with colibactin producers would benefit from colibactin resistance, we searched for more distant ClbS homologues (50% amino acid identity cut-off) in the genomes of bacteria from two specific niches in which *pks* encoders are reported to exist: the human gastrointestinal tract and the honey bee gut^{5,29}. We found multiple *clbS*-like genes in *pks*[−] human-associated bacteria, including *Escherichia albertii* 07-3866, *Kluyvera intestini* and *Metakosakonia* sp. MRY16-398, the latter two of which were isolated from patients with gastric cancer and patients with sigmoid colon diverticulitis, respectively^{30,31}. We also identified a *clbS*-like gene in *Snodgrasella alvi*, a *pks*[−] core member of the honey bee gut³² (Extended Data Fig. 4a).

To assess whether these homologues could protect against colibactin-induced phage lysis, we heterologously expressed a subset of the identified ClbS-like proteins in the *E. coli* lambda lysogen or reporter strain and co-cultured these bacteria with *pks*⁺ *E. coli*. All four ClbS-like proteins attenuated DNA damage and prophage induction, both in terms of reporter output and plaques produced, suggesting the potential for the bacteria harbouring these genes to be protected from colibactin (Fig. 3a). Removing the niche-specific criteria and further lowering the cut-off in our search led us to uncover a wider range of ClbS-like proteins (25–80% amino acid identity relative to *E. coli* ClbS), an additional six of which we chose as a representative panel for heterologous expression and evaluation in our assays (Extended Data Fig. 4a). A summary of all ClbS-like proteins identified in our search is presented in Supplementary Table 1 (BLASTp 5,000 hits; [Methods](#)). Every ClbS-like protein tested in our panel provided protection against colibactin-induced DNA damage and prophage induction (Fig. 3a). Collectively, these results show that protection from colibactin can be gained through distantly related ClbS-like proteins that are found in bacteria that lack all other *pks* genes.

Fig. 3: ClbS and ClbS-like proteins from diverse bacteria provide protection against colibactin-activated prophage induction.

 figure 3

a, Plaque assay (images, left) and P_R -*lux* reporter output (bar graph, right) obtained from *pks*⁺ *E. coli* co-cultured with *pks*[−] *E. coli* harbouring a vector encoding the *clbS*-like gene of the indicated organism or the pTrc- $\Delta clbS$ vector. For plaque assays, the *pks*[−] *E. coli* harboured phage lambda; for the P_R -*lux* reporter assay, the *pks*[−] *E. coli* harboured the reporter plasmid. The heat map and clustering of the ClbS-like proteins are based on amino acid identity to *pks*⁺ *E. coli* ClbS. *Metakosakonia* sp. and *K. intestinalis* share the same ClbS sequence. **b**, Schematic of co-culture experiment between *pks*⁺ *E. coli* with *E. coli* harbouring the *Metakosakonia*-derived prophage reporter (P_{Metako} -*lux*) and a second vector containing the *clbS*-like gene from the same organism (pTrc-*clbS*_{Metako}) or pTrc- $\Delta clbS$. **c**, P_{Metako} -*lux* reporter output from co-cultures as described in **b**. Grey bars indicate the reporter response in monoculture to MMC. **d**, Schematic of co-culture experiment between *pks*⁺ *E. coli* with an isolate of *E. albertii* that natively encodes a *clbS*-like gene in its genome and harbours a prophage (*albertii_phi12*). **e**, Plaque assay obtained from co-cultures as described in **d**. The supernatants were serially diluted (twofold) and spotted on *E. coli* BW25113 to measure plaque formation. **f**, P_R -*lux* reporter output obtained from culturing *pks*⁺ or *pks*[−] *E. coli* with *pks*[−] *E. coli* harbouring the reporter plasmid or *pks*[−] *E. coli* that was recombineered to encode *clbS*_{albertii} from the same chromosomal locus in *E. coli* as it occurs in *E. albertii* (designated *E. coli*::*clbS*_{albertii}). In **a** (plaque assay), **e**, data are shown as a single representative image from $n = 3$ biological replicates; for **a** (*lux* reporter), **c**, **f**, data are represented as mean \pm s.d. with $n = 3$ biological replicates and RLU as in Fig. 1d.

[Source data](#)

Resistance as a phage-silencing strategy

To investigate the effect of colibactin resistance on prophage induction in non-colibactin-producing bacteria, we focused on two human-associated *clbS*⁺ organisms from our panel: *Metakosakonia* sp. MRY16-398 and *E. albertii* 07-3866, both of which harbour predicted DNA-damage-responsive prophages (Extended Data Fig. 4b–d, [Supplementary Discussion](#)). In *Metakosakonia* sp. MRY16-398, one of the predicted prophages corresponds to an uncharacterized 40-kb element. We synthesized a region of approximately 1 kb from this *Metakosakonia* prophage, encompassing the putative immunity region (containing a possible clI-like repressor; [Supplementary Discussion](#)), and fused the counter-oriented promoter to *lux* on a plasmid, called P_{Metako}-*lux* (Fig. 3b). When introduced into *recA*⁺ *E. coli*, the activity of P_{Metako}-*lux* was activated both by MMC and by co-culture with *pks*⁺ *E. coli* (Fig. 3c), suggesting its DNA damage inducibility. Next, to determine whether the *clbS*-like gene encoded by *Metakosakonia* sp. MRY16-398 (*clbS*_{Metako}) affects induction of the *Metakosakonia* phage, we introduced plasmid-based *clbS*_{Metako} into the reporter strain (resulting in P_{Metako}-*lux* + pTrc-*clbS*_{Metako}). We found that MMC continued to activate reporter expression, whereas co-culture with *pks*⁺ *E. coli* did not (Fig. 3c). Although we could not obtain an isolate of *Metakosakonia* MRY16-398 for these investigations, the results predict that if the ClbS protein is expressed in this *Metakosakonia* host, the organism will be resistant to the prophage-inducing effects of colibactin.

As another example, we turned to an available human-associated *clbS*⁺ isolate of *E. albertii* (Fig. 3d). *Escherichia albertii* 07-3866 was isolated from human faeces³³, encodes a ClbS homologue that is unique from those of *Metakosakonia* sp. MRY16-398 and *pks*⁺ *E. coli* (Extended Data Fig. 4a), and harbours multiple predicted prophages (Extended Data Fig. 4c). When exposed to MMC, lysates of *E. albertii* 07-3866 cultures formed distinct plaques on *E. coli*, indicating that *E. albertii* 07-3866 harbours a DNA-damage-inducible prophage (Fig. 3e). In contrast to treatment with MMC, co-culture of *E. albertii* 07-3866 with *pks*⁺ *E. coli* did not lead to plaque formation (Fig. 3e). We investigated whether the failure of this strain to produce phages specifically during *pks*⁺ co-culture could be explained by the expression of *E. albertii* ClbS. *Escherichia albertii* is related to *E. coli*, and the region that surrounds *clbS* in the *E. albertii* 07-3866 genome is highly conserved in *E. coli* (around 90% nucleotide identity in an approximately 18-kb vicinity). We transferred the *clbS* locus from *E. albertii* to the same relative location in the *pks*[–] *E. coli* genome. As shown in Fig. 3f, when co-cultured with *pks*⁺ *E. coli*, *pks*[–] *E. coli* harbouring the chromosomally integrated *E. albertii* *clbS* exhibited a reduction of approximately 50% in P_R-*lux* reporter activity relative to the unprotected, wild-type *clbS*[–] strain. The results of these experiments suggest that native *clbS* expression levels in *E. albertii* are sufficient to attenuate colibactin-specific prophage induction. More generally, our data from both *Metakosakonia* sp. and *E. albertii* lead us to propose that *clbS*⁺ organisms

are protected from colibactin-mediated prophage induction. These results also imply that the acquisition of orphan *clbS* genes is an effective strategy for prophage-carrying bacteria to resist the production of colibactin by neighbouring community members.

Discussion

The knowledge that colibactin induces prophages in diverse bacteria, combined with the finding that non-colibactin-producing bacteria from distinct environmental origins have functional *clbS*-like genes, leads us to speculate that colibactin production is more widespread than currently recognized, and that this genotoxin is likely to have evolved to target bacteria rather than a mammalian host. So far, studies of colibactin have primarily focused on its role in carcinogenesis, but this activity raises important questions with regard to the evolutionary role of the toxin for the producing bacterium. Colibactin genes have also been implicated in siderophore biosynthesis and microcin export, suggesting that these factors may collectively be involved in bacterial competition^{34,35}. Although other functions of colibactin may exist, our discovery that it induces prophages provides one mechanism by which production of and immunity to this natural product might confer a competitive advantage over other microorganisms. For example, because cell lysis is an irreversible consequence of prophage induction²², this mechanism could explain a previously reported observation of *pks*-dependent growth inhibition of a subset of *S. aureus* strains, a bacterium with an evolutionary history shaped by phage activity^{17,36} ([Supplementary Discussion](#)). Moreover, the broad-spectrum activity of colibactin in inducing prophages across distinct bacteria suggests that this natural product could have effects on many members of a community, potentially accounting for colibactin-associated changes in the composition of the gut microbiome that have previously been observed in animal models¹⁶. Beyond bacteria, our observation that exposure to colibactin increases the production of Stx in mixed communities hints at mechanisms by which this natural product could affect host health and highlights how inducing prophages may regulate other behaviours within the microbial community.

Our study underscores major gaps in our understanding of the molecular mechanisms that underlie prophage induction in microbiomes. MMC and ultraviolet light are the most common methods of activating prophage induction in the laboratory; however, the ecologically relevant triggers for prophages found in natural environments remain largely unidentified. Previous work has shown that the human gut commensal bacterium, *Lactobacillus reuteri*, harbours a prophage that undergoes induction during gastrointestinal transit in response to dietary fructose and short-chain fatty acids³⁷. In the vaginal community, metabolism of benzo[a]pyrene—a constituent of tobacco smoke—and subsequent secretion in the vagina induces multiple *Lactobacillus* prophages³⁸. In the nasal microbial community, hydrogen-peroxide-producing

Streptococcus has been shown to selectively eliminate prophage-carrying *S. aureus*³⁹. Unlike benzo[a]pyrene, which humans encounter through outside exposures, and hydrogen peroxide, which has a wide range of biological targets and proposed functions, colibactin is a complex natural product produced by human gut bacteria. By uncovering the phage-inducing activity of colibactin-producing bacteria, our findings reveal a previously unrecognized mechanism by which colibactin and potentially other DNA-damaging natural products may shape microbial communities. More generally, the modulation of phage behaviours represents a distinct and underappreciated ecological role for microbial natural products. Our findings add to this growing understanding^{14,40,41,42,43} and, notably, demonstrate phage induction by a natural product in co-culture. Finally, as links between the human gut virome and diseases continue to be established⁴⁴, our findings set the stage for further investigations of how gut bacterial metabolite production modulates phage behaviours and may influence human disease.

Methods

Bacterial strains, plasmids and routine cultivation

Bacterial strains and plasmids used in these studies are listed in Supplementary Table 2 and Supplementary Table 3, respectively. Unless otherwise noted, *E. coli* DH10β (NEB) was used for all strain construction and propagated aerobically in Luria-Bertani (LB-Lennox, RPI) broth at 37 °C. All experiments involving faecal communities were performed in an anaerobic chamber (70% N₂, 25% CO₂, 5% H₂). Oligonucleotides (Sigma) and dsDNA gene blocks (IDT) used in plasmid construction are listed in Supplementary Table 4. Plasmid construction steps and recombineering were performed using enzymes obtained from NEB (NEBuilder HiFi DNA assembly master mix, T4 DNA ligase and DpnI) and lambda red (pKD46 and pKD3), respectively. Sequencing of all inserts was performed using Sanger sequencing. Plasmid sequencing of P_R-lux revealed that the vector consists of two copies of the DNA-damage-responsive element (cI and P_R). Growth, reporter and lysis assays were all carried out in M9 medium supplemented with 0.4% casamino acids (M9-CAS, Quality Biological) unless otherwise specified. Antibiotics, inducers and indicators were used at the following concentrations: 100 µg ml⁻¹ ampicillin (IBI Scientific), 50 µg ml⁻¹ kanamycin (VWR), 25 µg ml⁻¹ chloramphenicol (Sigma), 100 ng ml⁻¹ MMC (Sigma), 40 µg ml⁻¹ 5-bromo-4-chloro-3-indolyl β-D-galactosidase (X-gal, Takara Bio), and 500 µM isopropyl β-D-1-thiogalactopyranoside (IPTG, Teknova), unless otherwise specified.

Growth and competition assays

For growth inhibition by cell-free fluids

Overnight cultures of wild-type *E. coli* BW25113 harbouring either BAC-*pks* or the empty BAC were centrifuged (16,100g and 1 min) and the supernatant was passed through a 0.22-µm filter (Corning Spin-X). Growth of non-colibactin-producing *E. coli* cultures was assayed in fresh LB in the presence of varying amounts of each supernatant (5%, 10%, 20%, 50% v/v). OD₆₀₀ was measured at regular intervals using a BioTek Synergy HTX multi-mode plate-reader.

For testing ClbS protection from cell-free fluids

Overnight cultures of wild-type *E. coli* BW25113 harbouring either pTrc-*clbS* or pTrc- Δ *clbS* were centrifuged (16,100g and 1 min) before addition at 10% v/v to co-cultures containing a 1:1 ratio of *E. coli* BW25113 harbouring the P_R-*lux* reporter and *E. coli* BW25113 harbouring either BAC-*pks* or the empty BAC. Bioluminescence was measured after 24 h and quantified in a plate-reader as outlined below (see ‘*E. coli*-based reporter assay’).

For *E. coli*–*E. coli* competition assays

Overnight cultures of lacZ⁺ *E. coli* MG1655 (K1lacZ, Addgene: 52696) harbouring BAC-*pks* were back-diluted 1:100 into fresh M9-CAS and mixed in a 1:1 ratio with a similarly back-diluted culture of lacZ⁻ *E. coli* MG1655 (delta-Z, Addgene: 52706) harbouring the empty BAC. The co-cultures were incubated at 37 °C, and, at regular intervals, an aliquot was taken for differential plating on LB supplemented with X-gal and IPTG. Both BAC combinations (*pks*⁺ versus empty) and marker combinations (lacZ⁺ versus lacZ⁻) were tested to rule out the influence of carrying the lacZ marker.

For assaying RecA-dependent growth of *pks*⁺ Δ *clbS* *E. coli*

Overnight cultures of wild-type *E. coli* BW25113 or wild-type *E. coli* DH10β, each individually harbouring BAC-*pks* or BAC-*pks* Δ *clbS*, were back-diluted 1:100 into fresh M9-CAS. The monocultures were incubated at 37 °C and the OD_{600 nm} readings were obtained after 24 h.

For *E. coli*–*S. aureus* competition assays

S. aureus RN450 lysogenic for phi80α and *S. aureus* RN450 lysogenic for phi11 were grown overnight at 37 °C in fresh brain heart infusion (BHI) medium, and *E. coli* BW25113 harbouring BAC-*pks* or empty BAC were grown overnight at 37 °C in fresh

LB broth supplemented with chloramphenicol. The overnight cultures were back-diluted 1:100 into fresh BHI medium and mixed in a 1:1 ratio and incubated at 37 °C for 24 h. The cultures were plated on LB agar supplemented with Cm for *E. coli* colony-forming units (CFUs), and mannitol salt phenol-red agar (Sigma) for *S. aureus* CFUs.

For differential MMC susceptibility of phage-free *S. aureus* and *E. coli*

lacZ[−] *E. coli* MG1655 (delta-Z, Addgene: 52706) and *S. aureus* RN450 were grown overnight at 37 °C in fresh LB and BHI media, respectively. The overnight cultures were back-diluted 1:100 into the same respective fresh medium and a twofold dilution series of MMC was added to achieve a final concentration ranging from 78 ng ml^{−1} to 5,000 ng ml^{−1}. Cultures were subsequently incubated overnight at 37 °C and OD_{600 nm} readings were obtained after 24 h. Normalized OD_{600 nm} was calculated as the OD_{600 nm} at a given MMC concentration relative to the OD_{600 nm} of the same strain to which no MMC was added (defined as 100%).

Production and isolation of phage lambda by MMC induction

An overnight culture of the lambda lysogen was back-diluted 1:100 into fresh LB and incubated at 37 °C. After reaching an OD_{600 nm} of 0.4–0.5, MMC (500 ng ml^{−1} final concentration) was added and the cultures were returned to 37 °C for an additional 3–5 h, over which time noticeable clearing occurred. After chloroform treatment and centrifugation (16,100g and 1 min), the clarified lysates were filter-sterilized and stored at 4 °C before use.

Quantification of phage induction by colibactin

***E. coli*-based reporter assay**

Overnight cultures were back-diluted 1:100 into fresh M9-CAS medium with appropriate antibiotics before being dispensed (200 µl) into white-walled 96-well plates (Corning 3610). For co-culture experiments, the two cultures were mixed 1:1 immediately after back-dilution. Monoculture controls for each strain were prepared by adding 100 µl of the back-diluted cultures to an equivalent volume of M9-CAS. For DNA interference experiments, herring sperm DNA (Promega) was used. To test DNA with varying AT richness, complementary oligonucleotide pairs (JWO-1046 and JWO-1047) and (JWO-1044 and JWO-1045) were annealed in 10 mM aqueous Tris-HCl buffer, and the resulting duplexes were added to the wells at the indicated concentrations. Plates were shaken at 37 °C and the OD_{600 nm} and bioluminescence

readings were obtained after 24 h. Relative light units (RLU) were calculated by dividing the bioluminescence by the OD_{600 nm}.

Phage quantification for phages of *E. coli*, *S. Typhimurium*, *S. aureus*, *E. albertii* 07-3866 and *E. faecium* E1007

Preparing and measuring viral titres from co-cultures with phage-infected isolates was carried out according to the identical conditions used for the reporter assays with the exception that the reporter strain was substituted for the relevant lysogen. Co-cultures with phage-infected *E. coli*, *S. Typhimurium* and *E. albertii* were conducted in M9-CAS, whereas co-cultures with phage-infected *S. aureus* and *E. faecium* were conducted in BHI as the growth medium. To prepare phage lysates, cultures were transferred after 24 h co-culture to microcentrifuge tubes and centrifuged at 16,100g for 1 min. The supernatant was removed and passed through a 0.22-μm filter. For phage quantification by plaque assays, supernatants were diluted logarithmically from 10⁰ to 10⁻⁵, and 10 μl spotted on top agar (preparation below) containing the relevant indicator. For *E. albertii* 07-3866 phi12, 2-fold dilutions of the supernatants instead of 10-fold were used. In the case of quantifying *S. Typhimurium* phages from faecal communities, culture supernatants were concentrated approximately 40-fold from their starting volume in protein concentrators (Pierce, 100 kDa MWCO, spin columns) before use in plaque assays. For phage quantification by qPCR, supernatants were diluted 100-fold, treated with DNase (Promega) to remove residual DNA, then boiled to release encapsidated phage DNA. Host (JWO-1120 and JWO-1121) and phage (JWO-1116 and JWO-1117) specific primer pairs were used for PCR amplification using the Luna Universal qPCR kit (NEB) in a CFX96 real-time PCR detection system (Bio-Rad). Data were processed and analysed by comparing the relative amplification within samples of phage-specific primer pairs to host-specific primer pairs (Pfaffl method) using the Gene Expression calculator in the CFX Manager software (Bio-Rad).

Preparation of top agar

The indicators used to assay each phage-bacteria system were as follows: for lambda-*E. coli* and phi12-*E. albertii* (wild-type *E. coli* BW25113 or the lambda-resistant *lamB*::*kan* mutant); for P22-S. Typhimurium (*S. Typhimurium* D23580ΔΦ); for BTP1-*S. Typhimurium* (*S. Typhimurium* SNW22 D23580 ΔBTP1); for Gifsy-1-*S. Typhimurium* (*S. Typhimurium* D23580 ΔΦ Δ*waaG*::*aph*); for phi80α and phi11 (*S. aureus* RN450). In each case, overnight cultures of the relevant indicator strains were back-diluted 1:100 into LB (for *E. coli* and *S. Typhimurium*) or BHI (for *S. aureus*) and incubated at 37 °C. At an OD_{600 nm} of 0.3–0.5, *E. coli* and *S. Typhimurium* cultures were diluted 1:10 into molten LB-agar (0.6%) supplemented with 10 mM

MgSO_4 and 0.2% maltose and poured onto a LB-agar (1.5%) plate. For *S. aureus*, cultures were back-diluted 1:10 into molten tryptic soy agar (0.6%) supplemented with 10 mM CaCl_2 and poured onto a denser layer (1.5%) of the same agar.

ELISA for $\text{Stx}_{2\text{dact}}$ detection

Detection of $\text{Stx}_{2\text{dact}}$ from both aerobic co-cultures and faecal communities was performed using the Premier EHEC test kit, which specifically detects Shiga toxins I and II (Meridian Biosciences), following the manufacturer's instructions with the following modifications: for aerobic co-cultures, overnight monocultures of *C. rodentium* harbouring $stx_{2\text{dact}}$ were back-diluted 1:100 and co-cultured in M9-CAS at a 1:1 ratio with *E. coli* BW25113 harbouring either BAC-*pks* or the empty BAC. For faecal community experiments, anaerobic monocultures of *C. rodentium* harbouring $stx_{2\text{dact}}$ were mixed with faecal communities in BHI as described in the relevant section below. To verify toxin production in response to a known DNA-damaging agent under these conditions, MMC (1.5 $\mu\text{g ml}^{-1}$ final concentration) was added to aerobic cultures of exponentially growing $stx_{2\text{dact}}$ -harbouring *C. rodentium* in M9-CAS. In all cases, samples collected after 24-h incubations (exact volumes detailed below) were diluted in 200 μl of diluent buffer provided by the manufacturer before addition to Stx-specific antibody-coated microwells. The use of kit-provided positive and negative controls as well as all wash and substrate addition steps were carried out exactly according to the manufacturer-supplied protocol. The stop reagent was added approximately 2–5 min after adding the final substrate to each well, at which time the images used in Fig. 3c were taken. Absorbance at 450 nm ($\text{Abs}_{450\text{ nm}}$) was measured using a plate-reader. According to the manufacturer, $\text{Abs}_{450\text{ nm}}$ values ≥ 0.180 are considered a positive test result. For aerobic experiments including MMC controls, 2 μl of culture supernatants were used as the sample input. For faecal community experiments, culture supernatants were first concentrated approximately 20-fold from the initial volume in protein concentrators (Pierce, 30 kDa MWCO, spin columns). Forty microlitres of the concentrated retentate was used as the sample input.

Faecal sample processing

Faecal pellets from C57BL/6J mice from the Jackson Laboratory (which lack Enterobacteriaceae and do not contain colibactin-producing organisms) were suspended in pre-reduced PBS supplemented with 0.1% l-cysteine (5% w/v), then left to stand to allow insoluble particles to settle. The supernatant was carefully removed and mixed with an equal volume of 40% glycerol. Aliquots (50 μl) of this suspension were stored at -80°C until required.

Ex vivo culture with faecal communities

An aliquot of the faecal suspension prepared above was thawed and inoculated into BHI (1:100) and incubated at 37 °C in an anaerobic chamber alongside the relevant human-associated phage-containing bacteria and *E. coli* BW25113 harbouring either BAC-*pks* or the empty BAC. After 24 h incubation, the overnight cultures were back-diluted (1:1,000) and mixed in equal proportions in fresh BHI, then incubated for a further 24 h. Phages and toxin produced from faecal communities were measured in the same assays used in two-way cultures, involving plaque assays for *S. Typhimurium* (BTP1 and Gifsy-1) and *S. aureus* (phi80α and phi11), qPCR for *E. faecium* (phi1), and Stx ELISA for *C. rodentium* (*stx*_{2dact}).

Assaying protection by *clbS*-like open reading frames

For reporter assays, each of the *clbS*-like open reading frames (ORFs) (or the pTrc-Δ*clbS* construct) were transformed into *E. coli* BW25113 harbouring the P_R-*lux* reporter. After overnight growth of each strain in monoculture, strains were back-diluted 1:100 and co-cultured in M9-CAS at a 1:1 ratio with *E. coli* BW25113 harbouring BAC-*pks*. Bioluminescence was measured after 24 h incubation at 37 °C in a plate-reader as detailed for all other *E. coli*-based reporter assays above. For measuring protection by the *clbS*-like ORFs from phage induction, the same *clbS*-like ORF-encoding constructs from the reporter assay were individually transformed into a *E. coli* BW25113 lambda lysogen. An identical dilution and co-culture procedure to that of *E. coli* BW25113 harbouring BAC-*pks* was used, after which phage production was measured by plaque assay as described in the relevant section above. To measure protection provided by a chromosomal copy of *E. albertii*-encoded *clbS* (*clbS*_{albertii}), the locus surrounding *clbS*_{albertii} from the *E. albertii* 07-3866 genome was PCR-amplified and transferred using lambda-red recombineering into wild-type *E. coli* BW25113 (JSO-1966–1973; Supplementary Table 4). The P_R-*lux* reporter plasmid was introduced into the resulting strain, *E. coli*::*clbS*_{albertii}, and measured for its ability to be induced by colibactin using the identical co-culture procedure as that used for *E. coli*-based reporter assays, as noted in the relevant section above.

Quantification of N-myristoyl-d-asparagine prodrug production by *pks* + *E. coli*

For culture conditions and sample preparation

Overnight cultures of *E. coli* BW25113 harbouring either BAC-*pks* or the empty BAC were back-diluted 1:100 and co-cultured in M9-CAS at a 1:1 ratio with phage-free *E.*

coli BW25113 or lambda-infected BW25113. Cultures (1 ml) were dispensed into deep-well plates (VWR) and incubated with shaking at 37 °C. After 24 h, 10 µl deuterated (d27) *N*-myristoyl-d-asparagine (10 µM in DMSO stock solution) was added to each sample. Samples were flash-frozen in liquid nitrogen, lyophilized for 48 h, then reconstituted in methanol (1 ml) and vortexed for 1 min. Three hundred microlitres of the mixture was filtered through a 0.22 µm filter (Pall) before mass spectrometry analysis.

For prodrug quantification

Analysis of the *N*-myristoyl-d-asparagine prodrug in samples was performed using an ultra-high performance liquid chromatography tandem mass spectrometry (UHPLC–MS/MS) system model Xevo TQ-S (Waters). The mass spectrometer system consists of a triple quadrupole equipped with a dual-spray electrospray ionization (ESI) source. Samples were analysed using an Agilent Poroshell 120 EC-C18 column (2.7 mm, 4.6 mm × 50 mm) with the following elution conditions: isocratic hold at 90% solvent A in solvent B for 0.5 min; linear gradient from 90% to 5% solvent A in solvent B from 0.5–2 min; isocratic hold at 5% solvent A from 2–3 min, gradient from 5% to 98% solvent A in solvent B from 3–3.5 min; isocratic hold at 98% solvent A in solvent B from 3.5–4 min (solvent A: 95% water + 5% methanol + 0.03% ammonium hydroxide; solvent B: 80% isopropanol + 15% methanol + 5% water; flow rate = 0.75 ml min⁻¹; injection volume = 5 µl). The mass spectrometer was run in negative-mode MRM with a Cone voltage of 50 V, monitoring transitions of *m/z* 341 → *m/z* 114 (retention time (rt) = 2.2 min, collision energy (CE) = 24 V) for the prodrug scaffold and *m/z* 368 → *m/z* 114 (rt = 2.2 min, CE = 28 V) for the deuterated internal standard (d27-*N*-myristoyl-d-asparagine). For all samples, peak areas for the *m/z* 341 → *m/z* 114 were normalized to the *m/z* 368 → *m/z* 114 transition for the same sample, and then normalized values compared to a standard curve of unlabelled *N*-myristoyl-d-asparagine containing 100 nM d27- *N*-myristoyl-d-asparagine, which was run in triplicate.

Bioinformatic analyses

NCBI tBLASTN (nr/nt database, expect threshold = 0.05, word size = 6, BLOSUM62 matrix) was used to identify *clbS* genes that match *E. coli* ClbS (WP_000290498) but that are found outside of *pks* clusters. The more distantly related ClbS-like proteins examined in this study (Fig. 3d) were compiled from BLASTp results using *E. coli* ClbS as the query (nr protein sequences database, expect threshold = 0.05, word size = 6, BLOSUM62 matrix, 5,000 entries). After excluding entries that occur in genomes with *pks* clusters, the isolation source of the remaining hits was considered in identifying bee gut and human-associated isolates. Other members in the representative panel selected for cloning and heterologous expression were chosen

heuristically and to cover the range in per cent identities returned by the BLAST search (spanning *Mixta theicola* having 80% pairwise identity and *Bifidobacterium longum* with 26.8% pairwise identity to *E. coli* ClbS). The genomes encoding *clbS*-like genes in the representative panel were submitted to PHASTER for identification of prophage regions. Genes encoded by predicted intact prophages (score higher than 90) were further analysed by domain analysis (InterPro) for features matching the lambda repressor (DNA-binding and peptidase domains), as mentioned in the main text and [Supplementary Discussion](#), and shown in Extended Data Fig. 4d.

Quantification and statistical analysis

Software used to collect and analyse data generated in this study consisted of: GraphPad Prism 9 for analysis of growth- and reporter-based experiments; Gen5 v.3 for collection of growth- and reporter-based experiments; Bio-Rad CFX Manager 3.0 for quantification and analysis of qPCR data; ImageJ 1.53c for colony counting in competition experiments; and Geneious Prime 2020 for analysis of publicly available data and primer design. Data are presented as mean \pm s.d. unless otherwise indicated in the figure legends. The number of independent biological replicates for each experiment is indicated for each experiment and included in the legend.

Reporting summary

Further information on research design is available in the [Nature Research Reporting Summary](#) linked to this paper.

Data availability

All unprocessed plaque assay images (Figs. 1c, 2a, b, 3a, Extended Data Figs. 1c, 2c, f, h, 3g) and source data (Figs. 1b, d, 2c, d, f–h, 3a, c, Extended Data Figs. 1a, b, d, e, 2b, e, g, 3a, d–f, 4b, c) generated in the course of this study are available without restriction and deposited on Zenodo (<https://doi.org/10.5281/zenodo.4683077>). Total PFU data are available in Supplementary Table 5, and total CFU and growth data are available in Supplementary Table 6 (Supplementary Fig. 1 in the Supplementary Discussion). Identifiers for all entries in NCBI BLAST results are listed in Supplementary Table 1. Protein accession numbers for the relevant ClbS sequences tested in this study are as follows: *E. coli* CFT073 ([WP_000290498](#)), *M. theicola* ([PNS10644](#)), *S. erythrinae* ([WP_132453050](#)), *Gibbsiella quercinecans* ([WP_095844971](#)), *S. alvi* ([WP_025331471](#)), *F. perrara* ([WP_039103908](#)), *Metakosakonia* sp. ([BBE76153](#)), *K. intestini* ([PWF54517](#)), *E. albertii* ([WP_000115842](#)), *E. coli* 69 ([QDM73539](#)), *Dickeya dadantii* ([WP_038909824](#)) and *B. longum* ([WP_193641739](#)). Accession numbers used for the design of qPCR primers

and reporter construction are: *E. faecium* E1007 ([AHWP00000000](#)), *E. coli* BW25113 and lambda ([NZ_CP009273](#) and [NC_001416.1](#)), *E. albertii* 07-3866 ([NZ_CP030781](#)) and *Metakosakonia* sp. ([AP018756](#)). Accession and identifier information can be found at NCBI. [Source data](#) are provided with this paper.

References

1. Nougayrède, J.-P. et al. *Escherichia coli* induces DNA double-strand breaks in eukaryotic cells. *Science* **313**, 848–851 (2006).
2. Auvray, F. et al. Insights into the acquisition of the *pks* island and production of colibactin in the *Escherichia coli* population. *Microb. Genomics* **7**, 000579 (2021).
3. Dougherty, M. W. & Jobin, C. Shining a light on colibactin biology. *Toxins* **13**, 346 (2021).
4. Bondarev, V. et al. The genus *Pseudovibrio* contains metabolically versatile bacteria adapted for symbiosis. *Environ. Microbiol.* **15**, 2095–2113 (2013).
5. Engel, P., Vizcaino, M. I. & Crawford, J. M. Gut symbionts from distinct hosts exhibit genotoxic activity via divergent colibactin biosynthesis pathways. *Appl. Environ. Microbiol.* **81**, 1502–1512 (2015).
6. Moretti, C. et al. *Erwinia oleae* sp. nov., isolated from olive knots caused by *Pseudomonas savastanoi* pv. *savastanoi*. *Int. J. Syst. Evol. Microbiol.* **61**, 2745–2752 (2011).
7. Wilson, M. R. et al. The human gut bacterial genotoxin colibactin alkylates DNA. *Science* **363**, eaar7785 (2019).
8. Dziubańska-Kusibab, P. J. et al. Colibactin DNA-damage signature indicates mutational impact in colorectal cancer. *Nat. Med.* **26**, 1063–1069 (2020).
9. Plequezuelos-Manzano, C. et al. Mutational signature in colorectal cancer caused by genotoxic *pks*⁺ *E. coli*. *Nature* **580**, 269–273 (2020).
10. Faïs, T., Delmas, J., Barnich, N., Bonnet, R. & Dalmasso, G. Colibactin: more than a new bacterial toxin. *Toxins* **10**, 151 (2018).
11. Williams, P. C., Wernke, K. M., Tirla, A. & Herzon, S. B. Employing chemical synthesis to study the structure and function of colibactin, a “dark matter” metabolite. *Nat. Prod. Rep.* **37**, 1532–1548 (2020).

12. Balskus, E. P. Colibactin: understanding an elusive gut bacterial genotoxin. *Nat. Prod. Rep.* **32**, 1534–1540 (2015).
13. Wernke, K. M. et al. Probing microbiome genotoxicity: a stable colibactin provides insight into structure–activity relationships and facilitates mechanism of action studies. *J. Am. Chem. Soc.* **143**, 15824–15833 (2021).
14. Jiang, Y. et al. Reactivity of an unusual amidase may explain colibactin’s DNA cross-linking activity. *J. Am. Chem. Soc.* **141**, 11489–11496 (2019).
15. Xue, M. et al. Structure elucidation of colibactin and its DNA cross-links. *Science* **365**, eaax2685 (2019).
16. Tronnet, S. et al. The genotoxin colibactin shapes gut microbiota in mice. *mSphere* **5**, e00589-20 (2020).
17. Faïs, T. et al. Antibiotic activity of *Escherichia coli* against multiresistant *Staphylococcus aureus*. *Antimicrob. Agents Chemother.* **60**, 6986–6988 (2016).
18. Bossuet-Greif, N. et al. *Escherichia coli* ClbS is a colibactin resistance protein. *Mol. Microbiol.* **99**, 897–908 (2016).
19. Tripathi, P. et al. ClbS is a cyclopropane hydrolase that confers colibactin resistance. *J. Am. Chem. Soc.* **139**, 17719–17722 (2017).
20. Dubois, D. et al. ClbP is a prototype of a peptidase subgroup involved in biosynthesis of nonribosomal peptides. *J. Biol. Chem.* **286**, 35562–35570 (2011).
21. Brotherton, C. A. & Balskus, E. P. A prodrug resistance mechanism is involved in colibactin biosynthesis and cytotoxicity. *J. Am. Chem. Soc.* **135**, 3359–3362 (2013).
22. Ofir, G. & Sorek, R. Contemporary phage biology: from classic models to new insights. *Cell* **172**, 1260–1270 (2018).
23. Gimble, F. S. & Sauer, R. T. λ Repressor mutants that are better substrates for RecA-mediated cleavage. *J. Mol. Biol.* **206**, 29–39 (1989).
24. Arthur, J. C. et al. Intestinal inflammation targets cancer-inducing activity of the microbiota. *Science* **338**, 120–123 (2012).
25. Lobel, L., Cao, Y. G., Fenn, K., Glickman, J. N. & Garrett, W. S. Diet posttranslationally modifies the mouse gut microbial proteome to modulate renal function. *Science* **369**, 1518–1524 (2020).

26. Sheldon, P. J., Mao, Y., He, M. & Sherman, D. H. Mitomycin resistance in *Streptomyces lavendulae* includes a novel drug-binding-protein-dependent export system. *J. Bacteriol.* **181**, 2507–2512 (1999).
27. Martin, T. W. et al. Molecular basis of mitomycin C resistance in *Streptomyces*: structure and function of the MRD protein. *Structure* **10**, 933–942 (2002).
28. Tripathi, P. & Bruner, S. D. Structural basis for the interactions of the colibactin resistance gene product ClbS with DNA. *Biochemistry* **60**, 1619–1625 (2021).
29. Putze, J. et al. genetic structure and distribution of the colibactin genomic island among members of the family Enterobacteriaceae. *Infect. Immun.* **77**, 4696–4703 (2009).
30. Sekizuka, T. et al. Complete genome sequence of *bla_{IMP-6}*-positive *Metakosakonia* sp. MRY16-398 isolate from the ascites of a diverticulitis patient. *Front. Microbiol.* **9**, 2853 (2018).
31. Tetz, G. et al. Complete genome sequence of *Kluyvera intestini* sp. nov., isolated from the stomach of a patient with gastric cancer. *Genome Announc.* **5**, e01184-17 (2017).
32. Kwong, W. K. & Moran, N. A. Gut microbial communities of social bees. *Nat. Rev. Microbiol.* **14**, 374–384 (2016).
33. Lindsey, R. L., Rowe, L. A., Batra, D., Smith, P. & Strockbine, N. A. PacBio genome sequences of eight *Escherichia albertii* strains isolated from humans in the United States. *Microbiol. Resour. Announc.* **8**, e01663-18 (2019).
34. Martin, P. et al. Interplay between siderophores and colibactin genotoxin biosynthetic pathways in *Escherichia coli*. *PLoS Pathog.* **9**, e1003437 (2013).
35. Massip, C. et al. Deciphering the interplay between the genotoxic and probiotic activities of *Escherichia coli* Nissle 1917. *PLoS Pathog.* **15**, e1008029 (2019).
36. Xia, G. & Wolz, C. Phages of *Staphylococcus aureus* and their impact on host evolution. *Infect. Genet. Evol.* **21**, 593–601 (2014).
37. Oh, J.-H. et al. Dietary fructose and microbiota-derived short-chain fatty acids promote bacteriophage production in the gut symbiont *Lactobacillus reuteri*. *Cell Host Microbe* **25**, 273–284 (2019).
38. Pavlova, S. I., Kiliç, A. O., Mou, S. M. & Tao, L. Phage infection in vaginal lactobacilli: an in vitro study. *Infect. Dis. Obstet. Gynecol.* **5**, 36–44 (1997).

39. Selva, L. et al. Killing niche competitors by remote-control bacteriophage induction. *Proc. Natl Acad. Sci. USA* **106**, 1234–1238 (2009).
40. Kronheim, S. et al. A chemical defence against phage infection. *Nature* **564**, 283–286 (2018).
41. Kever, L. et al. Aminoglycoside antibiotics inhibit phage infection by blocking an early step of the phage infection cycle. Preprint at <https://doi.org/10.1101/2021.05.02.442312> (2021).
42. Jancheva, M. & Böttcher, T. A metabolite of *Pseudomonas* triggers prophage-selective lysogenic to lytic conversion in *Staphylococcus aureus*. *J. Am. Chem. Soc.* **143**, 8344–8351 (2021).
43. Silpe, J. E. & Bassler, B. L. A host-produced quorum-sensing autoinducer controls a phage lysis-lysogeny decision. *Cell.* **176**, 268–280 (2019).
44. Santiago-Rodriguez, T. M. & Hollister, E. B. Human virome and disease: high-throughput sequencing for virus discovery, identification of phage-bacteria dysbiosis and development of therapeutic approaches with emphasis on the human gut. *Viruses* **11**, E656 (2019).

Acknowledgements

We thank all members of the E.P.B. laboratory for insightful discussions; K. Papenfort for feedback; the laboratory of J. R. Penadés (Imperial College London) for sharing *S. aureus* strains; the laboratory of J. M. Leong (Tufts University) for sharing *C. rodentium*; and the laboratory of W. Garrett (Harvard School of Public Health) for sharing of faecal pellets. This work was supported by the National Institutes of Health (NIH) grant R01 CA208834. J.W.H.W. was supported by the A*STAR NSS (PhD) predoctoral fellowship. S.V.O. and M.B. were partially supported by the NIH NIGMS award R35GM133700, the David and Lucile Packard Foundation, and the Pew Charitable Trusts. The content is solely the responsibility of the authors and does not necessarily represent the official views of the funders.

Author information

Author notes

1. These authors contributed equally: Justin E. Silpe, Joel W. H. Wong

Affiliations

1. Department of Chemistry and Chemical Biology, Harvard University, Cambridge, MA, USA

Justin E. Silpe, Joel W. H. Wong & Emily P. Balskus

2. Department of Biomedical Informatics and Laboratory of Systems Pharmacology, Harvard Medical School, Boston, MA, USA

Siân V. Owen & Michael Baym

3. Howard Hughes Medical Institute, Harvard University, Cambridge, MA, USA

Emily P. Balskus

Contributions

J.E.S., J.W.H.W. and E.P.B. conceived the project. J.E.S. and J.W.H.W. contributed equally to this work and ordering of authorship was determined in no particular order. J.E.S. and J.W.H.W. constructed strains, conducted all bioinformatic analyses and performed all growth-based-, reporter-based- and plaque assays. S.V.O. assisted in constructing and acquiring *S. Typhimurium* and *S. aureus* strains. All authors interpreted data, provided critical feedback and wrote the paper.

Corresponding author

Correspondence to [Emily P. Balskus](#).

Ethics declarations

Competing interests

The authors declare no competing interests.

Peer review

Peer review information

Nature thanks Breck Duerkop and the other, anonymous, reviewer(s) for their contribution to the peer review of this work. Peer reviewer reports are available.

Additional information

Publisher's note Springer Nature remains neutral with regard to jurisdictional claims in published maps and institutional affiliations.

Extended data figures and tables

Extended Data Fig. 1 Colibactin production does not generally inhibit bacterial growth but induces DNA damage.

a, Growth of *pks*[−] *E. coli* grown in the presence of the indicated relative volume of cell-free fluids from overnight cultures of *pks*⁺ *E. coli*, *pks*[−] *E. coli* or without cell-free fluids added (top row). **b**, Growth and frequency of *pks*[−] and *pks*⁺ *E. coli* in co-culture as in Fig. 1b but with the *pks* and *lacZ* combination swapped. Upper, total culture density of *pks*[−] *lacZ*⁺ *E. coli* co-cultured with *pks*⁺ *lacZ*[−] *E. coli* at a starting ratio of 1:1; lower, the proportion of *lacZ*⁺ versus *lacZ*[−] within the same co-culture based on differential blue-white plating over time. **c**, Plaque assay obtained after co-culturing *pks*⁺ or *pks*[−] *E. coli* with a lambda lysogen separated by a 0.4 μm membrane. Where indicated, MMC was added to the opposing side of the membrane from the lambda lysogen. **d**, Concentration of the colibactin prodrug motif *N*-myristoyl-D-asparagine obtained from *pks*[−] or *pks*⁺ *E. coli* in monoculture and in co-culture with lysogenic and non-lysogenic (phage-free) *E. coli*. **e**, P_R-*lux* output in *recA*⁺ (black) and Δ*recA* (white) *E. coli* harbouring the reporter plasmid in the absence and presence of MMC. For e, RLU as in Fig. 1d. Data represented as mean of n = 3 biological replicates (a), as mean ± s.d. with n = 3 biological replicates (b, d, e), or n = 3 biological replicates from which a single representative image is shown (c).

[Source data](#)

Extended Data Fig. 2 Prophage induction is dependent on colibactin-mediated DNA alkylation and addition of extracellular DNA ameliorates this effect.

a, Schematic of co-culture experiment with a colibactin biosynthesis-defective Δ(*clbP*) *pks* strain. **b**, P_R-*lux* output from reporter cells co-cultured with *E. coli* BW25113 (*pks*⁺, *pks*[−], and *pks*⁺Δ*clbP*; black bars) or native-colibactin producing *E. coli*, NC101 (WT and Δ*clbP*; white bars). **c**, Plaque assays obtained from analogous incubations as in b but with a lambda lysogen used in place of the reporter strain. **d**, Schematic of co-culture experiment in which extracellular DNA is added to the medium. **e**, P_R-*lux* output from reporter cells co-cultured with either *pks*⁺ or *pks*[−] *E. coli* and the indicated concentration of herring sperm DNA. **f**, Plaque assays of the analogous incubations as in e but with a lambda lysogen used in place of the reporter strain. **g**,

P_R -*lux* output from reporter cells co-cultured with *pks*⁺ *E. coli* in the presence of varying amounts of extracellular DNA (AT-rich and GC-rich DNA, black and white symbols, respectively). **h**, Plaque assays of the analogous incubations as in **g** but with a lambda lysogen used in place of the reporter strain. In **b, e, g**, RLU as in Fig. [1d](#). Data represented as mean \pm s.d. with n = 3 biological replicates (**b, e, g**); or n = 3 biological replicates from which a single representative image is shown (**c, f, h**).

[Source data](#)

[**Extended Data Fig. 3 ClbS provides intracellular protection from colibactin, and *clbS*-like genes are present in the genomes of diverse bacteria, including those that lack *pks*-biosynthetic genes.**](#)

a, 24 h growth of *recA*⁺ *E. coli* (BW25113, black bars) or $\Delta recA$ *E. coli* (DH10 β , white bars), each harbouring either the full *pks* cluster (*pks*⁺) or the cluster with *clbS* removed (*pks*⁺ $\Delta clbS$), as indicated. **b**, Genomic context of *clbS* found within the *E. coli pks* cluster encoded by a known colibactin-producing isolate (CFT073) as compared to *pks*⁻ isolates of *E. coli* that lack the colibactin biosynthetic genes but contain an identical *clbS* coding sequence (red) and truncated *clbQ* (purple) in regions flanked with predicted transposase-associated genes (green-coloured genes). Numbering above genomes denotes prophage genome size in base pairs. **c**, Schematic of co-culture experiment with the gene encoding colibactin resistance, *clbS*, expressed *in trans*. **d**, P_R -*lux* reporter output obtained from *pks*⁺ *E. coli* co-cultured with *pks*⁻ *E. coli* harbouring the reporter plasmid and either pTrc-*clbS* or the same vector with *clbS* removed (pTrc- $\Delta clbS$) expressed *in trans*. **e**, P_R -*lux* reporter output in the absence and presence of MMC in *E. coli* harbouring the P_R -*lux* reporter plasmid, the indicated second plasmid (pTrc-*clbS* or pTrc- $\Delta clbS$), and co-cultured with *pks*⁻ or *pks*⁺ *E. coli*. **f**, P_R -*lux* reporter output obtained from culturing *pks*⁺ or *pks*⁻ *E. coli* with *pks*⁻ *E. coli* harbouring the reporter plasmid to which cell-free supernatants of cells expressing *clbS* or a vector control ($\Delta clbS$) were added (right two bars). **g**, Upper: Plaque assays obtained from analogous incubations as in **d** but with a lambda lysogen used in place of the reporter strain. Lower: Plaque assays obtained from co-culturing *pks*⁺ *E. coli* with *S. Typhimurium* harbouring P22 and either pTrc-*clbS* or pTrc- $\Delta clbS$ expressed *in trans*. In **d, e** and **f**, RLU as in Fig. [1d](#). Data represented as mean \pm s.d. with n = 3 biological replicates (**a, d, e, f**); or n = 3 biological replicates from which a single representative image is shown (**g**).

[Source data](#)

Extended Data Fig. 4 Prophages with predicted DNA-damage-responsive repressors co-occur in *clbS*-encoding bacteria.

a, Genomic organization surrounding *clbS*-like genes encoded by diverse bacteria identified in this study. Purple-coloured genes denote the known *pks* biosynthetic genes. *E. coli* CFT073 and *F. perrara* were previously known to carry *pks*-associated *clbS*. Red-coloured genes denote *clbS*. The saturation of red for each *clbS* is proportional to the percent identity in amino acid sequence of that gene relative to *pks⁺ E. coli* (CFT073), as indicated in the key. **b**, Distribution of PHASTER-predicted prophage regions present in the 12 bacterial genomes that encode the *clbS*-like genes tested in Fig. 3a (genomic context for each shown in a). A total of 94 prophage regions were predicted, 38 of which are considered to be intact prophages. **c**, Number and distribution of intact prophages within each bacterial species from **b**. **d**, Organization of predicted intact prophages that encode prototypical DNA-damage-responsive repressors (12 from the 38 intact phages identified in **a** and **b**). Genes coloured according to predicted function, designated in the key. In **a** and **d**, numbering above genomes denotes size in base pairs. In **d**, domain analysis was used to predict the *cI*-like repressor (maroon genes) on the basis that it harbours a helix-turn-helix DNA-binding domain (blue, N-terminal domain) and a LexA-like, S24 peptidase domain (pink, C-terminal domain). The same two-domain architecture is found in the lambda *cI* repressor protein and confers an autoproteolytic mechanism in which the repressor is cleaved in the presence of a DNA-damage-induced, RecA-active protein complex, leading to phage lysis.

[Source data](#)

Supplementary information

Supplementary Information

This file contains additional discussion pertinent to study findings; the caption for Supplementary Table 1; Supplementary Tables 2–4; and the Supplementary References.

Reporting Summary

Peer Review File

Supplementary Tables 1.1 and 1.2

tBLASTn result of top 230 *clbS*-like genes encoding proteins matching *E. coli* ClbS, WP_000290498 (tab 1); BLASTp result of top 5,000 ClbS-like proteins using *E. coli* ClbS, WP_000290498 as query (tab 2, available as a separate Excel file).

Supplementary Table 5

PFU ml⁻¹ for each plaque assay used in this study (available as a separate Excel file).

Supplementary Table 6

CFU ml⁻¹ and OD_{600 nm} data displayed in Supplementary Discussion Fig. 1 (available as a separate Excel file).

Source data

Source Data Fig. 1

Source Data Fig. 2

Source Data Fig. 3

Source Data Extended Data Fig. 1

Source Data Extended Data Fig. 2

Source Data Extended Data Fig. 3

Source Data Extended Data Fig. 4

Rights and permissions

Open Access This article is licensed under a Creative Commons Attribution 4.0 International License, which permits use, sharing, adaptation, distribution and reproduction in any medium or format, as long as you give appropriate credit to the original author(s) and the source, provide a link to the Creative Commons license, and indicate if changes were made. The images or other third party material in this article are included in the article's Creative Commons license, unless indicated otherwise in a credit line to the material. If material is not included in the article's Creative Commons license and your intended use is not permitted by statutory regulation or exceeds the

permitted use, you will need to obtain permission directly from the copyright holder.
To view a copy of this license, visit <http://creativecommons.org/licenses/by/4.0/>.

[Reprints and Permissions](#)

About this article

Cite this article

Silpe, J.E., Wong, J.W.H., Owen, S.V. *et al.* The bacterial toxin colibactin triggers prophage induction. *Nature* **603**, 315–320 (2022). <https://doi.org/10.1038/s41586-022-04444-3>

- Received: 24 May 2021
- Accepted: 18 January 2022
- Published: 23 February 2022
- Issue Date: 10 March 2022
- DOI: <https://doi.org/10.1038/s41586-022-04444-3>

Share this article

Anyone you share the following link with will be able to read this content:

[Get shareable link](#)

Sorry, a shareable link is not currently available for this article.

[Copy to clipboard](#)

Provided by the Springer Nature SharedIt content-sharing initiative

This article was downloaded by **calibre** from <https://www.nature.com/articles/s41586-022-04444-3>

- Article
- [Published: 24 January 2022](#)

Clonally expanded B cells in multiple sclerosis bind EBV EBNA1 and GlialCAM

- [Tobias V. Lanz](#) ORCID: [orcid.org/0000-0001-7106-8801^{1,2,3,4}](https://orcid.org/0000-0001-7106-8801),
- [R. Camille Brewer](#) ORCID: [orcid.org/0000-0002-0342-1826^{1,4}](https://orcid.org/0000-0002-0342-1826),
- [Peggy P. Ho](#) ORCID: [orcid.org/0000-0002-6848-318X⁵](https://orcid.org/0000-0002-6848-318X),
- [Jae-Seung Moon](#) ORCID: [orcid.org/0000-0002-1983-465X^{1,4}](https://orcid.org/0000-0002-1983-465X),
- [Kevin M. Jude](#) ORCID: [orcid.org/0000-0002-3675-5136⁶](https://orcid.org/0000-0002-3675-5136),
- [Daniel Fernandez](#) ORCID: [orcid.org/0000-0002-6221-152X⁷](https://orcid.org/0000-0002-6221-152X),
- [Ricardo A. Fernandes](#)⁶,
- [Alejandro M. Gomez](#)^{1,4},
- [Gabriel-Stefan Nadj](#)^{1,4},
- [Christopher M. Bartley](#) ORCID: [orcid.org/0000-0002-1391-4130⁸](https://orcid.org/0000-0002-1391-4130),
- [Ryan D. Schubert](#)⁹,
- [Isobel A. Hawes](#)⁹,
- [Sara E. Vazquez](#)¹⁰,
- [Manasi Iyer](#)¹¹,
- [J. Bradley Zuchero](#)¹¹,
- [Bianca Teegen](#)¹²,
- [Jeffrey E. Dunn](#)¹³,
- [Christopher B. Lock](#) ORCID: [orcid.org/0000-0002-4087-5894¹³](https://orcid.org/0000-0002-4087-5894),
- [Lucas B. Kipp](#)¹³,
- [Victoria C. Cotham](#)^{14,15},
- [Beatrix M. Ueberheide](#)^{14,15},
- [Blake T. Aftab](#) ORCID: [orcid.org/0000-0003-4020-2718¹⁶](https://orcid.org/0000-0003-4020-2718),
- [Mark S. Anderson](#) ORCID: [orcid.org/0000-0002-3093-4758¹⁷](https://orcid.org/0000-0002-3093-4758),

- [Joseph L. DeRisi](#)^{10,18},
- [Michael R. Wilson](#) ORCID: orcid.org/0000-0002-8705-5084⁹,
- [Rachael J. M. Bashford-Rogers](#) ORCID: orcid.org/0000-0002-6838-0711¹⁹,
- [Michael Platten](#) ORCID: orcid.org/0000-0002-4746-887X^{2,3,20},
- [K. Christopher Garcia](#) ORCID: orcid.org/0000-0001-9273-0278⁶,
- [Lawrence Steinman](#) ORCID: orcid.org/0000-0002-2437-2250⁵ &
- [William H. Robinson](#) ORCID: orcid.org/0000-0003-4385-704X^{1,4}

Nature volume **603**, pages 321–327 (2022)

- 26k Accesses
- 7 Citations
- 855 Altmetric
- [Metrics details](#)

Subjects

- [Autoimmunity](#)
- [Multiple sclerosis](#)
- [Neuroimmunology](#)
- [VDJ recombination](#)

Abstract

Multiple sclerosis (MS) is a heterogenous autoimmune disease in which autoreactive lymphocytes attack the myelin sheath of the central nervous system. B lymphocytes in the cerebrospinal fluid (CSF) of patients with MS contribute to inflammation and secrete oligoclonal immunoglobulins^{1,2}. Epstein–Barr virus (EBV) infection has been epidemiologically linked to MS, but its pathological role remains unclear³. Here we demonstrate high-affinity molecular mimicry between the EBV transcription factor EBV nuclear antigen 1 (EBNA1) and the central nervous system protein glial cell

adhesion molecule (GlialCAM) and provide structural and *in vivo* functional evidence for its relevance. A cross-reactive CSF-derived antibody was initially identified by single-cell sequencing of the paired-chain B cell repertoire of MS blood and CSF, followed by protein microarray-based testing of recombinantly expressed CSF-derived antibodies against MS-associated viruses. Sequence analysis, affinity measurements and the crystal structure of the EBNA1–peptide epitope in complex with the autoreactive Fab fragment enabled tracking of the development of the naive EBNA1-restricted antibody to a mature EBNA1–GlialCAM cross-reactive antibody. Molecular mimicry is facilitated by a post-translational modification of GlialCAM. EBNA1 immunization exacerbates disease in a mouse model of MS, and anti-EBNA1 and anti-GlialCAM antibodies are prevalent in patients with MS. Our results provide a mechanistic link for the association between MS and EBV and could guide the development of new MS therapies.

This is a preview of subscription content

Access options

Subscribe to Nature+

Get immediate online access to the entire Nature family of 50+ journals

\$29.99

monthly

[Subscribe](#)

Subscribe to Journal

Get full journal access for 1 year

\$199.00

only \$3.90 per issue

Subscribe

All prices are NET prices.
VAT will be added later in the checkout.
Tax calculation will be finalised during checkout.

Buy article

Get time limited or full article access on ReadCube.

\$32.00

Buy

All prices are NET prices.

Additional access options:

- [Log in](#)
- [Learn about institutional subscriptions](#)

Fig. 1: B cell repertoires in MS blood and CSF.

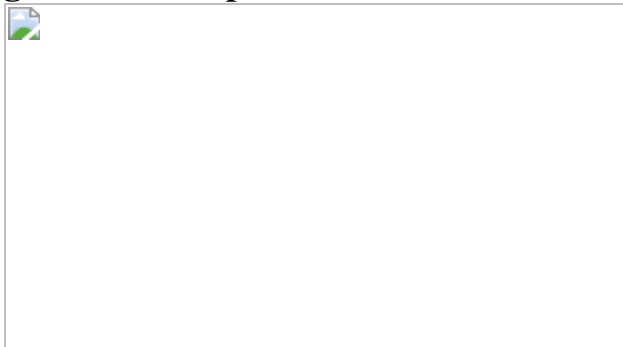


Fig. 2: MS CSF B cell mAb reactivity to EBV proteins and interaction of MS39p2w174 with EBNAL_{AA386–405}.

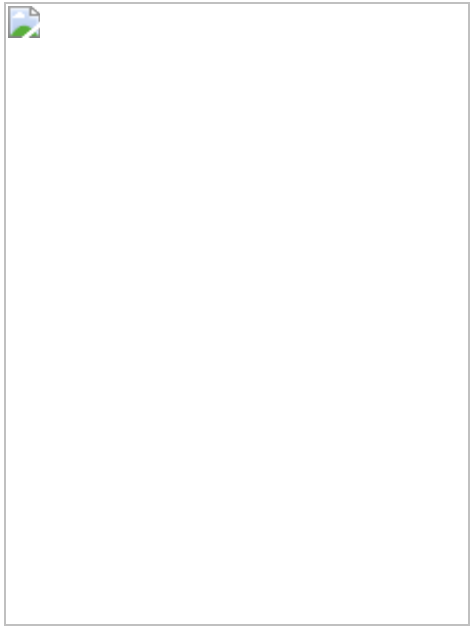


Fig. 3: Molecular mimicry between EBNA1 and GlialCAM.

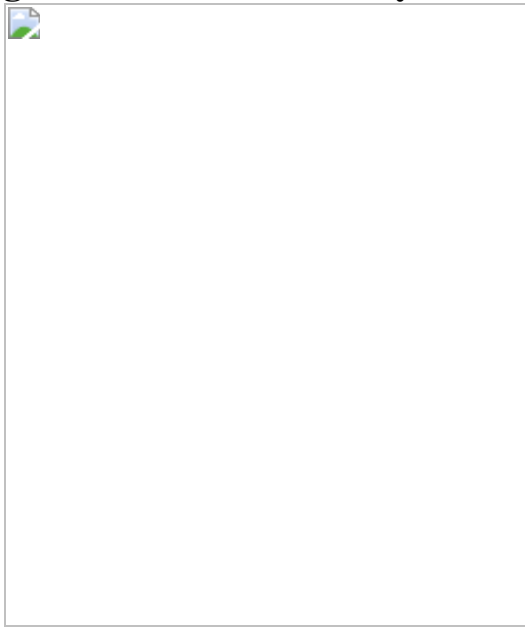
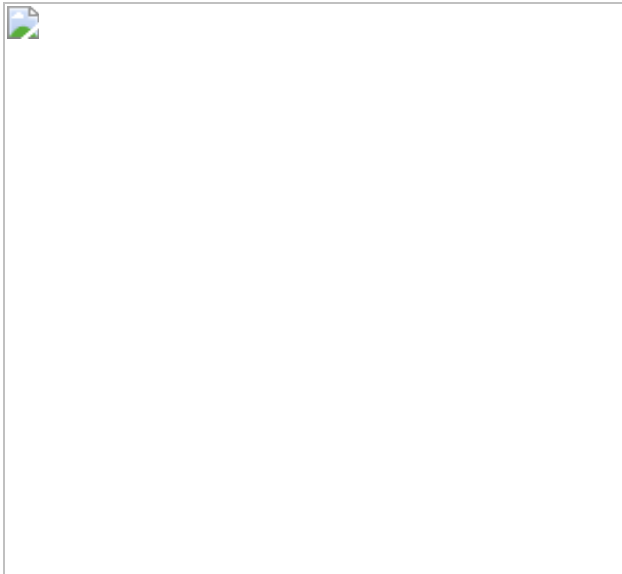


Fig. 4: Anti-EBNA1_{AA386-405} immunization exacerbates autoimmune-mediated demyelination in vivo.



Data availability

The genomic datasets analysed during the study have been uploaded to the Sequence Read Archive (<https://www.ncbi.nlm.nih.gov/sra>) with accession number [PRJNA780931](#). Mass spectrometry data are available at MassIVE (<https://massive.ucsd.edu>) with accession number MSV000086842. Structural data are available at PDB (<https://www.rcsb.org>) with the identifier [7K7R](#). [Source data](#) are provided with this paper.

References

1. Cencioni, M. T., Mattoscio, M., Magliozzi, R., Bar-Or, A. & Muraro, P. A. B cells in multiple sclerosis—from targeted depletion to immune reconstitution therapies. *Nat. Rev. Neurol.* **17**, 399–414 (2021).
2. Hauser, S. L. et al. Ocrelizumab versus interferon beta-1a in relapsing multiple sclerosis. *N. Engl. J. Med.* **376**, 221–234 (2017).
3. Bar-Or, A. et al. Epstein–Barr virus in multiple sclerosis: theory and emerging immunotherapies. *Trends Mol. Med.* **26**, 296–310 (2020).
4. Jarius, S. et al. The MRZ reaction as a highly specific marker of multiple sclerosis: re-evaluation and structured review of the literature.

J. Neurol. **264**, 453–466 (2017).

5. Wang, Z. et al. Antibodies from multiple sclerosis brain identified Epstein–Barr virus nuclear antigen 1 & 2 epitopes which are recognized by oligoclonal bands. *J. Neuroimmune Pharmacol.* **16**, 567–580 (2021).
6. Bjornevik, K. et al. Longitudinal analysis reveals high prevalence of Epstein-Barr virus associated with multiple sclerosis. *Science* **375**, 296–301 (2022).
7. Nielsen, T. R. et al. Effects of infectious mononucleosis and HLA-DRB1*15 in multiple sclerosis. *Mult. Scler.* **15**, 431–436 (2009).
8. Tengvall, K. et al. Molecular mimicry between anoctamin 2 and Epstein–Barr virus nuclear antigen 1 associates with multiple sclerosis risk. *Proc. Natl Acad. Sci. USA* **116**, 16955–16960 (2019).
9. Ruprecht, K. et al. Multiple sclerosis: the elevated antibody response to Epstein–Barr virus primarily targets, but is not confined to, the glycine–alanine repeat of Epstein–Barr nuclear antigen-1. *J. Neuroimmunol.* **272**, 56–61 (2014).
10. Jafari, N. et al. No evidence for intrathecal IgG synthesis to Epstein–Barr virus nuclear antigen-1 in multiple sclerosis. *J. Clin. Virol.* **49**, 26–31 (2010).
11. Salzer, J. et al. Epstein–Barr virus antibodies and vitamin D in prospective multiple sclerosis biobank samples. *Mult. Scler.* **19**, 1587–1591 (2013).
12. Sundqvist, E. et al. Epstein–Barr virus and multiple sclerosis: interaction with HLA. *Genes Immun.* **13**, 14–20 (2012).
13. Ramesh, A. et al. A pathogenic and clonally expanded B cell transcriptome in active multiple sclerosis. *Proc. Natl Acad. Sci. USA* **117**, 22932–22943 (2020).

14. Kowarik, M. C. et al. Immune cell subtyping in the cerebrospinal fluid of patients with neurological diseases. *J. Neurol.* **261**, 130–143 (2014).
15. Tan, Y.-C. et al. Barcode-enabled sequencing of plasmablast antibody repertoires in rheumatoid arthritis. *Arthritis Rheumatol.* **66**, 2706–2715 (2014).
16. Palanichamy, A. et al. Immunoglobulin class-switched B cells form an active immune axis between CNS and periphery in multiple sclerosis. *Sci. Transl. Med.* **6**, 248ra106 (2014).
17. von Büdingen, H.-C. et al. B cell exchange across the blood–brain barrier in multiple sclerosis. *J. Clin. Invest.* **122**, 4533–4543 (2012).
18. Rounds, W. H. et al. MSPrecise: a molecular diagnostic test for multiple sclerosis using next generation sequencing. *Gene* **572**, 191–197 (2015).
19. Bankoti, J. et al. In multiple sclerosis, oligoclonal bands connect to peripheral B-cell responses. *Ann. Neurol.* **75**, 266–276 (2014).
20. Mescheriakova, J. Y., van Nierop, G. P., van der Eijk, A. A., Kreft, K. L. & Hintzen, R. Q. EBNA-1 titer gradient in families with multiple sclerosis indicates a genetic contribution. *Neurol. Neuroimmunol. Neuroinflamm.* **7**, e872 (2020).
21. Berman, H. M. et al. The Protein Data Bank. *Acta Crystallogr. D* **58**, 899–907 (2002).
22. Jeong, J. S. et al. Rapid identification of monospecific monoclonal antibodies using a human proteome microarray. *Mol. Cell. Proteomics* **11**, O111.016253 (2012).
23. Uhlén, M. et al. Proteomics. Tissue-based map of the human proteome. *Science* **347**, 1260419 (2015).
24. Gilbert, A., Vidal, X. E., Estevez, R., Cohen-Salmon, M. & Boulay, A.-C. Postnatal development of the astrocyte perivascular

MLC1/GliaCAM complex defines a temporal window for the gliovascular unit maturation. *Brain Struct. Funct.* **224**, 1267–1278 (2019).

25. Favre-Kontula, L. et al. GliaCAM, an immunoglobulin-like cell adhesion molecule is expressed in glial cells of the central nervous system. *Glia* **56**, 633–645 (2008).
26. López-Hernández, T. et al. Mutant GliaCAM causes megalencephalic leukoencephalopathy with subcortical cysts, benign familial macrocephaly, and macrocephaly with retardation and autism. *Am. J. Hum. Genet.* **88**, 422–432 (2011).
27. Han, M. H. et al. Proteomic analysis of active multiple sclerosis lesions reveals therapeutic targets. *Nature* **451**, 1076–1081 (2008).
28. O'Donovan, B. et al. High-resolution epitope mapping of anti-Hu and anti-Yo autoimmunity by programmable phage display. *Brain Commun* **2**, fcaa059 (2020).
29. Bochkarev, A., Bochkareva, E., Frappier, L. & Edwards, A. M. The 2.2 Å structure of a permanganate-sensitive DNA site bound by the Epstein–Barr virus origin binding protein, EBNA1. *J. Mol. Biol.* **284**, 1273–1278 (1998).
30. Casciola-Rosen, L. A., Anhalt, G. & Rosen, A. Autoantigens targeted in systemic lupus erythematosus are clustered in two populations of surface structures on apoptotic keratinocytes. *J. Exp. Med.* **179**, 1317–1330 (1994).
31. Pisetsky, D. S. & Lipsky, P. E. New insights into the role of antinuclear antibodies in systemic lupus erythematosus. *Nat. Rev. Rheumatol.* **16**, 565–579 (2020).
32. Schellekens, G. A. et al. The diagnostic properties of rheumatoid arthritis antibodies recognizing a cyclic citrullinated peptide. *Arthritis Rheum.* **43**, 155–163 (2000).

33. Moh, M. C., Zhang, C., Luo, C., Lee, L. H. & Shen, S. Structural and functional analyses of a novel Ig-like cell adhesion molecule, hepaCAM, in the human breast carcinoma MCF7 cells. *J. Biol. Chem.* **280**, 27366–27374 (2005).
34. Britton, D. et al. Quantification of pancreatic cancer proteome and phosphorylome: indicates molecular events likely contributing to cancer and activity of drug targets. *PLoS ONE* **9**, e90948 (2014).
35. Herskowitz, J. H. et al. Phosphoproteomic analysis reveals site-specific changes in GFAP and NDRG2 phosphorylation in frontotemporal lobar degeneration. *J. Proteome Res.* **9**, 6368–6379 (2010).
36. Hornbeck, P. V., Chabra, I., Kornhauser, J. M., Skrzypek, E. & Zhang, B. PhosphoSite: a bioinformatics resource dedicated to physiological protein phosphorylation. *Proteomics* **4**, 1551–1561 (2004).
37. Zavala-Cerna, M. G. et al. The clinical significance of posttranslational modification of autoantigens. *Clin. Rev. Allergy Immunol.* **47**, 73–90 (2014).
38. Bashford-Rogers, R. J. M., Smith, K. G. C. & Thomas, D. C. Antibody repertoire analysis in polygenic autoimmune diseases. *Immunology* **155**, 3–17 (2018).
39. Obermeier, B. et al. Matching of oligoclonal immunoglobulin transcriptomes and proteomes of cerebrospinal fluid in multiple sclerosis. *Nat. Med.* **14**, 688–693 (2008).
40. Singh, V. et al. Cerebrospinal-fluid-derived immunoglobulin G of different multiple sclerosis patients shares mutated sequences in complementarity determining regions. *Mol. Cell. Proteomics* **12**, 3924–3934 (2013).
41. Colombo, M. et al. Accumulation of clonally related B lymphocytes in the cerebrospinal fluid of multiple sclerosis patients. *J. Immunol.* **164**, 2782–2789 (2000).

42. Terzoglou, A. G., Routsias, J. G., Avrameas, S., Moutsopoulos, H. M. & Tzioufas, A. G. Preferential recognition of the phosphorylated major linear B-cell epitope of La/SSB 349–368 aa by anti-La/SSB autoantibodies from patients with systemic autoimmune diseases. *Clin. Exp. Immunol.* **144**, 432–439 (2006).
43. International Multiple Sclerosis Genetics Consortium & The Wellcome Trust Case Control Consortium 2. Genetic risk and a primary role for cell-mediated immune mechanisms in multiple sclerosis. *Nature* **476**, 214–219 (2011).
44. Thompson, A. J. et al. Diagnosis of multiple sclerosis: 2017 revisions of the McDonald criteria. *Lancet Neurol.* **17**, 162–173 (2018).
45. Polman, C. H. et al. Diagnostic criteria for multiple sclerosis: 2010 revisions to the McDonald criteria. *Ann. Neurol.* **69**, 292–302 (2011).
46. Wingerchuk, D. M. et al. International consensus diagnostic criteria for neuromyelitis optica spectrum disorders. *Neurology* **85**, 177–189 (2015).
47. Tan, Y.-C. et al. High-throughput sequencing of natively paired antibody chains provides evidence for original antigenic sin shaping the antibody response to influenza vaccination. *Clin. Immunol.* **151**, 55–65 (2014).
48. Blum, L. K. et al. Circulating plasmablasts are elevated and produce pathogenic anti-endothelial cell autoantibodies in idiopathic pulmonary arterial hypertension. *Eur. J. Immunol.* **48**, 874–884 (2018).
49. Edgar, R. C. UPARSE: highly accurate OTU sequences from microbial amplicon reads. *Nat. Methods* **10**, 996–998 (2013).
50. Alamyar, E., Duroux, P., Lefranc, M.-P. & Giudicelli, V. IMGT® tools for the nucleotide analysis of immunoglobulin (IG) and T cell receptor (TR) V-(D)-J repertoires, polymorphisms, and IG mutations: IMGT/V-QUEST and IMGT/HighV-QUEST for NGS. *Methods Mol. Biol.* **882**, 569–604 (2012).

51. Edgar, R. C. MUSCLE: multiple sequence alignment with high accuracy and high throughput. *Nucleic Acids Res.* **32**, 1792–1797 (2004).
52. Guindon, S. et al. New algorithms and methods to estimate maximum-likelihood phylogenies: assessing the performance of PhyML 3.0. *Syst. Biol.* **59**, 307–321 (2010).
53. Huerta-Cepas, J., Serra, F. & Bork, P. ETE 3: reconstruction, analysis, and visualization of phylogenomic data. *Mol. Biol. Evol.* **33**, 1635–1638 (2016).
54. Bern, M., Kil, Y. J. & Becker, C. Byonic: advanced peptide and protein identification software. *Curr. Protoc. Bioinformatics Chapter 13*, Unit13.20 (2012).
55. Robinson, W. H. et al. Autoantigen microarrays for multiplex characterization of autoantibody responses. *Nat. Med.* **8**, 295–301 (2002).
56. Kuerten, S. Autoantibodies against central nervous system antigens in a subset of B cell-dominant multiple sclerosis patients. *Proc. Natl Acad. Sci. USA* **117**, 21512–21518 (2020).
57. Schubert, R. D. et al. Pan-viral serology implicates enteroviruses in acute flaccid myelitis. *Nat. Med.* **25**, 1748–1752 (2019).
58. Emery, B. & Dugas, J. C. Purification of oligodendrocyte lineage cells from mouse cortices by immunopanning. *Cold Spring Harb. Protoc.* **2013**, 854–868 (2013).
59. Obradovic, Z. et al. Predicting intrinsic disorder from amino acid sequence. *Proteins* **53**, 566–572 (2003).
60. Evans, P. R. & Murshudov, G. N. How good are my data and what is the resolution? *Acta Crystallogr. D* **69**, 1204–1214 (2013).

61. Tickle, I. STARANISO: use of a WebGL-based 3D interactive graphical display to represent and visualise data quality metrics for anisotropic macromolecular diffraction data. *Acta Crystallogr. A* **75**, e162 (2019).
62. McCoy, A. J. et al. Phaser crystallographic software. *J. Appl. Crystallogr.* **40**, 658–674 (2007).
63. Fouts, A. E. et al. Mechanism for neutralizing activity by the anti-CMV gH/gL monoclonal antibody MSL-109. *Proc. Natl Acad. Sci. USA* **111**, 8209–8214 (2014).
64. Emsley, P., Lohkamp, B., Scott, W. G. & Cowtan, K. Features and development of Coot. *Acta Crystallogr. D* **66**, 486–501 (2010).
65. Liebschner, D. et al. Macromolecular structure determination using X-rays, neutrons and electrons: recent developments in Phenix. *Acta Crystallogr. D* **75**, 861–877 (2019).
66. Afonine, P. V. et al. Towards automated crystallographic structure refinement with phenix.refine. *Acta Crystallogr. D* **68**, 352–367 (2012).
67. The PyMOL Molecular Graphics System, Version 2.1, Schrödinger, LLC.
68. Lanz, T. V. et al. Tryptophan-2,3-dioxygenase (TDO) deficiency is associated with subclinical neuroprotection in a mouse model of multiple sclerosis. *Sci Rep.* **7**, 41271 (2017).

Acknowledgements

We thank W. Wick for support with sample collection; B. Bell for advice on crystallization; G. Harauz for insightful discussions on poly-proline motifs; and the staff at SSRL for assistance with data collection. This work was supported by NIH R01 AR063676 and U19 AI110491 to W.H.R., the Juvenile Diabetes Research Foundation and Lupus Research Alliance

Funding to W.H.R. and T.V.L., the German Research Foundation (DFG, LA3657/1) to T.V.L., Atara to L.S. and P.P.H., and the German Research Foundation to M.P. (DFG, project 406052676; PL-315/5-1). The mass spectrometry experiments were in part supported by the NYU Grossman School of Medicine and a shared instrumentation grant (NIH 1S10OD010582-01A1). Use of the Stanford Synchrotron Radiation Lightsource, SLAC National Accelerator Laboratory, is supported by the US Department of Energy, Office of Science, Office of Basic Energy Sciences under contract number DE-AC02-76SF00515. The SSRL Structural Molecular Biology Program is supported by the DOE Office of Biological and Environmental Research, and by NIH GIGMS P30GM133894. C.M.B. is a Hanna H. Gray Fellow at the Howard Hughes Medical Institute. The contents of this publication are solely the responsibility of the authors and do not represent the official views of the NIGMS or the NIH.

Author information

Affiliations

1. Division of Immunology and Rheumatology, Department of Medicine, Stanford University School of Medicine, Stanford, CA, USA

Tobias V. Lanz, R. Camille Brewer, Jae-Seung Moon, Alejandro M. Gomez, Gabriel-Stefan Nadj & William H. Robinson

2. Department of Neurology, Mannheim Center for Translational Neurosciences (MCTN), Medical Faculty Mannheim, University of Heidelberg, Mannheim, Germany

Tobias V. Lanz & Michael Platten

3. Department of Neurology and National Center for Tumor Diseases, University Hospital Heidelberg, Heidelberg, Germany

Tobias V. Lanz & Michael Platten

4. The Geriatric Research, Education, and Clinical Center (GRECC), VA
Palo Alto Health Care System, Palo Alto, CA, USA

Tobias V. Lanz, R. Camille Brewer, Jae-Seung Moon, Alejandro M. Gomez, Gabriel-Stefan Nadj & William H. Robinson

5. Department of Neurology and Neurological Sciences, Stanford University School of Medicine, Beckman Center for Molecular Medicine, Stanford, CA, USA

Peggy P. Ho & Lawrence Steinman

6. Department of Molecular and Cellular Physiology, Stanford University School of Medicine, Beckman Center for Molecular Medicine, Stanford, CA, USA

Kevin M. Jude, Ricardo A. Fernandes & K. Christopher Garcia

7. Macromolecular Structure Knowledge Center, Stanford ChEM-H Institute, Stanford, CA, USA

Daniel Fernandez

8. Weill Institute for Neurosciences, Department of Psychiatry and Behavioral Sciences, University of California San Francisco, San Francisco, CA, USA

Christopher M. Bartley

9. Weill Institute for Neurosciences, Department of Neurology, University of California San Francisco, San Francisco, CA, USA

Ryan D. Schubert, Isobel A. Hawes & Michael R. Wilson

10. Department of Biochemistry and Biophysics, University of California San Francisco, San Francisco, CA, USA

Sara E. Vazquez & Joseph L. DeRisi

11. Department of Neurosurgery, Stanford University School of Medicine, Stanford, CA, USA

Manasi Iyer & J. Bradley Zuchero

12. Institute of Experimental Immunology, Euroimmun AG, Lubeck, Germany

Bianca Teegen

13. Division of Neuroimmunology, Department of Neurology and Neurological Sciences, Stanford University School of Medicine, Stanford, CA, USA

Jeffrey E. Dunn, Christopher B. Lock & Lucas B. Kipp

14. Department of Biochemistry and Molecular Pharmacology, NYU Perlmutter Cancer Center, NYU School of Medicine, New York, NY, USA

Victoria C. Cotham & Beatrix M. Ueberheide

15. NYU Langone Health Proteomics Laboratory, Division of Advanced Research Technologies, NYU School of Medicine, New York, NY, USA

Victoria C. Cotham & Beatrix M. Ueberheide

16. Preclinical Science and Translational Medicine, Atara Biotherapeutics, South San Francisco, CA, USA

Blake T. Aftab

17. Department of Medicine, Diabetes Center, University of California San Francisco, San Francisco, CA, USA

Mark S. Anderson

18. Chan Zuckerberg Biohub, University of California San Francisco, San Francisco, CA, USA

Joseph L. DeRisi

19. Wellcome Centre for Human Genetics, University of Oxford, Oxford, UK

Rachael J. M. Bashford-Rogers

20. DKTK Clinical Cooperation Unit Neuroimmunology and Brain Tumor Immunology, German Cancer Research Center (DKFZ), Heidelberg, Germany

Michael Platten

Contributions

Conceptualization: T.V.L., L.S. and W.H.R. Methodology: T.V.L., R.C.B., P.P.H., K.M.J., D.F., R.A.F., A.M.G., R.D.S., B.T., V.C.C., B.M.U., J.-S.M., M.I. and J.B.Z. Software: T.V.L., R.C.B., D.F., K.M.J. and V.C.C.

Validation: T.V.L., R.C.B., K.M.J., B.M.U., R.J.M.B.-R., K.C.G., L.S. and W.H.R. Formal analysis: T.V.L., R.C.B., K.M.J., D.F., A.M.G., C.M.B.,

V.C.C. and B.M.U. Investigation: T.V.L., R.C.B., P.P.H., D.F., G.-S.N.,

C.M.B., R.D.S., I.A.H., S.E.V., B.T., V.C.C., J.-S.M. and M.I. Resources: T.V.L., P.P.H., D.F., B.T., J.E.D., C.B.L., L.B.K., B.M.U., M.R.W., M.S.A., J.L.D., M.P., K.C.G., L.S. and W.H.R. Data curation: T.V.L., R.C.B.,

K.M.J., D.F., V.C.C. and B.M.U. Writing (original draft): T.V.L. Writing

(review and editing): T.V.L., R.C.B., P.P.H., L.S. and W.H.R. Visualization:

T.V.L., R.C.B. and K.M.J. Supervision: T.V.L. and W.H.R. Project

administration: T.V.L. and W.H.R. Funding acquisition, T.V.L., P.P.H.,

B.T.A., M.P., L.S. and W.H.R.

Corresponding author

Correspondence to [William H. Robinson](#).

Ethics declarations

Competing interests

W.H.R. owns equity in, serves as a consultant to and is a member of the Board of Directors of Atreca, Inc. L.S. owns equity in and serves as a consultant to Atreca, Inc. Stanford University is in the process of applying for a patent, US Patent and Trademark Office Serial No. 63/131,581, covering anti-EBV antibodies generated by sequencing B cell repertoires, which lists T.V.L. and W.H.R. as inventors. The remaining authors declare no competing interests.

Peer review

Peer review information

Nature thanks Paul Farrell, George Georgiou, Hartmut Wekerle and the other, anonymous, reviewer(s) for their contribution to the peer review of this work. Peer reviewer reports are available.

Additional information

Publisher's note Springer Nature remains neutral with regard to jurisdictional claims in published maps and institutional affiliations.

Extended data figures and tables

[Extended Data Fig. 1 Analysis of B cell phenotypes in MS blood and CSF.](#)

a–l, Flow cytometry data, **a,b**, representative flow cytometry plots are shown for **a**, blood and **b**, CSF. **c**, Plasmablasts as percent of all B cells in MS blood and CSF, means \pm SD of $n = 9$ patient samples, $**P = 0.004$, two-tailed Mann-Whitney test. **d**, Non-plasmablast B cell subsets as percent of all B cells in blood (red) and CSF (blue), means \pm SD of $n = 8$ patient

samples, *** $P = 0.0006$, two-tailed Mann-Whitney test, Holm-Sidak corrected for multiple comparisons. **e**, Integrin alpha-4 expression in non-plasmablast B cells (red) and plasmablasts (blue), mean MFI \pm SD of $n = 9$ patient samples, **** $P < 0.0001$, ** $P = 0.0013$, two-way ANOVA, Tukey adjusted for multiple comparisons, **f**, representative histogram showing integrin alpha-4 expression in non-plasmablast B cells (red) and plasmablasts (blue) in blood (top panel) and CSF (lower panel), **g**, HLA-DR expression in non-plasmablast B cells (red) and plasmablasts (blue) in blood and CSF, mean MFI \pm SD of $n = 9$ patient samples, **** $P < 0.0001$, *** $P = 0.0002$, two-way ANOVA, Tukey adjusted for multiple comparisons, and **h**, representative histogram showing HLA-DR expression in non-plasmablast B cells (red) and plasmablasts (blue) in blood (top panel), and CSF (lower panel). **i**, HLA-DR expression in patients carrying HLA-DRB1*15:01 (HLA-DR15, $n = 5$) vs. other HLA-genotypes (non-HLA-DR15, $n = 4$) in **i**, blood, and **j**, CSF, mean MFI \pm SD, significance levels calculated with two-way ANOVA, **k,l**, Immunoglobulin classes in **k**, non-plasmablast B cells and **l**, plasmablasts in blood (red) and CSF (blue), mean MFI \pm SD of $n = 9$ patient samples, **** $P < 0.0001$, two-way ANOVA, Holm-Sidak adjusted for multiple comparisons. Plasmablasts, PB; unswitched memory B cells, UM; switched memory B cells, SM; double negative B cells, DN.

[Source data](#)

[Extended Data Fig. 2 Extended BCR repertoire data.](#)

a–i, Single-cell BCR repertoire sequencing data, **a**, individual repertoires from all CSF B cells (top row) and subdivided into CSF plasmablasts (middle row) and non-plasmablast B cells (bottom row) of $n = 9$ MS patients. **b**, Individual repertoires of all CSF B cells (top row) and subdivided into CSF plasmablasts (middle row) and non-plasmablast B cells (bottom row) of $n = 3$ control patients. Numbers indicate number of sequences, inner circle: colored wedges represent clonal expansions and grey area represents singleton antibody sequences, outer circle: immunoglobulin classes, red: IgG, blue: IgA, green: IgM, sequence locations in outer circle correspond to inner circle. No non-plasmablast B cells were sorted for MS12 and C5. Only plasmablasts were sorted for

MS39. **c**, Clonality, percent of clonal sequences in CSF B cells are shown, comparing BCR repertoires of control patients ($n = 3$) to MS patients ($n = 9$). Data corresponds to data shown in (Fig. 1b) and is separated into immunoglobulin classes IgG (left), IgA (center), and IgM (right). Means \pm SD of individuals' repertoires are shown. **d**, Immunoglobulin class distribution, percent of IgG (left), IgA (center), and IgM (right) of all CSF B cells are shown for $n = 3$ control patients and $n = 9$ MS patients. Means \pm SD of individuals' repertoires are shown. **e**, IGHV and IGLV cumulated mutation count in plasmablasts in blood (red) vs. CSF (blue), means \pm SD of $n = 9$ patients samples. **f**, Mean HC CDR3 lengths (amino acid sequences) of plasmablasts in blood (red) vs. CSF (blue), means \pm SD of $n = 9$ patient samples. **g–i**, Immunoglobulin gene distribution in blood vs. CSF plasmablasts for **g**, IGLV, IGKV1-33, $****P < 10^{-6}$, IGLV3-21, $****P = 3 \times 10^{-6}$ according to unpaired two-tailed Student's t tests, Holm-Sidak adjusted for multiple comparisons, **h**, IGHJ, and **i**, IGLJ. Each dot represents the usage of one gene across $n = 9$ MS patient repertoires in the respective compartments. Linear regression lines and 95% confidence intervals are shown. **j**, Mass spectrometry data of purified CSF immunoglobulins, showing variable chain sequences that could be uniquely identified in singleton BCR sequences vs. plasmablast sequences, peptide-spectral matches (PSM) cutoff ≥ 10 , means \pm SD of $n = 9$ MS patients, $**P = 0.0012$. **k**, **l**, Same mass spectrometry data set as in (j), showing variable chain sequences that could be uniquely identified in non-plasmablast BCR sequences vs. plasmablast sequences, means \pm SD of $n = 7$ MS patients, **k**, PSM cutoff ≥ 1 , $**P = 0.007$, **l**, PSM cutoff ≥ 10 , $*P = 0.037$. **m**, Single-cell sequencing efficacy in non-plasmablast B cells (red) vs. plasmablasts (blue) in CSF. Fraction of sequences that passed filter thresholds are shown as percentages of the number of sorted cells in the respective group, means \pm SD of $n = 8$ patient samples (no non-PB value for MS39). **c**, **d**, **j–l**, P according to unpaired two-tailed Mann-Whitney test. **e–i**, P according to unpaired two-sided Student's t-test. Immunoglobulin heavy V gene, IGHV; Immunoglobulin heavy J gene, IGHJ; Immunoglobulin light V gene, IGLV; Immunoglobulin light J gene, IGLJ; peptide-spectral matches, PSM.

[Source data](#)

Extended Data Fig. 3 Phylogenetic trees of B cells from MS blood and CSF.

Blood plasmablasts (top rows) and CSF B cells (bottom rows) of $n = 9$ MS patients and CSF B cells of $n = 3$ control patients are shown. Each node represents the full-length heavy chain and light chain sequence of a single B cell. Trees are binned according to their IGHV families and genes, then the concatenated heavy chain and light chain sequences are clustered. IgG (red), IgA (blue), IgM (green). Smaller brighter circles indicate singleton B cells, larger darker circles indicate clonal expansions. Arrows indicate sequences that were expressed as mAbs, numbers indicate V-gene mutation loads in heavy and light chains. Immunoglobulin heavy V gene, IGHV.

[Source data](#)

Extended Data Fig. 4 Polyreactivity of recombinantly expressed antibodies.

a, ELISA data showing reactivity of recombinant mAbs against LPS (top), human insulin (middle), and dsDNA (bottom). Reactivity is represented in the order of decreasing reactivity to LPS in MS mAbs and control mAbs, respectively. Measurements were carried out in duplicates at 0.1, 1, and 10 $\mu\text{g/ml}$ mAb concentrations and the area under the curve (AUC) for each mAb is shown from one experiment. Commercial anti-LPS antibody (cyan), MS39p2w174 (red), germline (orange), control mAbs (blue).

[Source data](#)

Extended Data Fig. 5 MS CSF mAb reactivity to EBV and GlialCAM antigens.

a, mAb reactivities to EBV virus lysates and recombinant EBV proteins as well as to other virus lysates. Z-scores for each antigen are shown, measurement of one microarray experiment, measured in 8 technical replicates. **b**, mAb reactivities to LPS, Insulin, and dsDNA to assess polyreactivity. Z-scores of area under the curve (AUC) of ELISA

measurements at antibody concentrations of 0.1, 1, and 10 µg/ml are shown, each measurement was carried out in duplicates. **c**, mAb reactivities to GlialCAM proteins, peptides, and phosphorylated or citrullinated peptides. Mean reactivities (mean fluorescence intensity counts) are shown from one microarray experiment, measured in 8 technical replicates. Immediate early latency stage protein, IE; early, E; late, L; intracellular domain, ICD; extracellular domain, ECD; phosphorylated Serine, pSer; citrulline residue, Cit; _B - _E: duplicate probes of same / similar lysates and proteins (different preparations or batches).

[Source data](#)

Extended Data Fig. 6 MS CSF mAb reactivity to EBV peptides.

a, mAb reactivities to EBV peptides. Z-scores for each antigen are shown, measurement of one microarray experiment, measured in 8 technical replicates. Intracellular domain, ICD; extracellular domain, ECD; peptide mix, PM.

[Source data](#)

Extended Data Fig. 7 mAb reactivity to EBV peptides and extended structural data for the EBNA1_{AA386-405}/MS39p2w174-Fab complex.

a, mAb reactivities of selected reactive mAbs against the selected reactive peptide antigens. Z-scores for each antigen are shown, measurement of one microarray experiment, measured in 8 technical replicates. **b**, ELISA-based alanine-scan on EBNA1_{AA386-405}, corresponding to (Fig. 2e). Mean OD (450 nm) ± SD from three independent experiments, each carried out in triplicates. **c**, 20x image of protein crystals in hanging drop. **d**, Asymmetric unit containing two peptide-Fab complexes in a diagonal orientation, heavy chain (red/pink), light chain (blue/cyan), peptide (black/gray). **e**, EBNA1_{AA386-405} peptide and its 2mFoDFc map (contoured at 1σ) are shown, depicted on heavy chain (cyan) and light chain (pink) in surface representation. **f**, **g**, Amino acid sequences of variable regions of **f**, mAb

MS39p2w174 heavy chain and **g**, light chain. Bold font: CDR, regular font framework regions. Of the germline variable genes (bottom rows), only residues that differ from MS39p2w174 sequence are shown, red: residues that closely interact with EBNA1_{AA386-405} according to crystal structure. dots: gaps introduced during IMGT GapAlign for alignment and numbering purposes, numbers: residue numbers according to IMGT unique numbering. Intracellular domain, ICD; extracellular domain, ECD; heavy chain, HC; light chain, LC; complementarity determining region, CDR; framework region, FR; germline, GL.

[Source data](#)

Extended Data Fig. 8 Extended characteristics of GlialCAM_{AA370-389} and immunofluorescence stainings with MS39p2w174.

a, Phage display PhiP-Seq data, showing alignment of Pro/Arg-rich region and adjacent residues of all phage display peptides enriched above 100 / 10⁵ reads. **b**, Immunofluorescence of mouse brain slices stained with (i) control antibody, and (ii-iv) MS39p2w174 (green) and DAPI (blue). (i,ii) full brain, scale bars: 2000 μm, (iii) magnification of hippocampus with prominent MS39p2w174 staining, scale bar: 400 μm, and (iv) olfactory bulb with prominent MS39p2w174 staining in the olfactory nerve (oln), glomerular (gl), and external plexiform layers (epl), but not the mitral (ml), internal plexiform (ipl), or granule cell (gcl) layers, scale bar: 100 μm. **c**, Immunofluorescence of primary rat oligodendrocytes with isotype control antibody (top panel) and MS39p2w174 (bottom panel). **d**, K562 cells in culture, wildtype (left) and transduced with full-length GlialCAM (right). **e**, Immunofluorescence with MS39p2w174 on WT K562 cells (top) and GlialCAM-tg K562 cells (center and bottom). White arrow: single K562 cell, orange arrow: high intensity MS39p2w174 staining on the cell border between transgenic K562 cells in bulks. **c, e**, Scale bars: 40 μm. **b–e**, representative micrographs of at least two experiments. **f**, Overview of phosphorylated residues in GlialCAM, identified by mass spectrometry (phosphoSite.org). The two phosphorylated serine residues of interest are indicated with arrows. **g**, ELISA, measuring binding of MS39p2w174 to

native and citrullinated GlialCAM_{AA370-389} peptides, means of $n = 2$ independent experiments, each carried out in triplicates. Wildtype, WT; extracellular domain, ECD; intracellular domain, ICD; phosphorylated serine, pSer; citrulline residue, Cit.

[Source data](#)

Extended Data Fig. 9 Plasma reactivity against EBNA1 and GlialCAM proteins and peptides in healthy control individuals and MS patients.

a, ELISA measurement of antigen-specific IgG reactivity against peptides EBNA1_{AA386-405}, GlialCAM_{AA370-389}, phosphorylated GlialCAM_{AA370-389} pSer376, 2x-phosphorylated GlialCAM_{AA370-389} pSer376 pSer377, and scrambled peptide control in plasma samples of healthy control individuals ($n = 50$) and MS patients ($n = 71$). Means \pm SD in each patient group is shown. Representative OD (450 nm) measurements of two independent experiments, each carried out in duplicates. ** $P < 0.01$, *** $P < 0.001$ according to two-tailed Mann-Whitney test, Tukey corrected for multiple comparisons. **b**, ELISA measurements of antigen-specific IgG reactivity against GlialCAM full-length protein, GlialCAM_{AA370-389}, and phosphorylated GlialCAM_{AA370-389} pSer376 in plasma samples of a separate cohort of healthy control individuals ($n = 31$) and MS patients ($n = 67$). Means \pm SD across patient groups are shown. Representative OD (450 nm) measurements of two independent experiments, each carried out in duplicates. * $P < 0.05$, ** $P < 0.01$ according to two-tailed Mann-Whitney test, Tukey corrected for multiple comparisons. **c**, ELISA measurements of mAB MS39p2w174 binding to EBNA1_{AA386-405}, without interference as well as blocked with scrambled peptide control, EBNA1_{AA386-405}, and GlialCAM_{AA370-389} pSer376, as a positive control to (Fig. 3q). Mean OD (450 nm) \pm SD of quadruplicate measurements from $n = 1$ experiment are shown. * $P < 0.05$, ** $P < 0.01$, *** $P < 0.001$ according to one-way ANOVA, Tukey corrected for multiple comparisons.

[Source data](#)

Extended Data Fig. 10 T cell response against EBNA_{AA386-405}

a, ELISA data showing mouse plasma IgG responses against PLP_{AA139-151} at the indicated timepoints pre and post EAE induction, for scrambled peptide immunized mice (blue, $n = 10$) and EBNA1_{AA386-405} immunized mice (red, $n = 10$). Mean OD (450 nm) fold change \pm SD, significance levels according to unpaired two-tailed Mann-Whitney test. Means \pm SD, representative of three independent experiments, each carried out as triplicate measurements. **b**, T cell proliferation measurement by ³H-thymidine incorporation in splenocytes and lymph node cells of mice immunized with scrambled peptide (blue) and EBNA1_{AA386-405} (red). Cells from $n = 10$ mice per group were pooled and mean counts per minute (cpm) \pm SD of triplicate measurements are shown. $P = 8.9 \times 10^{-5}$, unpaired two-tailed Student's *t*-test, Holm-Sidak corrected for multiple comparisons. **c–h**, ELISA measurements of cytokines in cell culture supernatant of mouse splenocytes and lymph node cells of mice immunized with scrambled peptide (blue) or EBNA1_{AA386-405} (red) and re-stimulated with the indicated peptides. Cells from $n = 10$ mice per group were pooled and mean cpm \pm SD of six replicate measurements are shown. **c**, IFN- γ , **d**, TNF, **e**, IL-12, **f**, IL-10, **g**, IL-6, **h**, IL-17, * $P < 0.05$, significance levels according to unpaired two-tailed Mann-Whitney test, Holm-Sidak corrected for multiple comparisons. **i**, Representative Luxol Fast Blue stained spinal cords from scrambled peptide group (top panel) and EBNA1_{AA386-405} group (bottom panel). Scale bars left images: 200 μ m, right images: 50 μ m. **j**, Statistical evaluation of Luxol Fast Blue scores, means of at least 4 coronal spinal cord sections per mouse and means \pm SD for each group ($n = 9$) are shown. **** $P < 0.0001$, unpaired two-tailed Mann-Whitney test. **k, l**, Flow cytometry data of PBMC from healthy control individuals ($n = 6$, blue) and MS patients ($n = 7$, red), showing percent of **k**, IFN- γ + and **l**, IL-17+ CD4+ T cells in all CD4+ T cells. Mean MFI \pm SEM are shown for the respective groups. Significance levels were assessed by two-way ANOVA, followed by FDR calculation using the two-stage step-up method of Benjamini, Krieger and Yekutieli, *Significant at FDR < 0.1 . **m**, Flow cytometry data, representative dot plots are shown for two individuals from the data set

presented in Fig. 4f. Healthy control individual (left) and MS patient MS16 (right). Expression levels of Granzyme-B (GZMB) and IFN- γ are presented under the indicated stimulations.

[Source data](#)

Extended Data Table 1 Patient collective

Extended Data Table 2 MS39p2w174 binding peptides identified by 49-mer phage display

Supplementary information

[Supplementary Information](#)

This file contains Supplementary Tables 1–6, Supplementary Figs. 1 and 2, Supplementary Discussion and additional references.

[Reporting Summary](#)

[Peer Review File](#)

Source data

[Source Data Fig. 1](#)

[Source Data Fig. 2](#)

[Source Data Fig. 3](#)

[Source Data Fig. 4](#)

[Source Data Extended Data Fig. 1](#)

[Source Data Extended Data Fig. 2](#)

[**Source Data Extended Data Fig. 3**](#)

[**Source Data Extended Data Fig. 4**](#)

[**Source Data Extended Data Fig. 5**](#)

[**Source Data Extended Data Fig. 6**](#)

[**Source Data Extended Data Fig. 7**](#)

[**Source Data Extended Data Fig. 8**](#)

[**Source Data Extended Data Fig. 9**](#)

[**Source Data Extended Data Fig. 10**](#)

Rights and permissions

[Reprints and Permissions](#)

About this article

Cite this article

Lanz, T.V., Brewer, R.C., Ho, P.P. *et al.* Clonally expanded B cells in multiple sclerosis bind EBV EBNA1 and GlialCAM. *Nature* **603**, 321–327 (2022). <https://doi.org/10.1038/s41586-022-04432-7>

- Received: 06 August 2021
- Accepted: 14 January 2022
- Published: 24 January 2022
- Issue Date: 10 March 2022

- DOI: <https://doi.org/10.1038/s41586-022-04432-7>

Share this article

Anyone you share the following link with will be able to read this content:

[Get shareable link](#)

Sorry, a shareable link is not currently available for this article.

[Copy to clipboard](#)

Provided by the Springer Nature SharedIt content-sharing initiative

Further reading

- [**EBV linked to multiple sclerosis**](#)
 - Andrea Du Toit
Nature Reviews Microbiology (2022)
 - Hartmut Wekerle
Nature (2022)
 - Yvonne Bordon
Nature Reviews Immunology (2022)
- [**Epstein–Barr virus sparks brain autoimmunity in multiple sclerosis**](#)
- [**Linking Epstein-Barr virus infection to multiple sclerosis**](#)

[**Epstein–Barr virus sparks brain autoimmunity in multiple sclerosis**](#)

- Hartmut Wekerle

News & Views 15 Feb 2022

Molecular mimicry in MS

- Laurie A. Dempsey

Research Highlight 02 Mar 2022

This article was downloaded by **calibre** from <https://www.nature.com/articles/s41586-022-04432-7>

| [Section menu](#) | [Main menu](#) |

- Article
- [Published: 23 February 2022](#)

A trispecific antibody targeting HER2 and T cells inhibits breast cancer growth via CD4 cells

- [Edward Seung](#)^{1,2} na1,
- [Zhen Xing](#)¹ na1,
- [Lan Wu](#)^{1,2},
- [Ercole Rao](#)³,
- [Virna Cortez-Retamozo](#)¹,
- [Beatriz Ospina](#)¹,
- [Liqing Chen](#)¹,
- [Christian Beil](#)³,
- [Zhili Song](#)¹,
- [Bailin Zhang](#)¹,
- [Mikhail Levit](#)¹,
- [Gejing Deng](#)¹,
- [Andrew Hebert](#)¹,
- [Patrick Kirby](#)¹ nAff5,
- [Aiqun Li](#)¹,
- [Emma-Jane Poulton](#)¹,
- [Rita Vicente](#)⁴,
- [Audrey Garrigou](#)⁴,
- [Peter Piepenhagen](#)¹,
- [Greg Ulinski](#)¹,
- [Michele Sanicola-Nadel](#)¹ nAff6,
- [Dinesh S. Bangari](#) ORCID: orcid.org/0000-0002-9909-1146¹,
- [Huawei Qiu](#)¹,

- [Lily Pao](#) [ORCID: orcid.org/0000-0002-7626-2782¹](#),
- [Dmitri Wiederschain¹](#) [nAff7](#),
- [Ronnie Wei^{1,2}](#),
- [Zhi-yong Yang](#) [ORCID: orcid.org/0000-0002-9938-5929^{1,2}](#) &
- [Gary J. Nabel](#) [ORCID: orcid.org/0000-0003-0619-4419^{1,2}](#)

[*Nature*](#) volume **603**, pages 328–334 (2022)

- 10k Accesses
- 123 Altmetric
- [Metrics details](#)

Subjects

- [Cancer](#)
- [Immunology](#)

Abstract

Effective antitumour immunity depends on the orchestration of potent T cell responses against malignancies¹. Regression of human cancers has been induced by immune checkpoint inhibitors, T cell engagers or chimeric antigen receptor T cell therapies^{2,3,4}. Although CD8 T cells function as key effectors of these responses, the role of CD4 T cells beyond their helper function has not been defined. Here we demonstrate that a trispecific antibody to HER2, CD3 and CD28 stimulates regression of breast cancers in a humanized mouse model through a mechanism involving CD4-dependent inhibition of tumour cell cycle progression. Although CD8 T cells directly mediated tumour lysis in vitro, CD4 T cells exerted antiproliferative effects by blocking cancer cell cycle progression at G1/S. Furthermore, when T cell subsets were adoptively transferred into a humanized breast cancer tumour mouse model, CD4 T cells alone inhibited HER2⁺ breast cancer growth in vivo. RNA microarray analysis revealed that CD4 T cells markedly decreased tumour cell cycle

progression and proliferation, and also increased pro-inflammatory signalling pathways. Collectively, the trispecific antibody to HER2 induced T cell-dependent tumour regression through direct antitumour and indirect pro-inflammatory/immune effects driven by CD4 T cells.

This is a preview of subscription content

Access options

Subscribe to Nature+

Get immediate online access to the entire Nature family of 50+ journals

\$29.99

monthly

[Subscribe](#)

Subscribe to Journal

Get full journal access for 1 year

\$199.00

only \$3.90 per issue

[Subscribe](#)

All prices are NET prices.

VAT will be added later in the checkout.

Tax calculation will be finalised during checkout.

Buy article

Get time limited or full article access on ReadCube.

\$32.00

[Buy](#)

All prices are NET prices.

Additional access options:

- [Log in](#)
- [Learn about institutional subscriptions](#)

Fig. 1: Contribution of different arms of the trispecific antibody to HER2 on immune activation in vitro.

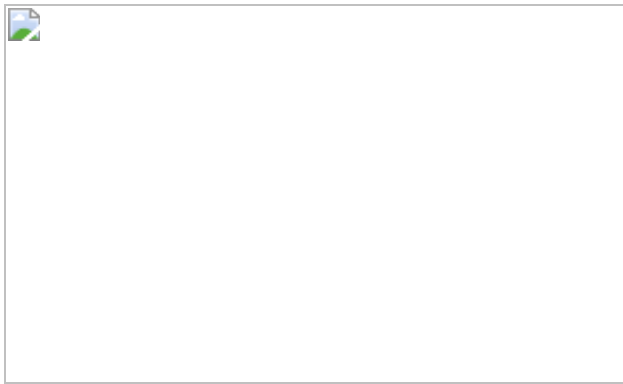


Fig. 2: Effect of the HER2 trispecific antibody on tumour growth in a humanized mouse model.

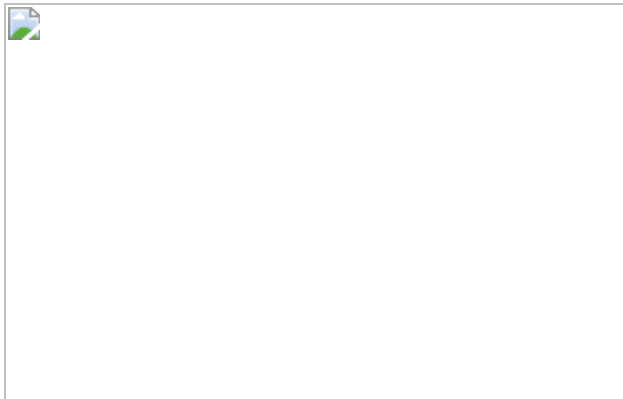


Fig. 3: The HER2 trispecific antibody-stimulated CD4⁺ T cell inhibited cell cycle progression and/or proliferation in HER2⁺ breast and gastric cancer cells.

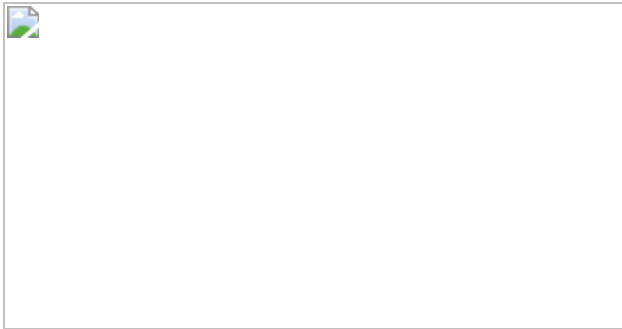


Fig. 4: HER2 trispecific antibody-stimulated CD4⁺ T cell inhibited cell cycle progression and/or proliferation and stimulated pro-inflammatory pathways in the breast cancer cell line HCC1954.

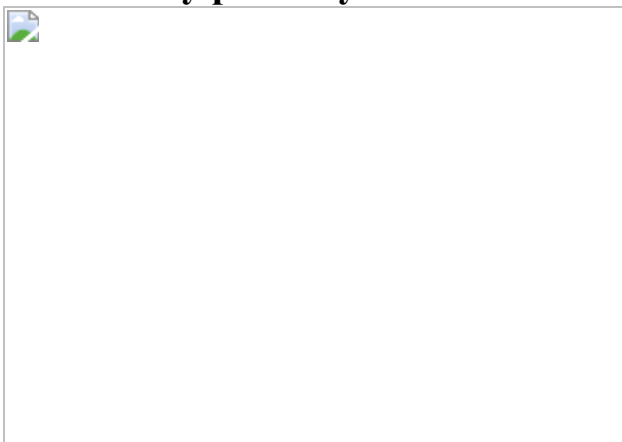


Fig. 5: Immune effects and cell binding of the HER2 trispecific antibody after dosing in NHPs.



Data availability

Source data used to generate graphs for Figs. 1, 2, 4 and 5, along with Extended Data Figs. 1, 2 and 4, are provided with this paper in spreadsheet format (in its Supplementary Information files). Further data that support the findings of this study are available from the corresponding authors on reasonable request. [Source data](#) are provided with this paper.

References

1. Waldman, A. D., Fritz, J. M. & Lenardo, M. J. A guide to cancer immunotherapy: from T cell basic science to clinical practice. *Nat. Rev. Immunol.* **20**, 651–668 (2020).
2. Goebeler, M. E. & Bargou, R. C. T cell-engaging therapies—BiTEs and beyond. *Nat. Rev. Clin. Oncol.* **17**, 418–434 (2020).
3. Porter, D. L., Levine, B. L., Kalos, M., Bagg, A. & June, C. H. Chimeric antigen receptor-modified T cells in chronic lymphoid leukemia. *N. Engl. J. Med.* **365**, 725–733 (2011).
4. Sharma, P. & Allison, J. P. The future of immune checkpoint therapy. *Science* **348**, 56–61 (2015).
5. Bhoj, V. G. et al. Persistence of long-lived plasma cells and humoral immunity in individuals responding to CD19-directed CAR T-cell therapy. *Blood* **128**, 360–370 (2016).
6. Leach, D. R., Krummel, M. F. & Allison, J. P. Enhancement of antitumor immunity by CTLA-4 blockade. *Science* **271**, 1734–1736 (1996).
7. Vesely, M. D., Kershaw, M. H., Schreiber, R. D. & Smyth, M. J. Natural innate and adaptive immunity to cancer. *Annu. Rev. Immunol.* **29**, 235–271 (2011).
8. Trabolsi, A., Arumov, A. & Schatz, J. H. T cell-activating bispecific antibodies in cancer therapy. *J. Immunol.* **203**, 585–592 (2019).

9. Wu, L. et al. Trispecific antibodies enhance the therapeutic efficacy of tumor-directed T cells through T cell receptor co-stimulation. *Nat. Cancer* **1**, 86–98 (2020).
10. Steinmetz, A. et al. CODV-Ig, a universal bispecific tetravalent and multifunctional immunoglobulin format for medical applications. *MAbs* **8**, 867–878 (2016).
11. Berchuck, A. et al. Overexpression of HER-2/neu is associated with poor survival in advanced epithelial ovarian cancer. *Cancer Res.* **50**, 4087–4091 (1990).
12. Burstein, H. J. The distinctive nature of HER2-positive breast cancers. *N. Engl. J. Med.* **353**, 1652–1654 (2005).
13. Gravalos, C. & Jimeno, A. HER2 in gastric cancer: a new prognostic factor and a novel therapeutic target. *Ann. Oncol.* **19**, 1523–1529 (2008).
14. Kim, E. K., Kim, K. A., Lee, C. Y. & Shim, H. S. The frequency and clinical impact of HER2 alterations in lung adenocarcinoma. *PLoS ONE* **12**, e0171280 (2017).
15. Pollock, N. I. & Grandis, J. R. HER2 as a therapeutic target in head and neck squamous cell carcinoma. *Clin. Cancer Res.* **21**, 526–533 (2015).
16. Santin, A. D. et al. Amplification of c-erbB2 oncogene: a major prognostic indicator in uterine serous papillary carcinoma. *Cancer* **104**, 1391–1397 (2005).
17. Siena, S. et al. Targeting the human epidermal growth factor receptor 2 (HER2) oncogene in colorectal cancer. *Ann. Oncol.* **29**, 1108–1119 (2018).
18. Slamon, D. J. et al. Human breast cancer: correlation of relapse and survival with amplification of the HER-2/neu oncogene. *Science* **235**, 177–182 (1987).

19. Yoon, H. H. et al. Association of HER2/ErbB2 expression and gene amplification with pathologic features and prognosis in esophageal adenocarcinomas. *Clin. Cancer Res.* **18**, 546–554 (2012).
20. Hicks, D. G. & Kulkarni, S. HER2⁺ breast cancer: review of biologic relevance and optimal use of diagnostic tools. *Am. J. Clin. Pathol.* **129**, 263–273 (2008).
21. Pohlmann, P. R., Mayer, I. A. & Mernaugh, R. Resistance to trastuzumab in breast cancer. *Clin. Cancer Res.* **15**, 7479–7491 (2009).
22. Shak, S. Overview of the trastuzumab (herceptin) anti-HER2 monoclonal antibody clinical program in HER2-overexpressing metastatic breast cancer. Herceptin Multinational Investigator Study Group. *Semin. Oncol.* **26**, 71–77 (1999).
23. Wang, J. & Xu, B. Targeted therapeutic options and future perspectives for HER2-positive breast cancer. *Signal Transduct. Target Ther.* **4**, 34 (2019).
24. Laux, I. et al. Response differences between human CD4(+) and CD8(+) T-cells during CD28 costimulation: implications for immune cell-based therapies and studies related to the expansion of double-positive T-cells during aging. *Clin. Immunol.* **96**, 187–197 (2000).
25. Brudno, J. N. & Kochenderfer, J. N. Toxicities of chimeric antigen receptor T cells: recognition and management. *Blood* **127**, 3321–3330 (2016).
26. Kroschinsky, F. et al. New drugs, new toxicities: severe side effects of modern targeted and immunotherapy of cancer and their management. *Crit. Care* **21**, 89 (2017).
27. Saber, H., Del Valle, P., Ricks, T. K. & Leighton, J. K. An FDA oncology analysis of CD3 bispecific constructs and first-in-human dose selection. *Regul. Toxicol. Pharmacol.* **90**, 144–152 (2017).

28. Baselga, J. et al. Phase II study of weekly intravenous trastuzumab (herceptin) in patients with HER2/neu-overexpressing metastatic breast cancer. *Semin. Oncol.* **26**, 78–83 (1999).
29. Zuch de Zafra, C. L. et al. Targeting multiple myeloma with AMG 424, a novel anti-CD38/CD3 bispecific T-cell-recruiting antibody optimized for cytotoxicity and cytokine release. *Clin. Cancer Res.* **25**, 3921–3933 (2019).
30. Harbeck, N. et al. HER2 dimerization inhibitor pertuzumab—mode of action and clinical data in breast cancer. *Breast Care (Basel)* **8**, 49–55 (2013).
31. Niculescu-Duvaz, I. Trastuzumab emtansine, an antibody-drug conjugate for the treatment of HER2⁺ metastatic breast cancer. *Curr. Opin. Mol. Ther.* **12**, 350–360 (2010).
32. Bang, Y. J. et al. First-in-human phase 1 study of margetuximab (MGAH22), an Fc-modified chimeric monoclonal antibody, in patients with HER2-positive advanced solid tumors. *Ann. Oncol.* **28**, 855–861 (2017).
33. Jones, K. L. & Buzdar, A. U. Evolving novel anti-HER2 strategies. *Lancet Oncol.* **10**, 1179–1187 (2009).
34. Mignot, F. et al. Concurrent administration of anti-HER2 therapy and radiotherapy: systematic review. *Radiother. Oncol.* **124**, 190–199 (2017).
35. Vu, T. & Claret, F. X. Trastuzumab: updated mechanisms of action and resistance in breast cancer. *Front. Oncol.* **2**, 62 (2012).
36. Buie, L. W., Pecoraro, J. J., Horvat, T. Z. & Daley, R. J. Blinatumomab: a first-in-class bispecific T-cell engager for precursor B-cell acute lymphoblastic leukemia. *Ann. Pharmacother.* **49**, 1057–1067 (2015).

37. Tran, B. et al. 609O Results from a phase I study of AMG 160, a half-life extended (HLE), PSMA-targeted, bispecific T-cell engager (BiTE®) immune therapy for metastatic castration-resistant prostate cancer (mCRPC). *Ann. Oncol.* **31**, s507 (2020).
38. Deegen, P. et al. The PSMA-targeting half-life extended BiTE therapy AMG 160 has potent antitumor activity in preclinical models of metastatic castration-resistant prostate cancer. *Clin. Cancer Res.* **27**, 2928–2937 (2021).
39. Raghu, G. et al. SAR156597 in idiopathic pulmonary fibrosis: a phase 2 placebo-controlled study (DRI11772). *Eur. Respir. J.* **52**, 1801130 (2018).
40. Merchant, A. M. et al. An efficient route to human bispecific IgG. *Nat. Biotechnol.* **16**, 677–681 (1998).
41. Xu, L. et al. Trispecific broadly neutralizing HIV antibodies mediate potent SHIV protection in macaques. *Science* **358**, 85–90 (2017).
42. Alegre, M. L. et al. A non-activating "humanized" anti-CD3 monoclonal antibody retains immunosuppressive properties in vivo. *Transplantation* **57**, 1537–1543 (1994).
43. Smith, K. B. & Ellis, S. A. Standardisation of a procedure for quantifying surface antigens by indirect immunofluorescence. *J. Immunol. Methods* **228**, 29–36 (1999).

Acknowledgements

We thank C. Lawendowski for excellent programme management; T. Schmidt, T. Bouquin, S. Rao, S. Sidhu, B. Thurberg, K. Klinger, J. Darbyshire, C. Dangler, Z. Jayyosi and C. J. Wei for organizational support; and J. Kingsbury, S. Kathuria, N. Maestrali, S. Somarriba, E. Deschamps, N. Couteault and L. Maton for technical support.

Author information

Author notes

1. Patrick Kirby

Present address: Dragonfly Therapeutics, Waltham, MA, USA

2. Michele Sanicola-Nadel

Present address: GSK, Waltham, MA, USA

3. Dmitri Wiederschain

Present address: Jounce Therapeutics, Cambridge, MA, USA

4. These authors contributed equally: Edward Seung, Zhen Xing

Affiliations

1. Sanofi R&D, North America, Cambridge, MA, USA

Edward Seung, Zhen Xing, Lan Wu, Virna Cortez-Retamozo, Beatriz Ospina, Liqing Chen, Zhili Song, Bailin Zhang, Mikhail Levit, Gejing Deng, Andrew Hebert, Patrick Kirby, Aiqun Li, Emma-Jane Poulton, Peter Piepenhagen, Greg Ulinski, Michele Sanicola-Nadel, Dinesh S. Bangari, Huawei Qiu, Lily Pao, Dmitri Wiederschain, Ronnie Wei, Zhi-yong Yang & Gary J. Nabel

2. ModeX Therapeutics, Natick, MA, USA

Edward Seung, Lan Wu, Ronnie Wei, Zhi-yong Yang & Gary J. Nabel

3. Sanofi R&D, Frankfurt, Frankfurt am Main, Germany

Ercole Rao & Christian Beil

4. Sanofi R&D, Montpellier, Montpellier, France

Rita Vicente & Audrey Garrigou

Contributions

Z.-y.Y., E.S., Z.X., E.R., R.W., V.C.-R., E.-J.P., P.K., R.V. and G.J.N. designed the research. Z.-y.Y., E.S., Z.X., E.R., R.V., V.C.-R., P.P., E.-J.P., P.K., C.B., B.Z. L.P., D.W. and G.J.N. led the research. E.S. and Z.X. designed and performed the experiments for the in vitro cellular assays. P.P. and G.U. designed and performed the imaging experiments. E.S., Z.-y.Y., V.C.-R., B.O., L.C. and D.S.B. designed and performed the mouse study experiments. B.Z., H.Q., M.L., G.D. and A.H. designed and performed the experiments to characterize antibodies. Z.S. performed the experiments to characterize tumour cell lines. E.S., P.K., A.L., E.-J.P., R.V. and A.G. designed, analysed or performed the NHP studies. Z.-y.Y., E.S., Z.X., L.W., V.C.-R., E.-J.P., R.V., A.L., M.S.-N., P.P. and G.J.N. analysed the data. Z.-y.Y., E.S., Z.X., R.W., V.C.-R., A.L., R.V. and G.J.N. wrote the paper. All authors reviewed and approved the final manuscript for submission and are accountable for the accuracy and integrity of the manuscript. The research conducted in this study by the authors has been used in the development of a therapeutic drug against tumours currently in a phase I clinical trial that started in August 2021 (ClinicalTrials.gov identifier [NCT05013554](#)).

Corresponding authors

Correspondence to [Lily Pao](#), [Zhi-yong Yang](#) or [Gary J. Nabel](#).

Ethics declarations

Competing interests

All authors are or were employees of Sanofi while engaged in this research project and may hold shares and/or stock options in the company. ModeX employees performed additional informatic evaluation of data, graphic illustration and writing at ModeX. Sanofi develops and manufactures cancer treatment medicines. ModeX is a private biotechnology company that develops multispecific antibodies for the treatment of cancers and viral diseases. G.J.N. formerly served as chief scientific officer of Sanofi. G.J.N., Z.-y.Y., E.R., R.W., E.S., L.W., Z.X., C.B. and H.Q. are listed on intellectual

properties developed and owned by Sanofi related to development of novel cancer treatments.

Peer review

Peer review information

Nature thanks the anonymous reviewers for their contribution to the peer review of this work. Peer reviewer reports are available.

Additional information

Publisher's note Springer Nature remains neutral with regard to jurisdictional claims in published maps and institutional affiliations.

Extended data figures and tables

[Extended Data Fig. 1 The effect of HER2 trispecific Ab on human T cell proliferation and cytotoxic granzyme expression in vitro.](#)

a, Surface expression of early T cell activation marker CD69 after one day stimulation by the HER2 trispecific Ab, the indicated single binding site inactivating mutants, or triple mutants, at 100 nM. The data are from a single experiment with PBMC from 3 donors. **b**, T cells were stimulated in the presence of the indicated mutants or wild type trispecific antibodies as described in Methods to determine the effects of CD28 co-stimulation on T cell proliferation in vitro. Lines in representative graph from one PBMC donor indicate fold change in cell numbers from Day 0 of viable T cells in vitro; 2 other PBMC donors demonstrated similar results. **c**, Stimulation of cytotoxic granzyme was measured in primary T cells in the presence of HCC1954 tumor cells and the trispecific Ab or indicated single mutant or triple mutant negative control (1 nM). Intracellular flow staining was used to determine percentage of CD8+ cells expressing Granzyme B. The representative graph is from a single experiment with one PBMC donor

performed in triplicate; a second experiment with same donor and two experiments with a second PBMC donor demonstrated similar results.

[Source data](#)

Extended Data Fig. 2 Cytolysis of BT20 and MDA-MB-468 breast tumor cell lines by T cells incubated with the HER2 trispecific Ab and mutants and correlation in target cell lysis with HER2 density on tumor cell lines.

a, Cytolysis of HER2-expressing breast cell line BT20, and HER2-negative breast cell line MDA-MB-468, were assessed with HER2 trispecific Ab in vitro using CD8+ as effector cells (E:T = 3:1). The crucial contribution of anti-HER2 arm of the trispecific Ab is demonstrated with the single binding site inactivating mutant. **b**, Correlation in target cell lysis with HER2 density on tumor cell lines. Additional breast tumor cell lines, along with gastric tumor cells lines, (HCC1954, MDAMB453, HCC1143, MDAMB231, OE.19, GSU, and MKN-45) were measured for HER2 surface protein expression using QIFI kit (Dako, Denmark) as described in Methods. Cytolysis of the tumor targets with HER2 trispecific Ab was assessed in vitro using CD8+ effector cells. The EC50 for target cytotoxicity was calculated for each tumor cell line (left) and the maximum percentage of dead target cells was also calculated for each tumor cell line (right).

[Source data](#)

Extended Data Fig. 3 HER2 trispecific Ab stimulated CD8+ T cell did not inhibit cell cycle progression/proliferation in multiple HER2 expressing cancer cell lines but upregulated proinflammatory pathways.

a, The antitumor effect of HER2 trispecific Ab against multiple tumor cell lines was evaluated with human CD8+ T cells as effector cells (E:T = 5:1). Breast cancer cell lines HCC1937, HCC70, BT549 and gastric cancer cell line OE19 were used as targets. After 1 day of incubation, the tumor cell lines did not exhibit cell cycle arrest at the G₁/S stage in cells that remained

alive based on flow cytometry. **b (left)**, Scatter plots of RNAs significantly upregulated (\geq 5-fold, red), or downregulated (\leq 5-fold, green), in HER2 trispecific Ab treated target cells compared to the control in presence of CD8+ effector cells. **b, (right)**, Enrichment analysis of gene sets in tumor cells after HER2 trispecific Ab treatment compared to control in the presence of CD8+ effector cells. Red bar = upregulation.

Extended Data Fig. 4 Inflammatory cytokines mediated T cell lysis of HER2+ tumor cells with the HER2 trispecific Ab.

Sorted CD4+ or CD8+ T cell subsets were obtained from ex vivo expanded human CD3+ T cells, as previously described, to be used as effectors against HER2+ breast cancer cell line (E:T = 3:1 (all subsets)) with HER2 Trispecific Ab. Neutralizing antibodies against TNF- α (5 μ g/mL, R&D systems), IFN- α (5 μ g/mL, PBL), or IFN- γ (5 μ g/mL, R&D systems) were added to tumor lysis assay against MDA-MB-453 tumor cells using CD4 or CD8 T cells as effectors (**a**). A representative graph is shown. The tumor lysis assay using neutralizing anti- TNF- α Ab was verified with CD4 T cells as effectors from different PBMC donor against HER2-expressing breast cancer cell lines MDA-MB-453 (**b, left**) or ZR-75-1 (**b, right**). The representative graphs are from two experiments using a single PBMC donor each.

[Source data](#)

Extended Data Fig. 5 Time lapse of Her2 Tri-specific antibody induced T-cell mediated killing of target HER2+ MDA-MB-453 breast cancer cells.

HER2+ MDA-MB-453 cells were labeled with CellVue Maroon dye (Invitrogen) and combined with PBMCs in 12-well plates. HER2 trispecific Ab was added at 1 μ g/ml concentration. Time lapse imaging was conducted for 24 h using a confocal microscope equipped with an environmental chamber which maintains cultures at 37 °C, 5% CO₂.

Extended Data Table 1 Characterization of HER2 trispecific Ab

Extended Data Table 2 Clinical observations and chemistry after single and multiple doses of trispecific Ab in NHPs

Extended Data Table 3 Serum pharmacokinetics after HER2 trispecific Ab treatment in NHPs

Supplementary information

[**Reporting Summary**](#)

[**Peer Review File**](#)

Source data

[**Source Data Fig. 1**](#)

[**Source Data Fig. 2**](#)

[**Source Data Fig. 4**](#)

[**Source Data Fig. 5**](#)

[**Source Data Extended Data Fig. 1**](#)

[**Source Data Extended Data Fig. 2**](#)

[**Source Data Extended Data Fig. 4**](#)

Rights and permissions

[**Reprints and Permissions**](#)

About this article

Cite this article

Seung, E., Xing, Z., Wu, L. *et al.* A trispecific antibody targeting HER2 and T cells inhibits breast cancer growth via CD4 cells. *Nature* **603**, 328–334 (2022). <https://doi.org/10.1038/s41586-022-04439-0>

- Received: 30 March 2021
- Accepted: 18 January 2022
- Published: 23 February 2022
- Issue Date: 10 March 2022
- DOI: <https://doi.org/10.1038/s41586-022-04439-0>

Share this article

Anyone you share the following link with will be able to read this content:

[Get shareable link](#)

Sorry, a shareable link is not currently available for this article.

[Copy to clipboard](#)

Provided by the Springer Nature SharedIt content-sharing initiative

This article was downloaded by **calibre** from <https://www.nature.com/articles/s41586-022-04439-0>

- Article
- [Published: 02 March 2022](#)

Silent mutations reveal therapeutic vulnerability in RAS Q61 cancers

- [Yoshihisa Kobayashi](#) ORCID: [orcid.org/0000-0003-2057-408X^{1,2,3}](https://orcid.org/0000-0003-2057-408X),
- [Chhayheng Chhoeu⁴](#),
- [Jiaqi Li¹](#),
- [Kristin S. Price](#) ORCID: [orcid.org/0000-0003-4300-6413⁵](https://orcid.org/0000-0003-4300-6413),
- [Lesli A. Kiedrowski⁵](#),
- [Jamie L. Hutchins⁵](#),
- [Aaron I. Hardin](#) ORCID: [orcid.org/0000-0003-1231-0658⁵](https://orcid.org/0000-0003-1231-0658),
- [Zihan Wei](#) ORCID: [orcid.org/0000-0001-9234-3497⁶](https://orcid.org/0000-0001-9234-3497),
- [Fangxin Hong^{6,7}](#),
- [Magda Bahcall^{1,2}](#),
- [Prafulla C. Gokhale](#) ORCID: [orcid.org/0000-0002-1974-5921^{4,8}](https://orcid.org/0000-0002-1974-5921) &
- [Pasi A. Jänne](#) ORCID: [orcid.org/0000-0002-7821-4928^{1,2,8,9}](https://orcid.org/0000-0002-7821-4928)

[Nature](#) volume 603, pages 335–342 (2022)

- 9285 Accesses
- 1 Citations
- 119 Altmetric
- [Metrics details](#)

Subjects

- [Cancer genetics](#)

- [RNA splicing](#)
- [Targeted therapies](#)

Abstract

RAS family members are the most frequently mutated oncogenes in human cancers. Although KRAS(G12C)-specific inhibitors show clinical activity in patients with cancer^{1,2,3}, there are no direct inhibitors of NRAS, HRAS or non-G12C KRAS variants. Here we uncover the requirement of the silent *KRAS*^{G60G} mutation for cells to produce a functional KRAS(Q61K). In the absence of this G60G mutation in *KRAS*^{Q61K}, a cryptic splice donor site is formed, promoting alternative splicing and premature protein termination. A G60G silent mutation eliminates the splice donor site, yielding a functional KRAS(Q61K) variant. We detected a concordance of *KRAS*^{Q61K} and a G60G/A59A silent mutation in three independent pan-cancer cohorts. The region around *RAS* Q61 is enriched in exonic splicing enhancer (ESE) motifs and we designed mutant-specific oligonucleotides to interfere with ESE-mediated splicing, rendering the RAS(Q61) protein non-functional in a mutant-selective manner. The induction of aberrant splicing by antisense oligonucleotides demonstrated therapeutic effects in vitro and in vivo. By studying the splicing necessary for a functional KRAS(Q61K), we uncover a mutant-selective treatment strategy for *RAS*^{Q61} cancer and expose a mutant-specific vulnerability, which could potentially be exploited for therapy in other genetic contexts.

This is a preview of subscription content

Access options

Subscribe to Nature+

Get immediate online access to the entire Nature family of 50+ journals

\$29.99

monthly

Subscribe

Subscribe to Journal

Get full journal access for 1 year

\$199.00

only \$3.90 per issue

Subscribe

All prices are NET prices.

VAT will be added later in the checkout.

Tax calculation will be finalised during checkout.

Buy article

Get time limited or full article access on ReadCube.

\$32.00

Buy

All prices are NET prices.

Additional access options:

- [Log in](#)
- [Learn about institutional subscriptions](#)

Fig. 1: KRAS^{Q61K} imparts resistance to osimertinib only in the presence of a concurrent KRAS^{G60G} silent mutation.

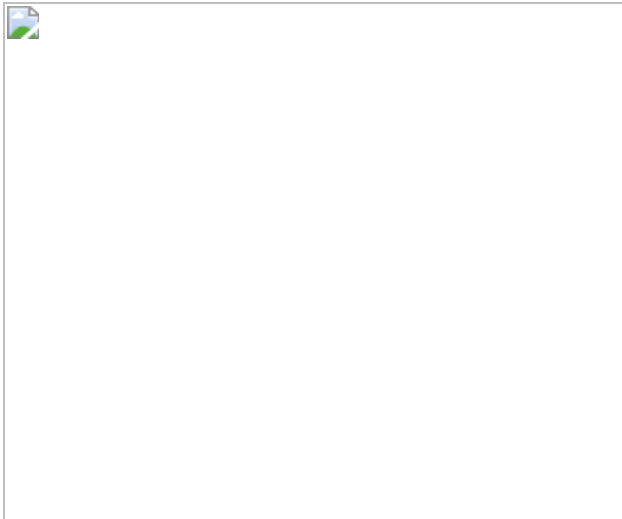


Fig. 2: $KRAS^{Q61K}$ co-occurs with the G60G silent mutation in three independent pan-cancer cohorts.

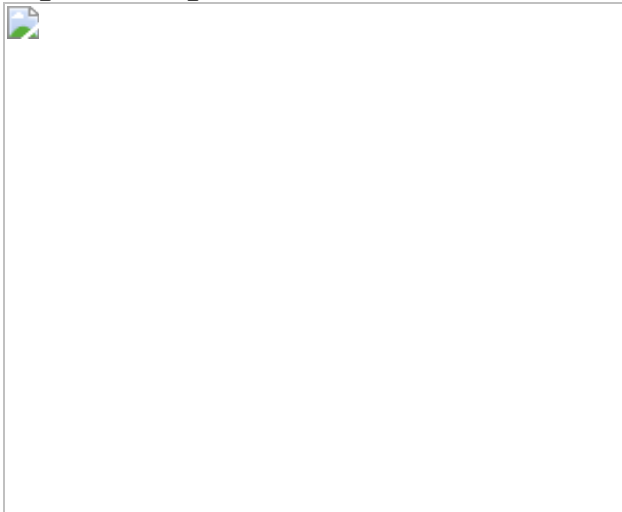


Fig. 3: Silent mutation in $KRAS^{G60G}$ is necessary for correct splicing of $KRAS^{Q61K}$.

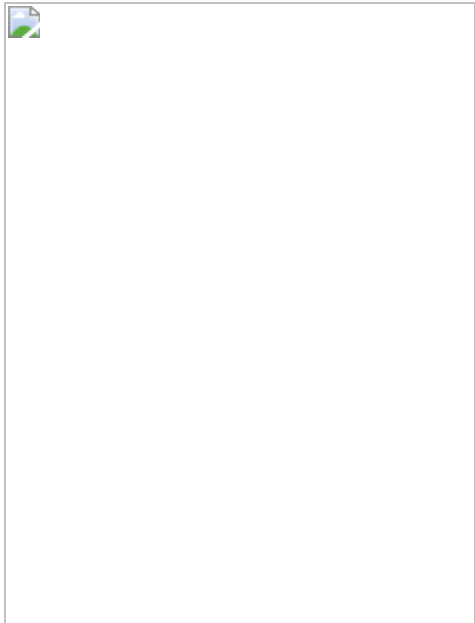
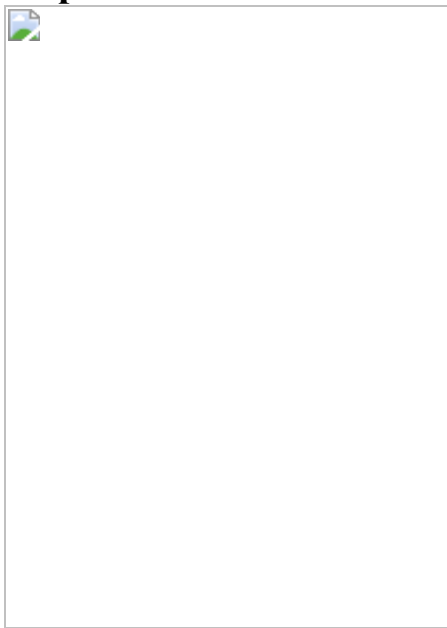


Fig. 4: Antisense oligonucleotide induces aberrant splicing and therapeutic effects in vitro and in vivo.



Data availability

FASTQ files from the Amplicon sequencing of *KRAS* are available from the Sequence Read Archive database under BioProject accession number [PRJNA789849](#). Non-synonymous and silent mutations in *KRAS*, *NRAS* and *HRAS* genes were obtained from TCGA pan-cancer cohort

(<https://portal.gdc.cancer.gov>). Data on exon 3 skipping at baseline in the TCGA cohort were obtained from TCGA SpliceSeq (<https://bioinformatics.mdanderson.org/public-software/tcgaspliceseq/>). Gene effect scores for dependency, evaluated by RNAi and CRISPR knockout, were obtained from Depmap (<https://depmap.org/portal/>). [Source data](#) are provided with this paper.

References

1. Ostrem, J. M., Peters, U., Sos, M. L., Wells, J. A. & Shokat, K. M. K-Ras(G12C) inhibitors allosterically control GTP affinity and effector interactions. *Nature* **503**, 548–551 (2013).
2. Canon, J. et al. The clinical KRAS(G12C) inhibitor AMG 510 drives anti-tumour immunity. *Nature* **575**, 217–223 (2019).
3. Hallin, J. et al. The KRAS(G12C) inhibitor MRTX849 provides insight toward therapeutic susceptibility of KRAS-mutant cancers in mouse models and patients. *Cancer Discov.* **10**, 54–71 (2020).
4. Middleton, G. et al. The National Lung Matrix Trial of personalized therapy in lung cancer. *Nature* **583**, 807–812 (2020).
5. Zehir, A. et al. Mutational landscape of metastatic cancer revealed from prospective clinical sequencing of 10,000 patients. *Nat. Med.* **23**, 703–713 (2017).
6. Ramalingam, S. S. et al. Overall survival with osimertinib in untreated, EGFR-mutated advanced NSCLC. *N. Engl. J. Med.* **382**, 41–50 (2020).
7. Diederichs, S. et al. The dark matter of the cancer genome: aberrations in regulatory elements, untranslated regions, splice sites, non-coding RNA and synonymous mutations. *EMBO Mol. Med.* **8**, 442–457 (2016).

8. Group, P. T. C. et al. Genomic basis for RNA alterations in cancer. *Nature* **578**, 129–136 (2020).
9. Consortium, A. P. G. AACR project GENIE: powering precision medicine through an international consortium. *Cancer Discov.* **7**, 818–831 (2017).
10. Janne, P. A. et al. Selumetinib plus docetaxel compared with docetaxel alone and progression-free survival in patients with KRAS-mutant advanced non-small cell lung cancer: the SELECT-1 randomized clinical trial. *JAMA* **317**, 1844–1853 (2017).
11. Kitai, H. et al. Epithelial-to-mesenchymal transition defines feedback activation of receptor tyrosine kinase signaling induced by MEK inhibition in KRAS-mutant lung cancer. *Cancer Discov.* **6**, 754–769 (2016).
12. Kruspig, B. et al. The ERBB network facilitates KRAS-driven lung tumorigenesis. *Sci. Transl. Med.* **10**, eaao2565 (2018).
13. Moll, H. P. et al. Afatinib restrains K-RAS-driven lung tumorigenesis. *Sci. Transl. Med.* **10**, eaao2301 (2018).
14. LaMarche, M. J. et al. Identification of TNO155, an allosteric SHP2 inhibitor for the treatment of cancer. *J. Med. Chem.* **63**, 13578–13594 (2020).
15. Hong, D. S. et al. KRAS(G12C) inhibition with sotorasib in advanced solid tumors. *N. Engl. J. Med.* **383**, 1207–1217 (2020).
16. Hunter, J. C. et al. Biochemical and structural analysis of common cancer-associated KRAS mutations. *Mol. Cancer Res.* **13**, 1325–1335 (2015).
17. Zhou, Z. W. et al. KRASQ61H preferentially signals through MAPK in a RAF dimer-dependent manner in non-small cell lung cancer. *Cancer Res.* **80**, 3719–3731 (2020).

18. Oxnard, G. R. et al. Assessment of resistance mechanisms and clinical implications in patients with EGFR T790M-positive lung cancer and acquired resistance to osimertinib. *JAMA Oncol.* **4**, 1527–1534 (2018).
19. Ramalingam, S. S. et al. Mechanisms of acquired resistance to first-line osimertinib: preliminary data from the phase III FLAURA study. *Ann. Oncol.* **29**, VIII740 (2018).
20. Reinert, T. et al. Analysis of plasma cell-free DNA by ultradeep sequencing in patients with stages I to III colorectal cancer. *JAMA Oncol.* **5**, 1124–1131 (2019).
21. Chabon, J. J. et al. Integrating genomic features for non-invasive early lung cancer detection. *Nature* **580**, 245–251 (2020).
22. Amendola, C. R. et al. KRAS4A directly regulates hexokinase 1. *Nature* **576**, 482–486 (2019).
23. Cartegni, L., Chew, S. L. & Krainer, A. R. Listening to silence and understanding nonsense: exonic mutations that affect splicing. *Nat. Rev. Genet.* **3**, 285–298 (2002).
24. Desmet, F. O. et al. Human Splicing Finder: an online bioinformatics tool to predict splicing signals. *Nucleic Acids Res.* **37**, e67 (2009).
25. McVety, S., Li, L., Gordon, P. H., Chong, G. & Foulkes, W. D. Disruption of an exon splicing enhancer in exon 3 of MLH1 is the cause of HNPCC in a Quebec family. *J. Med. Genet.* **43**, 153–156 (2006).
26. Khvorova, A. & Watts, J. K. The chemical evolution of oligonucleotide therapies of clinical utility. *Nat. Biotechnol.* **35**, 238–248 (2017).
27. Kim, J. et al. Patient-customized oligonucleotide therapy for a rare genetic disease. *N. Engl. J. Med.* **381**, 1644–1652 (2019).

28. Janes, M. R. et al. Targeting KRAS mutant cancers with a covalent G12C-specific inhibitor. *Cell* **172**, 578–589.e517 (2018).
29. Brant, R. et al. Clinically viable gene expression assays with potential for predicting benefit from MEK inhibitors. *Clin. Cancer Res.* **23**, 1471–1480 (2017).
30. Chang, M. T. et al. Identifying recurrent mutations in cancer reveals widespread lineage diversity and mutational specificity. *Nat. Biotechnol.* **34**, 155–163 (2016).
31. Zammarchi, F. et al. Antitumorigenic potential of STAT3 alternative splicing modulation. *Proc. Natl Acad. Sci. USA* **108**, 17779–17784 (2011).
32. Ross, S. J. et al. Targeting *KRAS*-dependent tumors with AZD4785, a high-affinity therapeutic antisense oligonucleotide inhibitor of *KRAS*. *Sci. Transl. Med.* **9**, eaal5253 (2017).
33. Amodio, V. et al. EGFR blockade reverts resistance to KRAS^{G12C} inhibition in colorectal cancer. *Cancer Discov.* **10**, 1129–1139 (2020).
34. Klein, A. F. et al. Peptide-conjugated oligonucleotides evoke long-lasting myotonic dystrophy correction in patient-derived cells and mice. *J. Clin. Invest.* **129**, 4739–4744 (2019).
35. Boisguerin, P. et al. Delivery of therapeutic oligonucleotides with cell penetrating peptides. *Adv. Drug Deliv. Rev.* **87**, 52–67 (2015).
36. Imbert, M., Dias-Florencio, G. & Goyenvalle, A. Viral vector-mediated antisense therapy for genetic diseases. *Genes* **8**, 51 (2017).
37. Sharma, Y. et al. A pan-cancer analysis of synonymous mutations. *Nat. Commun.* **10**, 2569 (2019).
38. Cartegni, L., Wang, J., Zhu, Z., Zhang, M. Q. & Krainer, A. R. ESEfinder: A web resource to identify exonic splicing enhancers. *Nucleic Acids Res.* **31**, 3568–3571 (2003).

39. Smith, P. J. et al. An increased specificity score matrix for the prediction of SF2/ASF-specific exonic splicing enhancers. *Hum. Mol. Genet.* **15**, 2490–2508 (2006).
40. Fairbrother, W. G. et al. RESCUE-ESE identifies candidate exonic splicing enhancers in vertebrate exons. *Nucleic Acids Res.* **32**, W187–W190 (2004).
41. Zhang, X. H. & Chasin, L. A. Computational definition of sequence motifs governing constitutive exon splicing. *Genes Dev.* **18**, 1241–1250 (2004).
42. Hori, S.-i et al. Ca²⁺ enrichment in culture medium potentiates effect of oligonucleotides. *Nucleic Acids Res.* **43**, e128 (2015).
43. Garcia, E. P. et al. Validation of OncoPanel: a targeted next-generation sequencing assay for the detection of somatic variants in cancer. *Arch. Pathol. Lab. Med.* **141**, 751–758 (2017).
44. Odegaard, J. I. et al. Validation of a plasma-based comprehensive cancer genotyping assay utilizing orthogonal tissue- and plasma-based methodologies. *Clin. Cancer Res.* **24**, 3539–3549 (2018).

Acknowledgements

Y.K. is supported in part by JSPS Overseas Research Fellowships, Uehara Memorial Foundation, SGH Foundation and Suzuki Memorial Foundation. P.A.J. is supported in part by the Cammarata Family Foundation Research Fund, the American Cancer Society Clinical Research Professor Grant (CRP-17-111-01-CDD), the Mark Foundation for Cancer Research (grant no. 19-029 MIA), the Mock Family Fund for Lung Cancer Research and the Goldstein Family Research Fund. We thank S. Obika and T. Nakayama for advice on antisense oligonucleotides; D. A. Barbie for helpful discussion; and E. F. Cohen for visualizing fastq data on *KRAS* transcript reads in IVG software.

Author information

Affiliations

1. Department of Medical Oncology, Dana-Farber Cancer Institute, Boston, MA, USA
Yoshihisa Kobayashi, Jiaqi Li, Magda Bahcall & Pasi A. Jänne
2. Department of Medicine, Harvard Medical School, Boston, MA, USA
Yoshihisa Kobayashi, Magda Bahcall & Pasi A. Jänne
3. Division of Molecular Pathology, National Cancer Center Research Institute, Tokyo, Japan
Yoshihisa Kobayashi
4. Experimental Therapeutics Core, Dana-Farber Cancer Institute, Boston, MA, USA
Chhayheng Chhoeu & Prafulla C. Gokhale
5. Department of Medical Affairs, Guardant Health, Redwood City, CA, USA
Kristin S. Price, Lesli A. Kiedrowski, Jamie L. Hutchins & Aaron I. Hardin
6. Department of Data Science, Dana-Farber Cancer Institute, Boston, MA, USA
Zihan Wei & Fangxin Hong
7. Harvard T. H. Chan School of Public Health, Boston, MA, USA
Fangxin Hong
8. Belfer Center for Applied Cancer Science, Dana-Farber Cancer Institute, Boston, MA, USA

Prafulla C. Gokhale & Pasi A. Jänne

9. Lowe Center for Thoracic Oncology, Dana-Farber Cancer Institute,
Boston, MA, USA

Pasi A. Jänne

Contributions

Y.K. conceptualized the study, collected data from TCGA and DFCI cohorts, designed antisense oligonucleotides, developed and executed in vitro experiments and wrote the paper. C.C. executed in vivo studies. J.L. executed in vitro experiments. K.S.P., L.A.K., J.L.H. and A.I.H. collected data from the Guardant Health cohort. Z.W. and F.H. performed statistical analyses. M.B. executed in vitro experiments, interpreted data, and wrote the paper. P.C.G. supervised and analysed in vivo studies. P.A.J. conducted and supervised all experiments, interpreted data and wrote the paper. All authors reviewed and commented on the paper.

Corresponding authors

Correspondence to [Yoshihisa Kobayashi](#) or [Pasi A. Jänne](#).

Ethics declarations

Competing interests

P.A.J. reports consulting fees from AstraZeneca, Boehringer-Ingelheim, Pfizer, Roche/Genentech, Takeda Oncology, ACEA Biosciences, Eli Lilly and Company, Araxes Pharma, Ignyta, Mirati Therapeutics, Novartis, Loxo Oncology, Daiichi Sankyo, Sanofi Oncology, Voronoi, SFJ Pharmaceuticals, Silicon Therapeutics, Nuvalent, Esai, Bayer, Biocartis, Allorion Therapeutics, Accutar Biotech and AbbVie; receiving post-marketing royalties from DFCI owned intellectual property on EGFR mutations licensed to Lab Corp; sponsored research agreements with AstraZeneca, Daichi-Sankyo, PUMA, Boehringer Ingelheim, Eli Lilly and

Company, Revolution Medicines and Astellas Pharmaceuticals; and stock ownership in Loxo Oncology and Gatekeeper Pharmaceuticals. K.S.P., L.A.K., J.L.H. and A.I.H. are employees and stockholders of Guardant Health. P.A.J. and Y.K. are inventors on a patent on the therapeutic use of mutant specific antisense oligonucleotides.

Peer review

Peer review information

Nature thanks the anonymous reviewers for their contribution to the peer review of this work.

Additional information

Publisher's note Springer Nature remains neutral with regard to jurisdictional claims in published maps and institutional affiliations.

Extended data figures and tables

Extended Data Fig. 1 CRISPR-Cas9 modified *EGFR* mutant PC-9 cells for evaluating oncogenicity of *KRAS* or *BRAF* mutations.

a, A schema of selection with EGFR inhibitor osimertinib. Majority of parental *EGFR*-mutant PC-9 cells are sensitive to osimertinib with only a small fraction exhibiting intrinsic resistance. In bulk CRISPR-Cas9 modified PC-9 cells, osimertinib treatment can lead to an increase in the fraction of cells harboring a resistance mutation such as *KRAS* G12C. **b**, Cell viability assay of parental and CRISPR-Cas9 modified PC-9 cells after 72 h of osimertinib treatment. Each clone has heterozygous *KRAS* mutations: GQ60GK c.180_181delinsCA plus Q61K, GQ60GK c.180_181delinsGA plus frameshift, and Q61K plus frameshift ($n = 3$ biological replicates, mean \pm s.d.). **c**, Knockdown of *KRAS* or *BRAF* in

CRISPR-Cas9-modified PC-9 clones following 48 h of *KRAS* or *BRAF* specific siRNA treatment are shown by western blot analyses.

Extended Data Fig. 2 Alternative splicing of KRAS in CRISPR-Cas9 modified PC-9 cells.

a, Images of *KRAS*-specific PCR amplicons of cDNA, generated from CRISPR-Cas9 modified PC-9 clones expressing different *KRAS* mutations in the presence or absence of osimertinib given the influence of upstream EGFR signals. Heterozygosity or homozygosity of *KRAS* mutants is shown for each clone. M: 100 bp-marker, m: mutant, wt: wild-type, fs: frameshift. **b**, Images of *KRAS*-specific PCR amplicons of cDNA, generated from additional CRISPR-Cas9 modified PC-9 clones expressing different *KRAS* mutations. **c**, Images of *KRAS*-specific PCR amplicons of cDNA, generated from *KRAS* mutant cell lines and CRISPR-Cas9 modified PC-9 clones expressing different *KRAS* mutations.

Extended Data Fig. 3 A strategy to convert the original KRAS GQ60GK into the non-functional Q61K by editing silent mutations using CRISPR-Cas9.

a, A schema of the proposed alternative treatment strategy using CRISPR-Cas9 editing with a mutant-specific sgRNA substituting the c.180 silent mutation with a cryptic splice donor nucleotide in order to promote exonic skipping leading to a premature STOP codon **b**, Allele frequencies of mutations, evaluated by next generation sequencing using DNA derived from bulk *KRAS* GQ60GK-mutant Calu6 and SNU668 cell lines, 48 h after CRISPR-Cas9 editing with indicated donor templates ($n = 1$). Allele frequency of original *KRAS* GQ60GK decreased by CRISPR editing with GQ60GK-specific sgRNA and allele frequency of non-functional Q61K increased only in the presence of donor template designed for Q61K. **c**, Relative expression of indicated *KRAS* isoforms, evaluated by qPCR in *KRAS* GQ60GK-mutant Calu6 and SNU668 cell lines, 48 h after CRISPR-Cas9 editing with indicated donor templates. Expression data are shown as relative to cell lines using Q61K template ($n = 3$ biological replicates, mean \pm s.d.). Although it is difficult to capture clones successfully converted to

non-functional Q61K due to their inability to grow, increased expression level of the KRAS isoform skipping 112 bp was confirmed in the remaining cells 2 days after CRISPR-editing.

Extended Data Fig. 4 Designing mutant-selective antisense oligos.

a, Structures of DNA, antisense oligo nucleotides with phosphorothioate (PS) + 2'-O-Methoxyethyl (2' MOE) modifications, and morpholino. In PS+2' MOE, a non-bridging oxygen is replaced by a sulfur atom in the phosphate backbone, and 2' position of the sugar moiety is modified. In morpholino, the sugar moiety is replaced with methylenemorpholine rings, and the anionic phosphates are replaced with non-ionic phosphorodiamidate linkages. **b**, Schema depicting the design of the *KRAS* GQ60GK c.180_181delinsCA, *NRAS* Q61K, and *HRAS* Q61L selective antisense oligo. The motifs for binding exonic splicing enhancers simulated using the Human Splicing Finder (top) and ESE finder (bottom) are shown. Matrices for SR proteins including SRSF1 (SF2/ASF and IgM-BRCA1), SRSF2 (SC35), SRSF5 (SRp40), and SRSF6 (SRp55) are shown.

Extended Data Fig. 5 Mutant selective inhibition of RAS using morpholino.

Raw NGS reads showing *KRAS* Q61L transcript were visualized using IGV 2.8.0 software.

Extended Data Fig. 6 *In vitro* sensitivity to MEK inhibitor and morpholino oligos in *RAS* mutant cells.

a, Cell viability assays of suspension cells after 8 days of 10 µM morpholino treatment were performed on ultra-low attachment plates (n = 6 biological replicates, mean ± s.d., ANOVA, followed by Dunnett's post-hoc test comparing to cells treated with DMSO, **p < 0.01). **b**, Cell viability assay of a panel of mutant *RAS* cell lines after 72 h of trametinib treatment in 2D adherent or 3D suspension culture (n = 3 biological replicates, mean ± s.d.). **c**, The correlation of growth inhibition by 10 nM trametinib in 2D or

3D culture and morpholino antisense oligo nucleotide in 17 *RAS* Q61X cell lines. **d**, Western blot analyses of signaling in *KRAS* wild-type cell lines were performed after 72 h treatment with 10nM trametinib, 10 μ M morpholino or respective controls. **e**, Relative expression of *ERK* signature genes, evaluated by qPCR in Calu6 and H650 cell lines treated with mutant-selective morpholino for 48 h. Expression data are normalized to readout of a control morpholino treatment. GUSB was used as an internal control. n = 3 biological replicates, mean \pm s.d., t test, **p < 0.01. **f**, Cell viability assays in suspension cells after 8 days of 50 nM afatinib, 10 μ g/ml cetuximub, and 10 μ M morpholino treatment were performed with the same method as **a** (n = 6 biological replicates, mean \pm s.d., ANOVA, followed by Dunnett's post-hoc test comparing to cells treated with DMSO, **p < 0.01). **g**, Western blot analyses of signaling in *NRAS* and *HRAS* mutant cell lines were performed after 72 h of treatment with 10 nM trametinib, 10 μ M morpholino, or DMSO.

Extended Data Fig. 7 Pre-treatment strategy using vivo-morpholino *in vitro* and *in vivo* H650 models.

a, Morpholino oligo pre-treatment strategy. H650 cells were pre-treated with 10 μ M control vivo-morpholino and target vivo-morpholino for 1 to 4 days as 3D suspension cells. After drug washout, cells were cultured in growth media and cell viability was evaluated on day 8 *in vitro*. Luciferase-expressing H650 cells were used for *in vivo* experiments. After pre-treatment with 10 μ M vivoMor-CTRL and target vivo-morpholino for 1 to 2 days as 3D suspension cells, drugs were washed out and cells were subcutaneously implanted into mice. *In vivo* imaging was performed twice a week. **b**, *In vitro* cell viability assays of H650 cells pre-treated with 10 μ M vivoMor-CTRL or vivoMor-4 for 1 to 4 days (n = 6 biological replicates, mean \pm s.d., t test, **p < 0.01). **c**, Volume change of pre-treated H650 xenograft tumors. H650 cells were pre-treated with vivoMor-CTRL or vivoMor-4 *in vitro* for 1 or 2 days prior to injection into nude mice (n = 10 per each group, mean \pm s.e.m., t-test and linear mixed growth models at day 22, **p < 0.01).

[Source data](#)

Extended Data Fig. 8 Intra-tumoral injection of vivo-morpholino in H650 xenograft models.

a, Images of KRAS-specific PCR amplicons generated from the cDNA of H650 xenograft tumors that were treated with daily intra-tumoral injection of morpholino for 7 days. Fraction of exon 3 skipping is defined as the band intensities of “skipped/(skipped + full-length)” as measured by ImageJ ($n = 1$). M: 100 bp-marker. **b**, Fractions of exon 3 skipping in samples shown in **(a)** were compared using t test, $**p < 0.01$, $n = 2–6$ mice in each group, box plots show minimum, lower quartile, median, upper quartile, and maximum. **c**, Relative expression of KRAS exon 3 skipping, evaluated by qPCR in tumor samples corresponding to **(a)** ($n = 3$ biological replicates, mean \pm s.e.m.). **d**, Body weight change of mice with H650 xenograft tumors treated with morpholino over time ($n = 10$ per each group, mean \pm s.e.m.).

[Source data](#)

Extended Data Fig. 9 Pre-treatment strategy and intra-tumoral injection of vivo-morpholino in Calu6 models.

a, *In vitro* cell viability assays of Calu6 cells pre-treated with 10 μ M vivoMor-CTRL or vivoMor-1 for 1 to 4 days ($n = 6$ biological replicates, mean \pm s.d., t test, $**p < 0.01$). **b**, Volume change of pre-treated Calu6 xenograft tumors. Calu6 cells were pre-treated with vivoMor-CTRL or vivoMor-1 *in vitro* for 24 h prior to injection into nude mice ($n = 10$ per each group, mean \pm s.e.m., t-test and linear mixed growth models, $*p < 0.05$, $**p < 0.01$). **c**, *In vivo* efficacy of Calu6 xenograft tumors treated with daily intra-tumoral injection of morpholino ($n = 10$ per each group, mean \pm s.e.m., t-test and linear mixed growth models, $**p < 0.01$). **d**, Body weight change of mice with Calu6 xenograft tumors treated with morpholino over time ($n = 10$ per each group, mean \pm s.e.m.).

[Source data](#)

Extended Data Fig. 10 Mutant selective inhibition of KRAS using PS+2'MOE antisense oligos.

a, Schema depicting the design of the KRAS GQ60GK c.180_181delinsCA selective antisense oligo by screening. **b**, Images of KRAS-specific PCR amplicons generated from the cDNA of cells treated with 6 kinds of PS+2' MOE antisense oligos for 48 h. Exon 3 skipping fraction is defined as the band intensities of “skipped/(skipped + full-length)” transcript as quantified by ImageJ. M: 100 bp-marker. n = 2 biological replicates, mean ± s.e.m. **c**, Images of KRAS-specific PCR amplicons in indicated cell lines with same method as b (n = 2 biological replicates, mean ± s.e.m.). **d**, Transcript reads of KRAS GQ60GK or Q61L versus wild-type in the intact full-length KRAS amplicon derived from mRNA of Calu6 and SW948 cells treated with PS+2' MOE antisense oligos (n = 1). **e**, Western blot analyses of signaling in KRAS mutant and wild-type cell lines were performed after 6 days of 0.5 μ M PS+2' MOE antisense oligos. **f**, Cell viability assays in suspension cells after 8 days of 0.5 μ M PS+2' MOE antisense oligos treatment were performed (n = 6 biological replicates, mean ± s.d., t test, **p < 0.01).

Supplementary information

Supplementary Information

This file contains Supplementary Figs. 1 and 2.

Reporting Summary

Supplementary Tables

This file contains Supplementary Tables 1–10

Source data

Source Data Fig. 4

[**Source Data Extended Data Fig. 7**](#)

[**Source Data Extended Data Fig. 8**](#)

[**Source Data Extended Data Fig. 9**](#)

Rights and permissions

[Reprints and Permissions](#)

About this article

Cite this article

Kobayashi, Y., Chhoeu, C., Li, J. *et al.* Silent mutations reveal therapeutic vulnerability in RAS Q61 cancers. *Nature* **603**, 335–342 (2022).
<https://doi.org/10.1038/s41586-022-04451-4>

- Received: 24 November 2020
- Accepted: 20 January 2022
- Published: 02 March 2022
- Issue Date: 10 March 2022
- DOI: <https://doi.org/10.1038/s41586-022-04451-4>

Share this article

Anyone you share the following link with will be able to read this content:

[Get shareable link](#)

Sorry, a shareable link is not currently available for this article.

[Copy to clipboard](#)

Provided by the Springer Nature SharedIt content-sharing initiative

This article was downloaded by **calibre** from <https://www.nature.com/articles/s41586-022-04451-4>

| [Section menu](#) | [Main menu](#) |

- Article
- Open Access
- [Published: 02 March 2022](#)

Structural basis for mismatch surveillance by CRISPR–Cas9

- [Jack P. K. Bravo](#)¹ ✉nal,
- [Mu-Sen Liu](#) ORCID: orcid.org/0000-0002-3220-9330¹ ✉nal,
- [Grace N. Hibshman](#)^{1,2},
- [Tyler L. Dangerfield](#)^{1,2},
- [Kyungseok Jung](#)¹,
- [Ryan S. McCool](#) ORCID: orcid.org/0000-0001-8833-8847^{1,2},
- [Kenneth A. Johnson](#) ORCID: orcid.org/0000-0002-6575-2823^{1,2} &
- [David W. Taylor](#) ORCID: orcid.org/0000-0002-6198-1194^{1,2,3,4}

Nature volume 603, pages 343–347 (2022)

- 92k Accesses
- 285 Altmetric
- [Metrics details](#)

Subjects

- [Cryoelectron microscopy](#)
- [DNA metabolism](#)
- [Enzyme mechanisms](#)
- [Genetic engineering](#)

Abstract

CRISPR–Cas9 as a programmable genome editing tool is hindered by off-target DNA cleavage^{1,2,3,4}, and the underlying mechanisms by which Cas9 recognizes mismatches are poorly understood^{5,6,7}. Although Cas9 variants with greater discrimination against mismatches have been designed^{8,9,10}, these suffer from substantially reduced rates of

on-target DNA cleavage^{5,11}. Here we used kinetics-guided cryo-electron microscopy to determine the structure of Cas9 at different stages of mismatch cleavage. We observed a distinct, linear conformation of the guide RNA–DNA duplex formed in the presence of mismatches, which prevents Cas9 activation. Although the canonical kinked guide RNA–DNA duplex conformation facilitates DNA cleavage, we observe that substrates that contain mismatches distal to the protospacer adjacent motif are stabilized by reorganization of a loop in the RuvC domain. Mutagenesis of mismatch-stabilizing residues reduces off-target DNA cleavage but maintains rapid on-target DNA cleavage. By targeting regions that are exclusively involved in mismatch tolerance, we provide a proof of concept for the design of next-generation high-fidelity Cas9 variants.

[Download PDF](#)

Main

For therapeutic applications of CRISPR–Cas9, off-target DNA cleavage must be minimized^{1,2,3}. Although a variety of high-fidelity Cas9 variants with improved mismatch discrimination have been developed^{7,9}, their enhanced specificity comes at the cost of severely reduced rates of on-target DNA cleavage^{5,11}. Mismatches induce alternative Cas9 conformations^{12,13}; however, the structures used to guide rational redesign of such variants were bound to on-target DNA and in inactive conformations^{14,15}. To understand the molecular mechanisms that govern off-target recognition, here we used kinetic analysis to guide sample preparation for cryo-electron microscopy (cryo-EM) and obtained structural snapshots of Cas9 pre-cleavage activation intermediates in the presence of various guide RNA–DNA target strand (gRNA–TS) mismatches.

Kinetics of Cas9 on mismatched DNA

We measured the rates of target strand cleavage by Cas9 in the presence of contiguous triple nucleotide mismatches at different positions along the gRNA–TS duplex (Extended Data Fig. 1a, Extended Data Table 1). Compared to rapid on-target cleavage (around 1.0 s^{-1}) the well-characterized protospacer adjacent motif (PAM)-distal 18–20 MM^{5,9,12,13} (three mismatches 18–20 bp distal from the PAM) caused a reduction in rate of around 40-fold. Other mismatches (6–8 MM, 9–11 MM and 15–17 MM) resulted in a greater-than-2,000-fold reduction in cleavage rates, with only 20% of the DNA cleaved after 2 h of incubation (Extended Data Fig. 1b).

Notably, the 12–14 MM allowed Cas9 activation but with rates around 10-fold slower than those of the 18–20 MM. Although Cas9 cleavage is markedly slower for both 12–

14 MM-and 18–20 MM-containing DNA than for on-target DNA, more than 80% of either substrate was cleaved within an hour of incubation with Cas9. This time frame for off-target cleavage poses problems for genome-editing applications, which typically occur on the time scale of days to weeks¹⁶.

Structures of Cas9 with mismatched DNA

To understand the structural basis for Cas9 activation of mismatched DNA, we vitrified Cas9 with 12–14 MM DNA after a 5-min reaction, in which only around 10% of DNA was cleaved (Extended Data Table 2). We determined a cryo-EM structure at a global resolution of 3.6 Å (Fig. 1a, Extended Data Fig. 2, Extended Data Table 3). The target-strand-cleaving HNH endonuclease domain was not observed, indicating conformational heterogeneity before activation^{17,18}. Of note, the distal end of the gRNA–TS duplex was in a linear conformation relative to the PAM-proximal DNA–DNA duplex—a state that differs from previously determined on-target DNA-bound Cas9 structures that depict a kinked duplex (around 70°)^{14,18}, although this state is reminiscent of early R-loop formation intermediates¹⁹.

Fig. 1: Mismatch-induced Cas9 conformational intermediates.

 **figure 1**

a, Cryo-EM reconstructions of Cas9 in complex with various partially mismatched DNA substrates, determined at nominal resolutions ranging from 2.8 to 3.6 Å. Cryo-EM structures are coloured according to the domain map for Cas9. Nucleotides are coloured: target strand (TS), green; NTS, pink; and gRNA, red. The fraction of target strand DNA cleaved by Cas9 containing contiguous triple mismatches at the position and time point used for structural determination is shown above each structure. **b**, Domain organization of SpCas9. CTD, C-terminal domain. **c**, Models of Cas9 in complex with mismatched DNA substrates shown as isosurface representations. The angle between PAM-proximal and PAM-distal duplexes (θ) is shown. θ is equivalent to around 25° for all linear conformations observed.

We then vitrified samples of Cas9 with 12–14 MM DNA after a 1-h incubation in which around 80% of the DNA was cleaved (Fig. 1b). Two distinct conformations were observed: a linear duplex conformation consistent with the 5-min structure of 12–14 MM and the kinked duplex conformation described above (Fig. 1a,c). The Cas9 conformations in the two 12–14 MM structures are identical (Fig. 2), but the PAM-distal gRNA–TS duplex end was shifted by around 30 Å and stably docked with REC3 (Fig. 2c). We propose that the linear duplex conformation corresponds to an early intermediate of Cas9, before HNH rearrangement and docking to cleave the DNA^{9,18}. This is supported by recent structural analyses of catalytically dead Cas9 in complex with various R-loop formation intermediates, several of which exhibit linear gRNA–TS duplex conformations that are similar to our linear duplex structures²⁰.

Fig. 2: Positions 12–14 of the gRNA–TS duplex occupy a blind spot for REC3 mismatch detection.

 figure 2

a, b, Structures of 12–14 MM at 5 min (a) and 1 h (b) in linear and kinked conformations, respectively. The position of the 12–14 MM is shown as light green and light pink for the gRNA and the target strand, respectively. Models are shown as isosurface representations. **c,** Conformational change of the PAM-distal gRNA–TS duplex. The Cas9 protein structure is largely unchanged (root-mean-square deviation (RMSD) of less than 2 Å for equivalent C-alpha atoms), but the PAM-distal gRNA–TS duplex end undergoes a 30 Å conformational change, docking with REC3. **d,** Close-up

view of positions 12–14, showing that because of the phase of the gRNA–TS duplex, REC3 makes no contacts with these base pairs. **e**, Schematic of interactions between REC3 and positions 9–17 of the gRNA–TS duplex. No interactions occur between Cas9 REC3 and positions 12–14 MM. Position 1 of the duplex is the first base of the target strand that hybridizes with the gRNA spacer.

Notably, positions 12–14 of the gRNA–TS make no direct contacts with the REC3 domain of Cas9 (Fig. 2). Although positions 9–11 and 15–17 make considerable contacts with REC3, the alignment of the gRNA–TS duplex leaves positions 12–14 without any engagement with this domain (Fig. 2d,e). Because REC3 has a critical role in sensing PAM-distal mismatches⁹, the 12–14 MM is likely to be able to evade mismatch discrimination by REC3 as it is positioned in a blind spot.

We reasoned that mismatches that prevent the PAM-distal gRNA–TS duplex from docking on REC3 would be unable to assume the kinked conformation, leading to considerably reduced DNA cleavage. To test this hypothesis, we determined a structure of Cas9 with 15–17 MM double-stranded DNA (dsDNA) substrate after 1 h of incubation with the enzyme (Fig. 1b). This mismatch inhibits cleavage by Cas9, but still permits DNA binding as measured by high-throughput profiling²¹. We observed only the linear duplex conformation (Fig. 1a,c). These structures support a model in which a linear duplex conformation precedes the canonical kinked duplex conformation that is required for activation, and mismatches that block formation of the kinked conformation escape DNA cleavage by Cas9.

The 18–20 mismatch supports Cas9 activation

We next sought to understand how certain mismatches can evade Cas9 discrimination to allow more efficient Cas9 activation and DNA cleavage relative to other mismatches. We examined Cas9 after incubation with 18–20 MM DNA at the 1-min time point at which around 65% of the DNA was cleaved (Extended Data Fig. 1b), to determine whether this more tolerated mismatch undergoes the same structural transition as that of 12–14 MM DNA. Consistent with the fraction of product formation, we observed a mixed population of particles including the linear (Fig. 1a,c) and the kinked duplex conformation. In the kinked duplex structure, we observed HNH docked at the target site scissile phosphate, indicating the fully active conformation. This arrangement of HNH is entirely consistent with the previously observed active Cas9 conformation^{12,18}. These results suggest that the population of particles showing a linear conformation represents an early intermediate in the pathway, and that the kinking of the gRNA–TS duplex is linked to HNH docking.

We observed target strand cleavage between nucleotides 3 and 4 (Fig. 3, Extended Data Fig. 3) and non-target strand (NTS) cleavage at the canonical site three bases

upstream from the PAM. We report a direct observation of an RuvC active site with the non-target strand bound in the product state (Fig. 3, Extended Data Fig. 3). R986 is in the ‘down’ conformation, stabilizing the two magnesium ions as predicted by molecular dynamics simulations²² (Fig. 3), whereas F916 wedges between the −2 and −3 bases through stacking interactions and positions the −3 position within the RuvC active site. These observations are in agreement with previous structural and mutagenesis studies^{23,24}. Our structure suggests a histidine-mediated catalytic mechanism, consistent with two-metal-ion-dependent catalysis²⁵ and supported by quantum-classical simulations²⁶. Furthermore, our product state reveals that the two Mg²⁺ ions are around 4.2 Å from each other, in agreement with the product state of the histidine-mediated mechanism (Extended Data Fig. 3).

Fig. 3: Linkers L1 and L2 mediate the structural transition to the active state.

 figure 3



a, Overview of the 18–20 MM active conformation. **b, c**, Detailed view of HNH (**b**) and RuvC (**c**) active sites. **d**, Docking of the L1 linker helix against the PAM-distal gRNA–TS duplex, shown as an isosurface representation. **e**, Interactions of L1 and L2 regions with the minor groove of the gRNA–TS duplex. HNH extending from L1 and L2 linkers has been removed for clarity and does not interact with this region of the gRNA–TS duplex.

The fully active configuration requires marked conformational rearrangements, including an approximately 140° rotation of the HNH domain from the inactive state. Furthermore, our structures reveal the molecular mechanisms that underlie this rearrangement. The L1 and L2 linker domains tether HNH to the rest of Cas9 and are often missing from crystal structures, presumably owing to their intrinsic flexibility. However, in our active structure, we observe high-quality density for both L1 and L2. Notably, the L1 helix docks against the minor groove of the PAM-distal gRNA–TS duplex and forms an extended network of interactions, including multiple water-mediated hydrogen bonds with both strands (Fig. 3). As L1 docks on the minor groove, these interactions are gRNA–TS structure-specific rather than sequence-specific and can only occur when the PAM-distal duplex end is in the kinked conformation. This provides a structural basis for our observation that the kinked duplex conformation is an intermediate that precedes Cas9 activation and DNA cleavage. Comparisons of our model with Cas9 structures in inactive (Electron Microscopy Data Bank (EMDB) code EMD-3276) and active (EMD-0584) conformations confirmed that L1 docking against the gRNA–TS duplex is correlated with HNH rearrangement and Cas9 activation (Extended Data Fig. 4). Furthermore, our observation of L1 and L2 ‘locking’ HNH in an active conformation is supported by the slow rate of dissociation of Cas9 from target DNA after cleavage²⁷.

Residue F916 stabilizes the NTS and is within the L2 linker domain; however, within the inactive Cas9 conformation, L2 is positioned more than 20 Å away from the RuvC active site. L1-facilitated positioning of HNH on the target strand enables relocation of L2, which in turn enables positioning of the NTS within the RuvC active site (Extended Data Fig. 4). This mechanism provides a structural explanation for the observed coupling of target strand and NTS cleavage, in which HNH docking precedes alignment of the NTS at the RuvC site for cleavage^{5,28}. The HNH and RuvC cleavage reactions appear to occur simultaneously because the alignment is rate-limiting.

Although previous studies have noted the importance of L1 docking onto the gRNA–TS duplex for HNH repositioning^{23,29}, our observation that a linear gRNA–TS duplex conformation induced by PAM-distal mismatches precludes L1 docking provides a structural explanation for why certain PAM-distal mismatched substrates are able to bind Cas9, while not triggering rapid DNA cleavage²¹.

The 18–20 mismatch reorders an RuvC loop

The 18–20 MM contains an unusual duplex conformation at the site of the mismatch. The C:C mismatch at position 18 on the target strand, TS(18), is stabilized by stacking interactions with adjacent Watson–Crick base pairs. However, the gRNA is otherwise distorted with gRNA position 2 (gRNA(2)) flipped out by around 180° so that gRNA(1) then intercalates between TS(19) and TS(20). TS(19) participates in water-

mediated hydrogen bonds to Q1027, and TS(20) resumes base-pairing with NTS (Fig. 4, Extended Data Fig. 5).

Fig. 4: Stabilization of distorted 18–20 MM by the RuvC domain and improved fidelity of SuperFi-Cas9.

 figure 4

a, Overall structure of the 18–20 MM active conformation viewed from the back. **b, c**, Magnified views of Cas9 interacting with the distal end of the duplex. Flipped gRNA base position 2 is accommodated by stacking interactions and hydrogen bonding with RuvC tyrosine side-chains, whereas a network of interactions (including a water-mediated hydrogen bond) stabilizes the stretched target strand configuration, which allows TS(20) to resume base-pairing with the NTS. **d**, Schematic of distorted PAM-distal gRNA–TS duplex. Red circles correspond to water molecules. **e**, Kinetics of on-target and off-target (18–20 MM) Mg^{2+} -initiated cleavage by the 7-D Cas9 mutant (SuperFi-Cas9). **f, g**, Cleavage competition assay for wild-type Cas9 (**f**) and SuperFi-Cas9 (**g**). 25 nM of either Cas9 variant was mixed with 50 nM of each substrate and the cleaved DNA product was monitored. Discrimination in favour of the on-target DNA is defined by the ratio of amplitudes for on-target and off-target product formed.

This unusual nucleic acid conformation is stabilized by RuvC and appears to facilitate the binding of this mismatch. The residues within RuvC that contact and stabilize this distorted configuration are absent in previous on-target structures^{14,15,18,30} (Extended Data Fig. 6), despite the overall similarity between our model and a previously determined active on-target Cas9 (Extended Data Fig. 7). This indicates that these resolved RuvC residues are involved only in mismatch binding and not in on-target activation (Fig. 4). Although this mechanism to accommodate certain mismatches may

provide an essential mechanism for bacteria to restrict phage variants, it is counterproductive for the use of Cas9 in gene editing.

Previous rationally engineered variants ‘hyper-accurate Cas9’ (HypaCas9; N692A, M694A, Q695A and H698A mutations) and ‘high-fidelity Cas9’ (Cas9-HF1; N467A, R661A, Q695A and Q926A mutations) achieve somewhat higher fidelity at the expense of up to 100-fold reduced efficiency of on-target DNA cleavage^{5,8,9}. The mutated residues are mainly located within the REC3 domain and make numerous interactions only with the kinked duplex end. Therefore, by abolishing interactions between REC3 and the PAM-distal duplex, these high-fidelity variants reduce the capacity of Cas9 to stabilize the kinked duplex configuration that is required for the docking of L1, and thereby reduce HNH repositioning and cleavage activity. Our data provide a structural explanation for why these high-fidelity Cas9 variants reduce the activation of Cas9⁹ by off-target substrates, but also reduce on-target Cas9 activity.

To test the role of this loop for mismatch stabilization, we designed a 7-D mutant (in which all seven of the stabilizing residues in Fig. 4b are mutated to aspartic acid) and tested the effects of this mutant on DNA cleavage. Although this 7-D mutant cleaved on-target DNA at a similar rate to wild-type *Streptococcus pyogenes* Cas9 (SpCas9) (2 s^{-1}), we observed that cleavage of 18–20 MM DNA was 500-fold slower (0.004 s^{-1}) (Fig. 4e). This indicates that this loop is critical for stabilizing the distorted mismatch-induced PAM-distal duplex conformation, thereby allowing the duplex to adopt the kinked conformation that is prerequisite for Cas9 activation. We refer to our designed high-fidelity variant that retains wild-type on-target cleavage rates as ‘SuperFi-Cas9’.

Because enzyme specificity is a kinetic phenomenon that is not determined solely by the rates of the chemical reaction, we performed a direct competition assay, in which on-target and off-target (18–20 MM) dsDNA substrates were mixed simultaneously with enzyme and cleavage was monitored over time. Although wild-type Cas9 showed some preference for on-target substrates (a 1.55-fold specificity ratio favouring the on-target over 18–20 MM off-target DNA), SuperFi-Cas9 showed rapid cleavage of on-target DNA and minimal cleavage of 18–20 MM DNA (6.3-fold preference for on-target DNA) (Fig. 4f,g). The ability to discriminate between on- and off-target DNA substrates without compromising DNA cleavage efficiency appears to be unique to SuperFi-Cas9¹¹. Although further studies are needed to fully define the kinetic basis for the change in discrimination, our current data constitute a proof of concept and provide a rationale for engineering improved variants of Cas9 using our structure.

Discussion

Through kinetics-guided structural determination, we have described a gRNA–TS duplex conformational intermediate that precedes Cas9 activation (Fig. 5). Notably,

we observe that the well-characterized and widespread off-target cleavage of DNA containing mismatches at the extreme PAM-distal end (positions 18–20 (refs. [5,9,12,31,32](#))) is attributed to a unique mechanism that stabilizes a highly distorted duplex conformation, involving a domain loop in RuvC that penetrates the duplex. This region is missing in previously determined structures of Cas9, which suggests that it has a role solely in mismatch tolerance at these positions. Our results provide molecular insights into the underlying structural mechanisms that govern off-target effects of Cas9, and provide a molecular blueprint for the design of next-generation high-fidelity Cas9 variants that reduce off-target DNA cleavage while retaining efficient cleavage of on-target DNA.

Fig. 5: Model for Cas9 activation.

 figure 5

During R-loop propagation (step 1), the gRNA–TS duplex adopts a linear conformation. After R-loop completion, the PAM-distal end of the linear duplex is captured by REC3 (steps 2 and 3). Mismatches in the PAM-distal region appear to prevent REC3 docking and thereby block subsequent steps of Cas9 activation. Once the kinked R-loop conformation has been formed, L1 and L2 linkers use the gRNA–TS duplex as a scaffold to position the HNH domain at the scissile phosphate of the target strand and to position the NTS in the RuvC site (step 4), which enables Cas9 to make a double-strand break (step 5). According to this model, mutations in the RuvC loop (corresponding to SuperFi-Cas9) inhibit formation of the kinked conformation and subsequent cleavage of the gRNA–TS duplex with mismatches at the PAM-distal end.

Methods

Protein expression and purification

SpCas9 was expressed and purified as described previously⁵.

Nucleic acid preparation

DNA duplexes (55 nt) were prepared from PAGE-purified oligonucleotides synthesized by Integrated DNA Technologies. DNA duplexes used in cleavage assays were prepared by mixing 6-FAM- or Cy3-labelled target strands with unlabelled non-target strands at a 1:1.15 molar ratio in annealing buffer (10 mM Tris-HCl pH 8, 50 mM NaCl and 1 mM EDTA), heating to 95 °C for 5 min, then cooling to room temperature over the course of 1 h. The sgRNA was purchased from Synthego and annealed in annealing buffer using the same protocol as for the duplex DNA substrates. The sequences of the synthesized oligonucleotides, including the positions of mismatches, are listed in Extended Data Table 1.

Kinetics

Buffer composition for kinetic reactions

Cleavage reactions were performed in 1× cleavage buffer (20 mM Tris-Cl, pH 7.5, 100 mM KCl, 5% glycerol and 1 mM DTT) at 37 °C.

DNA cleavage kinetics

The reaction of Cas9 with on- and off-target DNA was performed by preincubating Cas9.gRNA (28 nM active-site concentration of Cas9, 100 nM gRNA) with 10 nM DNA with a 6-FAM label on the target strand in the absence of Mg²⁺. The reaction was initiated by adding Mg²⁺ to 10 mM, then stopped at various times by mixing with 0.3 M EDTA (Extended Data Fig. 1). Products of the reaction were resolved and quantified using an Applied Biosystems DNA sequencer (ABI 3130xl)³³. Data were fit using either a single or a double-exponential equation, as shown below.

Single exponential equation:

$$\text{Y} = A_1 e^{-\lambda_1 t} + C \quad (1)$$

in which Y represents the concentration of the cleavage product, A_1 represents the amplitude and λ_1 represents the observed decay rate (eigenvalue). The half-life was calculated as $t_{1/2} = \ln(2)/\lambda_1$.

Double exponential equation:

$$\text{Y} = A_1 e^{-\lambda_1 t} + A_2 e^{-\lambda_2 t} + C \quad (2)$$

in which Y represents the concentration of the cleavage product, A_1 represents the amplitude and λ_1 represents the observed rate for the first phase. A_2 represents the amplitude and λ_2 represents the observed rate for the second phase.

Kinetic competition assay

Enzyme specificity is a kinetic phenomenon that is a function of all steps leading up to and including the first largely irreversible step in the pathway and it is common for mutants to introduce a change in specificity determining steps³⁴. Therefore, we designed an assay to monitor relative rates of cleavage for on- and off-target DNA when the enzyme was presented with both substrates simultaneously. The competition assay was performed by mixing a solution of 25 nM (active site concentration) Cas9 and 100 nM sgRNA, in the presence of 10 mM Mg²⁺, with 50 nM on-target DNA and 50 nM off-target DNA, in which the DNA contained a 5'-6-FAM label or a 5'-Cy3 label on the target or off-target DNA, respectively. Time points were collected by mixing with 0.3 M EDTA and reaction products were resolved and quantified by capillary electrophoresis, as described above. On-target cleavage data were fit to a single exponential function and off-target cleavage data were fit to a double exponential function. Discrimination was calculated as the ratio of the total amplitude of on-target cleavage divided by the amplitude for off-target cleavage to derive the relative specificity constants for the on-target DNA compared to the off-target DNA.

Cryo-EM sample preparation, data collection and processing

Cas9 in complex with various mismatched DNA substrates was frozen at different time points, on the basis of kinetic analysis (Extended Data Fig. 1). A non-productive mismatch complex (15–17 MM, 1 h); a slow productive mismatch (12–14) at early (5 min) and late (1 h) time points; and a fast productive mismatch (18–20, 1 min) were chosen. MDCC-Cas9 was used for structure determination to couple structural analysis with ongoing kinetic studies monitoring changes in fluorescence. It has previously been shown that the kinetics of MDCC-Cas9 were indistinguishable from those of wild-type enzyme⁵. The cleavage reaction was triggered by mixing 10 μM DNA duplex preincubated with 10 mM MgCl₂ and 8 μM MDCC-labelled Cas9: 8 μM gRNA was preincubated with 10 mM MgCl₂, in reaction buffer (19 mM Tris-Cl, pH 7.5, 95 mM KCl, 4.75% glycerol and 5 mM DTT) at a 1:1 ratio. Four microlitres of sample was applied to glow-discharged holey carbon grids (C-flat 2/2, Protochips), blotted for 1 s with a blot force of 4 and rapidly plunged into liquid nitrogen-cooled ethane using an FEI Vitrobot MarkIV. Reactions were quenched through vitrification.

Data were collected on an FEI Titan Krios cryo-electron microscope equipped with a K3 Summit direct electron detector (Gatan). Images were recorded with SerialEM³⁵

with a pixel size of 1.1 Å for 12–14 MM datasets, and 0.81 Å for 18–20 MM and 15–17 MM datasets, over a defocus range of −1.5 to −2.5 μm. During collection of the 12–14 MM 5-min time-point dataset, a preferred orientation was observed. To ameliorate this, a second dataset was collected at 30° tilt. Movies were recorded at 13.3 electrons per pixel per s for 6 s (80 frames) to give a total dose of 80 electrons per pixel. CTF correction, motion correction and particle picking were performed in real-time using cryoSPARC Live. Further data processing was performed with cryoSPARC v.3.2³⁶.

Multiple rounds of 3D classification within cryoSPARC yielded reconstructions of six distinct Cas9 complexes at resolutions ranging from 2.7 to 3.6 Å (Extended Data Table 3). To aid the separation of multiple Cas9 conformational states from within the same dataset, 3D variability analysis was performed within CryoSPARC. First and last frames from suitable eigenvector trajectory were then used as references for heterogeneous refinement (that is, reference-based 3D classification), and particles from resulting classes were refined using non-uniform refinement and used for final reconstructions³⁷. Active Cas9 (Protein Data Bank (PDB) code: 6O0X) was rigid-body fitted into each map using ChimeraX³⁸. Regions of the model not present in a given map were truncated, and flexible fitting was performed using Namdinator³⁹. Further modelling was performed using Isolde⁴⁰, and the models were ultimately subjected to real-space refinement as implemented in PHENIX.

Reporting summary

Further information on research design is available in the [Nature Research Reporting Summary](#) linked to this paper.

Data availability

The structures of 12–14 MM 5 min, 12–14 MM 60-min linear and 18–20 MM 1-min kinked active, and their associated atomic coordinates, have been deposited into the EMDB and the PDB with EMDB accession codes [EMD-24833](#), [EMD-24835](#) and [EMD-24838](#) and PDB accession codes [7S4U](#), [7S4V](#) and [7S4X](#), respectively. Maps of 12–14 MM 60-min linear, 15–17 MM 60-min linear and 18–20 1-min linear have been deposited into the EMDB with accession codes [EMD-23834](#), [EMD-24836](#) and [EMD-24837](#), respectively.

References

1. Jinek, M. et al. RNA-programmed genome editing in human cells. *eLife* **2**, e00471 (2013).

2. Cong, L. et al. Multiplex genome engineering using CRISPR/Cas systems. *Science* **339**, 819–823 (2013).
3. Fu, Y. et al. High-frequency off-target mutagenesis induced by CRISPR–Cas nucleases in human cells. *Nat. Biotechnol.* **31**, 822–826 (2013).
4. Doudna, J. A. The promise and challenge of therapeutic genome editing. *Nature* **578**, 229–236 (2020).
5. Liu, M. et al. Engineered CRISPR/Cas9 enzymes improve discrimination by slowing DNA cleavage to allow release of off-target DNA. *Nat. Commun.* **11**, 3576 (2020).
6. Kim, D., Luk, K., Wolfe, S. A. & Kim, J. S. Evaluating and enhancing target specificity of gene-editing nucleases and deaminases. *Annu. Rev. Biochem.* **88**, 191–220 (2019).
7. Slaymaker, I. M. & Gaudelli, N. M. Engineering Cas9 for human genome editing. *Curr. Opin. Struct. Biol.* **69**, 86–98 (2021).
8. Kleinstiver, B. P. et al. High-fidelity CRISPR–Cas9 nucleases with no detectable genome-wide off-target effects. *Nature* **529**, 490–495 (2016).
9. Chen, J. S. et al. Enhanced proofreading governs CRISPR–Cas9 targeting accuracy. *Nature* **550**, 407–410 (2017).
10. Slaymaker, I. M. et al. Rationally engineered Cas9 nucleases with improved specificity. *Science* **351**, 84–88 (2016).
11. Kim, N. et al. Prediction of the sequence-specific cleavage activity of Cas9 variants. *Nat. Biotechnol.* **38**, 1328–1336 (2020).
12. Sternberg, S. H., Lafrance, B., Kaplan, M. & Doudna, J. A. Conformational control of DNA target cleavage by CRISPR–Cas9. *Nature* **527**, 110–113 (2015).
13. Singh, D. et al. Mechanisms of improved specificity of engineered Cas9s revealed by single-molecule FRET analysis. *Nat. Struct. Mol. Biol.* **25**, 347–354 (2018).
14. Jiang, F. et al. Structures of a CRISPR–Cas9 R-loop complex primed for DNA cleavage. *Science* **351**, 867–871 (2016).
15. Anders, C., Niewoehner, O., Duerst, A. & Jinek, M. Structural basis of PAM-dependent target DNA recognition by the Cas9 endonuclease. *Nature* **513**, 569–

573 (2014).

16. Ran, F. A. et al. Genome engineering using the CRISPR–Cas9 system. *Nat. Protoc.* **8**, 2281–2308 (2013).
17. Dagdas, Y. S., Chen, J. S., Sternberg, S. H., Doudna, J. A. & Yildiz, A. A conformational checkpoint between DNA binding and cleavage by CRISPR–Cas9. *Sci. Adv.* **3**, eaao0027 (2017).
18. Zhu, X. et al. Cryo-EM structures reveal coordinated domain motions that govern DNA cleavage by Cas9. *Nat. Struct. Mol. Biol.* **26**, 679–685 (2019).
19. Cofsky, J. C., Soczek, K. M., Knott, G. J., Nogales, E. & Doudna, J. A. CRISPR–Cas9 bends and twists DNA to read its sequence. Preprint at <https://doi.org/10.1101/2021.09.06.459219> (2021).
20. Pacesa, M. & Jinek, M. Mechanism of R-loop formation and conformational activation of Cas9. Preprint at <https://doi.org/10.1101/2021.09.16.460614> (2021).
21. Jones, S. K. et al. Massively parallel kinetic profiling of natural and engineered CRISPR nucleases. *Nat. Biotechnol.* **39**, 84–93 (2021).
22. Palermo, G. Structure and dynamics of the CRISPR–Cas9 catalytic complex. *J. Chem. Inf. Model.* **59**, 2394–2406 (2019).
23. Zhang, Y. et al. Catalytic-state structure and engineering of *Streptococcus thermophilus* Cas9. *Nat. Catal.* **3**, 813–823 (2020).
24. Jinek, M. et al. Structures of Cas9 endonucleases reveal RNA-mediated conformational activation. *Science* **343**, 1247997 (2014).
25. Steitz, T. A. & Steitz, J. A. A general two-metal-ion mechanism for catalytic RNA. *Proc. Natl Acad. Sci. USA* **90**, 6498–6502 (1993).
26. Casalino, L., Nierzwicki, Ł., Jinek, M. & Palermo, G. Catalytic mechanism of non-target DNA cleavage in CRISPR–Cas9 revealed by ab initio molecular dynamics. *ACS Catal.* **10**, 13596–13605 (2020).
27. Aldag, P. et al. Probing the stability of the SpCas9–DNA complex after cleavage. *Nucleic Acids Res.* **49**, 12411–12421 (2021).
28. Gong, S., Yu, H. H., Johnson, K. A. & Taylor, D. W. DNA unwinding is the primary determinant of CRISPR–Cas9 activity. *Cell Rep.* **22**, 359–371 (2018).

29. Sun, W. et al. Structures of *Neisseria meningitidis* Cas9 complexes in catalytically poised and anti-CRISPR-inhibited states. *Mol. Cell* **76**, 938–952 (2019).
30. Nishimasu, H. et al. Crystal structure of Cas9 in complex with guide RNA and target DNA. *Cell* **156**, 935–949 (2014).
31. Tsai, S. Q. et al. GUIDE-seq enables genome-wide profiling of off-target cleavage by CRISPR-Cas nucleases. *Nat. Biotechnol.* **33**, 187–198 (2015).
32. Kuscu, C., Arslan, S., Singh, R., Thorpe, J. & Adli, M. Genome-wide analysis reveals characteristics of off-target sites bound by the Cas9 endonuclease. *Nat. Biotechnol.* **32**, 677–683 (2014).
33. Dangerfield, T. L., Huang, N. Z. & Johnson, K. A. High throughput quantification of short nucleic acid samples by capillary electrophoresis with automated data processing. *Anal. Biochem.* **629**, 114239 (2021).
34. Johnson, K. A. *Kinetic Analysis for the New Enzymology* (KinTek, 2019).
35. Mastronarde, D. N. Automated electron microscope tomography using robust prediction of specimen movements. *J. Struct. Biol.* **152**, 36–51 (2005).
36. Punjani, A., Rubinstein, J. L., Fleet, D. J. & Brubaker, M. A. CryoSPARC: algorithms for rapid unsupervised cryo-EM structure determination. *Nat. Methods* **14**, 290–296 (2017).
37. Punjani, A., Zhang, H. & Fleet, D. J. Non-uniform refinement: adaptive regularization improves single-particle cryo-EM reconstruction. *Nat. Methods* **17**, 1214–1221 (2020).
38. Pettersen, E. F. et al. UCSF ChimeraX: structure visualization for researchers, educators, and developers. *Protein Sci.* **30**, 70–82 (2021).
39. Kidmose, R. T. et al. Namdinator—automatic molecular dynamics flexible fitting of structural models into cryo-EM and crystallography experimental maps. *IUCrJ* **6**, 526–531 (2019).
40. Croll, T. I. ISOLDE: a physically realistic environment for model building into low-resolution electron-density maps. *Acta Crystallogr. D* **74**, 519–530 (2018).
41. Pausch, P. et al. DNA interference states of the hypercompact CRISPR–CasΦ effector. *Nat. Struct. Mol. Biol.* **28**, 652–661 (2021).

42. Huang, X. et al. Structural basis for two metal-ion catalysis of DNA cleavage by Cas12i2. *Nat. Commun.* **11**, 5241 (2020).
43. Nishimasu, H. et al. Crystal structure of *Staphylococcus aureus* Cas9. *Cell* **162**, 1113–1126 (2015).

Acknowledgements

This work was supported in part by Welch Foundation grants F-1604 (to K.A.J.) and F-1938 (to D.W.T.), and by a Robert J. Kleberg, Jr. and Helen C. Kleberg Foundation Medical Research Grant (to D.W.T.). D.W.T is a CPRIT Scholar supported by the Cancer Prevention and Research Institute of Texas (RR160088). We thank G. Palermo and members of her group for discussions.

Author information

Author notes

1. These authors contributed equally: Jack P. K. Bravo, Mu-Sen Liu

Affiliations

1. Department of Molecular Biosciences, University of Texas at Austin, Austin, TX, USA

Jack P. K. Bravo, Mu-Sen Liu, Grace N. Hibshman, Tyler L. Dangerfield, Kyungseok Jung, Ryan S. McCool, Kenneth A. Johnson & David W. Taylor

2. Interdisciplinary Life Sciences Graduate Programs, University of Texas at Austin, Austin, TX, USA

Grace N. Hibshman, Tyler L. Dangerfield, Ryan S. McCool, Kenneth A. Johnson & David W. Taylor

3. Center for Systems and Synthetic Biology, University of Texas at Austin, Austin, TX, USA

David W. Taylor

4. Livestrong Cancer Institutes, Dell Medical School, University of Texas at Austin, Austin, TX, USA

David W. Taylor

Contributions

J.P.K.B. prepared samples for and performed cryo-EM, structure determination and modelling. M.-S.L. performed initial kinetic studies. K.J. purified SpCas9 and MDCC-Cas9 used for structure determination and kinetic analysis. R.S.M. assisted with preliminary analysis of the 12–14 MM 5-min structure. G.N.H. cloned, expressed and purified SuperFi-Cas9 mutants. G.N.H. and T.L.D. performed kinetic analysis of SuperFi-Cas9 versus wild-type enzyme. J.P.K.B., M.-S.L., D.W.T., T.L.D. and K.A.J. analysed and interpreted the data and wrote the manuscript. D.W.T. and K.A.J. supervised and secured funding for the studies.

Corresponding authors

Correspondence to [Kenneth A. Johnson](#) or [David W. Taylor](#).

Ethics declarations

Competing interests

J.P.K.B., M.-S.L., G.N.H., T.L.D., K.A.J. and D.W.T. are inventors on a patent application based on this research titled ‘Methods and compositions for improved Cas9 specificity’ filed by the Board of Regents, The University of Texas System. The US Patent and Trademark Office (USPTO) has assigned US application no. 63/243,481 to this application, and the filing date of 13 September 2021. K.A.J. is the president of KinTek, which provided the chemical-quench flow instruments and the KinTek Explorer software used in this study.

Peer review

Peer review information

Nature thanks Daan Swarts, John van der Oost and the other, anonymous, reviewer(s) for their contribution to the peer review of this work. Peer reviewer reports are available.

Additional information

Publisher's note Springer Nature remains neutral with regard to jurisdictional claims in published maps and institutional affiliations.

Extended data figures and tables

Extended Data Fig. 1 Kinetic basis for mismatch discrimination by Cas9.

a, Schematic representation of mismatch constructs used for kinetic analysis. **b**, Time course of cleavage of on-target and mismatched DNA (10 nM) by Cas9. Magenta arrows correspond to time-points used to prepare cryo-EM samples. A_{obs} corresponds to amplitude of product formed (i.e. total cleavage). For 12–14 MM, target strand cleavage is shown with larger filled circles, while NTS cleavage is given with smaller open circles. For other mismatches we only show target strand cleavage. We previously reported NTS cleavage data for on-target²⁸ and 18–20 MM substrates⁵.

Extended Data Fig. 2 Resolution estimates and orientation distributions of cryo-EM maps.

a, Unsharpened maps coloured according to local resolution. **b**, Gold-standard FSC curves for cryo-EM reconstructions. Resolutions were estimated at FSC=0.143. **c**, Euler diagrams showing orientation distributions of cryo-EM reconstructions.

Extended Data Fig. 3 Representative cryo-EM densities for 18–20 MM 1-min kinked (product) structure.

a, HNH active site, showing cleaved target strand. **b**, L1 linker docked on PAM-distal kinked gRNA–TS duplex. Two water molecules are involved within the network of interactions that stabilize the L1 helix conformation. **c**, RuvC active site, showing cleaved NTS, and positioning of two Mg²⁺ ions. **d**, RuvC DNA cleavage mechanism. This is a typical two-metal-ion mechanism as described in²⁵ and agrees with QM/MM simulations for histidine-mediated activation²⁶, and the proposed mechanisms of Cas12j and Cas12i^{41,42}.

Extended Data Fig. 4 Structural analysis of Cas9.

a, Left, comparison of Cas9 protein only between 12–14 MM 60 min linear (colour) and 12–14 MM 1-h kinked (grey) models. Right, comparison of Cas9 protein only active conformation (18–20 MM 1 min linear, colour) and kinked pre-active (12–14 MM 60 min kinked, grey) models. While there is no significant conformational change

associated between transition from linear to kinked pre-active (root-mean standard deviation (RMSD) between equivalent C α atoms of 1.904 Å), the change from kinked pre-active to active conformations is associated with a larger conformational change (4.647 Å, most of which occurs within the REC3 domain). **b**, Close-up view of REC3 conformational changes that occur upon activation, as viewed from one angle. REC3 moves forwards towards the kinked duplex by ~15 Å upon activation and HNH repositioning. **c**, Schematic representation of Cas9–nucleic acid contacts in the context of 18–20 MM. Residues mutated in SuperFi-Cas9 are denoted by an asterisk. **d**, Conformations of HNH domain (green) and L1 (gold) and L2 (purple) linkers in the context of Cas9 binary complex (i.e. with gRNA, PDB 4ZT0), Cas9–gRNA complex bound to dsDNA in an inactive conformation (PDB 5F9R), and in the active Cas9 18–20 MM structure presented in this work. Upon activation, HNH is repositioned at the target strand cleavage site, driven by large conformational changes in the L1 and L2 linkers. **e**, Comparison with the active Cas9 18–20 MM structure presented in this work and previously determined cryo-EM maps (transparent grey) of inactive (left, EMD-3276¹⁴) and active (right, EMD-0584¹⁸) Cas9 bound to on-target dsDNA. The inactive Cas9 has no density for L1 helix at the kinked distal-docked gRNA–TS site, whereas there is clear density for L1 at this site in the active Cas9 cryo-EM map. **f**, Mapping of residues mutated to alanine in selected high-fidelity Cas9 variants. EvoCas9 (yellow) – M495, Y515, R661, K526. Cas9-HF1 (red) – N497, R661, Q695, Q926. HypaCas9 (blue) – N692, M694, Q695, H698. Residues shared between Cas9-HF-1 and either EvoCas9 or HypaCas9 are shown as orange and purple, respectively.

Extended Data Fig. 5 Representative cryo-EM density for the RuvC loop.

Two different views are shown (**a**, **b**). Unsharpened and B-factor sharpened maps are shown for each view with the RuvC loop shown as dark magenta. Key residues involved in stabilizing this distorted conformation are labelled.

Extended Data Fig. 6 RuvC loop in on-target SpCas9 structures.

a, On-target inactive Cas9 bound to dsDNA (PDB 4UN3)¹⁵. RuvC loop is missing between 1013–1029. **b**, On-target inactive (primed – HNH rearranged and adjacent to target strand scissile phosphate) Cas9 bound to dsDNA (PDB 5F9R)¹⁴. RuvC loop has been built primarily as alanine ‘stub’ residues, but electron density is very poor and diffuse for this region. **c**, On-target inactive Cas9 bound to dsDNA (PDB 4OO8)⁴³. RuvC loop is missing between 1017–1028. **d**, On-target active Cas9 bound to dsDNA in postcatalysis state¹⁸. RuvC loop is missing between 1001–1077. **e**, On-target active Cas9 bound to dsDNA in product state¹⁸. RuvC loop is missing between 1000–1075. In **a–c**, electron density is displayed as a grey surface, and in **d**, **e** cryo-EM density is

shown as a grey surface. In all structures, missing residues are depicted as a red dashed line with the RuvC loop in **b** shown as magenta. Position of RuvC loop is denoted by a black dashed box in the left panel for each model.

Extended Data Fig. 7 Comparison of Cas9 with previous structures.

a, Comparison of 18–20 MM kinked product state Cas9 with a selection of previously determined structures. RMSD between equivalent C-alpha atoms is shown. **b**, Alignment of HNH from the 18–20 MM kinked product state presented here (transparent grey) and the previously determined ‘post-catalysis’ state (PDB 6O0Y). The catalytically competent HNH conformation between these two structures is highly similar.

Extended Data Table 1 List of nucleotide sequences used in the study

Extended Data Table 2 Correlation between fraction of DNA cleaved and fraction of cryo-EM particles in linear or kinked duplex conformations

Extended Data Table 3 Cryo-EM data collection, refinement and validation statistics

Supplementary information

Reporting Summary

Peer Review File

Rights and permissions

Open Access This article is licensed under a Creative Commons Attribution 4.0 International License, which permits use, sharing, adaptation, distribution and reproduction in any medium or format, as long as you give appropriate credit to the original author(s) and the source, provide a link to the Creative Commons license, and indicate if changes were made. The images or other third party material in this article are included in the article’s Creative Commons license, unless indicated otherwise in a credit line to the material. If material is not included in the article’s Creative Commons license and your intended use is not permitted by statutory regulation or exceeds the permitted use, you will need to obtain permission directly from the copyright holder. To view a copy of this license, visit <http://creativecommons.org/licenses/by/4.0/>.

Reprints and Permissions

About this article

Cite this article

Bravo, J.P.K., Liu, M.S., Hibshman, G.N. *et al.* Structural basis for mismatch surveillance by CRISPR–Cas9. *Nature* **603**, 343–347 (2022).
<https://doi.org/10.1038/s41586-022-04470-1>

- Received: 13 September 2021
- Accepted: 25 January 2022
- Published: 02 March 2022
- Issue Date: 10 March 2022
- DOI: <https://doi.org/10.1038/s41586-022-04470-1>

Share this article

Anyone you share the following link with will be able to read this content:

[Get shareable link](#)

Sorry, a shareable link is not currently available for this article.

[Copy to clipboard](#)

Provided by the Springer Nature SharedIt content-sharing initiative

This article was downloaded by **calibre** from <https://www.nature.com/articles/s41586-022-04470-1>

| [Section menu](#) | [Main menu](#) |

- Matters Arising
- [Published: 09 March 2022](#)

Aquaculture will continue to depend more on land than sea

- [Wenbo Zhang](#) ORCID: [orcid.org/0000-0003-3765-3980¹](https://orcid.org/0000-0003-3765-3980),
- [Ben Belton^{2,3}](#),
- [Peter Edwards⁴](#),
- [Patrik J. G. Henriksson](#) ORCID: [orcid.org/0000-0002-3439-623X^{3,5,6}](https://orcid.org/0000-0002-3439-623X),
- [David C. Little](#) ORCID: [orcid.org/0000-0002-6095-3191⁷](https://orcid.org/0000-0002-6095-3191),
- [Richard Newton⁷](#) &
- [Max Troell](#) ORCID: [orcid.org/0000-0002-7509-8140^{5,6}](https://orcid.org/0000-0002-7509-8140)

[Nature](#) volume **603**, pages E2–E4 (2022)

- 1205 Accesses
- 13 Altmetric
- [Metrics details](#)

Subjects

- [Agriculture](#)
- [Developing world](#)
- [Environmental economics](#)
- [Interdisciplinary studies](#)
- [Sustainability](#)

The [Original Article](#) was published on 19 August 2020

arising from C. Costello et al. *Nature* <https://doi.org/10.1038/s41586-020-2616-y> (2020)

This is a preview of subscription content

Access options

Subscribe to Nature+

Get immediate online access to the entire Nature family of 50+ journals

\$29.99

monthly

[Subscribe](#)

Subscribe to Journal

Get full journal access for 1 year

\$199.00

only \$3.90 per issue

[Subscribe](#)

All prices are NET prices.

VAT will be added later in the checkout.

Tax calculation will be finalised during checkout.

Buy article

Get time limited or full article access on ReadCube.

\$32.00

[Buy](#)

All prices are NET prices.

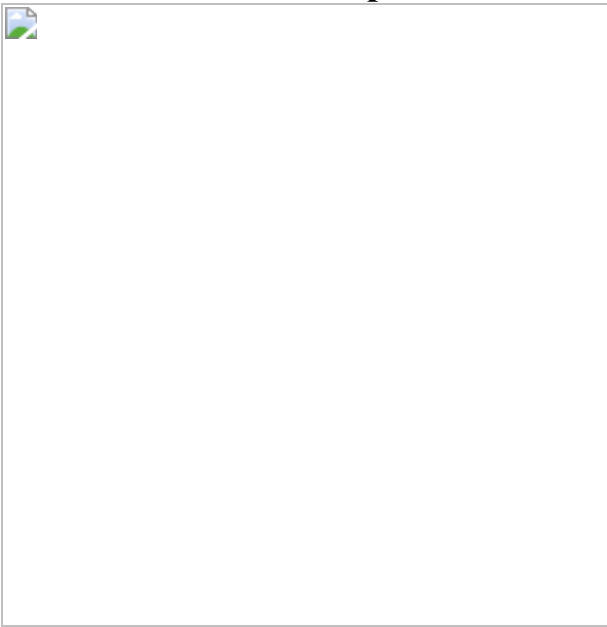
Additional access options:

- [Log in](#)
- [Learn about institutional subscriptions](#)

Fig. 1: Aquaculture and capture fisheries production, and publications related to aquaculture policy.



Fig. 2: Production, price, natural trophic level and the correlation between trophic level and price of the top 20 brackishwater, marine and freshwater finfish species.



Data availability

Secondary data were obtained from several sources: FAO statistics (www.fao.org/fishery/statistics/software/fishstatj/en), Fishbase (www.fishbase.org) and Web of Science (www.webofscience.com/). All

data analysed in this study are either included in the [Supplementary Information](#) or available on GitHub (<https://github.com/AquacultureFuture/LandAndSea>).

References

1. Edwards, P., Zhang, W., Belton, B. & Little, D. C. Misunderstandings, myths and mantras in aquaculture: its contribution to world food supplies has been systematically over reported. *Mar. Policy* **106**, 103547 (2019).
2. *The State of World Fisheries and Aquaculture 2020. Sustainability in Action* (FAO, 2020).
3. Costello, C. et al. The future of food from the sea. *Nature* **588**, 95–100 (2020).
4. Belton, B. et al. Farming fish in the sea will not nourish the world. *Nat. Commun.* **11**, 5804 (2020).
5. Edwards, P. Aquaculture environment interactions: past, present and likely future trends. *Aquaculture* **447**, 2–14 (2015).
6. Gentry, R. R. et al. Mapping the global potential for marine aquaculture. *Nat. Ecol. Evol.* **1**, 1317–1324 (2017).
7. Cottrell, R. S. et al. Considering land-sea interactions and trade-offs for food and biodiversity. *Glob. Chang. Biol.* **24**, 580–596 (2018).
8. Troell, M., Jonell, M. & Henriksson, P. J. G. Ocean space for seafood. *Nat. Ecol. Evol.* **1**, 1224–1225 (2017).
9. Pahlow, M., van Oel, P. R., Mekonnen, M. M. & Hoekstra, A. Y. Increasing pressure on freshwater resources due to terrestrial feed ingredients for aquaculture production. *Sci. Total Environ.* **536**, 847–857 (2015).

10. Gephart, J. A. et al. The ‘seafood gap’ in the food-water nexus literature—issues surrounding freshwater use in seafood production chains. *Adv. Water Resour.* **110**, 505–514 (2017).
11. Gephart, J. A. et al. Environmental performance of blue foods. *Nature* **597**, 360–365 (2021).
12. Belton, B., Bush, S. R. & Little, D. C. Not just for the wealthy: Rethinking farmed fish consumption in the Global South. *Glob. Food Sec.* **16**, 85–92 (2018).
13. Zhang, W. et al. Fishing for feed in China: facts, impacts and implications. *Fish Fish.* **21**, 47–62 (2020).
14. *Fishery and Aquaculture Statistics* (FAO, 2021).
15. Oyinlola, M. A., Reygondeau, G., Wabnitz, C. C. C., Troell, M. & Cheung, W. W. L. Global estimation of areas with suitable environmental conditions for mariculture species. *PLoS ONE* **13**, 0191086 (2018).

Acknowledgements

W.Z. was supported by the iFISH Program from China Blue Sustainability Institute. B.B. and P.J.G.H. were supported by the CGIAR Research Program on Fish Agri-Food Systems (FISH) led by WorldFish; P.J.G.H. was supported by the CGIAR Research Program on Climate Change, Agriculture and Food Security (CCAFS) supported by contributors to the CGIAR Trust Fund. P.J.G.H. and M.T. acknowledge the Kjell and Märta Beijer Foundation for supporting this work through the Beijer Institute’s Aquaculture and Sustainable Seafood Programme, and the SEAWIN Project funded by FORMAS (2016-00227). P.J.G.H. was partially funded by FORMAS Inequality and the Biosphere Project (2020-00454). D.C.L. and R.N. were funded by the European Union’s HORIZON 2020 Framework Programme under grant agreement no. 773330 (GAIN).

Author information

Affiliations

1. National Demonstration Center for Experimental Fisheries Science Education, Shanghai Engineering Research Center of Aquaculture, Centre for Research on Environmental Ecology and Fish Nutrition of the Ministry of Agriculture, Shanghai Ocean University, Shanghai, China

Wenbo Zhang

2. Department of Agricultural, Food and Resource Economics, Michigan State University, East Lansing, MI, USA

Ben Belton

3. WorldFish, Jalan Batu Maung, Penang, Malaysia

Ben Belton & Patrik J. G. Henriksson

4. School of Environment, Resources and Development, Asian Institute of Technology, Khlong Luang, Pathum Thani, Thailand

Peter Edwards

5. Stockholm Resilience Centre, Stockholm University, Stockholm, Sweden

Patrik J. G. Henriksson & Max Troell

6. Beijer Institute of Ecological Economics, The Royal Swedish Academy of Science, Stockholm, Sweden

Patrik J. G. Henriksson & Max Troell

7. Institute of Aquaculture, University of Stirling, Stirling, UK

David C. Little & Richard Newton

Contributions

W.Z., B.B., P.E., P.J.G.H., D.C.L., R.N. and M.T. conceived the idea and designed the study. W.Z., B.B. and P.J.G.H. collected and analysed the data. W.Z., B.B., P.E., P.J.G.H., D.C.L., R.N. and M.T. wrote the paper. W.Z. is lead author. All other co-authors contributed equally and are listed alphabetically by surname.

Corresponding author

Correspondence to [Wenbo Zhang](#).

Ethics declarations

Competing interests

W.Z. is a member of the BAP Committee on Climate Action. He has no affiliation with any for-profit company. B.B. has no competing interests. P.E. is an Emeritus Professor with no commercial interests. P.J.G.H. is a member of the BAP Committee on Climate Action and scientific advisor for SeaBOS. D.C.L. has received in-kind and financial support from a wide range of commercial and non-commercial entities, serves as a committee member for standards organizations and is a director of a commercial tilapia hatchery in Thailand. R.N. is the chair of the BAP committee on climate action. M.T. is a member of the program committee for the Marine and Coastal Science for Management (WIOMSA/MASMA), member of Action Areas and Solution Clusters Working Groups—Blue foods, United Nations Forum on Sustainability Standards (UNFSS), scientific lead for SeaBOS, and a review editor for Aquaculture Environment Interactions.

Additional information

Publisher's note Springer Nature remains neutral with regard to jurisdictional claims in published maps and institutional affiliations.

Supplementary information

Supplementary Information

This file contains Supplementary Information, including Supplementary Figs. 1–12, Tables 1–3 and references.

Rights and permissions

Reprints and Permissions

About this article

Cite this article

Zhang, W., Belton, B., Edwards, P. *et al.* Aquaculture will continue to depend more on land than sea. *Nature* **603**, E2–E4 (2022).
<https://doi.org/10.1038/s41586-021-04331-3>

- Received: 21 February 2021
- Accepted: 10 December 2021
- Published: 09 March 2022
- Issue Date: 10 March 2022
- DOI: <https://doi.org/10.1038/s41586-021-04331-3>

Share this article

Anyone you share the following link with will be able to read this content:

[Get shareable link](#)

Sorry, a shareable link is not currently available for this article.

[Copy to clipboard](#)

Provided by the Springer Nature SharedIt content-sharing initiative

This article was downloaded by **calibre** from <https://www.nature.com/articles/s41586-021-04331-3>

| [Section menu](#) | [Main menu](#) |

Amendments & Corrections

- **Publisher Correction: Indo-Pacific Walker circulation drove Pleistocene African aridification** [23 February 2022]

Publisher Correction •

- Publisher Correction
- [Published: 23 February 2022](#)

Publisher Correction: Indo-Pacific Walker circulation drove Pleistocene African aridification

- [H. J. L. van der Lubbe](#) ORCID: [orcid.org/0000-0001-7545-6502](#)^{1,2},
- [I. R. Hall](#) ORCID: [orcid.org/0000-0001-6960-1419](#)¹,
- [S. Barker](#)¹,
- [S. R. Hemming](#) ORCID: [orcid.org/0000-0001-8117-2303](#)³,
- [T. F. Baars](#) ORCID: [orcid.org/0000-0003-3163-4885](#)⁴,
- [A. Starr](#) ORCID: [orcid.org/0000-0003-1854-4412](#)¹,
- [J. Just](#) ORCID: [orcid.org/0000-0002-5257-604X](#)⁵,
- [B. C. Backeberg](#)^{6,7,8} &
- [J. C. A. Joordens](#) ORCID: [orcid.org/0000-0002-5757-1168](#)^{9,10,11}

Nature volume 603, pages E5–E6 (2022)

- 757 Accesses
- 1 Altmetric
- [Metrics details](#)

Subjects

- [Palaeoceanography](#)
- [Palaeoclimate](#)

The [Original Article](#) was published on 27 October 2021

[Download PDF](#)

Correction to: *Nature* <https://doi.org/10.1038/s41586-021-03896-3> Published online 27 October 2021

In this Article, a processing error led to the wrong versions of Fig. 3 and Extended Data Fig. 4 being published. Figure 3e did not include the entirety of the eastern Africa soil carbonate $\delta^{13}\text{C}$ database as compiled by ref. ¹³. Fig. 3 of the original Article has been corrected, and Fig. 1 of this Amendment shows the original and corrected Fig. 3 side by side, for transparency. In the Methods section of the original Article, there are further details about how this record has been produced. The last paragraph of the Methods has been corrected; the original text was: “On the basis of ref. ¹³, time series of $\delta^{13}\text{C}$ values from soil carbonate were combined for the Omo-Turkana Basin and the southern Kenyan-Tanzanian sites using their medians, and interquartile ranges using six-data-point bins.” Furthermore, the original version of Extended Data Fig. 4 did not display data from eastern African hominin site Afar; the figure and caption have been updated accordingly, and the original and corrected versions are shown as Fig. 2 to this Amendment. These changes do not alter any inferences drawn from the data. These errors have been corrected in the online version of the Article.

Fig. 1: This figure shows the original and corrected Fig. 3 of the original Article

 **figure 1**

Fig. 2: This figure shows the original and corrected Extended Data Fig. 4 of the original Article



Author information

Affiliations

1. School of Earth and Environmental Sciences, Cardiff University, Cardiff, UK

H. J. L. van der Lubbe, I. R. Hall, S. Barker & A. Starr

2. Department of Earth Sciences, Faculty of Science, Vrije Universiteit (VU),
Amsterdam, the Netherlands

H. J. L. van der Lubbe

3. Earth and Environmental Sciences, Lamont-Doherty Earth Observatory,
Palisades, NY, USA

S. R. Hemming

4. Department of Geosciences and Engineering, Delft University of Technology, TU
Delft, the Netherlands

T. F. Baars

5. Department of Geosciences, Universität Bremen, Bremen, Germany

J. Just

6. Deltares, Delft, the Netherlands

B. C. Backeberg

7. Nansen Environmental and Remote Sensing Center, Bergen, Norway

B. C. Backeberg

8. Nansen-Tutu Centre for Marine Environmental Research, Cape Town, South
Africa

B. C. Backeberg

9. Naturalis Biodiversity Center, Leiden, the Netherlands

J. C. A. Joordens

10. Faculty of Science and Engineering, Maastricht University, Maastricht, the
Netherlands

J. C. A. Joordens

11. Faculty of Archaeology, Leiden University, Leiden, the Netherlands

J. C. A. Joordens

Corresponding authors

Correspondence to [H. J. L. van der Lubbe](#) or [I. R. Hall](#).

Rights and permissions

[Reprints and Permissions](#)

About this article

Cite this article

van der Lubbe, H.J.L., Hall, I.R., Barker, S. *et al.* Publisher Correction: Indo-Pacific Walker circulation drove Pleistocene African aridification. *Nature* **603**, E5–E6 (2022). <https://doi.org/10.1038/s41586-021-04193-9>

- Published: 23 February 2022
- Issue Date: 10 March 2022
- DOI: <https://doi.org/10.1038/s41586-021-04193-9>

Share this article

Anyone you share the following link with will be able to read this content:

[Get shareable link](#)

Sorry, a shareable link is not currently available for this article.

[Copy to clipboard](#)

Provided by the Springer Nature SharedIt content-sharing initiative

This article was downloaded by **calibre** from <https://www.nature.com/articles/s41586-021-04193-9>

Nature Index